

MICROBEAM ANALYSIS

1984

A. D. Romig Jr. and J. I. Goldstein, *Editors*

Proceedings of the 19th Annual Conference
of the
Microbeam Analysis Society
Bethlehem, Pennsylvania, 16-20 July 1984



San Francisco Press, Inc.

Box 6800, San Francisco, CA 94101-6800

PUBLISHER'S NOTICE

The Microbeam Analysis Society (MAS) and its publisher since 1979, San Francisco Press, Inc., are not responsible for the information and views presented in this volume by the several contributors.

Back issues of MICROBEAM ANALYSIS are available as follows:

<i>1974, 1975, 1976 (spiral bound)</i>	<i>\$25 each</i>
<i>1979, 1980, 1981</i>	<i>\$25 each</i>
<i>1982</i>	<i>\$42.50</i>
<i>1983, 1984</i>	<i>\$30 each</i>

Beginning with 1983 San Francisco Press, Inc., is also the publisher of the EMSA Proceedings (abstracts from the annual meeting of the Electron Microscopy Society of America), available at \$45.

MAS and EMSA members prepaying by personal check receive a 20% discount from the above prices. All overseas orders must be prepaid. California purchasers add sales tax.

San Francisco Press, Inc., is also publisher of L. Marton's EARLY HISTORY OF ELECTRON MICROSCOPY (\$5) and ANALYTICAL ELECTRON MICROSCOPY--1981 (\$25) & 1984 (\$30) which are the Proceedings of the two AEM Workshops.

Foreword

It has been our privilege to serve as technical program chairmen for the 19th Annual conference of the Microbeam Analysis Society (Lehigh University, Bethlehem, Pennsylvania, 16-20 July 1984), a joint meeting with the 4th Workshop in Analytical Electron Microscopy. We are particularly pleased with the quality and quantity of the more than ninety papers. In addition, we are pleased with the large number of non-U.S. participants. We extend our sincere appreciation to our colleagues who served as session chairmen and so helped make the fine quality of this year's meeting possible. The sessions this year included some topics of ongoing, yearly interest and others that were special topics not routinely included in our program. The program also included several tutorials and discussion groups.

This year's program again was unique in that it was run concurrently with the AEM workshop, arranged by David Joy (Bell Laboratories) and David Williams (Lehigh). This year, the AEM workshop was jointly sponsored by the Microbeam Analysis Society (U.S.) and the Metals Society (U.K.). The first joint MAS-AEM conference in Vail, Colorado (1981), was a technical success, in part due to the fact that AEM and conventional bulk sample microanalysis are complementary techniques. AEM has extended conventional electron-probe microanalysis to much finer spatial resolution with the additional capability to perform crystallographic experiments on areas much smaller than normally associated with conventional selected area diffraction. Depending on the relative evolution of conventional electron microprobe, and AEM techniques, this kind of joint program may again serve a useful purpose. (The AEM papers are being published by San Francisco Press in a separate volume.)

As evidenced by the large number of fine papers submitted this year in areas spanning fundamental, theoretical, and experimental development to applications of microanalysis, the members of MAS continue to be leaders in the development of microanalytical techniques. This year's contributions clearly demonstrate that the MAS members' technical interests, with respect to techniques and applications, continue to broaden and evolve with time. MAS members will doubtless remain at the forefront of many microbeam techniques.

We wish also to extend our appreciation to the officers of MAS for 1984: David Joy, Bell Laboratories (President), Chuck Fiori, National Institutes of Health (Secretary), and Mary Finn, Lincoln Laboratories (Treasurer), who helped make this conference possible.

In addition, the assistance of our conference coordinator Betty Zdinak (Lehigh), as well as Luz Kalaczik (Sandia) and Dave Humphreys (Sandia), is sincerely acknowledged. We also wish to thank the Sandia staff who volunteered their time to serve on the review committee for the technical papers.

For those who will participate in the 19th Conference, we hope the oral presentations and discussions will be fruitful and enlightening; these Proceedings should prove to be a valuable reference and reminder of the conference. For those who were unable to attend, the published Proceedings give a wealth of material on the art and science of microanalysis in 1984.

Alton D. Romig Jr.
Sandia National Laboratories, Albuquerque, N.M.

Joseph I. Goldstein
Lehigh University, Bethlehem, Pa.

*Technical Program Chairmen
Microbeam Analysis Society 1984*

Table of Contents*

Foreword	iii
Officers of the Microbeam Analysis Society	viii
Sustaining Members' Information.	ix
T-1. TUTORIALS.	1
McCarthy, Elementary stereology.	1
Romig, Introduction to analytical electron microscopy.	7
1. DESTRUCTIVE LASER MICROPROBE	14
Fletcher, Fatiadi, Structure of metal-coordinated polymers: Laser desorption of poly(4-vinylpyridine) and poly(4-vinylpyridine)-metal complexes	14
Morelli, Hercules, Laser microprobe mass spectrometry of organophosphorous compounds.	15
Mauney, Adams, Interpretation of ion kinetic energy distributions in laser microprobe mass analysis	19
Dingle, Griffiths, Laser-induced ion mass analysis by use of the LIMA-2A	23
Steel, Simons, Small, Newbury, Analysis of submicrometer particles by sequential AEM and LAMMA.	27
Schroder, Monitoring uptake and release of material by cells and cell-organelles by LAMMA	30
Clarke, Davey, Ruckman, Phenomenological aspects of laser-induced ion-mass analysis. .	31
Clarke, Davey, Ruckman, Detection of cluster ions by the LIMA technique.	40
2. SPECTRAL PROCESSING.	45
Swyt, Leapman, Removal of plural scattering in EELS: Practical considerations. . . .	45
3. CORROSION	49
Tatlock, Fox, Metal oxide interfaces in alumina forming iron-based alloys.	49
Friel, Mehta, Industrial atmosphere corrosion products on metallic coatings.	55
Guerra, Worrel, Corrosion of nickel in SO ₂ -O ₂ -SO ₃ -Ar atmospheres above 600 C	59
Heidersbach, Purcell, Analysis of corrosion products with the use of the Raman microprobe	61
Hess, Al-Saleh, Murakami, Sakurai, Pickering, APFIM studies of segregation and solute-defect interactions in metals	65
4. ELECTRON-BEAM LITHOGRAPHY.	68
Murray, Isaacson, Adesida, Kirkland, Direct measurements of the range of secondary electrons in low atomic number materials	68
Murray, Isaacson, Adesida, Fabrication of nanometer scale structures.	70
Craighead, ~10nm electron-beam lithography with an (S)TEM.	73
5. SEM CONTRAST AT HIGH MAGNIFICATION.	77
Peters, Scanning electron microscopy: Contrast at high magnification	77
Joy, Monte Carlo studies of high-resolution secondary imaging.	81
6. FAILURE ANALYSIS IN MICROELECTRONICS	87
Romig, Yost, Hlava, Intermetallic layer growth in Cu/Sn-In solder joints	87
Matson, Tsuo, Complementary use of electron channeling and EBIC for analysis of polycrystalline semiconductor materials	93

*An Author Index appears on p. 335.

Sheng, Cross-sectional transmission electron microscopy of electronic devices	97
Lin, EBIC microscopy for device diagnosis	99
 7. RAMAN AND IR.	 103
Doyle, Alvarez, Microfluorescence studies of zirconium oxide.	103
Boyer, Smith, Petrological applications of the Raman microprobe (RMP): Examples of the characterization of micron-sized minerals in eclogites	107
Sommer, Leidheiser, Characterization of phosphate conversion coatings by laser Raman spectroscopy.	111
Andersen, Integrating a Raman microprobe into a general microanalytical problem-solving scheme.	115
Soto, Adar, Raman microprobe characterization of ZrO ₂ inclusions in glass lightguides	121
Atalla, Agarwal, Raman microprobe optimization, and sampling technique for studies of plant cell walls	125
 8. FAILURE ANALYSIS IN POLYMERS, CERAMICS, AND COMPOSITES.	 127
Tighe, Microstructural analysis of creep failure in Si ₃ N ₄ and SiC	127
Hertzberg, Manson, Rimnac, Fracture surface morphology in engineering plastics. . .	131
Sarkar, Sakarcin, Porter, Microstructural characterization of creep failure in alumina.	135
 9. GEOLOGICAL APPLICATIONS	 139
Dilks, Park, Graham, Characterization of sandstones and their component minerals by quantitative EPMA point counting in the scanning electron microscope	139
Hollister, Crisp, Kulick, Maze, Sisson, Quantitative energy-dispersive analysis of rock-forming silicates	143
Hearn, Steinkampf, Brown, Characterization of secondary alteration in the Columbia River basalt by backscattered electron imaging and energy-dispersive x-ray spectroscopy.	145
Dilks, Graham, Quantitative compositional and morphological characterization of sandstones by backscattered electron image analysis.	149
Strope, A method of combating alkali metal loss during microbeam analysis of basaltic glass.	154
Calvo, Guilemany, Salazar, SEM study of the structures obtained in ore synthesis test: A genetical hypothesis.	157
 10. IMAGE ANALYSIS	 161
Russ, Russ, Enhancement and combination of x-ray maps and electron images	161
Rommel, Kirkendall, Quantitative analysis of positive battery plates by means of BSE image analysis	165
Benoit, Blanc, Lugand, Some examples of the use of digital images on Camebax. . . .	169
Bright, Computer matching two different images of the same particle field	173
Heinrich, Fiori, Choice of color scales in analytical maps	175
Tejeda, Dominguez, Fourier analysis and processing of high-resolution electron microscope images	177
Fiori, Swyt, Gorlen, Continuum correction of x-ray images in scanning electron column instruments.	179
 11. QUANTITATIVE ELECTRON PROBE.	 186
Tian, Russ, Surface tilt effects on the effective current factor.	186
Love, Scott, Sandborg, Soft x-ray analysis with the use of a 'windowless' ED system	191
Sewell, Love, Scott, Development of a new absorption correction for EPMA.	195
Newbury, Myklebust, Steel, Use of a Monte Carlo electron trajectory simulation for quantitative analysis of thick films in the electron-probe microanalyzer	198
Marinenko, Use and abuse of quantitative wavelength-dispersive x-ray microanalysis	201

Myklebust, Marinenko, A re-examination of the characteristic fluorescence correction.	205
Armstrong, Quantitative analysis of silicate and oxide minerals: A reevaluation of ZAF corrections and proposal for new Bence-Albee coefficients.	208
Armstrong, Buseck, A general characteristic fluorescence correction for particles, thin films, and thick specimens.	213
Lifshin, The x-ray continuum: A blessing and a curse.	215
Reffner, Improved EDX analysis by use of x-ray absorption filters	221
 12. ARCHAEOLOGICAL APPLICATIONS	 223
Yamada, Shimura, Use-wear analysis of stone tools with scanning electron microscope	223
Thorpe, Franklin, Microstructural analysis of copper artifacts from Batan Grande.	227
Gordon, The quality of wrought iron evaluated by microprobe analysis.	231
Todd, The relationship between ore, slag, and metal compositions in pre-industrial iron.	235
Notis, Moyer, Barnisin, Clemens, Microprobe analysis of early copper artifacts from the Northern Sinai and the Judean caves.	240
Roeder, Sculac, Notis, The precipitation of iron in early smelted copper from Timna.	243
Vecchio, Marder, An analytical structure determination of a Saugus pig.	247
Demortier, Milli- and microprobe PIXE for the analysis of ancient brazing of gold	249
Dodia, The use of SEM for pollen morphological studies of climate-sensitive species	253
Murata, Sasaki, The rust analysis of the Inariyama sword.	257
Liu, Chan, Notis, Pigott, Analytical electron microscopy of early steel from the Bacqah Valley, Jordan	261
 13. BIOLOGICAL APPLICATIONS.	 264
Thibaut, Ansel, Systematic researches in various fungal tissues studied by laser microscopy.	264
Brenna, Morrison, Low-temperature ashing preconcentration for elemental localization in ion microscopy.	265
Warner, Myers, Taylor, Water content determined from analysis of freeze-dried thin sections	267
Sauer, Watabe, X-ray microanalysis in the study of heavy-metal uptake by fish calcified tissues.	269
Tormey, Accuracy and precision of biological x-ray microanalysis: Cardiac muscle.	272
Izutsu, Johnson, Wang, Elemental analysis of labial glands in cystic fibrosis	277
Lange, Donovan, Abraham, A generalized approach for the analysis of isolated cells by electron-probe microanalysis	281
Abraham, Donovan, Lange, Application of electron-probe microanalysis to tissue culture studies of normal cellular physiology and genetic disease	285
Hagler, Cryotransfer of ultrathin cryosections for x-ray microanalysis.	290
 14. COMPUTER-ASSISTED ANALYSIS	 291
Bastin, Heijligers, Quantitative electron probe microanalysis of carbon in binary carbides	291
Mauney, Van Espen, Design at the software-operator interface: Considerations on programming for efficient use of modern instrumentation.	295
Heyman, The application of an automated microprobe procedure for the evaluation of elemental segregation in alloys.	299

15. MATERIALS APPLICATIONS	303
Sellamuthu, Goldstein, Segregation analysis of melt-grown crystals of Fe-Ni alloys with the use of electron microprobe	303
Simonsen, Hare, Russ, Effect of scale on intensities from heterogeneous aluminum bronzes.	306
Breen, Moran, Leimkuhler, Wide-angle ECP of insonated aluminum.	309
Tworok, Mehta, Characterization of the suspended solids in a steel plant effluent with the use of electron-optical and x-ray diffraction techniques.	312
Merchant, Notis, Goldstein, Morphological stability of β - γ phase interfaces in Ni-Cr-Al alloys.	315
Sicignano, Colak, Werkhoven, van der Weg, Enhancement of cathodoluminescence in ZnSe cooled to liquid-nitrogen temperatures with the use of an SEM	319
16. AUGER AND SIMS	321
Lang, Degreè, Influence of probe setting in SIMS quantitative analysis	321
Sherman, Auger spectroscopy of ceramic grain boundaries	323
Morris, Bakhru, Haberl, A scanning nuclear microscope	327
Robinson, Brown, Johnston, Lau, Increased reproducibility of high mass resolution SIMS	331
Robinson, Brown, The matrix effect in depth profiling of implants in $\text{Al}_x\text{Ga}_{1-x}\text{As}$ by secondary ion mass spectrometry.	333
Author index.	333

Officers of the Microbeam Analysis Society (1984)

MAS Executive Council

President: David C. Joy, Bell Laboratories
President-Elect: Dale E. Newbury, National Bureau of Standards
Past President: Roger D. Bolon, General Electric R&D Center
Treasurer: Mary C. Finn, Lincoln Laboratory
Secretary: Charles E. Fiori, National Institutes of Health,
Bldg. 13, Rm. 3W13, Bethesda, MD 20205
(301) 496-2599

Directors

John T. Armstrong, California Institute of Technology, Pasadena
William F. Chambers, Sandia Laboratories, Albuquerque, N.M.
Alton D. Romig Jr., Sandia Laboratories, Albuquerque, N.M.
Roy H. Geiss, IBM Research Division, San Jose, Calif.
Joseph H. Doyle, Rockwell International, Golden, Colo.
Ronald R. Warner, Procter and Gamble Co., Cincinnati, Ohio

Honorary Members

L. S. Birks, Naval Research Laboratory, USA
I. B. Borovskii, Academy of Sciences, USSR
Raymond Castaing, University of Paris (Orsay), France
V. E. Cosslett, University of Cambridge, Great Britain
Peter Duncumb, Tube Investments Research Laboratories, Great Britain
Gunji Shinoda, Osaka University, Japan

Sustaining Members' Information

AMRAY INC.

160 Middlesex Turnpike
Bedford, MA 01730

Contact: James Furlong, (617) 275-1400

Product Line: Largest manufacturer of scanning electron microscopes and accessories in the USA.

Sales Offices:

Warren Johnson, Cleveland, Ohio, (216) 579-0035
George Bruno, New York State, (617) 275-8310
Don Pollock, Lico, New England, (617) 275-8310
Ken Benoit, New Jersey, (609) 662-3922
Gene Werbeck, Los Angeles, Calif., (714) 848-1940
Dr. Bart Yatchmenoff, San Francisco, Calif., (415) 964-5900

BAUSCH & LOMB/ARL

9545 Wentworth Street
Sunland, CA 91040

Contact: Walter R. Haley, (213) 352-6011

Product Line: Nanolab scanning electron microscopes, SEMQ scanning electron microprobe x-ray analyzer, Omnicon image analysis system.

Sales Offices:

9545 Wentworth St., Sunland, CA 91040, (213) 352-6011
820 Linden Ave., Box 9189, Rochester, NY 14625, (716) 338-8209
340 Melvin Dr., Northbrook, IL 60062, (312) 498-0400
2131 Kingston Ct. SE, Marietta, GA 30067, (404) 952-9061
2930 Baseline Rd., Nepean, Ont., Canada K2H 8T5, (613) 820-9437

CAMBRIDGE INSTRUMENTS INC.

40 Robert Pitt Drive
Monsey, NY 10952

Contact: Peter W. Boutell, (914) 356-3331

Product Line: Research scanning electron microscopes and accessories, research production beam microfabrication systems, image analysis equipment.

Sales Offices:

Joe Barrett, Arizona, New Mexico, Texas, (602) 991-9458
John Pong, California, Nevada, Utah, Colorado, (714) 893-1609
Mike Webber, Florida, Georgia, Alabama, Tennessee, Virginia, (404) 926-9636
Brian Partridge, California, Washington, Montana, Idaho, (408) 734-2313
T. Rodkin, Maine, Vermont, Mass., Connecticut, R.I., (603) 465-7888

CAMECA INSTRUMENTS INC.

2001 West Main Street
Stamford, CT 06902

Contact: Harry Rundall, (203) 348-5252

Product Line: CAMBAX/MICRO fully automated microprocessor controlled electron microprobe. IIS-3F second-generation ion microanalyzer.

Sales Offices:

Thomas Fisher, 416 Ohio Ave., West Springfield, MA 01089, (413) 734-0617
R. Rattay, Dept. 559, Box 42999, Houston, TX 77042
Ms. E. Flentye, Box 2994, La Jolla, CA 92038-2994

EDAX INTERNATIONAL, INC.

Box 135
Prairie View, IL 60069

Contact: A. Devenish, (312) 634-0600

Product Line: Manufactures energy-dispersive x-ray analysis systems for x-ray microanalysis in SEMs, TEMs, and electron probes, as well as energy-dispersive x-ray fluorescence spectrometers. System configurations from basic qualitative to fully automated quantitative (with computer control and data processing) are available, including an automated WD/ED system with stage and spectrometer controls.

Sales Offices:

V. Balmer, 637 Sunnyside Rd., Vermilion, OH 44089
E. Martin, Box 547, New Rochelle, NY 10802
J. Moore, Box 2253, Boulder, CO 80306

EG&G ORTEC

100 Midland Road
Oak Ridge, TN 37830

Contact: Judy Potter, (615) 482-4411, Ext 506

Product Line: Energy-dispersive systems for electron optical microscopes of all types. Wavelength-dispersive system electronics. Backscattered electron detection systems.

Sales Offices:

Joe Redmon, Box 6041, Boston, MA 02209
Peeter Kark, 9401 Comprint Ct., Suite 101, Gaithersburg, MD 20760
Robert G. Bardorf, Box 3355, Oak Ridge, TN 37930
Dick Tischler, 21360 Center Ridge Rd., Rm. 304, Cleveland, OH 44116
Earl Klugman, 310 Melvin Dr., Northbrook, IL 60062
Val Johnson, Box 1678, Boulder, CO 80306
Bill Tucker, 2104 Courland Circle, Carrollton, TX 75007
John Telford, Bldg. 3, Suite 204, 300 120th Ave. NE, Bellevue, MA 98005
Alan Welco, 22971 Triton Way, Suite C, Laguna Hills, CA 92653
Ed Gooden, Box 14607, Albuquerque, NM 87919

GATAN, INCORPORATED

780 Commonwealth Drive
Warrendale, PA 15086

Contact: Terry Donovan, (412) 776-5260

Product Line: Specializes in equipment for electron microscopy; these products are: electron energy loss spectrometer (EELS), ion beam milling equipment, image intensifier system, analytical stages of beryllium construction, general EM specimen preparation equipment.

HITACHI SCIENTIFIC INSTRUMENTS
NISSEI SANGYO AMERICA, LTD.

460 E. Middlefield Road
Mountain View, CA 94043

Contact: Hideo Naito (415) 969-1100 (West); John Johnson, (301) 840-1650 (East)

Product Line: Transmission and scanning electron microscopes, atomic absorption UV-Vis

spectrophotometers and liquid chromatographs.

Sales Offices:

TEM/SEM: 1300 Quince Orchard Blvd., Gaithersburg, MD 20878, (301) 849-1650
AAA/AA: 825 Third Avenue, Suite 2620, New York, NY 10022, (212) 755-2900

INTERNATIONAL SCIENTIFIC INSTRUMENTS, INC.

3255-6C Scott Boulevard
Santa Clara, CA 95051

Contact: Donald J. Evins, (408) 727-9840

Product Line: Scanning electron microscopes with a full complement of accessories, including WDX spectrometers. The ISI SEM line includes: SX-25, SX-30, SS-40, SS-60, LaB6-SS-130T, and DS-130. Also in the product line is our new wafer inspection SEM, the IC-130/5 and IC-130/6. A complete line of scanning electron microscopes suited for any application and budget.

Sales Offices:

Bill Maguire, Avon Park South, 20 Tower Lane, Bldg. 2, Avon, CT 06001, (203) 677-0016
John Fitzpatrick, c/o Santa Clara address, (713) 777-0321
Richard Feller, 800 Roosevelt Rd., Glen Ellyn, IL 60137, (312) 469-8111

JEOL U.S.A., INC.

11 Dearborn Road
Peabody, MA 01960

Contact: Judy Hamilton, (617) 535-5900

Product Line: Manufacturers and dealers of scanning electron microscopes, transmission electron microscopes, scanning transmission electron microscopes, electron probe micro-analyzers, scanning Auger microprobes, energy loss analyzers, and electron beam writing equipment.

Sales Offices:

John Bonnici, American Office Mall, 275 Route #18, East Brunswick, NJ 08816, (201) 254-5600 or 5603
Thayer Brickman, 1633 Bayshore Highway, Suite 245, Burlingame, CA 94010, (415) 697-9220
Jack Francis, 1402 Rambling Hills Dr., Cincinnati, OH 45230, (513) 232-7350
Thomas V. Gildea, 11 Dearborn Rd., Peabody, MA 01960, (617) 535-5900
Ray Gundersdorff, 6236 Gilston Park Rd., Catonsville, MD 21228, (301) 953-2959
Mike Hassel Shearer, 7586 Parkview Mountain, Littleton, CO 80123, (303) 979-0169
Richard Lois, One Kingwood Place, Suite 122B, 600 Rockmead Dr., Kingwood, TX 77339, (713) 358-2121
Lewis McDonald, 3223 G Post Woods Dr., Atlanta, GA 30339, (404) 434-9724
Jean-Pierre Slakmon, Soquelec Ltd., 5757 Cavendish Blvd., Suite 101, Montreal, Quebec, Canada H4W 2W8, (514) 482-6427
Robert Steiner, 640 Pearson St., Suite 102, Des Plaines, IL 60016, (312) 825-7164

KEVEX CORPORATION

1101 Chess Drive
Foster City, CA 94404

Contact: Dana E. Kelley, (415) 573-5866

Product Line: Analytical systems for x-ray energy spectrometry, wavelength-dispersive x-ray spectrometry, Auger, and electron energy spectrometry. Detector-cryostats and analytical spectrometer systems are compatible with all electron microprobe, SEMs, and TEMs in current production. Systems are available for both qualitative and quantitative analysis.

Sales Offices:

Blaise Fleischmann, 6436 Barnaby St., NW, Washington, DC 20015

Dana Kelley, 1101 Chess Dr., Foster City, CA 94404
Frank Mannino, 627 Harvest Glen Dr., Richardson, TX 75081
Ken Matz, 702 Main St., Collegeville, PA 19426
Steve Miller, 602 S. Fairview, Park Ridge, IL 60068

KRISEL CONTROL, INC.

16 Farsta Court
Rockville, MD 20850

Contact: Christos Hadidiacos, (301) 762-1790

Product Line: Automation equipment for electron microprobe/microscope, featuring on-line data acquisition and reduction using Alpha and ZAF correction schemes. Single-crystal automation system for on-line data collection, centering, calculation of orientation matrix, and refinement of cell parameters for an x-ray diffractometer.

LINK SYSTEMS (USA), INC.

3290 W. Bayshore Road
Palo Alto, CA 94303

7 Valley Forge Drive
North East, MD 21901

Contact: Nathan Schneider, (415) 856-2726 (West) Barry Weavers, (301) 287-6030 (East)

Product Line: Energy-dispersive x-ray microanalysis systems including interface with software support for electron energy loss spectroscopy (EELS), Auger, ESCA, and cathodoluminescence acquisition and processing. Simultaneous data acquisition and processing from energy-dispersive and wavelength-dispersive spectrometers including control of the microscope stage and spectrometers for fully automated analysis. Digital image processing systems for picture capture, enhancement, noise reduction and analysis, picture annotation, storage, and retrieval. Scan converters for interfacing digital image processors to electron microscopes and IR, RADA, and SONAR instruments.

Sales Offices:

Int'l Instrument Corp., 64 E. Main St., Marlton, NJ 08053, (609) 983-6550
Pulcir, Inc., Box 357, Oak Ridge, TN 37830, (615) 483-6358
The Buhrke Co., 1500 Old County Rd., Belmont, CA 94002, (415) 592-2904
Barry Weavers, 7 Valley Forge Dr., North East, MD 21901

WALTER C. McCRONE ASSOCIATES, INC.

2820 South Michigan Avenue
Chicago, IL 60616

Contact: Ian Stewart, (312) 842-7100

Product Line: Ultramicroanalytical services in chemistry and physics.

MICRON, INC.

Box 3536
Wilmington, DE 19807

Contact: James F. Ficca Jr., (302) 998-1184

Product Line: Scanning electron microscopy, electron spectroscopy, electron probe x-ray analysis, transmission electron microscopy, quantitative image analysis, x-ray diffraction, x-ray fluorescence, optical microscopy and metallography, micro hardness, optical emission spectroscopy, differential scanning calorimetry, ultra microtomy, sample preparation.

MICROSPEC CORPORATION

265-G Sobrante Way
Sunnyvale, CA 94086

Contact: Richard C. Wolf, (408) 733-3540

Product Line: WDX-2A wavelength-dispersive x-ray spectrometer systems. X-ray microanalysis systems for use as accessories on scanning electron microscopes and other electron beam instruments. Capable of x-ray analysis of all elements down to beryllium, atomic number 4. Unique design permits attachment to most SEM electron columns.

PHILIPS ELECTRONIC INSTRUMENTS, INC.

85 McKee Drive
Mahwah, NJ 07430

Contact: John S. Fahy, (201) 529-3800

Product Line: Transmission analytical electron microscopes, scanning analytical electron microscopes, and analytical accessories for electron microscopes.

Sales Offices:

A. Hugo, 55 Virginia Ave., West Nyack, NY 10994
D. Ahr, 6231 Executive Blvd., Rockville, MD 20852
H. Ittner, 155 NE 100th St., Suite 403, Seattle, WA 98125
T. Bates, 7094 Peachtree Industrial Blvd., Suite 220, Norcross, GA 30071
B. Smick, Suite D45, 2525 East Oakton, Arlington Heights, IL 60005
Ms. Jo Long, 7302 Harwin Dr., Suite 106, Houston, TX 77036
S. Spiers, 3000 Scott Blvd., Suite 113, Santa Clara, CA 95050

PHYSICAL ELECTRONICS
DIVISION OF PERKIN-ELMER CORP.

6509 Flying Cloud Drive
Eden Prairie, MN 55344

Contact: Gary Muilenberg, (612) 828-6315

Product Line: Surface analysis instrumentation including Auger, ESCA, SIMS; also MBE.

Sales Offices:

John Callaghan, 415 W. Golf, Arlington Heights, Ill., (312) 228-0130
Edward Graney, 5 Progress St., Edison, N.J., (201) 561-6530
Leslie Holmes, 1011 S. Sherman St., Richardson, Tex., (214) 669-4400
Dan Jean, 2 Taunton St., Plainville, Mass., (617) 695-7181
Jude Koenig and Dixie Sinkovits, 151 Bernal Rd., San Jose, Calif., (408) 629-4343
Guy Messenger, 7310 Ritchie Hwy., Glen Burnie, Md., (301) 761-3053
Pete Seamans, 655 Deep Valley Dr., Rolling Hills, Calif., (213) 377-7750
Jerry Rosenthal, 1382 Old Freeport Rd., Pittsburgh, Pa., (412) 963-6717
Elm Sturkol, 6509 Flying Cloud Dr., Eden Prairie, Minn., (612) 828-6332

PRINCETON GAMMA-TECH, INC.

1200 State Road
Princeton, NJ 08540

Contact: Darlene Zimmerman, (609) 924-8980

Product Line: Energy-dispersive x-ray spectrometers and SYSTEM-4 analyzer for electron column applications including energy-dispersive x-ray microanalysis, WDS automation, digital beam control, high-resolution digital image collection and processing, image analysis and EELS. Dedicated XRF systems for a variety of industrial applications are also available.

Sales Offices:

Joe Piersante, Rt. 2, Box 50-A16, Gainesville, GA 30501, (404) 887-9100
Denny Cannon, Box 36157, Denver, CO 80236, (303) 978-0786
Tom Griffin, 701 Morewood Pkwy., Rockey River, OH 44116, (216) 331-0120
Jay Sylvester, 7111 Eckher Rd., San Antonio, TX 78238, (512) 680-3702
Jake Brown, 556 Weddell Dr., Suite 3, Sunnyvale, CA 94086, (408) 734-8124
Roland Marti, 5119 Edsel Ave., Los Angeles, CA 90066, (213) 823-1330
Art Merkle, 1025 Old Mill Grove Rd., Lake Zurich, IL 60047, (312) 540-0555

Scientific System Sales Corp:

333 Jericho Turnpike, Jericho, NY 11753, (516) 822-4880
203 Middlesex Turnpike, Burlington, MA 01803, (617) 273-1660
14300 Gallant Fox Lane, Suite 212, Bowie, MD 20715, (301) 262-4104

SPI SUPPLIES

DIVISION OF STRUCTURE PROBE, INC.

535 E. Gay Street
Box 342
West Chester, PA 19380

Contact: Betty Garber, (215) 436-5400

Product Line: SPI Supplies: Consumable supplies, film, and small instruments for EM labs. Specializing in innovative new products developed in Structure Probe's four East Coast labs: Plasma-Prep II, SPI-Sputter, Steadi-cool, field finder, immunological reagents. Structure Probe, Inc.: Analytical research services, electron microscopy, surface analysis, failure analysis, STEM, SEM, TEM, EDS, WDS, PSA.

Sales Offices:

535 E. Gay St., Box 342, West Chester, PA 19380, (215) 436-5400
230 Forrest St., Metuchen, NJ 08840, (201) 549-9350
63 Unquowa Rd., Fairfield, CT 06430, (203) 254-0000
1015 Merrick Road, Copiague, NY 11726, (516) 789-0100

C. M. TAYLOR CORPORATION

289 Leota Avenue
Sunnyvale, CA 94086

Contact: Dr. Charles M. Taylor, (408) 245-4229

Product Line: Various types of multi-element standards for microbeam analysis by SEM, microprobe, and ion probe using energy, wavelength, and mass spectrometers. The standards available exceed 175 different metals, alloys, glasses, compounds, or minerals. Bence-Albee standards are available. Also manufactures many types of sample holders, polishing jigs, and other types of equipment for sample preparation. Also offers analytical services to customers desiring electron-beam microprobe analysis using MAC-5 instrument. Have full ZAF correction capability for microprobe data, using FRAME B or Bence-Albee procedures.

M. E. TAYLOR ENGINEERING INC.

11506 Highview Avenue
Wheaton, MD 20902

Contact: M. E. (Gene) Taylor, (301) 942-3418

Product Line: Scintillators for SEMs and microprobes, backscatter and secondary electron detectors of the quartz light pipe/scintillator design. Other products include Brimrose image intensifiers, ISI filaments and apertures, specimen mounts, adhesive tabs, vacuum pump oil, and foreline traps. SEM accessories on display and SEM services at Micro Source.

Sales Offices:

Agar Aids, 66A Cambridge Rd., Stansted, Essex, England, OM24 8DA
Science Services, Badstr. 13, 8000 München 70, Federal Republic of Germany
Micro Source, 620 Hungerford Dr., #12, Rockville, MD 20850, (301) 251-0642

TRACOR NORTHERN

2551 West Beltline Highway
Middleton, WI 53562

Contact: John Benson, (608) 831-6511

Product Line: Wide range of data processing instrumentation for qualitative and quantitative x-ray analysis. Products include data acquisition, reduction, and automation for electron microprobe, SEM, TEM, and STEM. Featuring simultaneous EDS/WDS acquisition/reduction, digital beam control allowing for digital mapping, line scans, and other digital image processing. Also particle location, sizing, and elemental characterization. Flexible packaging allows instrument to be used also for ELS, Auger, ESCA, SIMS, etc. Other products are used in nuclear, optical, signal-averaging, and medical applications.

Sales Offices:

345 E. Middlefield Rd., Mountain View, CA 94043, (415) 967-0350

3040 Holcomb Bridge Rd., Norcross, GA 30071, (404) 449-4165

Franklin Park Office, 134 Franklin Corner Rd., Lawrenceville, NJ 08648, (609) 896-1114

Suite 1458, Bldg. A, Miamisburg Centerville Rd., Dayton, OH 45459, (513) 439-3990

T.1 Tutorials

ELEMENTARY STEREOLOGY

J. J. McCarthy

Stereology is a branch of applied mathematics which aims to provide a three-dimensional interpretation of two-dimensional images (sections and projections) by means of the theory of geometric probability. Stereological procedures are quite easy to learn; the symbols and formulas are quite simply defined and applied. The basis of stereology is rooted in rigorous mathematics, but only a knowledge of algebra and elementary statistics is required to obtain meaningful stereological results from many specimens. This paper introduces the terminology, parameters, and formulas of stereology, discusses procedures, and lists some of the common sources of error.

The Statistical Nature of Stereology

Statistical considerations play a central role in stereological analysis. Experimental designs must incorporate random sampling techniques, and the validity of all stereological results must be evaluated statistically. In general, anyone attempting to perform a stereological analysis should keep the following premises in mind:

- stereological procedures must measure large numbers of related structures
- the results of stereological analysis are average values of parameters that characterize the structure
- the procedure of sectioning allows only a restricted sample of the structure to be analyzed
- all stereological principles are based upon the study of geometric probability

Terminology and Basic Parameters

Most branches of science develop a distinct jargon and stereology is no exception. This section introduces some basic terminology and defines a few fundamental parameters.

Terms. The following terms are explained visually in Fig. 1.

Section: a plane without any thickness generated by a single cut through a solid specimen.

Slice: a section of finite thickness generated by two cuts.

Profile: a section or slice through an individual component of a solid.

Trace: a section of a two-dimensional surface, such as a membrane, or an interface; a trace appears as a line in the section.

Intercept: the length of that segment of a test line that falls on the area of a profile.

Intersection: the point of crossing of a test line with a trace.

Parameters. What specimen parameters can be obtained by stereological measurements, and which parameters are most informative for characterizing specimen structure? Most of this information is obtained from a few fundamental parameters.

Volume fraction V_V : the volume of the measured components per unit volume.

Surface density S_V : the surface area of the measured component per unit volume.

Line density L_V : the length of a filamentous structure per unit volume.

Numerical density N_V : the number of particles per unit volume.

The author is at Tracor Northern, Inc., 2551 West Beltline Highway, Middleton, WI 53562.

Mean caliper diameter of particles D: the mean distance between tangent planes to the particle over all possible particle orientations.

The first three parameters do not require that the specimen be composed of discrete particles or even that the shape of the structures in the specimen be known. That is not the case for the numerical density N_V or the mean diameter \bar{D} . In the case of those two parameters, both the shape and size distribution of the particles must be considered. This requirement complicates the stereological analysis of N_V and \bar{D} a great deal--to the extent that a general solution to the problem has not been derived. However, proven approaches are available for commonly encountered shapes such as spheres, cylinders, and ellipsoids.

Many additional parameters can be derived from the basic parameters as required for a specific analysis. Some of those additional parameters will be discussed in the following.

Estimation of Volume Fraction

In 1847 the French geologist Delesse proved that the volume fraction of various components making up a rock can be estimated by measuring the relative areas of the profiles of each component in random sections of the sample.¹

A mathematical proof of the Delesse principle is straightforward and can be found in the treatments of various authors, including Weibel,² DeHoff and Rhines,³ and Underwood.⁴ In general, the area fraction of profiles on sections is an unbiased estimate of the volume fraction of structures. Stated as an equation,

$$A_A = V_V \quad (1)$$

The principle of Delesse requires the estimation of the area of profiles on a section in order to determine the volume fraction of a particular phase. Three basic approaches are used to obtain the volume fraction, which are also the basic measurement procedures used to obtain most stereological data: areal analysis, lineal analysis, and point analysis (Fig. 2). The shaded areas in Figs. 2(b) and (c) indicate the estimate of profile area generally obtained from automatic image processing instruments. When stereological measurements are made, only the line segments or points within the profile boundary are counted and compared to the total line length or total point count.

Areal analysis is usually done either by direct measurement with a planimeter or by weighing profiles that have been cut from tracings of the profiles on the section. The area fraction is calculated by summation of the areas (or weights) of each profile and dividing by the total for the section. Both methods are very tedious and are thus seldom used.

Lineal analysis was first introduced by Rosiwal⁵ in 1898. The procedure is randomly to place or project on the section a test line of length L_T and measure the total length of the line segments L_i included in the profiles. The area fraction A_A is then equal to the ratio

$$L_i/L_T = L_L = A_A \quad (2)$$

This equation states that the lineal fraction occupied by a given phase is an unbiased estimate of the area fraction and hence the volume fraction of that phase.

In point analysis, a point or a grid of points is placed at random on a section. The probability that a given point will fall within a given phase is equal to the volume fraction of that phase. Therefore, the point fraction of a given phase is an unbiased estimator of the volume fraction of that phase. That is,

$$P_i/P_T = P_P = V_V \quad (3)$$

The relationships defined in the preceding paragraphs are valid for random test lines or points placed on a section, or for nonrandom arrays of points or grids placed at random on the section. Also, enough data must be collected to assure that adequate statistics are obtained. Combining equations (1) to (3), we arrive at a fundamental stereological result:

$$V_V = A_A = L_L = P_P \quad (4)$$

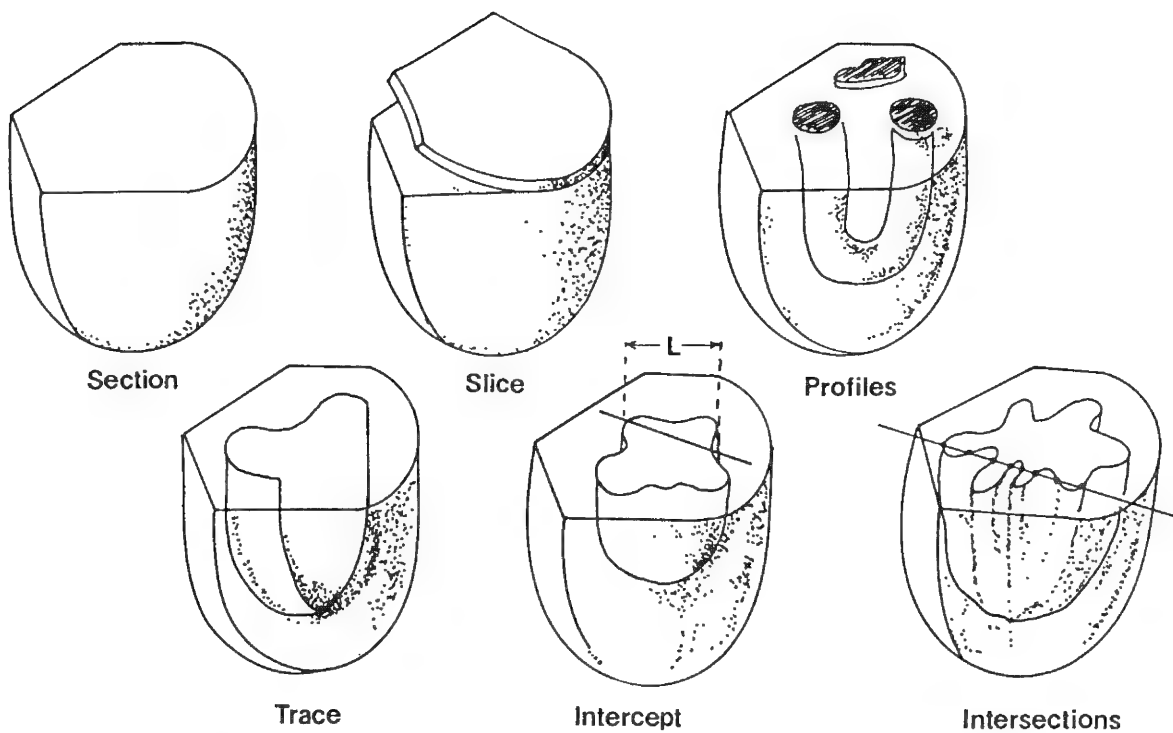


FIG. 1.--Visual explanation of terminology. (Adapted from Ref. 7.)

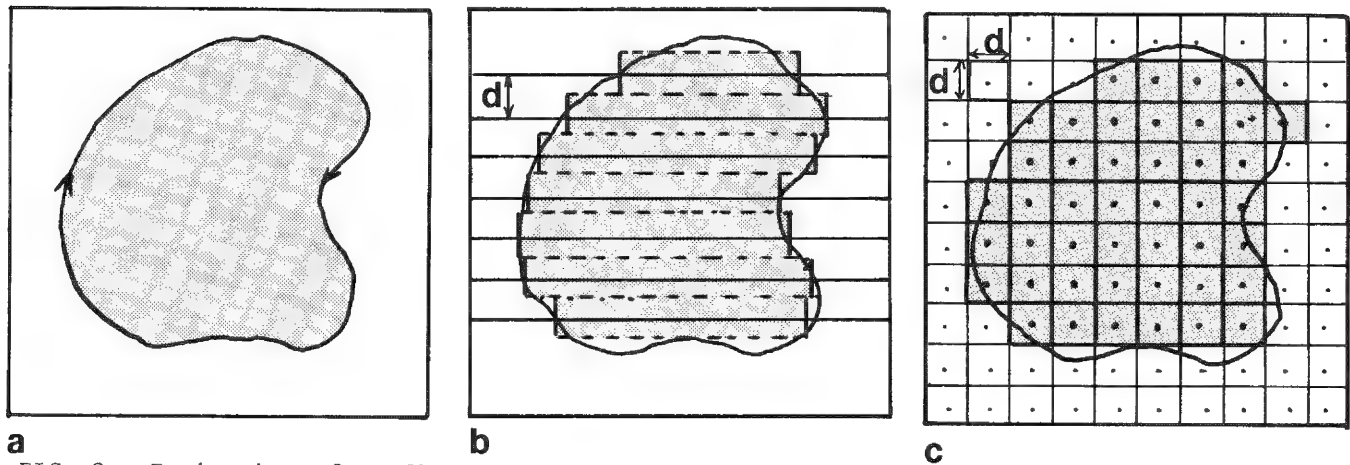


FIG. 2.--Estimation of profile area by (a) areal analysis; (b) lineal analysis; (c) point analysis.

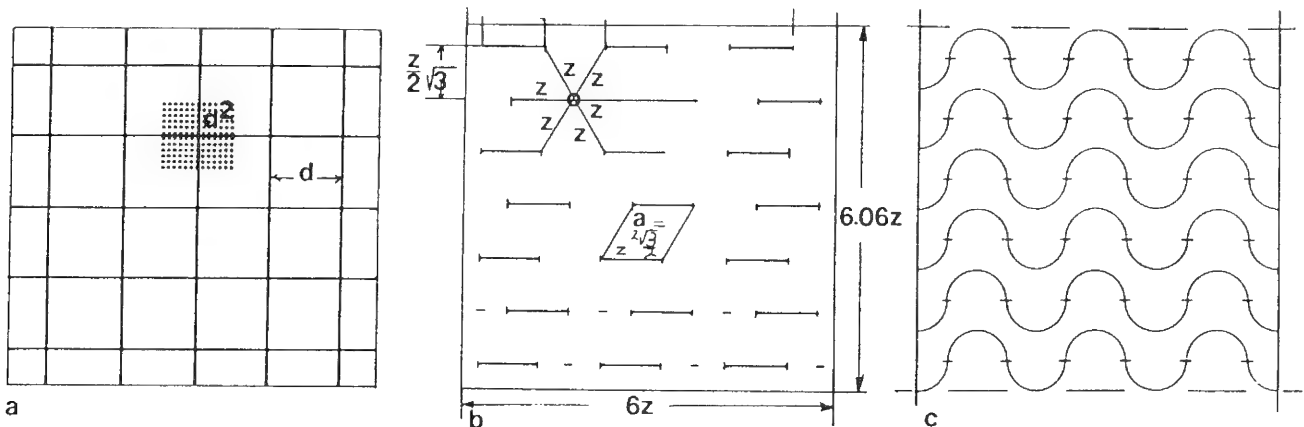


FIG. 3.--Common measurement test systems: (a) simple quadratic grid; (b) test system proposed by Weibel; (c) test system proposed by Murz. (Adapted from Ref. 2.)

Which method of analysis should be selected for a given volume estimate? Generally, point counting is more efficient than areal or lineal measurements. An estimate of the statistical accuracy of each method depends on the nature of the specimen and the measurement procedures. A complete discussion of these factors is given by DeHoff and Rhines.³ An estimate of the uncertainty of volume fractions obtained by point counting is presented in a later section of this paper.

Estimates of Surface Density and Line Density

Stereological techniques can also provide quantitative measurements of one- and two-dimensional features. Examples of these structural features include dislocation lines or the network of grain boundary lines in metal sections, and membranes in a section of tissue. These structures appear as traces in a two-dimensional section of the specimen, and represent boundaries in three-dimensions that occupy a specific surface area. Other structures are lines that transect the plane of the section and appear as points in the section. Examples include the intersection of three grain boundary surfaces, or the profiles of fibers or tubules in tissue sections. Three important general equations relate this type of feature (interfaces, lines and points) to their intersections with an arbitrary test line placed on the section. The equations are

$$L_A = (\pi/2)N_L \quad (5)$$

$$L_V = 2P_A \quad (6)$$

$$S_V = 2N_L \quad (7)$$

where L_A = the length of line (trace) per unit area

N_L = the number intersection of the trace per unit length of the test line (L)

L_V = length of a line (filamentous structure) per unit volume

P_A = the average number of transections of lineal objects with the plane of the section per unit area

S_V = surface area per unit volume

Estimates of Numerical Density N_V and Average Size \bar{D}

Determination of the number of particles per unit volume and the average size of particles is not easily done without prior knowledge of particle shape. Solutions have been obtained for specific particle shapes: sphere, ellipsoid of revolution, cylinder, and some others. DeHoff and Rhines³ have shown that, in general,

$$N_V = N_A/\bar{D} \quad (8)$$

where N_V = the number of objects per unit volume

N_A = number of profiles per unit area

\bar{D} = mean caliper diameter

Equation (8) requires two independent determinations: a count of N_A on sections and an estimation of mean particle diameter \bar{D} . There is a general relationship between the mean length of intercepts formed by a test line \bar{L} and the mean caliper diameter \bar{D} :

$$\bar{D} = k\bar{L} \quad (9)$$

where k is a shape coefficient; for spheres of equal diameter, $k = 3/2$. Underwood⁴ has presented an extensive table listing the relationship between the mean linear intercept \bar{L} and \bar{D} for solids of revolution and regular polyhedra.

Measurement Test Systems

Stereological measurements are made by counting of points, line intercepts, intersections or profiles, and by measurement of intercepts or mean intercept length on two-dimensional sections.

This information is commonly obtained by use of a test system composed of a regular array of points and line segments which can be superimposed on the image of the section. Several common test systems are shown in Fig. 3. All these test systems allow point, lineal, and areal measurements to be made by the combination of a known set of test points P_T with a known length of test lines L_T and test areas A_T . In fact, all three probes can be simply and quantitatively related to each other. Consider a test system composed of a grid of lines spaced a distance d apart. If the intersections of the grid lines are considered as "points" for point counting, there are the same number of squares of area d^2 and twice that number of line segments of length d . Such test systems are sometimes called coherent test systems. All the systems shown in Fig. 3 are coherent.

Manual measurements can be carried out by placing a test system over micrographs (photon or electron) of the section. Points and intercepts that lie on profiles or traces are counted and the length of intercepts are summed. Specimens that can be viewed in the optical microscope can be measured directly by means of a reticule on which an appropriate test system has been ruled. In either case, an examination of the statistical errors indicates that the accuracy of an analysis is principally determined by the number of observations, regardless of whether the observation is a measurement of intercepted area, length, or points. This conclusion is valid provided that the number of observations in a given test area is not too large, since statistical methods require a random sampling of the entire section. The optimum number of observations depends on many factors; for volume estimation by point counting it corresponds to about one test point per feature. If this condition is satisfied, for most types of structures, a volume fraction estimate by a systematic point count has a smaller error than either an areal or a lineal analysis with the same number of observations.

Method of Analysis

The first step of an analysis should be to determine the maximum error that can be tolerated. In the case of volume fraction measurements, DeHoff and Rhines³ have shown that the total number of points (P) needed to achieve a desired accuracy can be calculated from the following expression:

$$P = [V_V(1 - V_V)]/2\sigma_{V_V}$$

A rough estimate of the volume fraction V_V can be obtained from a measurement of a few points on the specimen and used to estimate the number of test points P . A difference in accuracy of 10% and 1% corresponds roughly to the difference between 30 min and 1 week of work!

The second step of an analysis is to choose a test system that will give the shortest counting time, by adjusting the number of points in the test system per frame to avoid counting errors. This step is often a matter of subjective judgment best determined by experience. If a test system with n test points is selected, then P/n fields of view will have to be examined in the analysis. In order to avoid any subjective bias, adjacent fields should be selected to give a uniform sampling of the entire section.

The third step of the analysis is to perform the measurement--point counting in the case of volume analysis. If an estimate of the experimental standard deviation is desired, separate subtotals of results should be kept at equal increments of the applied test points throughout the analysis. It is also a good idea to use the current estimate of the volume fraction to obtain a more reliable value of P and P/n to help determine when to stop the analysis.

Sources of Error

All stereological parameters are merely estimates of bulk properties obtained from the analysis of limited sections of a material. How well these parameters estimate the true

properties of the material can be determined solely by statistical methods in the absence of any systematic errors.

Stereological data must be treated statistically as mean estimates of the true parameter values. The error in these estimates can be determined from the standard deviation of repeated measurements. More complicated statistical analysis is required to estimate the total statistical error of data gathered from multiple sections of multiple specimens.

Systematic error rather than statistical error is often the limiting factor in most stereological analysis. Experimental errors arise from such limitations as the resolution of the microscope, effects of section thickness, etching effects, artifacts in the preparation, incorrect counting, and so forth. An illustration of the errors due to etching (or differential polishing) and section thickness when viewed in transmission is shown in Fig. 4. In both cases, the measured areal fraction exceeds the true volume fraction for the measured phase. This effect is known as the "Holmes effect" and a correction technique has been described by DeHoff and Rhines.³

A second major systematic error is related to sampling bias. These errors include non-random selection of test area, or nonrepresentative sampling within each area. Additional problems arise if the structures under study have a preferred orientation that is not taken into account in the sampling procedures. Errors from sampling bias can often represent the bulk of the total error of an analysis.

Conclusion

This paper has introduced the basic principles and procedures of stereological analysis. This type of analysis is derived from the theory of geometric probability, but the only mathematics required for applying stereology is simple algebra and elementary statistics. Although there are limitations to the applications of stereology, the field is still active and new developments are to be expected in the future.

References

1. M. A. Delesse, "Procédé mécanique pour déterminer la composition des roches," *C. R. Acad. Sci.* 25: 544, 1847.
2. E. R. Weibel, "Stereological techniques for electron microscopic morphometry," in M. A. Hayat, Ed., *Principles and Techniques of Electron Microscopy*, New York: Van Nostrand Reinhold, 1972, vol. 3.
3. R. T. DeHoff and F. N. Rhines, *Quantitative Microscopy*, New York: McGraw-Hill, 1968.
4. E. E. Underwood, *Quantitative Stereology*, Reading, Mass.: Addison-Wesley Publishing, 1970.
5. A. Rosiwal, "Ueber geometrische Gesternsanalysen usw.," *Verhandl. k.-k. geol. Reichsanstalt* 5-6: 143, 1898.
6. J. W. Chan and J. Nutting, "Transmission quantitative metallography," *Trans. AIME* 215: 526, 1959.
7. H. Elias and D. M. Hyde, "Elementary stereology," *Am. J. Anatomy* 159: 411, 1980.

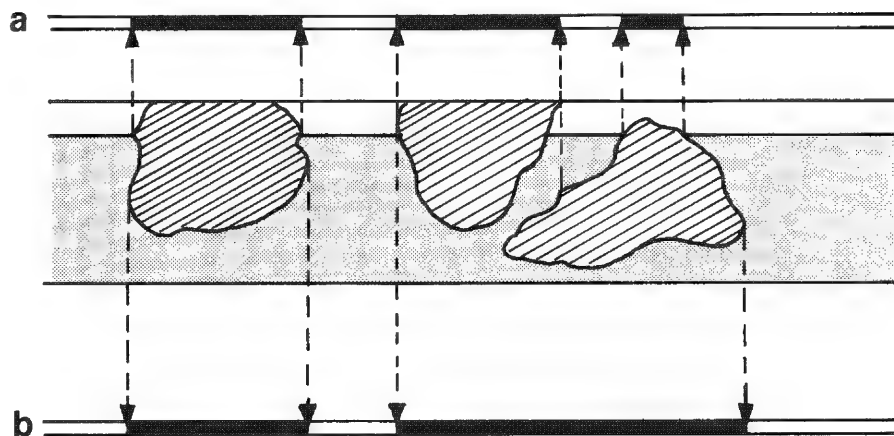


FIG. 4.--Example of error from (a) differential etching, (b) projected image viewed in transmission.

INTRODUCTION TO ANALYTICAL ELECTRON MICROSCOPY

A. D. Romig Jr.

The objective of this paper is to provide an introduction to the operating principles, capabilities, and limitations of analytical electron microscopy (AEM). No prior knowledge of the AEM is required, although a basic understanding of electron optics and x-ray microanalysis as it applies to scanning electron microscopy (SEM) and electron probe microanalysis (EPMA) is assumed.

Introduction

Analytical electron microscopy, compared to conventional transmission electron microscopy (TEM or CTM), implies the capability to extract quantitative data from the instrument. The TEM permits the user to image the sample with electrons which have been transmitted through the thin foil and thereby perform microstructural characterization. The TEM can also collect crystallographic data from areas of the sample as small as 1 μm in diameter via electron diffraction. The modern AEM has evolved from the TEM. Externally, the AEM resembles a traditional TEM and also requires the same thin foil (electron-transparent) samples. However, the AEM has several unique capabilities that distinguish it from the traditional TEM. The AEM can image the structure in several ways, including techniques normally associated with the conventional TEM and SEM. Imaging is possible with transmitted electrons, secondary electrons, and backscattered electrons. The AEM can also perform chemical analyses of small volumes of the sample via x-ray analysis, similar to the SEM and EPMA, and electron energy loss spectroscopy (EELS). In addition, the AEM can perform electron diffraction on very small volumes (10-100 nm in diameter). Such procedures are typically referred to as electron microdiffraction techniques.

In order to image with secondary electrons or backscattered electrons, one must focus the electron beam to a point probe and scan, or raster, the probe over the sample in a manner exactly analogous to the SEM. The secondary and backscattered electrons are collected and processed to produce the image exactly as in the SEM. The AEM can also collect and process transmitted electrons in an analogous way. If the beam raster is halted, the focused electron probe can be used to perform x-ray microanalysis, EELS, or electron microdiffraction on a small area of the sample. In this operating mode (scanned focused electron probe) the instrument is often referred to as a scanning transmission electron microscope (STEM). The acronyms AEM and STEM are often used interchangeably. The terms are not strictly interchangeable; STEM is an operating mode in many modern AEMs. To describe the AEM most efficiently, four specific aspects of the technique should be considered: (1) the microscope, (2) thin-foil x-ray analysis, (3) electron energy loss spectroscopy, and (4) electron microdiffraction.

The Microscope

Figure 1 shows the electron optical systems of the SEM, TEM, and AEM, respectively. All three instruments require a high-energy electron source or gun. The same basic source design can be used in all three instruments. However, the operating voltages are typically different. Most SEMs operate between 5 and 50 kV; 15 to 25 kV is typical. Virtually all TEMs and AEMs operate at voltages exceeding 80 kV; 100, 120, or 200 kV are most common. In all electron-optical instruments the electron source is a tungsten hairpin filament, LaB₆ filament,

The author is with Sandia National Laboratories, Albuquerque, NM 87185. This work was performed at Sandia National Laboratories and supported by the U. S. Department of Energy under contract DE--AC04--76DP00789.

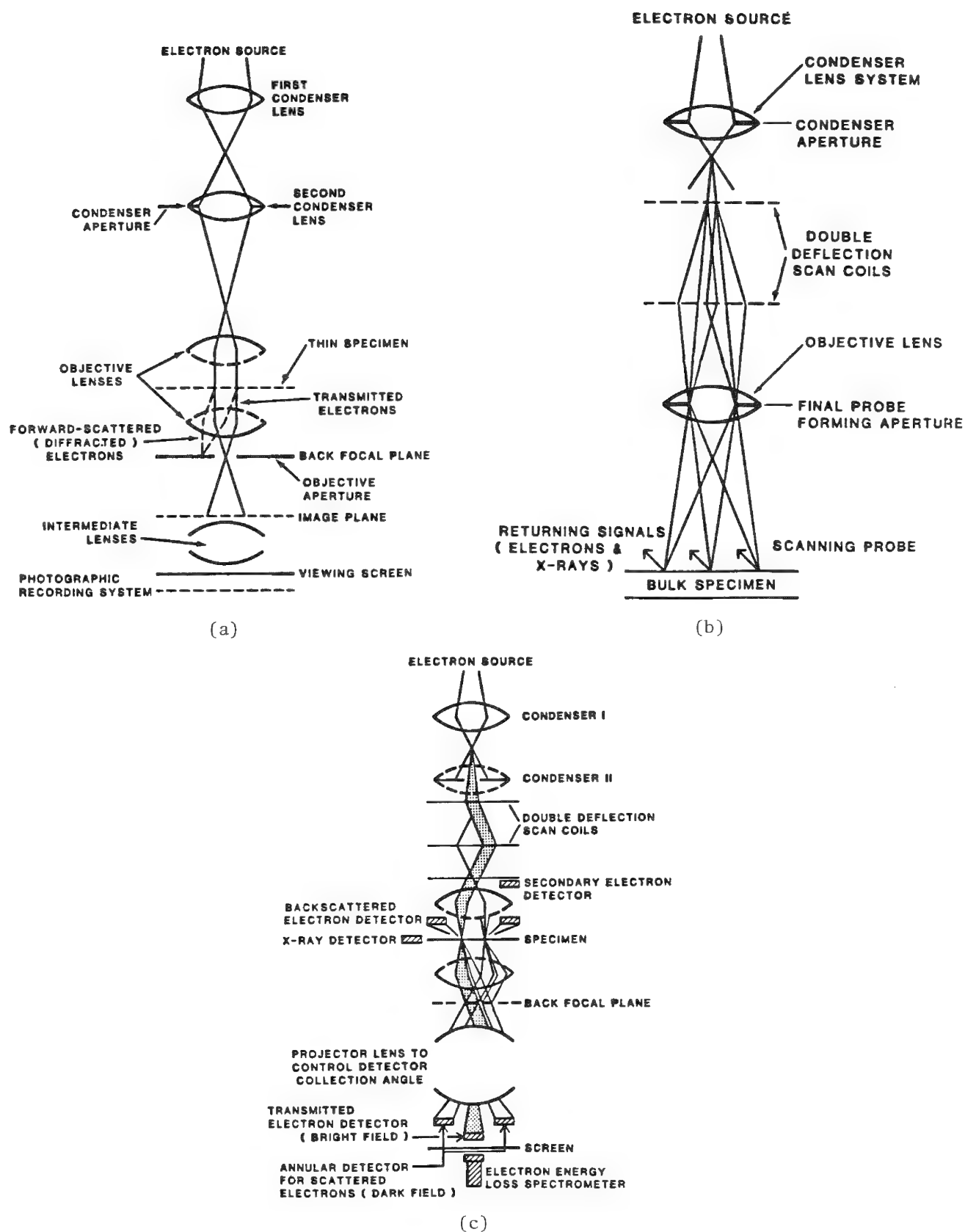


FIG. 1.--Electron-optical systems (adapted from Williams and Eddington¹⁶): (a) TEM, (b) SEM; (c) AEM.

or field-emission gun (FEG). A complete description of these electron sources is available in many basic electron optics texts.¹

The SEM and EPMA utilize a system of probe-forming lenses after the electron source in the column. These lenses focus the electron probe down to a diameter from a few nanometers to a few hundred nanometers. Electrostatic scan coils raster the electron beam over the surface of the sample. The incident high-energy electrons interact with the solid to produce signals, including secondary electrons, backscattered electrons, and characteristic x rays. These signals are detected electronically and processed to produce an image. The characteristic x-ray signal can be used to determine the chemical composition of a small volume, as small as 1 μm in diameter. The SEM does not require any post-specimen lenses since the sample is a bulk target and is therefore not electron transparent.

The conventional TEM uses a system of electromagnetic lenses which interact with the electron beam in a way analogous to the way in which ground glass lenses interact with visible light in an optical microscope. The electron beam is typically focused to a diameter of the order of micrometers. The electrons "flood" the sample and illuminate the entire area of interest. The electrons are transmitted through the sample and ultimately produce an image when they strike a fluorescent screen or photographic film. Contrast in the image is produced by one of several mechanisms. Most crystalline materials exhibit diffraction contrast; most amorphous materials, including most biological materials, exhibit absorption (amplitude) contrast.² After passing through the sample the electrons pass through a series of post-specimen lenses. Manipulation of these post-specimen lenses controls the magnification of the image and the choice of imaging mode, bright field (imaging with nondiffracted electrons) or dark field (imaging with a specific beam of diffracted electrons).

The modern AEM is a hybrid between the SEM and conventional TEM. A large number of modern AEMs, excluding the so-called dedicated STEMs,³ can in fact be operated as conventional TEMs. In the STEM mode the AEM rasters a point electron probe over the thin foil sample, exactly as in the SEM. The secondary electrons, backscattered electrons, and transmitted electrons can be collected and processed electronically and be used to produce "TV-like" images as with the SEM. If the beam raster is stopped and the beam placed at a point of interest the chemical composition can be determined by x-ray microanalysis and/or EELS. In the point mode it is also possible to perform electron microdiffraction. The post-specimen lenses in the AEM are primarily used to control bright-field and dark-field imaging with the transmitted electron signal. Contrast in the transmitted electron image is controlled by the post-specimen lenses.

Thin Foil X-ray Microanalysis

One consequence of the inelastic scattering events that occur when the high-energy incident electrons interact with the thin foil sample is the generation of characteristic x rays. These characteristic x rays can be used to perform qualitative and quantitative chemical analyses. Solid-state energy-dispersive spectrometers (EDS) are used almost exclusively to detect the x rays generated in thin foils in the AEM. Geometrical constraints and low x-ray count rate make the use of wavelength-dispersive crystals very difficult, although the first thin foil x-ray experiments were performed on a TEM equipped with diffraction crystals.⁴ One important limitation of x-ray analysis with an EDS system is the inability to detect elements with atomic numbers below that of Na ($Z = 11$). In the past few years this limitation has been somewhat overcome with the introduction of ultrathin window detectors, which allow one to detect the x rays from elements as light as carbon ($Z = 6$).⁵ The x-ray spectra generated from thin foil samples greatly resemble the x-ray spectra generated in bulk samples, but the x-ray intensity is much smaller due to the inherently lower rate of x-ray generation in thin foils. As a consequence, the accuracy and detectability limits in thin foil analysis are considerably poorer than in bulk sample analysis.⁶

If the foil is sufficiently thin, x-ray absorption and fluorescence effects can be neglected. If these effects can be neglected, the composition of the volume in which the x rays were generated can be related to the composition in that volume by the Cliff-Lorimer standardless-ratio relationship.⁴ For any two elements A and B, the composition ratio can be related to the characteristic x-ray intensity ratio by k_{AB} , the Cliff-Lorimer K-ratio, by

$$\frac{C_A}{C_B} = k_{AB} \frac{I_A}{I_B}$$

The constraining equation arises since the total of A and B must equal unity for an A-B binary sample. The value of k_{AB} can be determined experimentally from homogeneous samples of known composition or it can be calculated from physical constants including the ionization cross section and fluorescent yield.^{7,8} Much of the earliest work was standardized to the element Si. The k-factors were all expressed in terms of k_{ASi} . Figure 2 shows graphically the values of k_{ASi} for characteristic $K\alpha$ and $L\alpha$ x rays, respectively. This system of k-factor representation is actually quite convenient since any k_{AB} can be calculated from the ratio k_{ASi}/k_{BSi} . Referencing all elements to Si is convenient, especially for the analysis of geological materials. However, the Si reference is not sacred. Other investigators have referenced k-factors to other elements such as Fe⁹ and U.¹⁰ Although the preceding discussion referred specifically to a binary case, the procedure is readily extended to higher-order systems.

The standardless-ratio technique is easy to use and provides compositions by solution of a simple algebraic equation. Simple matrix algebra can be used to solve the equations even when the total number of elements is very large. The mathematical simplicity of this technique is in great contrast to the numerical iterative procedures associated with the ZAF (atomic number, absorption, fluorescence) correction required to reduce the x-ray data generated from bulk samples in the SEM or EPMA. The overriding caveat in the application of the standardless-ratio technique is the assumed absence of x-ray absorption and fluorescence effects. If these effects are significant, the standardless-ratio technique does not directly apply. Several criteria have been proposed to evaluate the significance of the effects in any given situation.^{7,12} If the effects are significant, corrections can be applied.^{9,11,12} However, these corrections result in numerical iteration of the Cliff-Lorimer equation and the solution can no longer be arrived at through simple matrix algebra.

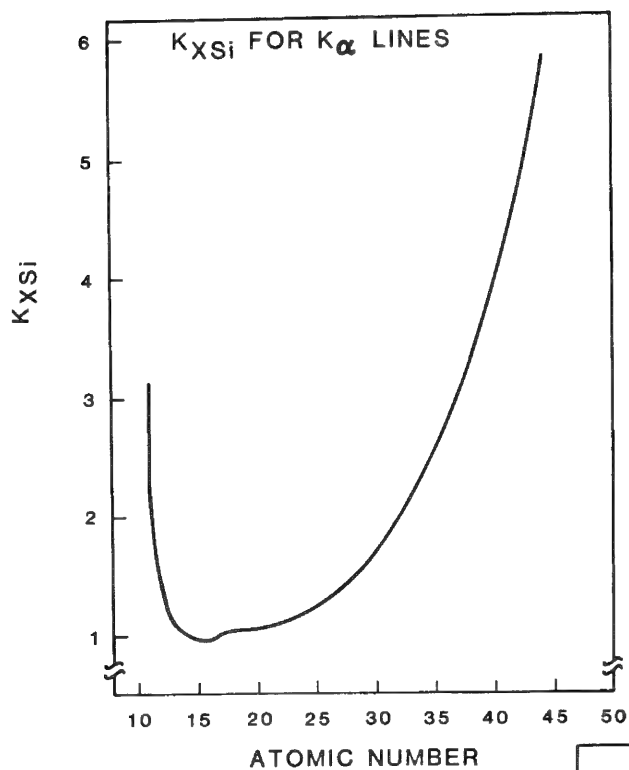
The principal advantage of x-ray analysis in thin foils relative to bulk samples is improved spatial resolution. In a bulk target, the volume of x-ray generation is defined by the electron scattering volume, which is essentially independent of the diameter of the incident electron beam. Due to these scattering effects, it is impossible to generate x rays from (and hence determine the chemical composition of) a volume much smaller than 1 μ m in diameter. Much better spatial resolutions, often better than 50 nm, are possible in thin foils because electron scattering is limited. Electron scattering in bulk samples versus thin foils and the influence of electron scattering on x-ray spatial resolution are shown schematically in Fig. 3. X-ray spatial resolution in thin foils can be estimated with analytical models,^{7,13} calculated by Monte Carlo techniques,¹⁴ or measured experimentally.^{6,8,10}

Electron Energy Loss Spectroscopy

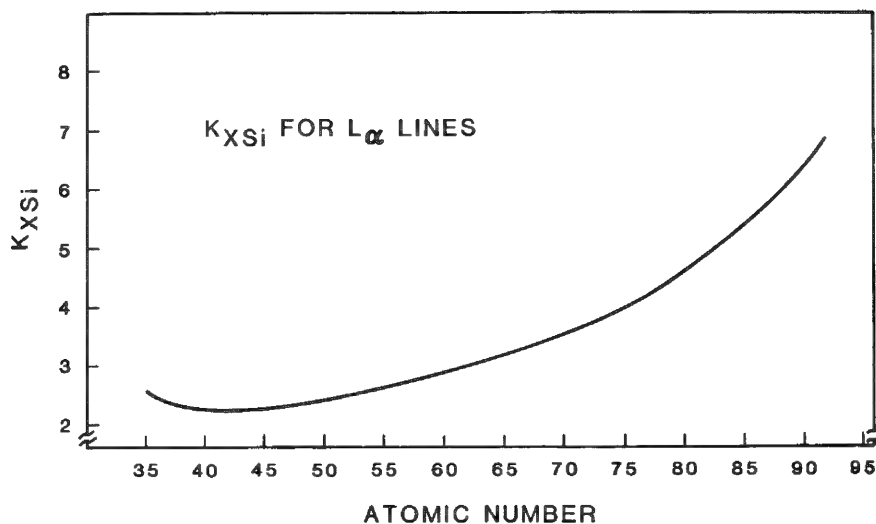
EELS studies the energy distribution of electrons which have been transmitted through the thin foil sample in an AEM. EELS, like x-ray microanalysis, is a technique that provides a method of identifying the elements present in the sample and further permits the quantification of the chemical composition. Unlike most EDS x-ray analyses, EELS is capable of detecting low-atomic-number elements. Ideally, one could detect hydrogen, but in practice elements with atomic numbers of 5 (boron) and greater are detectable.

When high-energy electrons pass through the thin foil they may undergo any one of several interactions. To describe these physical processes and understand how they are related to the properties of the specimen, it is instructive to examine the features of a typical EELS spectrum (Fig. 4).

Region 1, 0-10 eV, is the so-called "zero-loss" peak, which is the most intense portion of the EELS spectrum. It contains signals from three groups of electrons: (1) unscattered electrons which did not interact with the sample; (2) elastically scattered electrons which have been deflected by the nuclear charge of the atom; and (3) electrons which have generated "phonon excitations," or atomic vibrations in the sample. The zero-loss peak is of little direct value in microanalysis but is useful for calibration and normalization of EELS spectra.



(a)



(b)

FIG. 2.--Typical values of k_{AB1} for (a) characteristic K_{α} lines, (b) characteristic K_{β} lines.

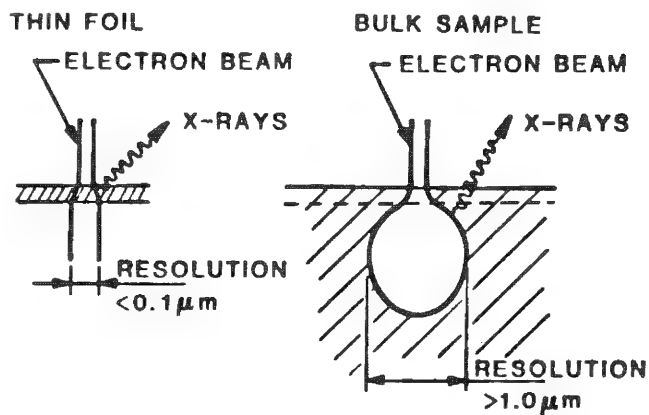


FIG. 3.--Electron-beam spreading in thin foils and bulk targets.

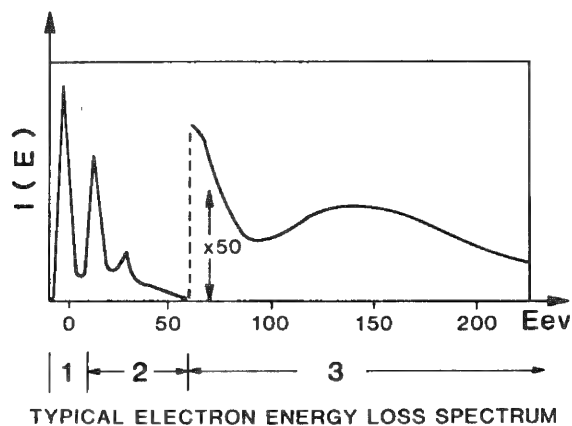


FIG. 4.-- Typical EELS spectrum: zero-loss (1), low-loss (2), and core-loss (3) regions are shown. Note scale amplification by $50\times$ in region 3.

Region 2, 10-60 eV, is the "low-loss" region. The low-loss peak is only 5-10% as intense as the zero-loss peak, but approximately 80% of the total transmitted electrons are contained in Regions 1 and 2. The structure in the low-loss region is due to direct electronic interactions between the incident electrons and the atomic electrons. The losses are due primarily to the excitation of electrons from the bound state including molecular orbitals and "plasmon excitations," which are interactions between the incident electrons and the "electron gas" in a metal. This region is of limited use in microanalysis, but plasmon excitations provide an accurate way to measure the thickness of the foil.

Finally, above 60 eV is Region 3, or the core-loss region. This region is quite weak and is often amplified on the viewing CRT (Fig. 4). Region 3 contains characteristic features, the core-losses due to inelastic interactions with the inner atomic shells, superimposed on a background intensity due to outer-shell excitations. As with characteristic x rays, the core losses are unique to the element in which they were generated and should be useful for qualitative chemical analysis. After background stripping, the integrated edge intensities can be used to determine the composition quantitatively. Careful examination of a core-loss edge will show a pre-ionization and extended fine structure (EXAFS) which provides information on the chemical bonding and crystallography of the sample.

EELS spectra are typically collected with a magnetic sector spectrometer mounted on the AEM below the fluorescent screen. The spectrometer discriminates among the electrons on the basis of their energy. The electrons are typically detected with a conventional scintillator-photomultiplier and processed by a multichannel analyzer (MCA).

Electron Diffraction

Of interest in the AEM is a special set of high-resolution electron diffraction techniques known as electron microdiffraction. Electron diffraction techniques in general are of use because they allow for the study of crystallographic features of the sample.

The oldest technique, also available in many conventional TEMs, is selected area diffraction (SAD). In SAD a special aperture, called the selected area aperture, is used. The aperture limits the area of the sample that contributes to the diffraction pattern. SAD can routinely be used to examine areas as small as 1 μm in diameter. However, smaller diffracting areas may be studied, but always with overlapping diffraction patterns from neighboring areas. Spherical aberration prevents the examination of areas smaller than 500 nm in diameter. However, several microdiffraction techniques are available to examine areas smaller than 500 nm in diameter.

The microdiffraction technique that offers the smallest spatial resolution is convergent-beam electron diffraction (CBED). In some AEMs this technique can be performed by simply focusing of the beam to a small spot and placing the beam at the position of interest. In most AEMs the technique is performed in the STEM mode in which the probe raster is stopped and the beam placed on the position of interest. The lens configuration used for CBED avoids difficulties with spherical aberration. Spot sizes as small as 3 nm are possible even with W-hairpin electron sources. Beam spreading in the thin foil usually limits the spatial resolution of the technique. A typical minimum area that could be examined with CBED is 30-50 nm. In some older AEMs the CBED technique is limited by sample contamination effects.

A second microdiffraction technique available in many AEMs is the focused-aperture method developed by Reicke.¹⁵ In this technique the second condensor aperture is used to limit the area accessible to the electron beam. The technique is not limited by spherical aberration effects and allows for the examination of areas as small as 50 nm.

The final microdiffraction technique of interest is the "rocking-beam technique."¹⁵ In the rocking-beam technique the beam is pivoted off the surface of the thin foil sample by the scan coils. Bright-field and dark-field reflections appear sequentially over the STEM detector located at the base of the AEM. The diffraction pattern is collected and displayed on the CRT, unlike in all the previously described techniques, in which the diffraction pattern is displayed on the fluorescent screen and recorded on photographic film. The spatial resolution of the rocking-beam technique can be as small as 50 nm.

Applications and Summary

The modern AEM is a hybrid instrument with the capabilities of both the conventional SEM and EPMA and the conventional TEM. With the large number of electron detection systems

on the AEM it is capable of imaging with transmitted electrons like the TEM and with secondary electrons and backscattered electrons like the SEM. Through the use of solid state x-ray detectors and EELS, the AEM can perform quantitative chemical analyses. The spatial resolution in these techniques is better by at least a factor of 20 than conventional analyses as performed in the EPMA. However, the sensitivity and detectability limits of chemical analysis in the AEM are about one order of magnitude larger than EPMA chemical analyses. Since the samples are thin foils, the AEM can perform crystallographic studies of materials with electron-diffraction techniques. Through microdiffraction techniques, the spatial resolution of crystallographic studies can be greatly improved relative to the conventional TEM.

The range of materials, including biological materials, that can be studied with the AEM is extensive. Identification of the chemical composition and crystallography of small particles is a widely used capability. The measurement of diffusion profiles over short distances and studies of grain boundary segregation are two additional common applications.¹⁶

General References

D. C. Joy, A. D. Romig Jr., J. I. Goldstein, and J. J. Hren, Eds., *Elements of Analytical Electron Microscopy*, New York: Plenum Press, 1984.

References

1. J. I. Goldstein et al., *Scanning Electron Microscopy and X-ray Microanalysis*, New York: Plenum Press, 1981, 19-31.
2. J. W. Edington, *Practical Electron Microscopy in Materials Science*, New York: Van Nostrand Reinhold, 1976, 109-116.
3. L. M. Brown, "Recent experiences with dedicated STEM," *Analytical Electron Microscopy Workshop*, Cornell University, 1978, 9-10.
4. G. Cliff and G. W. Lorimer, "The quantitative analyses of thin specimens," *J. Microsc.* 103: 203, 1975.
5. L. E. Thomas, "Microanalysis of light elements with an ultrathin window x-ray spectrometer," *Proc. 38th EMSA Meeting*, 1980, 90-91.
6. A. D. Romig Jr. and J. I. Goldstein, "Detectability limit and spatial resolution in STEM x-ray analysis," *Microbeam Analysis--1979*, 124-128.
7. J. I. Goldstein et al., "Quantitative x-ray microanalysis in the electron microscope," *SEM/1977*, 315-326.
8. A. D. Romig Jr., *X-Ray Microanalysis in the Analytical Electron Microscope*, SANDIA Report SAND82-2938, 1983.
9. J. E. Wood et al., "Experimental and theoretical determination of k_{AFe} factors," submitted to *J. Microsc.*, 1984.
10. A. D. Romig Jr., "Quantitative x-ray microanalysis of uranium alloys with the AEM," to be published in *J. Microsc.*, 1984.
11. R. Tixier et al., "Principles, limits and statistical evaluation of quantitative x-ray analysis," in *Quantitative Microanalysis with High Spatial Resolution*, London: The Metals Society, 1981, 15-23.
12. M. E. Twigg and H. L. Fraser, "A comparison of two models for the characteristic x-ray fluorescence correction in thin foil analysis," *J. Microsc.* 133: 61, 1984.
13. S. J. B. Reed, "The single-scattering model and spatial resolution in x-ray analysis of thin foils," *Ultramicroscopy* 7: 405, 1982.
14. D. E. Newbury and R. L. Myklebust, "A Monte Carlo electron trajectory simulation for AEM," *Analytical Electron Microscopy--1981*, 91-98.
15. J. B. Warren, "Microdiffraction," in J. J. Hren et al., Eds., *Introduction to Analytical Electron Microscopy*, New York: Plenum Press, 1979, 369-385.
16. D. B. Williams and J. W. Edington, "Practical electron microscopy in materials science: Analytical electron microscopy," *Norelco Reporter*. 28: 2, 1981.

1 Destructive Laser Microprobe

STRUCTURE OF METAL-COORDINATED POLYMERS: LASER DESORPTION OF POLY(4-VINYLPYRIDINE) AND POLY(4-VINYLPYRIDINE)-METAL COMPLEXES

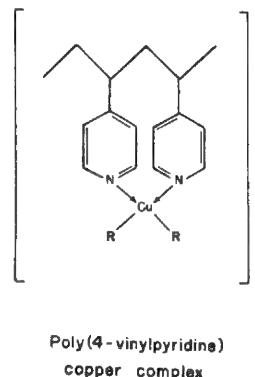
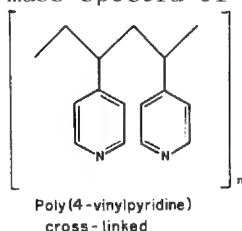
R. A. Fletcher and A. J. Fatiadi

Poly(4-vinylpyridine) (PVP) beads and PVP-metal complexes are being tested at NBS as possible column packing for the affinity chromatography of proteins. These 5-500 μ m-diameter nonvolatile solid particles were analyzed by laser desorption (LD) in a LAMMA 500.¹ The beads were mounted on a nickel TEM grid with no support film. Analysis was conducted by use of the 32 \times objective microscope lens and laser energy densities on the particle's surface of approximately 1 J/cm² (0.1-0.4 μ J laser energy). These values are similar to the energy levels used for surface analysis of asbestos fibers.² Only the edge of the sample PVP bead was irradiated.

Samples of the unwashed and aqueous-HCl treated PVP beads were analyzed by LD and the mass spectra of each were not found to be significantly different. The PVP chain upon laser ionization gives fragmentation patterns similar to polystyrene.³ Most of the fragment ions appear in the positive ion spectrum; the (pyridine + H)⁺ and (pyridine + C_mH_n)⁺ species from the polymeric backbone are present.

In the PVP polymer, the pendant moiety is thought to be exposed from the particle's surface and thus allows strong metal coordination to the pyridine nitrogen atoms. Copper ions have been added to form what is believed to be the coordinated PVP-Cu²⁺ complex,

where the copper ion extends out from the page as it would on the bead's surface and where R ligands can be H₂O, Cl⁻, Br⁻, F⁻, etc. Our efforts are directed toward verification of the molecular structure of these complexes. Laser desorption was performed in the same manner as described for uncomplexed PVP. The spectra contain Cu⁺ and PVP fragments, and there is some evidence of the Cu²⁺ molecular complex. Isotopic substitutions (with Cu⁶⁵) have been made to the above complex. Crystalline copper tetrapyridine sulfate [(C₅H₅N)₄Cu]SO₄ and 2,2' bipyridine copper complex have been analyzed by LD to aid in the molecular fragment identification. The mass spectra of 2,2'-dipyridyl and PVP copper complexes have been compared and our current work on these new types of immobilized organometallic complexes is under further study.



References

1. Certain commercial equipment, instruments, or materials are identified in this paper. Such identification does not imply recommendation or endorsement by the National Bureau of Standards, nor does it imply that the materials or equipment identified are necessarily the best available for the purpose.
2. J. K. De Waele, E. F. Vansant, P. Van Espen, and F. C. Adams, *Anal. Chem.* 55: 671-677, 1983.
3. J. A. Gardella and D. M. Hercules, *Fresenius Z. anal. Chem.* 308: 297-303, 1981.

The authors are with the Center for Analytical Chemistry at the National Bureau of Standards, Washington, DC 20234.

LASER MICROPROBE MASS SPECTROMETRY OF ORGANOPHOSPHOROUS COMPOUNDS

J. J. Morelli and D. M. Hercules

The analysis of environmental samples often imposes serious limits on analytical techniques. The problems environmental samples introduce are that their analytes occur in low concentrations and degrade in the biosphere. Furthermore, it is often necessary to acquire information on an analyte within a complex matrix. The advent and subsequent development of "soft ionization" mass spectrometry have given rise to analytical methods for environmental samples, especially biocides. These "soft ionization" techniques have the advantage of obtaining molecular weight information; however, the development of an organic microprobe would be of further value in studying biocides. A successful organic microprobe could be used both to identify and spatially resolve any component in a system. Laser Mass Spectrometry (LMS) with its spatial resolution of $\sim 4 \mu\text{m}$ represents a promising approach to this problem. A useful microprobe technique requires spatial resolution along with the capability of providing data to identify unequivocally the species of interest. The potential of LMS for analyzing organophosphorous (OP) pesticides has been evaluated using other mass spectral techniques as a basis for comparison.

Experimental

Mass spectra were obtained by a Leybold-Heraeus Laser Microprobe Mass Analyzer, LAMMA-1000, and a modified 3M Secondary Ion Mass Spectrometer, Model 610. These instruments are described elsewhere.¹⁻² LMS spectra were recorded with a Biomation transient recorder. Transfer and further manipulation of LMS data were performed with an HP-1000 series data system. A 3M digital processor was used for collecting SIMS data.

Pesticide samples were obtained from the Environmental Protection Agency Repository in Research Triangle Park, N.C. The purity of each sample was reported to be 95-99%; 300 MHz proton NMR was used for purity confirmation. Unless otherwise indicated, each sample for LMS study was placed on a piece of double-sided tape, which in turn was mounted on zinc foil. SIMS samples were prepared by evaporation of a methanol solution containing the sample on zinc foil.

Results

Most organophosphorous (OP) pesticides can be described by a general structural formula (Fig. 1), in which Z can vary from small aliphatic chains to heterocyclic aromatic ring systems; it may also contain various moieties such as halogens, carboxylic acids, and amines. R normally refers to small aliphatic groups.

The low molecular weight region of both positive and negative LMS spectra was heavily populated with ions which were difficult or impossible to interpret. For this reason, most spectra were obtained by sampling of the mass spectrum only above m/z 180.

Table 1 is a summary of the more important observations made from the LMS data, and also shows that the most prominent feature in the spectra was the presence of group transfers. Transfers of small alkyl and alkoxide groups (R^+ and OR^-) were seen most frequently, whereas the larger substituent transfers (Z^+) were rarely seen. Table 2 is a summary of generalized group transfers seen in LMS spectra of OP compounds.

To observe cation/anion transfers, a salt (KBr) was added to samples dissolved in methanol. The solution was then evaporated on gold foil. Cation/anion transfers were advantageous when mixtures were studied. To examine the utility of LMS for the analysis of OP pesticide mixtures, two similarly structured compounds, azinphos methyl and azinphos ethyl, were

The authors are at the Department of Chemistry, University of Pittsburgh, Pittsburgh, PA 15260.

Positive SIMS spectra of several pesticides were obtained for comparison. The positive spectra of potassium diethyl thiophosphate (KDEPT) showed a base peak at m/z 209, due to $[M + H]^+$. Also seen in SIMS spectra were the low mass fragments. Fragmentation in SIMS was significantly different from LMS. This result is contrary to observations reported for LMS/SIMS studies in other systems.⁴ Table 3 is a summary of the important observations made in SIMS studies of several OP pesticides.

Discussion

For further comparative purposes, review of previous reports on chemical ionization (CI) was found to be useful. The results are summarized as follows.

Varying the CI reagent gas has allowed researchers to categorize OP pesticides by their $[M - OZ]^+$ or $[M - Z]^-$ fragments.⁵⁻⁶ They are referred to as "group specific fragments" and are used to identify the class of OP pesticides present. Diethylphosphorothionates, diethylphosphorodithionates, and diethylphosphorothiolates are few examples of the variety of OP pesticide classes investigated. Work has also been focused on attempting the unequivocal determination of specific OP pesticides present in a sample.⁶⁻⁷ The procedure involves the proper selection of reagent gas, isobutane for positive ion chemical ionization (PICI) and dichloromethane for negative ion chemical ionization (NICI). Intense $[M + 1]^+$ peaks were seen for PICI, and frequently, chloride attachment in NICI. Bush et al., in a comparison of five CI ionization sources, has noted the variation of spectra with experimental conditions.⁸

SIMS has demonstrated the potential for providing both quasimolecular ions and group-specific fragments. Furthermore, SIMS spectra show a greater tendency to form odd-electron ions, which are extremely rare in LMS.

Although while LMS does not yield group-specific fragments, with the use of selected salts, unequivocal determination of OP pesticides is possible (Fig. 2). LMS also offers the added advantage over SIMS that charging effects are much less severe. This last point is significant when one considers the application of any technique for analyzing nonconductive organic sample in vitro.

From the work done with LMS and SIMS, the following useful comparisons can be made between these and other mass spectral techniques. The inherent advantage of both LMS and SIMS over CI is the capability to study materials of low volatility. LMS is more practical than SIMS for studying organic materials on nonconductive substrates since charging effects are less severe.

Conclusion

Although group-specific fragments are rarely seen in LMS, group transfers provide the information necessary to identify the OP compound present. Thus, LMS has proved successful for analyzing OP compounds. Other solid state mass spectral techniques have been applied to OP pesticides (SIMS, FDMS⁹), yet none offers both the spatial resolution and ease of analysis that LMS can provide. Charging effects in obtaining LMS spectra of OP compounds have proved to be minimal. This work, in combination with the inherent spatial resolution of LMS, justifies further investigation for determining the capabilities of LMS for microprobe analysis of OP pesticides on organic substrates.

References

1. H. J. Heinen, S. Meier, and H. Vogt, *Intern. J. Mass Spectrom. Ion Phys.* 47: 19-22, 1983.
2. J. A. Gardella Jr. and D. M. Hercules, *Anal. Chem.* 52: 226-232, 1980.
3. R. J. Conzemius and J. M. Capellen, *Intern. J. Mass Spectrom. Ion Phys.* 34: 197-271, 1980.
4. R. D. Macfarlane, *Acc. Chem. Res.* 15: 268-275, 1982.
5. H. J. Stan and G. Kellner, *Biomed. Mass Spec.* 9: 483-492, 1982.
6. H. J. Stan, *Z. anal. Chem.* 287: 483-492, 1977.
7. K. L. Busch, M. M. Bursey, J. R. Hass, and G. W. Sovocool, *Applied Spectroscopy* 32: 388-399, 1978.
9. H. R. Schulten and Si-En Sun, *Intern. J. Environ. Anal. Chem.* 10: 247-263, 1981.

INTERPRETATION OF ION KINETIC ENERGY DISTRIBUTIONS IN LASER MICROPROBE MASS ANALYSIS

Thad Mauney and Fred Adams

Ions formed in laser microprobe mass spectrometers have been reported to have energies from 5 to 30 eV, which are influenced by chemical and laser intensity effects.¹ We have developed a method, described in detail elsewhere,² for measurement of the kinetic energy distributions of ions formed in the LAMMA 500, made by Leybold-Heraeus (Cologne), which employs an ion reflector that precludes kinetic energy measurement directly from time of flight. In our procedure the ion reflector is used as an energy cutoff filter, and a cumulative distribution curve is obtained by varying the cutoff level over the energy domain of interest as repetitive spectra are acquired on a homogeneous specimen. The distribution curve accumulated reveals both the shape of the distribution and its center relative to the accelerating voltage. In this paper we discuss some of the processes that occur in the ionization region, which can be contributing factors to the specific kinetic energy distributions observed.

Results

In the examination of a vapor-deposited carbon film (Atomic Energy of Canada, Ltd., Ottawa) ten spectra were acquired at each reflector potential over the range from +40 to -100 V. The means of their integrated peak intensities³ form a cumulative distribution curve; for example, the negative carbon cluster ions from $m/e = 24, (C_2^-)$ to $m/e = 84, (C_7^-)$ (Fig. 1). To locate the medians of these distributions the Weibull function was fit to the data by nonlinear regression (simplex algorithm) and found to represent the data acceptably;² we do not interpret this result as the statistical form of the distributions. A 7.0V correction of the zero potential to compensate instrumental effects was established by use of a continuous beam of Na^+ ions emitted from a tungsten filament thermal source. Median kinetic energies obtained by this procedure for the various ions derived from elemental carbon foil are plotted in Fig. 2.

Processes Contributing to Kinetic Energy Distributions

The observed kinetic energy distributions can be decomposed into two major contributions: the distribution of initial velocities of ions due to processes in the laser plasma, and the distribution of the fraction of the acceleration potential imparted to each ion. The initial velocity of an ion due to plasma processes includes contributions from the following mechanisms.

1. Thermal collisions in the vapor phase, indicated schematically in Fig. 3 (Figs. 3 to 7 from Ref. 2), lead toward a Maxwell-Boltzmann distribution of velocities, to which temperatures estimated from local thermal equilibrium (LTE) model calculations should apply. These temperatures range from around 4900 K to around 13 000 K⁴⁻⁶ or 0.4 to 1.1 eV, but the widths of distributions observed in these experiments and others¹ exceed such values.

2. Hydrodynamic expansion of the vapor cloud results in high translational energies as the energy of random thermal motion and internal degrees of freedom are converted into linear motion. This process reduces the collisional temperature of the vapor and produces a kinetic energy distribution with a median greater than zero.

The authors are with the Department of Chemistry, University of Antwerp (UIA), B-2610 Wilrijk, Belgium. Eric Michiels of the UIA is thanked for critical discussions of the work. This research was conducted with the support of the Belgian Interministerial Commission on Science Policy through grant 80-85/10.

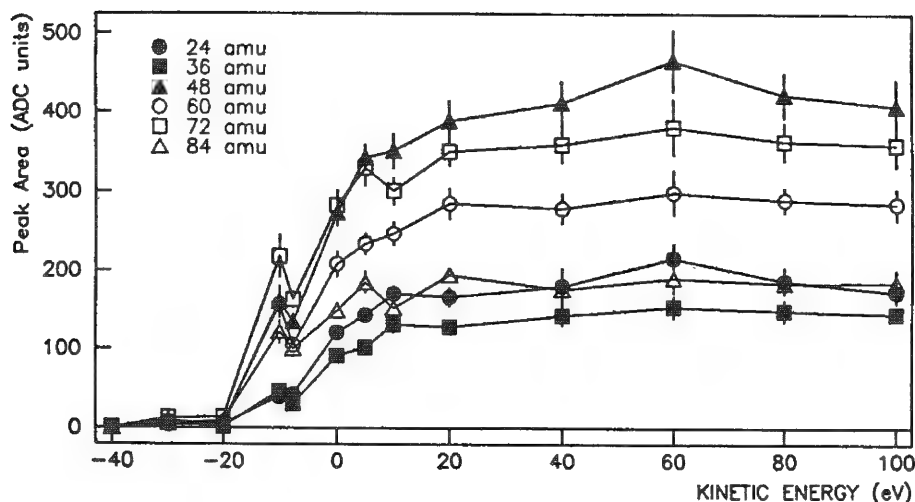


FIG. 1.--Intensities of various ions in negative spectra of carbon film as a function of reflector potential.

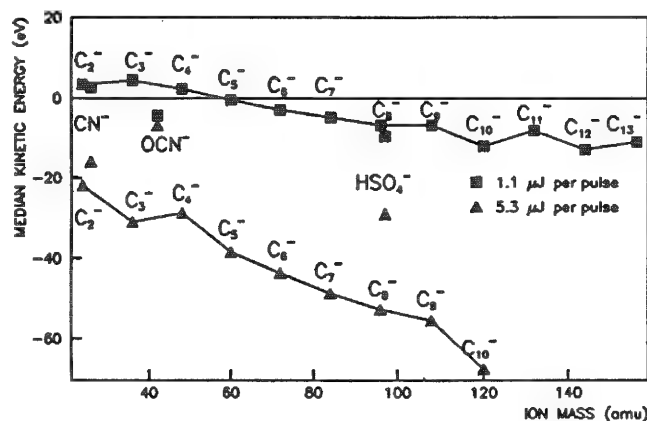


FIG. 2.--Median kinetic energies of negative ions derived from carbon foil; laser energies per pulse are approximate, TOF 3000 V, lens 1070 V, 32× objective lens.

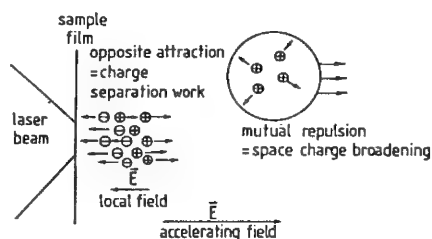


FIG. 4.--Velocity alteration by charge-charge interactions.

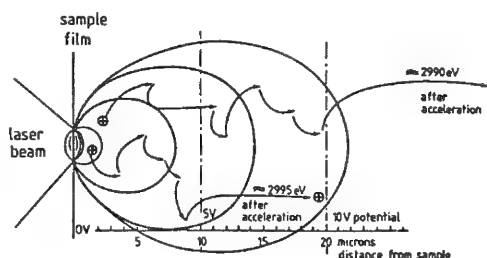


FIG. 6.--Loss of energy through collisions.

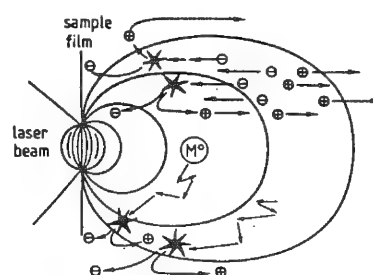


FIG. 3.--Initial velocity imparted by collisional processes.

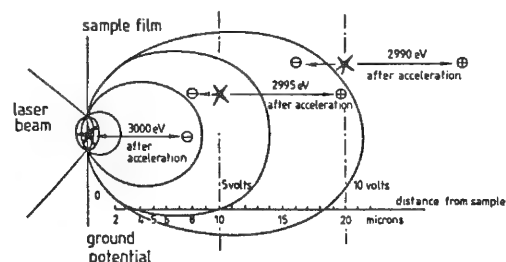


FIG. 5.--Incomplete acceleration due to down-field ion formation.

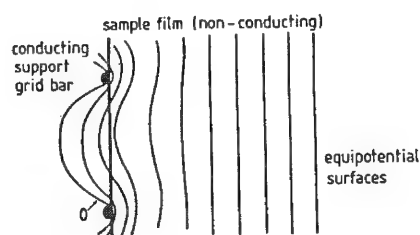


FIG. 7.--Deviation of potential at sample.

3. The space-charge effect of mutual repulsion between like-charged particles in the plasma (Fig. 4) tends to spread the velocities of ions so that the kinetic energy distribution becomes broader. This effect is proportional to ion density, and so would be most significant prior to plasma expansion. It could also result in concentration dependence.

4. Counterflow of the two polarities of charged species in the extracting field, included in Fig. 3, can cause some collisions to occur between the polarity not sampled (negative charges in the case of a positive ion spectrum) and other ions or neutrals. When such collisions result in ion production, a large fraction of the product ions can have velocity in the negative direction, which leads to distributions of energy with low or "negative" medians.

Extraction of ions from the source region may not impart the full potential energy to all of the ions for a variety of reasons. In the LAMMA 500 the full accelerating potential is constantly present in the ion-formation region, a situation that differs from pulsed extraction TOF spectrometers and from sources in which ions drift to the main slit due to thermal velocity or a small repeller potential. Mechanisms leading to incomplete acceleration include at least the following.

1. The position in space at which an ion is formed (Fig. 5) controls the potential through which it will be accelerated. If ions are formed by some process--collisional, unimolecular, or photolytic--after the precursor has drifted some distance downfield (toward the spectrometer), then the ion is accelerated only by the remaining part of the potential and the result is an apparent deficit of energy, or a "negative" initial kinetic energy.

2. Similarly, as indicated in Fig. 6, ions may undergo collisions as they traverse the vapor formed from the sample and lose energy of acceleration, and so appear with less than the full acceleration energy. After acceleration through only a few microns an ion has received more energy than the ionization potential of most elements, so these collisions could also contribute to downfield ion formation in the sense of the previous mechanism.

3. Deviation of the surface of zero voltage from the plane of the sample causes the entire vaporization and ionization process to occur at a locus from which acceleration will be incomplete. As illustrated in Figure 7, if the sample particle stands on a nonconducting film across a 100 μ m grid opening, electrostatic calculations predict a perturbation of about 3 V. Greater deviations can result if the insulating sample film accumulates static charge and so places the surface at some high and unknown potential.

4. If conductance of the sample support is low, collection of counter-ions (electrons and negative ions in the case of a positive-ions spectrum) can result in temporary accumulation of charge in the sample support near the microplasma, and so shift the median of the kinetic energy distribution by altering the potential through which ions are accelerated. The magnitude of this effect depends on the materials used, up to the static-charge case mentioned above. The sense of the effect is always toward reduction of the acceleration, i.e., an energy deficit.

5. The space-charge effect of attraction of the oppositely charged particles being separated from one another also reduces the effectiveness of the accelerating field (Fig. 4). As bunches of ions are separated, the work done is analogous to work done to separate the plates of a capacitor. This merges into the previous process as the counter-ions collide with the support and are conducted away in the solid.

6. Collision of ions with the accelerating electrode can deplete the charge there and briefly shift its potential. Zelenin et al.⁷ identified this as an important contribution to energy spread in spark source mass spectrometry; however, it is unlikely to be important in the LAMMA 500 because the entire drift tube forms the accelerating electrode.

Interpretation of Results

The trend among carbon ions plotted in Fig. 2 toward more negative kinetic energies for larger clusters suggests some possible interpretations for the distributions observed. The fact that different species possess different median energies indicates that the observed median is not a result of any process applying equally to all ions, such as the deviation of the accelerating potential, or a thermal-equilibrium kinetic-energy distribution. Species such as CN^- , OCN^- , and HSO_4^- , which lie off the trend of the carbon clusters C_n^- , demonstrate that the effect is not purely mass related, but is in some way chemically influenced. The

observation that many of the dominant species in the spectrum have distribution medians at negative values indicates that the occurrence of negative medians is not the result of a process that can produce only minor species such as counterflow collisions producing ions with negative net velocity. That leaves as reasonable possibilities incomplete acceleration due to the locus of ion formation, or energy-reducing collisions. For the actual dimensions involved, a deficit of 10 eV would imply a drift of only 20 μm through the 0.5V/ μm field prior to ionization or effective escape from the dense region. At present we cannot distinguish unambiguously the effects of positions of ion formation from the positions of collisions. The trend toward more negative values for larger clusters suggests, but does not prove, that if the dominant effect in shifting of energy distributions is in fact the position of ion formation, then the larger clusters are formed by recombination as the plasma cools rather than being formed initially and fragmenting as collisions proceed.

Conclusion

Kinetic-energy measurements are valuable sources of information about the plasma processes that occur in the LAMMA ion source. In this area much additional study will be required to make an adequate characterization of the system. In addition to the study of ion-formation processes, the kinetic energy measurement has practical applications in LAMMA analysis, such as the discrimination of chemically different species, or the removal from the spectrum of certain undesired ions. Measurement of kinetic energies has also allowed us to resolve the previously confusing dependence of spectral intensity on the einzel-lens potential. Results in this area are encouraging and lead to numerous questions, the answers to which should lead to improvement in the interpretability and reliability of practical LAMMA analysis.

References

1. F. Hillenkamp, E. Unsöld, R. Kaufmann, and R. Nitsche, *Appl. Phys.* 8: 341-348, 1975.
2. T. Mauney and F. Adams, "Ion kinetic energy measurement on laser induced plasmas in laser microprobe mass analysis (LAMMA), Part 1: Methodology," *Intl. J. Mass Spec. Ion Proc.*, in press.
3. Calculated with LAM, a FORTRAN program for LAMMA 500 control and data processing on a DEC SLI-11 minicomputer, available, with user manual, from one of the authors (T. Mauney), unpublished.
4. N. Fürstenau, *Fresenius Z. anal. Chem.* 308: 201-205, 1981.
5. U. Haas, P. Wieser, and R. Wurster, *Fresenius Z. anal. Chem.* 308: 270-273, 1981.
6. P. Surkyn and F. Adams, *J. Trace and Microprobe Techniques* 1: 79-114, 1982.
7. A. E. Zelenin, A. N. Pustovit, and G. G. Sikharulidze, *Sov. Phys. Tech. Phys.* 25: 1374-1379, 1981.

LASER-INDUCED ION MASS ANALYSIS BY USE OF THE LIMA-2A

Trevor Dingle and B. W. Griffiths

The laser-induced ion mass analyzer (LIMA-2A) manufactured by Cambridge Mass Spectrometry Ltd. utilizes an Nd:YAG, Q-switched laser that may be operated at twice the fundamental laser frequency (2f or 532nm wavelength) and four times the fundamental frequency (4f or 266nm wavelength). Thus, since the laser focusing (and viewing) objective lens is a Cassegrain reflecting lens¹ that does not suffer from chromatic aberrations or cutoff, 2f and 4f operation is possible. Most of the early work on LIMA has been at the 532nm (2f) wavelength. However, we have recently begun to use the 266nm (4f) wavelength more frequently, particularly because of the superior results it yields for organic samples. In this paper we describe some results we have obtained at 4f and contrast them with our previous experience at 2f, emphasizing the effect of the laser wavelength on the general performance of LIMA, before we discuss some results obtained on organic specimens.

Spatial Resolution

From simple diffraction theory, it would be expected that the 4f laser radiation should produce a smaller focused spot on the specimen. The 18× magnification Cassegrain objective used in LIMA-2A has an F number of approximately 1.5 and, accordingly, a focal diameter of less than 0.5 μm should result at 4f operation. However, as the physical properties of the sample ultimately limit the crater size produced, it is interesting to compare crater sizes obtained at 2f and 4f operation.

Typically, at 2f operation, with a steel sample at laser power densities sufficiently high to insure uniform ionization efficiency of the elements detected, a main crater just under 2 μm in diameter is produced.¹ In addition, an appreciable volume of material explodes out, recondenses on the sample, and extends out to a diameter of approximately 6 μm . We now find at 4f operation (Fig. 1), again at power densities sufficient for uniform elemental ionization, a main crater around 1 μm in diameter is produced with an exploded material diameter of approximately 3-4 μm . This result is not the ultimate spatial resolution achievable at 4f by means of the Cassegrain lens. On thin foil samples we can produce hole diameters of around 0.7 μm at laser power densities sufficient for good analytical results. Thus, our experience suggests that 4f operation does indeed yield higher analytical spatial resolution than 2f operation.

Mass Resolution

The laser-solid ionization process is still not fully understood, especially as to the precise influence of parameters such as laser power density and wavelength. However, one would expect the shorter-wavelength (and higher-energy) photons used at 4f to ionize high ionization potential elements more efficiently. Thus, it would seem that 4f operation offers the possibility of achieving similar sensitivities to 2f for certain elements but at a lower laser power density. Since the energy spread for the laser-generated ions decreases at lower laser power density, 4f operation has a lower energy spread of ions than 2f at the same elemental sensitivity. As energy spread, and hence time uncertainty, limit the mass resolution of the time-of-flight mass spectrometer used, we might expect better resolving power at 4f operation, particularly when looking for elements that are difficult to ionize, such as carbon, oxygen, and nitrogen. Although we have not yet completed a systematic investigation of this area, it is clear that in certain circumstances 4f irradiation provides improved spectral resolution for a given sensitivity on specific samples.

The authors are with Cambridge Mass Spectrometry Ltd., Cambridge Science Park, Milton Road, Cambridge, England CB4 4BH. They thank Dr. John Myatt of ICI Research Centre, Runcorn, England, for his collaboration in producing the LIMA organic results shown in this paper.

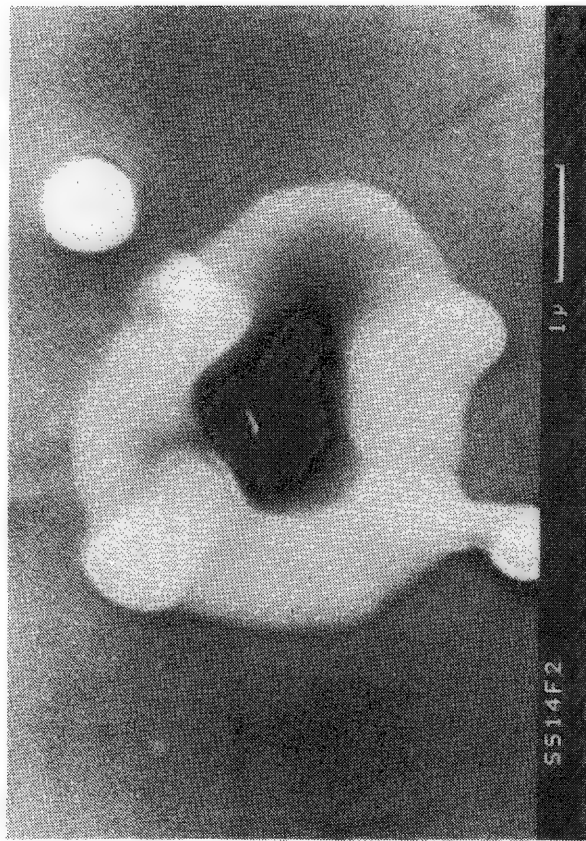


FIG. 1.--Single-shot 266nm-wavelength laser crater in stainless steel.

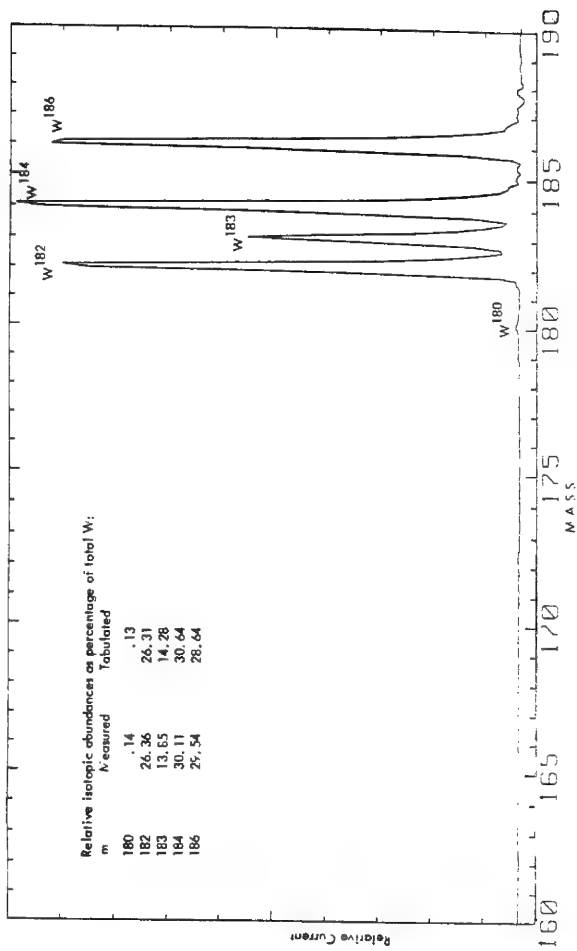


Fig. 2.--Tungsten isotopes.

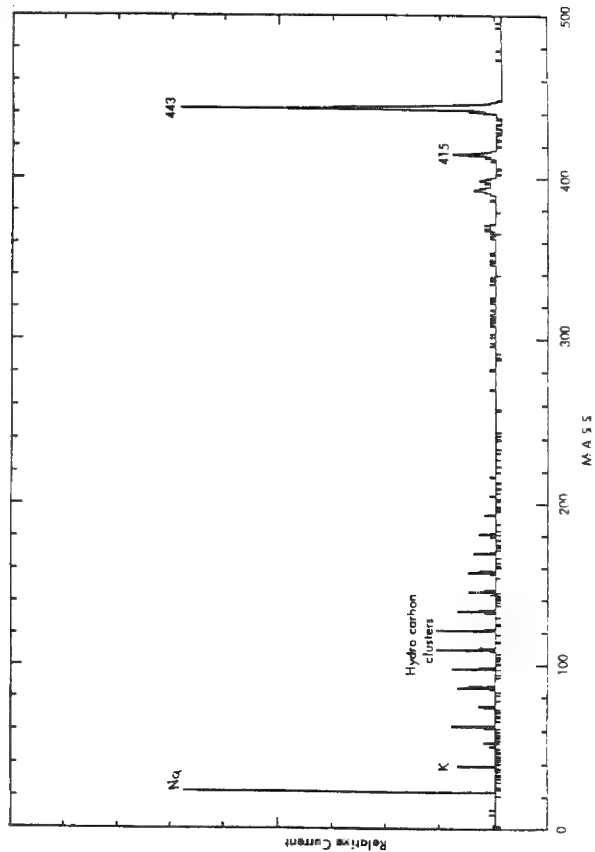


FIG. 3.--Positive-ion spectrum at 2f from rhodamine B.

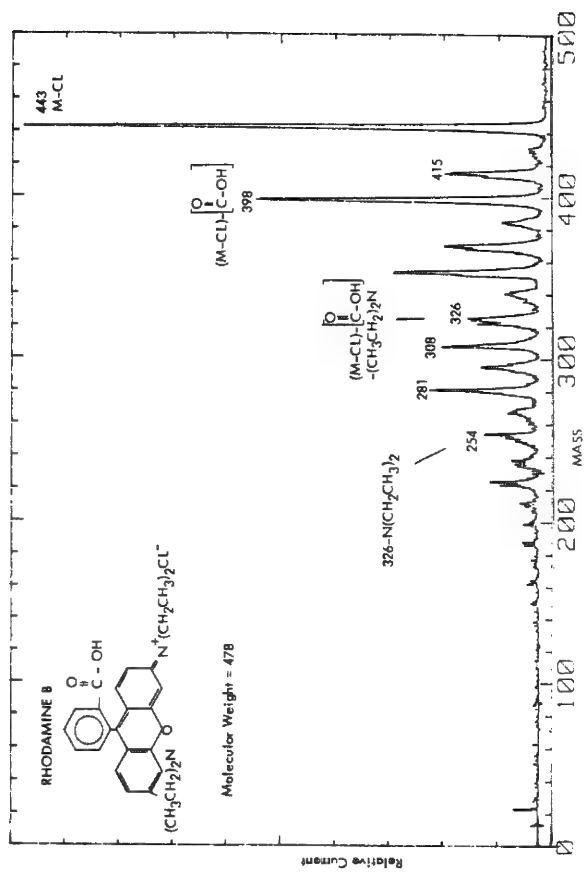


FIG. 4.--Positive spectrum from LIT-A at 4f.

Sensitivity

The practical sensitivity at 4f tends to be superior to 2f not because the ultimate ionization efficiency for all elements is better, but rather that, since the ionization efficiency at a given laser power density is more uniform for all the elements, the detection of a particular low-level element in a matrix is not so masked by large signals from an easily ionized matrix. Typically, detection limits in the 1-10ppm range are obtained for most elements with sub-ppm achievable for very easily ionized elements such as the alkali metals.

Reproducibility

The Nd:YAG laser pulse-to-pulse stability is better at 2f operation than at 4f. Thus, although the reproducibility of spectra depends on a large number of other factors, including the morphology of the sample and the accuracy of the laser focus position, it is interesting to see whether 4f operation is indeed less reproducible. We typically use a homogeneous sample containing elements such as iron and chromium, and ratio the areas under the prominent isotopes of each element. In practice, we find we can obtain a standard deviation of better than 8% for 9 laser shots at 4f, which is similar to 2f operation. Moreover, the accuracy of isotope ratios is not noticeably different at 2f and 4f. Figure 2 shows a typical isotope ratio spectrum obtained at 4f.

Organics

One of the major reasons for using 4f is the promise of achieving better results from organic molecules, since many of them have ionization potentials of around 10 eV and also many are relatively nonabsorbing in the visible. Figures 3 and 4 show positive ion spectra from Rhodamine B, an organic indicator dye, at 2f and 4f, respectively. In both cases we have found it necessary to use fine control of the laser power to get reproducible fragmentation and molecular information that is reasonably close to that achieved in electron impact mass spectra. It can be seen that the 4f operation does produce superior organic spectra. Figures 5, 6, and 7 show other typical positive-ion organic spectra, all at 4f. Figure 5 shows a spectrum of hexaphenyl, a relatively strong ring compound; Fig. 6, salphen, a more complex ring compound; Fig. 7, tetramethyltartaramide, a chain structure; and Fig. 8, diphenoxy benzene, a chain ring compound.

One interesting result we have recently obtained on LIMA at the suggestion of (and in conjunction with) Drs. Jopling and Gohlke of Eastman Kodak, is that nonionic organics can be ionized in solution with glycerine, and such substances would then yield a reproducible molecular peak. Thus a technique that is applied in Fast Atom Bombardment Mass Spectrometry has successfully produced molecular parent ion peaks at masses above 600 in the laser microprobe.

Conclusion

We still feel that a laser-induced ion mass analyzer should be constructed to operate at 2f and 4f because it may well be that 2f does produce superior results for some substances. However, our recent experience suggests that 4f has superior characteristics for a wide range of analysis problems.

References

1. C. A. Evans Jr., B. W. Griffiths, Trevor Dingle, M. J. Southon, and A. J. Ninham, "Microanalysis of bulk samples by laser-induced ion mass analysis," *Microbeam Analysis--1983*, 101-105.

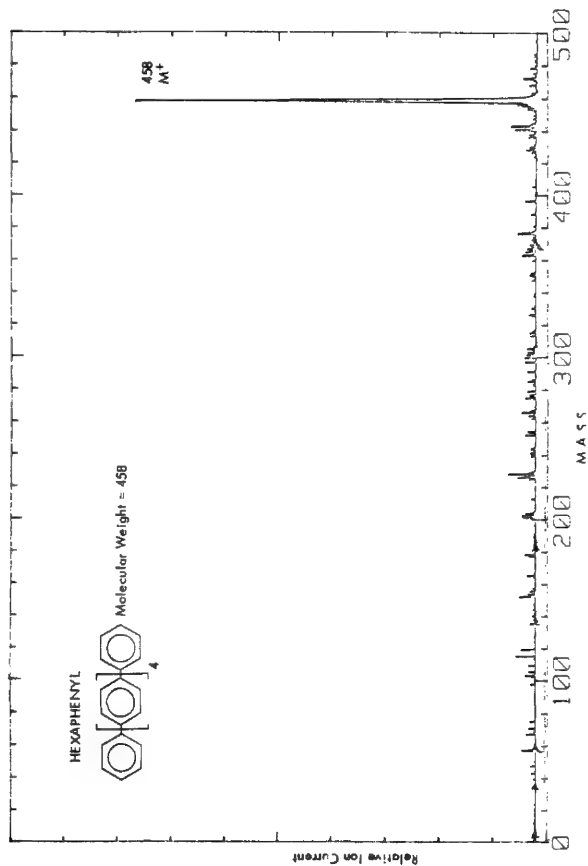


FIG. 5.--Hexaphenyl at 4f.

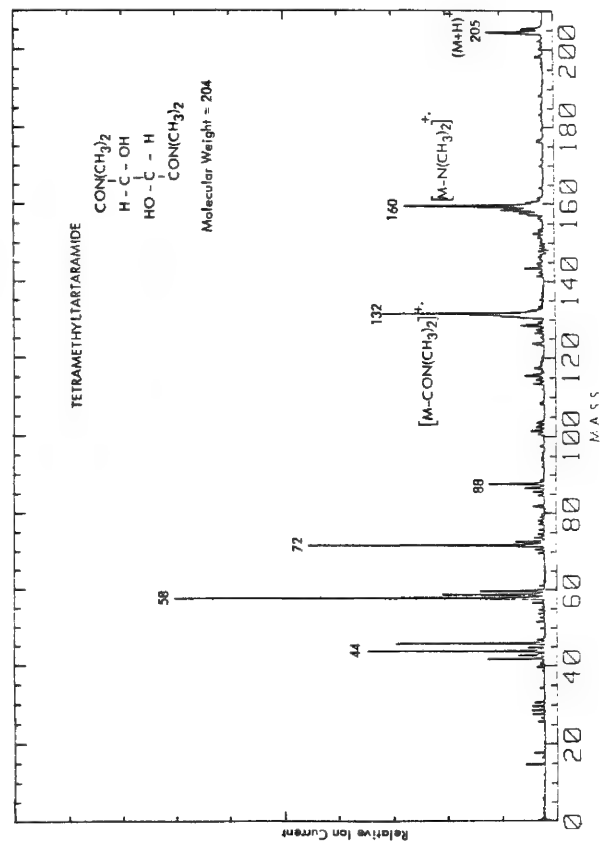


FIG. 7.--Tetramethyltartaramide at 4f.

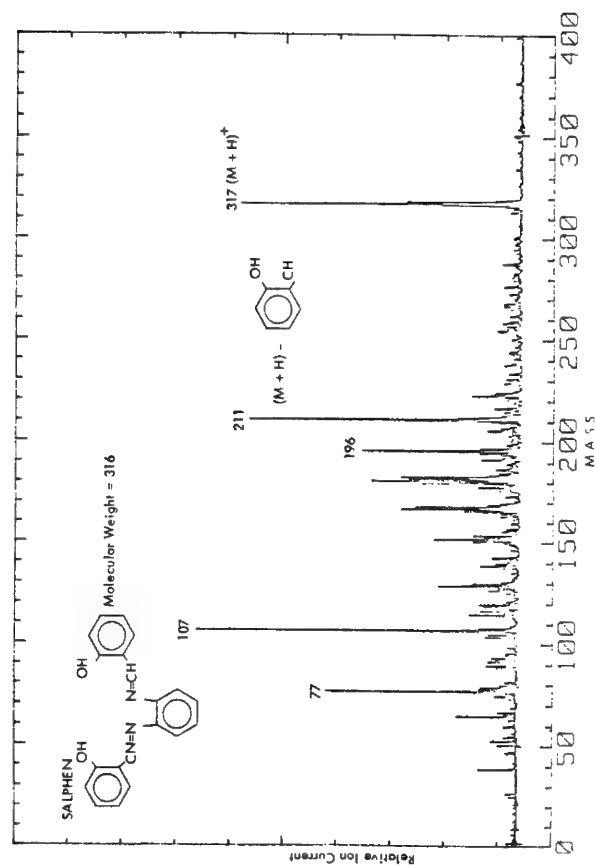


FIG. 6.--Salphen at 4f.

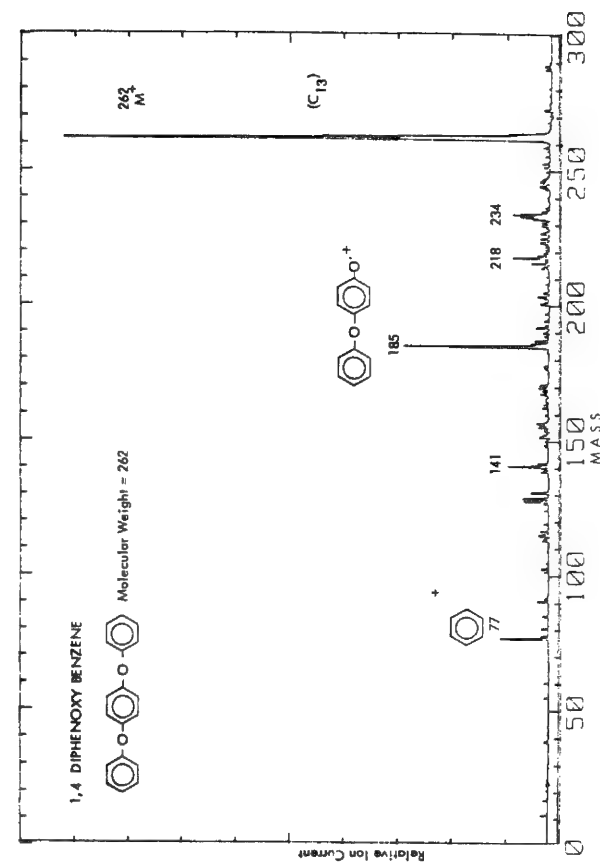


FIG. 8.--Diphenoxy benzene at 4f.

ANALYSIS OF SUBMICROMETER PARTICLES BY SEQUENTIAL AEM AND LAMMA

E. B. Steel, D. S. Simons, J. A. Small, and D. E. Newbury

If one combines the techniques of analytical electron microscopy (AEM) and laser microprobe mass spectrometry (LAMMA), one arrives at an almost complete definition of the morphology, composition (including major to trace chemistry, and isotopic abundance), and phase of individual submicrometer particles.¹ The AEM and LAMMA have complementary capabilities and limitations: where the AEM is analytically weak the LAMMA is strong and vice versa.

The AEM is capable of excellent imaging by conventional transmission electron microscopy or scanning microscopy. Quantitative analysis capabilities exist for determining major and minor chemical composition by energy-dispersive x-ray spectrometry (EDS) and electron energy loss spectrometry (EELS).² AEM also is able to define the phase or orientation of a specimen by electron diffraction of the crystal lattice. These analyses are usually nondestructive, which allows the same particle to be analyzed by LAMMA at some later time. However, some types of information cannot be collected on the AEM; for example, trace element and isotopic analysis are not feasible. Also, most EDS detectors cannot analyze elements lighter than atomic number 11, Na. No AEM technique can directly detect H or He and EELS is often not feasible for other light-element analysis due to sample thickness or chemical complexity.

The combination of pulsed-laser ionization and time-of-flight LAMMA mass spectrometry yields high sensitivity for most elements and gives isotopic analytical capabilities as well.^{3,4} The mass spectrometer permits the analysis of all elements including H and He. However, the LAMMA imaging is limited by the light microscope and quantitative chemical analysis is limited by the variation in ionization conditions from pulse to pulse and sample to sample.³ Also, the LAMMA gives little or no inorganic phase or structure information, although some progress has been made recently in that direction.⁵ LAMMA is definitely a destructive technique, since the area analyzed is vaporized by the laser pulse. Therefore, it is used after the AEM analysis has been completed.

Thus, the two techniques combined through sequential analysis on the same particles can accomplish an almost complete characterization of the particle's morphology, composition, and crystallography. Several applications are currently under investigation that use combined AEM and LAMMA, including a variety of air particulate samples and samples of geologic interest. An example of current research by these techniques is the study of zircons. Zircons (ZrSiO_4) contain relatively high concentrations of many unusual trace elements, whose variations have a variety of applications in the geological sciences. The general use of the trace elements includes the investigation of the origins of rocks or the magma from which the rocks formed. Moreover, the specific trace elements U, Th, and Pb can be used for radioisotopic age dating.⁶ Often the crystal structure of the zircons has been radiation damaged to such an extent that Pb, no longer tightly bonded into the crystal structure, can be partially lost, which makes the age-dating technique potentially inaccurate or at least difficult to reproduce and interpret on a macroscopic scale. Because of this radiation damage, zircons have also been used as models for radioactive waste containment systems.

In the present study, the AEM is used to determine the major and minor chemical composition as well as the crystallinity of submicrometer areas of a zircon, and then these same areas or particles are placed in the LAMMA for mass spectrometric analysis of the trace U, Th, and Pb isotopes.

The authors are with the Center for Analytical Chemistry, National Bureau of Standards, Washington, DC 20234.

Sample Preparation

A single zircon was ground and then deposited onto an indexed TEM grid with a Formvar support film. The indexing allows the same particles to be found and analyzed on both the AEM and LAMMA. (Particles that are too small to be seen on the light microscope of the LAMMA are located by the use of adjacent large particles to identify their position.) The specimens were then lightly carbon coated before AEM analysis. Standards for analysis were prepared in the same way from a mineral glass with a composition similar to zircon. The composition of the reference glass is given in Table 1.

Analysis

The AEM was used to (1) measure particle size and shape; (2) judge relative crystallinity by comparison of the electron diffraction patterns of the particles; and (3) determine major and minor elemental composition. This last included U and Th where these elements were greater than approximately 0.2 wt.%. Thus far Pb has been below the detection limit of the AEM.

The LAMMA was then used to (1) measure the relative abundance of U, Th, and Pb, where measurable; and (2) measure the relative abundance of the Pb isotopes, where measurable.

Figure 1 shows examples of the LAMMA spectra around the lead mass region of both the glass reference and a 0.5 μ m zircon particle. The Pb-204 peak is approximately 15 ppm by weight in the glass. The zircon mass spectrum shows trace rare earth elements and Pb-206 but the Pb-204 peak is below the detection limit. Figure 2 shows an x-ray spectrum of the particle whose mass spectrum is shown in Fig. 1 and qualitatively agrees with the LAMMA mass spectrum. The AEM EDS is not sensitive enough to detect the Th, Pb, or many of the rare earths and because of actual or potential x-ray peak overlaps the identification of the Yb and Ba were only made possible by comparison with the LAMMA spectra. Figure 3 shows the electron diffraction pattern from the same particle with diffuse diffraction maxima from the radiation damaged crystal structure.

Conclusions

The AEM and LAMMA analyses are complementary techniques. In complex systems it can be difficult or impossible positively to decipher the spectra from each individual technique, but in combination there are few ambiguous peaks. The combination of the AEM and LAMMA in sequential analyses yield results that can often define the morphology, major to trace chemical composition of all elements, isotopic abundance, and the phase of particles down to approximately 0.1 μ m.

References

1. Certain commercial equipment, instruments, or materials are identified in this paper. Such identification does not imply recommendation or endorsement by the National Bureau of Standards, nor does it imply that the materials or equipment identified are necessarily the best available for the purpose.
2. J. J. Hren, J. I. Goldstein, and D. C. Joy, Eds., *Analytical Electron Microscopy*, New York: Plenum Press, 1979.
3. P. Surkyn and F. Adams, "Laser microprobe mass analysis of glass particles," *J. Trace and Microprobe Tech.* 1: 79, 1982.
4. D. S. Simons, "Isotopic analysis with the laser microprobe mass analyzer," *Intern. J. Mass Spec. and Ion Proc.* 55: 15-30, 1983-84.
5. E. Michiels and R. Gijbels, "Fingerprint spectra in laser microprobe mass analysis of titanium oxides of different stoichiometry," *Spectrochim. Acta* 38B: 1347-1354, 1983.
6. G. Faure, *Principles of Isotope Geology*, New York: Wiley, 1977.

TABLE 1.--NBS Glass K2380 composition.

Compound	Li ₂ O	SiO ₂	CaO	Fe ₂ O ₃	ZrO ₂	BaO	HfO ₂	PbO	ThO ₂	UO ₂
Weight %	15	68	0.2	0.5	15	0.1	1.0	0.1	0.1	0.2

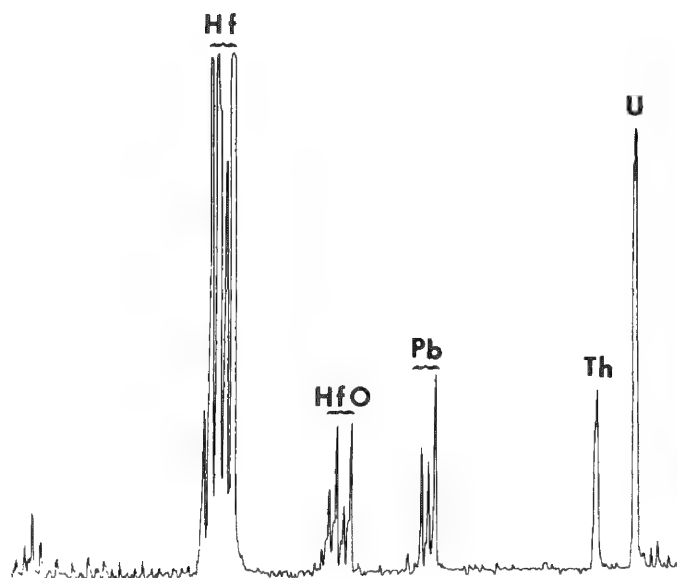
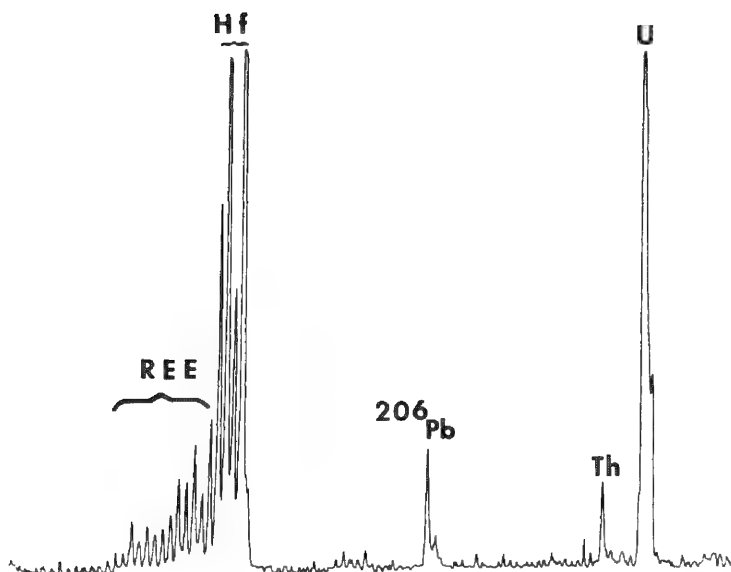


FIG. 1.--(a) LAMMA spectrum of 0.5µm zircon particle showing mass region from rare-earth elements (RRE) through U-238. This spectrum displays radiogenic Pb-206 peak at ~200 ppm, Yb and other trace rare-earth elements, U-238, Th-232, and array of Hf isotopes. (b) LAMMA spectrum of 0.5µm glass sherd as reference showing many of same peaks as (a) but noticeably lacking RRE peaks and displaying average crustal abundance of Pb isotopes and prominent Hf-oxide peaks.

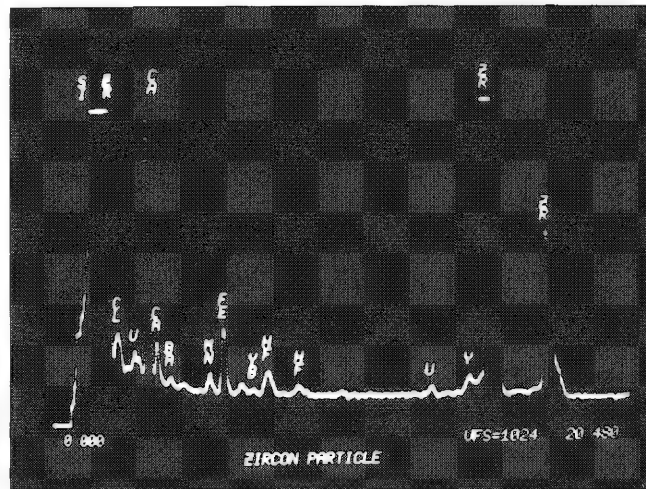


FIG. 2.--EDS x-ray spectrum of same particle analyzed in Fig. 1(a), showing major to minor elements occurring in particle.

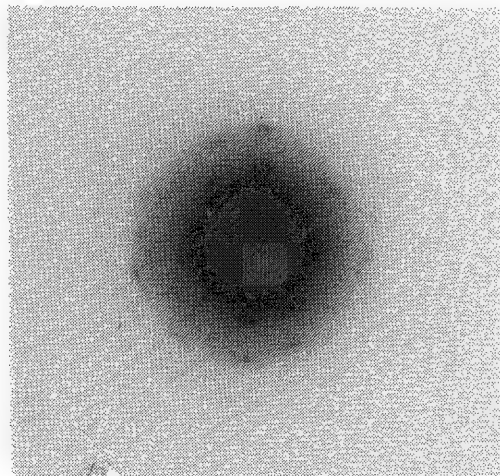


FIG. 3.--Electron diffraction pattern of particle analyzed in Figs. 1(a) and 2. This particle is radiation damaged due to radiogenic decay of the Th and U in zircon, but is still at least partially crystalline.

MONITORING UPTAKE AND RELEASE OF MATERIAL BY CELLS AND CELL-ORGANELLES BY LAMMA

W. H. Schröder

The combination of (1) a selected biological system with well-understood biological properties, (2) stable isotope labeling in physiological experiments, (3) adapted specimen preparation procedures, and (4) specialized standardization procedures for quantitative microbeam analysis has made it possible to monitor the uptake and release of material by photoreceptor cells and some of their organelles.

The rod, the major vertebrate photoreceptor, is an ideal system to study the function of cells and cell organelles with respect to the uptake and release of material and its regulation by microprobe techniques. Several reasons make the system especially suitable for our techniques, as follows.

In the analysis of diffusable materials--which is the typical case in samples of biological tissue--we face the problem that isolation of the sample in many cases already interferes severely with the system to be analyzed, and that diffusion has to be stopped as the first step of specimen preparation, usually by cryoprotocols. The retina may be isolated in the dark apparently without major damage to the cells of interest and allows for simple physiological tests on the quality of the preparation (test for light response of the receptors). The isolated retina is a fairly thin layer of tissue with the photoreceptors exposed on one surface. Therefore, these cells may be shock frozen without serious damage and processed further under conditions that limit diffusion of the element of interest.

In our experiments¹ we monitored uptake and release of Ca by rods as influenced by illumination. This seems to be a good way of demonstrating the possible power of the laser microprobe and the limitations imposed by the amount of information required from the samples to obtain quantitative data. To distinguish between Ca originally present in the cells from Ca taken up at a later point, the stable isotope ⁴⁴Ca was used in the incubation medium during the physiological experiments. (The accuracy of isotope ratio measurements will be demonstrated.)

The photoreceptors are different from most other cell types in that they are clearly divided into large structurally distinguished functional units. This feature makes it possible to analyze areas with different cell organelles separately within our spatial resolution of > 1 µm. The outer segments containing the disks (small membrane vesicles), the ellipsoid (a mitochondria-rich area), the cell nucleus, and an area without any larger organelles were analyzed separately.

The samples were shock frozen in freezing freon at -150 C, cryosubstituted, and plastic embedded. Sections were analyzed with a LAMMA 500 and an x-ray microprobe. Quantification was performed with the use of thin-film standards vacuum-deposited onto the sections.

References

1. W. H. Schröder and G. L. Fain, "Light-dependent Ca release from photoreceptors measured by laser micro mass analysis," *Nature* (in press).

The author is at the Institut für Neurobiologie, Kernforschungsanlage Jülich, D-5170 Jülich, Federal Republic of Germany.

PHENOMENOLOGICAL ASPECTS OF LASER-INDUCED ION-MASS ANALYSIS

N. S. Clarke, A. R. Davey, and J. C. Ruckman

The use of LIMA in the analysis of bulk solid state materials is described and examples are given. These examples illustrate some of the problems of interpretation of LIMA mass spectra that are of less significance in other mass-spectrometric techniques.

The technique of laser-induced ion-mass analysis (LIMA) is fast becoming an established tool for analysis of solid materials.^{1,2} Two instruments are commercially available that have been specifically designed for the analysis of *bulk* solids rather than thin foils: the LAMMA 1000 manufactured by Leybold-Heraeus in Germany, and the LIMA 2A manufactured by Cambridge Mass Spectrometry in England.^{3,4} We report here the results obtained from the prototype LIMA manufactured and designed by Cambridge Consultants Ltd (Fig. 1) according to specifications proposed by AWRE. This was the world's first commercial laser ionization, time-of-flight machine designed for analysis of bulk solids. The detailed theory and principles of operation of the AWRE LIMA have been published.⁵⁻⁷ Briefly, a pulse of laser energy evaporates and ionizes a small volume of a solid sample, typically 10 μm in diameter and 1 μm deep. The ions are separated according to their ratio of kinetic energy to charge and then spatially and temporally focused on to an electron multiplier. The ions are sequentially detected and the signals are digitized and stored by a fast transient recorder. The data can be output to a desk-top computer for further processing.

The analytical capabilities of LIMA are compared and contrasted with those of other physical bulk and surface analysis techniques in Fig. 2 and Table 1. The object of this paper is a discussion of the phenomena that occur as a result of the specific interactions within, and instrumental configurations of, the LIMA instrument during analysis, and their manifestation in the mass spectra. These phenomena are illustrated with examples. Recognition of the occurrence of these phenomena should enable workers in the field to interpret the mass spectral data more readily.

Discussion

LIMA can analyze any vacuum-compatible solid at ppm sensitivity, high spatial resolution, and with no intrinsic mass discrimination or matrix effects. Thus LIMA is comparable to, and has advantages over, dynamic SIMS. LIMA does not suffer to the same extent as SIMS from ion-molecule reactions as a result of probe-specimen interaction and the LIMA mass spectra are considerably simpler than the corresponding SIMS spectra. The LIMA spectrum of a pure silicon sample is shown in Fig. 3(a). The SIMS spectrum⁹ of a silicon sample is shown in Fig. 3(b). Even with energy filtering, the SIMS spectra contain Si_xO_y^+ ions, which make interpretation of the data more difficult than the corresponding LIMA spectra. Nevertheless, ion-molecule reactions occur in LIMA analysis. Figure 4 shows the mass spectrum of a mixture of oxalic acid and sodium chloride. The peaks due to $[\text{M} + 2\text{H}]^+$ and $[\text{M} + 3\text{H}]^+$ are clearly seen, and the successive replacement of hydrogen by sodium is shown by the peaks due to $[\text{M} + 2\text{H} + \text{Na}]^+$, $[\text{M} + \text{H} + 2\text{Na}]^+$, and $[\text{M} + 3\text{Na}]^+$. It has been suggested¹⁰ that this effect of addition of group I metal ions such as sodium to organic moieties can assist the elucidation of molecular structure by identifying the parent ion peak and shifting it to higher m/e , away from the potentially confusing $[\text{M} \pm x\text{H}]^+$ peaks.

The authors are with the Metallurgy Division, Atomic Weapons Research Establishment (AWRE), Aldermaston, England. (HMSO Copyright.) They acknowledge the assistance of the University of Loughborough Department of Physics and of Loughborough Consultants Ltd in the preparation of Table 1, as well as the aid of G. Lawrence of the AWRE Electron Metallography Group in the preparation of Fig. 2, and of Cambridge Mass Spectrometry Ltd for providing the data pertaining to Fig. 9.

TABLE 1.--Comparison of bulk and surface analytical techniques.

	LIMA	EPMA	Dynamic SIMS	Static SIMS	AUGER ELECTRON SPECTROSCOPY	X-RAY PHOTOELECTRON SPECTROSCOPY
PROBE	Photon $h\nu=2.3$ eV(2f) $h\nu=4.6$ eV(4f)	Electron 0.30 keV	Ion:Ar ⁺ ,Cs ⁺ ,O ₂ ⁺ O	Ions Ar ⁺ 0.1-5 keV	Electron 1-10 keV	X-rays 1254 eV 1487 eV
SECONDARY	Ion	X-ray	Ion	Ion	Auger electrons 0.02-2 keV	Photoelectrons 0.02-2 keV
MONITORED VARIABLE	Mass (m/e)	wavelength	Mass (m/e)	Mass (m/e)	electron energy	electron energy
CASTLE AND GOODHEW CLASSIFICATION ⁸	1,i,m	e,X,Eixy	1 ₂ ,i ₂ ,m	i ₂ i ₂ ,m	e ₁ ,e ₂ ,E	X,e,E
ELEMENT RANGE	H-U 0<m/e<1000	Z>5(B)	H-U 0<m/e<1000	H-U 0<m/e<1000	Z>3 (Li)	Z>2 He
DETECTION LIMIT	1 ppm atomic	100 ppm atomic	20 ppb atomic	1000 ppm atomic	1000 ppm atomic	5000 ppm atomic
SAMPLING DEPTH	1 μ m per shot can depth profile	1 μ m	1 nm can depth profile	1 nm	2 nm	2 nm
LATERAL RESOLUTION	10 μ m	1 μ m	0.5 μ m	1 mm	500Å	> 1 mm

TABLE 1 (Cont'd)

Technique	Advantages	Disadvantages
LIMA	Spatial resolution. High sensitivity for all elements and isotopes. Full periodic table coverage. Ultra rapid data acquisition. Chemical information from complex ion fragments. No restriction on electrical properties of sample. Narrow range of sensitivities.	No ultra high mass resolution. Quantification not achieved as yet. Reproducibility from shot to shot is a problem. Destructive.
EPMA	High spatial resolution. High elemental sensitivity. Elemental distribution mapping related to surface topographical imaging. Quantitative true micro analysis.	Cannot detect H, He, Li, Be.
Dynamic SIMS	High elemental sensitivity for all elements and isotopes. High depth resolution. Depth profiling. Quantitative with dilute systems (trace contaminants or dopants). Spatial resolution.	Not always quantitative for nondilute systems.
Static SIMS	High surface sensitivity. Chemical information in sputtered molecular fragments.	Wide range of sensitivities.
AES	High spatial resolution, imaging and mapping of sample possible. Rapid data acquisition. Quantification to $\pm 10\%$ with standards. High reproducibility. Narrow range of sensitivities. Amenable to depth profiling.	Beam damage on insulating samples. Charging problems on some rough insulator surfaces.
Photo-Electron Spectroscopy	Chemical information from chemical shift effects. No beam damage. Quantification to within $\pm 10\%$ with standards. High reproducibility. Narrow range of sensitivities.	No spatial resolution.

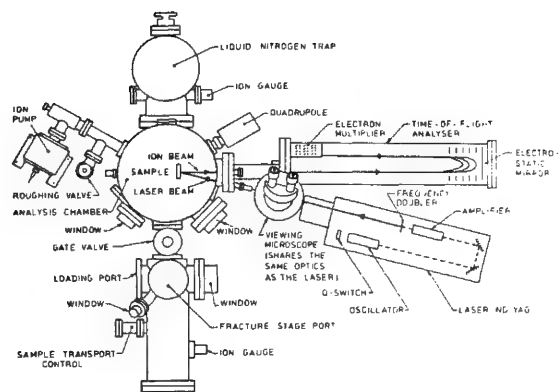


FIG. 1(a).--Schematic plan view of LIMA.

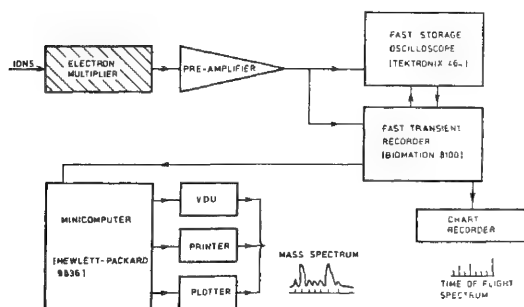


FIG. 1(b).--Data acquisition and processing.

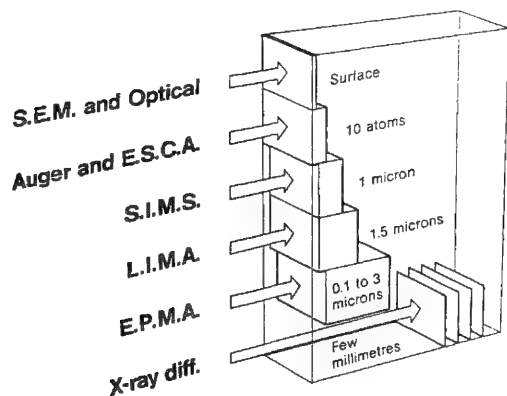


FIG. 2.--Surface and near-surface analytical techniques.

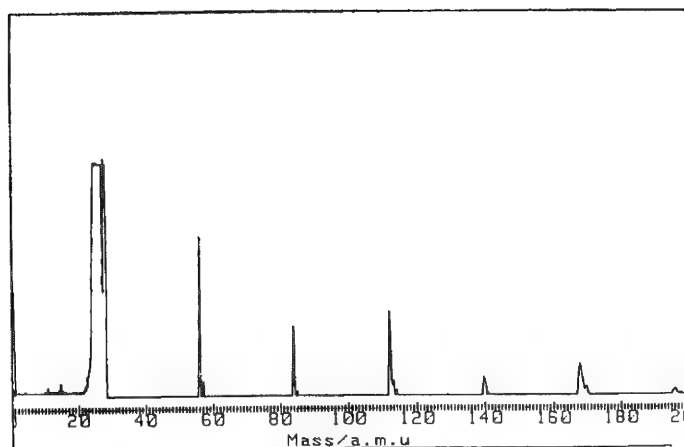


FIG. 3(a).--Silicon mass spectrum.

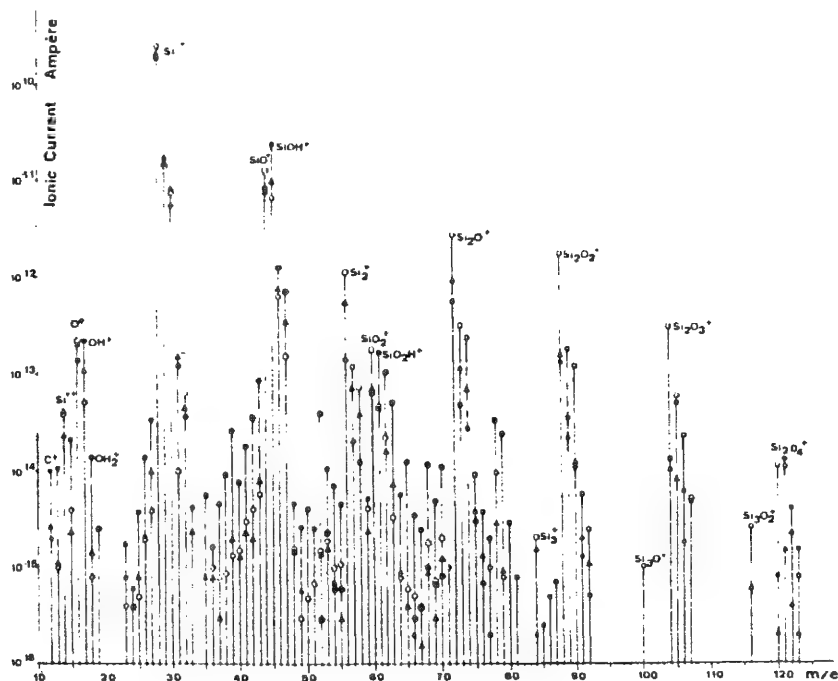
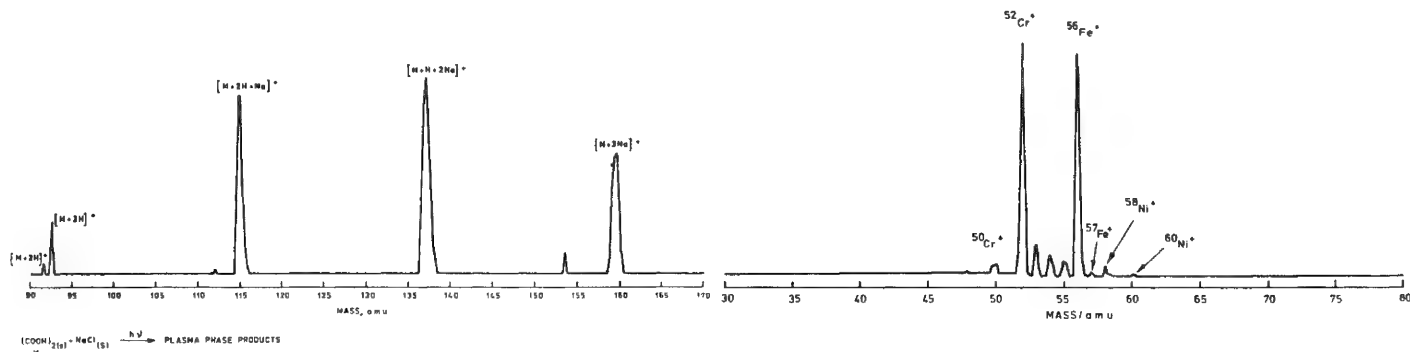


FIG. 3(b).--Pure silicon positive secondary ions spectrum; argon primary ions, oxygen blowing.



The performance and design of the transient recorder, and ion optics, do not permit ultra-high mass resolution to be achieved at present; interferences may occur. Isobaric interferences are illustrated in Fig. 5, which depicts the mass spectrum of stainless steel. Table 2 shows the isobaric interferences that occur. Fragment-ion interferences can also be found. A notable example is that of silicon hydrides with phosphorus: $^{28}\text{Si H}_3^+$, $^{29}\text{Si H}_2^+$, $^{30}\text{Si H}^+$ have $m/e = 31$, as does the $^{31}\text{P}^+$ ion. Figure 6 illustrates mass interferences in a mass spectrum of a stainless steel containing the elements H, Si, and P in trace amounts. Table 3 shows the occurrence of other interferences, which may be of importance in large biomolecule or polymer fragmentations.

The mode of analysis of LIMA causes multiply charged ions to traverse the TOF analyzer in a shorter time than singly charged ions of the same mass. Figure 7 shows the appearance of $^{52}\text{Cr}^{2+}$, $^{56}\text{Fe}^{2+}$, $^{58}\text{Ni}^{2+}$ at $m/e = 26, 28, 29$ in a stainless-steel spectrum obtained at high laser power.

Mechanisms by which fragmentations occur are not fully understood over the whole regime of LIMA analyses. Although "soft" ionizing techniques such as electron-impact ionization of vapor-phase organic molecules give characteristic fragmentation patterns that are predictive and useful diagnostic analytical aids, laser ionization of solids can give rise to nonspecific, nonreproducible fragmentations. This fact is illustrated by the fragmentation of certain polymers where fragments due to $\text{C}_n\text{H}_{2n+2}^+$ species appear that have become saturated due to the nonspecific reaction of hydrogen with unsaturated hydrocarbon fragments (Fig. 8). The mechanism of laser ionization possibly involves resonant multiphoton ionization (REMPI).¹¹ This mechanism can involve excited states of symmetries different from those of the ground or ionized states, which then fragment and produce ionic species not comparable with those formed as a result of one-photon or one-electron ionizations. The JK System 2000 laser fitted to the AWRE LIMA operates at 532 nm (2f). When the laser is operated at 266 nm (4f), as in the LIMA 2A, the likelihood of one-photon ionization increases and fragmentations become more akin to EI ionization. Figure 9 shows the LIMA mass spectrum of paraquat as the dimethyl ammonium dichloride. The EI mass spectrum contains similar peaks.¹⁶ The information contained in these spectra gives credence to the idea that one of the main mechanisms of laser-solid ionization, at least for organic materials, is REMPI.

The fragmentation of ionic solids is not well documented and in general the spectra are expected to be much simpler than for organics. Although much work needs to be done on the laser-induced ionization of inorganics, trends are observed in the analysis of ionic solids. For example, oxides give rise to the appearance of M_xO_y^+ ions, and the M^{z+} ion (where z is a stable oxidation state greater than unity) is rarely if ever observed. Figure 10 shows the fragmentation pattern of erbium oxide. The ions Er^+ , ErO^+ , ErO_2^+ , Er_2O^+ , Er_2O_2^+ , and Er_2O_3^+ are shown and the characteristic isotope ratio of erbium is superimposed on the Er_xO_y^+ ion signals.

Other phenomena that can complicate the mass spectra are concatenations exhibited by p-block elements (Fig. 11 shows the mass spectrum of sulfur¹³); and oligonuclear cluster ions formed by intermetallics (Fig. 12 shows some cluster ions formed during the laser ionization of a gold-silver alloy).

The ubiquitous contamination of samples by sodium and potassium can be surprisingly helpful. The assignment of neighboring peaks is often made easier, and the generation of a linear mass scale from the quadratic TOF raw data scale is facilitated, by the appearance of these alkali metal ion signals. In some cases this contamination can also be a nuisance where interferences occur, e.g., between $^{39}\text{K}^+$ and C_3H_3^+ .

The application of LIMA to the analysis of solid materials covers an extremely wide range. There is not enough space to document all the types of analyses; only a few examples will be given.

One of the early applications of LIMA was the analysis of embrittled reactor fuel cladding.¹² A Magnox alloy (AL80, E Ross UKAEA Springfields) was fractured at 77 K. Examination of the fracture surface showed it to be part intergranular and part transgranular. High magnification SEM photographs revealed the presence of grain boundary precipitates (insert, Fig. 13). Analysis of these precipitates by AES, SEM, and extraction replication techniques failed to yield any conclusions regarding their composition; two possibilities were the intermetallic MgBe or the hydride MgH_2 . LIMA analysis showed the complete absence of hydrogen in the transgranular fracture area. However, signals due to $^1\text{H}^+$ and $^1\text{H}_2^+$ were obtained from the intergranular area. It was concluded that the grain boundary precipitates were MgH_2 .

TABLE 2.--Mass spectrum of stainless steel.

Mass to Charge Ratio m/e	Assignment	Interference
50	$^{50}\text{Cr}^+$	
52	$^{52}\text{Cr}^+$ (83.76)*	
53	$^{53}\text{Cr}^+$ (9.55)	
54	$^{54}\text{Cr}^+$ (2.38), $^{54}\text{Fe}^+$ (5.82)	✓
55	$^{55}\text{Mn}^+$ (100)*	
56	$^{56}\text{Fe}^+$ (91.6)*	
57	^{57}Fe (2.19)	
58	^{58}Fe (0.33), ^{58}Ni (67.88)*	✓
60	^{60}Ni (26.23)	

^AB(%) refers to element B, isotopic mass A; (%) refers to % atomic abundance of isotope A in naturally occurring sample of B. (Percentages are those quoted by Roboz.¹⁵) *Denotes most abundant isotope.

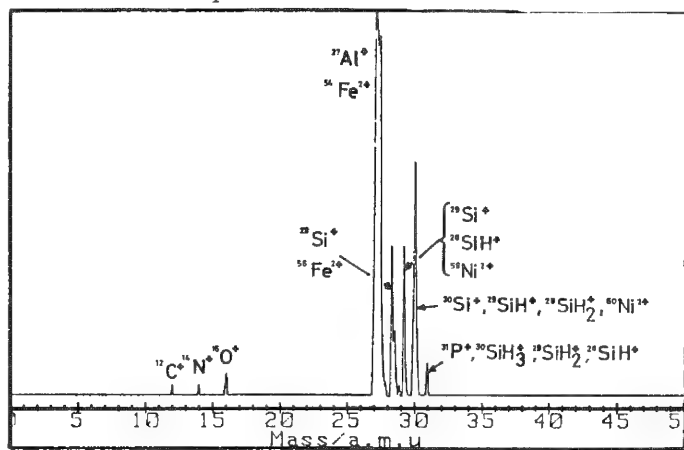


FIG. 6.--Mass interferences in stainless steel.

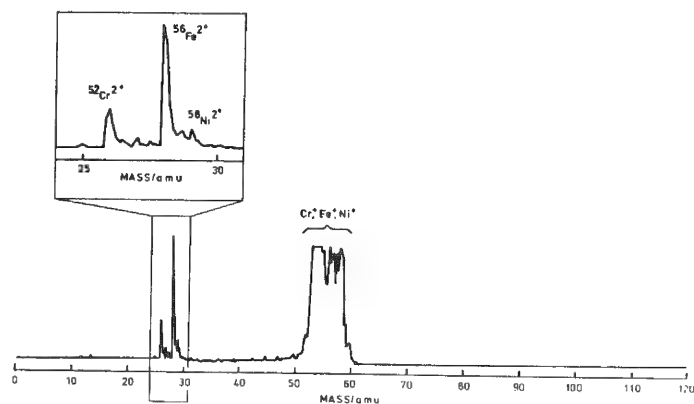


FIG. 7.--Doubly charged ions in stainless steel.

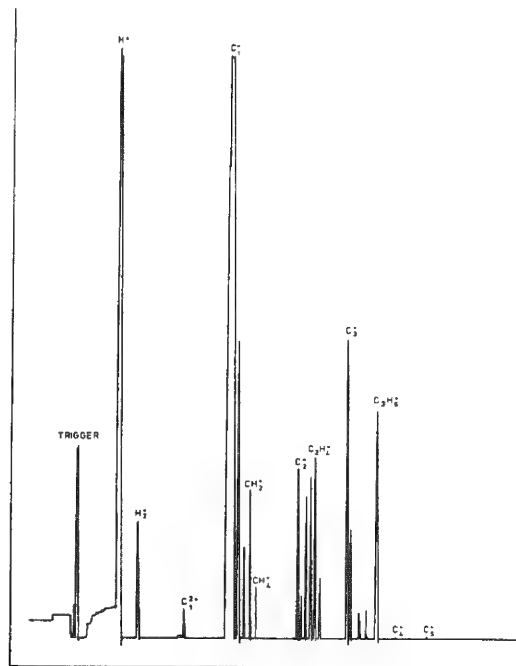


FIG. 8.--Mass spectrum of poly(ethylene) illustrating occurrence of nonspecific hydrocarbon fragments.

TABLE 3.--Organic fragmentation interferences.

Required Species	m/e	Interfering Ion
N	14	CH ⁺
NH ⁺	15	CH ₃ ⁺
O ⁺	16	CH ₄ ⁺
OH ⁺	17	NH ₃ ⁺
H ₂ O	18	NH ₄ ⁺
Mg ⁺	24	C ₂ ⁺

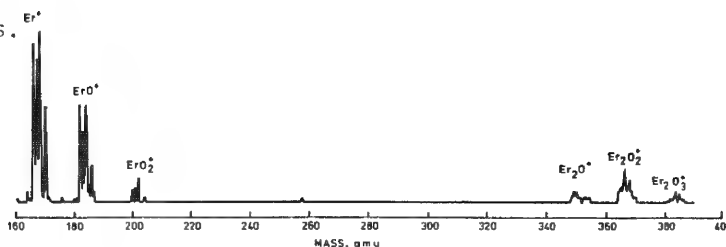
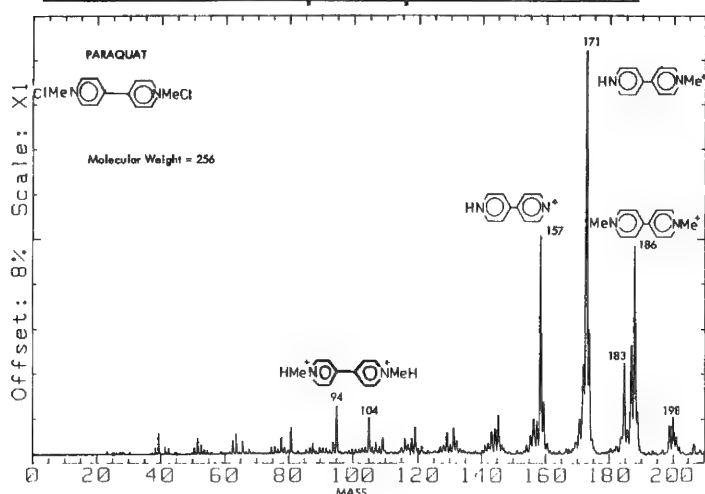


FIG. 10.--Erbium oxide.



CHLOROBENZ

FIG. 9.--Positive spectrum from LIMA at 4f.

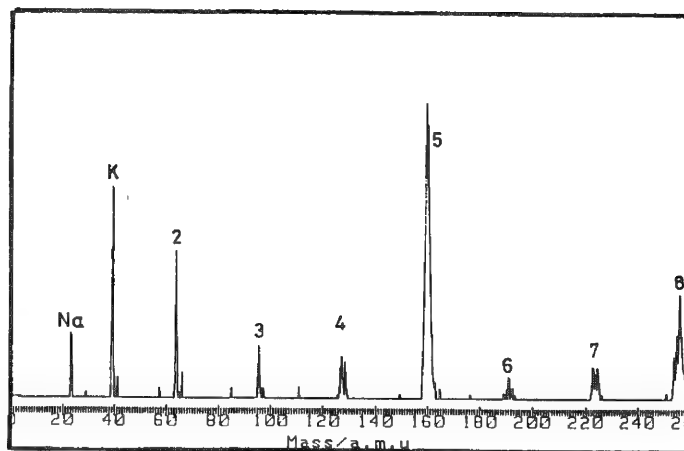


FIG. 11.--Sulfur mass spectrum.

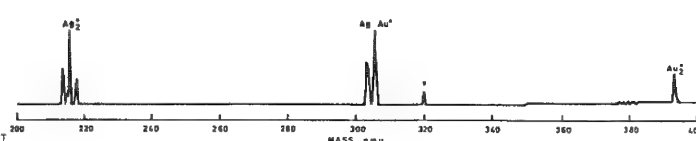


FIG. 12.--Cluster ions.

LIMA can resolve isotopes very well.¹² It is thus potentially very useful in studies where isotopic tracers or spikes are used. In medical research, for example, considerable medical and ethical problems are involved in the use of radioactive isotopes as tracers; the use of stable isotopes is to be encouraged. We have performed preliminary analyses on some pathological specimens as part of early work related to calcium metabolism in osteoporosis or muscular dystrophy patients. Figure 14 shows the LIMA mass spectrum of mouse femur and human thigh muscle.

The appearance of ⁴⁰Ca in the bone and not the muscle is significant. The ultimate object of the experiments was to detect changes in the ⁴⁰Ca/⁴⁴Ca ratio resulting from enrichment of the natural isotopic abundance of ⁴⁴Ca and then observing the appearance of the spike in tissues as the metal was metabolized. In principle LIMA was ideally suited to the task.

Figure 15 shows the LIMA spectrum of CaF₂. Integration of the ⁴⁰Ca⁺ and ⁴⁴Ca⁺ signals gave an isotopic abundance ratio of 2.06% ⁴⁴Ca in excellent agreement with the literature.¹⁵ However, the possibility of CO₂⁺ (m/e = 44) being a likely interference precluded the subsequent quantitative analysis of the "spike." Discussions with M. Jackson of University College Hospital in London revealed the possibility of the use of another calcium isotope as a spike, and the further application of LIMA to other isotopic studies in which the stable isotopes ⁶⁷Zn and ⁷⁴Se are used in relation to other different deficiency diseases.

LIMA has been used to provide analytical data on a host of other samples. We have analyzed polymers, ceramics, refractories, thin films on substrates, particles, inclusions, etc., and a forthcoming publication¹⁴ will be concerned with the many non-AWRE samples that have been analyzed by LIMA.

Conclusions

1. The phenomenological aspects of the generation of mass spectra from solids using LIMA have been described. These aspects have been illustrated with examples, and the use of LIMA in the solution of scientific, technological, and medical problems has been discussed.

2. The performance of LIMA and its role in bulk and surface analyses has been compared with other physical analysis techniques. The mass resolution of LIMA is not as high as that of SIMS, which means that interferences can occur, as illustrated by examples showing isobaric and fragment ion interferences. A particularly fruitful area of LIMA applications appears to be in isotopic studies, although interferences may require that the tracer or spike be chosen carefully.

3. The laser-solid ionization process at 532 nm produces fragmentations not directly comparable with other ionization techniques and means that, at present, existing libraries of mass spectra cannot be used for the interpretation of LIMA spectra. However, preliminary results at 266 nm indicate that one-photon ionizations can occur that produce fragmentations

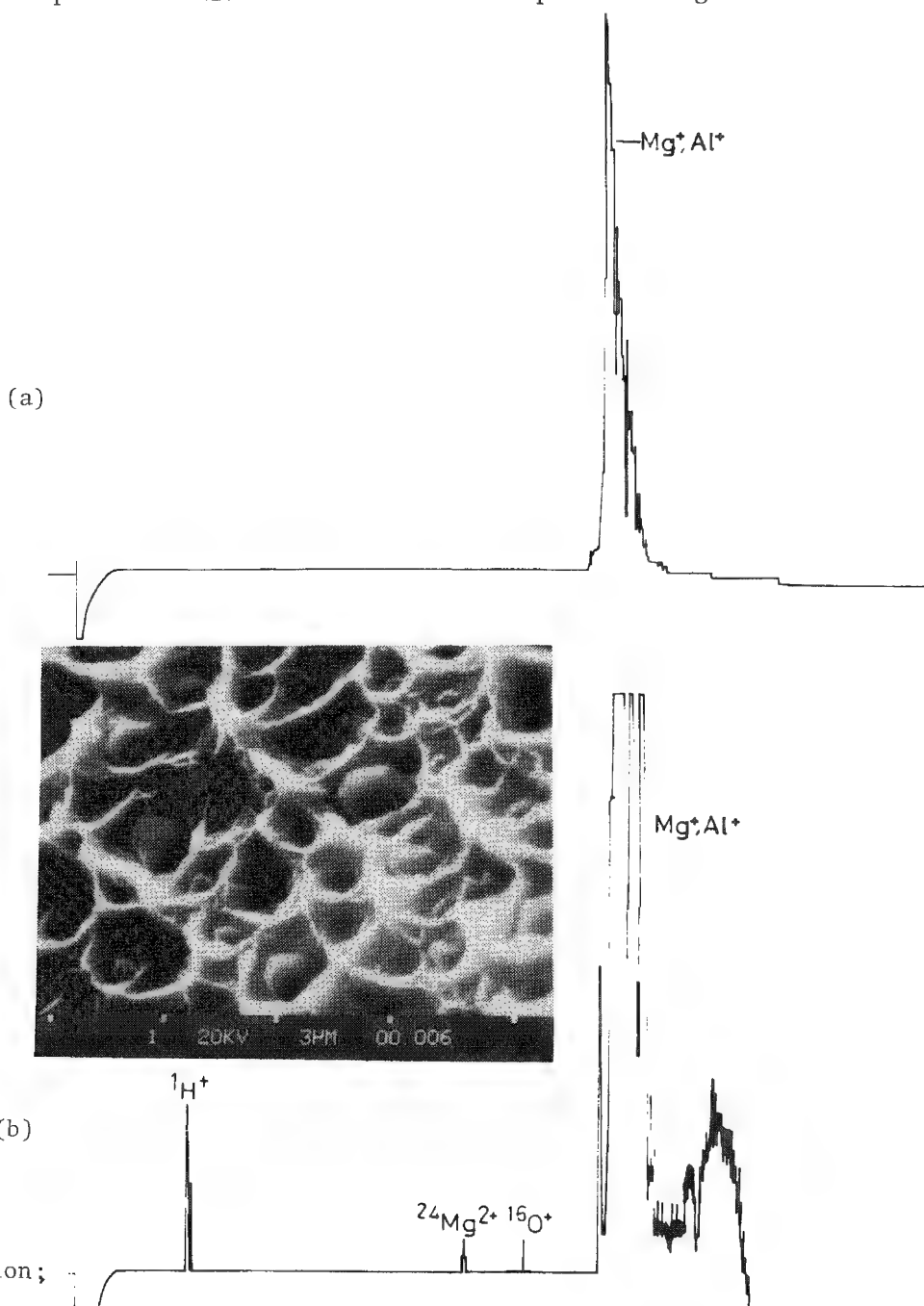


FIG. 13--Magnox alloy fracture surface: (a) transgranular region; (b) intergranular region.

similar to one-electron ionizations. Some trends in the fragmentation of inorganic solids have been established and it is anticipated that further work will enable the specific fragments formed from other giant structures to be characterized and comprehensive databases to be established.

4. The occurrence of ion-molecule reactions can be a difficulty in the assignment of peaks, but once the phenomenon has been recognized, the interpretation of mass spectra should become easier. Under suitable experimental conditions this phenomenon may be advantageously used in molecular-structure determinations and may offer deeper insight into the fundamental problems of laser-solid ionization, plasma chemistry, and laser-induced reactions.

5. Within the restrictions above the immediate advantages of LIMA over other techniques are full periodic table coverage and above, providing chemical information from elements, isotopes, and fragment ions; high sensitivity, high spatial resolution, freedom from contamination by the incident probe, relatively simple mass spectra, little or no specimen preparation, and no restriction on electrical properties of the sample.

References

1. R. J. Conzemius and J. M. Capellan, *Int. J. Mass Spectrom. Ion Phys.* 34: 197-271, 1980.
2. R. J. Conzemius, D. Simons, Z. Shankai, and G. D. Byrd, *Microbeam Analysis--1983*, 301-332.
3. M. J. Southon, presented to *RSC Conference Analytion '83*.
4. C. A. Evans Jr., B. W. Griffiths, T. Dingle, M. J. Southon, and A. J. Ninham, *Microbeam Analysis--1983*, 101.
5. J. C. Ruckman, A. R. Davey, and N. S. Clarke, *LIMA: A Novel Laser-induced Ion Mass Analyser*, AWRE Report 02/84, London: H. M. Stationery Office, 1984.
6. T. Dingle, B. W. Griffiths, and J. C. Ruckman, *Vacuum* 31: 571, 1981.
7. T. Dingle, B. W. Griffiths, and C. A. Evans Jr., *Microbeam Analysis--1982*, 365.
8. J. E. Castle and P. J. Goodhew, *Inst. Phys. Conf. Ser.* 68, 515.
9. B. Blanchard, *Int. J. Mass Spectrom. Ion Phys.* 45: 35-49, 1982.
10. F. P. Novak, K. Balasanmugam, K. Viswanadham, C. D. Parker, Z. A. Wilk, D. Mattern, and D. M. Hercules, *ibid.*, 53: 135-149, 1983.
11. D. H. Parker, in D. S. Kliger, Ed., *Ultrasensitive Laser Spectroscopy*, New York: Academic Press, 1983, Chap. 4.
12. J. C. Ruckman, A. R. Davey, and N. S. Clarke, "Laser-induced ion mass analysis: A novel technique for solid-state examination," submitted to *Vacuum* 84, *Inst. Phys. Conf.* April 1984, York, England.
13. N. S. Clarke, A. R. Davey, and J. C. Ruckman, "Detection of large-cluster ions by laser-induced ion mass analysis," submitted to *Chemical Communications*.
14. N. S. Clarke, A. R. Davey, and J. C. Ruckman, in preparation.
15. J. Roboz, *Introduction to Mass Spectrometry: Instrumentation and Techniques*, New York: Wiley, 1968.
16. M. Nicholson, AWRE Nuclear Chemistry Group, Aldermaston, private communication.

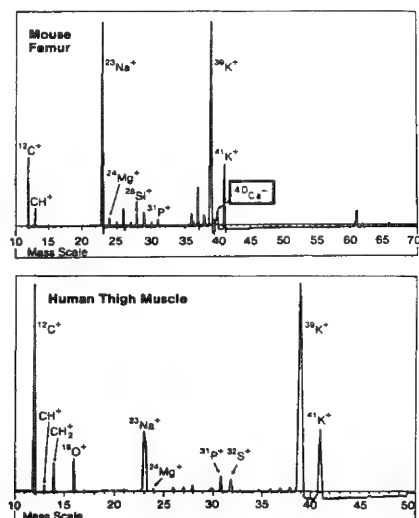


FIG. 14.--Biological samples.

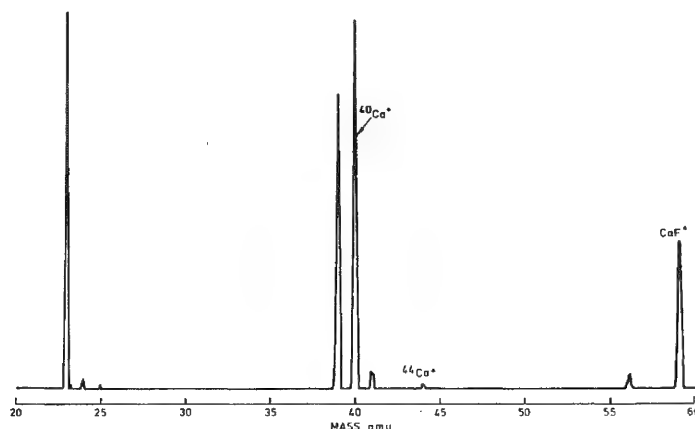


FIG. 15.--Calcium fluoride.

DETECTION OF CLUSTER IONS BY THE LIMA TECHNIQUE

N. S. Clarke, A. R. Davey, and J. C. Ruckman

This paper describes the results of LIMA investigations of nominally pure samples of s- and p-block elements, and some transition metal alloys. It is shown that to a greater or lesser sample-dependent degree, concatenation behavior is exhibited by certain elements, and inter-metallics in the plasma phase.

The laser-induced ion mass analyzer (LIMA) was originally designed to AWRE specifications for the detection and analysis of light elements in general and hydrogen in particular; these elements are inaccessible to most other microanalytical techniques. In response to the AWRE requirement the world's first commercial laser probe/time-of-flight mass spectrometer operating in the bulk-reflection mode rather than the thin-foil transmission mode was designed and built by Cambridge Consultants Ltd., England. The instrument is now commercially available from Cambridge Mass Spectrometry Ltd., England. After a feasibility study, the mass spectrometric analysis technique was chosen and developed because visible spectroscopic analysis of the light emitted by the plasma could not detect the visible electronic transitions of hydrogen, which were hidden by the continuum produced by the exciting (ruby) laser.¹ The time-of-flight (TOF) analyzer was incorporated into the construction because of its optimum performance in terms of resolution, detectable mass range, and sensitivity. The LIMA has proved itself to be an extremely versatile tool and has shown much potential for analytical work beyond the original design specification.

This work illustrates the application of the LIMA in fundamental studies of the plasma properties of elemental carbon, beryllium, silicon, and sulfur, and also of some transition metal systems. We do not propose to discuss here the theory or principles on which LIMA operates, nor the design nor construction of the AWRE LIMA.¹⁻³

Results and Discussion

Carbon Results. The carbon results are presented and discussed first. Three carbon samples were studied: graphite, vitreous carbon, and diamond.⁴ It is convenient to present and discuss these results collectively. Mass spectrometric studies of the carbon vapor over graphite have been made using spark-source⁵⁻⁷ or laser-ionization⁸⁻¹³ techniques. We have extended those observations by detecting very massive ions formed from the three types of carbon; the large range of m/e values spanned have enabled us to observe trends not noticed in earlier work because of the restricted detectable mass ranges. We have also been able to analyze the samples in the bulk reflection mode rather than as thin foils.^{12,13}

In the following, all spectra are of positive ions. Figure 1 shows the LIMA mass spectrum of a vitreous carbon sample. Figure 2 shows the spectrum of a graphite sample, and Fig. 3 shows the spectrum of a diamond sample. The vitreous carbon sample was nominally pure and was supplied by G. Lawrence of the Electron Metallography Group, Metallurgy Division, AWRE. The graphite sample was a portion of an arc electrode supplied by Polaron Equipment Ltd., England. The diamond was an industrial specimen such as is used in engraving and glass-cutting tools.

It is readily apparent that the vitreous carbon and graphite mass spectra are very similar in form; corresponding peak heights due to given $^{12}\text{C}_N^+$ ions have similar intensities relative to their neighbors in each of the two spectra. Ion signals corresponding to the odd-N series of ions are more intense than those due to the even-N series. For $N > 6$ there are maxima in the distribution of ion masses for both vitreous carbon and graphite at $N = 4n + 3$ (n finite, integral); i.e., ions of the $^{12}\text{C}_{4n+3}^+$ type. For both samples the mass range covers

The authors are with the Metallurgy Division, Atomic Weapons Research Establishment (AWRE), Aldermaston, England. (HMSO Copyright.)

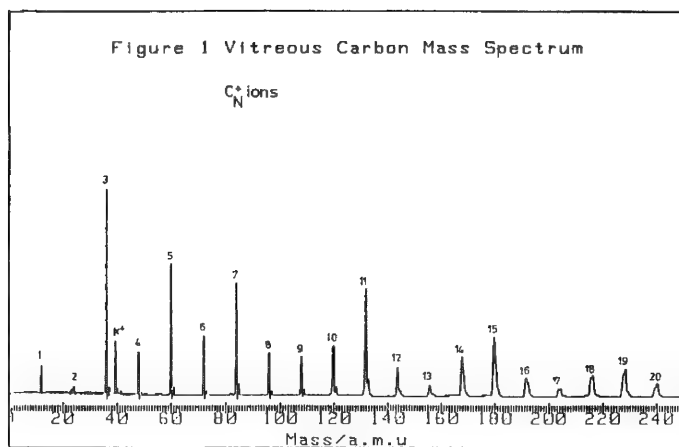


FIG. 1.--Vitreous carbon mass spectrum.

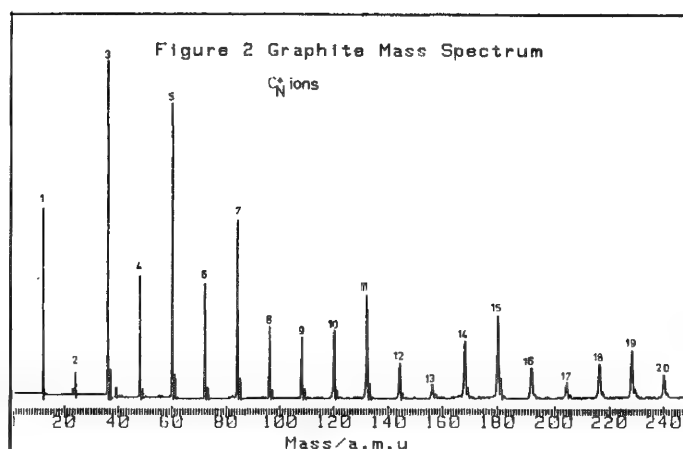


FIG. 2.--Graphite mass spectrum.

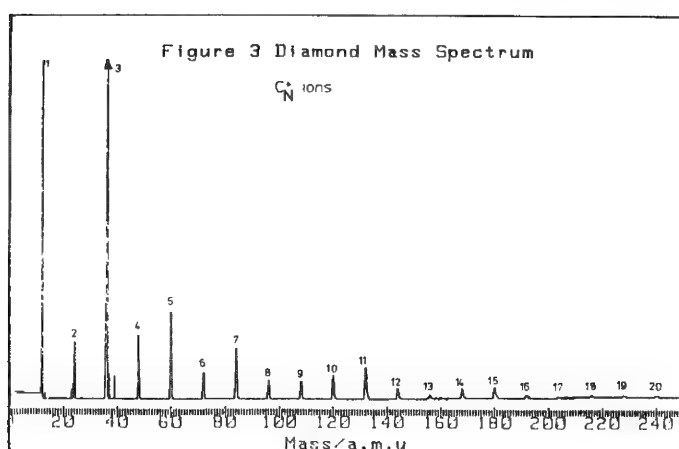


FIG. 3.--Diamond mass spectrum.

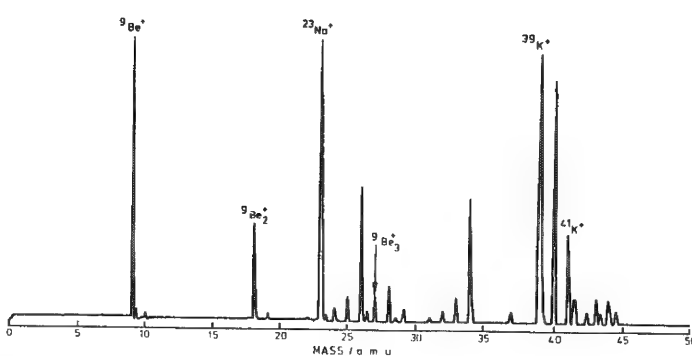


FIG. 4.--Beryllium sample.

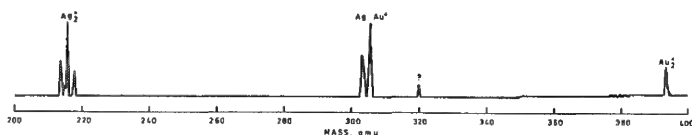


FIG. 5.--Cluster ions.

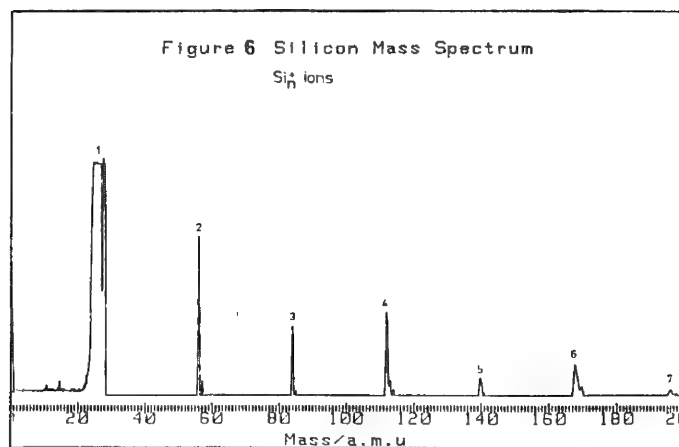


FIG. 6.--Silicon mass spectrum

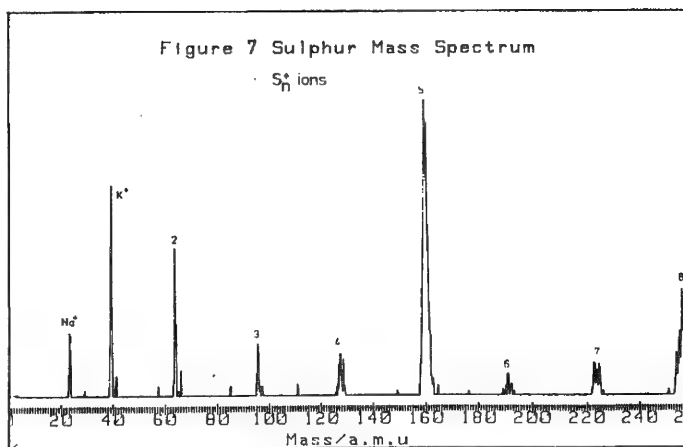


FIG. 7.--Sulfur mass spectrum.

the range $0 < m/e < 250$ and the heaviest ion signal shown is the $^{12}\text{C}_{20}^+$ peak ($N = 20, m/e = 240$). However, we have detected very massive ions with $N > 35$ for graphite and $N > 40$ for vitreous carbon. In all spectra the most intense feature is the peak at $m/e = 36$ due to the $^{12}\text{C}_3^+$ ion. Many workers have observed the pronounced thermodynamic and kinetic stability of this ion,^{13,14} and we have confirmed their findings.

The mass spectrum of diamond is systematically less intense in the region $N > 6$ than for the other carbon specimens and is weighted toward the low-mass region; however, in the high-mass range there are maxima in the distribution of ion masses again at $N = 4n + 3$. The most massive ion detected was the $^{12}\text{C}_{20}^+$ species. In semiquantitative terms, the laser power required to produce a given total ion current (as measured by the $^{12}\text{C}_3^+$ peak intensity) increased in the order vitreous carbon < graphite < diamond.

Discussion. The significant observation from the high mass regime, $N > 6$, for all carbon samples is the occurrence of stable ions at $N = 4n + 3$. On an electron-count basis, these ions contain 6, 10, 14, etc., π -electrons and are aromatically stabilized as predicted by semi-empirical molecular orbital theories. Huckel Molecular Orbital (HMO) theory predicts the stability of the $^{12}\text{C}_{4n+2}$ skeletal networks¹⁵ and by analogy that of the $^{12}\text{C}_{4n+3}$ ions. In view of the assumptions made in HMO theory, it is inferred that these stable ions are aromatic and thus cyclic and planar.

For all carbon samples, the high ionic mass distribution is fundamentally the same. We conclude that the distribution is independent of structure of the solid material and is therefore an intrinsic property of the carbon plasma. The systematically lower intensity in the high mass range for the diamond spectrum compared with the other samples can be empirically ascribed to its poor absorption of the laser energy and high enthalpy of vaporization, both of which require the use of high laser intensities to produce spectra, which tends to fragment the heavier ions.

The technological importance of these and other studies has wide-ranging implications. Within the scope of LIMA analyses the generation of a great many peaks at known values of m/e can provide an extremely accurate calibration of the instrument and accurate generation of linear mass scales from root-of-mass TOF raw data. This is because IUPAC conventions¹⁶ define the molar mass of carbon as $12.000000 \text{ g.mol}^{-1}$ exactly and thus the major peaks of the cluster ions appear at integral multiples of 12.000000 amu .

The many peaks in the carbon mass spectrum and the characteristic distribution of peak intensities serve as a "fingerprint" and enable the element to be easily identified. We have examined inclusions in beryllium pressings, the compositions of which were originally thought to be beryllium oxide. Techniques such as electron probe microanalysis and backscattered electron imaging failed to identify the inclusions. LIMA identified the inclusions as carbon by detecting the fingerprint mass spectrum.¹⁷ Other workers have identified inclusions in meteorites¹⁸ as carbon by observing this fingerprint. Similarly, the nonappearance of the fingerprint indicates the absence of bulk elemental carbon in an analysis zone. Freund and co-workers^{19,20} concluded that the nonappearance of the carbon fingerprint and the appearance of $^{12}\text{C}_1^+$ as the only carbon species in laser-probe analyses of forsterite (natural MgO) were consistent with the presence of atomically dispersed "carbonatic" carbon.

The polynuclear carbon cluster ions are expected to consist of conjugated carbon chains or rings depending on the value of N , and as such possess vacant bonding positions normally occupied by hydrogen in the corresponding hydrocarbon. The plasma temperature is variously estimated^{8-10,21,22} to be in the range 2000-10 000 K; these cluster ions are expected to be very reactive species. These conclusions have been confirmed by plasma quenching experiments,²³⁻²⁶ usually performed by laser irradiation of carbon targets in an atmosphere of reactant gas and detection of the products by mass spectrometry. The specificity of such quenching is surprising and it has been suggested^{27,28} that a laser and carbon target with a pure hydrogen feedstock could form the basis of a reactor for the specific synthesis of ethylene.

The interaction of the laser and target in LIMA can reproduce the high-temperature behavior of refractory materials. In relation to carbonaceous materials, the effect of variation of laser power on the LIMA mass spectrum of vitreous carbon and graphite can reflect the ablative properties of the materials,²⁹ which are important in such diverse fields as nuclear-reactor technology, rocket-engine nozzles, and re-entry heat shields.

The generation of the many types of ions from carbon targets both by laser-solid and spark techniques can explain the inhomogeneous deposit³⁰ formed when carbon arc or carbon sputter

coaters are used. It is conceivable that coaters could be constructed with a laser ion source and carbon targets in UHV chambers in conjunction with an ion mass filter. Precisely controlled carbon coatings could then be deposited by selection of suitable ions formed by the laser-carbon interaction.

It is possible to detect the $^{13}\text{C}/^{12}\text{C}$ isotope ratio by means of LIMA. Recent work with other analytical techniques³¹⁻³³ has revealed a variation in the ^{13}C abundance within certain individual diamonds between the exterior and the core. At present such studies require the laborious sectioning and combustion of large volumes of the sample. LIMA could be invaluable in such studies by dramatically reducing the data acquisition time and the volume of sample consumed.

Beryllium. Figure 4 shows the LIMA mass spectrum of a beryllium sample. Apart from the impurity peaks, the cluster ions observed were $^9\text{Be}_2^+$ and $^9\text{Be}_3^+$. The most massive ion detected was the trinuclear species, although the heptanuclear $^9\text{Be}_7^+$ has been detected in some SIMS studies.³⁴ The $^9\text{Be}_n^+$ cluster ion abundances are expected to decrease monotonically with increasing n . No aromatic stabilization can occur because each $^9\text{Be}_n^+$ ion contains an unpaired electron.

Gold-silver Alloy. Figure 5 shows the LIMA spectrum of a gold-silver alloy. Apart from the expected $^{107}\text{Ag}^+$, $^{109}\text{Ag}^+$, $^{197}\text{Au}^+$, and the ubiquitous contaminants $^{23}\text{Na}^+$, $^{39}\text{K}^+$, and $^{41}\text{K}^+$, the high mass region shows signals due to $^{107}\text{Ag}_2^+$, $(^{107}\text{Ag}^{109}\text{Ag})^+$, $^{109}\text{Ag}_2^+$, $(^{107}\text{Ag}, ^{197}\text{Au})^+$, $(^{109}\text{Ag}, ^{197}\text{Au})^+$, and $^{197}\text{Au}_2^+$. The relative intensities of the binuclear silver ions are in the ratio 1:2:1. This ratio arises from the binomial expansion of the nearly equal abundances of the 107 and 109 silver isotopes. A SIMS study of noble metals³⁵ demonstrated the existence of bi- and trinuclear silver cations, and also the existence of polynuclear silver anions. Furthermore, the existence of polynuclear copper cations and anions was demonstrated. In view of these observations and Joyes's subsequent theoretical discussion, it is seen that the bonding and stability of such ions can be reconciled in terms of linear combinations of atomic orbitals, LCAO. As a result of the symmetries and energies of the atomic orbitals available for bonding in silver and gold, it is seen that the generation of heteronuclear cluster ions can be explained in terms of LCAO.

Silicon. Figure 6 shows the positive ion LIMA mass spectrum of silicon; the sample was nominally pure and was supplied by J. R. Smith of the Electron Metallography Group, Metallurgy Division, AWRE. The Si_n^+ cluster ions are clearly seen; the heaviest ion detected was the Si_7^+ species. This result was irrespective of laser power or instrumental sensitivity; no larger ion was observed. The most intense ion signal detected was due to the Si^+ ion; thereafter the ion signal decreases in intensity as the cluster size increases. The ions with even numbers of nuclei give rise to signals which, as a series, are more intense than the series of signals due to ions with odd numbers of nuclei.

Sulfur. Figure 7 shows the positive-ion LIMA mass spectrum of sulfur. The sulfur was supplied in powder form and used without further purification. The powder was melted at 250 C and allowed to set into a solid mass. A portion of this mass was removed and inserted into the LIMA sample chamber. The mass spectrum shows strong impurity peaks due to sodium and potassium. The S_n^+ cluster ions are clearly seen; they extend to $n = 8$ only. A surprising result is the nonappearance of the mononuclear ion S^+ . The relative ion current decreases monotonically in the order $\text{S}_2^+ > \text{S}_3^+ > \text{S}_4^+$. The most intense signal in the whole spectrum occurs at $m/e = 160$, which corresponds to the very stable cyclo- or catena-pentasulfur cation. The S_6^+ and S_7^+ signals are weak and a strong signal due to the stable cyclo- or catena-octasulfur cation occurs at $m/e = 256$. Contributions to the signal width are rotations of the molecule as a whole, conformational changes during ion time of flight, and clusters containing sulfur isotopes; and of course space charge.

The p-block elements carbon, silicon, sulfur (and selenium) exhibit concatenation behavior in their solid-state, solution, and gaseous phase chemistries.³⁶ It is perhaps not surprising that such behavior is also exhibited by these elements in the laser-generated plasma such as is found under the LIMA analysis conditions.

Conclusions

1. The use of LIMA in fundamental studies of the plasma chemistry of some simple systems has been described. The mass spectra have been described and discussed in qualitative terms.

2. The unique ability of carbon to form large polynuclear clusters has been demonstrated and contrasted with the elements sulfur and silicon, which appear to form only small polynuclear cluster ions. There are alternations in the cluster-ion intensities as the cluster size increases for the carbon samples and maxima in the ion mass distributions. These maxima can be attributed to stable closed shell electronic configurations; i.e., singlet $^1\Sigma_g$ molecular states. The p-block elements sulfur and silicon exhibit stable cluster ions and those are again likely to be cyclic.

3. Beryllium forms oligonuclear cluster ions, none of which have closed electronic structures and are thus triplet $^3\Sigma$ states.

4. Homonuclear transition metal clusters have been observed by other workers and we have detected heteronuclear transition metal clusters within the same group.

References

1. J. C. Ruckman, A. R. Davey, and N. S. Clarke, *LIMA: A Novel Laser-induced Ion Mass Analyser*, AWRE Report 02/84, London: H. M. Stationery Office, 1984.
2. T. Dingle, B. W. Griffiths, and J. C. Ruckman, *Vacuum* 31: 571, 1981.
3. T. Dingle, B. W. Griffiths, J. C. Ruckman, and C. A. Evans Jr., *Microbeam Analysis--1982*, 365.
4. N. S. Clarke, A. R. Davey, and J. C. Ruckman, "Detection of large cluster ions by laser-induced ion mass analysis," submitted to *J. C. S. Chemical Communications*.
5. E. Dornenburger, H. Hintenberger, and J. Franzen, *Z. Naturforsch.* 16a: 532, 1961.
6. W. L. Baun, F. N. Hodgson, and M. Desjardins, *J. Chem. Phys.* 38: 2787, 1963.
7. H. Hintenberger, J. Franzen, and K. D. Schuy, *Z. Naturforsch.* 18a: 1236, 1963.
8. J. A. Howe, *J. Chem. Phys.* 39: 1362, 1963.
9. J. Berkowitz and W. A. Chupka, *ibid.*, 40: 2735, 1964.
10. P. D. Zavitsanos, *Carbon* 6: 731, 1968.
11. K. A. Lincoln, *Int. J. Mass Spectrom. Ion Phys.* 13: 45, 1974.
12. N. Furstenau, F. Hillenkamp, and R. Nitsche, *ibid.*, 31: 135, 1979.
13. N. Furstenau and F. Hillenkamp, *ibid.*, 37: 135, 1981.
14. A. B. Rakshit and D. I. Bohme, *ibid.*, 49: 275, 1983.
15. A. Streitwieser, *Molecular Orbital Theory*, New York: Wiley, 1961.
16. M. L. McGlashan, *Physico-chemical Quantities and Units*, RSC Monograph No. 15.
17. J. C. Ruckman, A. R. Davey, and N. S. Clarke, "Laser-induced ion mass analysis: A novel technique for solid-state analysis," submitted to *Inst. Phys. Conf. Vacuum*.
18. W. Herr, P. Englert, U. Herpers, E. A. Watts, and A. G. Whittaker, *J. Metro. Soc.* 15: 300, 1980.
19. F. Freund, H. Wengeler, H. Kathrein, and H. J. Heinen, *Mat. Res. Bull.* 15: 1019, 1980.
20. F. Freund, H. Kathrein, H. Wengeler, R. Knobel, and H. J. Heinen, *Geochimica et Cosmochimica Acta* 44: 1319, 1980.
21. K. S. Pitzer and E. Clementi, *J. Amer. Chem. Soc.* 21: 4477, 1959.
22. C. D. David and H. Weichel, *J. Appl. Phys.* 40: 3674, 1969.
23. R. L. Hanson, *Carbon* 16: 159, 1978.
24. R. Schaeffer and R. K. Pearson, *J. Amer. Chem. Soc.* 91: 153, 1969.
25. R. T. Meyer, A. W. Lynch, and J. M. Freese, *J. Phys. Chem.* 77: 1083-1092, 1973.
26. J. L. Schultz and A. G. Sharkey, *Carbon* 5: 57, 1967.
27. J. F. Asmus, Rec. 11th Symp. Electron, Ion, and Laser Beam Technol., San Francisco Press, 1973, 367.
28. W. W. Duley, *CO₂ Lasers Effects and Applications*, New York: Wiley, 1976.
29. K. A. Lincoln, *Proc. 3rd Int. Symp. High Temp. Technol. Pure Appl. Chem. Supp. Asilomar, Calif.*, 1967.
30. P. A. Echlin, University of Cambridge Department of Biology (private communication).
31. *Chem. Br.* March 1984.
32. H. J. Milledge, M. J. Mendelssohn, M. Seal, J. E. Rouse, P. K. Swart, and C. T. Pillinger, *Nature* 303: 791-793, 1983.
33. P. K. Swart, C. T. Pillinger, H. J. Milledge, and M. Seal, *ibid.*, 303: 793-795, 1983.
34. M. Leyleyter and P. Joyes, *Radiation Effects* 18: 105-110, 1973.
35. P. Joyes, *J. Phys. Chem. Solids*. 32: 1269-1275, 1971.
36. F. A. Cotton and G. Wilkinson, *Advanced Inorganic Chemistry*, New York: Wiley, 1972, 3d ed.

2 Spectral Processing

REMOVAL OF PLURAL SCATTERING IN EELS: PRACTICAL CONSIDERATIONS

C. R. Swyt and R. D. Leapman

The energy-loss spectrum from an ideally thin specimen is directly proportional to the inelastic cross section. To the extent that the physical origin of the cross section is understood, interpretation of the spectrum is then possible: edges can be identified unambiguously; fine structure is visible; background extrapolation can be performed and core edge areas accurately determined for quantitation. However, in most specimens there is some plural scattering that can complicate quantitation, obscure fine structure, and make even the identification of edges difficult. A method to extract the single scattering distribution (SSD) from a collected energy loss spectrum is thus often required. For most samples plural inelastic scattering will tend to affect the spectra very strongly when the thickness $t > \lambda_T$, where λ_T is the total mean free path for inelastic scattering. Typically λ_T ranges from 10 to 100 nm at 100keV beam energy.

Several workers have contributed methods of varying complexity and applicability. Among them are Daniels et al.¹ and Trebbia,² whose channel-by-channel iteration procedures are useful for low-energy losses and thin specimens (double scattering only). Misell and Jones³ presented a logarithmic series representation for the single scattering distribution. This, too, is limited to small specimen thickness because calculation of sufficient convolutions for convergence may otherwise become impractical. Recently Schattschneider⁴ has presented a solution that utilizes matrix methods for calculation of the n-fold convolutions. We shall discuss the algorithms we have found practical in our laboratory to extract a SSD from a collected spectrum. These algorithms are based on the complete plural scattering formulation presented by Johnson and Spence⁵ and utilized by Batson and Silcox.⁶ An algorithm employed by Egerton and Whelan⁷ and ourselves^{8,9} to recover the SSD from measured core edges is shown to be a special case of the general plural scattering representation. Some of the experimental factors which bear on the correctness of the derived SSD are presented.

The Algorithms

The complete plural scattering distribution can be expressed as a Poisson distribution in terms of n-fold convolutions of the single scattering cross section $S(E)$,

$$I(E) = \exp(-t\sigma_T) I_0(E) * [\delta(E) + tS(E) + (t^2/2!)S(E)*S(E) + \dots] \quad (1)$$

where $I_0(E)$ is the incident electron distribution, $\sigma_T = 1/\lambda_T = \int S(E)dE$ is the total scattering cross section, and $\delta(E)$ is the no-loss term. For simplicity the angular dependence has been omitted; i.e., it is assumed that scattering into all angles is collected, including elastic. Equation (1) can be inverted following Johnson and Spence⁵ by use of Fourier transforms (denoted by $\hat{}$) to give the SSD,

$$t\hat{S}(\hat{E}) = \ln\{\hat{I}(\hat{E})/[\hat{I}_0(\hat{E})\exp(-t/\lambda_T)]\} \quad (2)$$

We use this formulation in our algorithm for the SSD and write

$$t\hat{S}(\hat{E}) = \ln[|I_Z + \hat{I}_i(\hat{E})|/I_Z] \quad (3)$$

Here I_Z is the integrated intensity in the zero loss peak and $I_i(E)$ is the inelastic part of the spectrum, which excludes the zero-loss peak. This form is equivalent to a

The authors are at the Biomedical Engineering and Instrumentation Branch, National Institutes of Health, Bethesda, MD 20205.

delta-function representation of the zero-loss peak and produces a similar result as deconvolution by the instrumental broadening function to suppress noise. The absolute value of the Fourier coefficients of the measured spectrum are computed, as prescribed by Spence,¹⁰ to obtain a unique solution regardless of sample thickness, assuming there are no energy-gain processes contributing to the spectrum. The complete single-scattering derivation is useful for spectra where the dynamic range over the energies of interest permits acquisition with no change in incident intensity and for low energy-loss core edges where background subtraction may not be possible. Figure 1 shows the spectrum (curve A) from a carbon-coated oxidized aluminum film of thickness $0.92\lambda_T$ and the SSD (curve B) derived from Eq. (3). Intensity is removed at the second plasmon and the Al L_{23} edge is enhanced. The program utilizes a standard Digital Equipment Corp. fast Fourier transform (FFT) for 1024 points and runs on our DEC 11-60 computer in about 2 s. The speed of this FFT depends on integer arithmetic which requires scaling of the data to values $< 2^{15}$. This process causes truncation errors for core losses at higher energies, where the intensity may be considerably below that of the low-loss region. For this reason, and also because it may be more convenient to collect the core edge and low-loss distributions separately, we have made use of an algorithm for the SSD based on the separated distributions.⁷

The algorithm, which involves deconvolution of the measured core loss intensity by the measured low loss spectrum,⁷⁻⁹ can be derived directly from Eq. (1). Let us write the measured spectrum as the sum of a core edge contribution $I_C(E)$ and a much larger remaining portion $I'(E)$:

$$I(E) = I_C(E) + I'(E) \quad (4)$$

Similarly we write the SSD as the sum of a core edge contribution $S_C(E)$ and a remaining part $S'(E)$,

$$S(E) = S_C(E) + S'(E) \quad (5)$$

If $\hat{I}_C(\hat{E}) \ll \hat{I}'(\hat{E})$, which is generally true since the zero-loss intensity is much greater than the core-loss intensity, we can expand the logarithm term in Eq. (2) as

$$t[\hat{S}'(\hat{E}) + \hat{S}_C(\hat{E})] = \ln \hat{I}'(\hat{E}) + [\hat{I}_C(\hat{E})/\hat{I}'(\hat{E})] - \ln \hat{I}_0(E) + t\sigma_T \quad (6)$$

The FT of the intensity distribution without the core edge gives

$$t\hat{S}'(\hat{E}) = \ln \hat{I}'(\hat{E}) - \ln \hat{I}_0(\hat{E}) + t\sigma_T \quad (7)$$

Subtracting Eq. (7) from Eq. (6), we have

$$\hat{S}_C(\hat{E}) = \hat{I}_C(\hat{E})/\hat{I}'(\hat{E}) \quad (8)$$

This equation, which describes the deconvolution algorithm for core edges, is therefore a special case of the general single-scattering derivation. In our system derivation of the SSD from a background-subtracted core edge and the corresponding low-loss spectrum is completed in about 3 s. Figure 2 demonstrates the application of this algorithm to a spectrum from the carbon coated aluminum oxide sample analyzed in Fig. 1. Curve A shows the measured carbon K and oxygen K edges. Curve B shows the core edges after background subtraction and curve C is the deconvoluted spectrum which is strongly enhanced at threshold.

Experimental Considerations

In presenting their derivations for the SSD, the various authors have discussed limitations and requirements such as constant specimen thickness, extended energy range of collection, and correctness of intensity ratios. These limitations can be summarized in the fundamental requirement that the collected spectrum correctly represent the multiple scattering. Stephens¹¹ has discussed in some detail the effect of collection angle on the multiple-scattering spectrum: too small an angle results in a spectrum which underrepresents the amount of multiple scattering. Single-scattering derivations that do not account for the effects of convolution in energy and angle yield an SSD that is undercorrected for plural scattering.

FIG. 1.--Spectrum recorded at 100keV beam energy from carbon-coated oxidized aluminum film of thickness $t = 0.92\lambda_T$: (A) measured spectrum, (B) single-scattering distribution from Eq. (3). Aluminum L_{23} edge at 78 eV is more visible and second plasmon is removed in SSD.

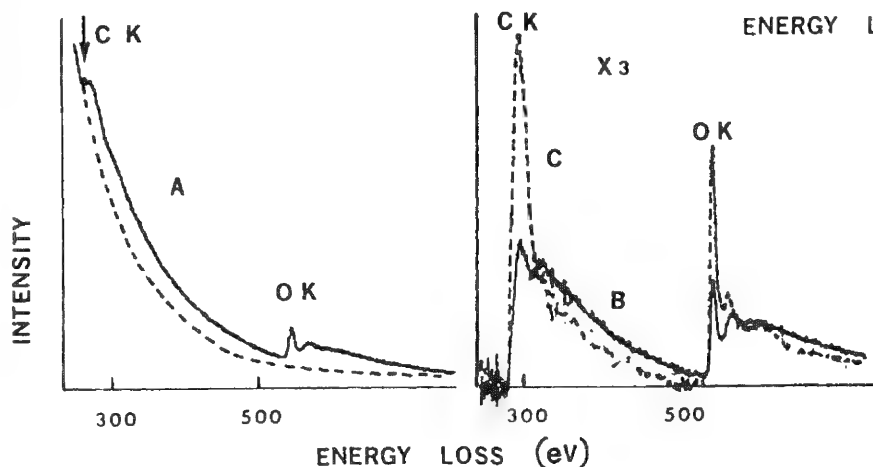
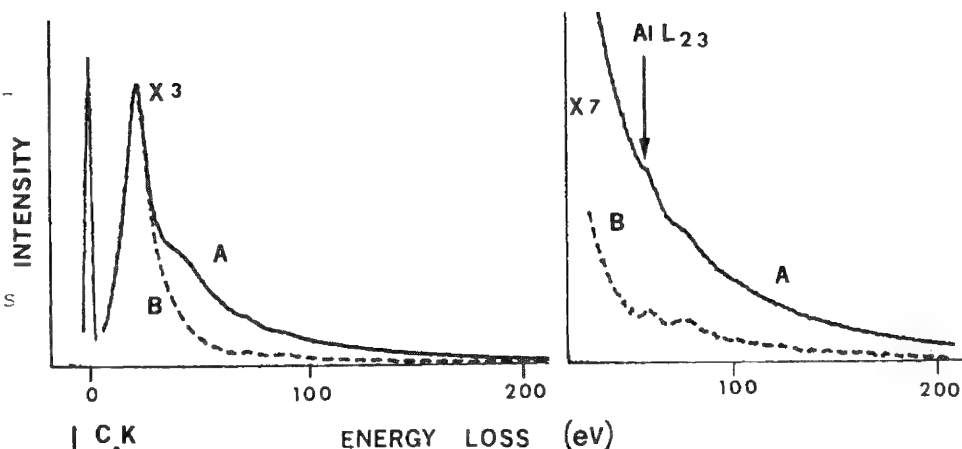


FIG. 2.--Core-loss spectrum from same sample as in Fig. 1: (A) measured spectrum showing background extrapolation, (C) carbon K and oxygen K edges with background subtracted, (c) single-scattering distribution from Eq. (5).

His calculations indicate that an accuracy better than 10% is obtained for a double-scattering correction if the collection angle is greater than 10 mrad. We have written a fairly simple program that has permitted us to study the effects on the derived SSD of some other experimental factors, such as nonuniform sample thickness, nonlinear detector response, and sample drift.

We start with a spectrum recorded at 100keV beam energy from a thin silicon oxide film coated with carbon of total thickness $0.2\lambda_T$. From this spectrum as input the program generates plural-scattering distributions for any specimen thickness, by means of the FT of Eq. (1), and allows for modifications to simulate various experimental conditions. The SSD derived from the generated spectra can then be compared with the original SSD to determine the errors that are introduced. Figure 3 simulates the effect arising when 10% of the area probed is holes in a sample $2.0\lambda_T$ thick. The SSD derived from Eq. (2) (curve C) is overestimated by up to 100% because too little plural scattering is removed. Figure 4 presents the effects of nonlinear detector response where the zero loss count rate is too high for single pulse detection. The sample is again of thickness $2.0\lambda_T$ and the zero loss peak intensity is reduced by 30%. The resulting SSD derived from Eq. (3) (curve C) is underestimated by up to 70% since too much plural scattering is removed. Oscillations and severe distortions are present. Figure 5 simulates the effects of contamination build-up or sample drift on the core edge deconvolution. Curve B is the core edge spectrum generated for a thickness of $1.0\lambda_T$ and curve C is the deconvoluted spectrum obtained from Eq. (8) with a low-loss spectrum corresponding to a sample of increased thickness, $1.5\lambda_T$. An error of more than 50% is observed with too much intensity removed from the spectrum above threshold.

Conclusions

Comparisons such as these illustrate what goes wrong with the SSD if the necessary experimental conditions are not satisfied. The results may help the experimentalist to recognize and correct a problem in the measurements. If these considerations are taken into account, it is possible to remove plural scattering from energy loss spectra on a regular basis. This allows more accurate information, both qualitative and quantitative, to be extracted from the data.

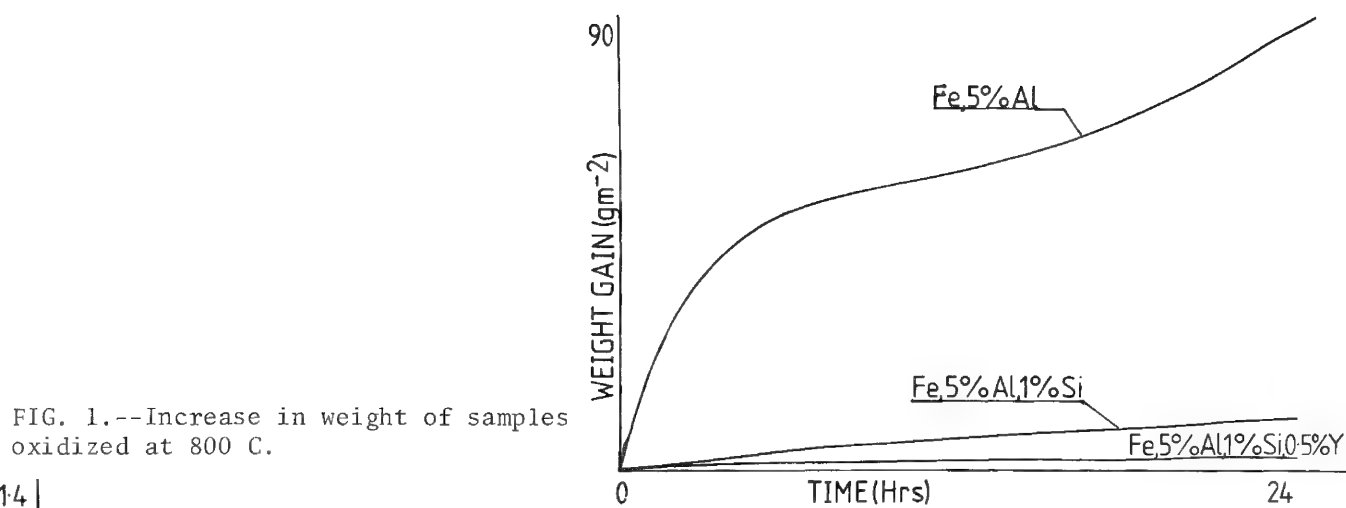


FIG. 1.--Increase in weight of samples oxidized at 800 C.

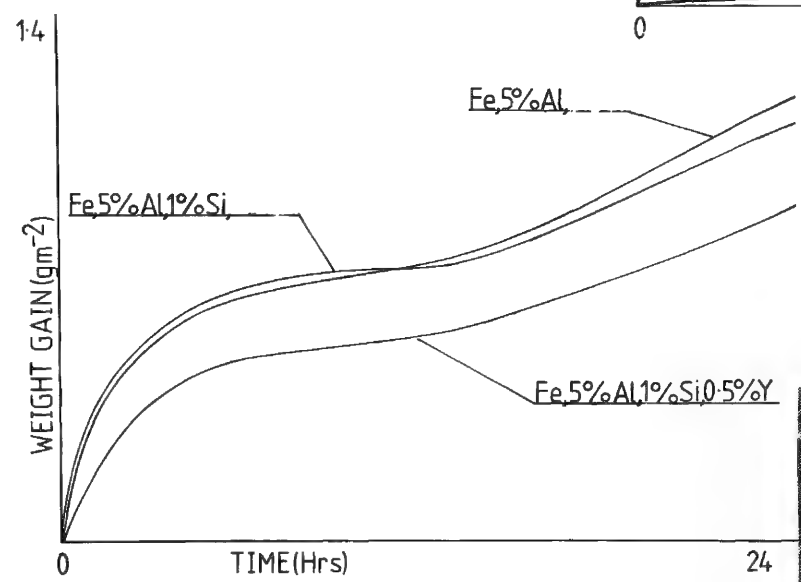


FIG. 2.--Increase in weight of samples oxidized at 1000 C.

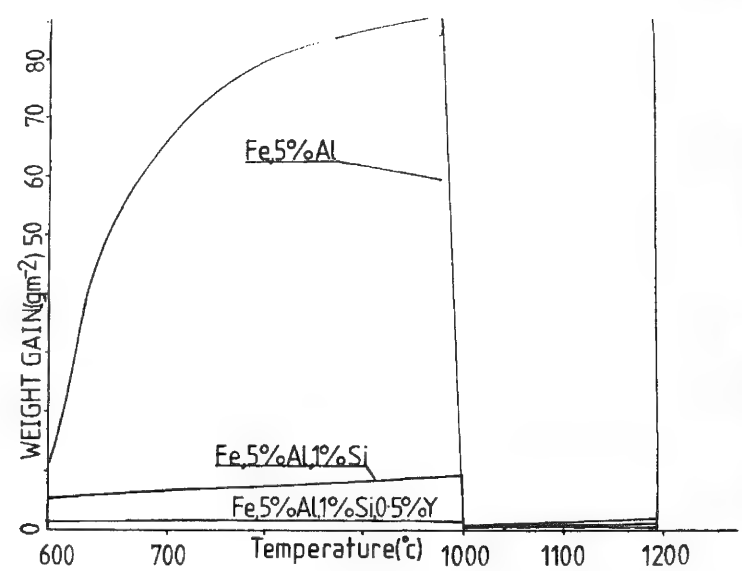


FIG. 3.--Weight gain for various temperatures, fixed time (24 h).

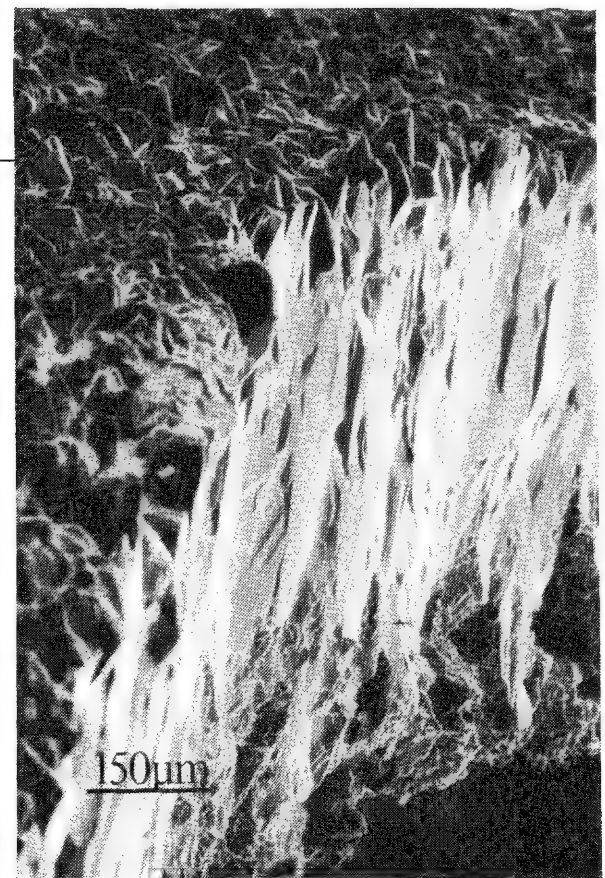


FIG. 4.--Iron oxide scale formed on Fe 5% Al after 24 h at 1200 C.

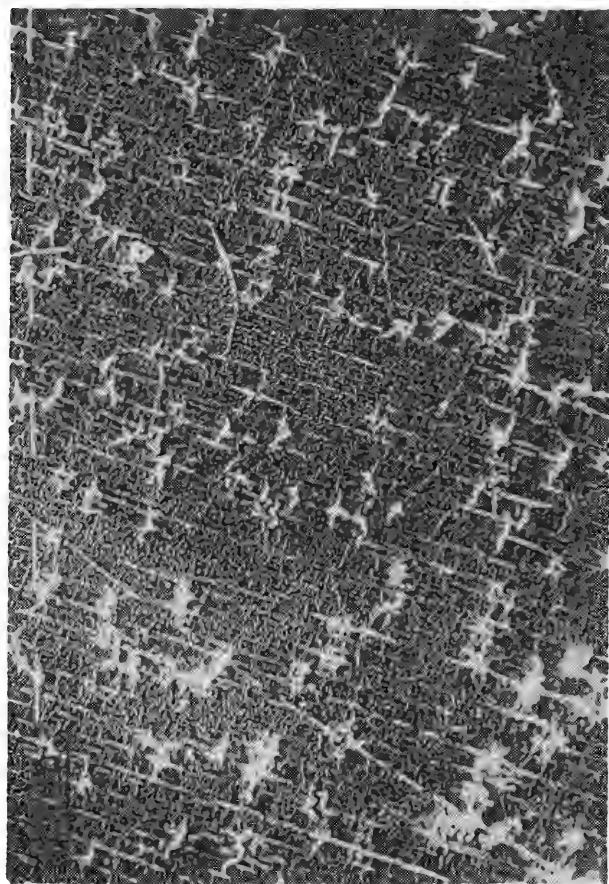


FIG. 5.--Convoluted alumina formed on Fe 5% Al after 10 h at 1000 C.

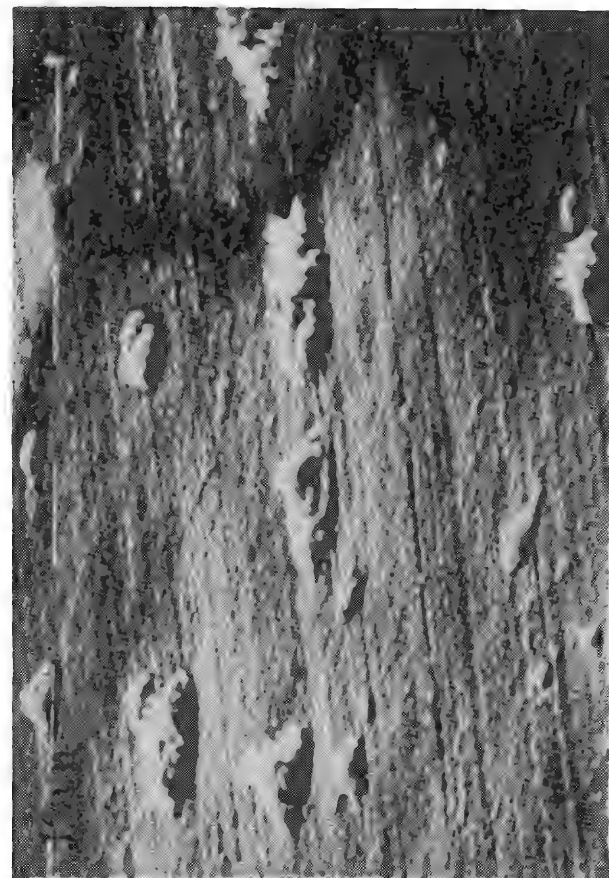


FIG. 6.--Flat alumina formed on Fe 5% Al 0.5% Y after 10 h at 1000 C.

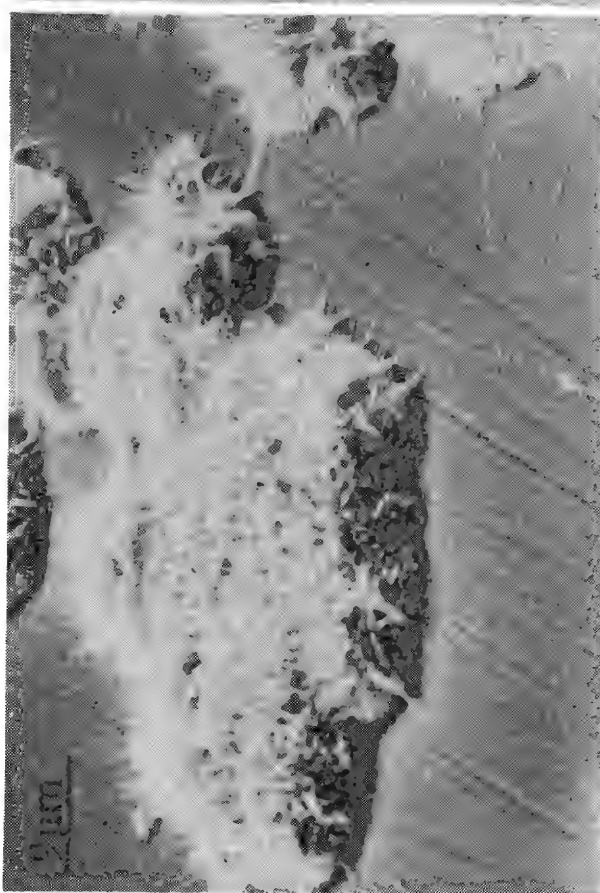


FIG. 7.--Iron oxide nodules and alumina formed at 600 C on Fe 5% Al 1% Si.

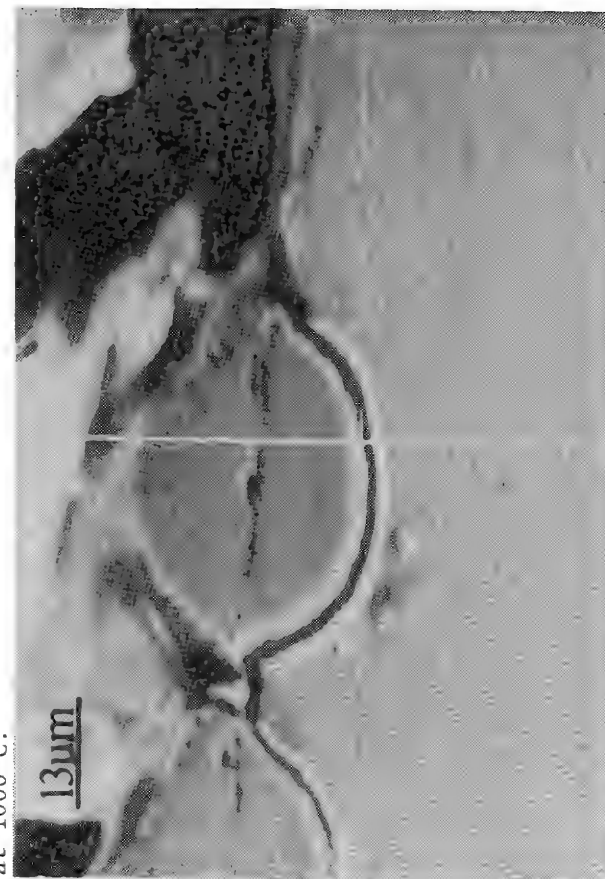


FIG. 8.--Cross section of iron oxide nodule at 600 C on Fe 5% Al 1% Si.

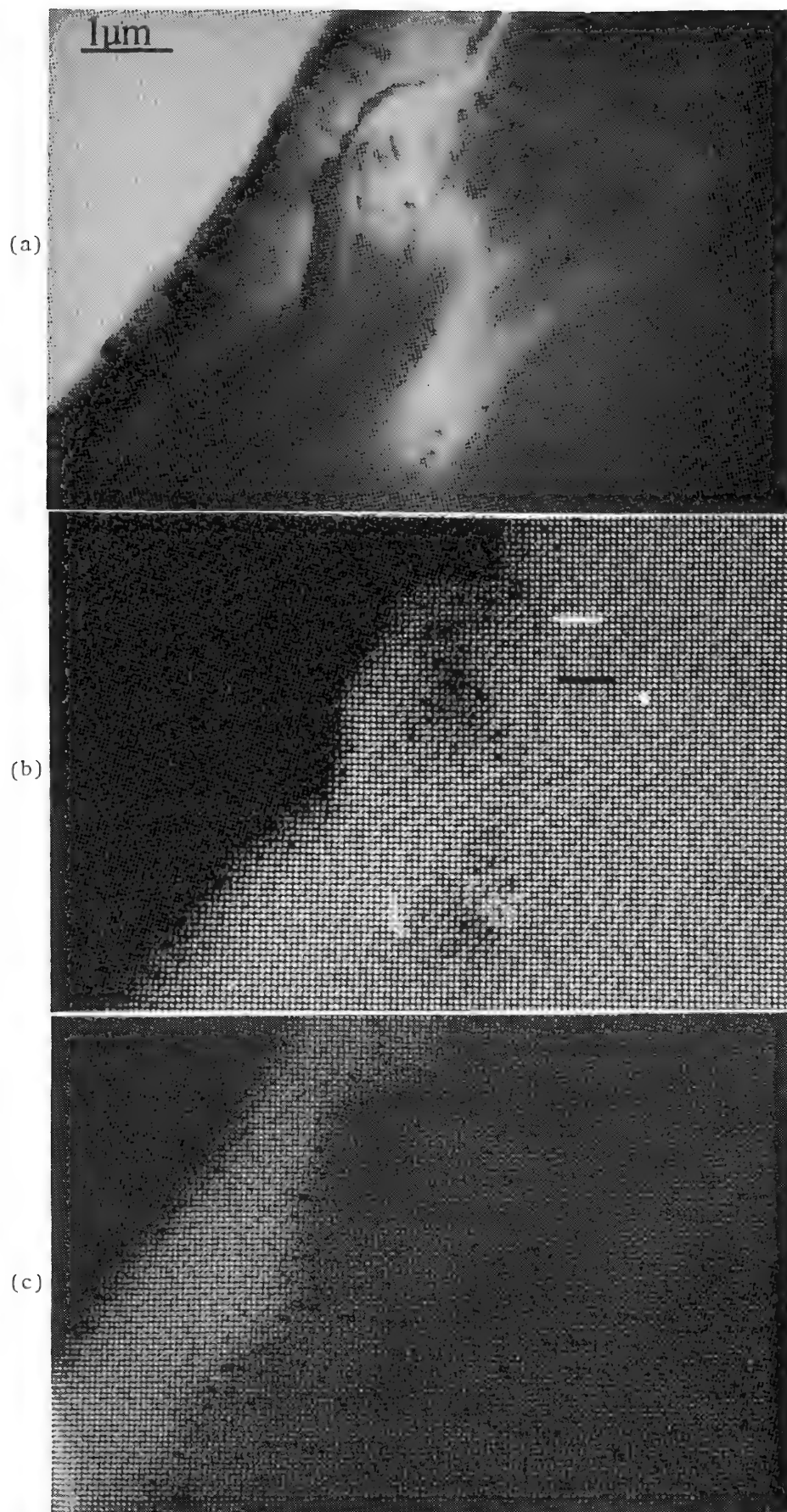


FIG. 9.--Metal/oxide interface in Fe 5% Al 1% Si 0.5% Y at 1000 C: (a) TEM image, (b) Fe map, (c) Al map.

less successful, since the magnetic field around the samples was affected by the ferritic nature of the base material and alignment proved very time consuming. However, EDX analysis and mapping produced some very interesting results, and typical examples are shown in Figs. 9 and 10.

Initial work has been concentrated on the alumina films formed at high temperatures (> 1000 C), which have been stabilized with yttrium additions. A TEM micrograph of metal oxide interface tested at 1000 C is shown in Fig. 9. The x-ray maps show that the scales are essentially pure $\alpha\text{-Al}_2\text{O}_3$ containing no detectable amounts of silicon either within the scale or at its base. Nor does the grain boundary at the center of the micrograph contain any alumina. Other boundaries do contain large amounts of aluminum, however, as shown in Fig. 10. A high yttrium signal is also detected in this region as can be seen in the x-ray maps. Little if any silicon was detected in either of these areas, although silicon is sometimes found associated with any iron oxide present. Elemental diffusion profiles have been obtained by line scanning across the oxide/metal interface and similar information has been obtained by XPS measurements on samples which have been sputter profiled up to depths of ~ 1 μm in a UHV environment.

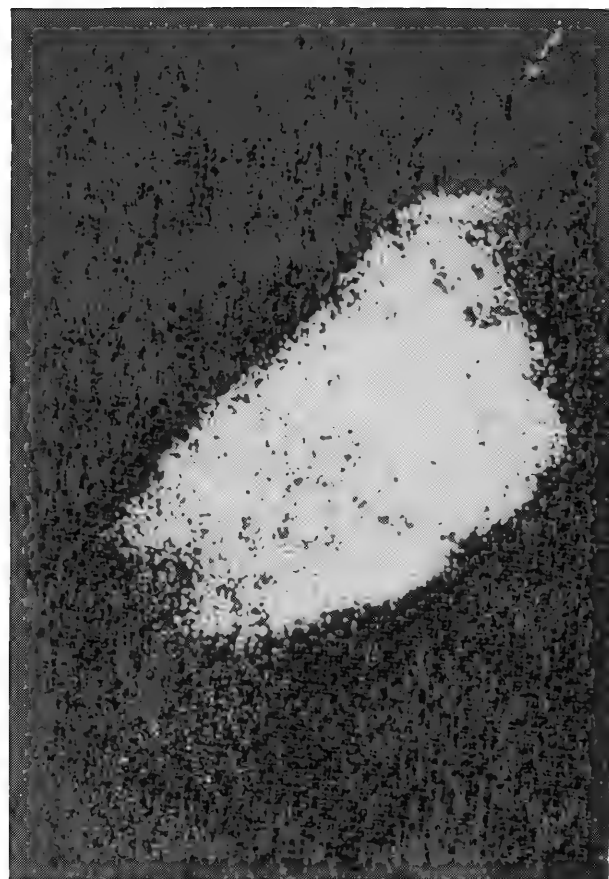
There are numerous theories as to the role of minor element additions such as those of yttrium and silicon on oxidation behavior. Among them are mechanical influences such as pegging or stress relieving,³ and diffusion effects such as oxygen "gettering"⁵ or ternary interactions. High spatial resolution investigations of the metal/oxide interface regions are now being used together with simple diffusion experiments to test these various theories. The results to date suggest that silicon and yttrium additions have a major effect on the oxidation resistance of Fe5Al, particularly below 1000 C, due to the formation of an alumina scale, but that the role of the silicon in Fe-Al is not the same as in the more familiar Fe-Cr system.

References

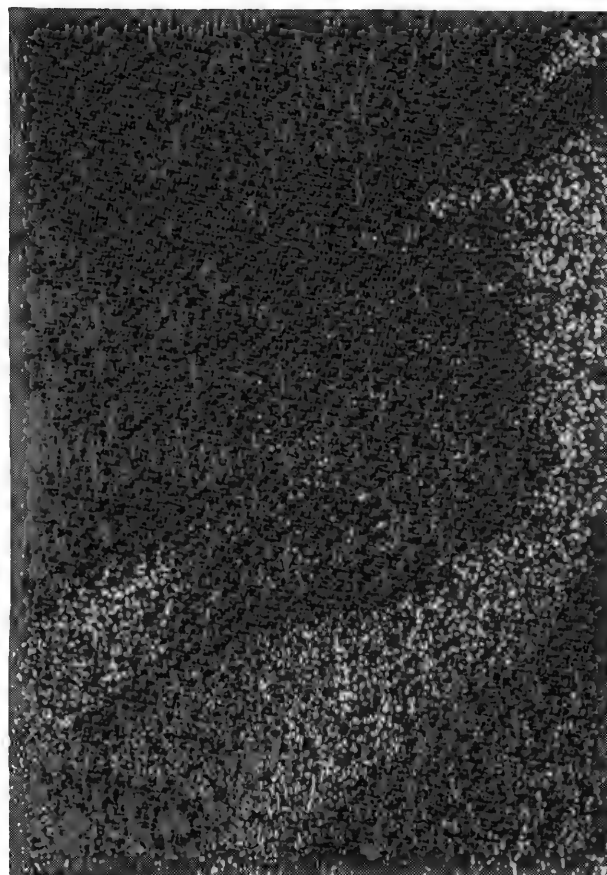
1. British patent application GB 2 019 886A. Fecralloy[®] is a registered trade mark of the UKAEA.
2. R. G. Miner and V. Nagarajan, *Oxid. Met.* 16: 295, 1981.
3. F. A. Golightly, F. H. Stott, and G. C. Woods, *ibid.*, 10: 163, 1976.
4. M. I. Manning and P. C. Rowlands, *Brit. Corr. J.* 15:184, 1980.
5. W. E. Boggs, *Oxid. Met.* 10: 277, 1976.



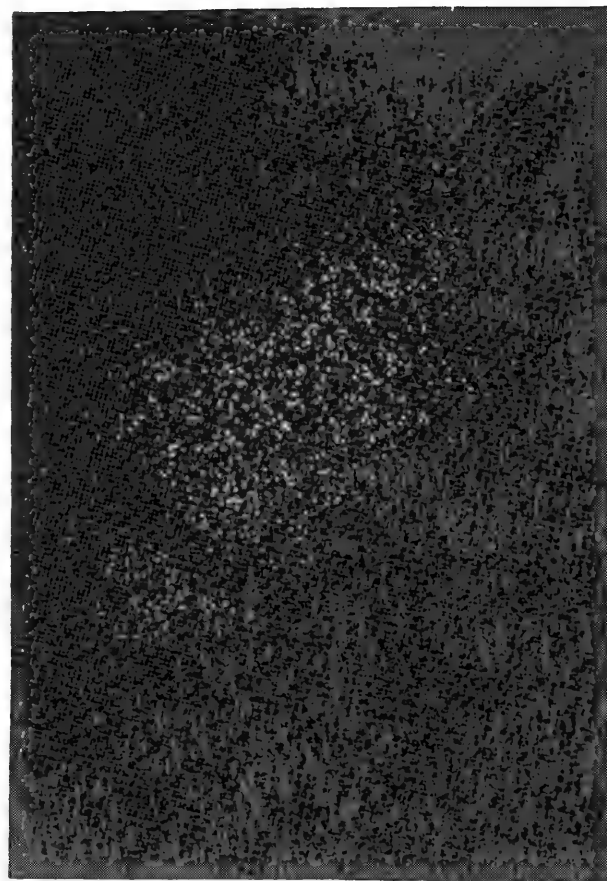
(a)



(b)



(c)



(d)

FIG. 10.--Oxidation down metal grain boundary in Fe 5% Al 1% Si 0.5% Y at 1000 C: (a) SED image, (b) Al map, (c) Fe map, (d) Y map.

INDUSTRIAL ATMOSPHERE CORROSION PRODUCTS ON METALLIC COATINGS

J. J. Friel and Sudhir Mehta

The atmospheric corrosion of metallic-coated sheet steel is a complex process involving numerous reactions that depend on the type of environment and length of exposure. The analysis of solid corrosion products formed on the surface of zinc or aluminum coatings can provide information about the nature of these reactions. However, such analysis is difficult owing to (1) limited mass, (2) interference from the substrate, and (3) lack of crystallinity. Because of these problems, little work has been done in this area in the past. One need not fully characterize the corrosion products to gain information about the corrosion reactions, but one must have sufficient chemical and structural data to identify each phase. In most cases the use of more than one technique is necessary to acquire this information.

X-ray diffraction (XRD) and infrared (IR) spectroscopy can be used to identify compounds when they are present in sufficient amount and when references are available. Surface techniques such as Auger electron spectroscopy (AES) and x-ray photoelectron spectroscopy (XPS) are useful in the determination of the chemical state of the elements on the surface. Electron microbeam instruments with wavelength- or energy-dispersive spectroscopy (WDS or EDS) provide information about the elements present and their associations, but interference from the substrate often makes identification ambiguous.

However, the analytical electron microscope (AEM) can overcome most of the limitations associated with the other techniques, if suitable extraction replicas can be prepared. In fact, we found that when data from the bulk techniques such as XRD were combined with those from microbeam techniques, the structure and composition of all solid corrosion products present on our samples could be determined.

Experimental

Panels of commercial metallic-coated sheet steel were examined after exposure to the industrial atmosphere in Bethlehem, Pa., for nine years. The samples are described in Table 1 along with original and present coating thicknesses determined metallographically. The skyward surface of each panel was examined, and the corrosion products were analyzed in situ in each test except for IR spectroscopy and AEM. Previous work dealing with the corrosion rates of these types of coatings along with corrosion product analysis by XRD was performed by Townsend and Zoccola.¹

The analytical instruments used were as follows: (1) Philips automated x-ray diffractometer scanned in steps of 0.02° two-theta and 2s/step with Cu radiation on coupons of coated steel; (2) Perkin-Elmer model 283B computer-controlled infrared spectrometer using KBr pellets containing scrapings from the surface of the coatings; (3) Physical Electronics model 548 x-ray photoelectron spectrometer using a magnesium x-ray source to excite photoelectrons over a 4mm^2 area of the surface with a pass energy of 50 eV; (4) Amray 1600 scanning electron microscope (SEM) operated at 15 kV normal to the surface; (5) ARL-EMX electron probe microanalyzer (EPMA) operated at 15 kV primarily to generate x-ray maps of Al, Zn, Fe, S, Si, O, and C, on the surface; and (6) Philips model EM400T analytical electron microscope operated at 120 kV to examine direct extraction replicas of the corrosion products.

The authors are at the Homer Research Laboratories of Bethlehem Steel Corp., Bethlehem, PA 18016. Mr. L. Allegra provided the weathered steel panels, and the aid of Drs. D. M. Follweiler and R. G. Hart is acknowledged for their assistance with the infrared spectroscopy and surface analysis, respectively.

Results

The galvanized steel sample produced the largest volume of corrosion products; the Al-coated type 2 and Galvalume coatings produced the least. The data provided by each analytical technique are shown in Table 2, along with interpretations consistent with the data. The XRD patterns are dominated by the metals in the coating, with only minor peaks representing the corrosion products. However, only those products are listed in Table 2. Zinc carbonate and zinc sulfate were found on the Zn-coated sample, but only oxides and hydrates of Al and Fe were found by XRD on the aluminum coatings. The Galvalume coating contained so few products that none could be identified by XRD. The IR data show the presence of hydrated Al-oxide and sulfate in the Al-containing coatings, and Zn-carbonate with alpha and delta-FeOOH in the zinc coating. The EDS analysis on the SEM revealed a prominent sulfur peak in areas of each sample plus a phase containing Al and Si in coatings that contained silicon. The SEM provided qualitative analysis of individual particles on the surface, but x rays from the substrate were always present.

The x-ray maps generated by the EPMA revealed an association of sulfur with oxygen, and the presence of sulfate was confirmed by a sulfur XPS peak at 172 eV and by the IR absorption. With the exception of a large oxygen peak, the elements detected on the surface by XPS were similar to those in the bulk as measured by EDS, but any subtle differences in the chemical state were obscured by charging.

The AEM, though, was the most informative of the analytical techniques used. By means of extraction replicas, we were able to observe individual particles pulled off the surface of the coatings. In this manner, it was possible to analyze corrosion products individually without interference from either adjacent particles or the substrate. In the Al-containing coatings, an amorphous sulfate of Al and Fe was common. Its presence was suggested by the other techniques; however, combined convergent-beam electron diffraction and EDS in the AEM conclusively proved its existence. In the Al-coated type 1 and Galvalume coatings, both of which contain silicon, an amorphous Al-silicate was also observed. Both the sulfate and silicate corrosion products were common, but their electron diffraction patterns, obtained in the microprobe mode, showed no crystallinity; accordingly, they were not detected by x-ray diffraction. In the case of the Zn-coated sample, the AEM data confirmed what was already known from XRD: an Fe-Zn-sulfate and Fe-oxide are the primary corrosion products.

Energy-dispersive spectra of the Al-Fe-sulfate on the Galvalume coating are shown in Figs. 1 (SEM spectrum) and 2 (AEM spectrum). The principal difference between them is a greater Al/Fe ratio in the SEM spectrum. This increase in Al is the result of Al x rays from the substrate. Some Cu from the grid is also seen in the AEM spectrum. Based on a synthesis of all the information disclosed by these techniques, a list of the probable solid corrosion products on these coatings is compiled in Table 3.

Discussion

Even with a combination of techniques, it is difficult to quantify the amount of each corrosion product, but it is possible to identify them. By use of replicas, we were able to extract numerous particles, mostly sulfates of Al and Fe, or of Zn on the Zn-coated sample. The sulfates were probably hydrated, and each one we checked by electron diffraction was amorphous. The second most abundant corrosion product was the amorphous Al-silicate on samples containing Si. Fe-oxides and some foreign material such as quartz, clays, and K-feldspar were also present. We concluded that the Al-silicate was a corrosion product, because of its lack of crystallinity and because it only occurred on the coatings containing silicon. The SEM and EPMA suggested that these phases were abundant, but they could not provide conclusive evidence. Oxides were harder to locate because oxygen could be measured with the EDS detector, and the high probe current necessary for WDS damages many hydrated phases.

Infrared and x-ray photoelectron spectroscopy proved the existence of sulfate, carbonate, and FeOOH, but otherwise were not very informative. The laser Raman microprobe might be useful as a molecular microbeam technique, but few standard spectra are yet available. The AEM is particularly well suited for the analysis of small particles and amorphous or microcrystalline materials. It is complementary to XRD, which can provide rapid identification of crystalline materials but only when they are present in sufficient amount. None of these techniques provide quantitative chemical analysis of the type of materials that

TABLE 1.--Sample description.

<u>Coating</u>	<u>Nominal Composition (wt%)</u>	<u>Coating Thickness (μm)</u>	
		<u>1974</u>	<u>1983</u>
Al-Coated type 1	Al9Si3Fe	23	17
Al-Coated type 2	Al	41	35
Galvanized	Zn	19	1
Galvalume*	Zn55Al1.6Si	20	18

*Galvalume Sheet Steel is Bethlehem Steel Corp's trademark for a product with the coating composition given above.

TABLE 2.--Analytical results and interpretation.

<u>Technique</u>	<u>Al-Coated type 1</u>	<u>Al-Coated type 2</u>	<u>Galvanized</u>	<u>Galvalume</u>
<u>IR</u> results interpretation	Al-O; SO_4 ; OH Al_2O_3 M- $\text{SO}_4(\text{OH}, \text{H}_2\text{O})$	SO_4 ; OH M- $\text{SO}_4(\text{OH}, \text{H}_2\text{O})$	FeOOH; CO_3 ; OH FeOOH; $\text{ZnCO}_3(\text{OH})$	Al-O; SO_4 ; OH Al_2O_3 M- $\text{SO}_4(\text{OH}, \text{H}_2\text{O})$
<u>SEM</u> results interpretation	Al,S,Fe,Si; Al,Si (Al,Fe)-sulfate Al-silicate	Al,S,Fe (Al,Fe)-sulfate	Zn,S,Fe,Al,Si; Fe (Zn,Fe)-sulfate Fe-oxide	Al,S,Fe,Zn,Si; Al,Si (Al,Fe)-sulfate; Al-silicate
<u>EPMA</u> results interpretation	Fe,O; Al,Fe,S,O; Fe-oxide; (Al,Fe)-sulfate Al-silicate	Al,Si Al,Fe,S,O	Zn,Fe,O (Zn,Fe)-oxide	Fe,S,O Fe-sulfate
<u>XPS</u> results	O,Fe,Al,Si,S	O,Fe,Al,S,Si	Zn,O,Fe,S	O,Al,Fe,S,Si
<u>AEM</u> results interpretation	Al,Fe,S; Si,Al; Fe (Al,Fe)-sulfate Al-silicate Fe-oxide	Fe,Al,S; Fe (Al,Fe)-sulfate Fe-oxide	Fe; Fe,Zn,S; Fe,Zn Fe-oxide (Fe,Zn)-sulfate (Fe,Zn)(CO_3, OH)	Al,Fe,S; Al,Si (Al,Fe)-sulfate Al-silicate
<u>XRD</u> results	$4\text{Al}_2\text{O}_3 \cdot \text{H}_2\text{O}$ Al_2O_3 ; Fe_3O_4	$4\text{Al}_2\text{O}_3 \cdot \text{H}_2\text{O}$; Fe_3O_4	ZnSO_4 ; $(\text{Fe}, \text{Zn})\text{CO}_3$ FeOOH; Fe_3O_4 $(\text{Fe}, \text{Zn})_5(\text{CO}_3)_2(\text{OH})_6$	No Products Identified

TABLE 3.--Probable solid corrosion products.

<u>Al-Coated type 1</u>	<u>Al-Coated type 2</u>	<u>Galvanized</u>	<u>Galvalume</u>
(Al,Fe)-sulfate	(Al,Fe)-sulfate	ZnSO_4	(Al,Fe)-sulfate
Fe_3O_4	Fe_3O_4	Fe_3O_4	Fe_3O_4
Al-silicate	$4\text{Al}_2\text{O}_3 \cdot \text{H}_2\text{O}$	FeOOH	Al-silicate
Al_2O_3	Al_2O_3	$(\text{Fe}, \text{Zn})\text{CO}_3$	
$4\text{Al}_2\text{O}_3 \cdot \text{H}_2\text{O}$		$\text{Zn}_5(\text{CO}_3)_2(\text{OH})_6$	

form as corrosion products, but such analysis is not essential to adequately identify the phases and interpret the reactions.

It is evident from these results that sulfur plays a dominant role in the atmospheric corrosion process at this site, since sulfates are the largest and most abundant solid corrosion products on each of these coatings. These sulfates contain Fe in varying amounts along with either Al or Zn from the coating as the principal cation. Inasmuch as the galvanized and Galvalume coatings contain no Fe, the source of the Fe must be atmospheric or the cut edges of the panels.

When Si is present in the coating, as in Al-coated type 1 in Galvalume, it is evidently reactive with Al in an industrial environment. The resulting Al-silicate is present as numerous submicron particles, but it does not constitute a large fraction of the total volume of corrosion products. No zinc corrosion products were found on the surface of the Galvalume coating; however, Zn and Fe compounds including sulfates and oxides or hydroxides do exist in the interdendritic regions where Zn metal had been. These products inhibit access of corrosive fluids through the coatings and thus account in part for the good corrosion resistance of this coating.

Conclusions

- By use of complementary techniques, it is possible to identify atmospheric corrosion products.
- Al-coated type 2 and Galvalume sheet produce the least volume of corrosion products.
- The most abundant Al-rich corrosion products are amorphous.
- Sulfur plays a dominant role in the corrosion of both Al- and Zn-coated steel in an industrial environment.

References

1. H. E. Townsend and J. C. Zoccola, "Atmospheric corrosion resistance of 55%Al-Zn-coated sheet steel: 13 year test results," *Materials Performance* 18: 13-20, 1979.

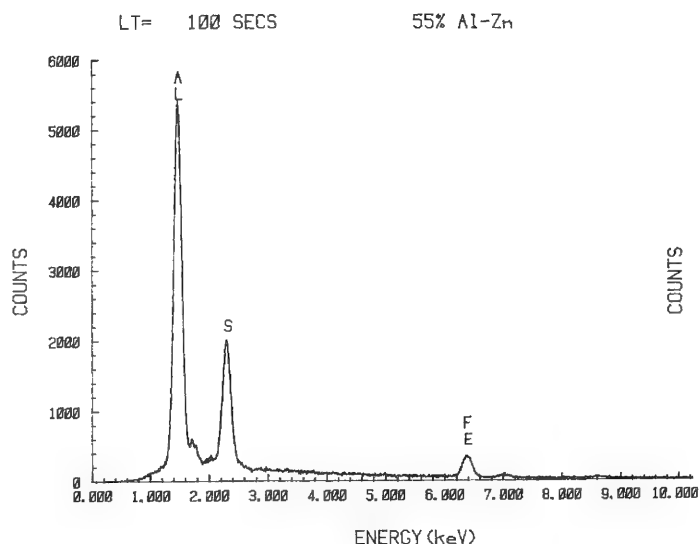


FIG. 1.--SEM/EDS spectrum of amorphous (Al,Fe)-sulfate on Zn55%Al-coated sheet steel.

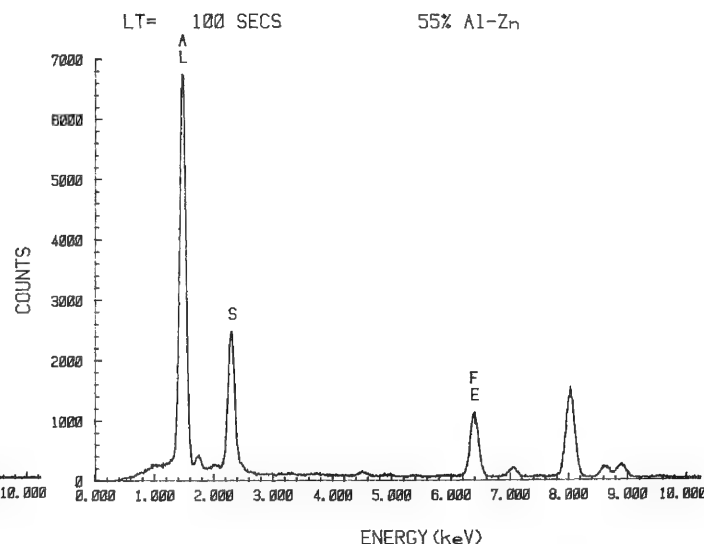


FIG. 2.--AEM/EDS spectrum of amorphous (Al,Fe)-sulfate on Zn55%Al-coated sheet steel.

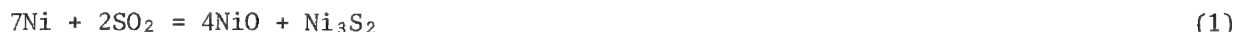
CORROSION OF NICKEL IN SO₂-O₂-SO₃-Ar ATMOSPHERES ABOVE 600 C

Victoria Guerra and W. L. Worrel

Studies of the corrosion of nickel in SO₂-O₂-SO₃ atmospheres have been done at total reaction gas pressures of 1 at.¹⁻⁴ This process usually results in fast reaction rates and very fast changes in product scale morphology. Because of the important relationship between scale morphology and reaction kinetics, this study aims at achieving a step-by-step understanding of the corrosion of nickel in SO₂-O₂-SO₃ atmospheres. To achieve this understanding, reaction products were characterized by x-ray diffraction, optical and scanning electron microscopy, EDC, and XPS during various states of the reaction.

Two reaction mechanisms have been proposed to explain the reaction of nickel with SO₂-O₂-SO₃. One involves the direct reaction of nickel with SO₂;^{3,4} the other involves the formation of a thin, unobservable NiSO₄ layer at the scale-gas interface.^{1,2}

The direct reaction mechanism is described by



It accounts for the observed sulfur-to-oxygen weight ratio of one and for the observed faster reaction rates in environments where SO₂ is the sole reacting species.

The sulfate intermediate mechanism is supposed to go in effect at temperatures and pressures at which sulfate is stable. It involves the formation of a thin sulfate layer at the scale-gas interface. The sulfate in turn reacts with the nickel dissolved in the scale to produce sulfide and oxide according to



This reaction can be used to account for the simultaneous presence of sulfide and oxide in the scale as well as for the increased rates observed at temperatures and pressures at which sulfate is stable. However, if NiSO₄ is present in the scale, reaction (3) is thermodynamically favored over (2):



The significance of the direct reaction and sulfate intermediate mechanisms in SO₂-O₂-SO₃-Ar environments is discussed below in light of recent experimental observations in the SEM.⁵

Experimental

Experiments were carried out on coupons of high-purity (99.999%) nickel provided by Johnson Matthey Chemicals, Ltd. The coupons were ground to 1 µm in alumina paste on felt. Thermogravimetric measurements were done on a Cahn 2000 electrobalance. The output of the balance was recorded by a Radio Shack TRS-80 computer at 2min intervals. The reaction products were identified by x-ray diffraction and ASCA. The scale morphology was studied under the scanning electron microscope.

Results

Reactions exhibited parabolic kinetics at all temperatures, which indicated that diffusion of ions through the product scale was the rate-limiting step.

The product layer consisted of an inner sulfide layer and an outer two-phase layer with varying degrees of sulfide dispersion. From 600 to 750 C, the sulfide dispersion was coarser than that produced in the absence of molecular oxygen, which resulted in a smaller diffusion path volume and slower reaction rates. Above 750 C an SO₂:O₂ ratio of 1:20 produced a "two-phase layer" that was mostly oxide. As a result, reaction rates were very slow, and diffusion of cations to the reaction interface occurred via the oxide grain

The authors are at the Department of Materials Science and Engineering, University of Pennsylvania, Philadelphia, PA 19104.

boundaries. At 1000 C the outer layer was all oxide, and the inner liquid sulfide layer enveloped the grains of the nickel substrate to form two-reaction interfaces, one at the sulfide-oxide interface, the other at the oxide-gas interface. Diffusion of cations through the product layer was the rate-determining step.

The mechanical properties of the product scales played an important role in the determination of the reaction mechanism below 800 C. At 600 C they were so brittle that any growth resulted in cracking of the scale, and the subsequent exposure of nonequilibrium phases (i.e., Ni_3S_2) to the gas phase. At 700 and 800 C growth stresses were relieved by the formation of cracks across the two-phase layer. As the reaction proceeded, the cracks became lined with Ni_3S_2 , which provided fast diffusion paths for nickel cations and thus prevented the scale from equilibrating with the gas.

Even though the reaction kinetics were parabolic, the scales were observed to be in equilibrium with the gas for very short periods of time. Sulfate was found on the surface at 700 and 800 C only 30 min after the beginning of the reaction. After that, the scale cracked, exposed the sulfate to high nickel activities, and caused it to decompose. At 600 C sulfate was found in the scale by ESCA. It was also only observed during the initial reaction stages.

Conclusions

Scale brittleness from 600 to 800 C results in high nickel activities at the scale-gas interface after an initial period of reaction, during which the scale tries to equilibrate with the gas. The high nickel activities preclude sulfate formation and thus a sulfate intermediate mechanism for scale growth.

References

1. C. B. Alcock, M. G. Hocking, and S. Zador, *Corr. Sci.* 9: 111, 1969.
2. M. G. Hocking and V. Vasantasree, *Corr. Sci.* 16: 261, 1972.
3. K. L. Luthra and W. L. Worrell, *Met. Trans.* 9A: 1055, 1978.
4. K. L. Luthra and W. L. Worrell, *Met. Trans.* 10A: 261, 1979.
5. V. Guerra, Ph. D. Thesis, Department of Materials Science and Engineering, University of Pennsylvania, 1984.

ANALYSIS OF CORROSION PRODUCTS WITH THE USE OF THE RAMAN MICROPROBE

R. Heidersbach and F. Purcell

Most metals are used in environments in which they are thermodynamically unstable. These unstable metals form reaction products on their surfaces which, if protective, prevent further reaction of the metal with the environment. Thus, many problems in corrosion science involve the understanding of these reaction product films, how they form, and how or why they become protective or nonprotective.

Many materials analysis techniques have been applied to the study of corrosion films. The ideal technique would be nondestructive, capable of in situ analysis, and capable of analyzing both the elemental chemistry and the molecular or crystal structure of the corrosion products film. Although no existing technique has all of these virtues, Raman spectroscopy is a technique offering several distinct advantages over other available analysis techniques.

The recent development of commercial Raman microprobes offers increased opportunities for understanding corrosion processes. The results of a preliminary study into the corrosion products formed weathering steels are used to illustrate the capabilities of this new instrument.

Weathering Steels

Weathering steels are a class of structural steels which, when used in some atmospheric exposure environments, develop a protective rust film that allows them to be used without being painted. They have been commercially available in the United States since the 1960s and have been used on a number of prominent buildings and other structures.¹ General guidelines on how they should be used were available in the 1960s.²⁻³ These guidelines included several precautions that were not always followed by designers.

Despite the generally favorable performance of weathering steel in many applications, there have been several notable failures or misapplications of these materials.^{1,4-6} The question of when and how these steels can be used has become controversial, especially in the United States, where the largest highway bridge completed in 1983 was made of weathering steel and located near another weathering-steel highway bridge involved in a widely publicized lawsuit.⁶

Weathering steels have been used for many years, yet no clear understanding of why they form protective films and why these films are sometimes nonprotective is available at present. One of the problems in understanding these films is the fact that a major fraction of these films is noncrystalline. Thus the use of x-ray diffraction, the most common means for structural analysis of corrosion products, will not work on weathering steels. This has led several researchers to use Mössbauer spectroscopy,⁷ infrared spectroscopy,⁸⁻¹⁰ or Raman spectroscopy⁹⁻¹¹ to analyze these noncrystalline corrosion products.

Scanning electron microscopy shows that weathering steel corrosion products have complicated morphologies.^{11,12} Thus, the development of the Raman microprobe, with improved spatial resolution over the above techniques, offers promise as an improved method of analyzing weathering steel corrosion products.¹³

Raman Microprobe

The Raman microprobe is an improved version of the laser Raman spectrometers that have been available since the early 1970s. These instruments use a laser beam narrowly focused

Author Heidersbach is at Oklahoma State University (Chemical Engineering), Stillwater, OK 74078; author Purcell is with Spex Industries, Edison, NJ 08820.

onto the sample. The wavelength of the incident radiation is several thousand Angstroms, so the incident radiation beam is of necessity several orders of magnitude wider than is possible with electron or x-ray devices. This seeming disadvantage is offset by a number of advantages inherent in Raman spectroscopy.

One of the principal advantages of Raman spectroscopy is the capability for in situ analysis of corrosion products as they form on metal surfaces in reactive environments.¹⁴⁻¹⁷ The lack of in situ capability in water or high-pressure gases is a major limitation of electron-beam instruments and other analytical instruments that operate in vacuum.¹⁷⁻¹⁹ Partial vacuums of any type may cause dehydration of corrosion products and alter the structure in significant ways.

Experimental

Loose nonprotective flaky rust was removed from the surface of two weathering steel structures. One was a 50-yr-old statue in the Midwest, and the other was an I-beam exposed to weathering in a research project.²⁵

Both samples were analyzed by means of a SPEX model 1482 micro-Raman illuminator. Details on the instrument used in this investigation are available in another report.²⁰ The incident-beam spot size was 1 μm and the laser power setting was 0.025 or 0.030 W.

Results

Figures 1 and 2 show Raman spectra obtained from the I-beam sample. The peaks in Fig. 1 correspond to published spectra for $\gamma\text{-FeOOH}$.¹⁰ The spectrum in Fig. 2 had only one peak and corresponds to Fe_3O_4 .^{12,21,22} Fe_3O_4 is reported to be formed by the reduction of $\gamma\text{-}$ or $\delta\text{-FeOOH}$ during the atmospheric corrosion of iron and steel.²² The difficulty of positive identification of Fe_3O_4 by x-ray diffraction is one of the reasons for interest in alternative means of identifying this species.⁷

Figure 3 shows the Raman spectrum obtained from the most prominent features on the exterior of the sample obtained from the naturally weathered structure. No identification of the peaks in this spectrum has been accomplished at the time of this writing. However, it is clear that this spectrum is different from either of those obtained from the I-beam sample. No location was found on the I-beam sample which produced spectra similar to that shown in Fig. 3.

Discussion and Conclusions

The results presented in this paper show that the Raman microprobe can be used to differentiate between corrosion products formed on metal surfaces in different locations.

The Raman microprobe is a promising new tool for the analysis of corrosion products. One possible problem with the use of this instrument is the possibility of radiation-induced alteration of the sample surface by the incident laser beam. This damage can be due to heating or photosensitivity.^{13,23} One means to minimize this problem is through the use of optical multichannel detectors that allow the measurement of Raman spectra in short periods of time. This procedure minimizes the exposure of the sample to the laser beam^{10,23} and allows film-development monitoring.²⁴ No evidence of radiation damage was noted on the samples investigated in this report.

The spectra and results presented in this paper represent a very limited sampling intended to demonstrate the capabilities of Raman microprobe analysis of corrosion products. They should not be interpreted as representative of the corrosion products formed on weathering steels under other conditions.

The reader is cautioned that weathering steels have been marketed in this country with two fundamentally different alloy chemistries. These different alloys may produce different corrosion products on their surfaces. A chemical analysis of the steel from the naturally weathered public structure is not available, so that this possible difference in the spectra reported here cannot be evaluated.

Most reported analyses of weathering steel corrosion products have been for supposedly protective films. The scales analyzed in this report were nonprotective. A detailed comparison of the mineralogy of protective and nonprotective scales is not available.

FIG. 1.--Raman spectrum from inclusion in corrosion product on I-beam sample.

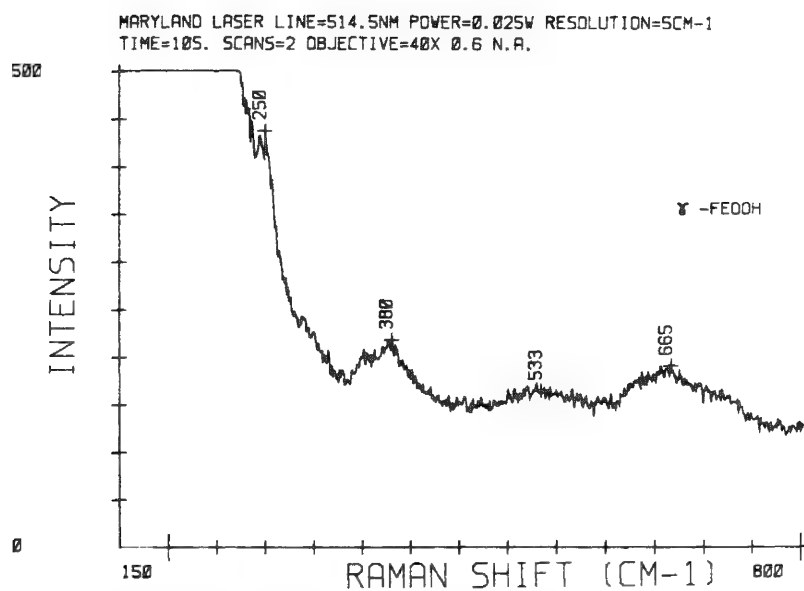


FIG. 2.--Fe₃O₄ spectrum from I-beam sample.

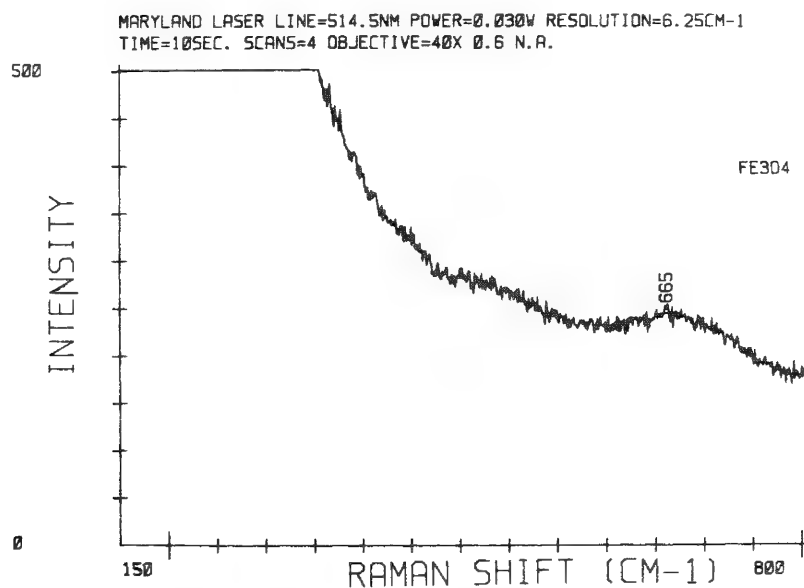
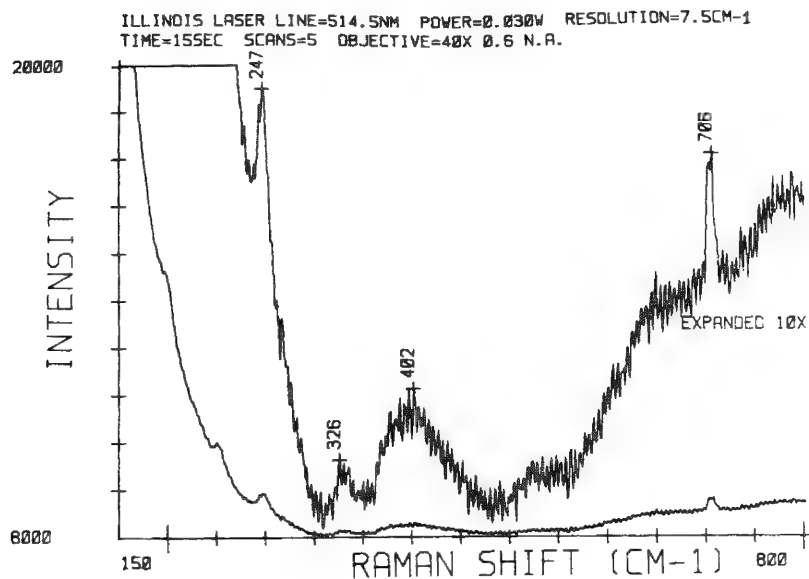


FIG. 3.--Unidentified spectrum from weathering steel statue.



References

1. P. Albrecht and A. Naeemi, *The Performance of Weathering Steel in Bridges*, Final Draft Report for the National Cooperative Highway Research Program, National Research Council, November 1983.
2. C. Larrabee and S. Coburn, "The atmospheric corrosion of steels as influenced by changes in chemical composition," *1st International Congress on Metallic Corrosion--1961*, London, 276-285.
3. R. Madison, "Unpainted steel for permanent structures," *Civil Engineering*, February 1966, p. 68.
4. J. D. Culp and G. L. Tinklenburg, *Interim Report of the Effects of Corrosion on Bridges of Unpainted A588 Steel and Painted Steel Types*, Michigan DOT Report R-1142, Lansing, Mich., June 1980.
5. G. L. Tinklenburg, "Corrosion of unpainted weathering steel: Causes and cure," *Proc. 2nd World Congress of Coatings Systems for Bridges and Steel Structures*, New York, October 1982.
6. J. Baron, *Painting and Wallcovering Contractor*, November 1983, 15-18.
7. H. Leidheiser and S. Music, "The atmospheric corrosion of iron as studied by Mössbauer spectroscopy," submitted to *Corrosion Science*.
8. T. Misawa et al., *Corrosion Science* 14: 279, 1974.
9. J. Keiser et al., *Corrosion Science* 23: 251, 1983.
10. J. Keiser et al., *American Laboratory* 14(No. 4): 17, 1982.
11. P. Fabis et al., *Oxidation of Metals* 16: 399-407, 1981.
12. B. deMeybaum and E. Ayllon, *Corrosion* 36: 345, 1980.
13. T. Doyle and J. Alvarez, "Analysis of TMI-2 samples using the molecular optical laser examiner," Winter 1982 Meeting, American Nuclear Society.
14. R. Thibeau et al., *J. Electrochem. Soc.* 127: 37, 1980.
15. R. Farrow et al., *Applied Physics Letters* 36: 212, 1980.
16. P. Fabis et al., *J. Materials for Energy Systems* 3: 66, 1981.
17. P. Fabis et al., *Corrosion* 37: 700, 1981.
18. R. Rapp, "In-situ studies of the oxidation of metals and alloys," *Proc. 8th Intern. Conf. Metallic Corrosion*, Mainz, September 1981, 674.
19. M. Janik-Czachor, "In-situ characterization of the metal solution interface by surface enhanced Raman spectroscopy," *ibid.*, 254-259.
20. F. Purcell and W. White, "A Raman microprobe study of phase-separated minerals," *Microbeam Analysis--1983*, 289-292.
21. J. Keiser et al., *Corrosion* 38: 357, 1982.
22. J. Keiser et al., *J. Electrochem. Soc.* 129: 2686-2689, 1982.
23. F. Purcell and E. Etz, "A new spectrograph with a multichannel optical detector for the Raman characterization of microparticles," *Microbeam Analysis--1983*, 301-306.
24. "Surface oxidation monitored," *Combustion Research News*, January 1984, p. 5.
25. P. Albrecht, "Fatigue testing of weathered A588 beams," Department of Civil Engineering, University of Maryland.

APFIM STUDIES OF SEGREGATION AND SOLUTE-DEFECT INTERACTIONS IN METALS

D. R. Hess, Kamal Al-Saleh, Kenji Murakami, Toshio Sakurai, and H. W. Pickering

The atom-probe field ion microscope (APFIM) is capable of obtaining both microstructural and chemical information from a sample on an atomistic scale not accessible by any other technique. A schematic of our APFIM is shown in Fig. 1. The sample is in the form of a sharp tip which has been electrochemically polished to an end radius of 100-1000 Å. After cooling the sample to 25 K by the use of a closed-cycle refrigeration system, pressure in the field ion microscope (FIM) chamber is in the 10^{-11} torr range. Image resolution of the FIM is on the order of a few Å and surface atoms are imaged. Mass resolution of the atom-probe [a time-of-flight (ToF) mass spectrometer containing a focusing lens], defined as the mass-to-charge ratio divided by the peak width at half-height, is better than 1000, which is more than sufficient to resolve metal isotopes and their hydrides. Detectability is close to the theoretical limit, which is determined mainly by the efficiency (55%) of the channel plate detector. The spectrometer is not limited to any particular elemental mass range, and light elements such as H, He, Be, C, N, and O can be detected as well as heavier elements. More complete descriptions of APFIM performance are available.¹⁻⁴

The characteristics mentioned above make the APFIM a rather unique analytical instrument and have allowed it to make valuable contributions in the structure and chemistry of grain boundaries and other interfaces, ordering and clustering, and precipitation.^{1,2} Metallurgical applications currently under investigation in our laboratory are described next.

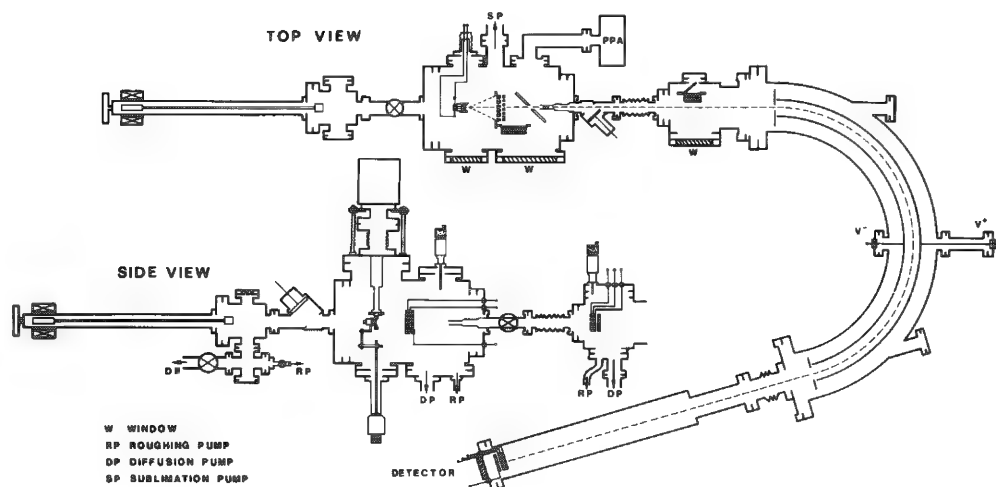


FIG. 1.--Schematic of high-performance focusing type of time-of-flight atom probe.

Authors Hess, Murakami, and Pickering are at the Pennsylvania State University's Department of Materials Science and Engineering (Metallurgy Section), University Park, Pa.; author Al-Saleh is at the Pennsylvania State University (Department of Physics); author Sakurai is at the University of Tokyo (Institute for Solid State Physics), Roppongi, Minato-ku, Tokyo, Japan. Support from DOE under contract DE-AC02-79ER10430 and the National Steel Corp. is gratefully acknowledged.

Segregation at Grain Boundaries

Although grain boundaries play an important role in the chemical and mechanical properties of polycrystalline materials, the application of the FIM and APFIM to their study has been limited⁵⁻⁸ because the observation of a grain boundary where it can be studied is rare, due to the small sample size. To overcome this problem two approaches are being used.

The first approach is the in situ formation of grain boundaries in the FIM sample by irradiation from its side with a pulsed Nd-YAG laser while observing the FIM image.⁹ This approach is currently being studied by T. Sakurai in his laboratory at the University of Tokyo. After the grain boundary is formed in a conventional FIM by laser irradiation, the tip is transferred to a high-performance ToF APFIM for analysis of grain boundary segregation.

When the laser power is small (0.2 mJ/pulse), irradiation produces evaporation of atoms at kink sites, essentially similar to field evaporation, but blunts the tip quicker than ordinary field evaporation. A slight increase in laser power causes random evaporation from the entire surface area and results in poor image quality. A further increase in laser power (0.3-0.5 mJ/pulse) produces rapid evaporation of surface layers and produces various defects, of which grain boundaries are one. Although the exact moment of grain-boundary formation cannot be predicted, a grain boundary is usually produced in less than 30 min of laser irradiation.

Figure 2 shows a W sample in which a grain boundary was formed after several minutes of laser irradiation with energy 0.5 mJ/pulse and the experiment carried out at 25 K. The grain boundary is indicated by arrows. From orientation analysis it is evident that the boundary is a twin boundary with respect to the [211] axis, and can also be described as a $\Sigma = 3$, with a rotation of 70.5° around the [100] axis. Further evaporation of surface layers did not change the geometrical structure of this surface, which suggests that the grain boundary is essentially parallel to the [100] axis. Similar results were obtained on other samples, and it seems that twin boundaries are often formed in this method. Grain boundaries were also produced at room temperature.

Grain boundaries formed in this way were found to disappear upon annealing at 1500 C, which suggests that they are not very stable. These boundaries may therefore differ in chemical and mechanical properties from naturally occurring grain boundaries. Furthermore, these boundaries disappeared after field evaporation of some tens of layers, which would suggest that they were not very deep.

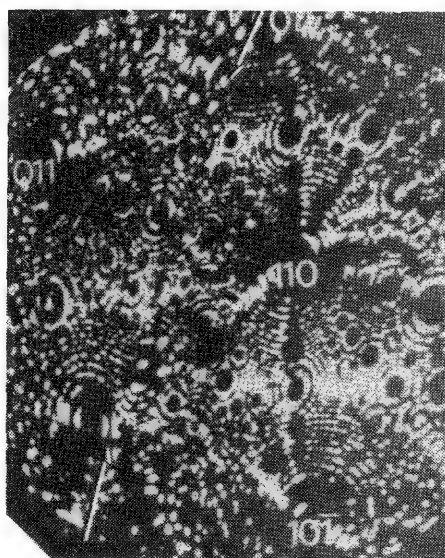


FIG. 2.--Field ion micrograph of W tip with grain boundary indicated by arrows.

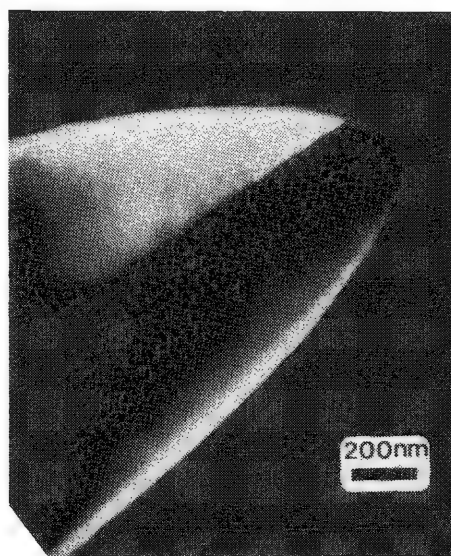


FIG. 3.--Dark-field TEM micrograph of Fe tip with grain boundary.

In order to evaluate the mechanism of grain boundary formation, surface temperature rise during laser irradiation was estimated. This estimate is based on the experimental observation that the evaporation field at a fixed evaporation rate decreases monotonically as the surface temperature increases and is a unique function of temperature.¹⁰ The maximum temperature obtained for the tip surface was 400 K, which precludes liquid-phase recrystallization. Therefore, the mechanism of formation is tentatively assigned to be due to solid-phase recrystallization initiated at existing defects and enhanced by the presence of large stresses due to the high imaging electric field and laser heating.

A W tip in which a grain boundary was produced was transferred to the APFIM and annealed in situ at 1500 C for 30 s in the presence of 2×10^{-6} torr O_2 . Comparing results obtained from this grain boundary with a similar experiment performed on a tip without a grain boundary indicates that there is an enrichment of oxygen along the grain boundary. The clean W surface resisted oxidation, but the grain boundary was subjected to heavy oxidation and formed WO and WO_2 .

The second approach is more conventional and involves the use of a Philips EM420 scanning transmission electron microscope (TEM). Since many more samples may be viewed in the TEM than in the APFIM, Fe samples are being screened in the TEM before they are placed in the APFIM for study. If a grain boundary is observed by dark-field imaging and selected-area electron diffraction in the TEM, the sample is kept for further study in the APFIM. Figure 3 is a TEM dark field image of an Fe sample that contains a grain boundary. Kikuchi lines in low camera length diffraction patterns will be used to determine the orientation between grains. It is also possible to etch samples further for better positioning of the boundary for APFIM study.

Oxidation of an Fe-0.63 wt.% Ti Alloy

The interaction of Ti with oxygen is of great interest in materials science. The APFIM can be used effectively to investigate the interaction. We have, using the APFIM, previously reported that Ti segregates to the surface upon annealing at and above 750 C in vacuum. Ti concentration at the surface is up to 20% and decreases gradually over several layers down to the bulk value. Ti is mainly in the elemental form, although a few percent of TiO were also found. This situation changes radically when the sample is annealed in oxygen. Upon annealing the sample in 10^{-7} torr O_2 at 850 C for an hour, the tip undergoes unexpected changes in its composition. The evaporation field, which is a measure of the surface composition, decreases by approximately 40%, and the detected signals are almost completely Ti compounds (Ti: 25%, TiO: 70%, and TiO_2 : 5%). Few Fe signals are detected. This composition persists up to over a few hundred layers (depending on annealing time) until it finally returns to the Fe-rich nominal bulk composition. Although this phenomenon is not yet completely understood, it appears that oxygen promotes Ti segregation and initiates Ti phase separation from the bulk.

References

1. S. S. Brenner and M. K. Miller, *J. Metals* 35: 54, 1983.
2. S. S. Brenner, *Surf. Sci.* 70: 427, 1978.
3. Toshio Sakurai and H. W. Pickering, "High performance time-of-flight atom-probe for hydrogen characterization in metals," in N. F. Fiore and B. J. Berkowitz, Eds., *Applications of Physics in the Steel Industry*, ASM-MSD, 1981, 171-181.
4. Young Kuk et al., "An atom-probe investigation of a microcrack associated with hydrogen in a Fe-Ti alloy," in Y. Yashiro and N. Igata, Eds., *27th Intern. Field Emission Symposium*, Tokyo: University of Tokyo, 1980, 260-266.
5. E. W. Mueller, *J. Appl. Phys.* 28: 1, 1975.
6. S. Ranganathan, *Acta Cryst.* 21: 197, 1966.
7. A. Henjered et al., *Scripta Met.* 17: 1275, 1983.
8. Toshio Sakurai et al., *Scripta Met.* 15: 535, 1981.
9. Toshio Sakurai et al., "In-situ formation of a grain boundary in field ion microscopy using a laser," in W. R. Graham and A. J. Melmed, Eds., *30th Intern. Field Emission Symposium*, Philadelphia: University of Pennsylvania, 1983, 107-109.
10. Shogo Nakamura and Tsukasa Kuroda, *Surf. Sci.* 17: 1346, 1969.

Electron-beam Lithography

DIRECT MEASUREMENTS OF THE RANGE OF SECONDARY ELECTRONS IN LOW ATOMIC NUMBER MATERIALS

Andrew Muray, Michael Isaacson, Illesanmi Adesida, and Earl Kirkland

In the past few years, the possibility of electron beam microfabrication on the nanometer scale has attracted interest. The ultimate limit to the scale of structures that can be fabricated by use of fast electrons for patterning is determined by the spatial distribution of the electron interactions in the sample and the mechanisms by which patterns are "developed" (i.e., bond breakage, scission, etc.). One particular aspect that has been under investigation has been the role that secondary electrons play in this size scale limit.

As one might expect, the spatial distribution of localization of secondary electrons is also important for determining the ultimate limit of resolution in conventional scanning electron microscopy in which the emitted "secondary" electrons are used as the signal. For these reasons, we have begun a program to obtain direct measurements of the range and distributions of these electrons in various materials. One measure is the escape depth λ of these electrons. This paper describes preliminary measurements of this quantity in a standard electron-beam resist polymer, polymethylmethacrylate (PMMA), and in other electronic materials.

Previously, calculations of the resolution of SEM secondary electron images due to the escape depth of these electrons utilized Monte Carlo calculations to simulate the "edge brightness effects" seen in high-magnification SEM images obtained with small probe sizes ($< 60 \text{ \AA}$ diameter).¹ Similar (though more extensive) Monte Carlo calculations have been made to try to deduce the energy dissipation profiles in PMMA due to secondary electrons.²⁻⁴ We are trying to develop a simple analytical model that might allow us to get a better feel for the salient features with which the secondary electrons limit the pattern size and spatial resolution in the SEM. Our model is of course based on certain simplifying approximations⁵ that can be actually achieved experimentally.

For our initial measurements, we have fabricated grooved and slotted structures.⁶ They consist of arrays 160 \AA wide $\times 600 \text{ \AA}$ high $\times 5000 \text{ \AA}$ long PMMA ridges on top of a 500 \AA thick single-crystal silicon substrate. Arrays in other materials are also being fabricated. Both the PMMA and Si substrate are thinner than one mean free path for inelastic scattering (of 100keV electrons). The walls of the PMMA are nearly vertical (a limitation at present). A $10\text{-}\mu\text{m}$ -diameter beam of convergence angle of 15 mrad is incident normal to the sample surface. As it scans across the edge of the PMMA the secondary-electron signal increases because some electrons escape through the side (vertical) walls. The decrease of this signal away from the edge can be related to the secondary-electron escape depth λ as follows.

For thin films less than one mean free path thick, there is on the average only one inelastic scattering event and therefore few secondary electrons are produced. Because of the kinematics of the scattering process, secondary electrons of energy $< 3 \text{ keV}$ are emitted near normal to the incident-beam direction. They are thus attenuated as $\exp(-x/\lambda)$ on the way of the sample sidewall, where x is the distance from the wall (within the PMMA). Thus, the signal of secondary electrons $S(x)$ as the beam is swept across the edge is just the convolution of $\exp(-x/\lambda)$ with the beam profile and the edge function. (We neglect for now the non-localization of the primary scattering event.) If we assume a perfect vertical wall and a Gaussian beam profile, this convolution is a simple analytical expression, which turns out to be essentially proportional to $\exp(-x/\lambda)$ when the beam diameter is less than λ . Thus, the slope of a semi-log plot of the signal against the distance x from the edge yields $-1/\lambda$.⁵

Authors Muray, Isaacson, and Kirkland are at the Cornell University School of Applied and Engineering Physics; author Adesida is at the Cornell University National Research and Resource Facility for Submicron Structures. This work was supported by NSF under grant ECS 8200312 to the NRRFSS and grant ECS 8205894.

In the case depicted here, our PMMA ridge width is not wide enough, so that there is some interference from both edges, which tends to decrease this slope by $\approx 20\%$ from $-1/\lambda$. In addition, the PMMA walls are not quite vertical. Typically, in the bright field signal, the 20-80% point is only 27 Å, which corresponds to a 1° wall angle. Since we have no tilt capabilities at present, we must live with this condition. With all these caveats, we can still put an upper limit on the escape depth of secondary electrons in PMMA at less than 40 Å. This result is consistent with Monte Carlo calculations^{2,3} and with measurements of the range of low-energy electrons in PMMA.⁷ We are now in the process of constructing more ideal samples and walls of various materials such as pure Si, Si₂N₃, and GaAs,⁸ and investigating the escape depth as a function of secondary-electron energy.

References

1. E. P. George and V. N. E. Robinson, *SEM/1980 I*, 393-406.
2. N. Samoto and R. Shimizu, *J. Appl. Phys.* 54: 3855, 1983.
3. D. Kyser, *J. Vac. Sci. Technol.* B1: 1391, 1983.
4. D. Joy, *Proc. 41st EMSA Meeting*, 1983, 90-91.
5. A. Muray et al., *Proc. 42nd EMSA Meeting*, 1984, 356.
6. A. Muray et al., *J. Vac. Sci. Technol.* B1: 1091, 1983.
7. S. A. Rishton et al., *Microcircuit Engineering*, Cambridge, 1982, 341-346.
8. A. Muray et al., *Microbeam Analysis--1984*, 70.

FABRICATION OF NANOMETER SCALE STRUCTURES

A. Muray, M. Isaacson, and I. Adesida

The first step in fabricating structures on the nanometer scale by pattern transfer techniques is to identify and characterize materials that exhibit "high resolution" when exposed to a focused electron beam and that can be used as a "resist" against etching or removal of the underlying substrate. By "high resolution" we mean materials whose degradation products, when developed, conform as closely as possible to the dimensions of the incident electron beam-exposure pattern. Thus, when using a 1nm-diameter beam we should like to determine whether we can pattern at 1nm feature-size resolution.

Our investigations have centered on the well known polymer polymethylacrylate (PMMA) and various metal halides, some of which are directly beam vaporizable.¹⁻³ The results presented here were obtained in a VG Microscopes Ltd. Model HB5 Scanning Transmission Electron Microscope (STEM) equipped with a 12-bit resolution pattern generator and a microcomputer-controlled energy-loss spectrometer. Exposure is usually carried out at 100 keV with a probe diameter of 0.5 nm and a current of 10^{-12} - 10^{-10} A.

Radiation damage caused by exposure to charged particles is familiar to electron microscopists and others, although the exact mechanisms are not known in many cases. Microscopists endeavor to minimize this damage; on the other hand, in the case of electron beam resists, the most useful materials are those in which the mechanism for damage is most efficient.

In PMMA, damage occurs by excitation of scission or crosslinking events. Since Monte Carlo calculations of the energy deposited by secondary electrons are in agreement with actual resist profiles, secondaries are presumably the source of these damage events.⁴⁻⁶ Measurement of the exposure distribution function (EDF) of 100keV electrons for thin PMMA on thin-film substrates indicate that a tail on the EDF extends out to at least 40 nm. This finding is consistent with the minimum linewidth separation that has been observed with the above exposure conditions. A linewidth dependence on dose is thus expected. Figure 1 shows measurements for single pass lines exposed at varying doses with development in 1:3 MIBK:ISO for 3.5 min. Within the limitations of these conditions various patterns can be exposed into PMMA and replicated into thin films by reactive ion etching (RIE). Examples of structures replicated into thin Si and Si₃N₄ thin windows (about 50-80 nm thick) are shown in Figs. 3-5. Figure 4 shows an ion-beam mask etched into silicon metallized with AuPd. Undercutting is observed to occur in the (110) direction in thin films of Si when etched with SF₆. However, since the etching selectivity to SF₆ between the PMMA and the Si is 1:7, patterns exposed into the PMMA are not greatly distorted. After a metal evaporation, the original pattern can be defined in the metal film.

The mechanism for the exposure of the metal halides such as NaCl, LiF, MgF₂, and AlF₃ appears to be different from PMMA, since much better resolution is observed (1-2 nm).^{2,7} Monitoring of the bright field or annular detector dark-field signal shows that mass loss occurs as a function of dose. More information can be obtained about the intermediate states if the energy-loss spectra of the region irradiated as a function of dose are recorded. Measurements on NaCl, which is one of the least sensitive metal halides, are shown in Fig. 2. Peaks 1 and 2 are the surface (3.8 eV) and volume (5.7 eV) plasma loss of metallic sodium, peak 3 is the NaCl plasma loss at 15.6 eV, and peak 5 at 33 eV is a core exciton doublet on the L₂₋₃ edge of Na. In spectra (a)-(f), the low-energy loss spectrum of the region irradiated is sequentially shown after dose increments. These data indicate that the following occurs: (1) Cl⁻ is removed from the lattice sites and leaves behind Na⁺, which then forms a metal. (2) After another increment, the Na also disappears from the irradiated region.

Authors Murray and Isaacson are at the Cornell University School of Applied and Engineering physics; author Adesida is at the Cornell University National Research and Resource Facility for Submicron Research (NRRFSS). This work was supported by NSF under grant ECS 8200312 to NRRFSS. We thank M. Scheinfein, B. Whitehead, and F. Johnson for helpful discussions and assistance, and J. Koumjian for technical assistance.

Similar results are found for the other metal halides above, although for MgF_2 the disappearance of the metallic state is not observed. This sequence of events is consistent with the model that excitons are formed in the irradiated regions which then decay by displacing the halide atoms.⁸ Displacement of the metal most likely occurs by electron nuclear collisions. Measurement of the EDF of these materials is in progress and should reveal the range of the excitons that are formed. The resolution limits of these materials are determined by the minimum separation between features before redeposition of materials occurs. This distance is found to be approximately 3-4 nm. Typical resolutions attainable in these materials is shown in Figs. 6-8.

For further processing these inorganic resists, it is desirable to transfer the patterns into the thin-film substrate. If exposure doses are reduced so that only partial mass loss has occurred, the irradiated regions become chemically altered. It is then possible to remove selectively the exposed or unexposed region in an appropriate solvent.⁹ For exposures where total mass loss has occurred, the resist can be directly used as a mask. Since many metal halides show low etch rates during RIE,⁷ transfer of nanometer-scale patterns into the substrate is possible.

The very high resolution (1-2 nm) of the metal halides has been demonstrated and the exciton model for damage is shown to be consistent with the intermediate states observed during exposure. The transfer of nanometer scale patterns exposed in PMMA into thin-film substrates shows that RIE is not a limiting step in the fabrication of such small structures.

References

1. M. Isaacson and A. Muray, "In situ vaporization of low molecular weight resists using 1/2 nm diameter electron beams," *J. Vac. Sci. Technol.* 19: 1117, 1981.
2. M. Isaacson, "Nanolithography," *Proc. 41st EMSA Meeting*, 1983, 92.
3. A. Muray et al., "Fabrication of apertures, slots and grooves at the 8-80 nm scale in silicon and thin metal films," *J. Vac. Sci. Technol.* B1: 1091, 1983.
4. S. A. Rishton et al., "Measurement of the effect of secondary electrons on the resolution limit of PMMA," *Microcircuit Engineering* (Grenoble), 1982, 341.
5. D. Joy, *Proc. 41st EMSA Meeting*, 1983, 90-91.
6. K. Murata et al., *J. Appl. Phys.* 52: 4396, 1981.
7. A. Muray et al., *Appl. Phys. Lett.* (submitted).
8. R. Kelly, "Phase changes in insulators produced by particle bombardment," *Nuclear Inst. and Meth.* 182/183: 351, 1983.
9. P. M. Mankiewich et al., "High resolution electron beam lithography in CaF_2 ," *Appl. Phys. Lett.* 44(4): 468, 1984.

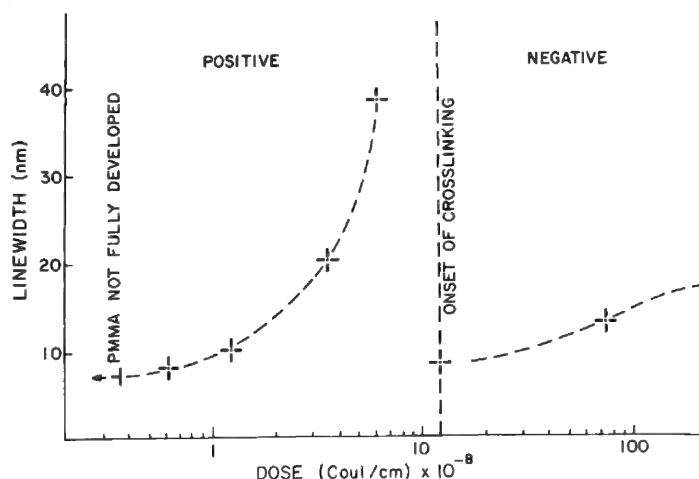


FIG. 1.--Linewidth vs dose for 60nm-thick PMMA single-crystal substrate. Exposure is at 100 keV with 0.5nm-diameter probe.

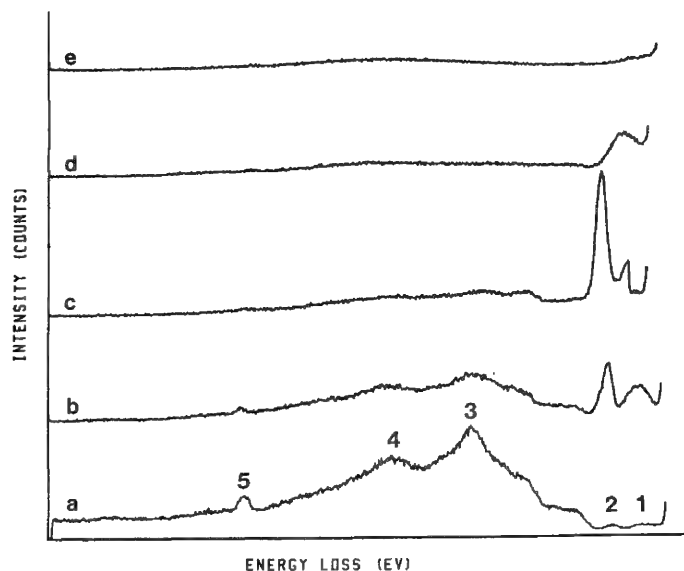


FIG. 2.--Sequence of energy loss spectra of NaCl after increments of dose have been received in regions examined. First dose increment received before spectra (a).

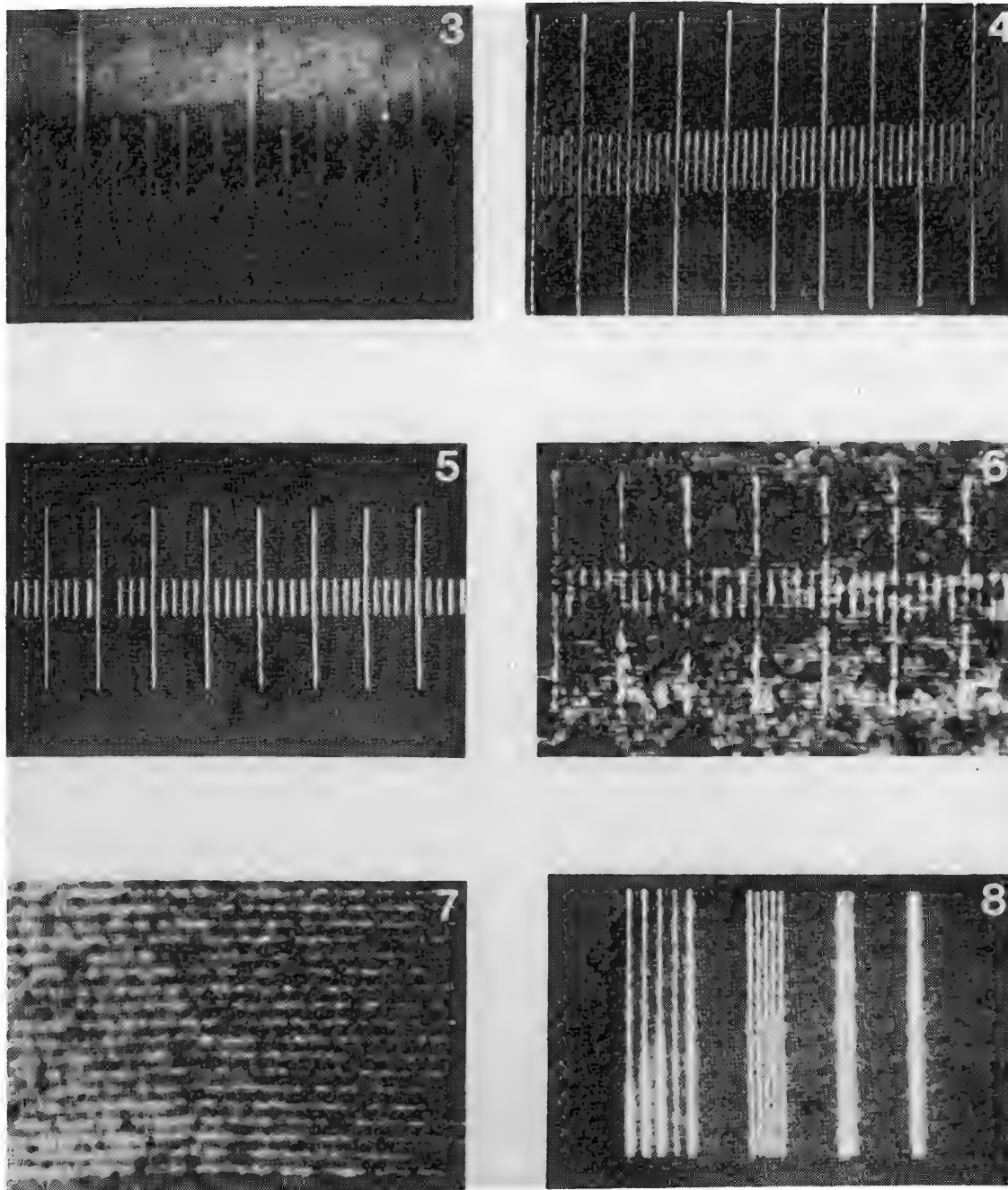


FIG. 3.--Grooves etched into 50nm-thick windows by reactive ion etching with SF_6 . Grooves 1270 nm apart, 30 nm deep. FIG. 4.--Grooves 30 nm deep etched into Si_3N_4 by reactive ion etching with CHF_3 . Groove spacing, 1270 nm. FIG. 5.--Ion-implantation mask fabricated by etching through window in exposed areas and metallizing mask with AuPd. FIG. 6.--Bright-field micrograph of calibration pattern exposed in LiF. Distance between neighboring lines, 12 nm. Note nonuniformity in exposure due to graininess of LiF film. FIG. 7.--Lines exposed in MgF_2 . Line separation, 12 nm. FIG. 8.--Spatial resolution test pattern exposed in AlF_3 . Line separation on left set of lines is 24 nm and decreases by factors of 2 from left to right.

~ 10 nm ELECTRON-BEAM LITHOGRAPHY WITH AN (S)TEM

H. G. Craighead

A variety of devices and structures with dimensions ≥ 10 nm have been fabricated by electron-beam lithography.¹ To accomplish this goal a modified (scanning) transmission electron microscope [(S)TEM] has been used as an electron-beam writing instrument, probing the size limits of conventional electron-beam lithography and studying novel electron-beam micro-fabrication techniques. In this paper an outline of techniques for fabricating ultrasmall structures with this type of instrument is given and specific examples are discussed.

Several features of this type of electron microscope facilitated the fabrication of very small structures. One was the availability of high beam energies, up to 120 keV. Another feature was the use of backscatter and secondary-electron imaging and smaller beam sizes than previously used for conventional resist techniques to form ultrasmall structures on bulk GaAs and Si.^{1,2} Dedicated STEMs with smaller beam sizes could not be used for the technologically important case of electron opaque samples.

For this lithography a DEC 11-23 microcomputer drove the x&y scan generator of the microscope with ± 5 V signals from two twelve bit digital-to-analog converters. Rather lengthy (5m) shielded cables transmitted the analog signal to the scan unit with no evidence of noise introduced by induced voltages. Pattern-generating software, written in BASIC, drove the beam in a vector-scan mode, tracing the pattern in a continuously connected path. Since there was no mechanism for blanking the beam during the exposure, the beam was dumped in the corner of the field at the beginning and end of the exposure. During the pattern writing the beam was rapidly scanned with sufficient speed to avoid exposure over the areas not to be exposed. The writing speed or maximum scan rate depends on the beam current and the sensitivity of the resist. For typical polymer resists the speed limiting factor was the response time of the scan coils, since more than enough beam current was available, even in the smallest probe, to expose the resist at the maximum scan rate. For the Philips 400T used for this work the maximum scan rate was ~ 1 ms/frame width.

For the highest-resolution lithography the shape and size of the electron beam spot was crucial. A $30\mu\text{m}$ -diameter condenser aperture was used to form a symmetric Gaussian-like beam. The danger of the beam profile with a sharp central spike and halo is that a perfectly acceptable scanning image can be obtained with this shape but it will broaden the written linewidth. A major advantage of the (S)TEM over a dedicated scanning instrument is the ability to image the probe with the post-specimen lenses. In this way the astigmatism can be corrected and uncertainties due to beam shape can be eliminated by direct observation. For this purpose the second condensor lens was used to focus the beam on the sample with the sample in objective lens image plane. Ultimately the objective-lens spherical aberration limits the useful field size. As a practical matter, I have found this to be a field width of about $15\mu\text{m}$ for the smallest resolution of about 10 nm on the Philips 400T.

The beam energy is important because of the dependence of primary beam spreading and the range of backscattered electrons. As has been discussed elsewhere,⁵ higher beam energies are desirable for thick substrates because of the larger backscatter range diluting the background exposure over a greater area, which increases the exposure latitude and decreases the proximity effects. This instrument had a beam energy that was variable over 20-120 keV and has been used to measure energy-dependent resist sensitivities and resolution.

As an example consider the specific case of lithography performed on a thick Si substrate

The author is with Bell Communications Research, Crawford's Corner Road, Holmdel, NJ 07733. This work was done at Bell Laboratories. He acknowledges helpful discussions with Richard McConville on the electron optics; R. E. Howard for help with the PMMA resist; useful discussions with P. F. Liao, M. Stern, L. D. Jackel, and E. L. Hu, and the technical assistance of P. Mankiewicz and J. E. Sweeney.

with a conventional electron-beam resist, polymethylmethacrylate (PMMA), and a lift-off procedure. The electron-beam resist was a 50nm thick layer of 950 000 molecular weight PMMA spun onto 3×8 mm crystals. This size sample fit directly in the side entry bulk specimen holder. In a series of tests, fields $15 \mu\text{m}$ square were filled with 50nm-spaced lines. The line dose exposure was 3×10^{-9} coul/cm at a beam current about 0.6×10^{-12} A at an energy of 120 keV. The exposed resist was developed in a cellosolve-methanol solution for 5 s; then a 15nm-thick layer $\text{Au}_{0.6}\text{Pd}_{0.4}$ alloy was deposited on the substrate at normal incidence from a thermal source. The patterns were "lifted off" in acetone and examined by secondary-electron imaging in the same microscope used for the exposure. A set of AuPd lines on Si is shown in Fig. 1. These lines were still wider than the incident electron beam, which indicated the existence of size-limiting effects other than the primary beam width, such as secondary-electron scattering or the molecular size of the resist. Joy and others have performed Monte Carlo calculations for the effect of fast lateral secondary electrons and obtained approximately a 10nm width, even with a much smaller electron beam spot size.⁴ This type of structure can be used for studies of localization and quantum effects.

As an example of another system for physical measurements, arrays of small metal particles were fabricated for optical and electromagnetic studies. In one sample, 3.6×10^5 gold particles were produced on a sapphire substrate. Problems of sample charging during the electron-beam writing required the deposition of a conducting film on the resist layer. The electron beam exposure time was of the order of 1 ms per point. Figure 2 is a scanning electron micrograph showing the regularity in shape and position of the gold particles.⁶ Heating the system after formation yielded rounder appearing particles and maintained the spatial periodicity.

The lithographically defined patterns can also be used as masks for the etching of patterns into bulk materials. By use of anisotropic reactive ion etching⁷ the metal pattern on the surface of a GaAs crystal can be transferred into the GaAs as in Figure 3, where an array of columns defined by NiCr metal spots was etched into the GaAs in a SiF_4 plasma. These particular structures are being studied for size-limited optical properties and enhanced Raman scattering.

Devices and structures have been made so small that the width of these structures was only tens of atoms. The materials problems at these small dimensions present new difficulties in fabrication. Dimensions smaller than the typical polycrystalline grain sizes of deposited films required dealing with this intrinsic inhomogeneity of the material. I have approached this problem by using very fine grained material or very large crystal size material where the entire device can be "cut" from a single crystal. The effects of electron scattering in the materials appear to be at least qualitatively understood. These examples suggest the versatility of the electron microscope in fabricating a range of structure with $>10\text{nm}$ resolution for experiments on bulk substrates. The indication is that we have neared the ultimate limit of conventional electron beam lithography. Novel studies on thin films and unconventional techniques have also been done in the same microscope system.

References

1. H. G. Craighead, *J. Appl. Phys.*, in press.
2. H. G. Craighead, R. E. Howard, L. D. Jackel, and P. M. Mankiewich, *Appl. Phys. Lett.* 42: 38, 1983.
3. H. G. Craighead, *Proc. 41st EMSA Meeting*, 1983, 102.
4. D. Joy, *Proc. 3rd Meeting Microscopy of Semiconductors*, Institute of Physics, London, 1983.
5. R. E. Howard, H. G. Craighead, L. D. Jackel, and P. M. Mankiewich, *J. Vac. Sci. Technol.* B1: 1101, 1983.
6. H. G. Craighead and G. A. Niklasson, *Appl. Phys. Lett.*, in press.
7. M. B. Stern and P. F. Liao, *J. Vac. Sci. Technol.* B1: 1053, 1983; M. Stern, H. G. Craighead, P. F. Liao, and P. M. Mankiewich, to be published.

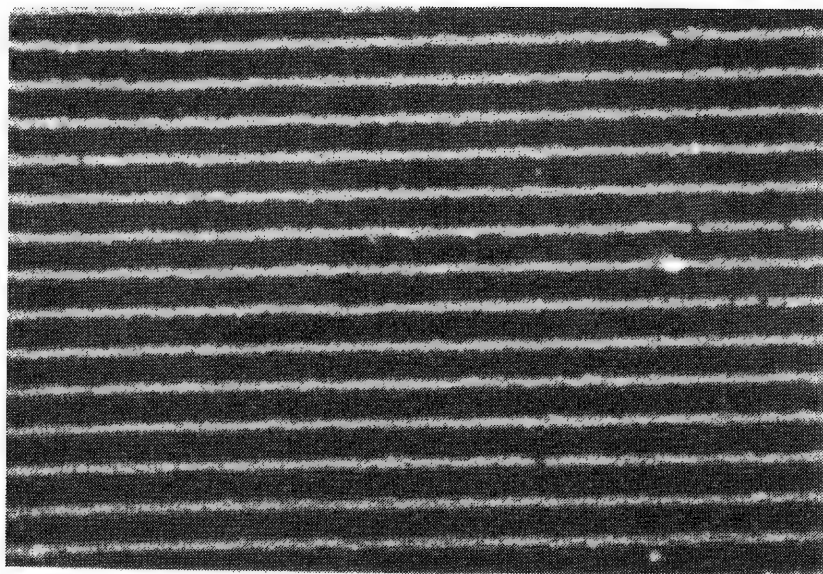
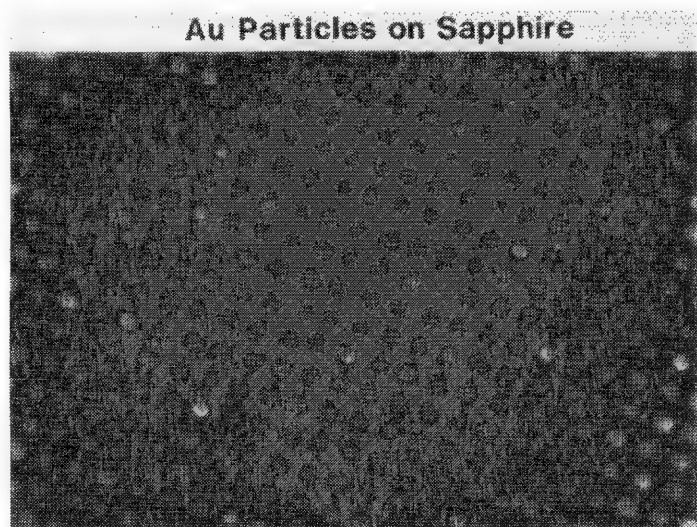


FIG. 1.--AuPd wires on Si.



Au Particles on Sapphire

100 nm

0.1 micron

FIG. 2.--Gold particles on sapphire.

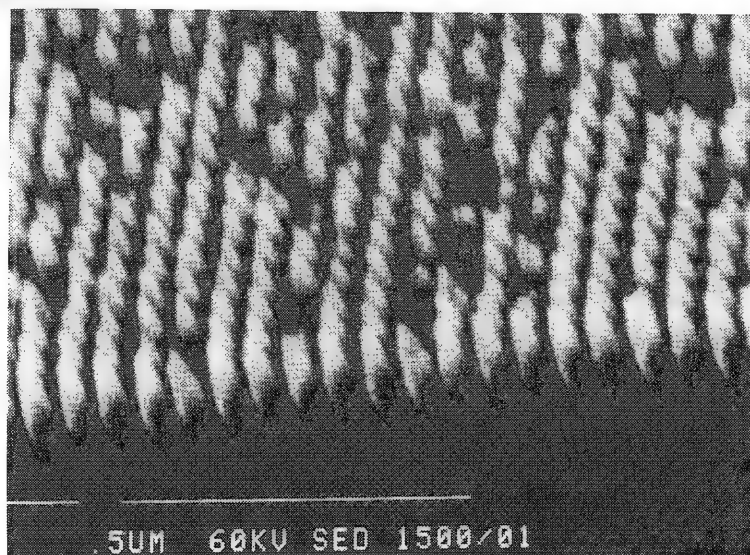


FIG. 3.--Etched GaAs columns.

.5UM 60KV SED 1500/01

SEM Contrast at High Magnification

SCANNING ELECTRON MICROSCOPY: CONTRAST AT HIGH MAGNIFICATION

Klaus-Ruediger Peters

In scanning electron microscopy (SEM), resolution and contrast on a specimen surface are functions of the spatial distribution of the collected fraction of the electrons produced by the probe's primary electrons (PE) in the specimen or in the microscope (Fig. 1). The size of the volume from which the signal is emitted depends on the range R of the electrons as well as on the topography of the specimen. The maximum resolution that can be obtained can be detected only above magnifications at which the signal source can be visualized.¹ High resolution depends on short-range signals which are produced by PE within the spot of impact and from a depth t from which the electrons can escape. Ultimately, the resolution is limited by the probe's diameter when the size of the latter is close to or larger than the range of the signal.

Two short range signals have been defined: (1) high-energy backscattered electrons (BSE-I), and (2) low-energy secondary electrons (SE-I). BSE-I can be collected from highly tilted surfaces and effectively separated by energy filtering from other BSE. They are defined as "low-energy-loss" electrons (LLE) and are emitted from a volume of $\sim 2-4$ nm in depth t but up to ~ 100 nm in length;² SE-I are collected, together with other SE, from untilted surfaces and are enriched by suppressing background SE.³ The background is produced by SE-II and SE-III generated by scattered PE in the specimen and in the microscope. The calculated escape depth of SE is ~ 1 nm and the range is established as $\sim 1-2$ nm.⁴ Although Monte Carlo calculations of SE-I contrasts have been available for some time,^{5,6} such contrasts have been only recently demonstrated by microscopy using a cold-cathode field-emission microscope (JEOL JFSM 30) with a beam diameter of $\sim 1-2$ nm, an acceleration voltage of 30 kV, a beam current of 10^{-11} A, and a working distance of 13 mm. The micrographs were taken at 200 000 \times CRT magnification and enlarged photographically to 500 000 \times (Figs. 2b, 3b).

The important types of contrasts detectable at high magnification on the surface of a bulk specimen are summarized in Fig. 2(a) and, as an example, a micrograph of gold crystals grown on bulk carbon and imaged with the SE-I imaging mode³ is shown in Fig. 2(b). On smooth surfaces, material contrasts are detected when the specimen is composed of layers of various materials. If the layer thickness exceeds t , the contrast depends predominantly on the atomic number Z of the layer's material (atomic number contrast). But if the layer is thinner than t , a thickness contrast is obtained. On uneven surfaces additional topographic contrasts are generated. They fall into two groups depending on the ratio of R to feature size d . For $R < d$, variations in facet orientation produce facet contrast

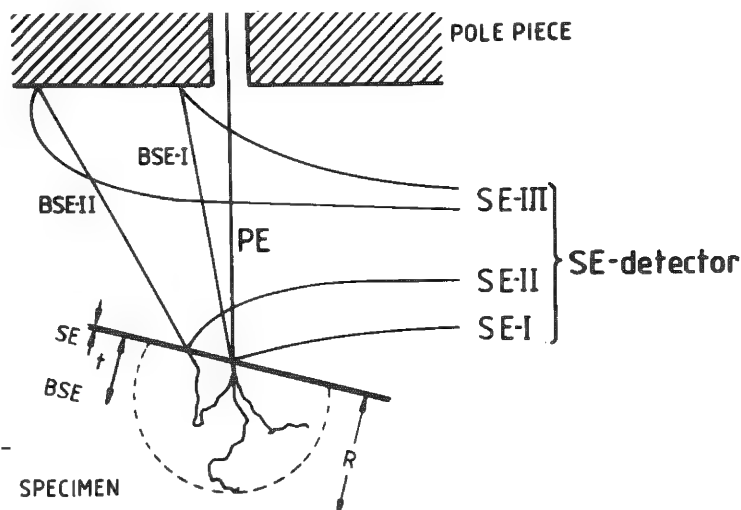
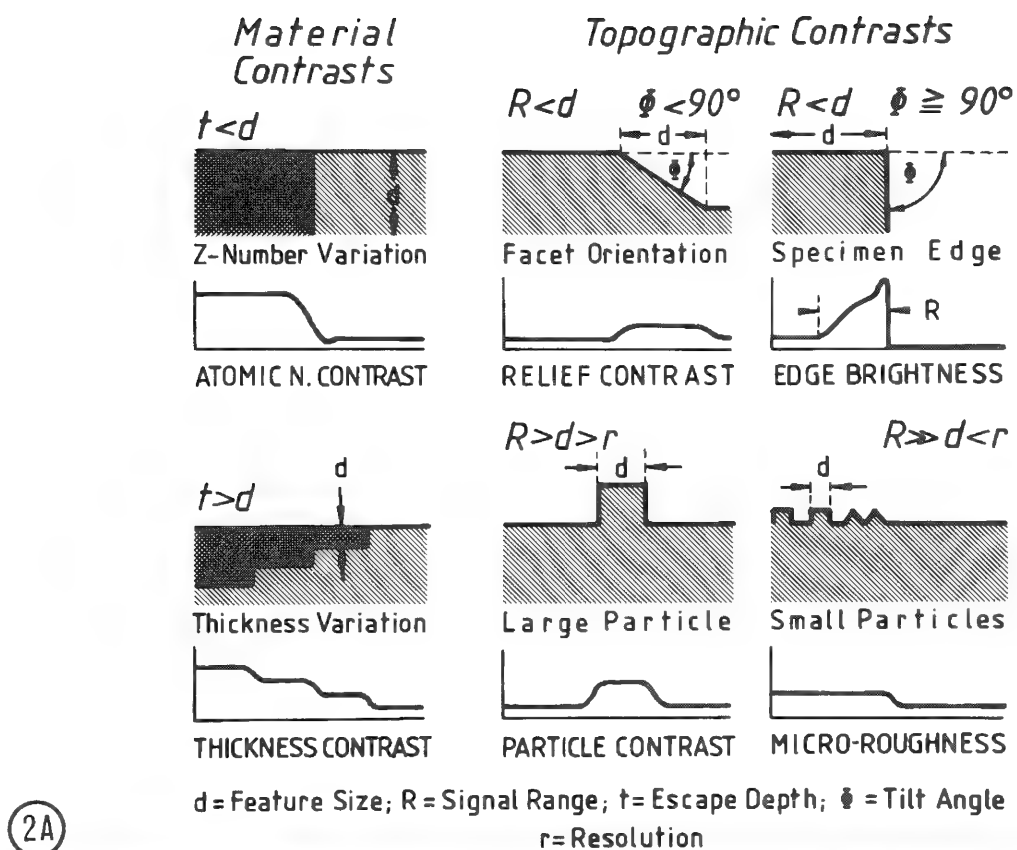


FIG. 1.--Range R of signals collected in SEM with large working distance; t = escape depth.

The author is at the Department of Cell Biology, Yale University School of Medicine, 333 Cedar Street, New Haven, CT 06510. The support by U.S. Public Health Service under Research Grant GM-21714 is acknowledged.



(2A)

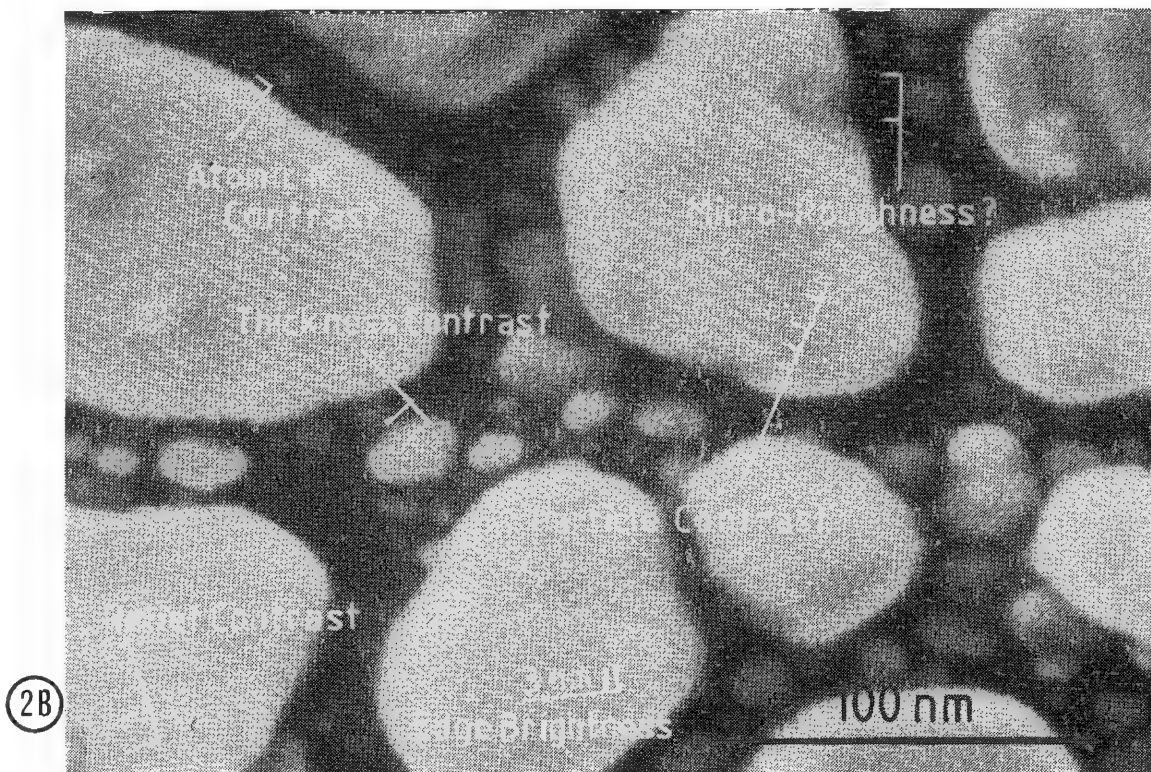


FIG. 2.--(a) Diagram and (b) micrograph of types of contrasts imaged on bulk sample of gold crystals grown on bulk carbon substrate; SE-I image mode, 500 000 \times .

and edge brightness. The width of the edge brightness is the sum of beam diameter and range and allows an easy assessment of these parameters. Particles smaller than R but greater than r ($R > d > r$) are resolved and imaged without edge brightness as bright disks with particle contrast. The width of particles imaged in particle contrast can also be used to estimate the signal range, since it is the sum of beam diameter plus two times the range. If the particles are so small that they are not resolved ($R \gg d < r$) they contribute an increase in background brightness which gives microroughness contrast.

Similar contrast principles apply for metal-coated specimens if the range of the signal equals or is larger than the thickness of the metal films (Fig. 3a). Variation in metal composition or isolated metal grains on the surface are imaged in atomic number contrast. For $t > d$ a thickness contrast results when the film thickness varies. By comparison with material contrasts, topographic contrasts are reduced in number. This result is shown in Fig. 3(b) for a T4 phage coated with a 2nm-thick continuous chromium film. On the titled facets of the phage head, a very small relief contrast is visible. At the edges of the particle a very strong contrast is prominent and overwhelms the minute relief contrast. These contrasts at edges are approximately proportional to the height of the edges. Features smaller than the thickness of the metal film become buried by the metal and are not resolved. Individual small crystals protruding on the metal film surface are expected to generate a microroughness contrast.

High-resolution contrasts on bulk specimens depend mainly on the signal range and the beam diameter. Only the latter may be reduced so as to improve resolution. However, on metal-coated specimens, resolution and contrast can be increased by use of metal films thinner than the signal range.¹ In fact, continuous 1nm-thick coatings give best SE-I contrasts and resolution.³

References

1. T. E. Everhart and M. S. Chung, "Idealized spatial emission distribution of secondary electrons," *J. Appl. Phys.* 43: 3708-3711, 1972.
2. O. C. Wells, "Resolution of the topographic image in the SEM," *SEM/1974* I, 1-8.
3. K.-R. Peters, "Generation, collection and properties of an SE-I enriched signal suitable for ultrahigh resolution SEM on bulk specimens," in D. F. Kyser et al., Eds., *Electron-beam Interactions with Solids*, SEM Inc., AMF, O'Hare, IL 60666, 1984, 363-372.
4. H. Seiler, "Einige aktuelle Probleme der Sekundärelektronenemission," *Z. angew. Phys.* 22: 249-263, 1967.
5. E. P. George and V. N. E. Robinson, "The influence of electron scattering on the detection of fine topographic detail in the scanning electron microscope (SEM)," *SEM/1977* I, 63-70.
6. D. C. Joy, "Contrast and resolution in the scanning electron microscope," *J. Microscopy*, 1984, in press.

Results

Secondaries can be generated both by incident electrons and exiting backscattered electrons. Following the scheme proposed by Drescher et al., secondaries formed by the incident beam are labelled SE1 and those produced by backscattered electrons are SE2.¹⁰ Because the SE1 signal carries information directly related to the position of the incident probe, it is this component which is the source of high resolution secondary imaging information, whereas the SE2 signal essentially mimics the resolution and contrast of the backscattered signals and so at high resolution contributes only a background to the desired contrast. A measure of the information content of the total secondary signal is the ratio $\delta_{SE1}/(\delta_{SE1} + \delta_{SE2})$, which can be calculated from the Monte Carlo model. The SE1 yield δ_{SE1} rises rapidly as the incident beam energy falls (Fig. 1) and eventually reaches a maximum value in excess of unity (although the model used here is not valid in that regime because the electrons are not "free"). The backscattered electrons for some incident energy E_0 have an energy distribution ranging from 0 to E_0 , the form of which can be calculated by means of another Monte Carlo simulation. This result can be convoluted with the SE1 yield data to give the SE2 yield δ_{SE2} (Fig. 1). The total secondary yield δ_{total} can be written as

$$\delta_{total} = \delta_{SE1} + \delta_{SE2} = \delta_{SE1}(1 + \beta\eta) \quad (5)$$

where η is the bulk backscattering coefficient and β then represents the enhanced efficiency of secondary electron production due to the lower average energy of the backscattered components. From the calculation outlined above β is found to be typically between 2 and 4 for materials such as carbon, aluminum, or copper, for energies in the range 5 to 30 keV, in good agreement with the experimental values of Drescher et al. and Kanter.^{10,11}

This result indicates that, for some materials, under 50% of the total secondary signal reaching the detector carries the desired high-resolution information. In fact the proportion is often even smaller, because in many SEMs up to 50% of the total detected signal arises from secondaries (SE3) produced at the polepiece or chamber walls by backscattered electrons, or secondaries (SE4) generated by hard x-ray fluorescence at apertures.¹² The true SE1 component may thus be as low as 25% of the total, depending on the specimen. Since we are assuming that high-resolution image information is carried only by the SE1 component, dilution of this contribution reduces the contrast. Since the threshold current required to observe some contrast level C varies as $1/C^2$, a reduction in contrast results in the need for more beam current and hence degraded spatial resolution. The attainment of high-resolution secondary-electron imaging therefore requires a strategy to enhance the SE1 component, reduce the SE2 contribution, and eliminate the SE3 and 4 components. Since the SE3 and 4 contributions can be eliminated by appropriate treatment of the microscope,¹³ the major task is that of improving the ratio between SE1 and SE2.

The ideal solution is to minimize the SE2 contribution by eliminating the backscattered electrons that produce it. Thus the ideal samples for high resolution are of low atomic number material, thin enough to be at least partially transparent to the beam, and supported on a nonscattering substrate. The fractional content of SE1 electrons in the total can be further enriched if the specimen is coated with a suitably chosen surface film. Since the escape depth of the secondaries is limited, the majority of SE1 signal comes from the first 2 to 3 nm of material (see for example Fig 4); the films thus need to be only of this order of thickness to have a significant effect. Figure 2 shows the SE1 yield δ_{SE1} at 20 keV for 2nm films of a variety of common coating materials; there is a monotonic rise with atomic number until about chromium and the yield then remains relatively constant until the heavy elements are reached. Any of the common transition or heavy metals is thus, in principle, a suitable candidate for the choice of a coating material since all will provide a considerable increase in the SE1 signal compared to that obtained from an uncoated sample such as a biological thin section. In this situation, provided that the SE2 component is small, the high-resolution secondary signal is dominated by the properties of the coating layer rather than those of the sample itself; the choice of the composition and thickness of the coating material must be therefore carefully considered, since the decision may significantly affect the information content and quality of the image.

This situation can be illustrated if we consider the topographic contrast that might result from such a film. Figure 3 shows the SE1 yield as a function of beam incidence angle

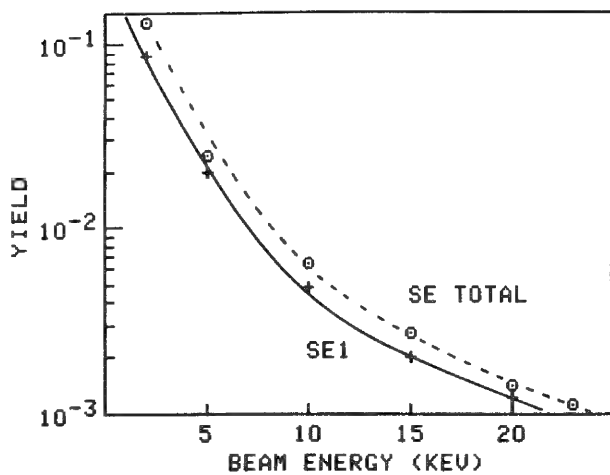


FIG. 1.--Computed total secondary, and SE1, yield from carbon vs beam energy computed by Monte Carlo Program.

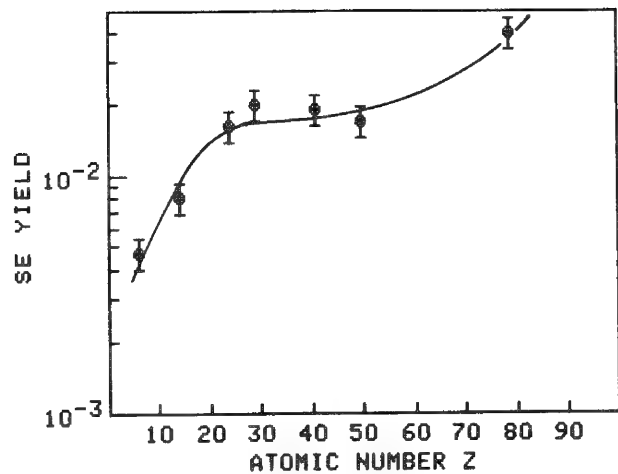


FIG. 2.--Variation of SE1 yield from 2nm-thick films of various materials at 20 keV.

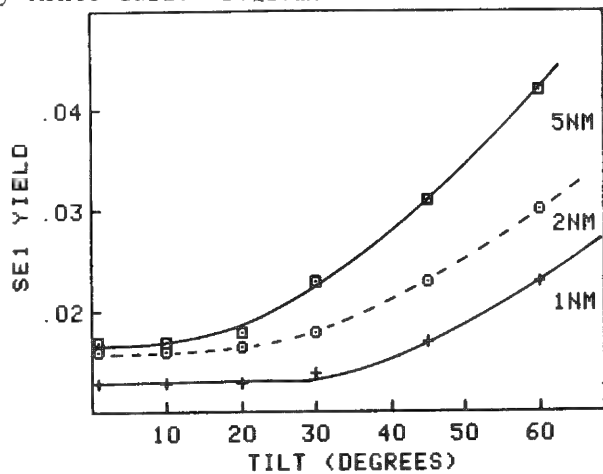


FIG. 3.--Variation of SE1 yield with tilt for Cr films 1, 2, and 5 nm thick at 20 keV.

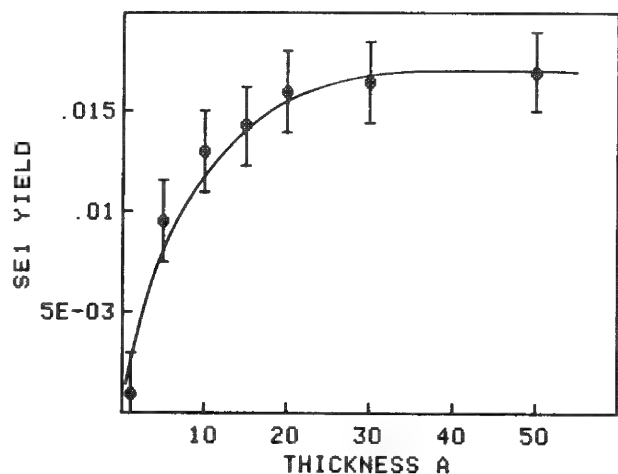


FIG. 3.--Variation of SE1 yield from Cr vs film thickness.

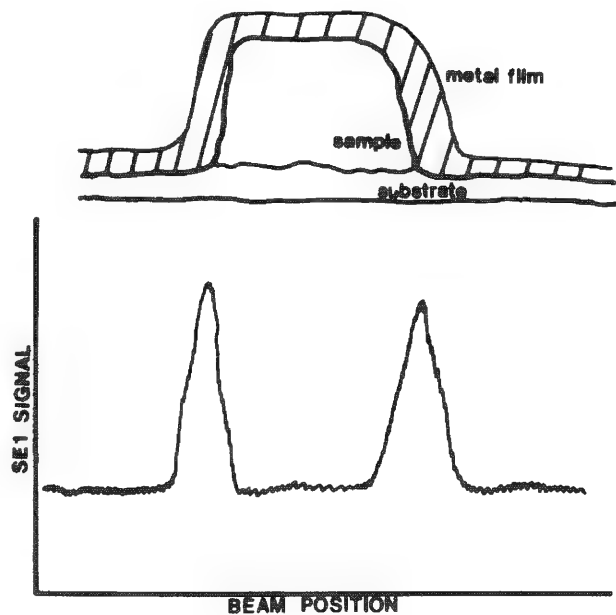


FIG. 5.--Sketch of thin film coating over a structure, and the corresponding SE1 "mass thickness" contrast.

at 20keV for thin films of Cr. The change of secondary yield with beam incidence angle, which would normally be the mechanism for "topographic contrast," is seen to be very small for both the 1 and 2nm films until the angle reaches 30° or 40°, although for a 5nm film of chromium the yield curve more closely follows the usual bulk behavior. With very thin coatings, therefore, topographic contrast is weak except at high values of surface inclination, and consequently surface detail will be absent except at major features such as cracks or an edge. However, contrast from surface relief can be obtained through an alternative process, called "mass thickness" contrast by Peters, the origin of which can be understood from Fig. 4.¹³ This figure shows the SE1 yield from Cr as a function of film thickness at 20 keV. This curve rises very rapidly with thickness and reaches 50% of its final value at only about 1 nm, but continues to increase until the thickness reaches about 5 nm. A similar curve could be generated for, say, gold; the only significant difference would be that the secondary yield reaches its plateau at a somewhat lower thickness because of the higher density of the material. If now a thin surface film is coated on to a rough surface, as sketched in Fig. 5, the actual thickness in the beam direction will be higher in some regions than others because of the topography. Provided that the nominal thickness of the layer is less than the value required to saturate the SE1 yield, the secondary signal will rise in these thicker areas. But if the film is too thick, this mode of contrast will be absent and only the residual normal topographic contrast discussed above will be present. Under the the conditions being considered here both mechanisms only produce significant contrast at edges, steps, or boundaries on the specimen. Less dramatic surface features will produce little or no contrast. However, since it is the edges and boundaries that identify the morphology of a sample, the ability of the coating film to enhance their visibility is of considerable importance in the high-resolution image, especially because the familiar "edge brightness" artifact (resulting from the enhanced escape probability of secondaries in the vicinity of an edge) disappears when the feature size drops below 10 nm.¹⁴

The choice of the material and thickness of the coating film can also affect the contrast indirectly, as shown in Fig. 6. Primary electrons scattered by passage through the film can, in some areas, re-enter the film at a distant point. If they do so they produce secondaries, called by Peters type 2A, which add to the background on which the SE1 signal is riding.¹³ The severity of this effect depends on the surface topography (since it changes both the probability the re-entry can occur and affect the angle at which the scattered electron meets the second surface) and the amount of scattering experienced by the beam in the film. Figure 6 shows the computed SE2A signal produced by a 20keV beam as it is scanned across a strip 10 nm wide and 10 nm high, coated with a 2nm layer of either Cr or Au. For Cr the level of SE2A production compared to the expected SE1 signal is negligible once the probe is a few nanometers past the edge. For the gold film, however, the SE2A signal is both much larger, and extends to 3 or 4 nm from the edge. Choosing a gold rather than a Cr layer can therefore lead to a reduction in the contrast and signal/noise ratio of the high-resolution secondary image even though both films are, by normal standards, very thin. In summary, the choice of the metal film coat parameters can be seen to be crucial to the success of high-resolution imaging, since they determine the type and magnitude of contrast available and the signal/noise ratio of the image.

Spatial Resolution

The final item to be examined is the likely spatial resolution of the SE1 image, which is determined by the profile of secondary emission from the surface. A guide to its general magnitude can be obtained by a look at the computed SE1 trajectories, for example in the top few tens of nanometers of a copper sample (Fig. 7a). The secondaries are generally clustered around the beam axis, but fast secondaries form a branch-like structure around this cluster that can extend for many nanometers. The trajectories shown are only plotted for energies down to 200 eV; therefore, to get the actual surface distribution, the effect of diffusion must again be considered. When that is done the profile is found to be as shown in Fig. 7(b). The shape is approximately Gaussian, but the top is flattened, and the tail is extended by the contribution from the fast secondaries. For this example, and for most other common materials, the full width at half maximum of the distribution is between 2 and 3 nm, which shows that the spatial resolution limit deduced from the Rayleigh criterion will be in the range 1-1.5 nm. It can be seen that some broadening of the primary beam occurs

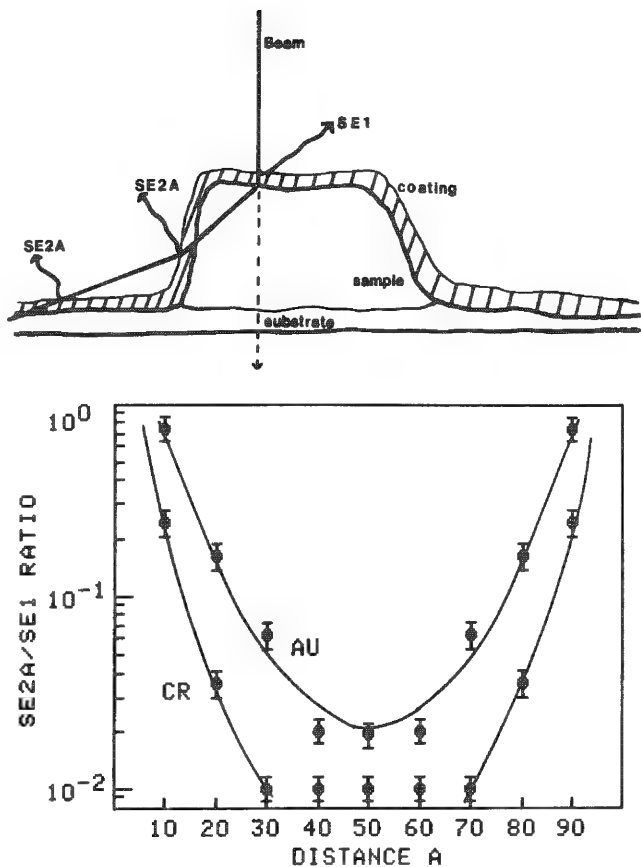


FIG. 6.--Sketch of origin of SE2A electrons, and computed ratio of SE2A and SE1 signals for 20keV probe of zero diameter traversing strip 10 nm high and 10 nm wide coated with 2 nm of chromium or gold.

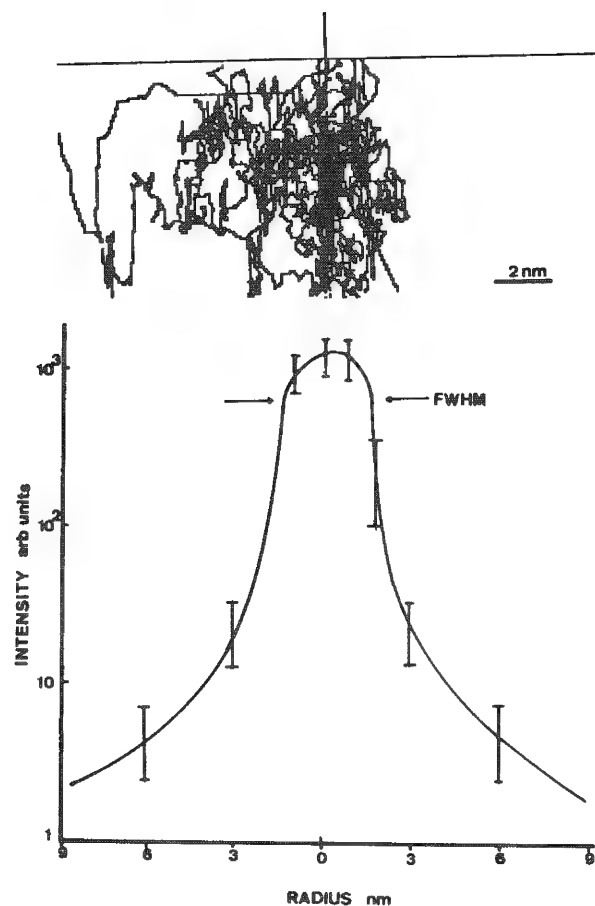


FIG. 7.--Computed secondary-electron trajectories in top 20 nm of copper sample at 20 keV, and corresponding surface distribution of SE1 secondary production.

even within a few nanometers of the surface; thus, on a thin film the resolution might be expected to show a slight improvement. This estimate of resolution should be treated with some caution, because the scattering event that produces a secondary is here assumed to occur at a point, rather than within some generation volume, but the result is in good agreement with recent experimental data.¹³

Conclusions

The Monte Carlo simulation demonstrates that the information content and interpretation of secondary electron images is greatly affected by the composition and characteristics of any surface coating applied to the sample. Under carefully chosen conditions a spatial resolution of the order of 1 nm should be attainable.

References

1. H. Seiler, "Secondary electron emission in the SEM," *J. Appl. Phys.* 54: R1, 1983.
2. C. J. D. Catto and K. C. A. Smith, "Resolution limits in surface scanning microscopy," *J. Microscopy* 98: 417, 1973.
3. K. Murata, "Monte Carlo calculations on electron scattering and secondary electron production in the SEM," *SEM/1973 II*, 267.
4. E. P. George and V. N. E. Robinson, "Dependence of SEM contrast on electron penetration," *SEM/1976 I*, 17.
5. R. D. Evans, *The Atomic Nucleus*, New York: McGraw-Hill, 1955.
6. D. C. Joy, "The ultimate spatial resolution limit of electron beam lithography," *Microelectronic Engineering* (in press). A copy of this program in APPLESOFT BASIC is available on request from the author.
7. H. Bruining, *Physics and Application of Secondary Electron Emission*, Oxford: Pergamon Press, 1954.
8. J. C. Ashley, "Simple model for electron inelastic mean free paths," *J. Electron Spectros. and Related Phenomena* 28: 177, 1982.
9. D. R. Penn, "Quantitative chemical analysis by ESCA," *ibid.*, 9: 29, 1976.
10. H. Drescher et al., "Rückstreuoeffizient und Sekundärelektronen-Ausbeute," *Z. angew. Phys.* 29: 331, 1970.
11. H. Kanter, "Contribution of backscattered electrons to secondary electron formation," *Phys. Rev.* 121: 681, 1961.
12. K.-R. Peters, "Validation of George and Robinson SE1 theorem," in *Proc. 40th EMSA Meeting*, 1982, 368.
13. K.-R. Peters, "Collection and properties of SE1 enriched signal," in D. Kyser, H. Niedrig, D. E. Newbury, and R. Shimizu, Eds., *Proc. Asilomar Meeting on Electron Interactions*, Chicago: SEM Inc., 1984, 363.
14. D. C. Joy, "Contrast and resolution in the scanning electron microscope," *J. Microscopy* (in press).

Failure Analysis in Microelectronics

INTERMETALLIC LAYER GROWTH IN Cu/Sn-In SOLDER JOINTS

A. D. Romig Jr., F. G. Yost, and P. F. Hlava

Metallurgical reactions often lead to the failure of engineering components. One type of reaction, often encountered in electronics applications, is the growth of intermetallic compounds between a base metal and a soldering alloy. The consequences of the formation of the intermetallic compound often include a degradation in the electrical, thermal, or mechanical properties of the solder joint. This paper concerns the study of the formation of intermetallic compounds between Cu base metal and a low-melting-point Sn-In solder. In this application, a thermal detent, the solder is intended to hold a spring-loaded Cu piston in a Cu cylinder. If the component is overheated the solder is intended to melt and release the piston from the cylinder. However, the intermetallic compounds that form have high melting points and could prevent the device from operating at the specified design temperature. It was the objective of this study to characterize the kinetics of formation for the intermetallic compounds. The characterization was performed with the use of optical metallography and electron microprobe analysis. Ultimately, the characterization of the kinetics of intermetallic layer growth will permit a prediction of the lifetime of the component.

Background

Two designs of thermal detents used in inertial switches may be susceptible to failure due to the formation of high-melting-point intermetallic compounds. Figure 1 shows schematically the design of the two detents. The basic design consists of a Cu cylinder, closed at one end, into which is placed a hollow Cu piston. The Cu cylinder and piston are dip-soldered together with a low-melting-point 50wt.%Sn/50wt.%In solder. A spring connects the piston to an external anchor point. As designed, the detent is intended to operate at approximately 120 C, which is just above the Sn-In eutectic temperature. At this temperature the solder melts and releases the piston from the cylinder. Examination of a number of detents manufactured nine to thirteen years ago¹ showed that intermetallic compounds had formed in the solder gap. The intermetallic compounds could freeze the detent and prevent it from operating at the design temperature. To predict the lifetime of these components one must characterize the formation and growth of these intermetallic compounds.

A controlled experiment was designed to determine the time-temperature parameters for layer growth. The literature on the subject was useful but did not specifically address the question of ternary Cu-Sn-In reactions. A number of references reported on layer growth in Cu-Sn²⁻⁷ and a number on Cu-In layer growth.⁸⁻¹⁰ At high temperatures layer growth in Cu-Sn is volume-diffusion controlled and is proportional to the square root of time, whereas at low temperatures intermetallic layer growth is interface controlled and is linearly proportional to time. Intermetallic layer growth in Cu-In is always volume-diffusion controlled. However, in other similar systems, the layer growth is always proportional to time, which indicates that growth is controlled by an interface reaction. The Au/In-Pb system forms intermetallic layers, which grow linearly with time.¹¹ These previous studies show that no one mechanism is universally responsible for layer growth in these kinds of alloy systems. There is no way to predict whether intermetallic layer growth in the Cu/Sn-In system will be controlled by volume diffusion or interface kinetics. In order to predict the kinetics of layer growth an experimental study was required.

Experimental Procedure

The procedure used in the experimental study was designed to simulate the production procedure actually used to manufacture the thermal detents. Two models of detent are to be

The authors are with Sandia National Laboratories, Albuquerque, NM 87185. This work was performed at Sandia National Laboratories, supported by the U.S. Department of Energy under contract DE-AC04-76DP00789.

considered, each with a slightly different processing history. The details of the procedure used to make the experimental diffusion couples, and equivalently the two thermal detent models (2560 and 2034), are given in Table 1. Note that the Cu base metal is dipped into the molten solder twice. The melting point of the solder is close to the Sn-In eutectic temperature, 117 C. The samples were then placed in alumina boats and aged in air. Only samples given the 3 s at 250 C and 40 s at 180 C processing cycle were aged. Aging temperatures were maintained to ± 2 C. Following the aging heat treatment the samples were quenched on an Al chill plate. The time-temperature heat treatment matrix is listed in Table 2.

The samples were sectioned (perpendicular to the plane of the Cu sheet), mounted, and polished (parallel to the plane of the Cu sheet). A chemical etch of 5% nitric acid and 2% hydrochloric acid in methanol, used at room temperature, emphasized the two-phase microstructure of the solder and highlighted the solder/intermetallic compound interface. The two-phase microstructure of the solder is shown in Fig. 2(a). The chemical etch did not delineate the Cu/intermetallic compound interface. A short exposure of about approximately 15 min to sulfur vapor highlighted the Cu/intermetallic compound interface. Figure 2(b) shows the appearance of the intermetallic compound after the complete metallographic preparation. The intermetallic compound layer thickness measurements were made optically at a magnification of 2000 \times . After repolishing, the elemental distribution of Cu, Sn, and In in the solder and intermetallic layers was investigated in the Cameca MBX electron microprobe. Several composition profiles were measured across the Cu/solder diffusion couples. The microprobe was operated at 15 kV at a beam current of 22 nA. The characteristic $K\alpha$ line for Cu and the characteristic $L\alpha$ lines for Sn and In were used in the analysis and were detected with the wavelength-dispersive system. The data were reduced with the ZAF routine in SANDIA-TASK.¹² Figure 3 shows typical concentration profiles. X-ray mapping was also done to give a qualitative indication of the elemental distribution. Figure 4(a) shows a secondary electron image of the intermetallic layer. Figures 4(b) and 4(c) show the elemental maps.

Results and Discussion

The microstructures and x-ray maps shown in Figs. 2(b), 4(a), and 4(c), respectively, show that the solder/intermetallic interface is not microscopically planar. The morphology of this interface introduces a systematic variation into the layer-thickness measurements. In order to improve the accuracy of the layer thickness measurements twenty (20) measurements were made on each sample which had been aged. To characterize completely the initial layer thickness produced during the dipping process, two hundred (200) measurements were made on the samples produced by each dipping process. The samples prepared by dipping with the process used for the Model 2560 had an initial intermetallic thickness of $3.4 \pm 0.4 \mu\text{m}$ (with errors of 1 S.D. throughout) and the samples prepared by the process used for the Model 2034 had an initial metallic layer thickness of $7.2 \pm 0.9 \mu\text{m}$. Several composition profiles, or traces, were measured across the as-dipped samples. The intermetallic layer thicknesses measured with the electron microprobe were consistent with the thickness measurements made by optical metallography. The electron microprobe data clearly show that the layer actually contained two distinct intermetallic compounds, $\text{Cu}_2(\text{Sn},\text{In})$ and $\text{Cu}_2\text{In}_3\text{Sn}$. The total intermetallic layer formed during the long-time dip was obviously thicker than the layer formed during the short time dip, but the layer thickness of the $\text{Cu}_2(\text{Sn},\text{In})$ remained essentially unchanged. All the growth appears to have occurred in the $\text{Cu}_2\text{In}_3\text{Sn}$ layer.

Figure 5 shows the results of the intermetallic layer growth measurements. The growth is predominantly linear with time. The samples heat treated at 70, 80, and 90 C all extrapolate linearly back to the initial layer thickness of approximately $3.4 \mu\text{m}$. The higher temperature data do not extrapolate linearly back to the initial thickness, although physically it must be the initial thickness. This behavior suggests that a different mechanism is responsible for layer growth at low temperatures than at high temperatures (especially high temperatures at short times). The linear-growth kinetics at low temperatures for all times and at high temperatures for long times suggest a growth mechanism controlled by interface kinetics, not volume diffusion. The growth at high temperatures and short times may be more parabolic, suggestive of a reaction controlled by volume diffusion.

During the linear-growth regime the layer growth may be described by the equation

$$\xi = \xi_0 + st$$

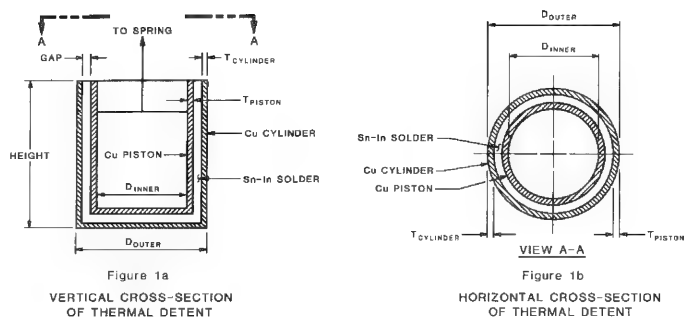


Figure 1a
VERTICAL CROSS-SECTION
OF THERMAL DETENT

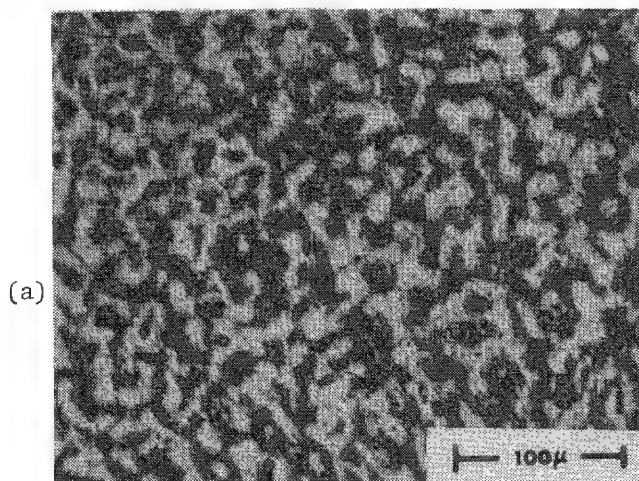
Figure 1b
HORIZONTAL CROSS-SECTION
OF THERMAL DETENT

DIMENSIONAL SUMMARY
(SCHEMATIC ONLY - NOT DRAWN TO SCALE)

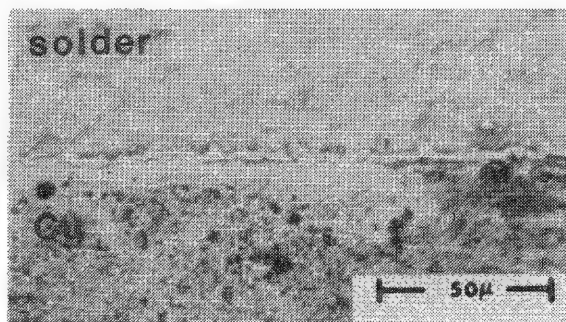
	MODEL 2560	MODEL 2034
HEIGHT	10.0mm	10.2mm
D _{OUTER}	4.7mm	3.1mm
D _{INNER}	2.3mm	1.9mm
T _{CYLINDER}	0.74mm	0.28mm
T _{PISTON}	0.40mm	0.26mm

NOMINAL GAP THICKNESS (BOTH MODELS) $\approx 100\mu\text{m}$ ($\pm 10\text{mm}$)

FIG. 1.--Schematic representation of thermal detents, Model 2034 and Model 2560.

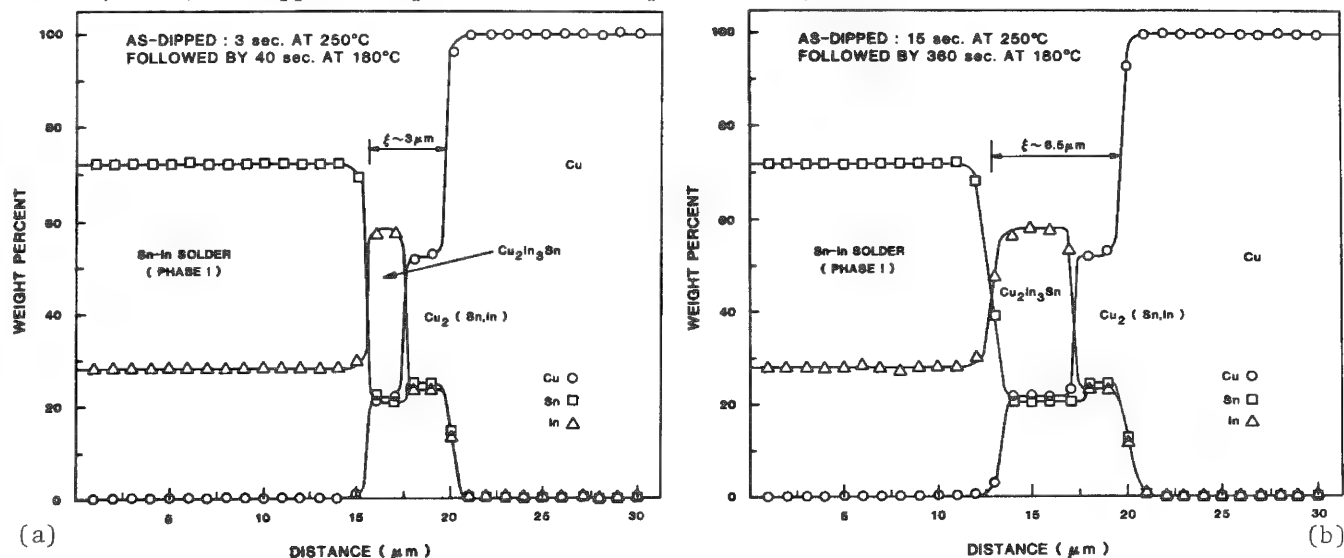


(a)



(b)

FIG. 2.--Optical micrographs: (a) Sn/In solder showing two-phase structure; (b) intermetallic layer. ("As-dipped" sample, Model 2034 process sequence, intermetallic layer $\sim 3\mu\text{m}$.)



(a)

(b)

FIG. 3.--Concentration profiles measured with electron microprobe: (a) "as-dipped" sample (Model 2034 sequence); (b) "as-dipped" sample (Model 2560 sequence).

TABLE 1.--Processing sequence to prepare actual components Model 2034 and Model 2560 and experimental Cu/Sn-In diffusion couples.

STARTING MATERIALS :

Cu sheet (1cm x 1cm x 0.51mm)
50wt%Sn-50wt%In solder (Cerroseal-35)

SAMPLE PREPARATION (CLEANING) :

Acid Pickle : (by volume)

3 parts phosphoric acid

3 parts acetic acid

1 part nitric acid

Rinse in Deionized Water

Degrease in Trichloroethylene

Flux with Kester Soldering Flux No. 1544

DIPPING :

(Model 2560)

(Model 2034)

15 sec. - 250°C

3 sec. - 250°C

Plate quenched

Plate quenched

360 sec. - 180°C

40 sec. - 180°C

Plate quenched

Plate quenched

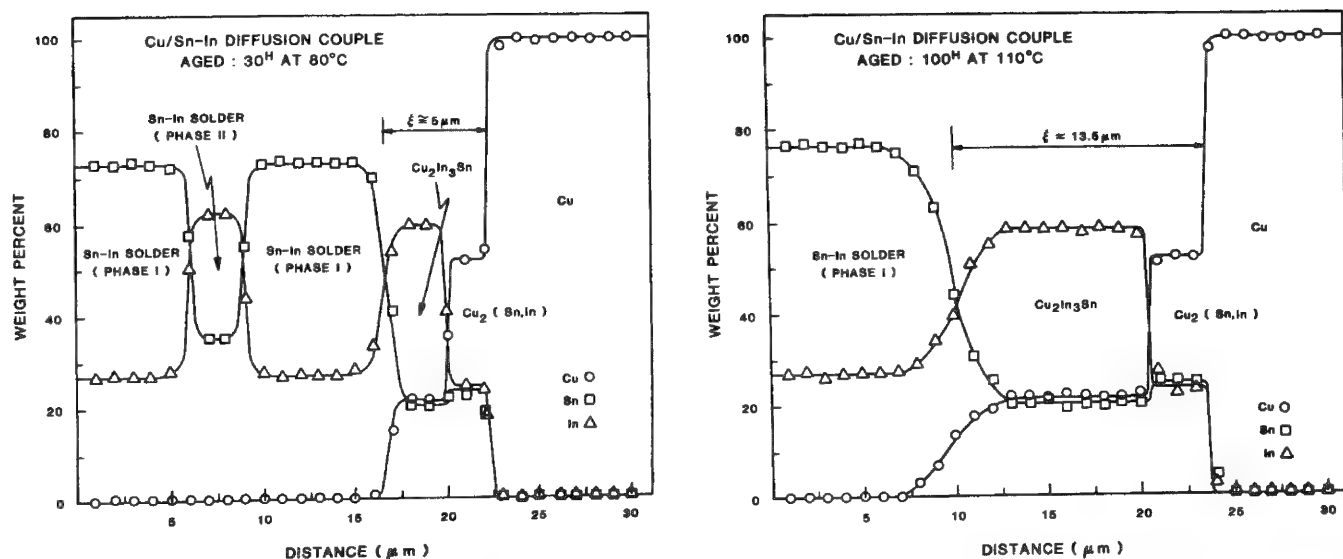


FIG. 3 (Cont'd).--Concentration profiles measured with electron microprobe: (c) sample aged for 30 h at 80 C; (d) sample aged for 100 h at 110 C.

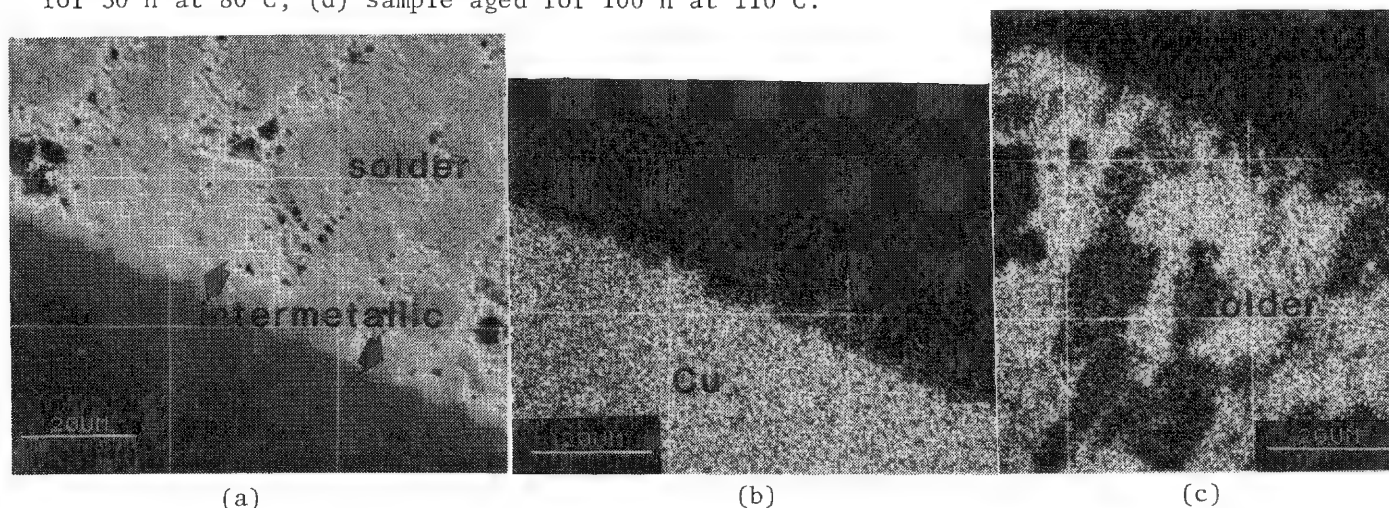


FIG. 4.--Sample aged for 200 h at 80 C: (a) secondary-electron image showing intermetallic layer between solder and Cu base metal (intermetallic layer $\sim 6 \mu\text{m}$); (b) Cu x-ray map; (c) Sn x-ray map. (Note two-phase structure in solder; Sn-rich phase is usually contiguous with intermetallic layer.)

TABLE 2.--Heat-treatment matrix for experimental diffusion couples.

TEMPERATURE (°C)	TIMES (HR.)
110	5, 10, 15, 20, 30, 40, 50, 75, 100
100	10, 15, 20, 30, 50, 75, 100
90	15, 20, 30, 50, 75, 100, 150
80	30, 40, 50, 75, 100, 150, 200
70	50, 75, 100, 150, 200, 250, 300
60	70, 100, 200, 300, 400, 500

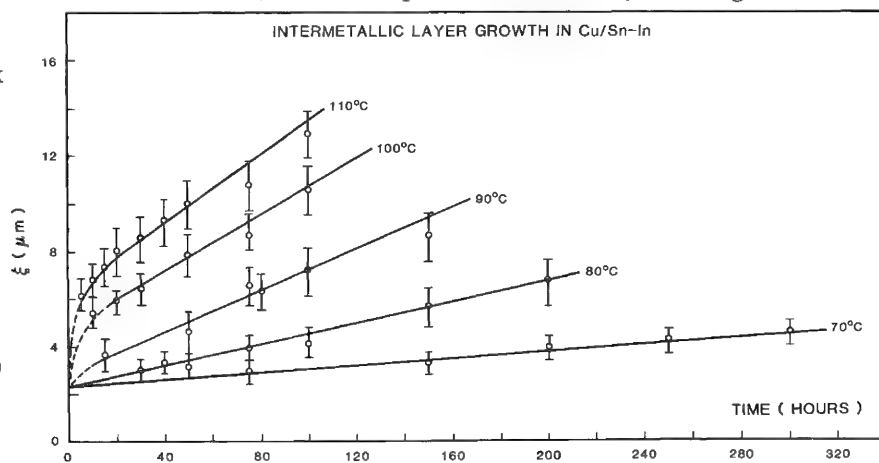


FIG. 5.--Results of layer-growth measurements. All samples used in this study had an initial layer thickness of $\sim 3.4 \mu\text{m}$. For these heat treatment times, layer growth that occurred at 60 C was not statistically significant.

where ξ is the total layer thickness at any time, ξ_0 is the initial layer thickness, t is time, and s is the layer growth coefficient, which is equal to the slope of the ξ -vs-time lines shown in Fig. 5. With the slopes from the linear portions of the curves in Fig. 5 it is possible to construct an Arrhenius plot of $\log s$ vs $1/T$, where T is absolute temperature, as shown in Fig. 6. Consistent with the earlier observation that the kinetics were controlled by several mechanisms, the curve in Fig. 6 breaks into two distinct regimes. The activation energy for each process can be determined since the slope is equal to $-Q/RT$, where Q is the activation energy, R is the gas constant, and T is absolute temperature. The low value of Q at high temperatures, 5300 cal/mole, is probably related to volume diffusion. In this regime the transfer of atoms across the interface is essentially instantaneous and the overall reaction is limited by volume diffusion. The role of volume diffusion is consistent with the fast diffusion of precious metals like Cu through metals like Sn, In, and Pb.¹³ At low temperatures the interface reaction, not volume diffusion, becomes the rate-limiting process. In this regime the activation energy increases to approximately 18 600 cal/mole. It is important not to misinterpret these results with respect to mechanisms. It is not possible, with the present data, to determine which interface reaction [solder/ $\text{Cu}_2\text{In}_3\text{Sn}$, $\text{Cu}_2\text{In}_3\text{Sn}/\text{Cu}_2(\text{Sn},\text{In})$, or $\text{Cu}_2(\text{Sn},\text{In})/\text{Cu}$] is rate limiting. Similarly, it is not possible to determine in which phase the volume diffusion is rate limiting. The activation energies determined from this analysis are for the overall process. The traces across the intermetallic layers measured with the electron microprobe show that during aging all layer growth appears to occur in the $\text{Cu}_2\text{In}_3\text{Sn}$. The initial 2 μm layer of $\text{Cu}_2(\text{Sn},\text{In})$ does not appear to grow at all during aging.

The microprobe analysis also revealed a nonequilibrium phase structure in the solder. The Sn-In phase diagram is shown in Fig. 7.¹⁴ The solder composition is very close to the eutectic composition. When the alloy liquid freezes it should partition into the equilibrium B and (Sn) phases, which are In rich and Sn rich, respectively. However, the microprobe analysis showed the solder to contain two nonequilibrium phases: Phase I, which contains approximately 77 wt%Sn/33 wt%In; and Phase II, which contains approximately 38 wt%Sn/62 wt%In. Phase I was almost always contiguous with the intermetallic layer. As shown in Fig. 7, these nonequilibrium phase compositions can be accounted for by the construction of metastable extensions of the liquidus lines. These nonequilibrium compositions are a consequence of the freezing kinetics in that the liquid had insufficient time to partition into the two equilibrium phases. Given sufficient time at elevated temperature the composition of the phases should adjust toward the equilibrium values. The nonequilibrium structure of the solder may influence the intermetallic-layer growth kinetics, but the nature or magnitude of the effect is unknown.

It is now possible to predict the rate of intermetallic layer growth at room temperature with the use of the low-temperature activation energy. The room temperature growth rate is the key to predicting the lifetime of the thermal detent. If the Cu piston is placed concentrically in the Cu cylinder, then the solder gap that the intermetallic compound must bridge to seize the assembly is 100 μm . For the initial layer thickness of 3.4 μm the time required to grow a layer 100 μm thick is approximately 8 years. In the actual device, layer growth proceeds from the Cu cylinder and the Cu piston. This process ultimately leads to a condition of soft impingement, or diffusion field overlap. The impingement effect slows the growth reaction and slightly extends the lifetime beyond the 8 yr prediction.

Conclusions

1. Cu reacts with the Sn-In solder to produce an intermetallic layer containing $\text{Cu}_2(\text{Sn},\text{In})$ and $\text{Cu}_2\text{In}_3\text{Sn}$.
2. A small amount of layer growth occurs when the solid Cu reacts with the molten solder, but the most significant growth occurs in the solid state.
3. In all cases the layer growth is dominated by the growth of $\text{Cu}_2\text{In}_3\text{Sn}$. An initial layer of $\text{Cu}_2(\text{Sn},\text{In})$ forms during the dipping but does not undergo subsequent growth.
4. The rate limiting mechanism changes with temperature. At high temperatures the growth appears to be limited by volume diffusion while at low temperature the growth appears limited by interface kinetics.
5. For a uniform gap of 100 μm , and neglecting the effects of impingement, the lifetime of the thermal detents at room temperature is estimated to be approximately 8 years.

References

1. F. G. Yost and A. D. Romig Jr., *Storage Life of Thermal Detents*, Sandia National Laboratories Report, to be published, 1984.
2. Louis Zakraysek, "Intermettalic growth in tin-rich solders," *Welding Research* 37: 536, 1972.
3. Masami Onishi and Hideo Fujibuchi, "Reaction diffusion in the Cu-Sn system," *Japan Inst. of Metals Trans.* 16: 539, 1975.
4. I. N. Revay, "Interdiffusion and formation of intermetallic compounds in tin-copper alloy surface coatings," *Surface Technology* 5: 57, 1977.
5. P. J. Kay and C. A. Mackay, "Barrier layers against diffusion," *Trans. Inst. Met. Finish.* 57: 169, 1979.
6. K. N. Tu and R. D. Thompson, "Kinetics of interfacial reaction in bimetallic Cu-Sn thin films," *Acta Metall.* 30: 947, 1982.
7. R. N. Chopra, M. N. Ohring, and R. S. Oswald, "Low temperature compound formation in Cu/Sn thin film couples," *Thin Solid Films* 94: 279, 1982.
8. R. W. Barnard, "Effects of interdiffusion on the properties of indium-plated contacts," *Plating* 61: 752, 1974.
9. B. G. Mellor and G. Z. Chadwick, "Volume diffusion coefficients in the beta phase region of the copper-indium system," *Metal Science* 8: 63, 1974.
10. N. A. Kermali and D. R. Gabe, "Diffusion coatings of indium on copper," *Surface Technology* 15: 1, 1982.
11. F. G. Yost, F. P. Ganyard, and M. M. Darnowsky, "Layer growth in Au-Pb/In solder joints," *Met. Trans.* 7A: 1141, 1976.
12. W. F. Chambers, *SANDIA--TASK '78: An Electron Microprobe Automation Program*, Sandia National Laboratories Report, SAND 78--1149, 1978.
13. W. K. Warburton and D. Turnbull, "Fast diffusion in alloys," *Thin Solid Films* 25: 71, 1975.
14. Max Hansen, *Constitution of Binary Alloys*, New York: McGraw-Hill, 2d ed., 1958, 860.

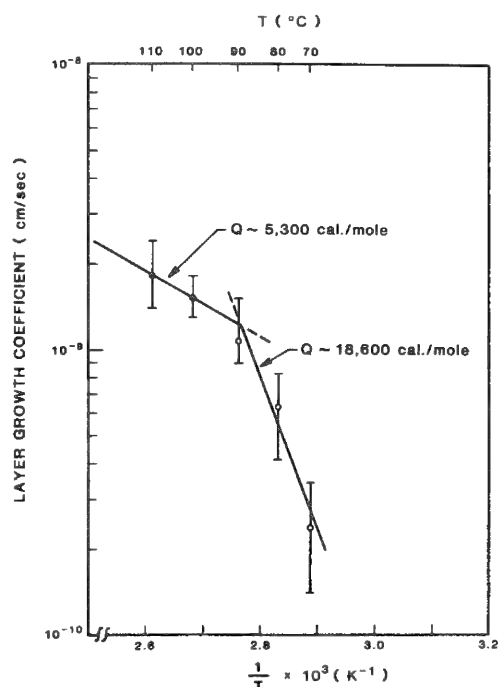


FIG. 6.--Arrhenius plot of intermetallic-layer growth coefficient for log s vs inverse temperature. Layer-growth coefficient equals slopes of curves of Fig. 5. Two slopes, each reflecting different activation energy, are apparent. Growth is limited by volume diffusion at high temperatures, by an interface reaction at low temperatures.

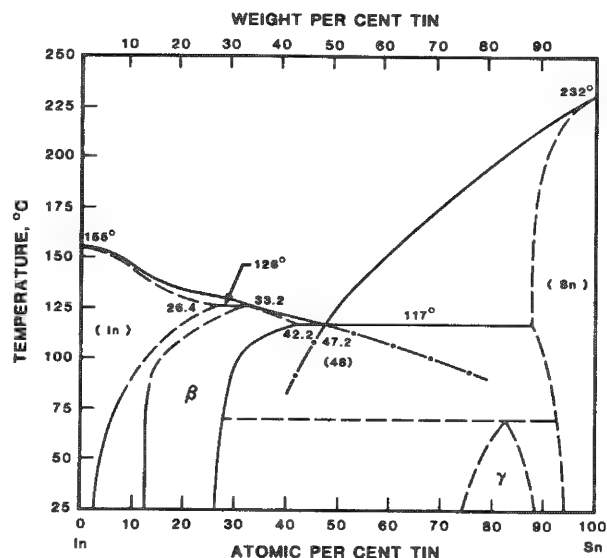


FIG. 7.--Sn-In phase diagram: metastable extensions of liquidus lines are shown to account for nonequilibrium compositions of coexisting solder phases.

COMPLEMENTARY USE OF ELECTRON CHANNELING AND EBIC FOR ANALYSIS OF POLYCRYSTALLINE SEMICONDUCTOR MATERIALS

R. J. Matson and Y. S. Tsuo

Considerable research is being conducted in low-cost polycrystalline semiconductors in the photovoltaic solar cell industry. The grain sizes of these polycrystalline materials are on the order of millimeters or less, and the electronic quality of individual grains is often related to their crystallographic orientations and intragrain defect structure.¹ We have found that the combination of secondary electron imaging (SEI), electron channeling,² and electron-beam-induced current (EBIC, also known as charge collection scanning electron microscopy)³ techniques in a scanning electron microscope (SEM) is quite useful for correlating morphology, crystallographic orientations, and the electronic quality of individual grains in polycrystalline semiconductor samples. It is also possible to obtain quantitative information about the minority carrier diffusion length of individual grains and the minority carrier recombination velocity at grain boundaries by the EBIC line scan method.⁴ The high spatial resolution obtainable with electron channeling and EBIC techniques and the ability to select among the SEI, EBIC, and electron channeling modes in the SEM make them far superior to conventional structural and electrical characterization techniques in the study of small-grained semiconductors. These techniques will be useful in the integrated circuits (IC) industry, where there is considerable current interest in recrystallized single-crystal or polycrystalline silicon islands on insulators used in the fabrication of three-dimensional ICs and large-area display-control circuits.

These techniques have been applied to the studies of two types of silicon sheets. Edge-supported pulling (ESP) silicon sheets⁵ made of polycrystalline silicon pulled vertically from the melt between two filaments were studied. These sheets contain long, narrow grains that run parallel to the growth direction. Low-angle silicon sheets (LASS)⁶ pulled almost horizontally from the melt at very high speeds, up to about 400 cm²/min, were also assessed. Large areas of single-crystal silicon are occasionally grown by the LASS method. However, single-crystal LASS sheets contain many defects which may result from the unusually high growth speeds.

Experimental Method

A JEOL JSM 35C SEM with a selected area diffraction component attachment was used in the experiment. An IC specimen holder was modified to operate at the 9mm working distance required for optimal electron channeling in this microscope. A GW Electronics Model 103B specimen current amplifier was used for EBIC imaging and a Keithley Model 427 current amplifier was used for digital quantitative EBIC images and linescans. The GW Electronics Model 130 backscattered electron imaging (BEI) detector and electronics were found to be optimal for acquiring clear electron channeling patterns (ECP). Restrained by a short working distance, the BEI unit, rather than the SEI unit, was used in a topographical mode to image topographical features such as grain boundaries and twin boundaries.

Various approaches can be taken to perform both electron channeling and EBIC analysis on the same area, depending on the requirements of the experiment. If the individual grains are relatively large and easy to locate, then the ECP work is done to establish the orientation of the grains; then, after a Schottky barrier device is made out of the material, the EBIC study is performed. Since the electron beam of the SEM is a constant-current source, the EBIC line scan traces and images reveal spatial variations in the charge collection efficiency of the Schottky barrier device. To measure the effective surface recombination

The authors are at the Solar Energy Research Institute (SERI), Golden, CO 80401. This work was supported by the U.S. Department of Energy under Contract EG-77-C01-4042.

velocity of minority carriers at a grain boundary, an EBIC line scan normal to the boundary is obtained. To be quantitatively useful, a digital linescan with a calibrated current amplifier, a computer, and a plotter are used to record the natural logarithm of the EBIC signal as a function of distance. One can also measure the minority carrier diffusion length within each grain by scanning the beam perpendicular to the edge of the front contact pad and recording the EBIC current as a function of distance from the contact pad.

If the grains are either difficult to locate or, as is often the case, there is significant local variation in the electrical activity along the length of the grain boundary such that one cannot easily locate specific areas, the electron channeling can be done through a thin Schottky barrier layer or a diffused p-n junction. The backscattered electrons used in electron channeling come from the top 1000 Å of the material, with the majority coming from the first few hundred Angstroms. Therefore, a thin Schottky barrier layer (≤ 100 Å) is necessary; even then, the ECP contrast is considerably degraded but possibly still useful for orientation purposes, depending on the original quality of the crystal. One method for performing EBIC analysis at the exact same location without compromising the ECP is to make a diffused p-n junction device. The presence of a heavily doped top layer for forming the junction does not notably degrade the ECP.

In the case of long, relatively parallel grains such as those found in ESP silicon sheets, one can evaporate a Schottky barrier across the grains. In the ECP mode, the sample is moved parallel to the evaporation line on the nonevaporated side until the ECP changes, whereupon the sample is moved laterally to the Schottky barrier part of the grain for EBIC analysis.

By switching between ECP, BEI, and EBIC while moving across the material, one can correlate the location, topography, electrical quality, crystalline orientation and even the crystalline quality for polycrystalline materials. Evaluating the crystalline quality requires measuring the relative peak heights (ECP contrast) and the shape of the peaks (ECP linewidths) shown by ECP linescans (intensity vs scan angle) normal to the crystalline bands.⁷

Applications

Complementary electron channeling and EBIC were first used in the study of ESP silicon sheets grown at SERI.⁸ In ESP Sheets, a fine-grained structure exists within a few millimeters of the filaments, and larger longitudinal and relatively parallel grains, several millimeters wide, dominate the rest of the sheet. The ESP sheets are usually 40 mm wide, and the average grain size of ESP sheets generally increases as the thickness of the crystal decreases. We studied the grain orientation distributions of ESP sheets with three different thicknesses: 110, 480, and 1100 μm . Figure 1 shows the grain orientations determined for these samples. The location of the dots inside the stereographic projection unit triangle indicates the direction of the surface normal of the longitudinal grains located several millimeters away from the filaments. The arrows attached to these dots within the triangle indicate the direction along which a particular grain was growing during the ribbon pulling. Figure 1 clearly shows that as the ESP silicon sheets get thinner, a dominant grain structure appears. This dominant grain structure consists of long grains with surface normals near the [011] direction. The plane that is parallel to the growth direction and perpendicular to the surfaces for most of these grains is very close to (11 $\bar{1}$).

EBIC images and linescans, such as those shown in Figs. 2 and 3, were also obtained on these ESP samples. The Schottky barrier device structure was made by evaporation of a layer of aluminum Schottky contact on the top of the device and a layer of gold ohmic contact on the back. The darker grains indicate a lower EBIC signal, caused by higher dislocation density within the grains. Correlation of the EBIC image intensities of the grains with the grain orientations showed that all the grains with bright EBIC images have surface normals oriented near [011]; i.e., the preferred grain orientation for thinner ESP silicon sheets.

This EBIC/ECP technique was also applied to LASS samples grown at the Energy Materials Corp. Probably because of the unusually high growth speed--the single-crystal LASS samples studied were grown at the speed of 210 cm^2/min --the defect structures we observed in these samples were rather unusual for single-crystal silicon. In addition to a relatively high density of electrically active dislocation networks, they also contain what appear to be inclusions such as that shown in the SEI in Fig. 4(a). The sample shown in Fig. 4(a) has been chemically etched to reveal the defects. The electron channeling patterns such as

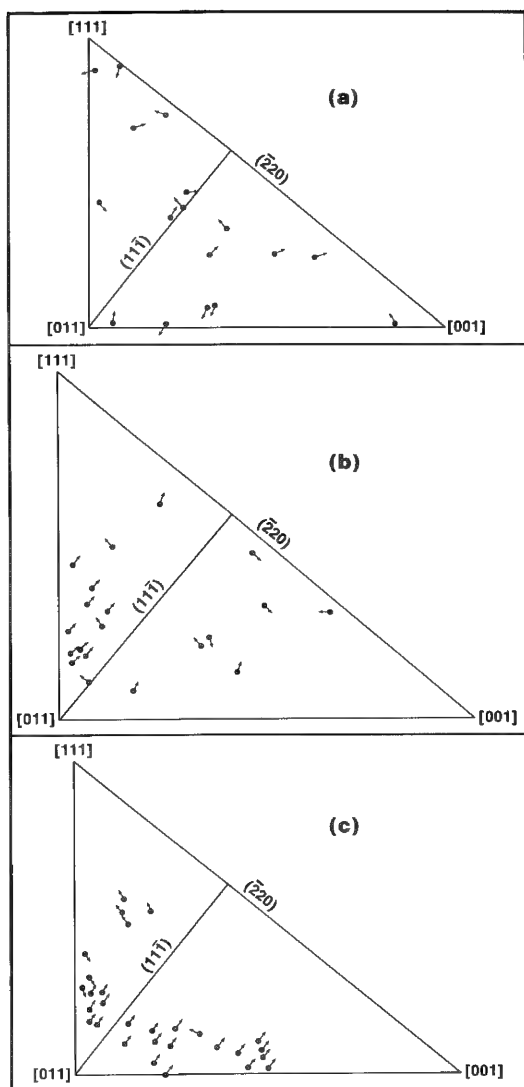


FIG. 1.--Grain orientations of ESP silicon sheets having average sheet thicknesses of 1100 μm (top), 480 μm (center), and 110 μm (bottom).

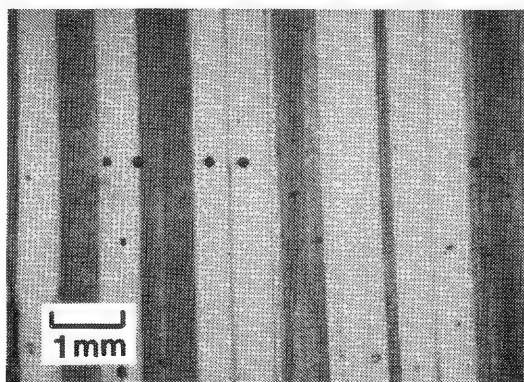


FIG. 2.--EBIC image of above 480 μm -thick sheet

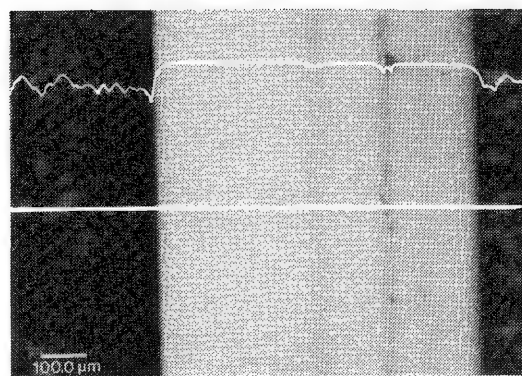


FIG. 3.--EBIC image and linescan of part of Fig. 1(b), both at 35 keV. Straight horizontal line shows position of linescan and zero beam current reference.

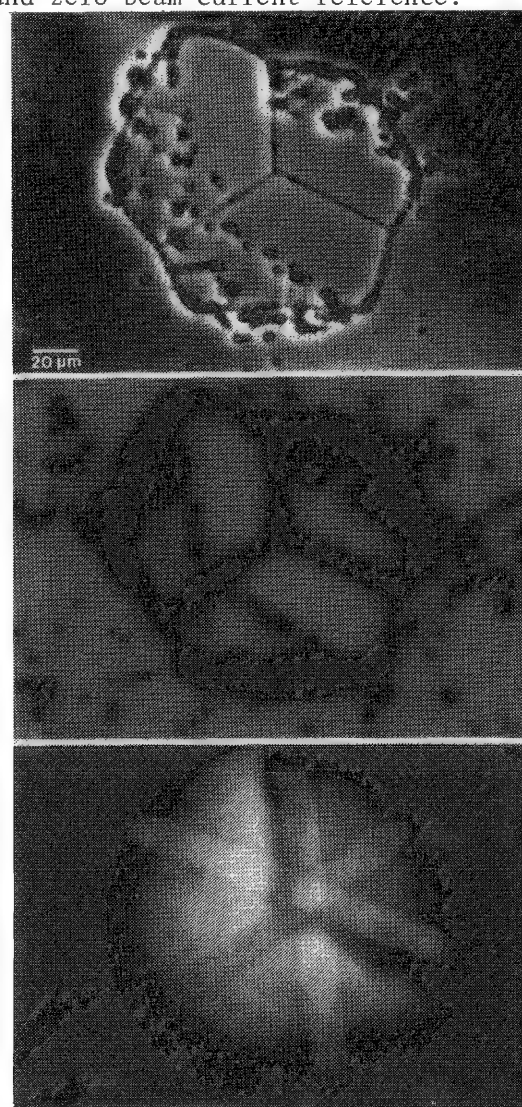


FIG. 4.--Defect structure in single-crystal LASS: (a) SEI image; (b) EBIC micrograph; (c) ECP superimposed on SEI image of center of defective area.

those shown in Fig. 4(c) indicate that these inclusions are actually silicon crystals with orientations identical or very similar to the rest of the crystal. Figure 4(c) is the superposition of the ECP taken at the center of Fig. 4(a) and the SEI of the location of the ECP at a magnification higher than that used in Fig. 4(a) and (b). The dark lines of the SEI in Fig. 4(c) show that the stacking faults occur along [220] planes. Figure 4(b) is an EBIC micrograph of the same area. The sample was mechanically and chemically polished to remove etch pits before being fabricated into Schottky barrier devices for EBIC studies. The EBIC images clearly illustrate the electrical activity of the various defects. They also show electrically active dislocations that were not revealed by chemical etching. In addition, our study showed that large, electrically active dislocation networks exist under the dendrites that appear on the LASS sheet's top surface during growth. Such information is not only useful from the device point of view, it may also provide insight into the mechanisms of defect growth in the LASS process.

Conclusion

By using a combination of secondary-electron imaging, electron channeling, and EBIC techniques in a SEM, we have discovered the existence of a dominant grain structure in thinner ESP silicon sheets and demonstrated that such grains have better electronic quality than random grains in ESP silicon sheets. We have also used this technique to correlate the structural and electrical properties of defects in low-angle silicon sheets. This technique has proven quite useful in correlating the structural and electrical properties of highly defected or polycrystalline semiconductor materials.

References

1. See, for example Y. S. Tsuo et al., "Grain boundary structures and properties in polycrystalline silicon," in Pike, Seager, and Leamy, Eds., *Grain Boundaries in Semiconductors*, New York: Elsevier Science Publishing, 1982, 155-166.
2. D. C. Joy et al., "Electron channeling patterns in the scanning electron microscope," *J. Appl. Phys.* 53(8): R51-80, 1982.
3. H. J. Leamy, "Charge collection scanning electron microscopy," *ibid.*, 53(6): R81-122.
4. P. E. Russell et al., "The effect of heat treatment on grain boundary properties in cast polycrystalline silicon," in Pike et al., Ref. 1, 185-191.
5. T. F. Ciszek and J. L. Hurd, "Melt growth of silicon sheets by edge-supported pulling," in K. V. Ravi and B. O'Mara, Eds., *Proc. Symp. Electronic and Optical Properties of Polycrystalline or Impure Semiconductors and Novel Silicon Growth Methods*, The Electrochemical Society, Pennington, N.J.: Proc. 80-5, 1980, 213-222.
6. D. N. Jewett et al., "Progress in growth of silicon ribbon by a low angle, high rate process," *Proc. 16th IEEE Photovoltaic Specialists Conference*, 1982, 86-89.
7. D. L. Davidson, "Assessment of defect density magnitude by changes in selected area electron channeling patterns," *SEM/1981 I*, 373-384.
8. Y. S. Tsuo et al., "Electron channeling and EBIC studies of edge-supported pulling silicon sheets," to be published in *IEEE Trans. Electron Devices*, May 1984.

CROSS-SECTIONAL TRANSMISSION ELECTRON MICROSCOPY OF ELECTRONIC DEVICES

T. T. Sheng

Cross-sectional transmission electron microscopy (XTEM) has become a well-established tool for materials research. In the past ten years XTEM has evolved into a valuable analysis tool for device evaluation. In silicon integrated circuit (SIC) processing, XTEM is routinely now used for the testing of process-related problems. However, direct application of silicon XTEM methods to III-V photonic materials technology was found to be difficult because of the extreme fragility and small size of lasers and other photonic devices compared with silicon devices.

The usefulness of TEM as a diagnostic tool resulted largely from the development of techniques for sample preparation. Sheng and Chang published the first results on SIC device analysis in 1976,¹ followed by a similar paper by W. Ham et al. in 1977.² A book by Marcus and Sheng on this subject was published in 1983.³ In this work, special methods for preparing cross sections of both silicon VLSI and photonic devices are presented, and the impact of TEM studies on device diagnostics programs is demonstrated.

Sample Preparation Technique

XTEM specimens of SIC or Josephson junction devices which contain multilayered structures prepared by mechanically thinning down to ~ 100 μm , followed by ion beam milling. Due to the slow ion milling rate of Au, Pb, and Al, thinning of such specimens requires exceedingly long times and leads to unavoidable deleterious effects. A prethinning "drill polishing" technique prior to ion milling has been developed that eliminates these difficulties and reduces ion milling time.

A grid reinforcement technique also has been developed to allow easier handling of III-V materials during sample preparation. The brittle material is bonded to a molybdenum grid during the entire sample-preparation procedure, which adds considerable strength and greatly improves the yield of successful samples. The molybdenum grid also serves as an etching mask by accurately positioning the masking grid and monitoring the perforation under a microscope. Since many perforations can be obtained in the selective area, the probability of success in obtaining a cross-section sample containing the device structure is greatly increased.

Results and Discussion

Figure 1 shows a cross section of a PbInAu Josephson junction device that clearly shows textural features of the various layers, the dielectric barrier interface, and the smooth interfaces. This is the first XTEM study of a complete Josephson device to be reported. This success was largely due to the development and use of a "drill polishing" technique prior to ion milling which uniformly thins down regions which differ markedly in their milling and/or etching rate, as mentioned earlier.

Figure 2 shows a TEM cross section of the quaternary active area of both etched mesa and V-groove heterostructure InGaAsP/InP long-wavelength lasers, which demonstrates that the heart of individual laser devices can now be reached. This area was considered to be inaccessible due to the brittle nature and small size of the material. From the micrograph, the dimensions and shape of these active layers can be easily determined.

Figure 3 shows a lower magnification XTEM of an etched mesa heterostructure InGaAsP/InP

The author is at AT&T Bell Laboratories, Murray Hill, NJ 07974. He wishes to acknowledge the support and encouragement of R. Edwards and R. B. Marcus, and technical discussions with S. N. G. Chu.

long-wavelength laser. No defects at most of the epitaxial interfaces or within the epilayers have been found. There is evidence for a spinodel structure within all InGaAsP quarternary layers, and an as yet unidentified defect at the mesa side wall/epi interface.

Conclusion

Thinning techniques are described for the preparation of cross-section samples for TEM studies of silicon, Josephson junction, and III-V compound semiconductor devices. The introduction of a grid-masking method for III-V devices enables more precise control over selection of the thinned region and greatly increases the success of obtaining a good XTEM sample. The masking grid also mechanically reinforces the thin cross section, which simplifies sample handling. This technique can also be applied to GaAlAs/GaAs devices, and greatly facilitates the preparation of plan-view TEM samples.

References

1. T. T. Sheng and C. C. Chang, *Trans. IEEE* ED-23: 531, 1976.
2. W. E. Ham et al., *RCA Rev.* 38: 351, 1977.
3. R. B. Marcus and T. T. Sheng, *Transmission Electron Microscopy of Silicon VLSI Circuits and Structures*, New York: Wiley, 1983.

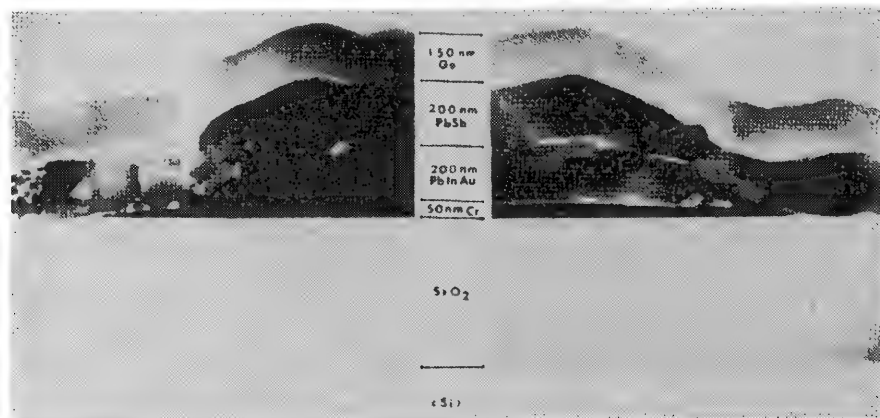


FIG. 1.--XTEM of Josephson junction device.

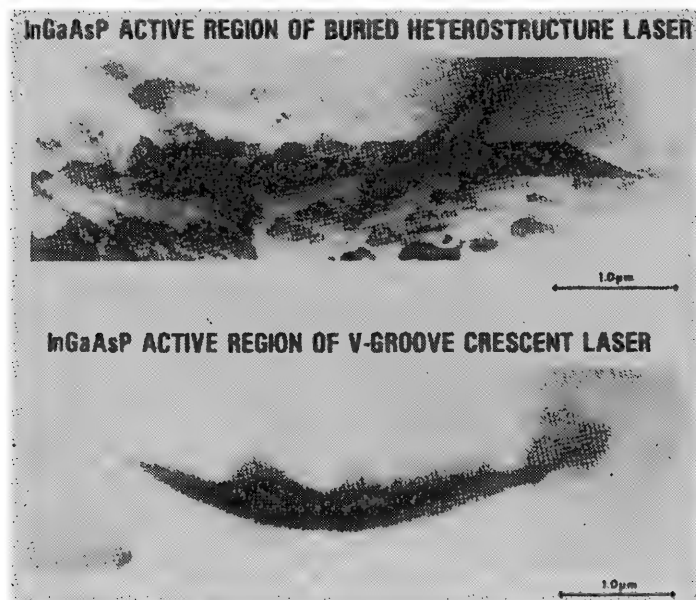


FIG. 2.--XTEM of active regions of InGaAsP/InP lasers.

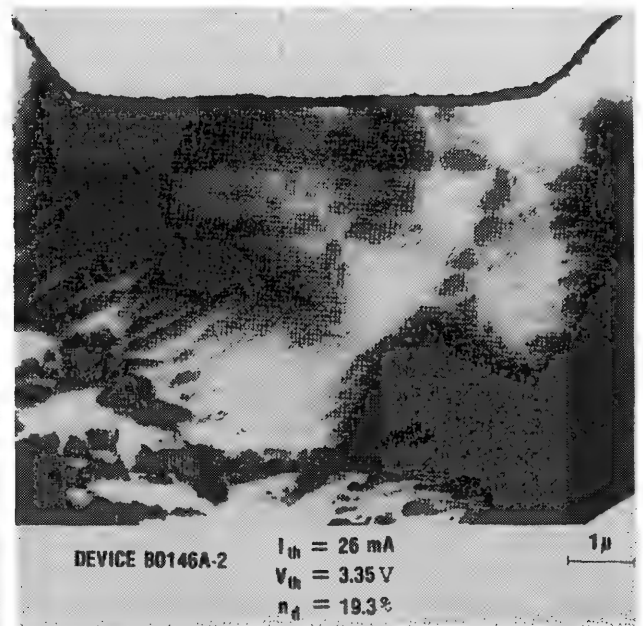


FIG. 3.--XTEM of etched mesa heterostructure InGaAsP/InP laser.

EBIC MICROSCOPY FOR DEVICE DIAGNOSIS

P. S. D. Lin

By detecting electrical signals induced by carriers injected into a device, electron beam injected carriers (EBIC) microscopy (also known as charge collection¹ or electron beam induced current microscopy) has the unique capability of providing information on a wide variety of semiconductor characteristics pertaining to carrier transport. Most previous EBIC microscopy studies focused on (1) "static" characteristics such as minority carrier diffusion length, lifetime, or surface recombination velocity,^{2,3} or (2) calculations and measurements of the induced current signal profile across a junction or near a defect.^{4,5} In these studies, the devices were not biased in operating condition. By collecting carriers injected into a device in its operating conditions, EBIC microscopy can examine the electrical and material structure of the device active under such conditions and thus provide leads vital to device quality improvement. We present cases studied in this approach and discuss future EBIC instrumentation needs. Overall, the goal is to open up the subject and illustrate that EBIC microscopy can be and needs to be broadened to tackle effectively the tasks in device diagnosis.

Device Case Studies

The fabrication of a device involves multiple steps that may interact with each other and result in defects in the end product, even though each step is known to be problem-free. Device testing engineers usually examine the electrical and optical characteristics of the device, but the processing engineers need additional information on the microscope structural defects that affect device performance. EBIC microscopy provides a tool that can detect the existence of abnormal junctions and electrically active defects and correlate them with the test results. To establish such correlations, one should examine in the EBIC mode devices biased in their operating or testing condition so that the effect of variations of internal field distribution on carriers transport can be examined. Following are four case studies:

1. *Leakage in MOS Capacitors with Thin Oxide.*⁶ Examination of MOS capacitors with excessive leakage current showed that such capacitors possess a high density ($10^4/\text{cm}^2$) of discrete spots (Fig. 1a, arrows) absent in capacitors with low leakage. Furthermore, when the field strength in the oxide was increased to about 6 MV/cm, the defects appeared as bright dots on a dark background. When the capacitors were stressed to breakdown, one of the EBIC spots invariably turned out to be the breakdown site. After EBIC had established the correlation between leakage and defects, transmission electron microscopy revealed that the defects originated from silicon stacking faults decorated with impurity atoms.⁶ Methods for avoiding the formation of silicon stacking faults during oxide growth were therefore devised and incorporated into device processing.

The method used in obtaining Fig. 1(b) differs from the conventional method of imaging MOS capacitors in that the latter utilizes the depletion region in silicon to separate the beam-injected carriers, whereas the capacitor in Fig. 1(b) was biased in accumulation. Thus there was no depletion layer in the silicon and a high electric field was set up across the oxide that regions of enhanced tunneling of beam generated carriers showed up as bright dots in the EBIC image.⁷

EBIC examination of MOS capacitors, utilizing the tunneling current, serves as an example that electron beam injected carriers can be used to reveal a variety of carrier transport phenomena in devices, in addition to the minority carriers drift-diffusion mechanism.

The author is at Bell Communications Research, Murray Hill, NJ 07974.

2. *Detection of Interfacial Junctions.* Compound semiconductor devices usually consist of multiple layers of semiconductor material of varied composition and dopant concentration. Crystallographic defects or transition layers due to chemical interaction or dopant redistribution may exist near a interface. Figure 2 provides an example of one of the latter cases. Here the background is a backscattered electron image of a multilayered GaAs/GaAlAs test chip. The straight horizontal line was where the beam scanned to acquire the two beam-induced current traces. One trace was obtained at zero bias; the other, at 0.4 V forward bias. On these EBIC traces, the only feature originally expected was a trough at layer 3, a layer of GaAlAs which borders n-type and p-type GaAs. The peak about 0.2 μm from the layer's 1-2 interface was not expected. Further analysis by secondary ion mass spectrometry (SIMS) showed that the dopant concentration was constant throughout layer 2; but whether the dopant atoms were activated or compensated remained uncertain. EBIC results indicated that the dopants in the first 0.2 μm of layer 2 most likely had been compensated by certain electrically active defects and turned either p-type or less n-type. The abnormal junction was eliminated by an increase in the dopant concentration in this layer.

3. *Metal-semiconductor Contacts.* An ohmic contact with negligible contact resistance is desirable for devices passing a current of high density. Various schemes exist, but thus far there appear to be few methods for checking the quality of such contacts. Again, EBIC microscopy provides a tool. Two examples are presented here.

Figure 3(a) shows the mirror face of a test chip of etched mesa buried heterostructure (EMBH) laser with a Au-Zn contact layer. A shallow junction is formed (Fig. 3b, right arrow) in the N-InP under the contact due to the in-diffusion of zinc. With the laser under reverse bias, EBIC microscopy detected the existence of premature-breakdown sites (left arrow in Fig. 3b) in lasers with noisy light output-vs-current characteristics. In an independent study, of this very system, Brasen, Vaidya, and Kammlott¹⁰ discovered that, due to metal migration induced by electric-field and temperature gradients, filaments nucleating at the Au contact were formed. Localized high electrical field at such filaments might have resulted in the premature-breakdown sites detected in our experiment.

In Fig. 4, the background is an edge-on view (secondary-electron image) of a GaAs/GaAlAs laser test chip with Au-Zn contact. The top signal trace is an EBIC signal recorded with the chip at zero bias. The peak corresponds to a pn junction. If the junction is forward biased, then most of the EBIC signal is inverted, except that some of the pn junction peak still remains (arrow on lower trace). The inversion of EBIC is tentatively attributed to carrier collection in the surface junction which has been widened or "enhanced" by biasing. This micrograph was obtained by blanking the electron beam and using a lock-in amplifier to extract the induced signal from a forward-current background. Further application of this effect to the determination of the width of the current confining stripe in proton-bombarded GaAs lasers is in progress.

EBIC Instrumentation for Device Diagnosis

Although EBIC has been widely practiced for years and the importance of proper instrumentation emphasized by many authors,^{2,12} existing EBIC detection systems appear to lack the full capability required for device diagnosis. One major problem is the low signal-to-noise ratio. Biasing a device in its operating condition to trace the source of leakage current often introduces a high background current that easily overwhelms the beam induced signal. Thus, many devices examined under conditions similar to those in obtaining Figs. 1(b) and 3(b) gave excessively noisy signals, so that EBIC imaging with usual instrumentation was not possible. To improve the signal-to-noise ratio, lock-in and/or signal integration technique is required in addition to the amplifiers. Other shortcomings include lack of conveniently organized bias supplies, calibration sources, beam-blanking controls, means for data recording and processing, etc. In short, there appears to be a need to devise for EBIC microscopy instrumentation packages which include the following components:

- (a) preamplifiers for quantitative measurements
- (b) device bias supply module
- (c) signal-to-noise improvement module
- (d) data processing module
- (e) automation module
- (f) accessories for device heating or illuminating in SEM

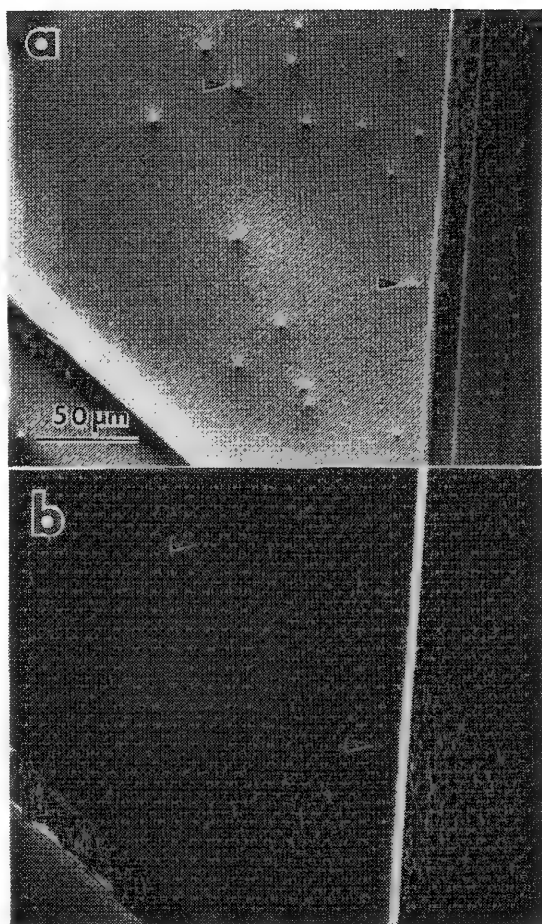


FIG. 1.--(a) EBIC image of MOS capacitor with 350 nm of doped polysilicon and 22 nm of oxide on p-type silicon substrate; field strength across oxide, 0.45 MV/cm. (b) Same capacitor as in (a), $E = 6.5$ MV/cm; arrow points to same defect sites as in (a), but tunneling of carriers enhanced at these sites.

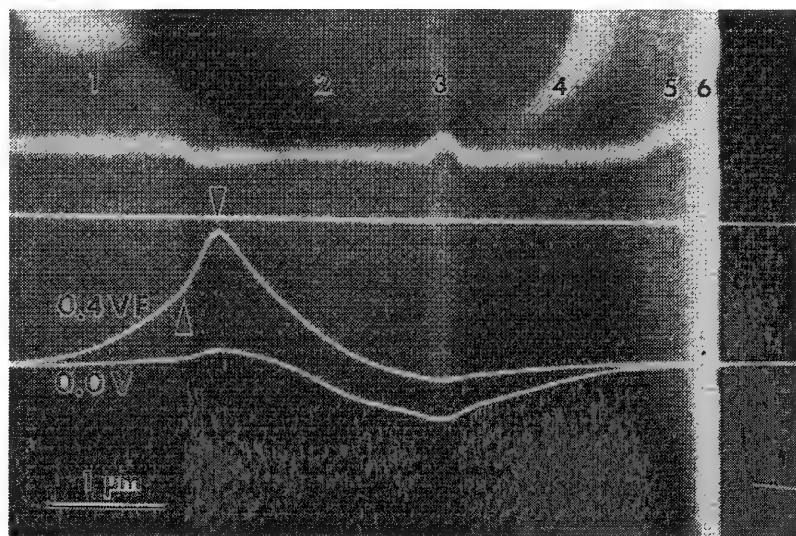


FIG. 2.--EBIC line scans across GaAs/GaAlAs test chip. Top trace contains peak enhanced upon forward biasing of chip; this transition layer results in high forward resistance, which inhibits current flow.

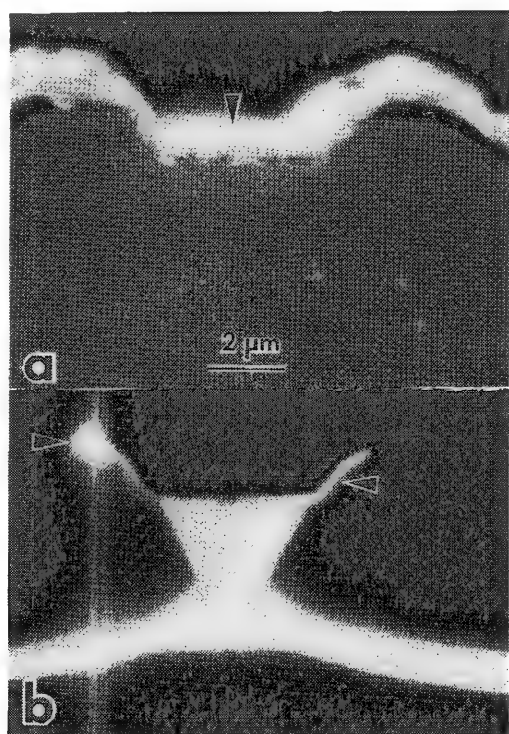


FIG. 3.--(a) Secondary electron image of InP-based etched mesa buried heterostructure laser test chip; arrow points to metal contact. (b) EBIC image of above laser; right arrow points to junction formed in InP under metal contact, left arrow indicates site of premature breakdown. Such breakdowns correlate with noise in light output.

With the recent growth in opto-electronics, such a package would be highly valued by the industry.

Conclusion

The cases presented here serve to illustrate that one can deduce important information on the internal field structure and defects of a device by examining in the EBIC mode devices biased in their operating or test conditions, and that correlation between electrical measurement data, device structure, and defect species can generally be established. Such information is vital to the improvement of device performance and reliability. Instrumentation developments are required in the direction of improving signal-to-noise ratio so that meaningful data can be extracted from the background signal due to leakage or forward junction current in the device. The EBIC microscopy for device diagnosis and analysis is only at its beginning. Many possibilities await exploration. Theoretical, experimental, and instrumental efforts are all in demand for meeting the immediate needs in semiconductor device research.

References

1. H. J. Leamy, "Charge collection microscopy," *J. Appl. Phys.* 53: R51, 1982.
2. D. B. Holt, "Conductive mode SEM," in D. B. Holt et al., Ed., *Quantitative Scanning Electron Microscopy*, New York: Academic Press, 1974, 213-286.
3. H. W. Marterx and O. Hildebrand, "Computer simulation of electron beam induced current (EBIC) linescans across PN-junctions," *SEM/1983 III*, 1197-1209.
4. C. Donolato, "Spatial resolution of SEM-EBIC images," *Sol. State Elect.* 22: 797-799, 1979.
5. S. Mil'shtein, D. C. Joy, and S. D. Ferris, "Defect characterization using SEM-CCM: Relative contrast measurements," to be published.
6. P. S. D. Lin, R. B. Marcus, and T. T. Sheng, "Leakage and breakdown in thin oxide capacitors: Correlation with decorated stacking faults," *J. Electrochem. Soc.* 130: 1878-1883, 1983.
7. P. S. D. Lin and H. J. Leamy, "Tunneling current microscopy," *Appl. Phys. Letters* 42: 717-719, 1983.
8. P. S. D. Lin et al., "Detection and elimination of abnormal interfacial layer in MOCVD GaAs/GaAlAs lasers," to be published.
9. P. S. D. Lin, P. D. Wright, and N. K. Dutta, "Studies of defects and structure of InGaAsP etched-mesa buried heterostructure lasers by scanning electron microscopy," to be published.
10. D. Brasen, S. Vaidya, and G. W. Kammlott, "Electro-thermomigration and filament growth in P-InP with Au contacts," to be published.
11. P. S. D. Lin and S. Y. Leung, "Nondestructive measurement of stripe width of proton bombarded GaAs/GaAlAs laser by EBIC microscopy," to be published.
12. B. A. Unvala et al., "A versatile quantitative detection system for conductive mode scanning electron microscopy," in A. G. Cullis and D. C. Joy, Eds., *Microscopy for Semiconductor Materials--1981*, 223-228.

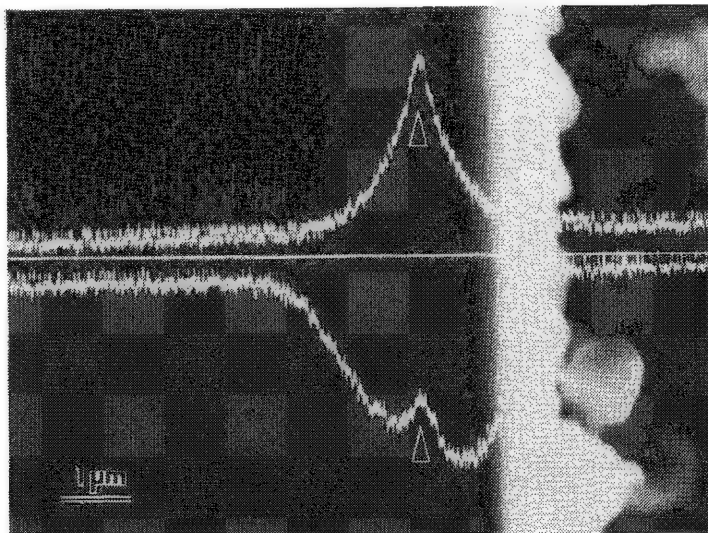


FIG. 4.--EBIC line scans superposed on secondary-electron image of GaAs/GaAlAs laser test chip. Top trace taken at zero bias, bottom trace at 1.2 V forward bias.

MICROFLUORESCENCE STUDIES OF ZIRCONIUM OXIDE

T. E. Doyle and J. L. Alvarez

We have experimented with titanium fluorescence in the various crystalline phases of ZrO_2 . This work was a direct result of micro-Raman analysis of filter debris samples from a nuclear test reactor. The titanium fluorescence in the micro-Raman spectra provides a method for differentiating between fabricated zirconia and oxidized fuel-rod cladding. We can conclude from the spectra that some of the observed cubic ZrO_2 in the samples was not from fabricated zirconia and is probably oxidized fuel-rod cladding. This work also suggests a novel and unexplored line of research in fission-product chemistry and detection.

Experimental

The samples were obtained from the Power Burst Facility (PBF), a reduced-scale nuclear test reactor where experimental fuel assemblies are subjected to high-temperature accident conditions. The samples consisted of debris retrieved from a filter in the coolant system. The debris was transported by water from the fuel assembly during a severe-fuel-damage test. Sources of ZrO_2 in the debris were fragments of zirconia fiberboard (used to insulate the fuel assembly), fragments of ZrO_2 spacers and ceramic-coated thermocouples, and oxidized fuel-rod cladding.

Debris particles were deposited on glass slides and placed under the microscope of a Raman microprobe for analysis. Spectra were taken of the particles by use of the 488.0nm blue line and 514.5nm green line of the argon ion laser as the excitation wavelengths. Spectra of a stabilized tetragonal ZrO_2 ceramic, a cubic ZrO_2 synthetic gemstone, and zirconia fiberboard particles were also obtained.

Results

Micro-Raman analysis of particles from the zirconia fiberboard which surrounded the PBF fuel bundle produced spectra of both monoclinic and tetragonal ZrO_2 . Cubic ZrO_2 was not detected. In addition, spectra of all fiberboard particles analyzed displayed strong, unique peaks at 963, 1026, and 1079 cm^{-1} with the 514.5nm green line of the argon ion laser as the excitation source (Fig. 1). Changing the lasing frequency to the 488.0nm blue line verified that these peaks were due to fluorescence. X-ray fluorescence revealed that the zirconia fiberboard contained more than trace quantities of yttrium, and evidently yttrium oxide (yttria) was used as a stabilizing agent for the ZrO_2 .

Both the tetragonal ZrO_2 ceramic and cubic ZrO_2 gemstone were yttria-stabilized, and both produced weaker fluorescence peaks than the zirconia fiberboard. Figure 2 is the spectrum of the gemstone. The 270 cm^{-1} peak is a plasma line of the 514.5nm green line, and a line from mercury lamps shows at 1127 cm^{-1} . The broad, asymmetrical peak at 601 cm^{-1} identifies cubic ZrO_2 ; the bands at 964, 1025, and 1097 cm^{-1} are fluorescence. Monoclinic ZrO_2 containing yttria (from destabilized tetragonal ZrO_2) also produced the same fluorescence peaks. The fluorescence peaks can be attributed to trace impurities of titanium in the ZrO_2 . The presence of yttria in the crystal lattice shifts the fluorescence peaks to wavelengths different from those of yttria-less ZrO_2 with titanium impurities. We used these fluorescence peaks as markers in the PBF filter debris examinations to differentiate between the yttria-stabilized zirconia fiberboard and the yttria-less oxidized fuel-rod cladding.

Monoclinic, tetragonal, and cubic ZrO_2 were identified in the PBF filter debris samples. One of the particles, identified as tetragonal ZrO_2 , produced the strong, unique fluorescence peaks indicating that it originated from the zirconia fiberboard. Spectra of other

The authors are at EG&G Idaho, Inc., Idaho Falls, ID 83415. Supported by the U.S. Department of Energy under DOE Contract DE-AC07-76ID01570.

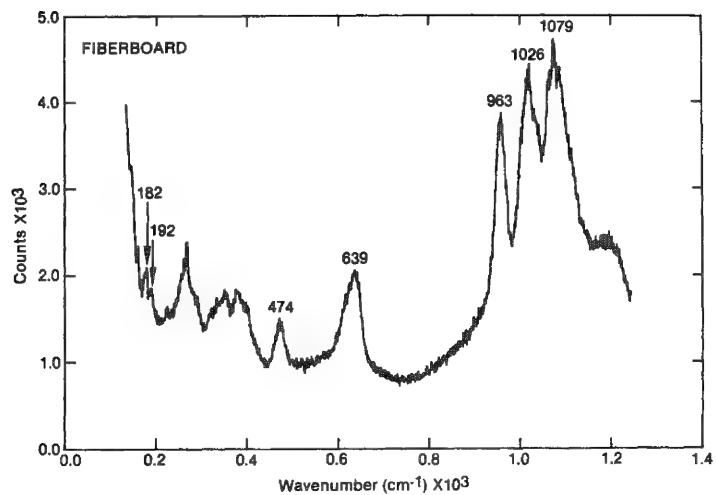


FIG. 1.--Spectrum of ZrO₂ fiberboard particle.

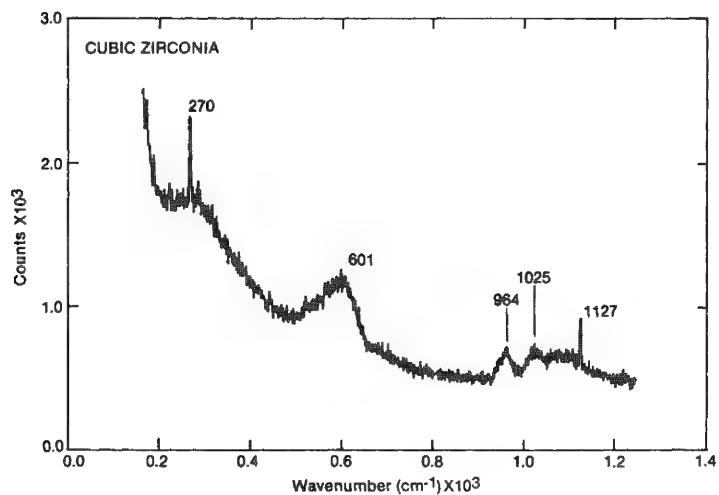


FIG. 2.--Spectrum of cubic ZrO₂ gemstone.

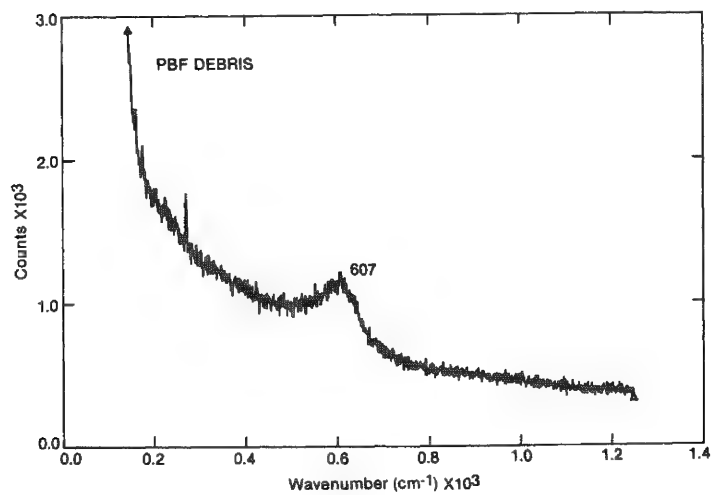


FIG. 3.--Spectrum of cubic ZrO₂ particle from PBF debris.

ZrO₂ particles, however, did not show fluorescence peaks. It is very probable that these particles came from oxidized fuel-rod cladding. Fuel-rod cladding has no titanium impurities. One particle was monoclinic and two other particles were cubic. Figure 3 is the spectrum of a cubic ZrO₂ particle.

Still other ZrO₂ particles, identified as tetragonal and cubic, produced spectra with fluorescence peaks similar to those of the ceramic and gemstone--weak but existing. These particles most likely originated from a third source of ZrO₂ in the PBF fuel assembly, the ZrO₂ spacers and ceramic-coated thermocouples. It seems highly unlikely that the titanium would diffuse or drift out of the ZrO₂ from the zirconia fiberboard. Zirconia fiberboard particles that were fragmented (crushed) and heated to 1000 C showed no reduction in fluorescence. It is possible that yttrium (possibly from fission products) would diffuse or fuse into ZrO₂ from oxidized fuel-rod cladding, but this too is unlikely because of the low fission-product yield of this particular severe-fuel-damage test.

Discussion

The presence of oxidized fuel-rod cladding as cubic ZrO₂ is interesting because cubic ZrO₂ is a high-temperature crystalline form of ZrO₂. ZrO₂ transforms to the cubic phase at 2200 C.¹ The phase transformation is reversible, so the ZrO₂ must be stabilized with an impurity to remain in the cubic form below 2200 C. An explanation that accounts for the cubic ZrO₂ is that oxidized cladding combined with an impurity, probably an oxide, to stabilize the cubic phase. An attempt to identify the impurity oxide by SEM-EDS analysis was not possible.

Cubic ZrO₂ grown on zirconium was detected by Ploc with the use of selected area electron diffraction.^{2,3} The formation of cubic and tetragonal ZrO₂ on zirconium and zircaloy-2 at low temperatures has been attributed to stress at the metal-oxide interface.⁴ The cubic ZrO₂ we observed were free particles not associated with a metal-oxide interface. The particles appeared to be single, translucent crystals, pentagonal and 5 μ m in diameter. If the particles had formed as an oxide film on the zirconium, the compressive stresses induced by the underlying atoms of the metal would have been relieved when the oxide separated. Consequently, the cubic phase would have transformed to the monoclinic. Yet the cubic phase was fully stabilized and not metastable, since all attempts to induce a phase transformation by laser heating failed. Because the cubic phase in ZrO₂ cannot be quenched,⁵ an impurity must be present in the particles to stabilize the ZrO₂. The most probable form of the stabilizing impurity would be an oxide such as CaO or UO₂.

Our interest in ZrO₂ reactions with fission products led us to acquire spectra of CaZrO₃, SrZrO₃, and BaZrO₃. The compounds fluoresced in the same spectral region as yttria-stabilized ZrO₂ ceramics. The zirconates were examined because a stable phase which forms in irradiated UO₂ fuel at high temperatures is (Ba,Sr)ZrO₃.⁶ All three zirconates produced strong, sharp fluorescence peaks in the wavenumber region between 900 and 1400 cm⁻¹. (The 514.5nm green line was the excitation source.) The wavelengths of the peaks are unique for each zirconate species, and for the yttria-stabilized zirconia as well. Table 1 lists the wavenumber assignments of the fluorescence peaks for each species.

The fine-structured fluorescence has been observed in ZrO₂ by Asher et al.⁷ They ascribe the sharp fluorescence features in ZrO₂ spectra to trace impurities of titanium (140 ppm) in the ZrO₂ lattice. The fine structure arises from phonon-mediated de-excitation of excited states. It appears that this phenomenon occurs with CaZrO₃, SrZrO₃, and BaZrO₃, although these species fluoresce more intensely than ZrO₂. Because the frequencies of the fluorescence peaks correspond directly to discrete phonon energies, fluorescence can be used to determine the phonon modes of cubic ZrO₂ and various zirconate compounds. This technique would be especially useful since the Raman spectra of cubic ZrO₂ and many zirconates are weak and yield limited information on the phonon modes.

Although the fluorescence we observed in yttria-stabilized ZrO₂ was not due to rare-earth fluorescence, the subject of rare-earth fluorescence in crystalline lattices may lead to a novel approach in fission-product research with the use of the Raman microprobe. The fluorescence of the lanthanides (Ln) in inorganic crystals may provide a sensitive technique for detecting these fission products. Although fluorescence is a more intense phenomenon than the Raman effect, it will never approach the sensitivity of radioisotope identification with the use of gamma-ray spectroscopy. As an example of the use of this technique, a trace quantity of a fission product which has either diffused or fused into ZrO₂ may produce a characteristic fluorescence signature as observed with titanium in ZrO₂. Schleifer et al.⁶ found that uranium, zirconium, and the rare earths in irradiated UO₂ fuel form a stable

TABLE 1.--Wavenumber assignments of fluorescence peaks in ZrO₂ mixed-oxide compounds.

Compound	Fluorescence Peaks (cm ⁻¹)					
	963	1026	1079	1201		
ZrO ₂ -Y ₂ O ₃						
CaZrO ₃	1037	1076	1092	1132	1253	1309
SrZrO ₃	1013	1046	1061	1090	1208	1255
BaZrO ₃	963	1006	1072	1081	1094	1150
BaZrO ₃ (cont.)	1174	1203	1226	1275		

phase consisting of a UO₂-ZrO₂-Ln₂O₃ solid solution. The solid solution has a cubic fluorite structure and is formed at high temperatures. Microfluorescence would reveal the presence of Ln impurities, and micro-Raman analysis would provide information on the oxide's composition and crystalline structure.

Summary

Microfluorescence has been used to identify the origin of ZrO₂ particles resulting from severe nuclear fuel damage. The ZrO₂ particles found in the PBF filter debris samples have been identified as:

1. particles from the zirconia fiberboard
2. fragments of ZrO₂ spacers and ceramic-coated thermocouples
3. oxidized fuel-rod cladding

The spectra of the cubic ZrO₂ particles without fluorescence peaks strongly suggest the following:

1. The cubic ZrO₂ particles are oxidized fuel-rod cladding.
2. The cubic phase was stabilized with an impurity.
3. The temperature of the ZrO₂ exceeded the ZrO₂-impurity eutectic point.

Investigations of lanthanide fluorescence in ZrO₂ may lead to a novel approach in fission-product chemistry and detection with the use of the Raman microprobe.

References

1. G. M. Wolten, "Diffusionless phase transformations in zirconia and hafnia," *J. Am. Ceram. Soc.* 46: 418-422, 1963.
2. R. A. Ploc, "A transmission electron diffraction study of ZrO₂ on α -Zr (0001), *J. Nucl. Mater.* 110: 59-64, 1982.
3. R. A. Ploc, "The lattice parameter of cubic ZrO₂ formed on zirconium," *J. Nucl. Mater.* 99: 124-128, 1981.
4. C. Roy and G. David, "X-ray diffraction analyses of zirconia films on zirconium and zircaloy-2," *J. Nucl. Mater.* 37: 71-81, 1970.
5. W. A. Lambertson and M. H. Mueller, "Uranium oxide phase equilibrium systems: III. UO₂-ZrO₂," *J. Am. Ceram. Soc.* 36: 365-368, 1953.
6. F. Schleifer et al., "Solid solutions and phase equilibria in (U, Zr, Ln) oxides in the temperature range 1270-1670 K," *J. Nucl. Mater.* 101: 150-161, 1981.
7. I. M. Asher et al., "Laser excited luminescence spectra of zirconia," *J. Phys. Chem. Solids* 37: 221-225, 1976.

PETROLOGICAL APPLICATIONS OF THE RAMAN MICROPROBE (RMP): EXAMPLES OF THE CHARACTERIZATION OF MICRON-SIZED MINERALS IN ECLOGITES

Helgard Boyer and D. C. Smith

Eclogites are high-pressure metamorphic rocks essentially composed of clinopyroxene and garnet without primary plagioclase. Like other metamorphic rocks, they may have experienced more than one period of recrystallization, and hence they often contain reaction products in the form of oriented or non-oriented intergrowths (symplectites, kelyphites) of two or more minerals of which one or more may be a microphase (1 - 50 μm wide). Accurate characterization of such microphases is necessary for a proper interpretation of the mineral reactions concerned and for geothermobarometric estimations of the geological history of the rocks.

Transmission optical microscopy (TOM) may provide several indications of the nature of these microphases, but their small size usually prohibits definitive identification. X-ray diffraction (XRD) of single crystals is impracticable because of their small size, and powder XRD is confronted with problems of mineral separation. Electron diffraction by transmission electron microscopy (TEM) can determine the crystal structure, but it requires time-consuming sample preparation and rare isolated microphases would also require extra careful manipulation. Electron microprobe analysis (EMP) can provide the mineral chemistry, but it cannot (a) distinguish between polymorphs and (b) analyze microphases that lie below the surface of the 30-50 μm -thick polished microprobe slide. Similarly, the ion microprobe (IMP) cannot distinguish between polymorphs and furthermore its analyses below the surface are destructive. The Raman microprobe (RMP) can provide spectra from microphases below the surface and, when compared with a series of standard spectra from larger known minerals, one can characterize the structure and perhaps the chemistry of such microphases.

By identifying crystals difficult or impossible to identify by other means, RMP offers a valuable tool for petrology. Some examples of cases histories and work in progress on diverse eclogites of geodynamical importance are briefly discussed here.

Coesite Relics in Quartz

An eclogite from Grytting, Norway (sample C51 gt), contains a microphase which, from TOM and petrographic observation, seemed to be coesite, the very high pressure polymorph of crystalline SiO_2 (Fig. 1). If true, it would indicate pressures > 30 kbar and would thus have far-reaching implications for the international controversy over the petrogenesis of Norwegian eclogites,^{1,2} and also for the role of effective pressure in metamorphism and in the geodynamics of lithospheric plate collision in general.³ The RMP spectrum of several such microphases (Fig. 2) showed all the characteristic coesite peaks as determined on other known coesites,⁴ and thus definitively confirmed the TOM interpretation. The main peak of coesite is situated at 521 cm^{-1} , i.e., at 55 cm^{-1} higher frequency than the main Raman line of quartz, so that these two forms can be easily distinguished. The superposition of the less intense quartz Raman spectrum on that of coesite visible in Fig. 2 originates from submicron-sized quartz crystallites, not from the surrounding matrix. A detailed discussion of the RMP peaks from natural and synthetic coesites is given by Boyer et al.⁴ It might have been possible to confirm the coesite structure by XRD or by TEM on the largest crystal (45 \times 90 μm), but the nondestructive, convenient, reliable, and relatively rapid nature of the RMP measurements clearly made RMP the superior technique.

Author Boyer is with Instruments SA, Jobin Yvon, 16, rue du Canal, F-91163 Longjumeau Cédex, France; author Smith is at the Laboratoire de Minéralogie, CNRS Lab. - Associé n° LA 286, Muséum National d'Histoire Naturelle, 61, rue Buffon, F-75005 Paris, France.

Quartz Needles in Clinopyroxene

Parallel needles of a mineral $\sim 5 \mu\text{m}$ wide occur uniformly throughout millimetric grains of clinopyroxene in several eclogites in Norway and one in Greenland at Rendeelv (sample 104 406; Fig. 3).⁵ Their few measurable TOM properties are compatible with those of many minerals including quartz and coesite. EMP analyses of needles reaching the surface established the needle composition as pure SiO_2 at Rendeelv and thus lead to the interpretation of exsolution of SiO_2 from a pre-existing nonstoichiometric supersilicic clinopyroxene;^{5,6} however, which polymorph was present remained unknown. RMP spectra of needles below the surface (Fig. 4) yielded strong quartz lines, in particular the main line at 466 cm^{-1} ; no coesite lines; and some superimposed lines from the host clinopyroxene monocrystal (e.g., at 671 cm^{-1}), thus confirming the quartz structure of these needles.

Two Norwegian eclogites from quite different localities at Eide (sample E2) and at Hessdalen (sample C254) present identical textures but because of differences in their local geological environment it was desirable to make sure that these needles really were of quartz, especially since some other thicker needles at Eide were known by EMP analysis to be composed of plagioclase (Smith, unpublished data). RMP spectra (Fig. 5) of needles below the surface at both localities were essentially similar in showing several quartz lines (e.g., 465 and 205 cm^{-1}) and several clinopyroxene lines including the strongest one at 676 cm^{-1} . Figure 5(b) presents two parts of spectra collected between 450 and 530 cm^{-1} with normalized intensities; one of them was recorded from the host clinopyroxene the other from the same needle as in Fig. 5(a). Their comparison clearly attributes the 465 cm^{-1} line to the needle and the 516 cm^{-1} line to the host crystal.

Colored Microphases in Plagioclase

Preliminary data may be mentioned from a brief study of associated green and brown microphases in a symplectite with plagioclase occurring as a reaction corona around kyanite in a partly retrogressed eclogite at Rekvika, Norway (sample D115). The TOM properties of the green microphase, principally isotropism, are compatible with those of an Mg-Al-rich spinel; those few measurable on the brown microphase do not clearly indicate any particular mineral.

Prominent Raman bands of cubic Mg-Al-rich spinel (our reference sample A77 from Hessdalen, Norway) occur at 406 , 622 , and 752 cm^{-1} (Fig. 6a). Several green microphases below the surface in sample D115 yielded quite similar spectra, which thus strongly supports the provisional TOM identification. The RMP spectrum from the brown microphase contain bands at 261 , 530 , and 834 cm^{-1} (Fig. 6b). The latter two bands were also found in a brown microphase in sample 93 bz from another eclogite occurrence at Rekvika, known from TOM and EMP analysis to be the Fe^{2+} equivalent of a Cr-Zn-högbomite, an Al-Mg-Ti oxide chemically similar to the spinel group but different in structure.⁷ It is thus probable that the brown microphase in sample D115 is also a member of the högbomite mineral group. Final determination must await the collection of more detailed RMP spectra, which may be more difficult to obtain since the fine intense Raman lines (e.g., Figs. 2, 4, and 5) are replaced by less intense and broader bands, but this initial work is at least encouraging for further petrological applications.

Conclusions

The rapidity, reliability, convenience, and nondestructive aspects of RMP make this technique superior to those of XRD and TEM for the identification of mineral structures in microphases; furthermore, RMP is the only practicable technique for such determinations in particularly small and rare microphases.

References

1. D. C. Smith, "A tectonic melange of foreign eclogites and ultramafites in the Basal Gneiss Region, West Norway," *Nature* 287: 366-368, 1980.
2. D. C. Smith, "A review of the controversial eclogites in the Caledonides," 1st Int. Eclogite Conf., *Terra Cognita* 2: 304, 1982.
3. D. C. Smith, "Coesite in the Caledonides: Implications for geodynamics" (in preparation).
4. H. Boyer, D. C. Smith, C. Chopin, and B. Lasnier, "Natural and synthetic coesites

determined with a Raman microprobe" (in preparation).

5. D. C. Smith; R. F. Cheeney, "Orientated needles of quartz in clinopyroxene: Evidence for exsolution of SiO_2 from a non-stoichiometric supersilicic 'clinopyroxene'," *26th Int. Geol. Cong.*, Paris, Abstracts 02.3.1: 145, 1980.

6. D. C. Smith, "On the characterization and credibility of supersilicic stoichiometric and subsilicic pyroxenes," *3rd Int. Kimberlite Conf., Terra Cognita 2*: 223, 1982.

7. D. C. Smith, "Remarques cristallographiques et pétrogénétiques sur les minéraux inhabituels dans les éclogites de Liset et Rekvika, Norvège," *10^e Réunion Ann. Sci. Terre*, Bordeaux, 1984.

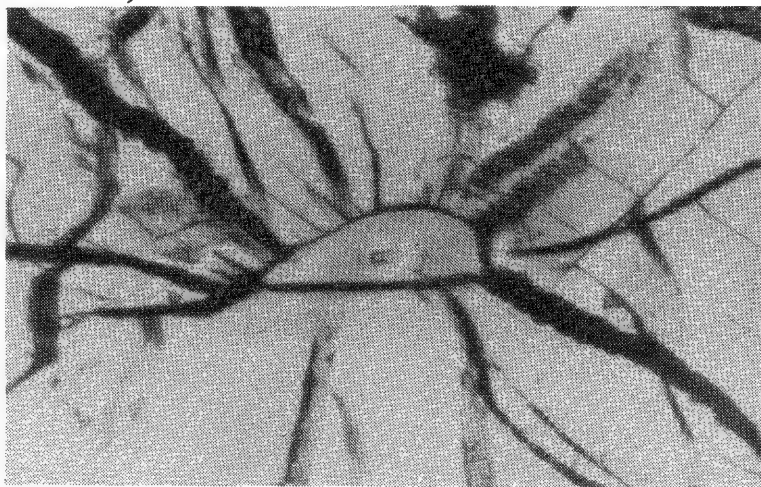


FIG. 1.--Relict 8 μm -wide coesite crystal (No. CS5) in center of 160 μm -long polycrystalline quartz inclusion. Fractures radiating from inclusion are due to volume expansion from transformation of larger crystal into quartz. Sample C51gt, Grytting, Norway.

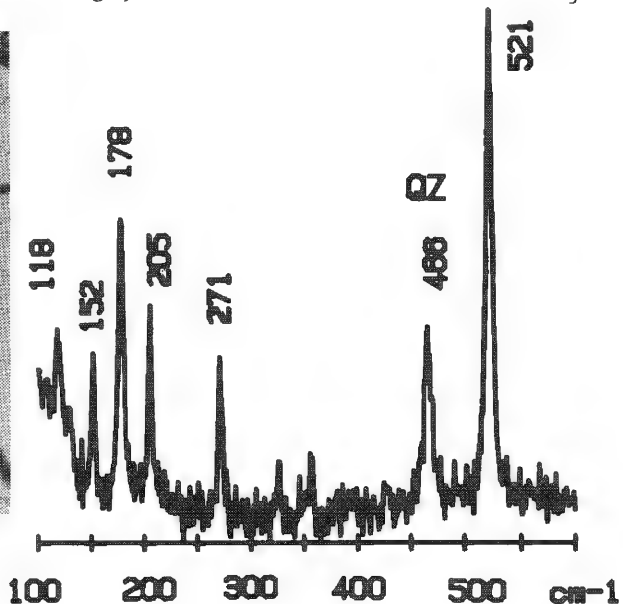


FIG. 2.--Raman microprobe (RMP) spectrum from coesite relict (No. CS3) in sample C51gt showing all essential lines of coesite (main peak, 521 cm^{-1}) and main peak of quartz (QZ) at 466 cm^{-1} .



FIG. 3.--Parallel needles of quartz $\sim 5 \mu\text{m}$ wide and $\sim 200 \mu\text{m}$ long in clinopyroxene host grain. Although needles appear abundant, they occur regularly at all depths into crystal such that very few actually occur in plane of microscope slide surface. Sample 104406, Rendeelv, Greenland.

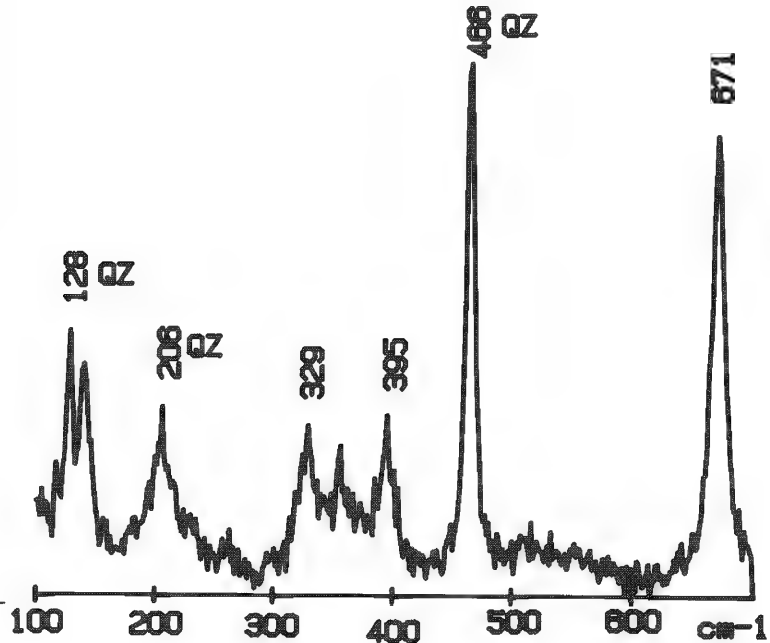


FIG. 4.--RMP spectrum from quartz needle shallowly embedded within clinopyroxene in crystal of Fig. 3

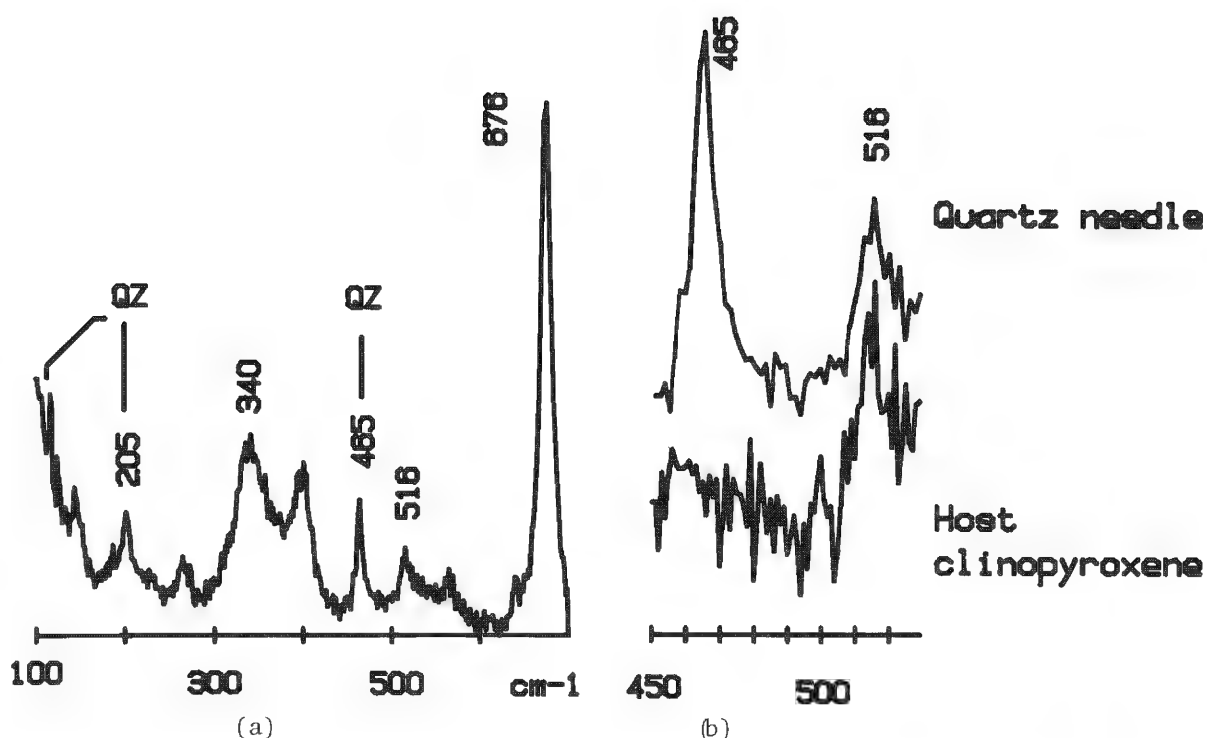


FIG. 5.--(a) RMP spectrum from quartz needle deeply embedded within clinopyroxene, sample E2 Eide, Norway; (b) partial RMP spectra from host clinopyroxene and same quartz needle, showing appearance of main quartz line and of 516cm^{-1} line attributed to clinopyroxene.

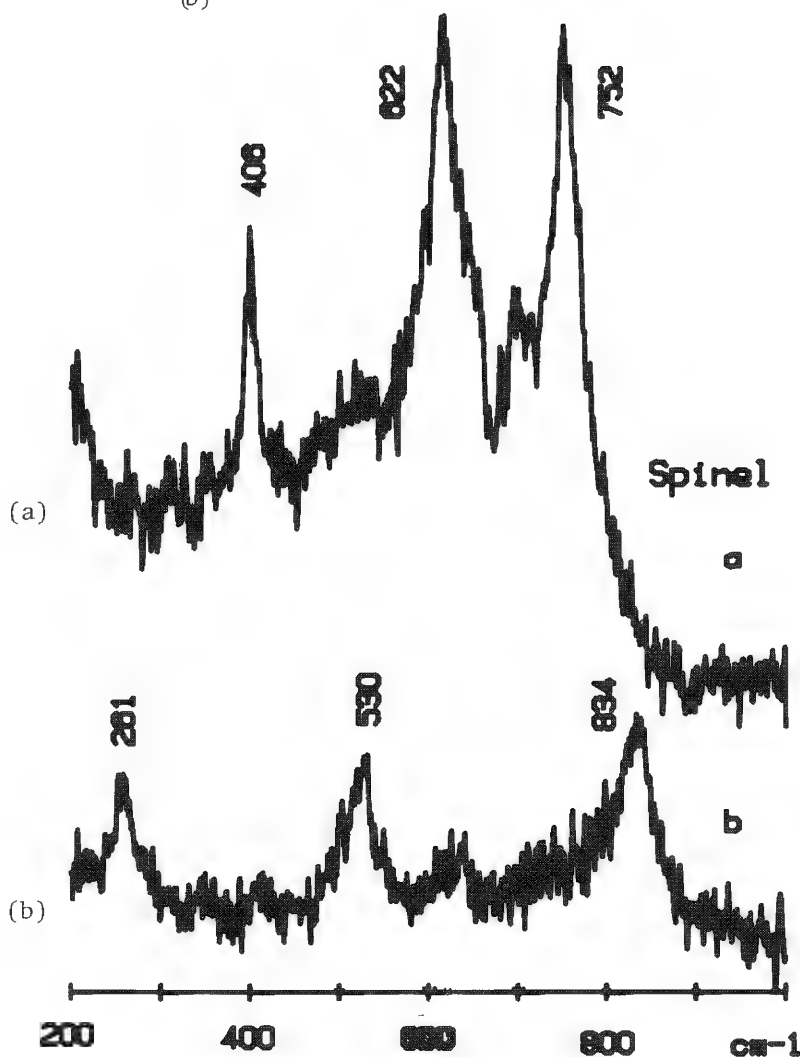


FIG. 6.--(a) RMP spectrum from Mg-Al-rich spinel $[(\text{Mg},\text{Fe})\text{Al}_2\text{O}_4]$ with $\text{Mg}/(\text{Mg} + \text{Fe}^{2+}) = 0.66$ and traces of Fe^{3+} , Cr, Mn, and Ni] in retrogressed garnet-ultrabasic, sample A77, Hessdalen, Norway; (b) RMP spectrum from brown microphase in symplectite with plagioclase, sample D115, Rekvika, Norway.

CHARACTERIZATION OF PHOSPHATE CONVERSION COATINGS BY LASER RAMAN SPECTROSCOPY

A. J. Sommer and Henry Leidheiser Jr.

Phosphate conversion coatings have long been used to enhance the corrosion resistance of metal and metal alloys. Phosphating also increases the surface area of the metal and thus provides a compatible surface for the adhesion of organic polymer coatings. Many proprietary formulations are in use, but the major systems are based on iron phosphate, zinc phosphate, and manganese phosphate. Phosphate coatings are formed as a consequence of the high pH generated at the cathodic sites during superficial corrosion of the metal substrate. The crystallizing phosphate often incorporates metal ions of the substrate metal, so that the composition of the phosphate is complex.

Two problems that face the phosphating industry are (a) the need for phosphate coatings of consistently high quality, and (b) accelerated tests to evaluate these coatings.¹ Phosphating formulations are constantly being modified to accommodate to commercial requirements, which leads to changes in the molecular composition, structure, and corrosion resistance of the product. Phosphate coatings are at present evaluated by a salt spray test that may take up to several hundred hours.¹ There is a growing need for a technique that enables the characterization of coatings produced from new formulations and at the same time yields information concerning the quality of the coating. In this investigation laser Raman spectroscopy with microprobe capabilities has been chosen as a candidate technique for the examination of phosphates on a steel surface.

The instrument is a Raman microprobe recently developed at the University of Lille in France by Delhaye et al.^{2,3} The microprobe incorporates an optical microscope into the source optics of a Raman spectrometer, which results in a spatial resolution on the order of $1\text{ }\mu\text{m}^2$. This feature facilitates the analysis and identification of microcrystallites in the phosphate coatings. Further, Raman spectra of micrometer-sized particles are simply related to spectra obtained for macroscopic single crystals of the same compound.⁴

Experimental

Spectra were recorded on an Instruments S.A. Molecular Optics Laser Examiner Raman Microprobe. A Spectra Physics Model 164 Argon ion laser served as the source for which the 514.5nm excitation line was used. Scattered radiation was collected 180° to the incident with a $100\times$ (0.90 NA) metallurgical objective from Leitz. Detection was accomplished with a Model 126 wide range photometer from Pacific Precision Instruments and an RCA 31034 photomultiplier tube cooled to -30°C , in a Products for Research thermoelectric housing (Model TE-104RF).

Each spectrum presented is the result of co-adding four separate spectra, recorded at different sample locations. Spectra were recorded at the rate of $50\text{ cm}^{-1}/\text{min}$ and a 1s time constant. Spectral slit width was 5 cm^{-1} and the wavenumber accuracy $\pm 2\text{ cm}^{-1}$. The samples were focused so as to give the maximum signal-to-noise ratio with power at the sample less than 40 mW.

Phosphated steel samples were supplied by Parker Surface Treatment Products, a division of Occidental Chemical Corp. Reference mineral samples were obtained from Wards National Scientific Establishment, mounted in epoxy and polished to yield a flat surface.

The authors are at the Department of Chemistry and Center for Surface and Coatings Research, Lehigh University, Bethlehem, PA 18015.

Results and Discussion

Phosphated steel samples were characterized by a comparison of Raman spectra of mineral samples to spectra recorded for phosphated steel. In the case of the iron phosphated samples, only the Raman spectrum of the phosphate coating was recorded. Carbon, a common contaminant on the steel surface, was identified and found to be present in the zinc phosphate coating.

Iron Phosphate System. Iron phosphate coatings are the most economical to produce and offer excellent paint adhesion. The structure of the coating is amorphous and consists mainly of paramagnetic iron(III) compounds.⁵ The Raman spectrum of iron phosphated steel is presented in Fig. 1. The most prominent feature is the band centered around 1025 cm^{-1} shift. This band is located in a region where most phosphates exhibit strong Raman transitions due to the ν_1 symmetric stretching mode of vibration for the PO_4^{3-} tetrahedra. The relative intensity and the breadth of the band are supportive of the amorphous structure. An identical experiment was conducted for a polished steel sample. The resulting spectrum exhibited no band in this region.

Manganese Phosphate System. Manganese phosphate coatings display a very crystalline structure for which the main constituent is hureaulite.⁶ Hureaulite is an acid phosphate of manganese constructed of PO_4 tetrahedra and octahedral units of MnO_6 or FeO_6 . The Raman spectrum for the mineral hureaulite is illustrated in Fig. 2 along with the spectrum of manganese phosphated steel. The most intense peak at 952 cm^{-1} shift can be attributed to the ν_1 symmetric stretching mode of vibration for the PO_4^{3-} tetrahedra. The remaining Raman vibrational transitions give rise to band shifts at 416 and 459 cm^{-1} (ν_2 modes); 533 and 581 cm^{-1} (ν_4 modes); and 1050, 1081, and 1112 cm^{-1} (ν_3 modes). The mode assignments were based on similar assignments for hydroxyapatite.⁷

Zinc Phosphate System. Zinc phosphate coatings are widely used throughout the automotive industry due to their maximum corrosion resistance and excellent paint adhesion. The coatings are characteristic of a two-phase crystalline system comprised of hopeite and phosphophyllite. The relative amount of each phase present depends on the iron concentration in the phosphating solution.⁸ Hopeite is the predominant form at low iron concentrations. More phosphophyllite is included as the iron concentration is increased. The Raman spectra of the minerals phosphophyllite and hopeite are displayed in Figs. 3 and 4, respectively.

Phosphophyllite and hopeite are similarly constructed with PO_4 and ZnO_4 tetrahedra. However, the latter contains $\text{ZnO}_4(\text{H}_2\text{O})_2$ octahedra and the former $\text{FeO}_2(\text{H}_2\text{O})_4$ octahedra.⁹ The strongest Raman transition associated with the ν_3 symmetric stretching mode of vibration for PO_4^{3-} is located at 995 cm^{-1} shift for both minerals. The remaining transitions for which the modes of vibration can be assigned are located at 584 and 596 cm^{-1} (ν_4 modes) for phosphophyllite and hopeite, respectively; 942, 1072, and 1138 cm^{-1} (ν_3 modes) for phosphophyllite; and 940, 1058, and 1148 cm^{-1} for hopeite. In each case the ν_2 mode of vibration was not assigned due to overlapping transitions at low wavenumbers. The transitions at low wavenumbers may be the result of metal-oxygen bonding modes.

The Raman spectrum of zinc phosphated steel is compared to the spectrum of hopeite in Fig. 4. This comparison indicates that, on the average, hopeite is the dominant constituent for this particular sample. All the transitions occurring for phosphated steel correspond to those of hopeite with the exception of two peaks located at 1343 and 1603 cm^{-1} shift. These two signatures were attributed to amorphous carbon. Carbon adversely affects the quality of the phosphate coating,¹⁰⁻¹² since it increases the porosity of the coating, which leads to reduced paint performance. Two sources of carbon have been proposed: (1) decomposed rolling-mill lubricants present on the steel prior to phosphating; or (2) improper rinsing after cleansing, in which case the source may result from reduced surfactants in the cleansing solution. The Raman spectra of carbon, uncleaned Q-panel steel, and zinc phosphated steel are displayed in Fig. 5. The spectra indicate the source of carbon is present on the surface of steel prior to the cleaning step before phosphating. Raman spectroscopy is a useful technique for detecting the presence of carbon on the surface of steel.

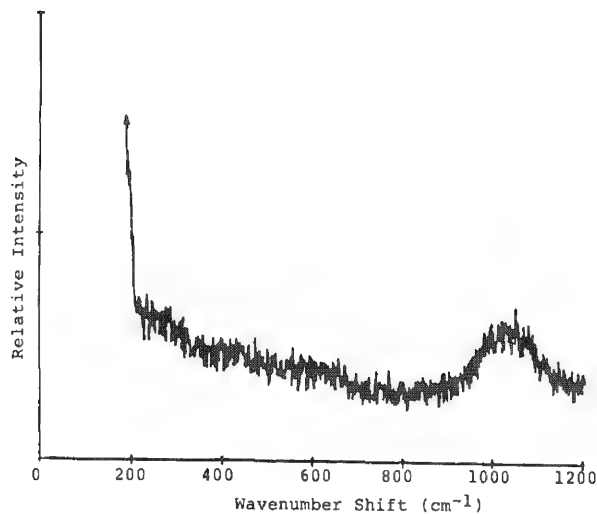


FIG. 1.--Iron phosphated steel.

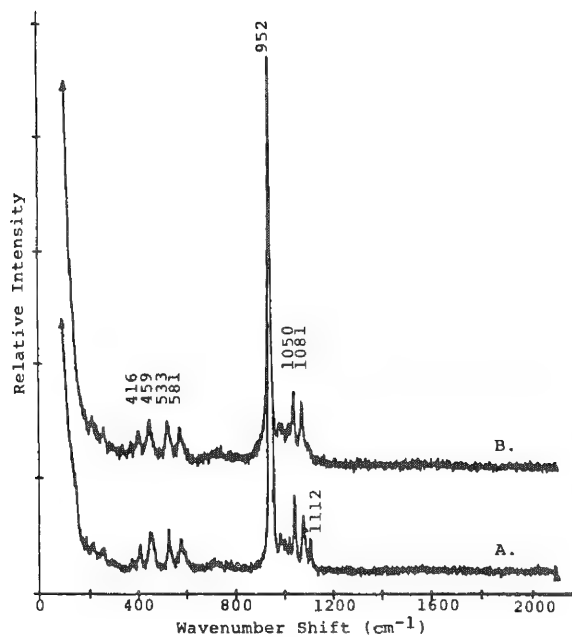


FIG. 2.--Hureaulite (A); zinc phosphated steel (B).

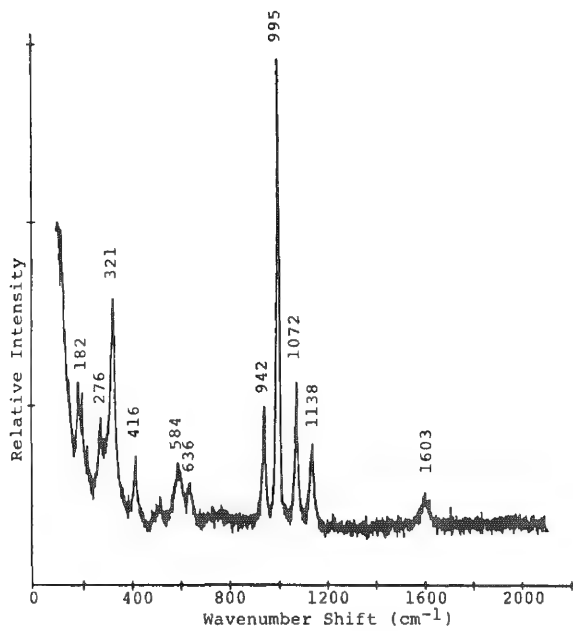


FIG. 3.--Phosphophyllite.

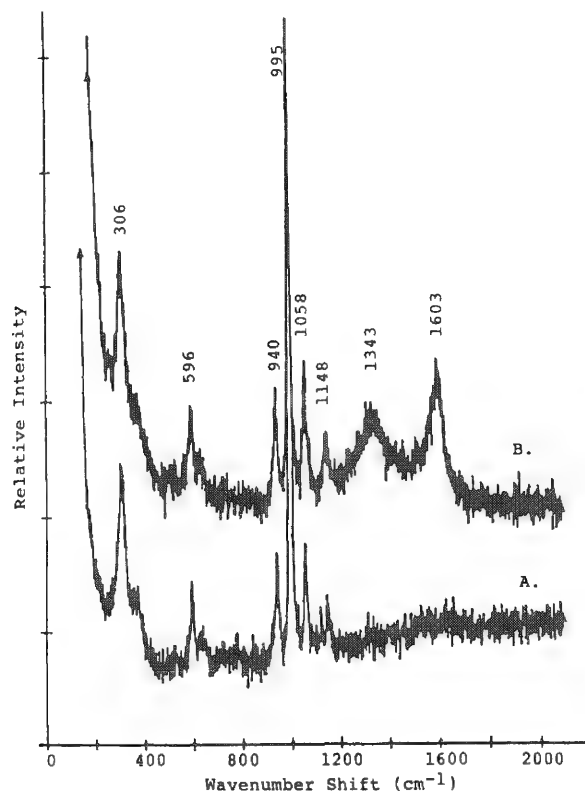


FIG. 4.--Hopeite (A); zinc phosphated steel (B).

Conclusion

Preliminary results presented in this investigation illustrate that laser Raman micro-probe spectroscopy is a very useful tool for the study of phosphated steel surfaces. The technique not only allows characterization of phosphate coatings but also provides information important to the service life of the coatings.

References

1. R. W. Zurilla and V. Hospadaruk, SAE Tech. Paper 780 187, 1978.
2. M. Delhaye and P. Dhamelinourt, *J. Raman Spectrosc.* 3: 33, 1975.
3. P. Dhamelinourt, F. Wallert, M. Lechlerg, A. T. N'Guyen, and D. O. London, *Anal. Chem.* 51: 414A, 1979.
4. G. J. Rosasco, in R. J. H. Clark and R. E. Hester, Eds., *Advances in Infrared and Raman Spectroscopy*, London: Heydon and Sons, 1980, Chap. 4.
5. Y. Ujihira and K. Nomura, *J. Phys.* 41: C1-392, 1980.
6. G. Lorin, *Phosphating of Metals*, Finishing Publications Ltd, 1974, Chap. 4.
7. K. C. Blakeslee and R. A. Condrate, *J. Amer. Cer. Soc.* 54: 559-563, 1971.
8. G. Lorin, *Phosphating of Metals*, Finishing Publications Ltd, 1974, Chap. 4.
9. D. E. C. Corbridge, *The Structural Chemistry of Phosphorus*, New York: Elsevier, 1974.
10. J. A. Karagol and D. L. Jordan, *Corrosion* 38(No. 4): 102, 1982.
11. M. Shigeyoshi, *J. Coatings Technology* 55: 43, 1983.
12. R. A. Iezze and H. Leidheiser Jr., *Corrosion* 37: 28, 1981.
13. R. W. Zurilla and V. Hospadaruk, SAE Tech. Paper 780 187, 1978.

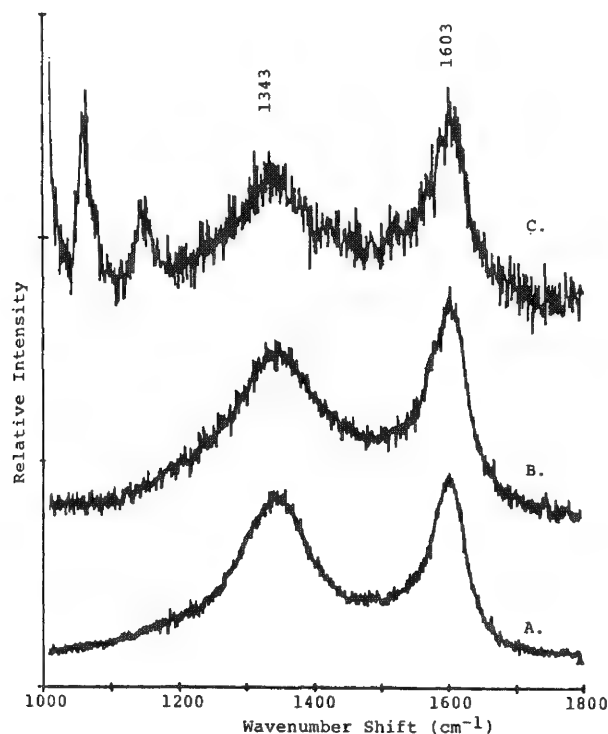


FIG. 5.--Carbon (A); Q-panel steel (B); zinc phosphated steel (C).

INTEGRATING A RAMAN MICROPROBE INTO A GENERAL MICROANALYTICAL PROBLEM-SOLVING SCHEME

M. E. Andersen

The Raman microprobe is a relatively new microbeam instrument that is gradually being incorporated into general microanalysis laboratories. As with all microanalytical tools it occupies a special niche in the analytical environment. For certain types of analyses it is unique in its capabilities; for other sorts it offers information similar to that obtainable with other instruments. The applicability of this or any instrument to a particular problem is determined by a variety of considerations.

Capabilities and Limitations of the Raman Microprobe

What does the Raman microprobe, MOLE, offer to the microanalyst? The instrument uses a small probe diameter approximately 0.5-2 μm in size, depending on the numerical aperture of the objective selected and the wavelength of the laser selected. High numerical apertures yield small probe diameters and large solid angles of collection. This microprobe, when used in conjunction with a spatial filter in the optical path, allows a spatial resolution of the order of about 1 μm .¹ The instrument is designed around a light microscope, which can be configured so that it has polarized light microscopical capabilities. This feature is useful, for example, when birefringent samples are to be imaged. In addition, positioning of a sample on the microscope stage is simple and straightforward. Because it is a standard microscope a wide variety of objectives can be utilized for analysis depending upon sample constraints. (For best results one must match the objective to the instrument.²) For instance, long-working-distance objectives can be utilized for the analysis of inclusions deep within a transparent sample. Low-magnification objectives can be utilized for analyzing large areas of a sample. Immersion objectives can be used for obtaining very high numerical apertures and also for examining samples immersed in a liquid.

Information can be derived for both inorganic and organic samples, whether crystalline or amorphous. Transparent and opaque particles can be examined on both transparent and opaque substrates. The technique is usually inherently nondestructive; samples can often be analyzed with little or no sample preparation. Information about a crystalline phase can be obtained on a micro scale far superior to that available by x-ray diffraction techniques. Inclusions in transparent media can be analyzed whether they are solid, liquid, or vapor. The MOLE, in particular, has a unique imaging capability allowing one to map any Raman or fluorescence emission from a sample on a micro scale. For Raman and optical microanalysis, particles are usually mounted on a glass slide. Particles can be also mounted on sodium chloride or potassium bromide substrates, which are used for infrared analysis without interference, or on beryllium metal, which is widely used in electron microprobe and scanning electron microscope (SEM) applications and thus minimizes the requirements of particle manipulation.

Raman analysis suffers three major limitations: (1) fluorescence or luminescence, (2) laser-induced thermal or photo decomposition, and (3) a limited reference data collection. Fluorescence or luminescence are terms used in the present context to describe the emission of light in the Stokes region of a Raman spectrum. The fluorescence level can sometimes be so great that the weak Raman signal is completely lost in the noise. Often the fluorescence level decays with time down to a value so low that the Raman signal can be detected. One may also attempt to reduce fluorescence by using a different exciting laser line. However, sometimes the fluorescence is so great that no Raman spectrum can be recorded. Laser-induced thermal or photo decomposition may also cause problems with a sample, particularly when a

The author is at W. C. McCrone Associates, Inc., 2820 South Michigan Avenue, Chicago, IL 60616. He thanks John Delly for the optical micrographs, Debbie Palenik for the transmission electron microscopy, Ralph Hinch for x-ray diffraction, and Jim Gerakaris and Chris Bajenski for assistance in preparing this paper.

highly focused laser beam is used in which power levels can approach 1 MW/cm^2 at a sample. These problems can often be overcome by cooling of the particle by immersion in water, reduction of the power density at the sample, or changing of the laser exciting line. The data collections available for x-ray diffraction and infrared spectroscopy are vastly larger than those available for Raman and often, if one is successful in recording a Raman spectrum, the identity of the material can still not be uniquely determined because of a lack of reference materials.

General Approach to Microanalysis of Particles

When many particles are available for analysis, the first step is to characterize the material optically. If more than one optically distinct component is present, one must follow this characterization by a physical separation of the components from each other and from whatever substrate or matrix with which they are associated. Such a separation permits the direct analysis of the sample without spectral contamination from the matrix or substrate. Such particle manipulation techniques have been discussed in detail.³ The separated sample is then mounted for analysis on a noninterfering substrate. Once separated, the primary criterion for selection of an instrument, in addition to the type of information desired, is the size of the particle of interest.

The workhorses in the analytical laboratory are the optical microscope and the electron microprobe/SEM. The optical microscope reveals a wide range of information about a sample: its morphology, crystallinity, color, refractive indices, and (with mechanical tests) the brittleness or plasticity. Microchemical tests such as an iodine starch reaction can also be applied to samples. The electron microprobe/SEM combination yields elemental information as well as information on the distribution of elements within a particular particle and any morphological detailed structure of its surface.

If the sample is determined at this stage to be organic, two pathways are available. If the sample is larger than about $25 \mu\text{m}$, and transparent to infrared radiation (that is, not loaded with inorganic filler materials), it can be analyzed directly by a micro infrared technique. The Raman microprobe is an alternative technique for analysis of particles bigger than $25 \mu\text{m}$, but is in general not preferred because of problems described previously. There is no routine alternative to the Raman microprobe for obtaining molecular information from particles smaller than $25 \mu\text{m}$.

If a sample is inorganic and more information than its elemental composition is required, one may use techniques such as x-ray or electron diffraction. If a particle or a group of particles is about $10 \mu\text{m}$, x-ray diffraction with a micro camera can be used.⁴ For smaller particles, transmission electron microscopy can be employed, with the use of electron diffraction techniques to obtain more information.

An alternative and more rapid technique for inorganic particles of about $10 \mu\text{m}$ or smaller is the Raman microprobe. Here the information available again depends on a set of standard reference spectra. Even if the material is noncrystalline, functional group assignments can often be made based on the Raman spectrum of the amorphous inorganic particle.

Sometimes a problem arises in which only a single particle is available for analysis or in which separation of the particle from a matrix is extremely difficult. Under these circumstances one must be quite careful in arranging the sequence of analytical tools employed so that the analysis will not be destructive and hinder subsequent analyses. Under these circumstances the Raman microprobe is often one of the first tools utilized because other microbeam instruments usually cause damage to the particle. To minimize sample handling, such a particle is usually mounted directly on a beryllium substrate if it appears optically to be inorganic, since the next step is elemental analysis in the electron microprobe/SEM. If it appears optically to be organic, however, such a particle is often mounted on a salt plate for analysis if its size is borderline in terms of the size for infrared analysis. Occasionally, however, this sequence cannot be followed and a particle is submitted for analysis by Raman *after* it has been examined by SEM/EMP. If no destruction of the sample has occurred due to the electron beam the sample can still be analyzed. Any conductive coating applied to a sample such as carbon or gold inhibits analysis of the particle by the Raman microprobe. Carbon films can be removed by low-temperature ashing with an oxygen plasma. With a gold coating the only hope is to flip the particle over and analyze its underside.

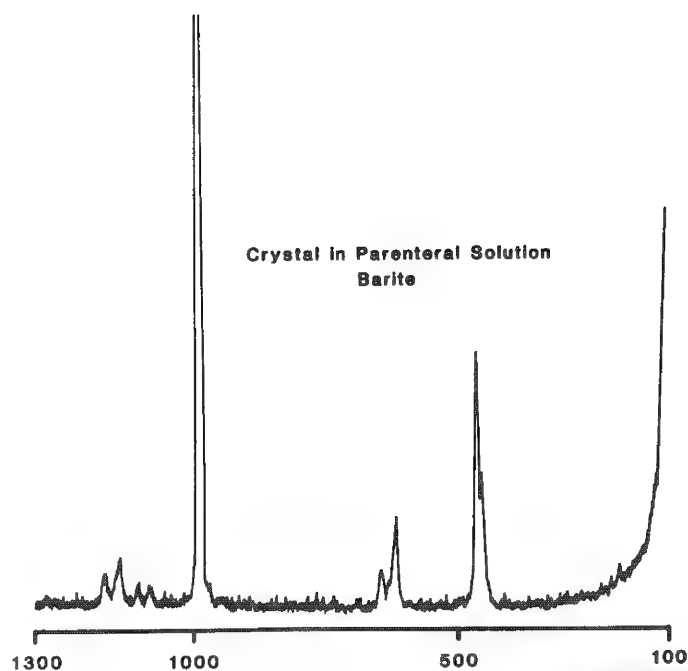


FIG. 1.--Raman spectrum of 15µm crystal removed from filter and mounted on glass slide.

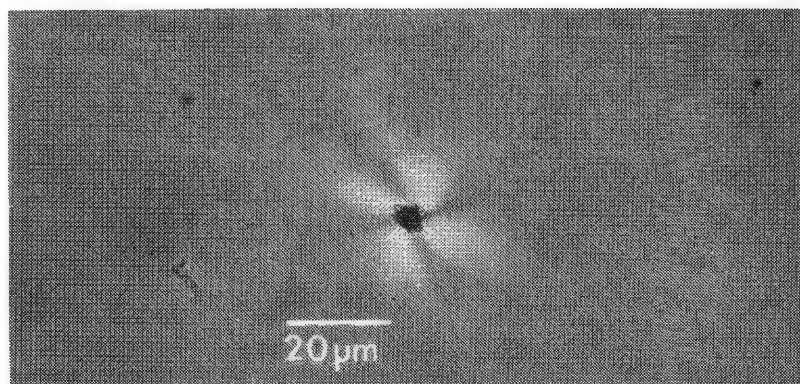


FIG. 2.--Inclusion in polymer film surrounded by strain birefringence.

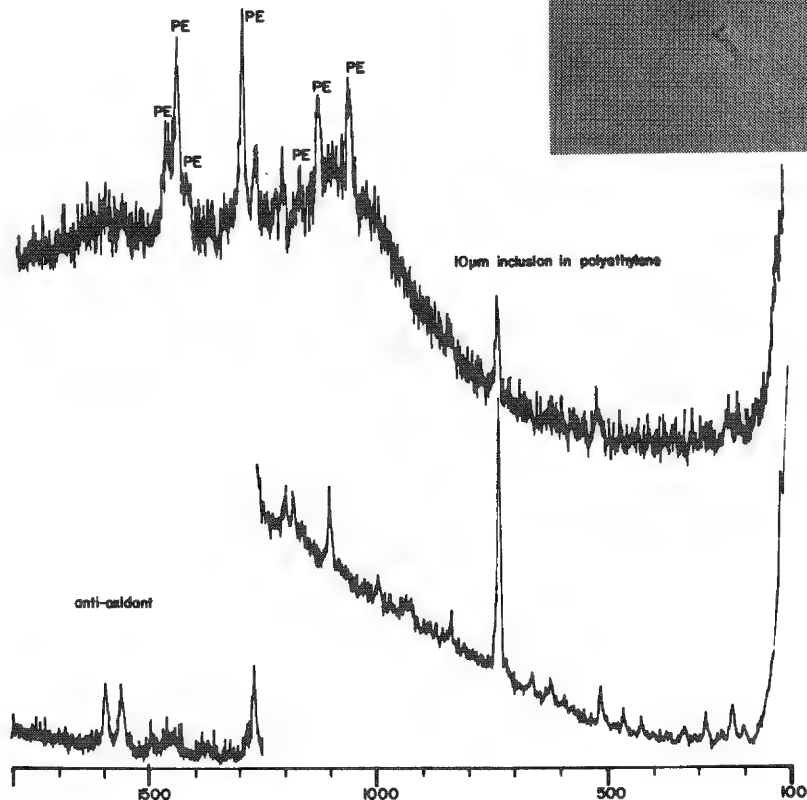


FIG. 3.--Raman spectra of inclusion in polymer film compared with that of anti-oxidant additive.

Case Histories

A few case histories will now be presented to demonstrate the integration of the Raman microprobe with other instruments in a microanalytical laboratory. A parenteral solution was found to contain a very low concentration of 2-20 μ m particles. These particles were filtered and observed microscopically to be highly birefringent and crystalline in appearance. In this circumstance, the particle was examined by the Raman microprobe on the same glass slide used for polarized light microscopical observation. A very strong spectrum was obtained that identified the unknown as barite, barium sulfate (Fig. 1). Here the Raman microprobe was selected because of the speed of the analysis and a lack of a requirement for any sample preparation. The parenteral solution contained bisulfate ions that had probably decomposed to form sulfate. The barium came from the glass vial.

As another example, a polymer was submitted with inclusions that had caused a product failure. The inclusions were readily visible under polarized light (Fig. 2). A region of the polymer containing the inclusion was extracted and examined by electron microprobe, and a low level of sulfur was detected in that region. Analysis of another inclusion by Raman microprobe identified the contaminant as an anti-oxidant that had been added to the polymer but had not dissolved sufficiently (Fig. 3).

Numerous birefringent particles were present in a tissue sample and their identity was desired for a legal case (Fig. 4). Beyond the simple identification of these crystals, an overwhelming volume of additional proof was required such that a jury would be completely convinced of the accuracy of the identification. A dry unstained tissue section was immersed in water for analysis by the Raman microprobe. Water immersion was required because of the highly light-scattering characteristics of the dried tissue. The birefringent particles could then be located and a spectrum was obtained (Fig. 5). The particles were identified as talc. As is the case with all microanalysis, however, only a few particles in a field of hundreds could be reasonably identified. A "bulk" analysis was wanted to determine whether any extraneous materials were present. Because the material was crystalline, a portion of the section was excised and mounted for analysis by x-ray diffraction. The x-ray diffraction pattern matched perfectly the talc pattern recorded in the reference data collection and thus the crystals in the sample were identified as being predominantly talc. In addition, the examination by polarized light microscopy showed that the optical properties of the crystals were identical throughout the section.

Figure 6 is a photomicrograph of an inclusion in glass. This inclusion was bright yellow in color and strongly birefringent. The Raman spectrum (Fig. 7) of the birefringent particles was quite intense but did not match any available references. The particles were extracted from the glass and mounted for analysis by electron microprobe. The spectrum (Fig. 8) indicated the presence of sodium, arsenic, and sulfur in the approximate atomic ratios of 1:1:2. No oxygen or carbon was found in association with these elements. A variety of sodium, arsenic, and sulfur containing compounds is possible and to prove precisely which one was present in the glass required diffraction analysis. Because of the difficulty of sample removal and the small amount of sample available, transmission electron microscopy was performed to obtain the diffraction pattern shown in Fig. 9. This diffraction pattern was matched with the reference x-ray diffraction data pattern of NaAsS₂. The Raman microprobe was then used so as rapidly to confirm the presence of this material in additional samples.

Fluorescence is frequently a problem in the analysis of samples by the Raman microprobe. It can be useful, however, in finding a region of interest. In this way, the Raman microprobe is actually a fluorescence microscope of extraordinary sensitivity. A piece of metal had contaminants on its surface as seen by scanning electron microscopy. However, the surface was quite rough and highly light scattering and the contamination could not be easily located optically. In addition, the defect was practically transparent. However, use of the Raman microprobe as a fluorescence microscope quickly located the area of interest, which was brightly fluorescing (Fig. 10). Fortunately, the fluorescence diminished rapidly during exposure to the laser beam and a Raman spectrum was obtained that identified the contaminant as stearic acid, a mold release agent.

Conclusion

As with all microanalytical tools, the Raman microprobe has unique capabilities in special circumstances. As a general tool, however, it has both strengths and weaknesses. Where

it is weak the evidence gathered can still be useful when used in conjunction with other data obtained with additional microanalytical tools. In this manner its utility is greatly increased.

References

1. M. E. Andersen, "Molecular optical laser examiner (MOLE) application to problems encountered by electron microscopists in the analysis of polymers," in Clara Craver, Ed., *Polymer Characterization, Advances in Chemistry Series 203*, Washington, D. C.: Am. Chem. Soc., 1983, 383-400.
2. P. Dhamelincourt, "Instrumentation and recent application in micro Raman spectroscopy," *Microbeam Analysis--1982*, 261-269.
3. A. S. Teetsov, "Techniques of small particle manipulation," *Microscope* 25: 103, 1977.
4. W. C. McCrone and J. G. Delly, *The Particle Atlas*, Ann Arbor, Mich.: Ann Arbor Science Publishers, 1973, 2d ed., Vol. 1, pp. 119-129.

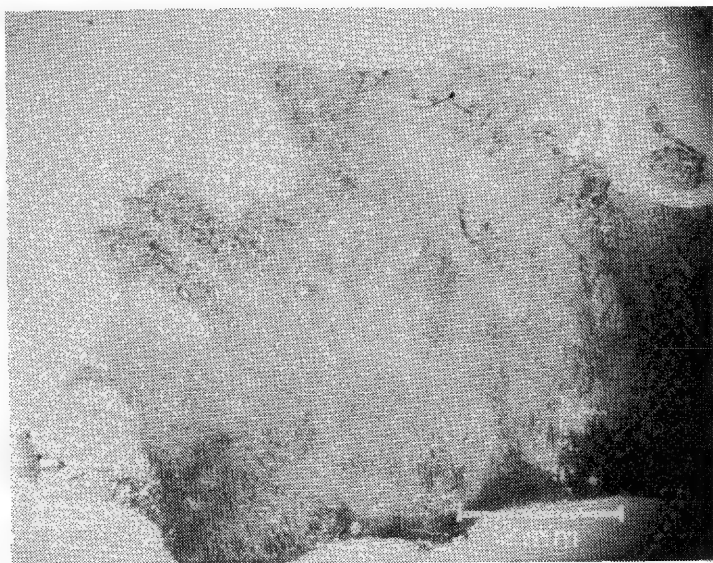


FIG. 4.--Tissue section with birefringent particles.

FIG. 5.--Raman spectrum of 15 μm birefringent talc particle in tissue.

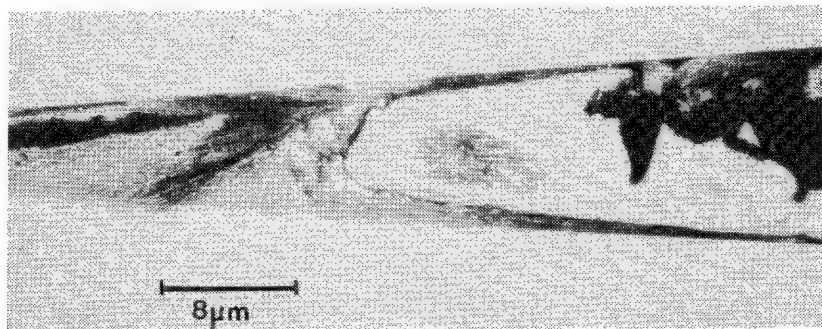
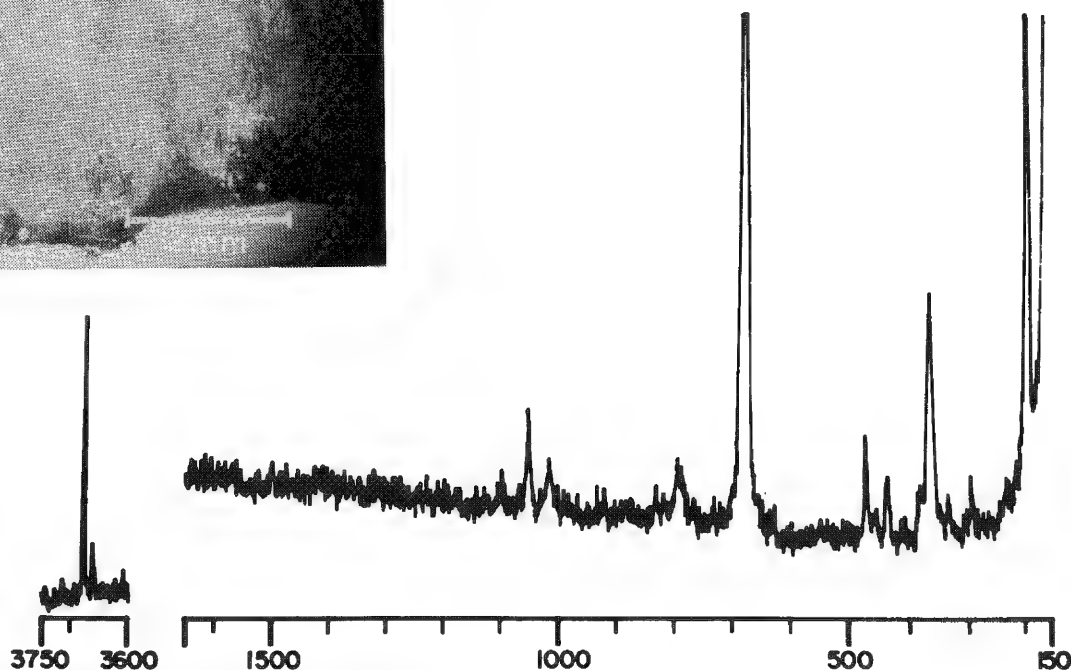


FIG. 6.--Inclusion in glass.

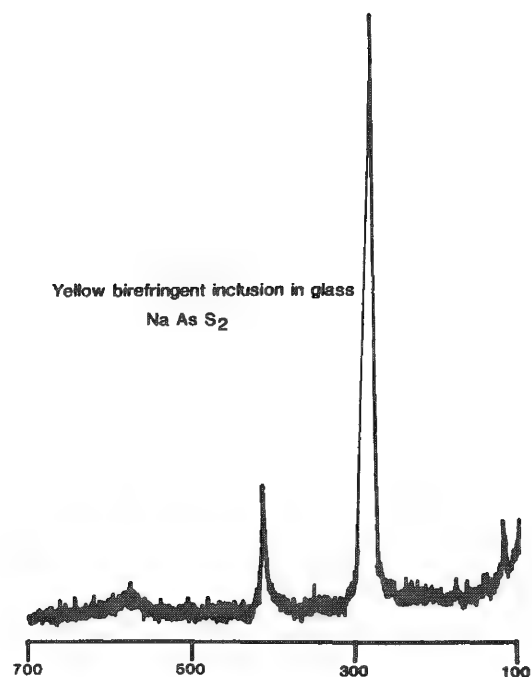


FIG. 7.--Raman spectrum of inclusion in glass.

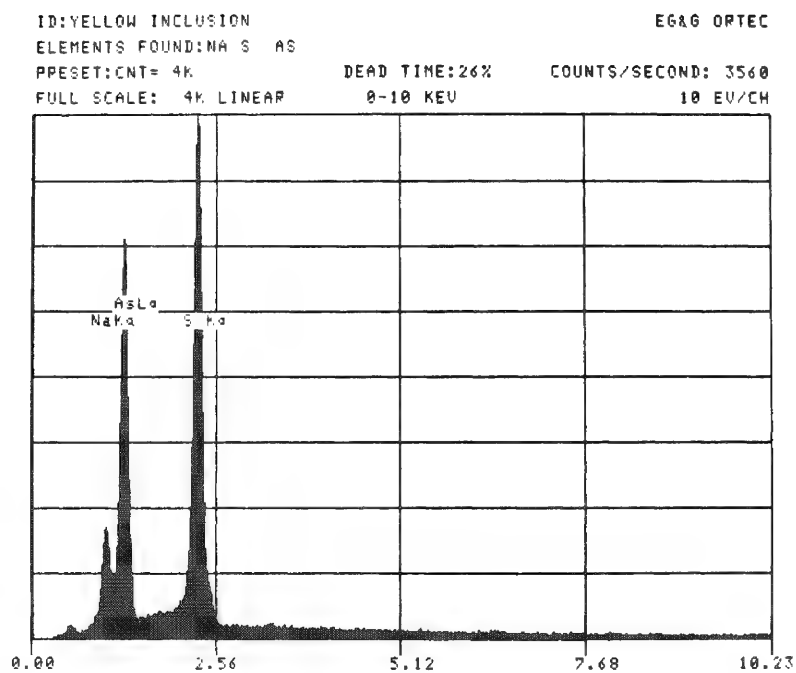


FIG. 8.--EDS spectrum of inclusion extracted from glass.

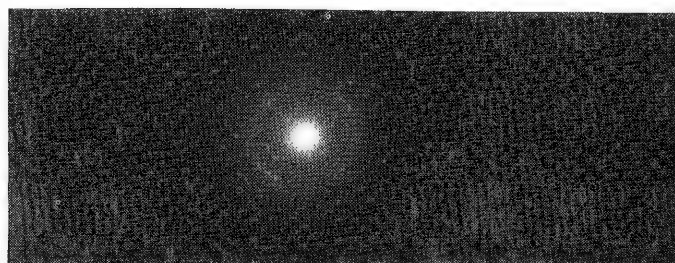


FIG. 9.--Selected Area Electron Diffraction pattern of inclusion extracted from glass.

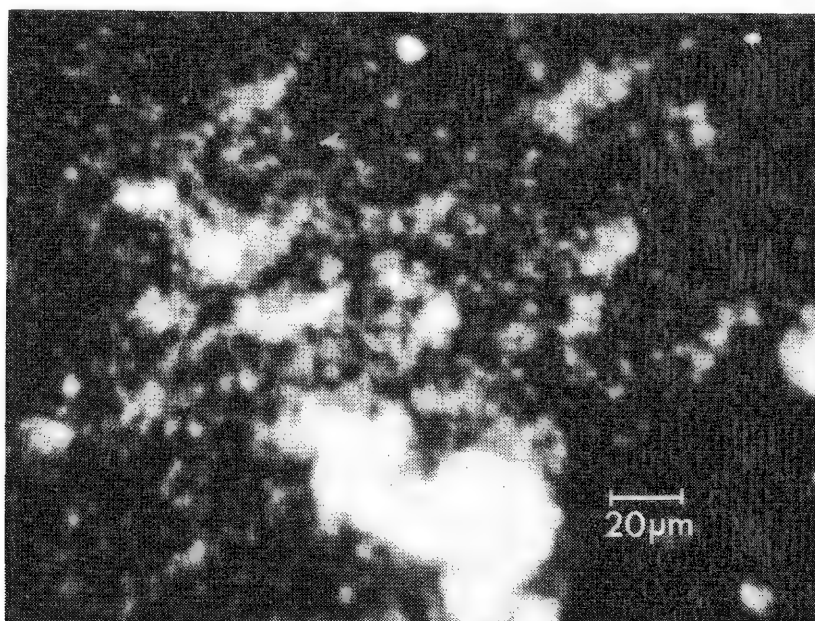


FIG. 10.--MOLE image of fluorescing area of metal.

RAMAN MICROPROBE CHARACTERIZATION OF ZrO_2 INCLUSIONS IN GLASS LIGHTGUIDES

Luis Soto and Fran Adar

The inductively heated zirconia furnace is widely used as a heat source for fiber drawing both in the United States and in Europe. Record lengths of high-strength glass fiber have been achieved by use of the zirconia furnace.¹ The strength of glass fibers depends on the distribution of microscopic defects along a given length. Surface flaws related to zirconia particle inclusions can cause low-strength fiber breaks.² These inclusions are usually 1-10 μm in diameter and can be found embedded on the outer surface of the fiber or just lodged between the fiber and the protective polymer coating. Figure 1 shows a scanning electron micrograph of a fiber fracture surface with a zirconia inclusion. The characterization of these inclusions is complicated because there are two possible sources of zirconia particulate within the furnace: the yttria-stabilized zirconia susceptor and the granular zirconia insulation known as "grog," which surrounds the susceptor. In order to differentiate unambiguously between the two sources, a technique capable of positive identification of some property of both materials is needed. Raman microprobe spectroscopy is such a technique, whereas energy-dispersive x-ray analysis in the SEM is only capable of positive identification of one of the two sources. Monoclinic and tetragonal zirconia have distinct and characteristic Raman spectra.³ The susceptor material is a mixture of the cubic and the tetragonal polymorphs; the grog is composed entirely of monoclinic zirconia. With a Raman microprobe it is possible to measure Raman spectra with high spatial resolution.^{4,5} Clarke and Adar⁶ have shown that the technique is capable of distinguishing between the monoclinic and tetragonal polymorphs of zirconia with a spatial resolution of approximately 1 μm .

Experimental

In this study we examined the fracture surfaces of fibers that failed during proof testing due to the presence of zirconia inclusions. Samples of the susceptor material and of the grog were used for reference. Powders of the reference materials were prepared by grinding with a boron carbide mortar and pestle used to avoid contamination.

Conditions, kept constant in recording all spectra, were: Excitation $\lambda = 487.987 \text{ nm}$; slits, 300 μm ; data points spaced by 1 cm^{-1} . The spectra of the powdered reference materials were recorded with a 50 \times , 0.6 NA objective; laser power = 10 mW at the sample; and counting time of 0.5 s/point. For the spectra of the inclusions a 100 \times , 0.9 NA objective was used; laser power = 10 mW at the sample; and counting times of 1 s/point for the spectrum shown in Fig. 2(c) and 8 s/point for the spectrum shown in Fig. 3(c).

Results and Discussion

Raman spectra of the region 100-300 cm^{-1} of the susceptor, the grog, and a particle inclusion are shown in Fig. 2. The susceptor spectrum shows two bands at 148 and 264 cm^{-1} . As mentioned previously, the susceptor material is mostly cubic zirconia with some fraction of tetragonal phase present. The Raman bands for the cubic polymorph are weak and overlap with tetragonal bands, so that the spectrum of the susceptor looks like a typical spectrum of tetragonal zirconia.

The grog spectrum shows a doublet at 181 and 192 cm^{-1} and weaker bands at 105 and 224 cm^{-1} , typical of monoclinic zirconia. A spectrum from a $2 \times 4 \mu\text{m}$ zirconia inclusion on a glass lightguide also shows the 181-192 cm^{-1} doublet and the band at 224 cm^{-1} . This clearly shows that the inclusion is monoclinic zirconia, which is positive evidence that this

Luis Soto is with AT&T Bell Laboratories, Murray Hill, NJ 07974; Fran Adar is with Instruments SA Inc., Metuchen, NJ 08840

TABLE 1.--Band positions of fluorescence lines observed in grog and inclusion.

Shift (cm ⁻¹)	Wavelength (nm)
1210	518.6
1232	519.2
1265	520.1
1307	521.2
1338	522.1
1395	523.6
1453	525.2
1473	525.8
1491	526.3
1511	526.8
1563	528.3
1710	532.4
1744	533.4
1914	538.3
1940	539.0
1969	539.9
2007	541.0
2052	542.3
2091	543.4
2151	545.2
2203	546.8
2227	547.5
2258	548.4
2279	549.0
2329	550.6
2378	552.0
2449	554.2
2506	556.0
2573	558.1
2606	559.1
2664	560.9
2713	562.4

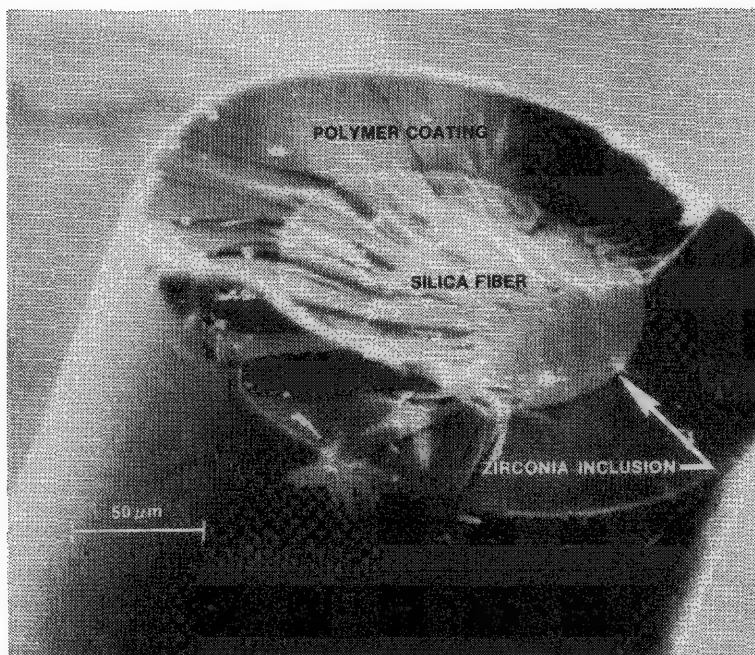


FIG. 1.--SEM micrograph of optical fiber fracture surface showing zirconia inclusion.

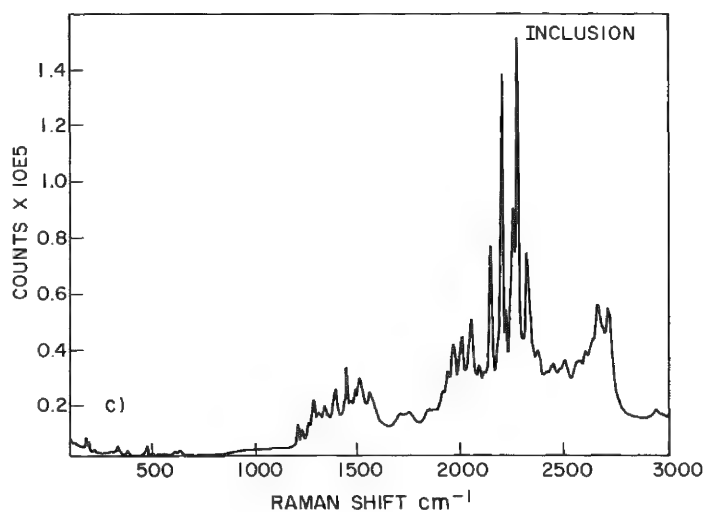
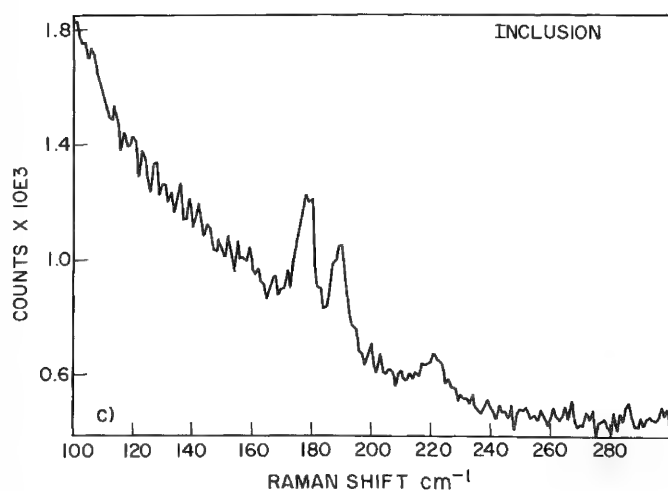
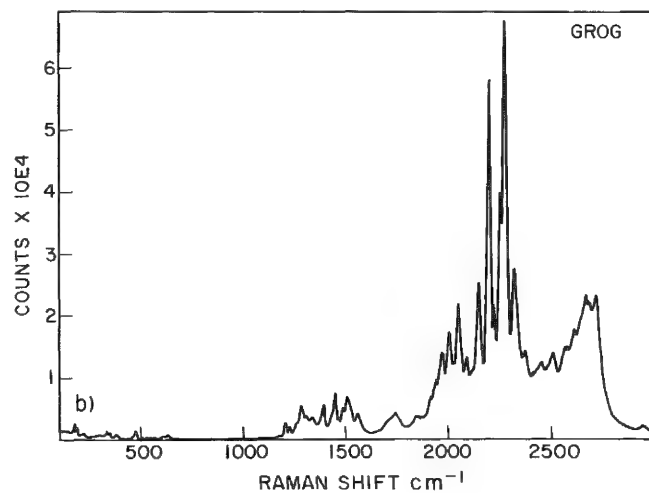
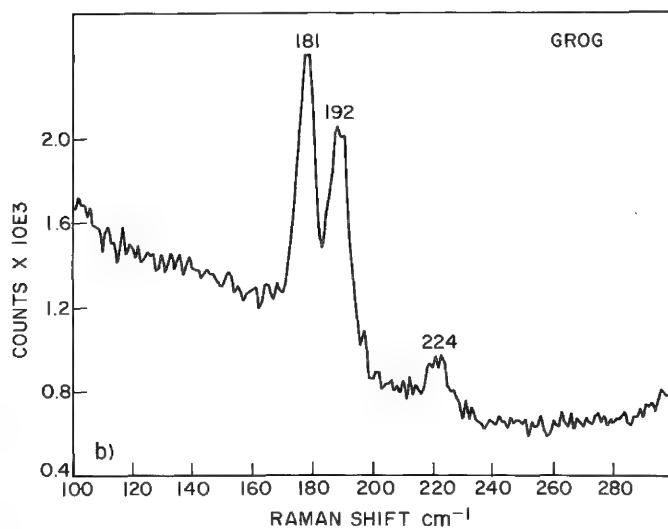
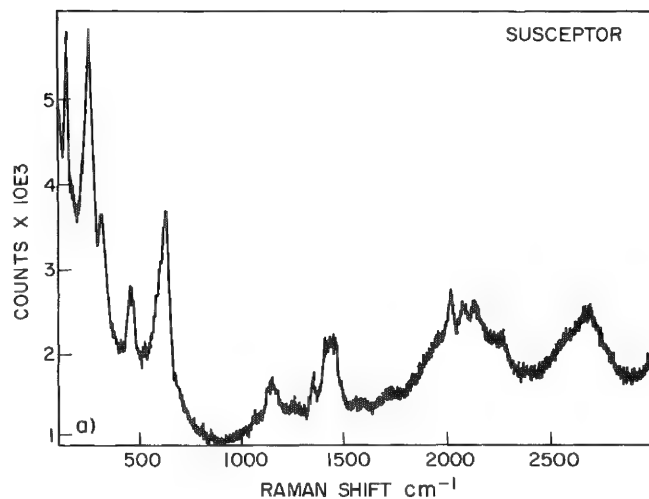
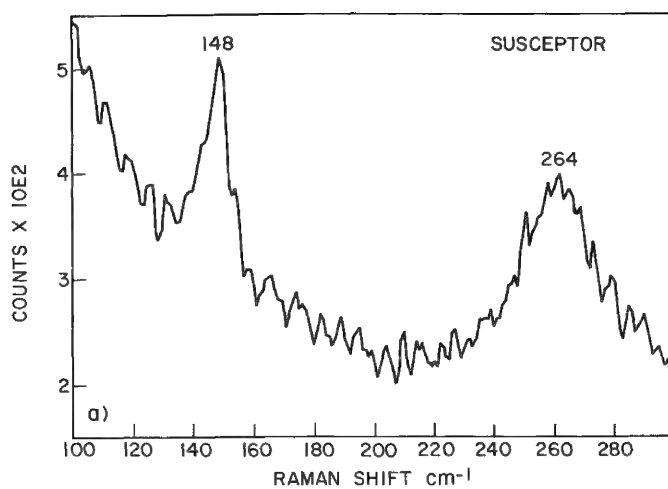


FIG. 2.--Raman spectra between 100 and 300 cm^{-1} : (a) susceptor, (b) grog, (c) inclusion.

FIG. 3.--Raman and fluorescence spectra between 100 and 3000 cm^{-1} : (a) susceptor, (b) grog, (c) inclusion.

particular inclusion came from the grog and not from the susceptor.

Laser-excited fluorescence was also measured in the susceptor material, the grog, and an inclusion. Raman and fluorescence spectra for the region $100\text{--}3000\text{ cm}^{-1}$ are shown in Fig. 3. The spectrum of the susceptor material exhibits broadband fluorescence. The intensities of the Raman and fluorescence bands in the susceptor are of the same order of magnitude. The fluorescence spectra of the grog and the inclusion exhibit intense sharp lines that arise from excitations of rare-earth impurities. The strongest bands are two orders of magnitude more intense than the Raman lines. The inclusion fluorescence spectrum is identical to that of the grog preference.

The position of the fluorescence bands observed in the grog and the particle inclusion are listed in Table 1. All 32 lines were observed in both spectra. D'Silva and Fassel have reported x-ray excited fluorescence spectra of zirconia and uranium oxide.⁷ In both materials they observed an erbium line at 550.7 nm that corresponds to the line that we observed at 550.6 nm. This is the only line that we have been able to identify precisely. Burke and Wood have reported x-ray excited fluorescence of rare earth ions in yttria.⁸ There are four ions that fluoresce in the region 510–560 nm: terbium, erbium, holmium, and europium. These are probably the ions which give rise to the fluorescence bands observed. In comparing the positions of rare-earth ion fluorescence lines in two different materials one must keep in mind that there are shifts in band position caused by crystal field splitting. Porter et al. have studied laser-excited fluorescence spectra of the $7F_0 \rightarrow 5D_0$ transition of Eu^{+3} in eighteen different materials.⁹ The observed band positions vary by $\pm 2\text{ nm}$; therefore, general comparisons of the spectra of rare earth ions in Y_2O_3 and ZrO_2 are valid.

Conclusions

We have shown that the Raman microprobe is an ideal tool for the characterization and differentiation of zirconia inclusions in glass lightguides. Both Raman and fluorescence spectra can be easily obtained on $1\mu\text{m}$ inclusions. The yttria-stabilized zirconia susceptor material contains tetragonal phase, whereas the granular insulation material or grog is entirely made up of monoclinic zirconia. The Raman spectra are distinctly different for the tetragonal and monoclinic polymorphs of zirconia. Furthermore, rare-earth impurities in the grog give rise to characteristic fluorescence lines that can be used to "fingerprint" a particular source of zirconia. On the basis of these two criteria the source of the inclusions can be definitively determined.

References

1. F. V. DiMarcello, C. R. Kurkjian, and J. C. Williams, "Fiber drawing and strength properties," in Tingye Li, Ed., *Advances in Optical Fiber Communications*, New York: Academic Press, 1984.
2. B. K. Tariyal and J. M. Seibert, "Factors affecting low strength breaks: Fractographic analysis," *Appl. Opt.* 21: 1716, 1982.
3. V. G. Keramidas and W. B. White, "Raman scattering study of the crystallization and phase transformation of ZrO_2 ," *J. Am. Ceram. Soc.* 57: 22–24, 1974.
4. M. Delhaye and P. Dhamelincourt, "Raman microprobe and microscope with laser excitation," *J. Raman Spectrosc.* 3: 33–43, 1975.
5. E. S. Etz, "Raman microprobe analysis, principles and applications," *SEM/1979*, 67–82.
6. D. R. Clarke and Fran Adar, "Measurement of the crystallographically transformed zone produced by fracture in ceramics containing tetragonal zirconia," *J. Am. Ceram. Soc.* 65: 284–288, 1982.
7. A. P. D'Silva and V. A. Fassel, "Direct determination of rare earth nuclear poisons in zirconia," *Anal. Chem.* 46: 996–999, 1974.
8. W. E. Burke and D. L. Wood, "Rare earth analysis by x-ray-excited optical fluorescence," *Advan. X-ray Anal.* 11: 204–213, 1968.
9. L. C. Porter, J. R. Akse, M. V. Johnson, and J. C. Wright, "Host materials for laser-excited fluorescence of lanthanide probe ions," *Appl. Spec.* 37: 360–371, 1983.

RAMAN MICROPROBE OPTIMIZATION, AND SAMPLING TECHNIQUE FOR STUDIES OF PLANT CELL WALLS

R. H. Atalla and U. P. Agarwal

The Raman microprobe¹ has made possible in situ studies on plant cell walls in which molecular structure and organization in the native state of woody tissue have been explored.^{2,3} In the course of these explorations some new procedures were developed; they are outlined in this report.

The experimental objectives were acquisition of Raman spectra from microscopic domains in specific morphological features in the cell walls, and observation of changes in the spectra when the polarization of the exciting radiation was rotated relative to the morphological features. The system used is based on an Instruments S.A. Ramanor HG2S equipped with a modified Nachet NS 400 microscope.

Two types of procedural development are described. The first is concerned with optimization of the microprobe system and analysis of polarization effects. The second concerns sample preparation.

Instrument Optimization

Three factors were integrated in optimization of the Raman microprobe system. The first was based on the realization that dichroism in the optics of the microprobe and the monochromator could confound the analysis of spectrum variation as the polarization of incident light was altered relative to the morphological features. The decision was therefore made to keep the plane of incident polarization stationary with respect to the optical system. Rotation of polarization relative to morphological features was accomplished instead by installation of a rotating stage on the microprobe, and rotation of the samples about the optical axis.

The second modification grew out of the observation that the dichroism of the microprobe favored a polarization that is least efficiently transmitted by the monochromator. This problem was dealt with by the installation of a polarization scrambler along the optical axis of the microprobe. A significant increase in throughput was observed after installation of the scrambler.

The third factor was a procedural one for alignment of the overall system. The usual procedures for aligning such systems involve mounting a helium neon laser in place of the photomultiplier tube and aligning the components so as to maintain the beam along the optical axis of the system. To complete the alignment we mounted a micrometer slide above a front surface mirror on the stage of the microprobe, illuminating with the laser exciting line, and following the image of the micrometer through the several optical components in the microprobe and the monochromator. At each stage the components were aligned to obtain a centered image. Upon completion of the process, an image of the micrometer slide could be observed in the plane of the photocathode of the photomultiplier tube. Upon conclusion of this procedure we observed significant improvement in the quality of the signals.

Sample Preparation and Mounting

In the preliminary studies the samples sectioned to approximately 20-30 μ m thickness were extracted and washed, then dried in air and mounted on slides. The Raman spectra recorded from such samples showed weak Raman peaks superimposed on a strong fluorescent background (Fig. 1a). The cell walls frequently decomposed at higher laser powers. In an attempt to

The authors are at The Institute of Paper Chemistry, Appleton, WI 54912. This work was supported by the Biological Energy Research Program of the Department of Energy under Contract DE-AC02-82ER/2056.

obtain better quality spectra, wet mounting of the samples was tested.

In the wet-mounting procedure the samples were placed on a slide, covered with water, and sandwiched with a glass cover slip. A thin layer of silicone grease was deposited around the cover slip to prevent water evaporation. In this procedure the sample could withstand higher power levels of the incident laser light and the background fluorescence was significantly reduced. In addition, in some instances H_2O was replaced with D_2O as the immersion medium in order to avoid overlap between the OH stretching bands and the CH stretching bands. However, the presence of the cover slips resulted in additional broad spectral features that could easily be assigned to the silicates in the glass (Fig. 1b). Use of quartz cover slips instead of the glass ones improved the situation only marginally. The spectra of the cover slips might have been accounted for by subtraction, except that the relative intensities of the features varied from cover slip to cover slip, and sometimes from point to point within the same cover slip. This finding is not inconsistent with minor variation in the composition of the glass.

In order to avoid the contributions of the spectra of the cover slips, a new procedure was developed based on drilling small holes in the center of the cover slips, immersing in water or D_2O , and using a liquid immersion objective. With the help of adhesive, a flat-base Pyrex glass beaker was fixed to a slide in a manner that allowed transmitted light to pass through. On the inner side of the bottom yet another portion of a glass slide was attached. The wet sample was sandwiched as before, between the cover slip and the slide portion so that the cover slip held the sample immobile on the slide portion. D_2O was slowly added into the beaker until complete immersion of the sample took place. The beaker was then mounted on the stage of the microprobe, and the water immersion objective lowered into the D_2O . In order to avoid evaporation of the D_2O , or exchange with atmospheric moisture, a thin layer of mineral oil was placed on the surface of the D_2O , after the objective was submerged in the medium. This procedure has resulted in acquisition of the best spectra obtained so far from native woody tissue (Fig. 1c).

Immersion in D_2O accomplishes a number of objectives. In addition to providing a heat sink to dissipate energy absorbed by the sample, the D_2O appears to quench the fluorescence of the native samples. Clearly it prevents dehydration of the samples, and it provides assurance that any spectral features observed in the OH stretching region are primarily associated with the woody tissue rather than absorbed H_2O .

References

1. G. J. Rosasco, R. J. H. Clark, and R. E. Hester, Eds., *Advances in Infrared and Raman Spectroscopy*, London: Heyden and Sons, 1980. vol. 7, chapter 4.
2. R. H. Atalla, DOE Report DOE/ER/12056-1.
3. U. P. Agarwal and R. H. Atalla, to be published.

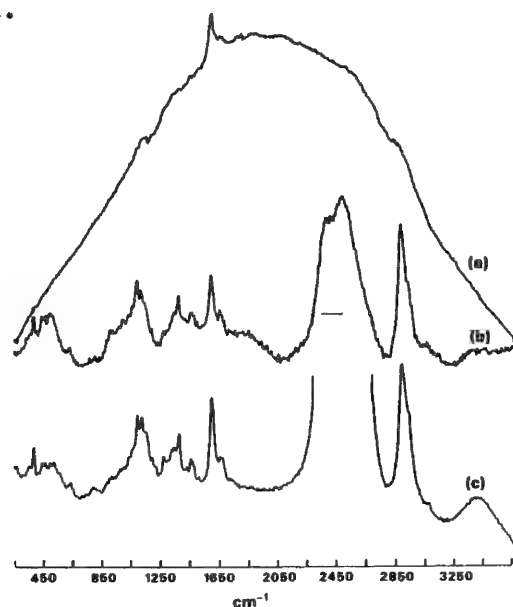


FIG. 1.--Polarized Raman spectra of plant cell wall cross sections, electric vector parallel to the plane of the cell wall: (a) air-dried sample; (b) wet sample sandwiched between glass slide and cover slip; (c) D_2O -immersed sample (cover slip with a 'hole' used and D_2O peak truncated).

Failure Analysis in Polymers, Ceramics, and Composites

MICROSTRUCTURAL ANALYSIS OF CREEP FAILURE IN Si_3N_4 AND SiC

N. J. Tighe

Advanced ceramics such as silicon nitride and silicon carbide are being used in high-temperature, high-stress heat-engine applications where catastrophic failure must be avoided. It is necessary to develop the required design parameters and to predict lifetimes for these materials. Therefore extensive fracture mechanics studies are being carried out and the failure mechanisms are being identified in terms of the appropriate thermal and mechanical stress environments.^{1,2} Identification of the microstructural elements that cause failure is being carried out by analytical scanning transmission electron microscopy (STEM). Silicon carbide and silicon nitride fail by mechanisms that involve crack propagation from pre-existing flaws or from flaws that develop during the exposure to a simulated service environment. The pre-existing flaw population consists of inclusions, pores, and surface preparation damage; the flaw population that develops during exposure includes cavities, oxidation pits, microcracks, and reaction products from bonding phases and inclusions. Silicon nitride and silicon carbide are compounds of several crystalline and amorphous phases and the identification of the microstructural elements that relate to the failure mechanisms requires considerable structural and chemical analysis. Examination of fracture interfaces by light microscopy and by scanning electron microscopy can locate the fracture initiation site and show the path of the crack across the interface. In order to identify the specific flaw population that is responsible for the failure, the higher resolution analytical capabilities of the STEM are used to examine the test specimens. The effectiveness of the STEM techniques for failure analysis is demonstrated with examples from recent fracture mechanics test programs.

Experimental

The microstructural elements that affect failure during long-term exposure experiments on silicon nitride and silicon carbide are: (a) amorphous or crystalline bonding phases, (b) inclusions and pores within grains and at triple junctions, and (c) cracks and defects introduced by surface grinding. Static load experiments were done with four-point bend bars at temperatures up to 1500 C for times up to 1000 h. Specimens fail by premature fracture as a result of crack growth or by excessive bending as a result of creep. The experiments were used to develop reliability maps that show the stress-time evolution of strength. Specimens were broken at temperature during the course of the experiments in order to obtain strength distributions at specific time intervals for the reliability assessment. The microstructural elements that were related to strength changes and to failures were identified from specimens selected from specific regions of the reliability maps.

Specimens for the STEM examination were prepared by slicing of sections from cross sections and from tensile and compressive sides of the test bars with a diamond saw. The sections were ground to approximately 100 μm -thick slices, and 3mm disks were cut and ion thinned to electron transparency. The ion thinning was carried out from one or both sides, depending on the information required from the specimen. The relatively thick slices were used in order to eliminate confusion between damage associated with specimen preparation and damage associated with the deformation from the static load tests. The oxide scale was removed from the tensile and compressive surfaces by careful polishing or by ion sputtering. Silicon nitride foils were coated with carbon to prevent charging but the coating was not needed on

The author is at the National Bureau of Standards, Washington, DC 20234. The work was supported in part by the U.S. Air Force Office of Scientific Research and by the U.S. Army Materials and Mechanics Research Center under contract DOE-1A-DE-A101-77-CS5-1017.

silicon carbide foils. The micrographs in Fig. 1 are examples of crack growth information that was obtained from surface and subsurface examination. The specimen is a hot pressed silicon nitride that showed creep cracking at 1400 C. The conventional TEM³ showed extensive grain boundary separation and oxide along grain boundary interfaces that is characteristic of grain boundary sliding mechanism of creep. Examination of the surface with secondary electrons in an STEM showed the path of primary crack from the thinned region to edge of the disk and the arrays of smaller cracks and cavities associated with creep. The amorphous phase softened at the test temperature and was pulled across the crack from between the grain boundaries as the specimen bent. The tungsten inclusions contained in the specimen were identified and then associated with cavities and surface pits by imaging with the back-scattered electrons. The amorphous phase was shown to be a magnesium silicate glass⁴ by element analysis with the use of EDS and EELS and diffraction analysis. Such a comprehensive analysis of a single specimen demonstrates the approach used for failure analysis.

The micrographs in Fig. 2 are examples of the identification of the nucleation and growth of cavities during creep of yttria-doped silicon nitride.⁵ This ceramic has a crystalline yttrium silicate bonding phase rather than an amorphous phase as in the previous example. The extent of the cavitation decreased with distance from the tensile surface to the neutral axis and these changes were revealed when serial sections were made. The progression in Fig. 2 shows the extensive grain-boundary cracks at the tensile surface, the nucleation and growth stage a few micrometers below the tensile surface, and the initial diffusion growth of the yttria phase into a crack-like configuration. Diffraction analysis shows the changing yttria phase.

The flaw population responsible for the changes in strength and failures in alpha silicon carbide and static load experiments is identified in the examples shown in Fig. 3. The as-sintered silicon carbide was found to have graphitic inclusions at triple junctions and within grains. These graphitic inclusions had a fibrous texture from which elliptical diffraction patterns could be formed. The inclusions were well bonded to the silicon carbide grains and had an amorphous background with Si and Ca present. The carbon was identified by EELS. There was considerable microcracking near grain boundaries and along faults in the silicon carbide. Boron was found by small-angle neutron scattering (SANS) and by EELS analysis. The microcracks were not found in annealed samples. In samples from the static load experiments the microscopy analysis showed that the graphitic inclusions caused several reactions. At the surface, they oxidized and produced cavities. Below the tensile surface they interacted with the stress field around them and caused cracks within grains and some dislocation activity. The presence of the graphitic inclusions in the alpha silicon carbide had not been anticipated or identified from regular SEM analysis. The complete analytical capabilities of the STEM were required to identify the inclusions and to indicate their role in the strength degradation and failure process.

Conclusions

The results of the STEM analysis of silicon nitride and silicon carbide provided the information on failure mechanisms that was required to predict lifetimes from fracture mechanics tests carried out in high-temperature, high-stress conditions.

References

1. N. J. Tighe and S. M. Wiederhorn, "Effects of oxidation on the reliability of silicon nitride," in R. C. Bradt et al., Eds., *Fracture Mechanics of Ceramics*, New York: Plenum, 1983, 403-423.
2. S. M. Wiederhorn and N. J. Tighe, "Structural reliability of yttria-doped hot-pressed silicon nitride at elevated temperatures," *J. Amer. Ceram. Soc.* 66: 884-889, 1983.
3. N. J. Tighe, "The structure of slow-crack interfaces in silicon nitride," *J. Mat. Sci.* 13: 1781-1786, 1978.
4. D. R. Clarke, "Grain boundary phases in a hot-pressed MgO fluxed silicon nitride," *J. Amer. Ceram. Soc.* 60: 491-495, 1977.
5. N. J. Tighe, S. M. Wiederhorn, T.-J. Chuang, and C. L. McDaniel, "Creep cavitation and crack growth in silicon nitride," in R. Tressler, Ed., *Plastic Deformation of Ceramics*, in press.

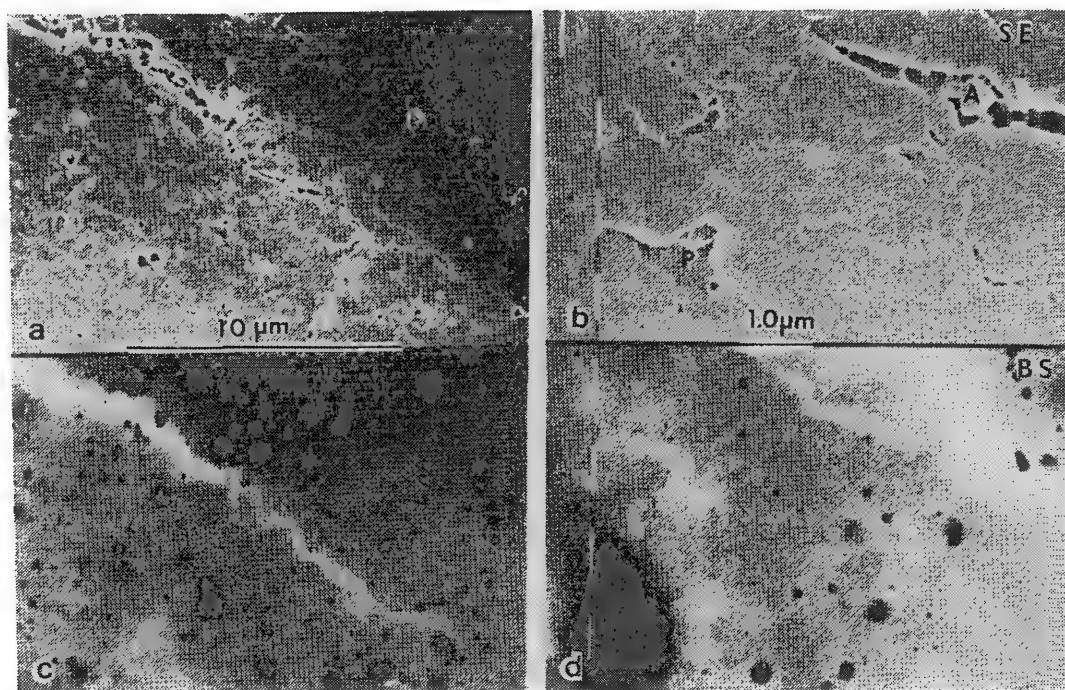


FIG. 1.--Microstructural characteristics of creep in specimen tested at 1400 C in air: (a) and (b) secondary-electron images of primary crack; (c) backscattered electron image of tungsten and iron based particles as dark images.

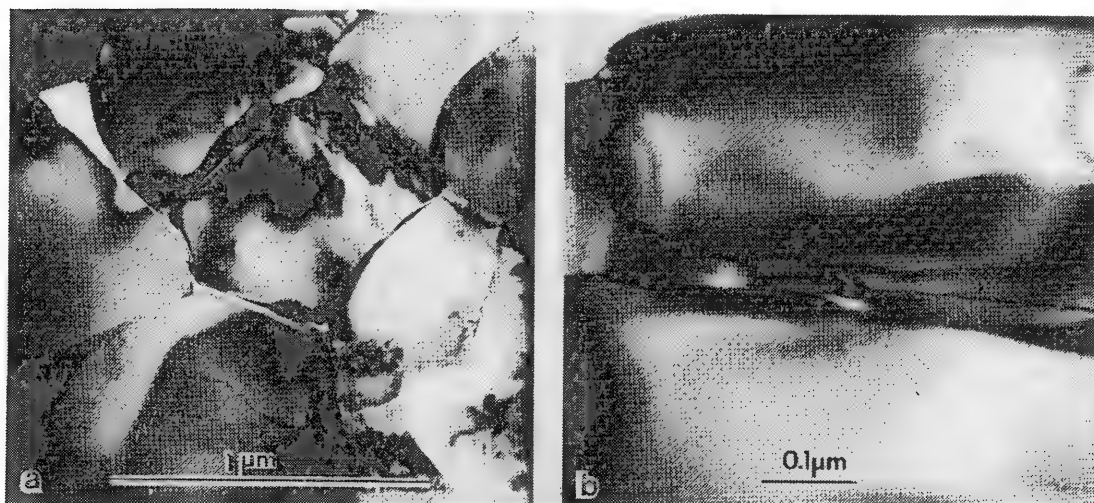


FIG. 2.--Microstructural characteristics of creep cavitation in yttria-doped silicon nitride after 117 h at 1300 C with 350 MPa load: (a) cavitation along grain boundaries approximately 5 μm beneath tensile surface; (b) crack-like diffusional zone and grain boundary crack approximately 30 μm beneath tensile surface.

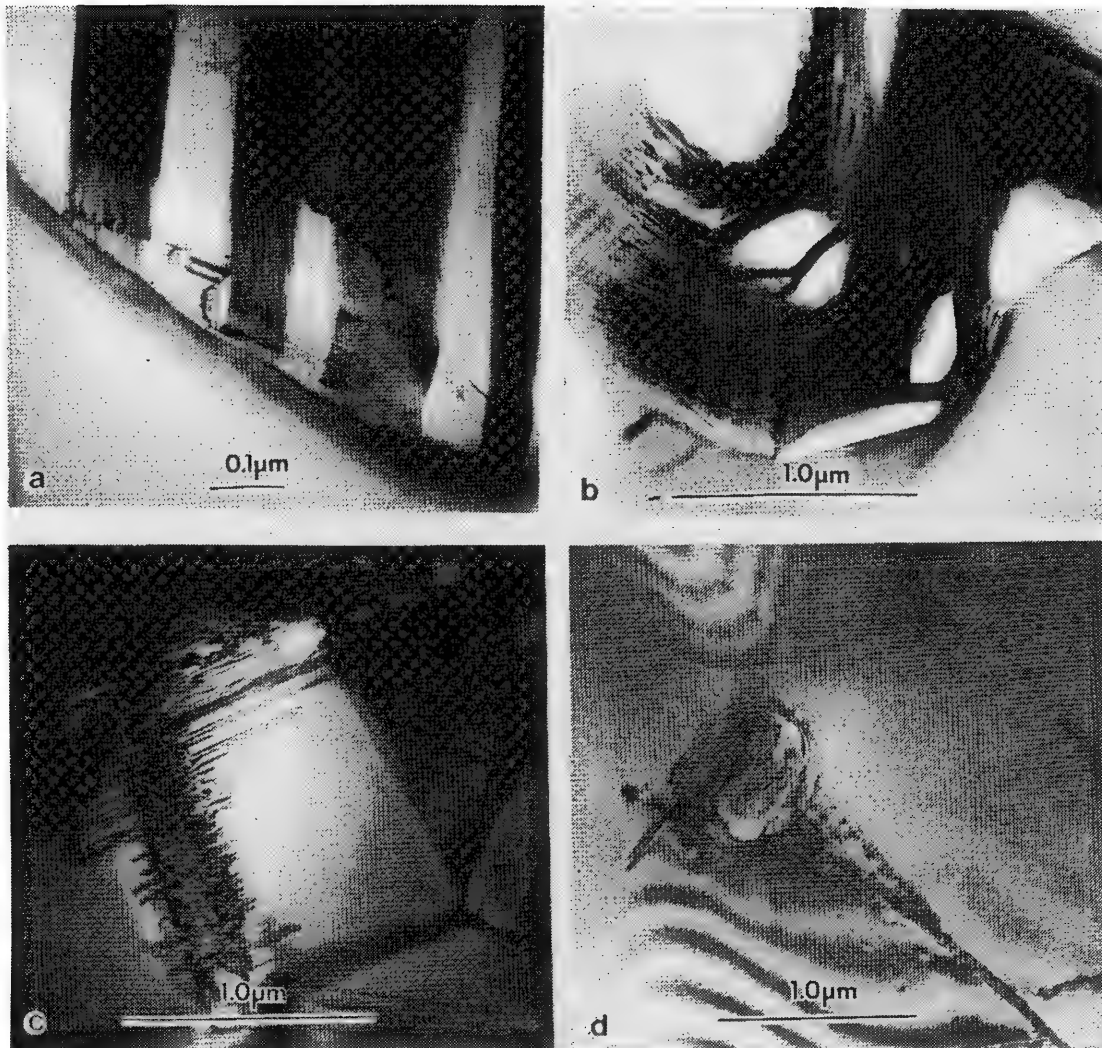


FIG. 3.--Microstructural elements in silicon carbide: (a) microcracks near grain boundary in as-sintered sample; (b) fibrous graphitic phase in as-received sample; (c) faults and initial grinding damage near tensile surface of specimen after 300 h at 1300 C; (d) crack associated with graphitic inclusion in 300h specimen.

FRACTURE SURFACE MORPHOLOGY IN ENGINEERING PLASTICS

R. W. Hertzberg, J. A. Manson, and C. M. Rimnac

The analysis of a polymer fracture surface generated during monotonic or cyclic loading can provide much useful information pertaining to those fracture mechanisms responsible for the material's failure and to the deformation mechanisms that preceded final separation. For amorphous polymers [e.g., poly(vinyl chloride), poly(methyl methacrylate), polystyrene], one particular deformation mechanism, crazing, can play an important role in crack growth. A craze is a region of expanded polymeric material that is composed of fibrils of polymer material oriented in the direction of the principal tensile load and interconnected with a void network; the density of this structure is about 50% of the uncrazed polymer matrix. Though a polymer craze is capable of supporting load, it is a weakened structure relative to the surrounding polymer matrix and thus is often a precursor to crack growth. Crazes also develop in amorphous regions of semicrystalline solids and serve to initiate cracks in these materials. In addition, spherulites have been shown to deform and leave characteristic patterns on the fracture surfaces.

The objective of this paper is to examine the fracture surface micromorphology in amorphous and semicrystalline polymers as well as their composites. To this end, scanning electron microscope images are presented and efforts made to distinguish between fracture markings produced under monotonic and cyclic loading conditions.

Experimental Procedures

Various engineering plastics were fractured under monotonic and cyclic loading conditions. Fractured surfaces were then studied by use of an ETEC Autoscan scanning electron microscope (SEM) at an accelerating voltage of 20 kV. Specimens were mounted on aluminum stubs and sputter-coated with a gold-palladium alloy prior to examination.

Fractographic Observations

Amorphous Polymers. Under monotonic loading conditions, rapid fracture usually occurs by passage of a crack through a bundle of crazes that form at the advancing crack tip. The crack advances in discrete bursts associated with different bundles of crazes and thus leaves a series of bands--called hackle markings--on the fracture surface (Fig. 1a).¹⁻⁴ Closer examination of a hackle band reveals another common polymeric fracture surface feature, referred to as the patch morphology (Fig. 1b). This morphology results from the crack front jumping randomly within a single craze from one craze-matrix interface to the other. Thus, patches of craze matter are left on either half of the fracture surface and match with depressions on the mating surface. Within a hackle band the patches decrease in size in the direction of crack growth (Fig. 1b).

Craze formation and breakdown has also been shown to dominate the fracture of amorphous polymers under cyclic loading conditions.⁵ In such cases one, or at the most a few, crazes form in the damage zone at the crack tip. The principal craze then develops and gradually breaks down over several hundred to thousands of loading cycles. When the craze fibrils are sufficiently weakened, the crack front advances by striking through the craze. As this process is repeated, a series of bands lying perpendicular to the direction of crack growth is developed with each band representing a single craze (Fig. 2a). The width of these bands has been shown to vary with the second power of the crack tip stress intensity factor and corresponds to the size of the plastic zone at the advancing crack tip. Because the crack front advances discontinuously by this process, these markings are known as discontinuous growth

Authors Hertzberg and Manson are at Lehigh University, Bethlehem, PA 18015; Rimnac is at the Hospital for Special Surgery, New York, NY 10021.

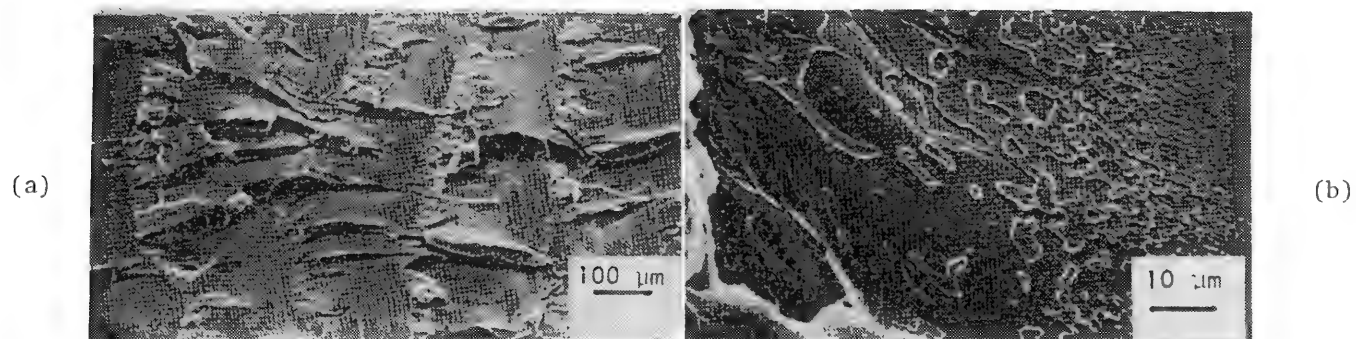


FIG. 1.--(a) Hackle-type fast fracture bands in amorphous plastics; (b) patch-type morphology.

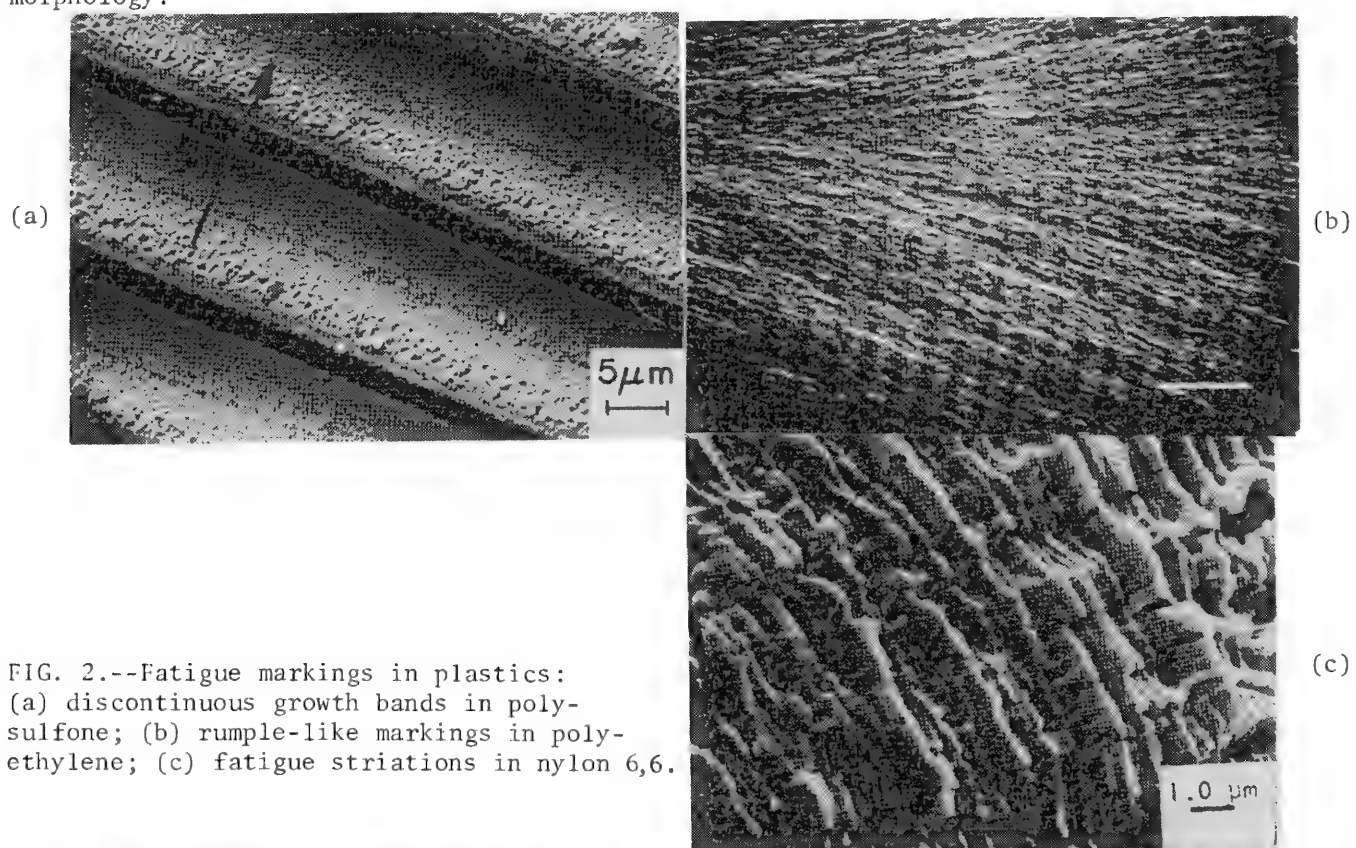


FIG. 2.--Fatigue markings in plastics:
(a) discontinuous growth bands in poly-sulfone;
(b) rumple-like markings in poly-ethylene;
(c) fatigue striations in nylon 6,6.

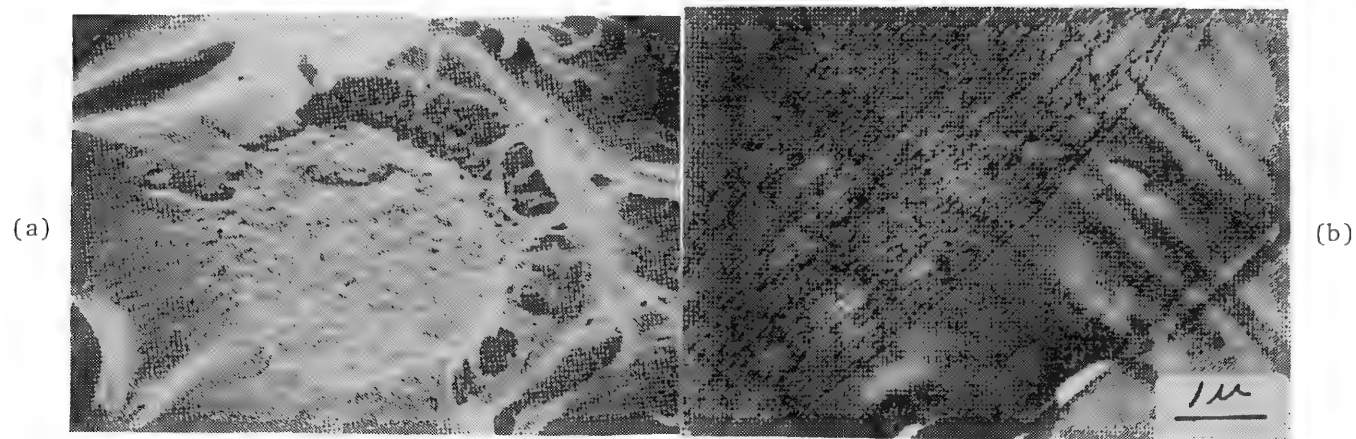


FIG. 3.--(a) Fracture of duplex-phase rubber particle in toughened plastic; (b) TEM image showing OsO_4 -stained rubbery phase.

bands. The discontinuous growth band is composed of microvoids that decrease in diameter from the beginning to the end of each band. The change in void diameter is thought to reflect the decreasing craze opening displacement with increasing distance from the crack tip. Surrounding these voids are masses of broken fibrils that had previously carried the load across the craze.

Microstructural features can also be identified on impact modified polymer fracture surfaces. Figure 3(a) shows a failed duplex-phase rubber particle on a fracture surface created under monotonic loading conditions.⁶ The character of these duplex particles is shown clearly in Fig. 3(b), where the osmium-tetroxide stained rubbery phase is seen. The islands of clear matter are regions of amorphous matrix.

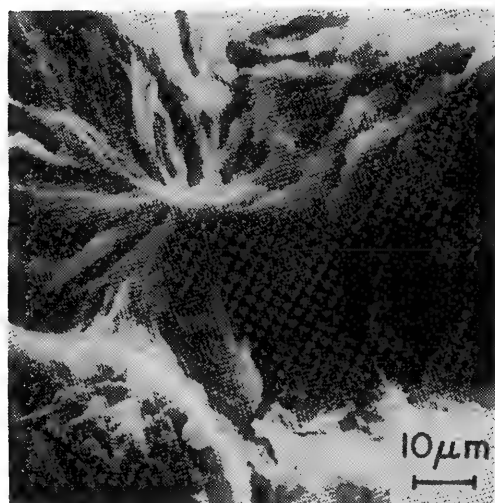
Semicrystalline Polymers. Fracture surfaces in semicrystalline polymers occasionally reveal the underlying microstructure of the material that results from the crack path either following around or passing through a spherulite (Fig. 4a).⁷ Note the radial pattern that reflects the morphology typical of spherulitic microstructures. On the other hand, the extensive amount of plastic deformation that is exhibited by most semicrystalline materials often obscures the details of the microstructure as noted for the case of room-temperature tearing in polyethylene (Fig. 4b); by sharp contrast, rapid bending of the same material at 6 C reveals a distinctly different fracture surface appearance that includes highly drawn tufts of material (Fig. 4c). With decreasing test temperature, these tufts become shorter and more widely spaced. Images similar to that shown in Fig. 4(c) are commonplace in certain service failures of polyethylene pipe.

The fatigue fracture surfaces in semicrystalline polymers often take on a rumpled appearance indicative of extensive amounts of crack tip deformation (Fig. 2b);⁸ in this figure, the crack direction is from the right to left. No connection can be made between the width of these rumple bands and the macroscopic growth rate. On the other hand, different fatigue bands (called fatigue striations) (Fig. 2c) are sometimes observed in all polymers at high growth rates and correspond closely to the average crack growth rate within the material. The presence of these striations is very useful in performing a quantitative failure analysis since the striation width varies with the magnitude of the crack tip stress field.

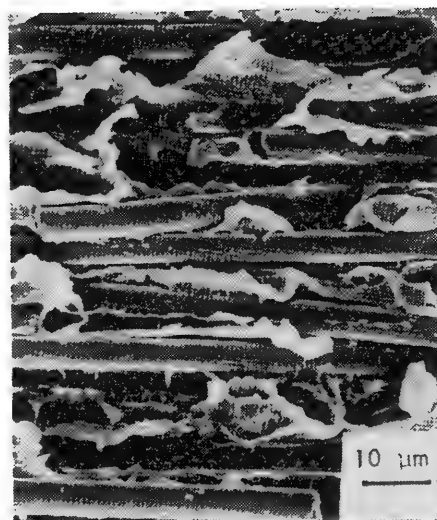
Composites. Fracture surfaces of polymers containing rigid particles or fibers can help in the qualitative, and sometimes quantitative, analysis of the characteristics and relative importance of failure in the matrix, the reinforcement, or the interface (Fig. 5). For example, in a well-bonded glass-fiber-reinforced nylon 6,12 undergoing slow fatigue crack propagation,⁹ the mode of failure depends on fiber orientation. With fibers *transverse* to the loading direction, both interfacial failure and extensive drawing and retraction of the matrix occur (Fig. 5a). In contrast, with parallel fibers, more brittle failure occurs in the matrix as well as in the fibers (Fig. 5b). With fast fracture (either under cyclic or monotonic loads), adhesion remains high even with transverse fibers (not shown), and considerable fiber pull-out is seen (Fig. 5c). Environmental effects can also be monitored; thus, water decreases interfacial adhesion and increases the plasticity and extent of retraction of the matrix.⁹

References

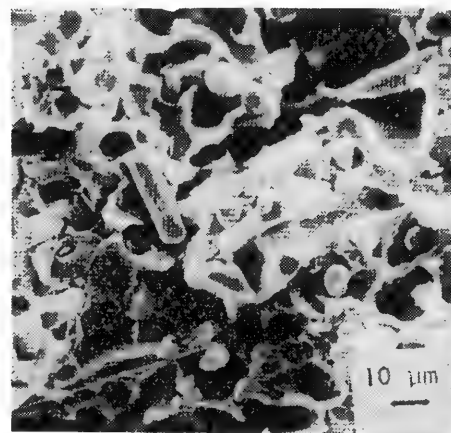
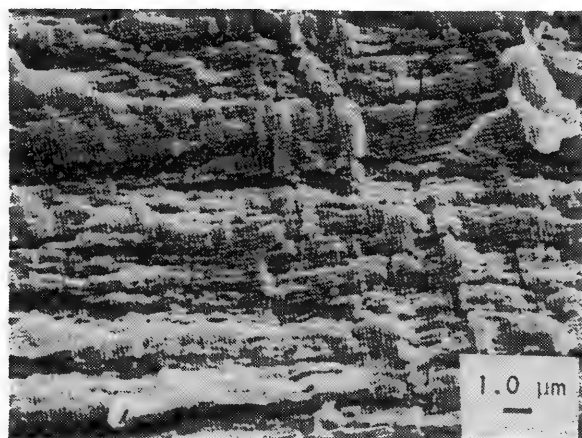
1. D. Hull, *Polymeric Materials*, Metals Park, Ohio: ASM, 1975, 487.
2. J. Murray and D. Hull, *Polymer* 10: 451, 1969.
3. J. Murray and D. Hull, *J. Polym. Sci.* 8(A-2): 583, 1970.
4. D. Hull, *J. Mater. Sci.* 5: 357, 1970.
5. R. W. Hertzberg and J. A. Manson, *Fatigue of Engineering Plastics*, New York: Academic Press, 1982.
6. C. M. Rimnac, R. W. Hertzberg, and J. A. Manson, *Polymer* 23: 1977, 1982.
7. R. W. Hertzberg, M. D. Skibo, and J. A. Manson, *J. Mater. Sci.* 13: 1038-1044, 1978.
8. P. E. Bretz, R. W. Hertzberg, and J. A. Manson, *ibid.*, 16: 2070-2078, 1981.
9. R. W. Lang, J. A. Manson, and R. W. Hertzberg, *Polym. Eng. Sci.* 22: 982-987, 1982.



(a)



(b)



(c)

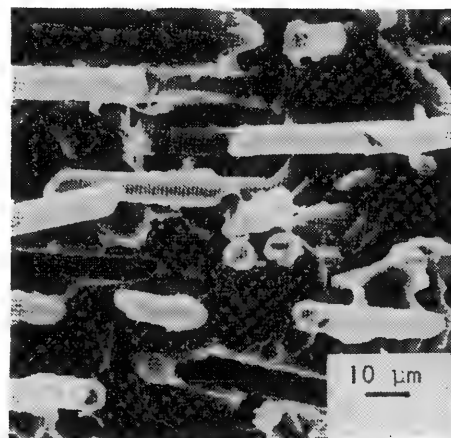
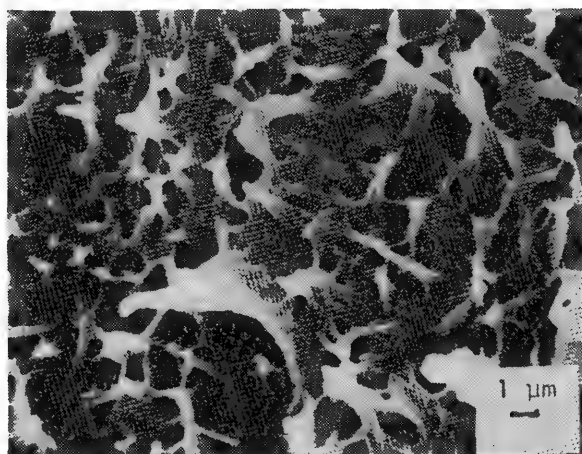


FIG. 4.--(a) Transspherulitic fracture in polyacetal; (b) room-temperature tearing in polyethylene; (c) rapid fracture in polyethylene at 6 °C.

FIG. 5.--Fracture in glass-fiber-reinforced nylon: (a) load transverse to fibers; (b) load parallel to fibers; (c) rapid fracture.

MICROSTRUCTURAL CHARACTERIZATION OF CREEP FAILURE IN ALUMINA

Dipankar Sarkar, Metin Sakarcı, and J. R. Porter

Aluminum oxide fails under high-temperature tensile creep conditions by a process of grain-boundary cavitation followed by cavity coalescence. In the present study, both commercial hot-pressed alumina samples and laboratory hot-pressed samples have been investigated. Mechanical testing under four-point flexure conditions have yielded a creep stress exponent $n = 1.7$, a result not immediately explicable in terms of existing steady-state creep models.¹ At sufficiently high temperatures, hot pressed alumina will desinter, when annealed in oxidizing environments, as a result of internal gas forming reactions.² A comparison between cavitation induced by tensile stress and by internal gas pressure has therefore been made.

One important observation is that the cavitation process is inhomogeneous, with only a small number of grain-boundary facets developing cavities. Potential explanations for cavitation inhomogeneity include variable normal tensile stresses on grain boundary facets, variable extent of grain boundary sliding on different facets, variable additive segregation to different facets, and variable boundary energies leading to variable cavity tip dihedral angles.

Mechanical Properties

Commercial hot pressed alumina samples, doped with 0.1% MgO and 0.15% NiO, were deformed in four-point flexure at 1400 C to a maximum outer fiber strain of 7%. Figure 1 shows the computed outer-fiber stress/strain curve, where the stress exponent n in the expression $\dot{\epsilon} = \sigma^n$ is 1.7, where $\dot{\epsilon}$ is the outer fiber strain rate and σ is the outer fiber stress. The circles represent tests on commercial alumina samples. The square represents a test on laboratory hot-pressed alumina doped with 250ppm MgO. At low stresses, the creep tests did not reach a steady-state deformation rate due to concurrent grain growth. For this data point, values of deformation rate were taken early in the test. The value for n observed was comparable to that found in earlier work and cannot be explained in terms of existing diffusion creep models.¹ The laboratory hot-pressed alumina and the commercial alumina have a comparable grain size and the similar creep behavior is expected.

Cavitation

At 1400 C, there was no evidence of desintering during air annealing and the cavitation was attributed to the applied stress. Desintering was observed during air annealing at 1600 C, with cavities initiating at grain boundary triple points. Figure 2 shows two fracture surfaces after annealing for 1 and 32 h, respectively. After 1 h, cavities had a rounded tetrahedron appearance, although some cavities developed a crack-like nature after 32 h.

After mechanical testing at 1400 C, cavitation was observed, although the extent of cavitation was less than that observed under similar conditions on similar material.¹ Figure 3 shows a transmission electron micrograph of a section of the sample parallel to the tensile surface from a region just below the surface. The specimen was deformed at 6.9 MPa and had developed triple-point cavities on some of the triple points.

Analytical electron microscopy (AEM) was used to characterize the deformed alumina samples further with particular attention focused on characterizing grain boundaries. In well-annealed, undeformed, hot-pressed alumina, the grain boundaries tend to be planar. After deformation, the boundaries become nonplanar with nonuniform curvature. A nonplanar boundary is arrowed in Fig. 3. Cavities have developed at some grain boundary facets. However,

The authors are at the Department of Materials Science, University of Southern California, Los Angeles, CA 90089-0241. They wish to acknowledge the support of the National Science Foundation under Grant DMR-8217120.

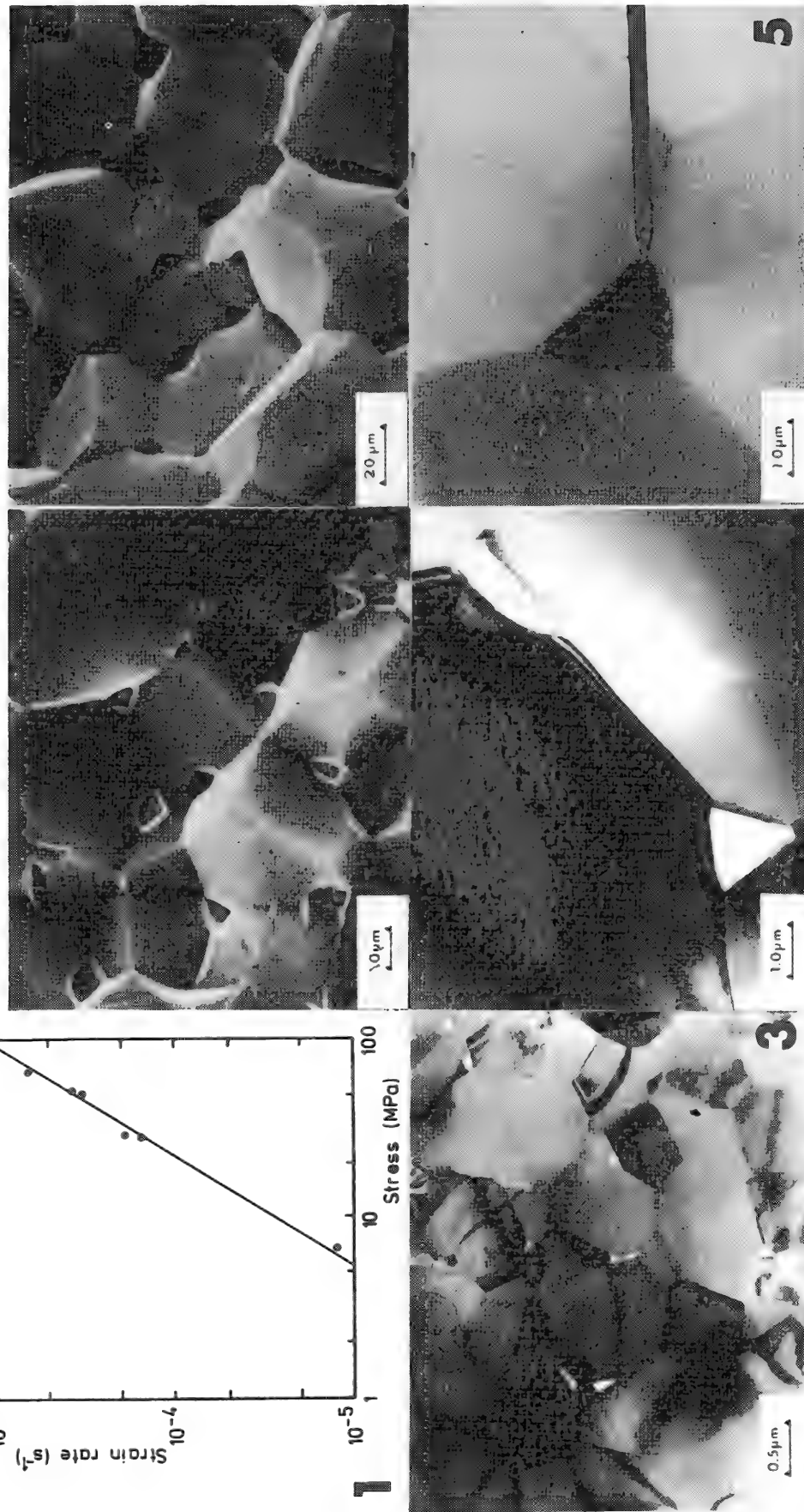
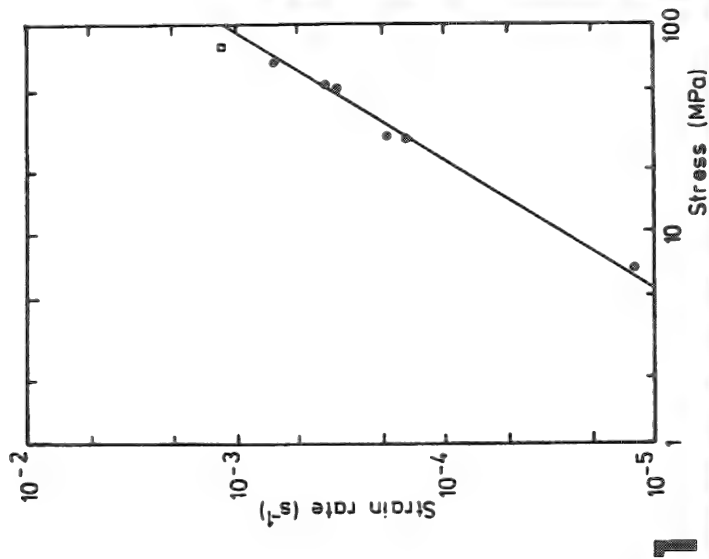


FIG. 1.--Outer fiber stress-outer fiber strain rate curve for alumina deformed in flexure at 1400 C. Circles represent commercial alumina, square represents alumina doped with 250 ppm MgO. FIG. 2.--Desintered alumina; samples were annealed at 1600 C for (a) 1 h, (b) 32 h. FIG. 3.--Inhomogeneous distribution of creep cavities in alumina deformed at 1400 C with outer fiber stress of 6.9 MPa. FIG. 4.--Facetted crack-like creep cavity. FIG. 5.--Spinel grain in Mg-doped alumina.

not all crack-like cavities have the ideal shapes predicted by the Chuang and Rice model.³ Many of the crack-like cavities have faceted surfaces (Fig. 4), the existence of which modifies cavity growth kinetics.

One aspect of the program is to identify the role of sintering additives in the development of creep cavities. Sintering additives are known to affect grain growth in alumina; and certain additives, for example calcium, are known to segregate strongly to grain boundaries. However, there is little evidence for magnesium segregation to grain boundaries. Although magnesium could be detected in small, spinel oxide grains (Fig. 5), magnesium segregation to grain boundaries in the deformed alumina samples could not be detected by energy-dispersive x-ray analysis (EDS), with a 5nm probe positioned over boundaries inclined parallel to the beam, in keeping with other published work.⁴ A similar technique was able to detect silicon segregation to grain boundaries in hot-pressed alumina doped with 250 ppm silicon (Fig. 6). At this level of doping, there was no detectable grain boundary phase.

A few of the grain boundaries were observed to have a periodic structure (Fig. 7). Grain boundary dislocation motion has been postulated as a mechanism of grain boundary migration and grain-boundary sliding and both processes are involved in creep cavitation. Periodic boundaries are predicted to have a lower grain boundary energy than nonperiodic boundaries. Consequently, a cavity growing on a periodic boundary would have a larger dihedral angle at the cavity tip than a cavity on a nonperiodic boundary. No cavities have been observed to grow on periodic boundaries in the deformed samples investigated, which suggests that such boundaries do indeed have a low energy, and therefore have a reduced tendency to cavitate.

References

1. J. R. Porter, W. Blumenthal, and A. G. Evans, "Creep fracture in ceramic polycrystals--I. Creep cavitation effects in polycrystalline alumina," *Acta Metall.* 29: 1899-1906, 1981.
2. S. J. Bennison and M. P. Harmer, "Grain growth and cavity formation in MgO doped Al_2O_3 ," *Advances in Ceramics*, 1983, vol. 6.
3. T. J. Chuang and J. R. Rice, "The shape of intergranular creep cracks growing by surface diffusion," *Acta Metall.* 21: 1625-1628, 1973.
4. D. R. Clarke, "Grain-boundary segregation in magnesia doped alumina," *J. Am. Ceram. Soc.* 63: 339-341-1980.

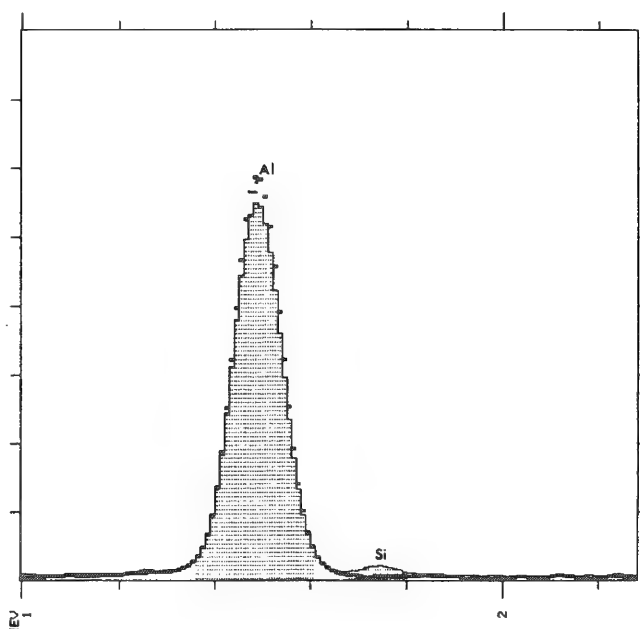


FIG. 6.--Two superimposed EDS spectra from grain boundary (with Si peak) and from grain interior (no Si peak), showing Si segregation to grain boundaries in alumina doped with 250 ppm Si.

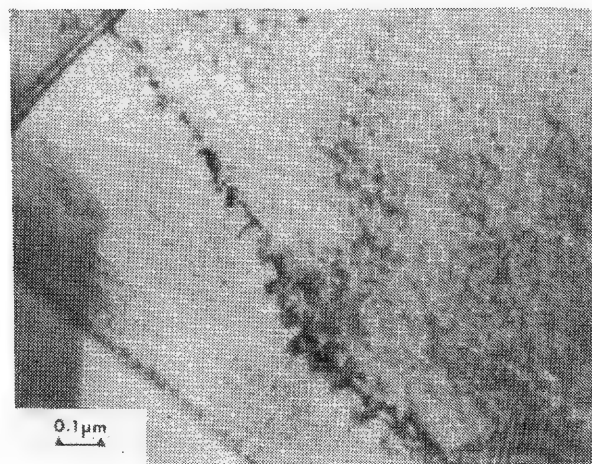


FIG. 7.--Periodic boundaries in Mg-doped alumina.

9 Geological Applications

CHARACTERIZATION OF SANDSTONES AND THEIR COMPONENT MINERALS BY QUANTITATIVE EPMA POINT COUNTING IN THE SCANNING ELECTRON MICROSCOPE

A. Dilks, D. Park, and S. C. Graham

With the advent of computer-controlled data acquisition and stage movements in the scanning electron microscope, large-area, quantitative electron probe microanalysis (EPMA) has become a reality. We describe a point-counting procedure that uses EPMA for sandstones. A typical analysis, driven by a L 860/500 minicomputer, involves the measurement of the concentrations of fifteen elements at each of 500 points arranged in a regular array on the sandstone section. Sorting of the data, according to simple element concentration criteria, into the various minerals and pores is achieved after transfer of the data to a mainframe computer where statistical analyses and graphical presentations can be performed routinely. Where analysis points include two or more phases in the specimen they are separated on the assumption that a linear combination of their element compositions exists. An important advantage of EPMA point counting over the corresponding optical method lies in its ability to provide spatial (x-y coordinates) and element-compositional information on the minerals. For example, ternary plots within the albite-orthoclase-anorthite system for feldspars, or the magnesite-calcite-siderite system for carbonates are readily constructed, as are plots of magnesium, potassium, and iron distributions in clay minerals. In addition, the EPMA method is fully automated and requires minimal operator involvement. This work is restricted to the study of sandstones, though similar methods have been applied by other laboratories to other types of rock.^{1,2}

Experimental

The sandstones studied in this work were prepared as flat polished sections of arbitrary thickness impregnated with epoxy resin as discussed elsewhere.^{3,4} The SEM used was a JEOL JXA 733 equipped with a LINK systems energy-dispersive (ED) x-ray analyzer and 860/500 minicomputer. The LINK 860 minicomputer was programmed to drive the X, Y specimen stage to position the sandstone section such that the SEM primary electron beam became incident in turn on 500 points set in a array of 20 rows × 25 columns. The spacing between the points was 0.4 mm, which is approximately the largest dimension of the largest particle in the specimens studied. At each point the microscope performed a full quantitative elemental analysis by EPMA and stored the x, y coordinates and concentrations of 15 elements on floppy disk. The electron beam energy was 20 keV, the beam current 1.2 nA, and the counting time per point 100 s. The total analysis time was 18 h but required less than 1 h of operator time. Following the analysis in the SEM, the x, y coordinates and concentrations of Na, Mg, Al, Si, P, S, Cl, K, Ca, Ti, Cr, Mn, Fe, Zr, and O (oxygen calculated by difference) for each point were transferred to our IBM 4341 mainframe computer for sorting, statistical analysis, and graphical presentation.

Results and Discussion

Table 1 lists the minerals found to be present in the sandstone along with their idealized chemical formulas. Also shown in Table 1 are the threshold criteria used for data re-

The authors are at Shell Research Ltd., Thornton Research Centre, P. O. Box 1, Chester, England CH1 3SH.

TABLE 1.--Retrieval criteria and number of points retrieved.

Phase	Retrieval thresholds, % ^a	Number of points retrieved		Composition, % ^a
		Directly	Indirectly ^d	
Pore	O > 90 ^b	21	25.3	9.3
Kaolinite [Al ₂ Si ₂ O ₅ (OH) ₄]	Al > 12 O > 50	50	13.9	12.8
Quartz [SiO ₂]	Si > 35	326	7.9	66.8
Na-feldspar [NaAlSi ₃ O ₈]	Na > 5	8	1.8	2.0
K-feldspar [KAlSi ₃ O ₈]	K > 10	33	3.5	7.3
Anatase [TiO ₂]	Ti > 35	4	1.6	1.1
Pyrite [FeS ₂]	Fe > 35	1	0.9	0.4
Zircon [ZrSiO ₄]	Zr > 35	0	0.3	0.1
Others ^c			1.8	0.4

a) All percentages are by weight.

b) In the e.p.m.a. analysis carbon is not included and oxygen is calculated by difference. Pores therefore appear to be largely "O".

c) Mainly apatite and an unidentified mineral containing Fe, Mn, Al, Si and some Ca.

d) For example, since potassium is only found in significant quantities in potassium feldspar for this specimen, the number of the remaining points attributable to this mineral is the sum of the potassium contents of the points divided by 0.14, the weight fraction of potassium in the pure mineral.

Hence, $N(\text{potassium feldspar}) = \sum_{i=1}^n K_i / 0.14$, where N is the number of points, i is the analysis point, and n is the total number of remaining points. All other minerals can be treated similarly.

trieval. For example, setting the criterion that silicon exceeds 35% by weight retrieves all points where quartz has been analyzed. The criterion $Al > 12\%$ retrieves all points where kaolinite has been analyzed, and the criterion $K > 10\%$ retrieves all points where potassium feldspar has been analyzed. Ambiguities at this stage are readily resolved either by straightforward visual inspection of the retrieved data or by application of further criteria. For example, for the set of points retrieved as potassium feldspar we find that no points have a chlorine content exceeding 0.05%, which confirms the absence of sylvite (KCl) and illustrates the advantages of the simplistic retrieval approach.

Table 1 also shows the number of points retrieved directly for each mineral by application of the criteria. About 90% of the points are retrieved directly in this way, leaving only 57 points unretrieved. Two possibilities exist for the unretrieved points: either the analysis point is a new mineral not included in the original set, or the analysis point is at a boundary and so straddles two or more different phases (minerals or epoxy resin in pores). The partitioning of these points among the various minerals is straightforward, based on the approximation that each measured elemental composition is a linear combination of the compositions of all phases present. After all minerals are assigned, the balance is assumed to be pores. The points assigned to each phase in this way are again listed in Table 1 as indirectly retrieved points.

In principle, a fully comprehensive set of conditional retrieval criteria, based on the presence of one or more elements with concentrations falling between predetermined values, could be set up to analyze unknown specimens that might contain a wide range of minerals. We believe, however, that the opposite approach is more profitable; namely, the one in which the simplest possible retrieval criteria are used initially and modified and made more complex only when necessary. Notwithstanding the simplistic retrieval, we have preferred to obtain a fully quantitative elemental analysis at each point, using the ZAF-4 correction procedure. In doing that we have found that, although the retrieval thresholds are coarse for this specimen, the measured composition of each mineral approximates the idealized chemical formula very closely. The final column in Table 1 expresses the total number of points for each phase as the composition of the sandstone. The compositions of sandstones determined in this way agree very well with the compositions determined by other methods, e.g., optical point counting³ or back-scattered electron image analysis.^{3,4}

An important advantage of quantitative EPMA point counting over the corresponding optical method lies in its ability to provide spatial (x-y coordinates) and element-compositional information on the minerals. Ternary plots within the albite-orthoclase-anorthite system for feldspars, or the magnesite-calcite-siderite system for carbonates are readily constructed. Figure 1, for example, shows the carbonate ternary plot for a specimen found to contain 19% carbonates by the EPMA method. In this particular example, all carbonate points were retrieved according to the criterion that $Mg + Ca + Fe > 30\%$ by weight, and Fig. 1 was obtained by a plot of Mg vs Ca vs Fe concentrations for this subset of the data. The graphical representation clearly demonstrates that the carbonates present in the sandstone are siderite and ankerite.

For the same sample, Fig. 2 shows plots of the potassium and iron contents of the clay minerals. In contrast to the sample discussed with reference to Table 1, this sample clearly shows a significant amount of illite clay, containing potassium and iron that is readily quantified by the EPMA method.

Conclusion

Quantitative EPMA can be used in a point-counting mode to provide a quantitative analysis of a relatively large area of a sandstone section. An important advantage of this method over the corresponding optical method lies in its ability to provide spatial and element compositional information on the minerals.

References

1. P. F. Hlava, W. F. Chambers, W. C. Lugh, and T. M. Gerlach, paper presented at 16th Annual Conference of the Microbeam Analysis Society, Vail, Colo., 1981.
2. J. E. Quick, A. A. Chodos, and A. L. Albee, *Microbeam Analysis-1981*, page 143.
3. A. Dilks, D. Park, and S. C. Graham, in preparation.
4. A. Dilks and S. C. Graham, *Microbeam Analysis--1984*, 149.

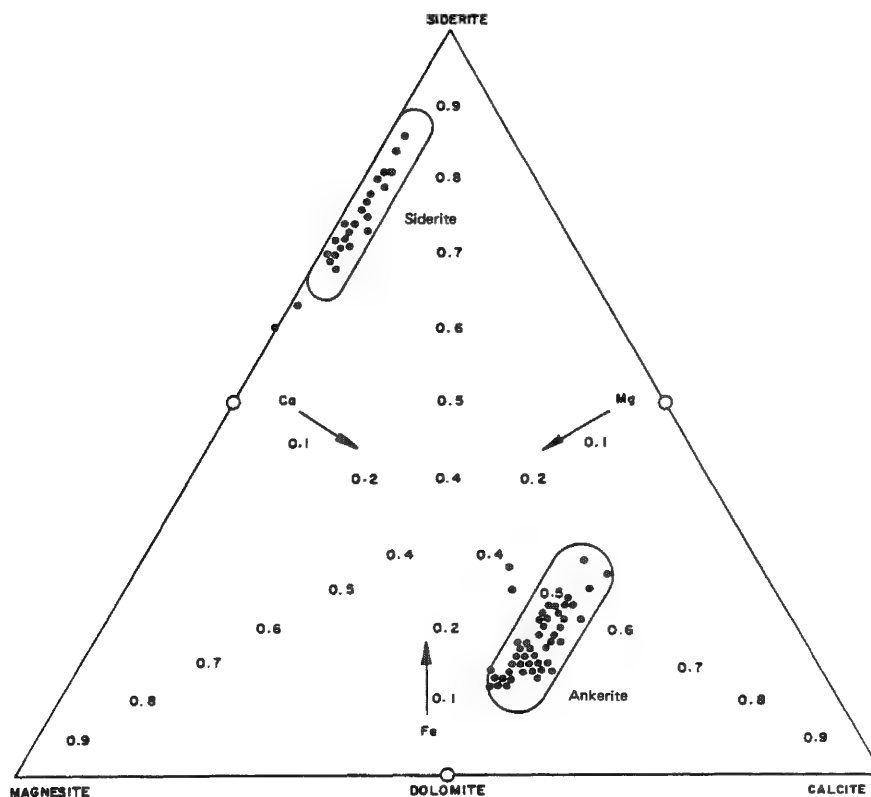


FIG. 1.--Carbonate ternary plot derived from EPMA point counting.

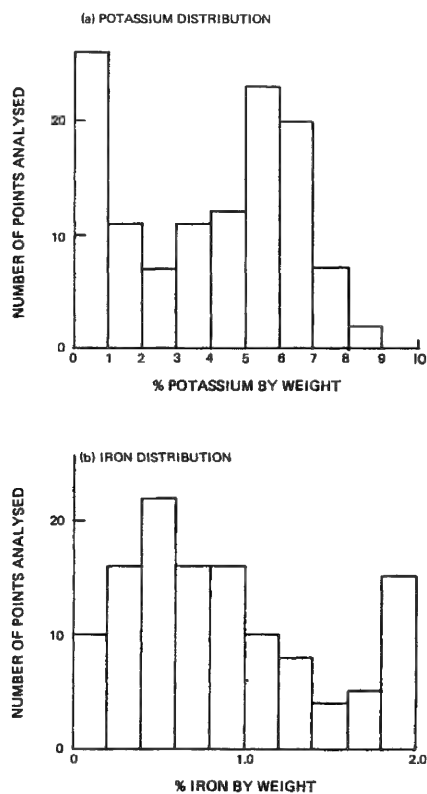


FIG. 2.--Potassium and iron distributions for clay minerals in a sandstone. Results derived from EPMA point counting.

QUANTITATIVE ENERGY-DISPERSIVE ANALYSIS OF ROCK-FORMING SILICATES

L. S. Hollister, J. A. Crisp, C. G. Kulick, Will Maze, and V. B. Sisson

The Princeton microprobe consists of a 1968 ARL-EMX wavelength-dispersive system (WDS) 32K plus a 1978 TN Tracor Northern energy-dispersive system (EDS) with a dual floppy disk 32K computer and manufacturer-supplied software. With this equipment we have achieved a level of speed and accuracy sufficient for most geologic applications. At our conditions of operation, 3-4 averaged 50s EDS analyses for concentrations greater than 10% and 10 averaged 50s EDS analyses for concentrations of 0.5-1% are equivalent to 5 averaged 10s WDS analyses. In the present paper we give accuracy of the EDS system for common elements in silicates as a function of concentration and atomic number, describe our procedure, and note a few limitations.

Most of our data compare EDS with WDS analyses for the same spot on mineral grains. This procedure minimizes potential errors from differences in characteristics between standard and sample. The Bence-Albee correction procedure is used for both systems. The data were collected over the past year and were supplied by the co-authors and M. L. Crawford (Bryn Mawr College), M. Colucci (Rutgers University), G. Grissom, M. L. Hill, and K. Peters. Thus, the conclusions hold for routine use by various operators and for changes over time in instrument characteristics.

Our results are given in Table 1. Accuracy is reported for single EDS analyses and for averages of 5-10 repeat analyses. Errors are given in relative weight % for approximately one σ . Minerals analyzed include hornblende, pyroxene, garnet, muscovite, feldspar, biotite, cordierite, olivine, and scapolite.

We operate at 15 kV and 0.2 μ A beam current (equivalent to about 0.02 μ A sample current) for both EDS and WDS. Beam current is held constant during analysis; drift, monitored on a digital meter, is less than 1 part in 500 over several hours. With a 5 μ m beam diameter, Na counts are not lost in albite during the time of analysis. The EDS detector window is set to yield a count rate for the total EDS spectrum of 1200-1500 cps, which thus minimizes dead time and pulse pile-up effects.

The spectra accumulation time for the standards is set for 100 s. We use a 4 μ s rise time for the amplifier and set the lower energy limit of the spectrum at 0.83 keV. This combination eliminates low-energy transient signals. The energy windows (keV) for standard elements, and the standards, are given in Table 2. Only the $K\alpha$ peak is used for Cr and Mn because of overlaps in our standards of $CrK\beta$ with $MnK\alpha$, and $MnK\beta$ with $FeK\alpha$, respectively. The EDS accuracy is poor for Mn in Cr-rich samples, Fe in Mn-rich samples, and for Ti and Ba when they occur together.

With the energy ranges listed in Table 2 we can analyze for 13 elements simultaneously. The spectra accumulation time for the unknowns is set for 50 s. A complete analysis for 10 elements, including calculation of cation proportions, takes 3.5 min.

The standards data are stored on disk. A complete standard set takes about 8 h to acquire but yields accurate analyses literally "forever." More than 5 sets of standard peak counts are taken, and, when one is obtained near the average of the previous results, it is stored on disk.

After warm-up (30 min usually sufficient) the calibration of the energy spectrum is checked on tephroite (Si, Mn). We then analyze a standard anhydrous mineral to establish the drift factor relative to the stored standards data. We are ready to run unknowns after about 1 h, and proceed to take data at a rate of about fifteen 10-element reduced analyses per hour. While the computer is reducing the data, we can also operate the WDS system, without extending analysis time, to collect data for 3 elements for which greater accuracy is required. This is an operator choice, but is recommended for concentrations below 0.5%

The authors are at the Department of Geological and Geophysical Sciences, Princeton University, Princeton, NJ 08544. NSF support is acknowledged.

and, of course, for cases of spectra overlaps. The WDS data, reduced separately, can be later combined with the EDS data.

Although the error ranges given in Table 1 are valid as stated, they are not all normally distributed. EDS analyses for Si are slightly higher than the WDS results; and, if Mg is present, EDS analyses for Al are systematically lower than WDS values.

Important factors in obtaining accurate EDS analyses include constant bias voltage on the filament, stability of the beam, uniform carbon coats, meticulously clean sample holders, and choice of energy windows (Table 2).

TABLE 1.--Relative percentage errors for EDS analyses.

Wt. % range	Elements	% error (single) ^a	% error (multiple) ^b
0.1 - 0.5	K,Ca,Mn,Mg,Fe	n.d.	20
0.5 - 1	K	10	n.d.
0.5 - 5	Na,Mg	10	10
5 - 10	K,Na	n.d.	5
5 - 10	Al	7	4
5 - 10	Ti	5	2
10 - 15	Na,Mg	5	4
10 - 15	K,Ca,Fe	n.d.	2
15 - 20	Al	3	1
20 - 25	Al,Mn,Fe	3	2
30 - 45	Al,Si	2	1
40 - 70	Si	1	1

^aFor single EDS analysis.

^bFor average of 5-10 repeat EDS analyses.

TABLE 2.--Element peak energy windows (keV) and standards.

Na	0.83-1.21	albite	Ca	3.29-4.42	wollastonite
Mg	0.83-1.49	forsterite	Ba	4.14-5.36	Ba-glass
Al	1.02-2.03	corundum	Ti	4.05-5.28	rutile
Si	1.22-2.33	wollastonite	Cr	5.10-5.77	chromite
P	1.64-2.36	apatite	Mn	5.22-6.19	tephroite
Cl	2.39-3.08	apatite	Fe	6.05-7.48	hematite
K	2.94-3.93	orthoclase	Zn	8.20-9.07	gahnite

CHARACTERIZATION OF SECONDARY ALTERATION IN THE COLUMBIA RIVER BASALT BY BACKSCATTERED ELECTRON IMAGING AND ENERGY-DISPERSIVE X-RAY SPECTROSCOPY

P. P. Hearn, W. C. Steinkampf, and Z. A. Brown

The thick sequences of flood basalts which underlie the Columbia River basin are important aquifers, providing water for both agricultural and domestic use. Secondary alteration in these rocks occurs primarily as coatings or fillings in fractures and vesicles; alteration is generally believed to have occurred at low temperatures (<100 C) by reaction with meteoric waters. The distribution and compositional variation of secondary minerals are therefore of major interest, since they may reflect the chemical evolution and flowpaths of groundwaters traveling through the basalt aquifers.

The nature and scope of secondary alteration in Pasco Basin basalts have been described by Ames¹ and also by Benson and Teague;² those interested in a more detailed treatment of the subject may wish to refer to these studies. This paper focuses on the compositional variation of the major alteration products and on present formulas based on the mean composition of these phases, and suggests possible reactions for the observed sequence of alteration. This work is part of a larger study of groundwater geochemistry initiated by the U.S. Geological Survey, with the ultimate goal of developing a solute transport model for basalt aquifers.

Sample Preparation and Analysis

Fifteen samples of drill cuttings were obtained from water wells in the central and northeast Pasco Basin; ten drill-core samples were also obtained from Rockwell Hanford Operations from two test wells within the Hanford Test Area (Wells DH-4 and DC-14). Depths of the well-cutting samples range from 85 to 365 m; depths of the drill-core samples range from 276 to 1441 m. Polished thin-sections or polished chips imbedded in epoxy were carbon coated and examined with an ETEC Autoscan scanning electron microscope equipped with an EDAX model 9100 Energy Dispersive X-ray Spectrometer (SEM/EDS). Discrete phases within altered zones were selected for analysis by means of a backscattered electron detector. EDS analyses were made on $10 \times 10 \mu\text{m}$ areas at an accelerating voltage of 18.5 kV and a count time of 30 s. Glass reference standards were prepared from USGS rock standards.

In addition to SEM/EDS analysis, microsamples of altered basalt fragments from well cuttings and scrapings of vesicle linings from rock core samples were collected for a more accurate major oxide analysis. Following fusion of samples in a lithium tetraborate flux and dissolution in 1% HNO_3 , major oxides were determined by inductively coupled argon plasma arc spectrometry. Major oxides were also measured in representative splits of bulk samples by wavelength x-ray fluorescence.

Results

The primary alteration products found were smectite, zeolites, various forms of silica, and iron oxides. Smectite is ubiquitous in both shallow and deep samples; its composition is closest to that of nontronite, but is higher in magnesium than is normal for this mineral (Fig. 4). Clinoptilolite, the major zeolite observed, occurs in abundance only at depths greater than 300 m below the surface. Iron oxide was found only in samples above 300 m; free silica was more abundant below this depth. These large-scale vertical changes are often reproduced in the sequences of alteration observed in closed vesicles (Fig. 1). The

The authors are with the U.S. Geological Survey in Reston, Va. (Hearn and Brown) and in Tacoma, Wash. (Steinkampf). The authors thank Blair Jones, Warren Wood, Leslie Ruppert, and Richard Larson for reviewing the manuscript.

general sequence of formation is smectite \pm iron oxide \rightarrow clinoptilolite \rightarrow silica. This sequence is consistent with the findings of earlier studies.^{1,2}

Smectite often appears admixed with phases of similar composition, but with substantially higher iron contents ("fs" in Fig. 1). Analyses of these zones are suggestive of a mixture of smectite and amorphous iron oxide. Several generations of compositionally distinct smectite are often present; backscattered electron images and EDS analyses show each generation to be relatively uniform in composition (Fig. 2).

A formula was computed from each smectite and clinoptilolite analysis on the basis of a smectite half-cell with 11 oxygens and a clinoptilolite half-cell with 36 oxygens (Table 1). Smectite analyses were rejected if the computed formula did not satisfy the following conditions: (1) Si atoms in half cell ≥ 3 and ≤ 4 ; (2) sum of octahedral ions > 2 ; interlayer charge ≤ 0.75 .

Although the low sample density precluded the evaluation of lateral variation in the composition of smectites and clinoptilolites, some changes in the chemistry of these minerals are apparent with depth. The plot of the octahedral ions Fe, Mg, and Al (Fig. 3)



FIG. 1.--Backscattered electron image of vesicle lining showing sequence of formation of alteration products: smectite + Fe-oxide \rightarrow smectite (S) \rightarrow clinoptilolite (C) \rightarrow silica (Si). (Scale bar, 500 μm .)

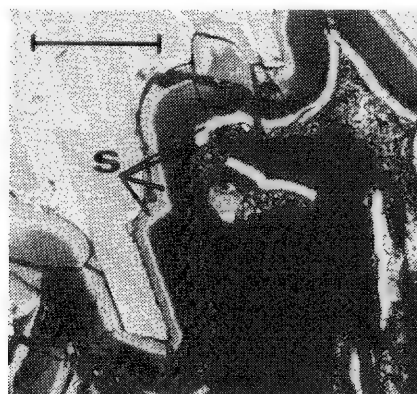


FIG. 2.--Backscattered electron image of vesicle lining showing multiple generations of smectite (S). (Scale bar, 100 μm .)

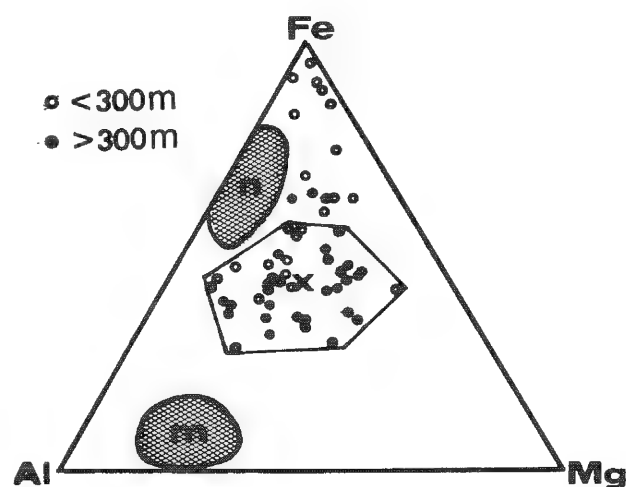


FIG. 3.--Molar plot of octahedral ions Fe, Mg, and Al in smectites. Polygon encloses analyses that satisfy unit-cell criteria. Hatched zones indicate range of composition reported for montmorillonites (M) and nontronites (N).^{3,4} "X" indicates mean composition.

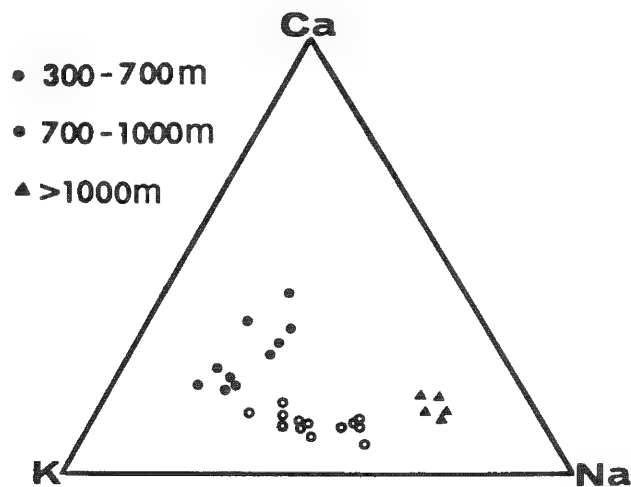


FIG. 4.--Molar plot of exchange ions Ca, K, and Na in clinoptilolites.

shows smectites from depths greater than 300 m to be slightly enriched in iron relative to the smectites from deeper sites. Furthermore, the analyses that do not yield an acceptable formula are predominantly from shallow samples, and generally fall along a line between the mean smectite composition and the iron corner of the triangle. This trend suggests that shallow smectites may contain finely admixed but discrete particles of amorphous iron oxide; zones containing more than 90% Fe as Fe_2O_3 were observed in several shallow samples.

A trend with depth is also apparent in the molar plot of exchange ions for clinoptilolites (Fig. 4). The data show a progressive increase in sodium relative to potassium within the depth interval from 300 to 1000 m. This trend is consistent with observations of high Na^+ in deeper groundwaters in the Pasco Basin.

Overall trends in the process of secondary alteration can be seen from a comparison of analyses of hand-separated alteration products with analyses of bulk samples (Table 2). Values for both well cuttings and vesicle scrapings are indicative of the retention of Fe and Mg in smectite and the accompanying loss of Na, Ca, and K to solution in groundwater. The vesicle scrapings generally contain more smectite and less altered glass than the altered fragments from well cuttings. This composition is reflected by the lower Al and Ti ratios: smectite is depleted in both these elements relative to volcanic glass. The mechanisms causing the enrichment of K in these samples are less clear, but may be possibly a combination of potassium uptake by the precipitation of clinoptilolite and migration of K^+ into smectite exchange sites.

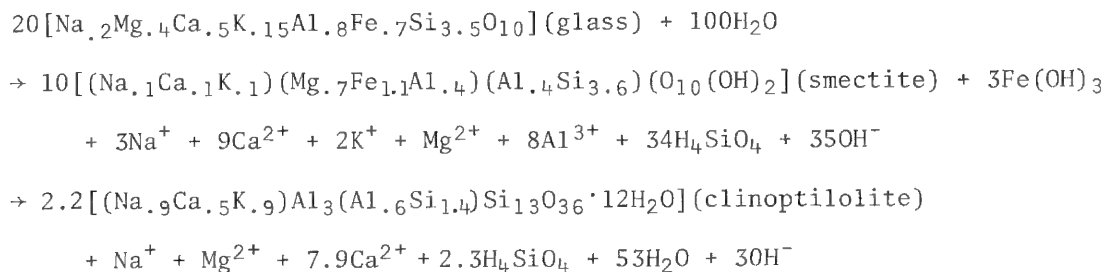
Discussion and Conclusions

Compositional variations in secondary alteration are a complex function of several variables, including (1) relative proportions and reactivities of crystalline and glassy components in the parent basalt, (2) groundwater flux, and (3) position along groundwater flow paths.

Basalt flows are commonly divided into two structural units: a lower zone of tightly jointed, vertically trending columns termed *collonade*, and an upper zone of more irregularly jointed and scoriaceous *entablature*.⁵ Distinct differences in the composition and relative abundance of glass, and hydraulic conductivity in the collonade and entablature zones of Pasco Basin basalts have been documented.^{6,7} Unfortunately, the actual distribution of these units within a single flow is largely random on a regional scale; quantitative modeling that takes these variations into account is therefore extremely difficult.

Although quantitative modeling is not as yet possible due to the problems mentioned above, knowledge of the composition and basic sequence of formation of the primary alteration products does permit one to write reactions that describe the process of alteration in a very general manner. In the following hypothetical reactions, the primary reactant phase is assumed to be volcanic glass. A representative formula was computed from microprobe analyses of Wanapum glasses.⁸

Smectite and iron hydroxide form from glass by simple hydrolysis; the products of the reaction left in solution in turn combine to form clinoptilolite:



The hydroxyl produced by these reactions will be buffered by HCO_3^- , or by sulfuric acid produced from the oxidation of pyrite; excess Ca^{2+} is precipitated as calcite.

These reactions do not uniquely describe the alteration process; other scenarios involving bicarbonate and sulfate ions are also possible. However, the reactions demonstrate the possibility of deriving the primary alteration products from volcanic glass and suggest the relative proportions of products that should be formed. When combined with water-chemistry data, the results of this work may serve as a basis for future attempts to quantify the basalt-groundwater system.

References

1. L. L. Ames, *Hanford Basalt Flow Mineralogy*, Battelle Institute Pacific Northwest Laboratory PNL-2847, 1980.
2. L. V. Benson and L. S. Teague, "Diagenesis of basalts from the Pasco Basin, Washington: I. Distribution and composition of secondary mineral phases," *J. Sed. Petrology* 52: 595-613, 1982.
3. W. A. Deer, R. A. Howie, and J. Zussman, *Rock Forming Minerals*, v. 3: Sheet Silicates, London: Clowes & Sons, 1967.
4. R. E. Grim, *Clay Mineralogy*, New York: McGraw-Hill, 1968.
5. D. A. Swanson and T. L. Wright, "Bedrock geology of the Northern Columbia Plateau and adjacent areas, in V. R. Baker and D. Nummedal, Eds., *The Channeled Scabland: A Guide to the Geomorphology of the Columbia Basin*, Washington, D.C.: National Aeronautics and Space Administration, 1978.
6. C. C. Allen and M. B. Strobe, "Microcharacterization of basalt: Considerations for a nuclear waste repository," in *Microbeam Analysis--1983*, 51-53.
7. D. B. Sapik and H. H. Bauer, U. S. Geological Survey, Tacoma Wash., unpublished report.
8. T. L. Wright et al., *Major Oxide, Trace Element, and Glass Chemistry of Columbia River Basalt Samples Collected Between 1971 and 1977*, Washington, D.C.: U. S. Geological Survey, Open-file Report 79-711, 1979.

TABLE 1.--Mean formulas for smectite and clinoptilolite computed from EDS analyses.

Smectite -	$(\text{Na}_{.1}\text{Ca}_{.1}\text{K}_{.1})(\text{Mg}_{.7}\text{Fe}_{1.1}\text{Al}_{.4})\text{Al}_{.4}\text{Si}_{3.6}\text{O}_{10}(\text{OH})_2$	(n=40)
Clinoptilolite -	$(\text{Na}_{.9}\text{K}_{.9}\text{Ca}_{.5})\text{Al}_3(\text{Al}_{.6}\text{Si}_{1.4})\text{Si}_{13}\text{O}_{36}\cdot 12\text{H}_2\text{O}$	(n=30)

TABLE 2.--Average changes in major element chemistry in altered fragments and vesicle scrapings relative to bulk samples. Values reported as ratios of altered fragment to bulk sample on a water-free basis.

	Si	Al	Fe	Mg	Na	Ca	K	Ti
Palagonitized fragments from well cuttings	1.10	0.97	1.42	1.39	0.20	0.24	0.35	0.80
Scrapings of vesicles from rock cores	1.15	0.60	1.35	1.70	0.41	0.40	1.25	0.50

QUANTITATIVE COMPOSITIONAL AND MORPHOLOGICAL CHARACTERIZATION OF SANDSTONES BY BACKSCATTERED ELECTRON IMAGE ANALYSIS

A. Dilks and S. C. Graham

The backscattered electron (b.e.) imaging mode of the scanning electron microscope has received relatively little attention to date in mineralogy, but promises to be extremely valuable for large-area mineralogical characterization from the standpoints of both composition and morphology.¹

In this paper we describe a quantitative method for both compositional and morphological characterization of sandstones by means of a Kontron SEM-IPS image analyzer coupled directly to a JEOL JXA 733 scanning electron microscope equipped with an annular, semiconductor backscattered electron detector. The method, involving intermediate image storage and parallel-array processing, has many advantages, including precise definition of segmentation thresholds, the quantitative separation of the phases with the same gray level but different morphologies, the rapid acquisition and analysis of data, and the retention of the two-dimensional image information that after segmentation can be quantified within the realms of mathematical morphology.² Both the compositional and morphological analyses are capable of being fully automated.

Experimental

The oil-reservoir sandstone studied in this work was from the North Sea basin and was prepared as a flat polished section as follows. A small piece (ca 15 mm cube) of the sandstone was immersed in Araldite epoxy resin and placed in a vacuum chamber and cycled between atmospheric pressure and ca 0.2 Torr three times to remove trapped air from the specimen and to impregnate it with the resin. This vacuum impregnation of the sandstone increases its mechanical stability during subsequent preparation, and provides a constant, dark gray level for the pores in the b.e. image. After curing overnight, a flat section of the sandstone was exposed by sectioning with a diamond saw and the surface was polished successively with decreasing grades of Hyprez diamond paste and finished with 1/4 μm diamond. Finally the specimen was coated with ca 15 nm of evaporated carbon to avoid electrical charging problems and mounted in the horizontal plane in the SEM. The signal from the b.e. detector was amplified to give a dynamic range of ca 0-6 V and was fed both to a digital voltmeter for calibration purposes,¹ and to the analog-to-digital converters at the input of the image analyzer. The images were stored and processed as 512×512 by 8 bit pixel arrays giving a resolution of 256 gray levels.

Results and Discussion

Compositional Analysis. Figure 1(a) is a backscattered electron image of an area ca 1 mm square of the sandstone specimen. Since the sandstone was carefully polished flat, the contrast in Fig. 1(a) is due almost entirely to the different compositions of the phases³ (so-called atomic-number contrast) and the distinction of the phases in the image is quite striking. The minerals identified by electron-probe microanalysis (EPMA) point analyses of several particles are indicated. The brightest particle is zircon and then, in decreasing backscattered electron intensity, we have pyrite, anatase, potassium feldspar, quartz, kaolinite, and, appearing black in the image, epoxy-resin-filled porespace.

The pixel intensity histogram of the image displayed in Fig. 1(a) is plotted in Fig. 2. As might have been expected, the histogram is highly structured, consistent with the large

The authors are at Shell Research Ltd., Thornton Research Centre, P.O. Box 1, Chester, England CH1 3SH.

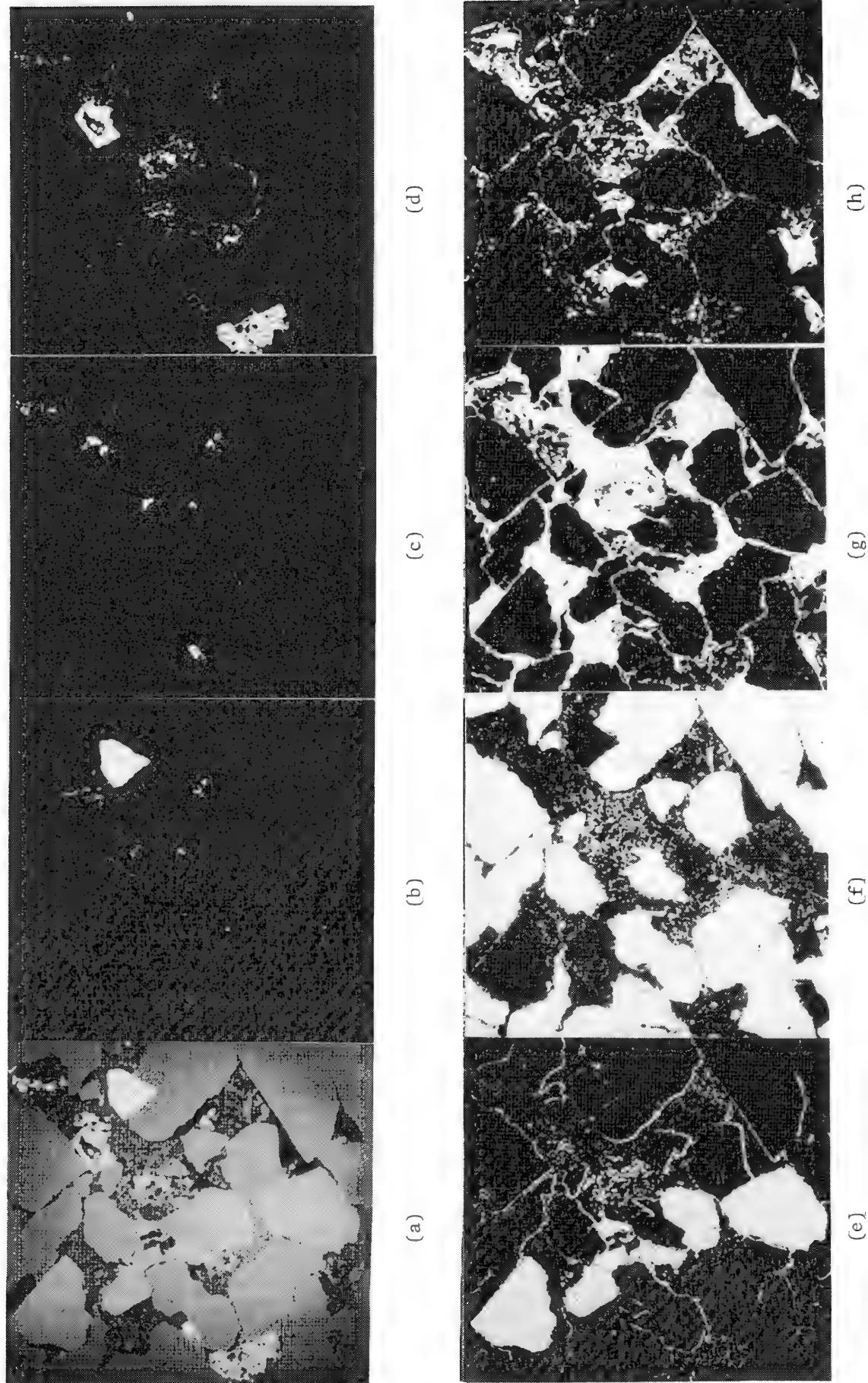


FIG. 1.--Digitized backscattered-electron image of 1×1 mm area of sandstone section. Segmented binary images obtained from (a) by application of thresholds defined in Fig. 2 are shown in: (b) zircon, (c) pyrite, (d) anatase, (e) potassium feldspar, (f) quartz, (g) kaolinite, (h) pores.

variety of phases in the image. The extreme sharpness of the peak for quartz at 100-101 units demonstrates the high contrast uniformity throughout the image.

The sharpest peaks in the histogram occur for the solid, relatively large detrital grains, quartz, potassium feldspar, and zircon, and these peaks tail off more slowly on the higher intensity side (right) than on the lower intensity side (left). By examination of the image using the zoom and cursor-gray-level-direct-readout facilities of the image analyzer we found that the high-intensity tail is due to enhanced backscattered electron emission from the edges of the grains in contact with epoxy-resin in the pores which, by virtue of its low average atomic number, offers a less absorbing pathway for the escape of backscattered electrons. For the potassium feldspar, anatase, and zircon, this tail does not interfere very much with any other phase and the amount of pyrite present is generally small throughout this sandstone.

The gray level of quartz on the other hand is close to that of potassium feldspar and, as can be seen from the histogram in Fig. 2, the high-intensity tail of the former extends significantly beneath the peak of the latter. Coupled with the fact that quartz is the most abundant mineral in the sandstone, the contribution of quartz to the segmented image for the feldspar is unacceptably high and must be removed by a mathematical opening^{1,2} transformation performed on the binary image before measurement of the feldspar area (i.e., the quartz outlines and feldspar particles having the same gray level are separated, based on their respective morphologies in the image; see Fig. 1e).

The kaolinite exhibits a very broad distribution of gray levels because the particles are small and approach in size the sampling volume ($\sim 0.2 \mu\text{m}$ dia. $\times 1 \mu\text{m}$ deep) of the backscattered electron imaging mode. Thus the volume from which backscattered electrons are collected for a single pixel in the image often contains both kaolinite and pore (epoxy resin) and thus has an intermediate gray level. However, this distribution of gray levels has been demonstrated¹ to fall off rapidly above the calculated gray level for pure kaolinite, as might have been expected, and has a negligible effect on the quartz peak (Fig. 2).

Based on the careful consideration of pixel intensity histograms of several image fields, segmentation thresholds were set to define windows in the gray-level spectrum for each mineral phase. These thresholds are shown in Fig. 2 and the corresponding segmented, binary images from Fig. 1(a) are shown in Figs. 1(b)-(h).

The measurement of the area for each phase is then straightforward: the image analyzer counts the number of white pixels in each binary image. The opened binary image was used for potassium feldspar and the difference in area between the opened and direct binary images for this segmentation window was added to the quartz area measured, since this difference represents quartz outlines. In this study we have analyzed 36 image fields, each $1 \times 1 \text{ mm}$, spread over a total area of 60 mm^2 ; the results are summarized in Table 1. For comparison we have included in Table 1 the results from an EPMA point count (500 equally spaced points) of the same area of the sandstone.⁴ The agreement between the two sets of results is very good.

Morphological Analysis. We have quantified the morphology of the various phases in the sandstone specimen under investigation in this paper by applying a series of two-dimensional (2-d) openings to each phase,¹ as described by Serra.² This method complies with our criteria that it must be totally objective and amenable to automation in a way that implies that the images themselves need never be viewed by an operator. The same mathematical operation is performed on every pixel in the images and there is no need to separate or identify individual particles or features. We find this approach particularly useful for describing pore structures where an analogy with particle sizing does not exist.

The opening transformation operates on a binary, segmented image of a given mineral phase (Fig. 1) and first erodes the image with a given structuring element, then dilates it with the same element.² All features smaller in size than the structuring element disappear and the difference in area of the white phase in the transformed and original images is a measure of the total quantity of these features. By repeating this operation with a series of structuring elements of increasing size [in this work we have used squares of $(2n + 1) \times (2n + 1)$ pixels] a histogram of total area of features of given size against the size can be plotted that describes the 2-d morphology of the phase.^{1,2} Rapid quantitative analysis of the mineral phases in sandstones can therefore, in principle, be obtained by this morphological opening procedure since little or no interaction with an operator is required.

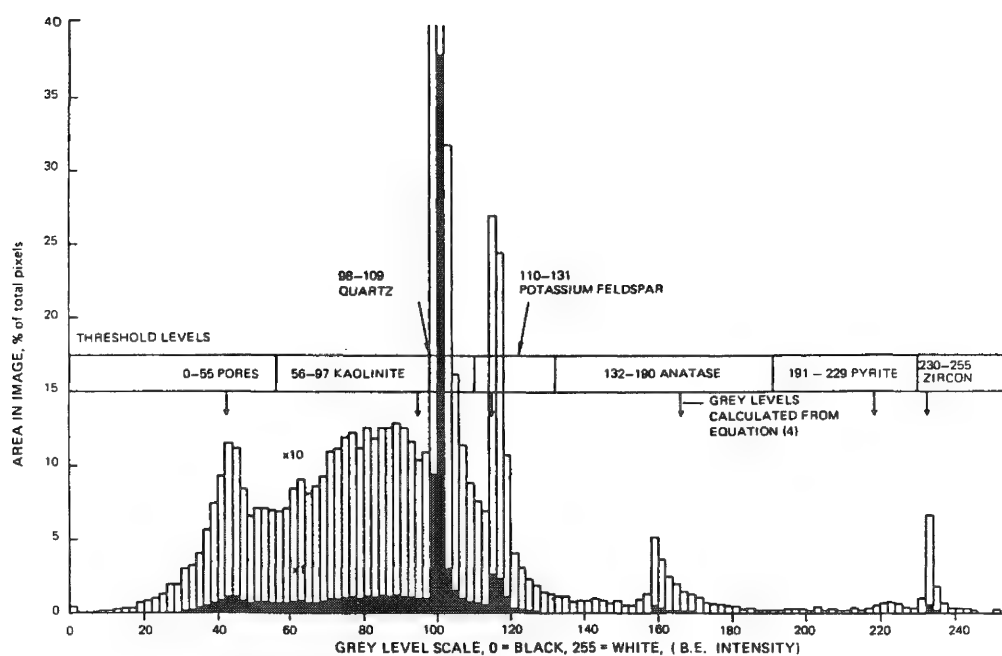


FIG. 2.--Pixel intensity histogram for image in Fig. 1(a).

TABLE 1.--Results of compositional analysis compared to results obtained by EPMA point counting.

Mineral phase	Quantity determined by b.e. image analysis, %		Quantity determined by e.p.m.a. point counting, %	
	Mean	St. error	Mean	St. error
Pores	8.6	0.4	9.3	1.3
Kaolinite	17.9	0.6	12.8	1.5
Quartz	65.5	1.1	66.8	2.1
Na-feldspar ^a	-	-	2.0	0.6
K-feldspar	6.8	1.0	7.3	1.2
Anatase ^b	1.0	0.1	1.5	0.5
Pyrite	0.16	0.03	0.4	0.3
Zircon	0.06	0.04	0.1	0.1

a) Na-feldspar is not distinguished from quartz in the b.e. image analysis since their back-scatter coefficients are very similar.

b) Includes a small amount of apatite in both analyses.

Both particles and pores can be characterized; for example, Fig. 3(a) shows the histogram of 2-d openings for the pores in the sandstone averaged over 12 image fields. The histogram for the actual porespace is sharply peaked at the origin, clearly indicating the spikiness of the larger pore shapes and the large number of small pores; this interpretation is confirmed by comparison with Fig. 1. The concept of particle size is not clear cut for the pores, not least because there is no simple idealized structure for the pores similar to that of spheres for quartz grains, for example. Nevertheless, even for totally connected porosity the 2-d morphological opening procedure provides a quantitative analysis that can be summed over many image fields to produce a characteristic histogram for the specimen. Furthermore, given the existence of some model that has pore throats, channels, and cavities, for example, the experimentally obtained histogram can be compared with that generated from the model. Figure 3 provides an interesting comparison of the morphology of the actual pores in the sandstone with that of the potentially available porespace based on the sandstone with all the kaolinite removed. The latter hypothetical situation was achieved by segmenting the images between gray levels of 0 and 97 (see Fig. 2), which includes the kaolinite that is then reassigned as further porespace. In going from Fig. 3(a) to Fig. 3(b) the increase in total area beneath the histogram is about a factor of 3, which corresponds to the increase in porosity. The change in the shape of the histogram, however, corresponds to the change in 2-d morphology, which is intimately related to permeability. In Fig. 3(b) the pores are not only bigger but have much more open and rounded structures.

Conclusion

Backscattered electron imaging in the scanning electron microscope provides a powerful method for quantitative analysis of sandstones when coupled directly to a parallel-array-processor-based image analyzer. Compositional analysis can be achieved by segmentation and measurement of the area of each phase in the image, and the results can be averaged over many fields covering a large area of the specimen. Agreement with point-counting methods is found to be very good. Two-dimensional morphological analysis can be achieved completely objectively by the method of 2-d openings and again the information can be readily summed over many image fields, giving a totally representative description of the sandstone section.

References

1. A. Dilks and S. C. Graham, submitted to *J. Sedimentary Petrology*.
2. J. Serra, *Image Analysis and Mathematical Morphology*, London: Academic Press, 1982.
3. J. I. Goldstein, D. E. Newbury, P. Echlin, D. C. Joy, C. Fiori, and E. Lifshin, *Scanning Electron Microscopy*, New York: Plenum Press, 1981.
4. A. Dilks, D. Park, and S. C. Graham, *Microbeam Analysis--1984*, 139.

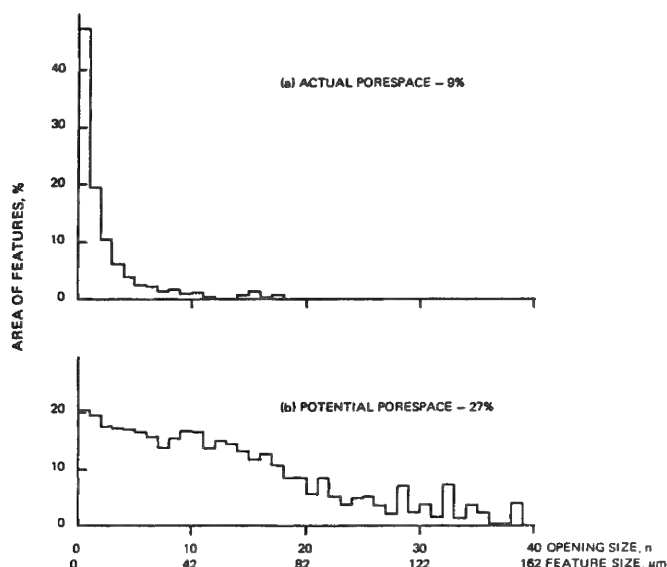


FIG. 3.--Histograms of 2-d openings for actual porespace and potential porespace (clay removed), each summed over 12 image fields.

A METHOD OF COMBATING ALKALI METAL LOSS DURING MICROBEAM ANALYSIS OF BASALTIC GLASS

M. B. Strobe

As part of the U.S. Department of Energy's search for a geologic repository for high-level nuclear waste, the suitability of basalt is being investigated. The Basalt Waste Isolation Project is involved in the characterization of the basalt and associated geologic materials in order to evaluate the feasibility of placing a nuclear waste repository in the basalt beneath the Hanford Site. The microchemical analysis of these materials is an important aspect of this evaluation.

One of the problems encountered in the analysis of glass and plagioclase with an electron microprobe is the migration of alkali metals, notably Na and K, under electron bombardment. Various investigators¹⁻⁵ have studied this migration mechanism and arrived at methods of combating Na and K loss. The techniques used include cooling the sample to cryogenic temperatures, defocusing the electron beam, and mathematical or graphic solutions. All the techniques work but have some drawbacks.

Discussion

Cryogenic cooling does not affect the basic heat-transfer ability of a specimen. The effect is merely one of starting at a lower temperature and thus gaining a little more time to gather data. Many laboratories have no sample cooling devices on their microprobes. Also, cooling the specimen, checking and recording temperature, keeping the dewar filled, etc., constitute delays and details that reduce the efficiency of the data-gathering process, especially when large numbers of samples have to be analyzed.

Varying amounts of calcium, magnesium, and iron in the specimen greatly affect the speed of Na and K migration, which interferes with graphic methods unless standards of very similar composition are run for each and every specimen. This same interference makes mathematic projection of data uncertain. The main problem with defocusing the beam lies in the uncertainty of the area being bombarded at the edges of the beam, and in a repeatable defocusing.

Experiment

A great deal of concern has been expressed by all investigators for obtaining sodium and potassium counts first and quickly. Frequently, beam current is dropped to avoid scaring off the touchy ions. Figure 1 shows the count rates for Na and Si in an albite standard, with a 1 μm diameter beam at 100 nA. Not only is Na depleted but Si counts are increased. Thus, even though Na is analyzed first the results can be erroneous with totals going well over 100%. Other elements (Al, Ca) can be affected as well. When glasses are analyzed and as many as 10 or 12 elements are to be measured, sample irradiation time may be relatively long and increased totals will become evident. Reduction of beam current definitely helps but is often not feasible because trace amounts of elements such as Cr, Mn, Ti, P, S, Cl, and others call for either larger currents or inordinately longer count times.

We have found that by rastering the beam most problems of elemental depletion and enrichment are overcome. At about 20 000 \times , which gives the equivalent of a square area of 5 μm being irradiated, the effect of beam heating is reduced to the point at which damage is negligible for a considerable period of time. A magnification of $\sim 5000\times$ can be used without significant spectrometer defocusing but the area under study is usually small enough to demand 20 000 \times . A 100nA beam spread out over a 25 μm^2 area is reduced to a beam density of 4 nA/ μm^2 .

The author is with the Materials Testing Group of the Basalt Waste Isolation Project of Rockwell International, Box 800, Richland, WA 99352.

Figures 2 and 3 demonstrate the effect of beam rastering on count rate, not only on glass but also on plagioclase, another mineral sensitive to beam heating. With count times of 5 s per element and three spectrometers, data for 12 elements can be gathered in less than 60 s. Typical results are in Table 1.⁶

In addition, when large numbers of points are to be analyzed, the points can be pre-selected if the beam current is lowered to <100 nA, the specimen is inspected in SEM mode, and points are stored to be analyzed later under probe strength currents. For our use, a magnification of not more than 4000× is quite sufficient to observe the basalt thin section and save points. Moving the electron beam across the specimen as suggested by Heinrich⁷ helps to homogenize the standard and assures good standards data from glass and albite standards. A Cameca MBX microprobe with Tracor Northern automation and SANDIA TASK⁸ was used for all analysis.

Summary

The count rate curves for glass and plagioclase clearly show that the method outlined holds alkali elements stable long enough to obtain good data. The table of analysis for basalt glass compares favorably with those of many other investigators.

We have devised a simple, pragmatic approach that can be adopted by any laboratory and gives results equal to other methods. By reducing total count times, analyzing beam-sensitive elements first, using a rastered beam, and preselecting points to be analyzed using a low energy beam, we essentially eliminate alkali metal loss, even when beam currents as high as 100 nA are used.

References

1. M. P. Borom and R. E. Hannerman, "Local compositional changes in alkali silicate glasses during electron microprobe analysis," *J. Appl. Phys.* 38: 2406-2410, 1967.
2. A. K. Varshneya, A. R. Cooper, and M. Cable, "Changes in composition during electron microprobe analysis of K₂O-SrO-SiO₂ glass," *J. Appl. Phys.* 37: 2199-2202, 1966.
3. P. J. Goodhew and J. E. C. Gully, "The determination of alkali metals in glass," *Glass Technology* 15: 123-126, 1975.
4. C. H. Nielsen and H. Sigurdsson, "Quantitative methods for electron microprobe analysis of sodium in natural and synthetic glasses," *Am. Mineralogist* 66: 547-552, 1981.
5. L. F. Vassamillet and V. E. Caldwell, "Electron-probe microanalysis of alkali metals in glasses," *J. Appl. Phys.* 40: 1637, 1969.
6. C. C. Allen and M. B. Strobe, "Microcharacterization of basalt: Considerations for a nuclear waste repository," *Microbeam Analysis--1983*, 51-53.
7. K. F. J. Heinrich, *Electron Beam X-ray Microanalysis*, New York: Van Nostrand Reinhold, 1981.
8. W. F. Chambers, *Sandia-Task '78: An Electron Microprobe Automation Program*, Sand 78-1149, 1978.

TABLE 1.--Basalt glass analysis.

	wt%	σ	Counts per Second per Nanoamp
SiO ₂	62.6	2.0	500.0
TiO ₂	1.6	0.5	5.0
Al ₂ O ₃	13.7	0.7	90.0
FeO	7.8	1.6	35.0
MgO	0.5	0.4	2.5
CaO	3.7	0.7	12.0
Na ₂ O	4.6	0.4	10.0
K ₂ O	2.6	0.3	9.0
P ₂ O ₅	0.7	0.2	0.5
	97.8		

Avg. of 60 points
 $\sigma = 1$ standard deviation

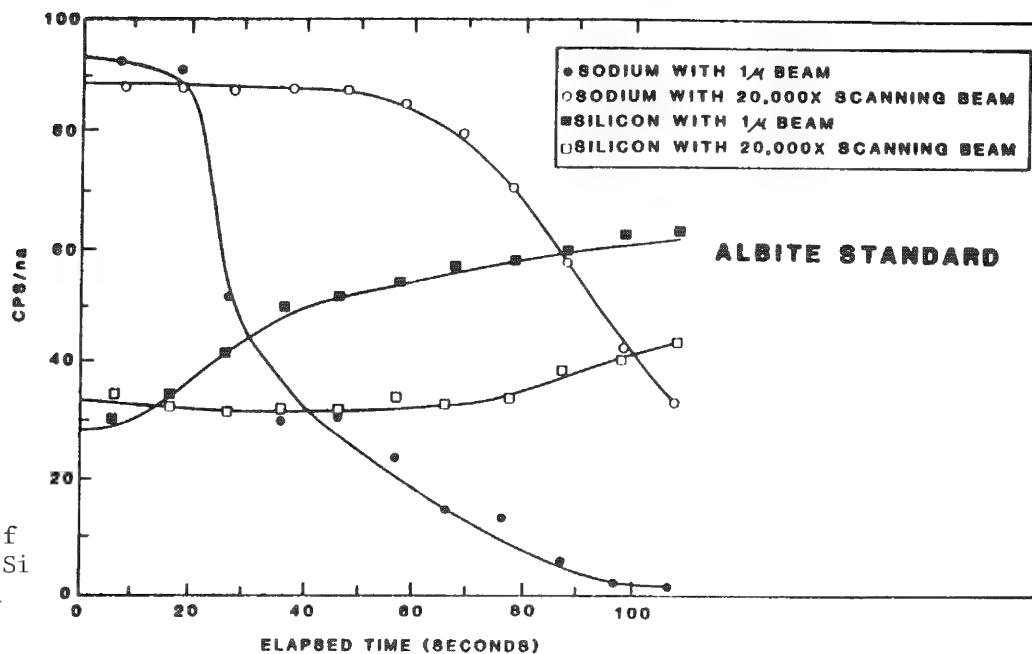


FIG. 1.--Comparison of stability for Na and Si counts with rastered beam and stationary beam.

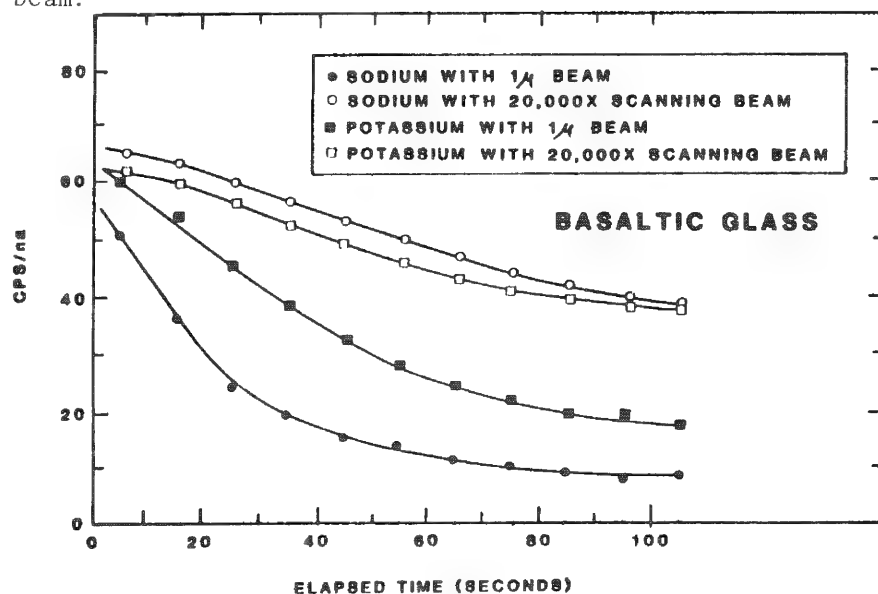


FIG. 2.--Comparison of stability for Na and K counts with rastered beam and stationary beam.

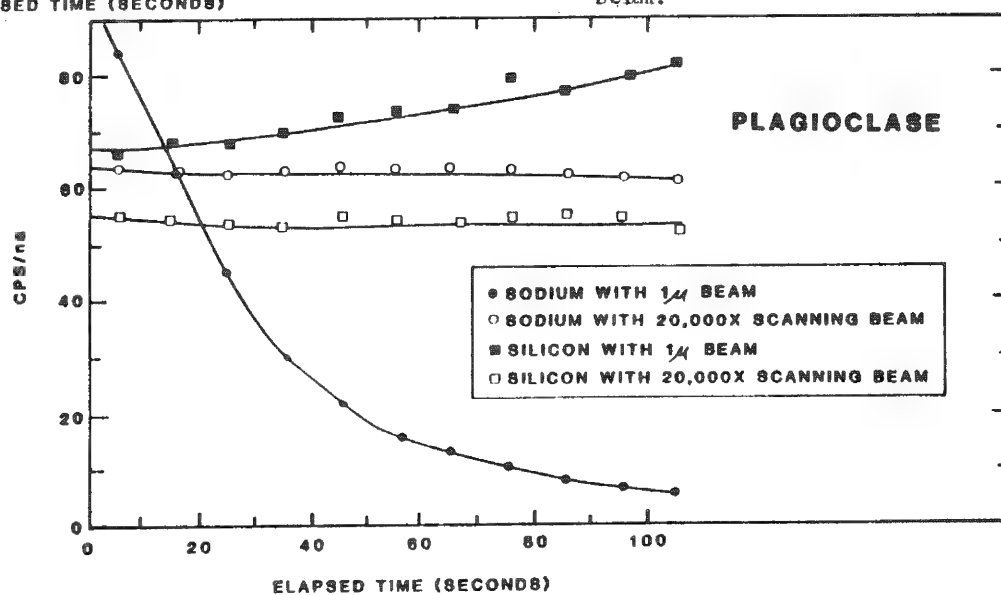


FIG. 3.--Comparison of stability for Na and Si counts with rastered beam and stationary beam.

SEM STUDY OF THE STRUCTURES OBTAINED IN ORE SYNTHESIS TEST: A GENESIC HYPOTHESIS

F. A. Calvo, J. Ma Guilemany, J. Ma Gomez de Salazar

The results obtained during the past few years on the SEM study of the structure of Spanish mercury ores¹⁻³ led us to a hypothesis about the genesis of these ores: either impregnation of a host rock by magmatic (fluid) cinnabar (ores of Almadén, Entredicho, Las Cuevas, Caunedo, Tarna, Soterraña), or condensation of a cinnabar vapor phase (Chovar ore). According to this hypothesis, different experiments on "synthesis" have been carried out, using both molten cinnabar and vapor cinnabar in order to obtain the reimpregnation of an "empty" host rock.

Structures of the Natural and "Synthetic" Ores

Impregnation by Molten Phase. The structure of the natural ores is characterized by the cinnabar being placed allotriomorphically between the crystals, idiomorphic or not, of the host rock minerals. Although there is no coherence between the cinnabar and these minerals, both are in very close contact, which makes the ores very compact. On the surface of the massive cinnabar, the most small details of the crystals can be seen reproduced as if they were "cast" in cinnabar (Fig. 1).

For the synthesis experiments of impregnation by molten cinnabar, a vertical furnace was designed equipped with thermal cycling programming. Maximum testing temperatures were between 800 and 850 C. Demineralized samples of Almadén ore were used for remineralization experiments.

The mercury sulfide and quartzite samples were placed inside a closed quartz tube under vacuum (0.01 Torr.) Reimpregnation took place under HgS vapor pressure at the working temperature.

The product ("syntheticose") obtained has the following characteristics:

1. Cinnabar is allotriomorphic to the constituents of the host rock (Fig. 2); compare with the natural ore (Fig. 1).
2. There is no cohesion between the cinnabar and the crystals of the host rock (Fig. 3); compare with the natural ore (Fig. 4).
3. Transcrystalline fracture in cinnabar, either in natural ores or in the synthetic, shows a similar morphology.
4. Quartz crystal surfaces were not affected by temperature during the synthesis process (Figs. 2 and 3).
5. Cinnabar in the syntheticose follows the contour of the crystals of the host rock (Fig. 5) as it does in the natural ore (Fig. 6).
6. Quartz crystals appear "cast" on cinnabar in natural ore (Fig. 7). However, in the "synthetic ore" the "casting" we are getting is less perfect (Fig. 8). The imperfect reproduction is explained by the lack of fluidity or pressure due to the experimental conditions.
7. Polycrystalline and polyhedral cinnabar was found in the synthetic ore as it was in nature.

Impregnation in Vapor Phase. In Chovar ore, cinnabar mineralizes an argillitic rock, in the form of microcrystals 0.4 μm in size (Figs. 9 and 11).

Various devices were set up to vaporize HgS, which eventually would condense on previously demineralized argillites. The HgS was introduced in glass tubes which were heated up; its vapor diffused to various compartments into which demineralized argillite had been introduced. The glass tubes were closed under vacuum (0.01 Torr).

Depending on the condensation temperature a great many solid forms of HgS were obtained.

Authors Calvo and Gomez are at the Departamento de Metalurgia, Facultad de Ciencias Químicas, Universidad Complutense, Madrid 3, Spain; author Guilemany is at the Departamento de Metalurgia, Facultad de Química, Universidad de Barcelona.

Some of them are very similar to the HgS crystals found in Chovar ore. Particular characteristics of the condensation products out of the HgS vapor phase were:

1. Cinnabar was deposited in a powdery form on top of the argilitic rock (Fig. 10). Cinnabar does not fill up the cavities of the rock, just as is the case in the mineralization of the natural ore (Fig. 9).
2. The cinnabar so deposited is resolved into polyhedral microcrystals (Fig. 12), as is observed in the natural ore (Fig. 11).
3. There is no coherence between the cinnabar and the rock crystals.

Conclusions

1. The structure of the "synthetic ore" obtained by impregnation of quartzite rocks by molten HgS seems to confirm the proposed genetic hypothesis for the Spanish mercury ores; i.e., mineralization by fluid cinnabar of magmatic origin.
2. Experimental HgS deposits on demineralized argilitic rock from HgS vapor support the genetic hypothesis of the peculiar Chovar ore being mineralized by HgS vapor of magmatic origin.

References

1. F. A. Calvo, J. Ma Guilemany, and J. Ma Gomez de Salazar, "The contribution of SEM-EDAX and EPMA to the study of the structure and genesis of Spanish mercury ores," *EUREM Electron Microscopy 1980/I*, 456-457.
2. F. A. Calvo, J. Ma Guilemany, and J. Ma Gomez de Salazar, "Microstructure of Entredicho mercury ore (Ciudad Real, Spain)," *Microbeam Analysis--1982*, 435-440.
3. F. A. Calvo, J. Ma Guilemany, and J. Ma Gomez de Salazar, "The application of SEM and XRMA to the study of the structure and composition of Spanish mercury ores: A genetic hypothesis," *Scanning* 5: 32-38, 1983.

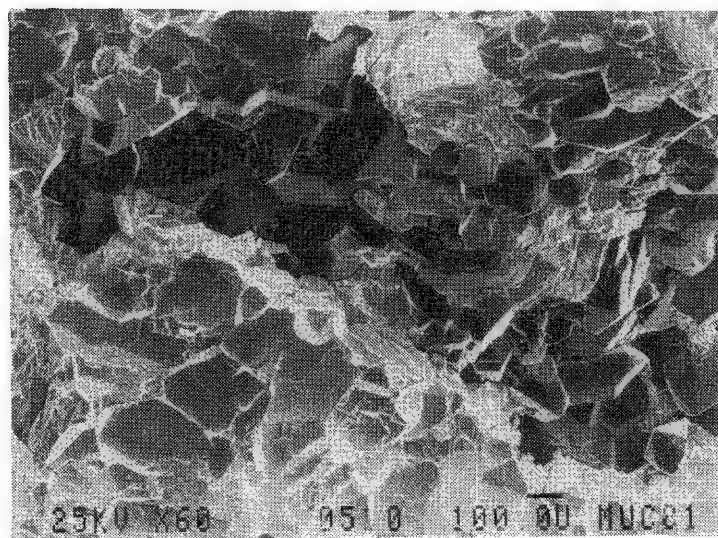


FIG. 1.--Entredicho ore: allotropic cinnabar in quartzite. ($\times 60$.)

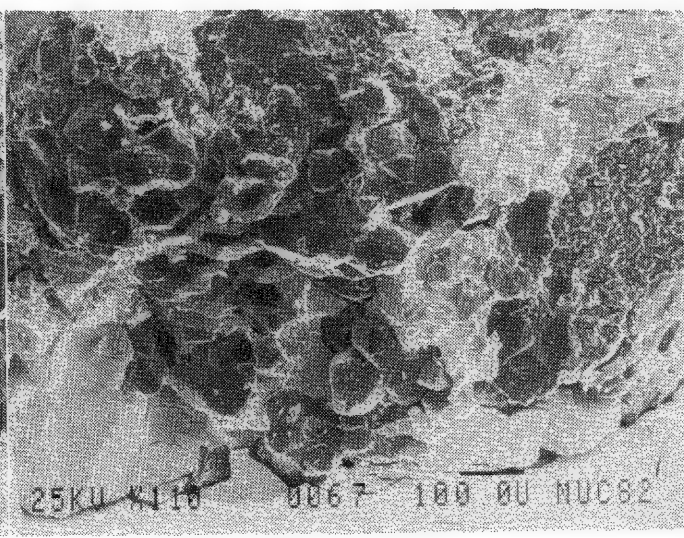


FIG. 2.--"Synthetic" ore: allotropic cinnabar in previously demineralized quartzite. ($\times 110$.)

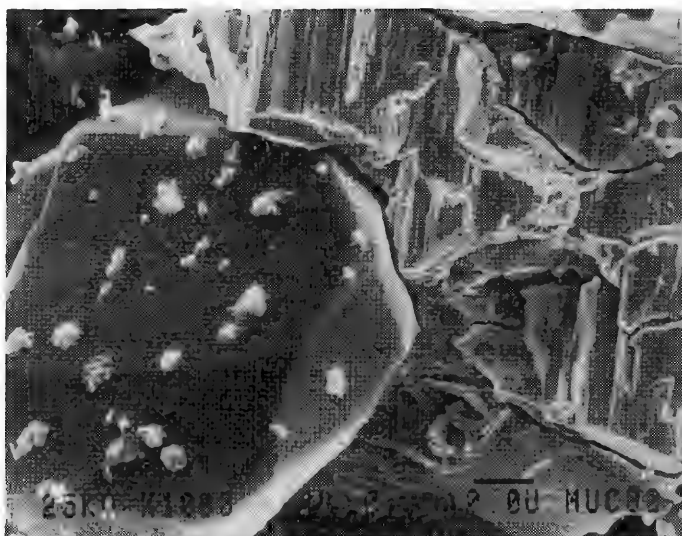


FIG. 3.--"Synthetic" ore test: incoherence between cinnabar, allotriomorphic cinnabar, and quartz. ($\times 1000$.)

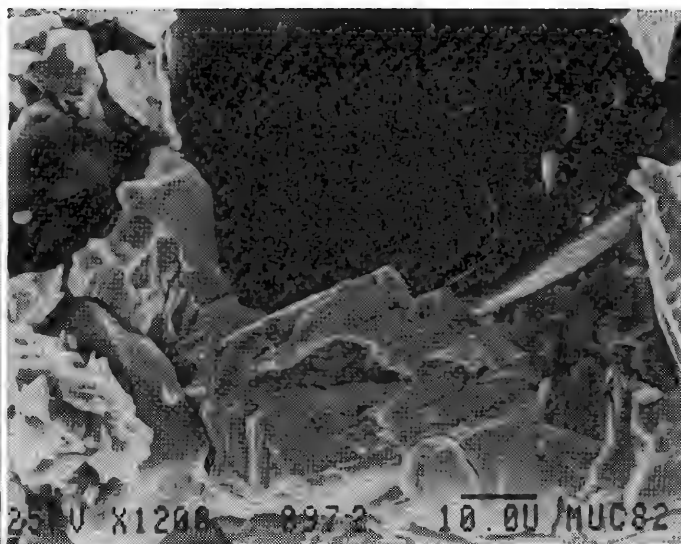


FIG. 4.--Usagre ore: incoherence between cinnabar and quartz. ($\times 1000$.)

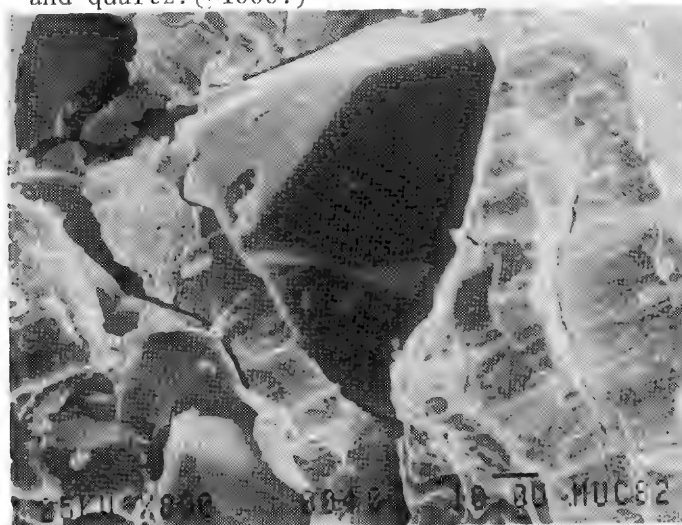


FIG. 5.--"Synthetic" ore: quartz crystals being cast on cinnabar. ($\times 800$.)

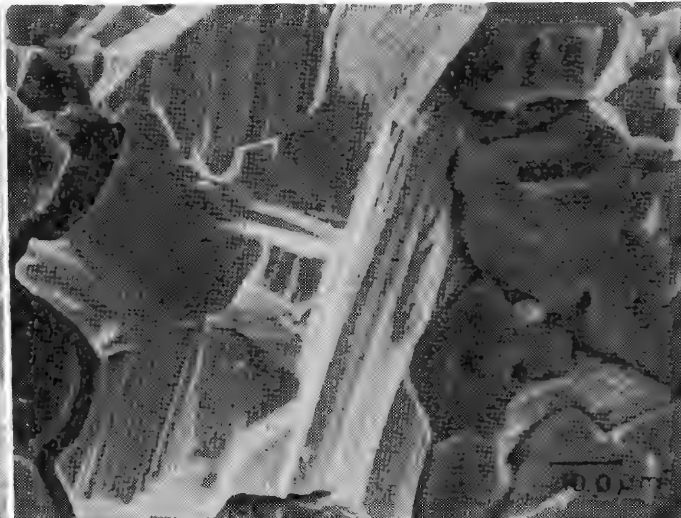
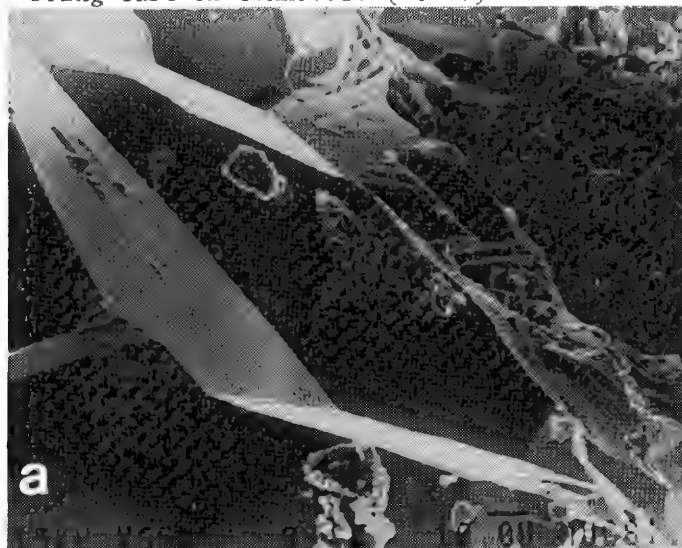


FIG. 6.--Tarna ore: quartz crystals being cast on cinnabar. ($\times 1275$.)



a



b

FIG. 7.--Entredicho ore: (a) quartz crystals; (b) "cast" on cinnabar of quartz crystals in (a). ($\times 650$.)

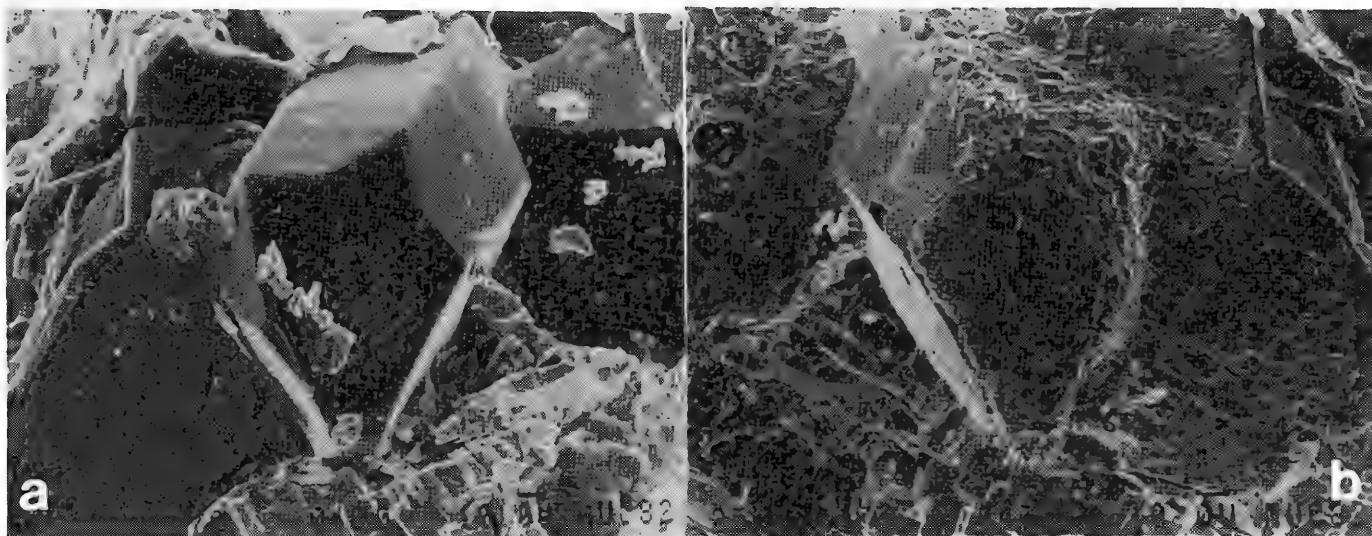


FIG. 8.--"Synthetic" ore: (a) quartz crystal; (b) "cast" on cinnabar of quartz crystal in (a). ($\times 470$.)

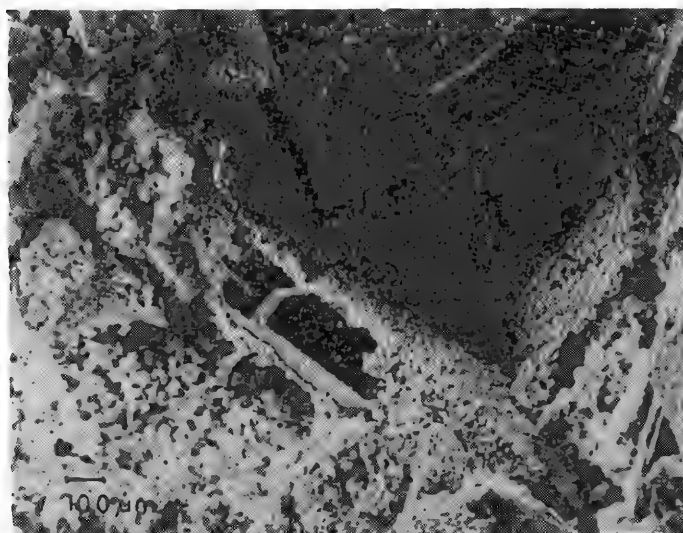


FIG. 9.--Chovar ore: microcrystals of cinnabar on quartz crystals of argilitic rock. ($\times 500$.)

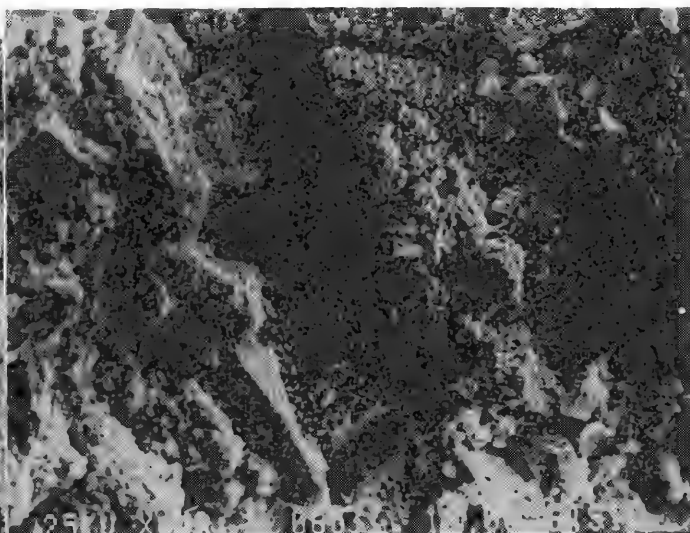


FIG. 10.--"Synthetic" ore: microcrystals of cinnabar obtained by HgS vapor condensation on quartz crystals of demineralized argilitic rock. ($\times 400$.)

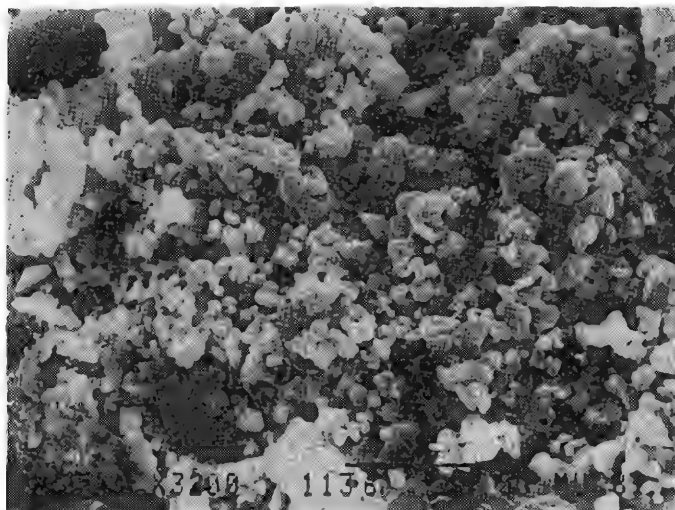


FIG. 11.--Chovar ore: detail of microcrystal-line cinnabar deposit. ($\times 3200$.)

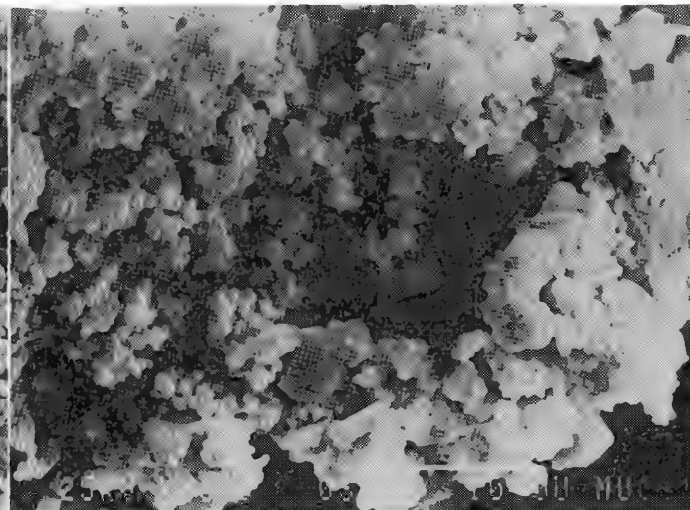


FIG. 12.--"Synthetic" ore test: polyhedral microcrystals of cinnabar obtained by HgS vapor condensation. ($\times 3600$.)

10 Image Analysis

ENHANCEMENT AND COMBINATION OF X-RAY MAPS AND ELECTRON IMAGES

J. Christian Russ and John C. Russ

We have previously described methods for manual and automatic measurement of video images obtained from scanning electron microscopes.^{1,2} The manual techniques require the operator to mark, outline, or select features using a light pen or graphics tablet while viewing the image on a video monitor, whereas the automatic methods first store the image internally within the computer memory and then discriminate features from background or each other using the gray scale (64 brightness levels) at each point of the image (256 points wide).

When the image is stored internally, it becomes possible to carry out various image processing steps,³ including the combination of one image with others previously acquired and stored (internally or on disk). Initially this was done as a precursor to image measurement, i.e., for better discrimination of the features to be counted and measured. Actual use has shown that in many cases the processing and combination steps produce images that reveal their content information to the operator's view better as well. Redisplay of the processed images (using either gray scale or false color) and hard-copy printouts of the images may in some cases be the desired end result of the processing, rather than further measurement steps.

Each image requires 64K bytes of internal storage. In the computer we are using (Apple IIe with extended memory and peripheral cards for video interfacing, RGB or gray display controller, fast co-processor, large-capacity disk drives, etc.), two such images can be stored, along with the programs. This memory is used as a primary image page and a secondary one. All operations (smoothing, differentiation, etc., as will be described) are carried out on the primary image, which can also be moved to or swapped with the secondary one. The images may also be added, in fractions of 1/4, 1/2, or 3/4. Along with storage or recall to/from disk, this feature allows rather flexible image manipulation.

In addition to the gray-level images, the programs can also derive and manipulate binary (black/white) images. These occupy only 8K of memory, and are normally used for feature counting and measurement, by selecting a gray scale range to encompass the features of interest. They can also be combined and manipulated in several useful ways. For example, Fig. 1 shows a binary image from pigment particles in a secondary-electron image. The particles have a distinct brightness as compared to the substrate, and so can be readily distinguished. However, the edges are quite rough, and some of the features touch each other (which causes errors in counting or measuring them). This problem can be alleviated with an etching and plating operation, as shown in the figure. Individual picture points (pixels) along the periphery of each feature are removed or added according to a simple algorithm that counts the number of touching neighbors, with the result that smoother outlines and separation of contacts is obtained.

Typical x-ray "dot" maps can also be processed by this method. Sparse dot maps generally have disconnected points. A "plating" operation expands each point and produces filled areas, as shown in Fig. 2. These features are then enlarged relative to the original feature. However, the logical AND of the derived ("filled") dot image with the smoothed binary electron image reveals only features that contain the element of the original x-ray map. This information can be used for measuring purposes, for instance to obtain a size-distribution plot for the sulfur-containing pigment particles.

The programs also allow other logical operations (NOT, OR, Exclusive-OR), and sequences of stored images may be used, so that more elaborate combinations of elements, and images recorded using other signals in the SEM can be combined as required.

The most common operations carried out on the gray-scale images are noise smoothing and

Author J. Christian Russ is at the University of Michigan, Ann Arbor; author John C. Russ is at North Carolina State University in Raleigh.

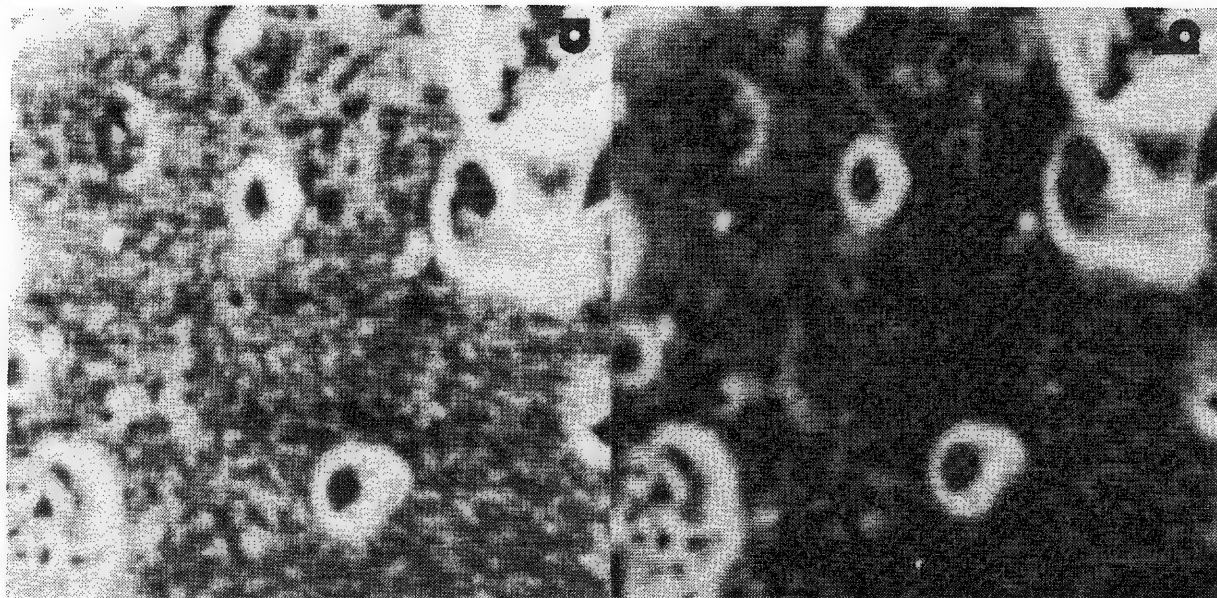


FIG. 3



FIG. 2

FIG. 1

edge sharpening. The former operation is appropriate both for "noisy" secondary electron or backscattered electron images, and for x-ray dot images where the number of recorded pulses is great enough to produce a gray scale. (The number of x-ray counts at each image point is taken as the brightness value. For most real images, this may require extremely long recording times; even then, the counting statistics are poor and the image is "noisy.") Smoothing simply replaces the brightness of each point with a weighted average of that and its neighbors, a direct two-dimensional analog to the smoothing commonly applied to energy-dispersive x-ray spectra. Depending on the weighting factors, the amount of smoothing (and concurrent loss of lateral resolution) can be controlled. Figure 3 shows an example.

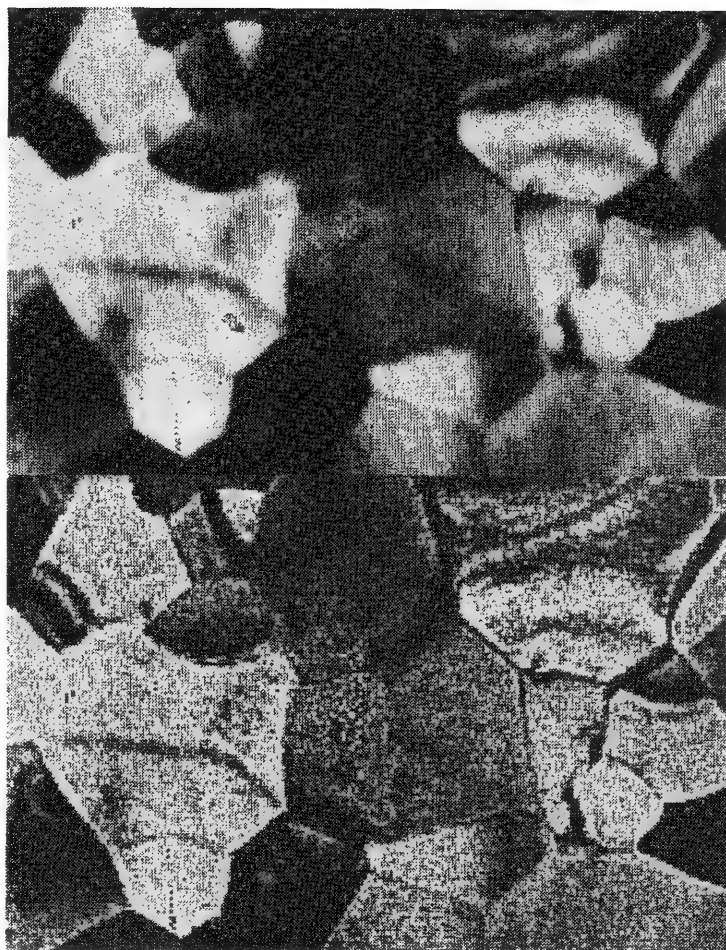
Edge sharpening is carried out in similar ways, with Laplacian operators on each image point and its neighbors. Depending on the values used in the operator, it is possible to suppress the original gray scale of the image completely and keep only edge information, or to retain varying amounts of the gray scale to improve recognition of the features in the image. Figure 4 shows an example. Many other operators can be applied, among them texture extractors (to reveal structure in the image that has a particular orientation, but may be visually hidden by the clutter of other information in the original image), and directional differentiation (to create a pseudo-three-dimensional relief effect).

In addition to the processing of the image, redisplay of the stored gray-scale information can be carried out by use of either gray-scale substitution or false color. The substitution of gray-scale values allows any portion of the original gray-scale range to be expanded, either linearly or logarithmically, to cover the full brightness range of the display. An additional mode, histogram equalization, shifts the brightness values nonlinearly to devote equal areas on the displayed image to each brightness level. This procedure expands the local brightness range (to show details) in regions of rapid change. Figure 5 shows the effect of shifting gray scale to separate features from background, for the same specimen described in Figs. 1 and 2.

There seems to be great interest in displaying false-color images. It is technically very easy to do, by use of standard RGB video display monitors and controllers. Instead of a translation table from one shade of gray to another, the table contains the colors that correspond to various brightnesses in the original image. With the controller we are using, up to sixteen display colors can be selected from a palette of 4096 shades and colors. If these colors are arranged in a logical progression (e.g., varying in brightness for a single color, or shading gradually from one color to another), the images still look quite "normal" and can be visually recognized, but they really do not show any more information than the original gray-scale image. On the other hand, when bizarre colors are used (e.g., 16 large steps around the color wheel), the visual image is broken up. Normal features become difficult to recognize, but small brightness variations, which may correspond to information that is hard to discern in the original image, become evident. This mode of operation is useful in only very limited cases. (Note: because of reproduction costs, no color images are included in the printed paper, but were shown at the meeting presentation.)

References

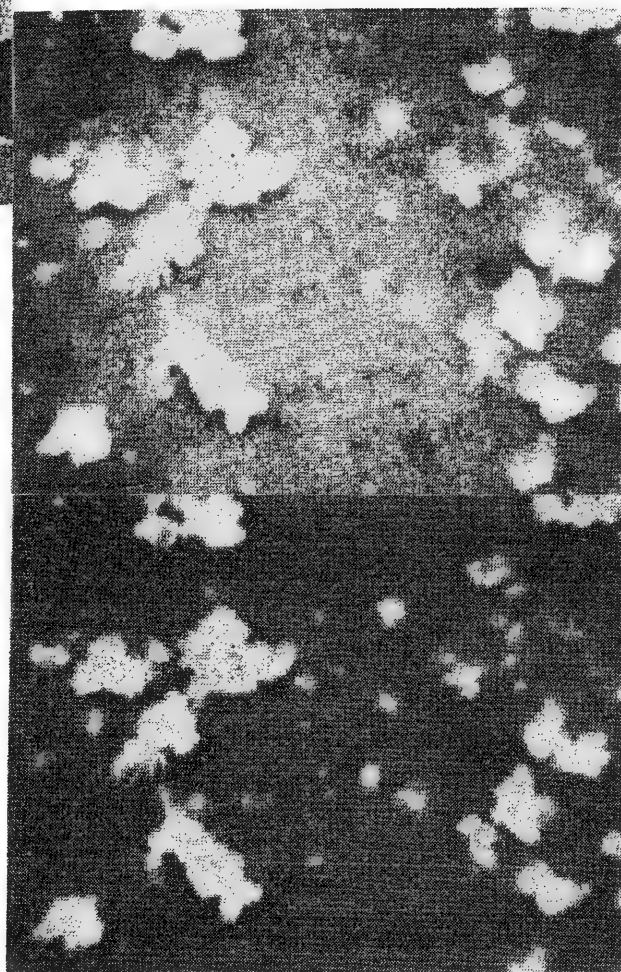
1. T. M. Hare, J. C. Russ, and J. C. Russ, "Image measuring algorithms for a small computer," *Microbeam Analysis--1982*, 509-516.
2. J. C. Russ and W. D. Stewart, "Quantitative image measurement using a microcomputer system," *American Laboratory*, Dec. 1983, 70-75.
3. J. C. Russ and J. C. Russ, "Image processing in a general purpose microcomputer," *J. Microscopy*, in press.



(a)

(b)

FIG. 4



(a)

(b)

FIG. 5

QUANTITATIVE ANALYSIS OF POSITIVE BATTERY PLATES BY MEANS OF BSE IMAGE ANALYSIS

T. P. Remmel and T. D. Kirkendall

Nickel-hydrogen (Ni-H₂) battery cells, offering improved performance and higher energy density per pound, are rapidly replacing nickel-cadmium as the main power storage medium for longer-life spacecraft applications.¹ The positive plates used in the Ni-H₂ cell consist of a nickel screen substrate, which acts as the backbone for a sintered nickel-powder network that is about 80% porous. Nickel hydroxide, which is electrochemically impregnated into the pores of the plate, serves as the active material for the cell. Distribution of the various components throughout the thickness of a plate affect its performance; therefore, the ability to measure the active material and void distributions is important in assessing the effect of variables in the impregnation process and in correlating component distributions with cell performance.

By quantitative image analysis, techniques were developed to measure the distribution of the components through the cross section of the plate. Backscattered electron (BSE) images of metallographically polished sections of the plates were digitized and gray-level analyzed to discriminate between the three components--nickel sinter, nickel hydroxide, and void. Quantitative analysis for intensity levels corresponding to the three components on a line-by-line basis yielded the distribution of the three phases through the thickness of the plate.

Method

A Tracor Northern (TN) Digital Beam Control System was used to digitize 256 × 256 pixel images with an 8-bit analog-to-digital converter on the video (BSE) signal.² The image acquisition software used was the TN Image Processing Program (IPP) with in-house routines written for image analysis and data output. The PDP-11/23-based computer system, with 128 kbytes, has sufficient memory for the image and operating software to be resident during processing. Archival storage is on either a 30-Mbyte Winchester or a 0.5-Mbyte floppy disk.

The analysis and processing of a battery plate image are shown in Fig. 1. A digitized BSE image of a polished plate section taken at about 1000× magnification is shown in Fig. 1(a). The white areas of the image correspond to the nickel sinter, the gray to the nickel hydroxide, and the black to the voids. The gray-level histogram for the 65 536 pixel image is shown in Fig. 1(b). Peaks corresponding to the three components of the plate are clearly distinguished. By segmentation of the 256 levels of the histogram into three intensity windows encompassing the peak, all pixels of the image can be identified with one of the three plate components. Thus, the image in Fig. 1(a), which contains about 200 gray levels, can then be transformed into an image with only three levels (Fig. 1c). Once transformed, data in the image can be readily processed and analyzed, and calculation of the area fractions of the three components is a trivial matter. Also, different intensity transforms can be used to display photographically the components separately or in combination (Fig. 1d).

Distribution Profile Analysis

An analog BSE image of a cross section of the entire positive battery-plate thickness is shown in Fig. 2. The circular wires of the nickel substrate screen are evident. Measurement of the distribution of the three components across the thickness of the plate is similar to that discussed above, with a few modifications. The magnification used is much lower,

The authors are with COMSAT Laboratories, Clarksburg, MD 20871. This paper is based on work performed at COMSAT Laboratories under the sponsorship of the Communications Satellite Corporation.

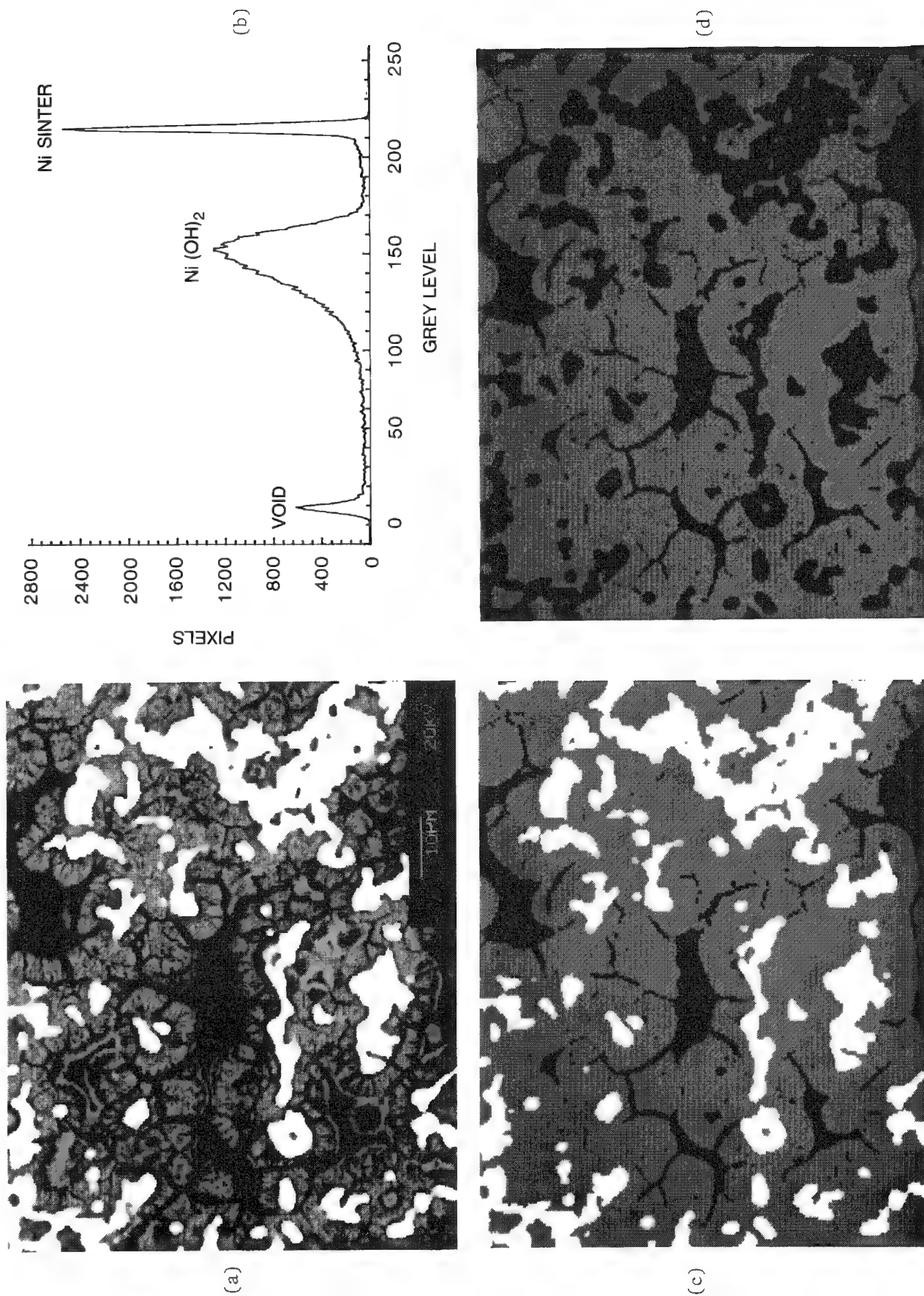


FIG. 1.--Analysis and processing of battery plate image: (a) 256 × 256 pixel, digitized BSE image of sectioned positive battery plate; (b) gray-level histogram of BSE image in (a); (c) BSE image of (a) after gray-level transformation into three levels corresponding to Ni (white), Ni(OH)₂ (gray), void (black); (d) processed BSE image showing only gray phase of (c) representing distribution of Ni(OH)₂.

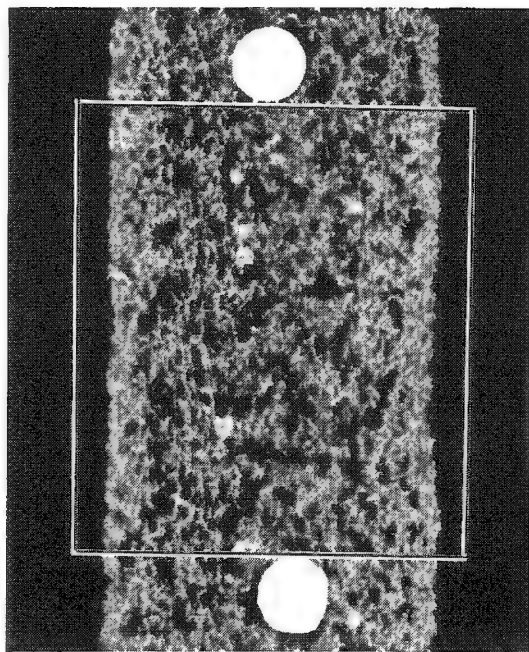


FIG. 2.--Analog BSE image of positive battery plate cross section

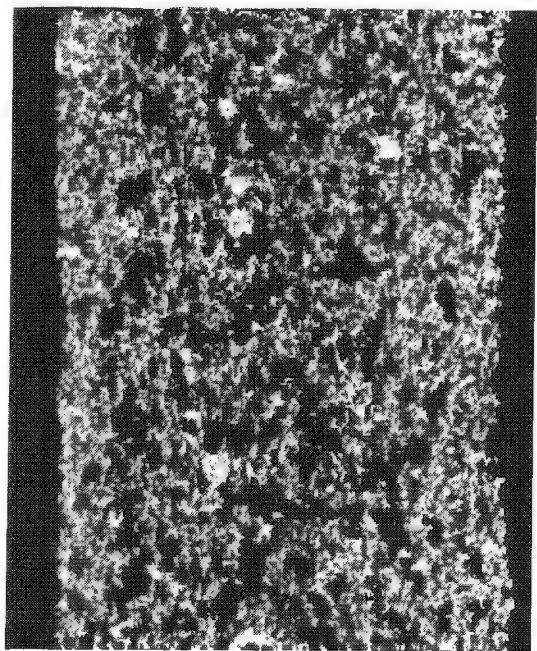


FIG. 3.--256 \times 256 pixel, digitized image of area defined by rectangle in Fig. 2

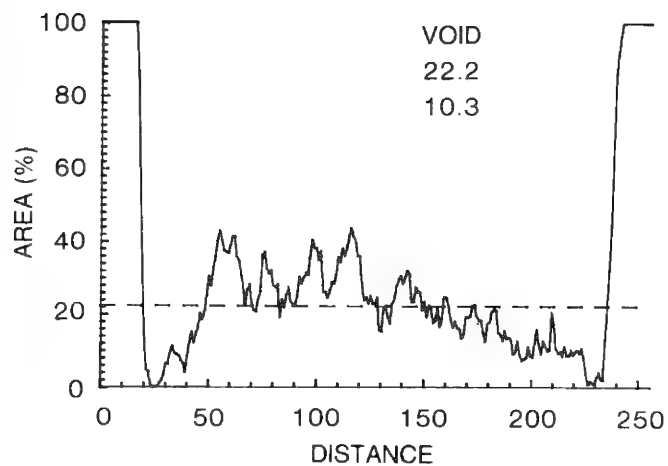
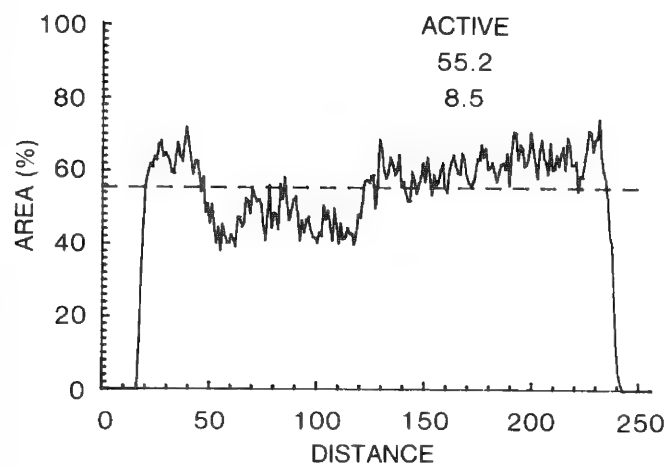
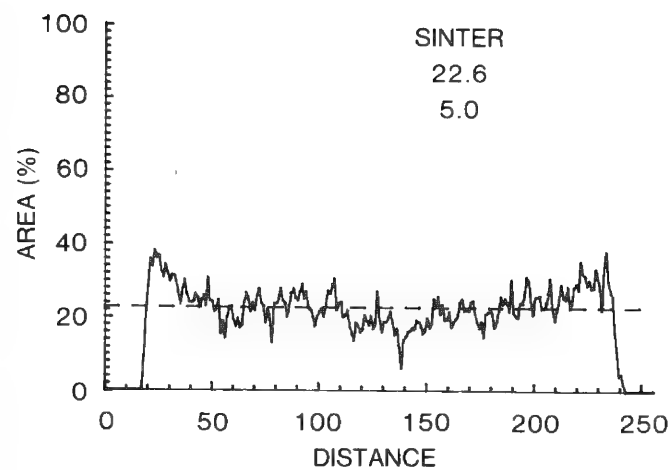


FIG. 4.--Distribution profiles for sinter, active material, and void for image in Fig. 3.

about 60 \times , with the image including the full thickness of the plate but excluding the substrate wires, as shown by the white rectangle in Fig. 2. At this magnification, the pixel size is the same order of magnitude as the nickel sinter ($\sim 5 \mu\text{m}$); therefore, the image becomes a statistical sampling of the battery plate components. The digitized image corresponding to the area defined in Fig. 2 is shown in Fig. 3. Histogram analysis and image intensity transformation are accomplished as described previously. To measure the distribution of components in cross section, image analysis is conducted in a line-by-line mode, with the area fractions of the three components calculated for each line of the image (256 in all). These area fractions are then plotted against distance through the plate (in this case, arbitrary units are used) to yield distribution profiles of the three components.

Statistical analysis of each profile is performed to yield the mean and standard deviation of the component fractions across the thickness of the plate. Distribution profiles of the three components for the digital image in Fig. 3 are shown in Fig. 4. Distance zero corresponds to the left side of the image; 255 corresponds to the right side. Dashed lines represent the mean area fraction across the plate. The numerical value of the mean is listed immediately beneath the component description, along with the standard deviation. Typically, to improve statistics, three areas of a plate are analyzed and the profiles combined to form an average profile that is representative of the plate.

Conclusions

A method has been developed to perform quantitative analysis and transformation of BSE images. Measurement of component distribution profiles through positive battery plates by this method has proved to be useful in the evaluation of electrochemical factors that affect impregnation and battery life. The method could be applied to any multiphase system that exhibits distinct gray-level separation of its phases with the BSE imaging mode. However, this technique uses only a fraction of the potential of quantitative image analysis. More sophisticated processing algorithms could be applied to derive additional morphological characteristics of the images, such as texture or periodicity.^{3,4}

References

1. J. D. Dunlop and J. F. Stockel, "Nickel-hydrogen battery technology--development and status," *J. Energy* 6(No. 1): 28-33, 1982.
2. J. J. McCarthy, G. S. Fritz, and R. J. Lee, "Acquisition, storage, and display of video and x-ray images," *Microbeam Analysis--1981*, 30-34.
3. N. K. Tovey and V. N. Sokolov, "Quantitative SEM methods for soil fabric analysis," *SEM/1981 I*, 537-554.
4. A. V. Jones and K. C. A. Smith, "Image processing for scanning microscopists," *SEM/1978 I*, 13-26.

SOME EXAMPLES OF THE USE OF DIGITAL IMAGES ON CAMEBAX

Danièle Benoit, Michel Blanc, and Laurent Lugand

Most EDS manufacturers are now developing image analysis programs for size classification of various phases or automatic x-ray analysis of particles. At IRSID an SEM and an image analyzer (Leitz texture analyzer) are used in the study of materials such as sinter at high magnification.¹ The Camebax-Microbeam system has also been used for two applications in this field, with off-line image processing on a VAX computer. The first is the use of digital x-ray maps for the study of microsegregation in steel when large areas of the specimen are to be observed. The possibilities of high stable beam currents and good peak-to-background ratios offers some advantages for the EPMA + WDS analysis over a SEM + EDS configuration. The second application concerns the digitalizing of electron images and their processing to obtain some metallurgical parameters.

Digital X-ray Maps for the Study of Solidification Structures in Steels

Aims. For studies of carbon steel brittleness occurring during slab cooling, some experiments on unidirectional solidification have been carried out to go further into solidification modeling; the specimen is quenched from a partially solidified state. The observation of samples taken perpendicularly to the growth direction enables the morphology of the dendritic structure and its evolution to be determined, as well as the lateral growth of the dendrites and their mean perimeter values. Applied to the continuous casting process, this method is used to evaluate the possibility of breaking the dendrite tips by liquid stirring to obtain a large zone of equiaxed crystals, and to evaluate the fluid flow of segregated liquid in the interdendritic channels. All these parameters can be measured on x-ray maps but some of them probably could be determined by linear analysis.

Improvements in Camebax Software. For the recording of raw intensities, only the size of the matrix and the counting time per point have been changed in the standard MICMAP program. Variable matrix sizes up to 256^2 points are allowed with an optional choice of distance between points and lines. The MAP2D visualization has been modified for graphics display on a Benson plotter connected to the VAX computer (Fig. 1). The reasons are file size and processing time. A new three-dimensional visualization program has been written, which is useful in the identification of the formation of minor phases such as manganese sulfides (Fig. 2).

Measurement of perimeters that could be performed with the contour-following algorithm used for isoconcentration visualization is a pixel-to-pixel method that consumes a long CPU time. Furthermore, this is not the right perimeter for solidification models because it includes the length of all pseudopodes that appear during the quench. That is why, in order to obtain specific dendrite perimeters, size of primary dendrite arms, and solid and liquid fractions, a VAX image processing has been developed.

Numerical Treatment of Camebax X-ray Maps. There is indeed an efficient and simple method for evaluating the perimeters in a binary image. It consists of measuring the number N_L of 0-1 transitions per unit length averaged over several directions; the perimeter per unit area is then equal to πN_L .²

The first problem in obtaining a satisfactory binary image is the choice of the threshold. It must tally with the solid concentration at the solid-liquid transition, which is easily determined from precise linear analysis. For maps, it is not feasible to spend a

The authors are with IRSID, F-78105 Saint Germain-en-Laye, France. The experimental help of MM. Blaizot and Petitgand is gratefully acknowledged.

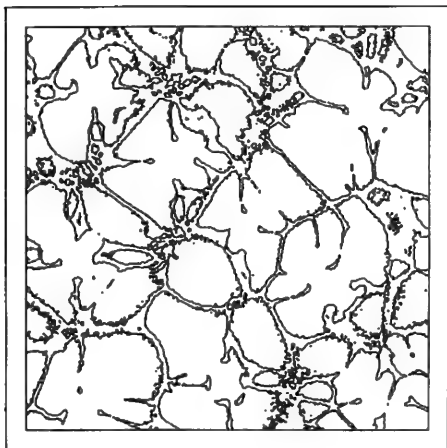


FIG. 1.--Two-dimensional graph (MAP2D type) 256^2 image of Mn $(1.28 \text{ mm})^2$.

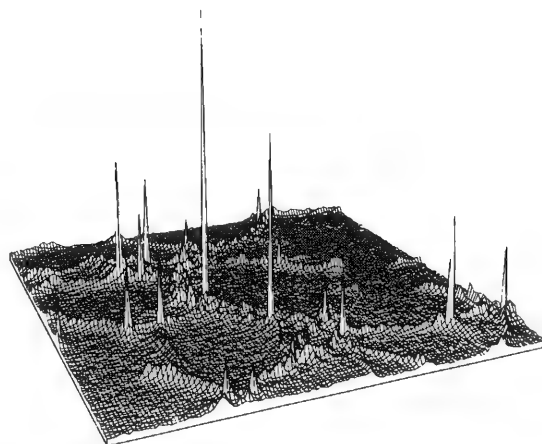


FIG. 2.--Three-dimensional graph 118^2 image of Mn $(590 \mu\text{m})^2$.

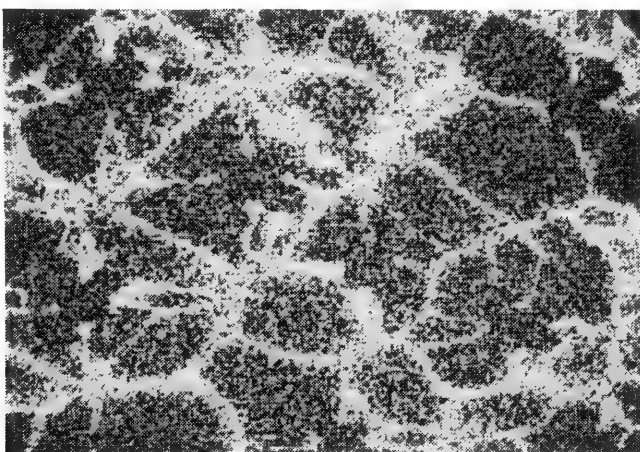


FIG. 3.-- 256^2 raw image of Mn as visualized on VAX, 1 s/point.

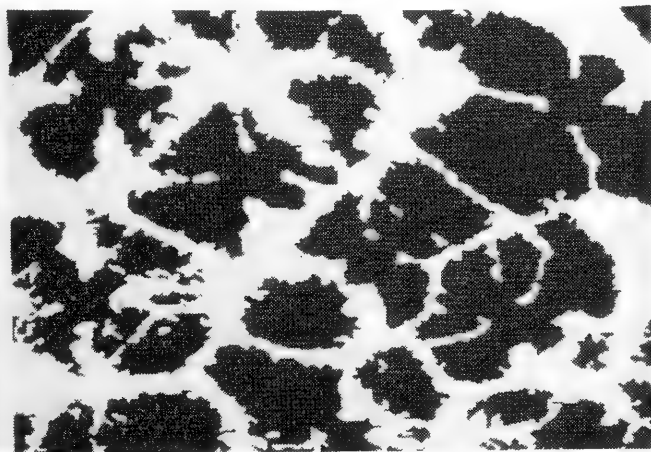


FIG. 4.--Image of Fig. 3 after VAX processing.

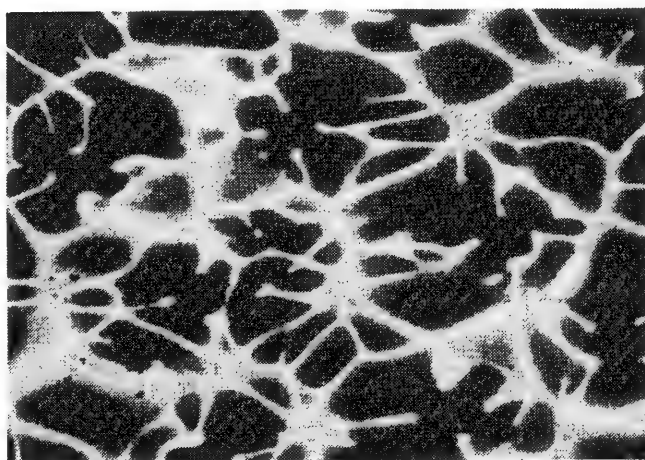


FIG. 5.-- 256^2 raw image of Mn recorded with 3 s/point.

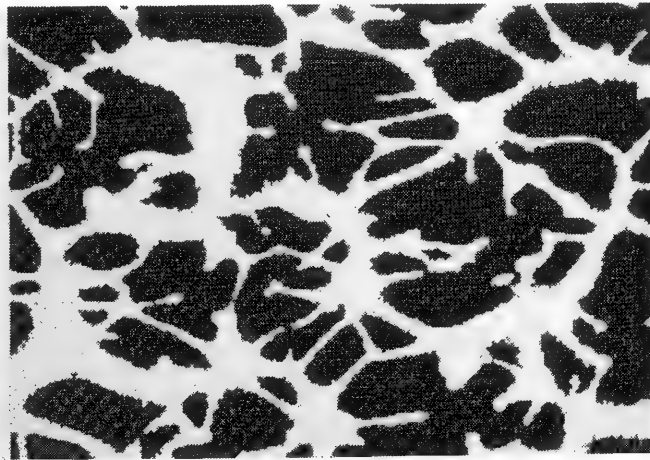


FIG. 6.--Image of Fig. 5 after VAX processing; counting-time effect, cf. Fig. 4.

long time per point, so that the quality of the binary image is impaired by the counting statistic noise. When the counting time is 1 s, the signal-to-noise ratio is too poor for the later processing (Figs. 3 and 4). A time of 3 s yields an acceptable contrast (Fig. 5) and has been chosen for this study despite the resulting long recording time.

To reduce the effect of the remaining noise as well as the contribution of the pseudopores on the length, we apply a low-pass filter on the digital image and a "closing" (dilation followed by erosion) on the thresholded image (Fig. 6).

Digital Crystalline-contrast (CC) Pictures for a Study of Sheet Steel Recrystallization

Aims. To optimize the manufacturing of deep drawing steels, one must determine the temperature of recrystallization in continuous and batch annealing processes. Quantitative optical metallography is generally inadequate when precise determination of the beginning and the end of recrystallization is necessary (Figs. 7 and 8).³ Numerical processing of CC images on the VAX has been applied to this problem for future adaptation to on-line processing with an SEM instrument.

Software Development on Camebax-Microbeam. An original program has been written to record digital electron images. It simply uses the MICBEA library. The monitoring of the beam is done on a square grid; for most applications a 512^2 pixels image with 256 gray levels gives good results. Multiple recording per point can be performed if the signal is too noisy.

Identification of Recrystallized Grains in Deformed Areas on the VAX. Although relatively easy to identify with the naked eye, the various types of grains cannot be readily characterized in a form that is suitable for a computer. The recrystallized grains have two main properties: relatively uniform gray levels and polygonal shapes. In the case of the image shown in Fig. 9, this latter property could not be used because many of the grain boundaries are interrupted by etch-pitting. The local variation of gray level has thus been used to identify the grains.

First, a median filter is introduced to reduce the high-frequency noise. The processing is then based on the thresholding of variance over adjacent pixels (Fig. 10). The large areas of low variance corresponding to recrystallized grains are assigned to a black level; unrecrystallized areas with high variance are represented by a mixture of small black and white spots. To eliminate the latter a dilatation is performed, black spots smaller than the minimum surface of a grain are removed, and erosions are performed to compensate for the previous dilatation and eliminate the noise in the grains. The recrystallized grains appear black on a white background (Fig. 11). The processing time is about 6 min CPU on the VAX 11/780 for a 512^2 image.

Conclusions

We have shown how x-ray and electron image processing can be used in some metallurgical applications. Programs written for x-ray map analysis could be applied to any other analytical technique with the same data recording scheme. Programs used for electron image recording will be later used for automated analysis of phases detected by their gray levels. The same electron-image processing will be used for SEM or TEM pictures. At IRSID we plan to interconnect all these instruments to the VAX via Ethernet and to improve the image processing speed.

References

1. Dominique Jeulin, "Morphological SEM picture processing," *J. Microscopie et Spectroscopie Electroniques* 8: 1-18, 1983.
2. E. E. Underwood, *Quantitative Stereology*, Reading, Mass.: Addison-Wesley, 1970.
3. Jean Philibert and Roland Tixier, "Effets de contraste cristallin en microscopie électronique à balayage," *Micron* 1: 174-186, 1969.

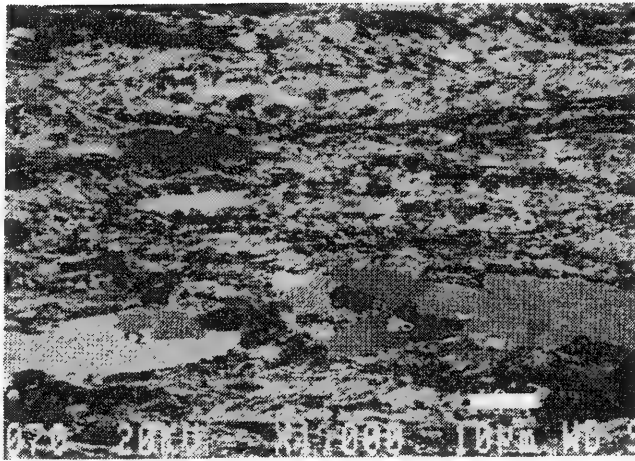


FIG. 7.--Crystalline-contrast picture of low-carbon steel sheet at beginning of recrystallization.

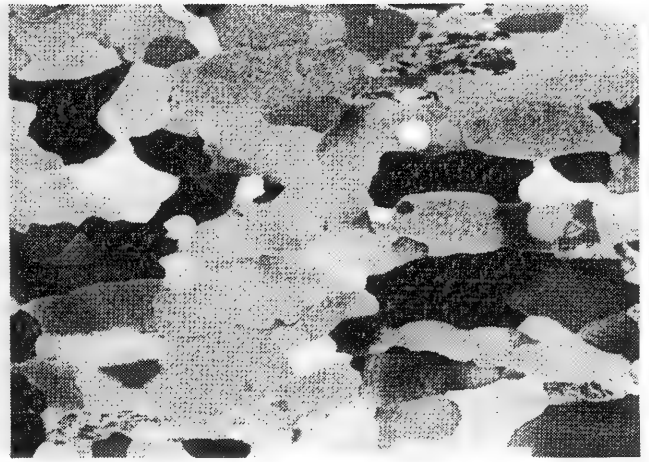


FIG. 8.--Crystalline-contrast picture of low-carbon steel sheet at end of recrystallization.

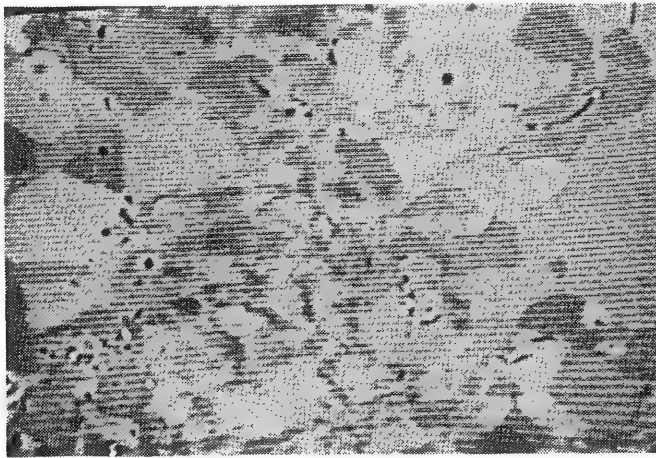


FIG. 9.--Raw digital electron image as visualized on VAX, 512^2 pixels.

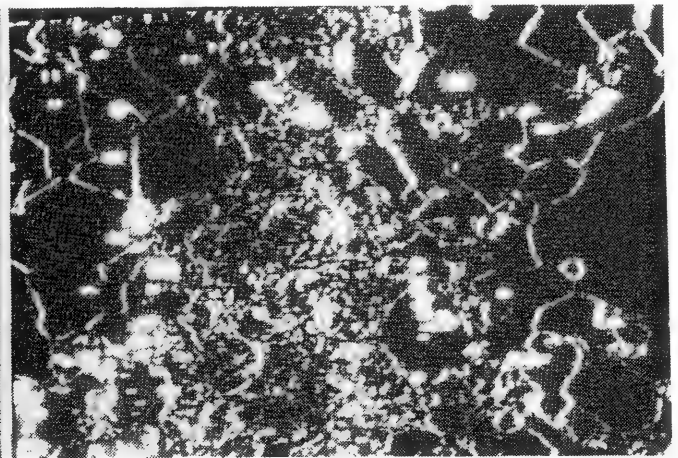


FIG. 10.--Local variance image of electron image shown in Fig. 9.

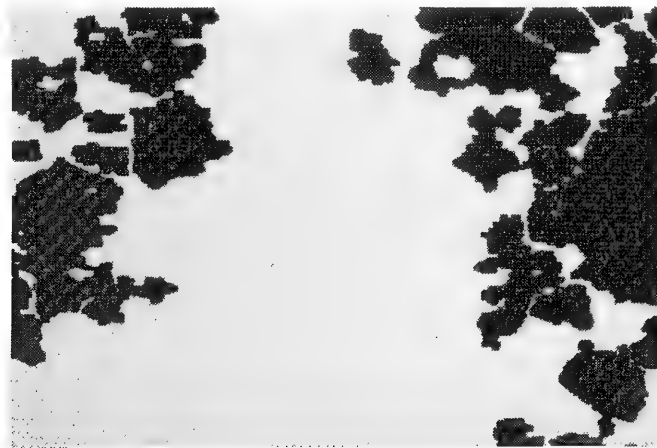


FIG. 11.--Final image showing recrystallized grains fraction.

COMPUTER MATCHING TWO DIFFERENT IMAGES OF THE SAME PARTICLE FIELD

D. S. Bright

In analytical microscopy, images taken from a variety of instruments are stored on mass storage and transferred to a computer for processing and analysis. When comparing these images under computer control, one often has the problem of matching images of the same field of view taken from different instruments where nonlinear geometric distortions occur. Often we wish to analyze the data with as little human intervention as possible. The situation described below involves the chemical analysis of inorganic particulate matter, where we seek to determine the nature of the particles themselves and not their positions as such. The images are presented in the computer as 512×512 pixel arrays, where each pixel (or dot in the image) can have an intensity in the range of 0 to 255 and where the particles under analysis are represented by groups of contiguous pixels with intensity levels that are sufficiently different from the relatively constant background intensity to distinguish them from the background. The first stage of analyzing the images is to form a binary image by choosing an intensity threshold such that the computer is able to separate the particle pixels from the background pixels. The TEM and SEM images that have been overlapped in Fig. 1 are typical results of thresholding. Once the images are thresholded so that the operator is satisfied that the particles in question are represented in each image, the matching is at-

The case in point is where two images of particles on a substrate were taken with an analytical electron microscope. One image was taken in the STEM (transmission) mode and the other was taken in the SEM backscatter mode. A detector near the sample is charged when the SEM image is being taken, and is neutral otherwise. The charged detector causes enough nonlinear distortion of the SEM image to prevent superposition of the two images by translation, rotation, and scaling.

Solution

Although the distortion over the whole image is large, it is relatively small for small pieces of the image: corresponding small areas of each image are *almost* superimposable. Therefore, reliable matches can be made if they are done over small overlapping areas and one at a time. One accomplishes this goal by representing each image as a list of objects, each characterized by its size and position. It is these objects that are manipulated and matched, rather than portions of images represented by arrays of pixels. This methodology has been used successfully with a different matching algorithm.¹

The two images were preprocessed to provide binary images (SEM and TEM parts of the figure) that represented the particles in the original images, by thresholding to select all the particles with little (but not zero) noise in the background. An area of the image corresponding to a particle is usually covered by a group of pixels that are above threshold and that are all contiguous. (That is, they are all interconnected via the 4-neighborhood of each pixel.) Such groups of pixels that form connected homogeneous regions of the image we call *blobs*.

The matching algorithm uses two lists of blobs, where each blob is given a unique name and represents a particle or noise. Associated with this name are various characteristics of the particle such as its area and centroid.

The problem can then be represented in this way:

- (a) given a list of particles in the form of blobs from the TEM image, and a similar list from the SEM image,
- (b) return a list of matched particles, i.e., a list of pairs of names where the members of the pair denote the same particle in the two images.

How the Matching Algorithm Works

Correspondence of particles in the images is generated from three particles at a time. If three particles in one image correspond with three in another, then they represent the

The author is with the Center for Analytical Chemistry, National Bureau of Standards, Washington, DC 20234.

same three actual particles. Considering the triangles formed by the centers of the three particles in each image, we note that

(a) the lengths of the sides of the two triangles correspond (we assume the images to be of approximately the same scale; if not, the matching algorithm can be used with minor changes);

(b) the angles match (which eliminates chances of mirror images of triangles being matched accidentally); and

(c) the areas of the blobs will correspond, where ratios of areas of corresponding blobs are compared because the TEM images are solid but the STEM images are hollow (Fig. 1), have fewer pixels, and thus have less area.

Based on the above criterion for matching, a search is first done to find an initial set of three blobs in one image that corresponds to a similar set in the other image. This triplet is used to begin the set of matched blobs. This matched set is used as a basis for testing the remaining unmatched blobs one at a time.

To get the initial matched set of three particles, the largest blob in each list is chosen and two neighboring blobs are sought to confirm the match. If no such neighbors can be found, then the largest blobs in each list do not correspond and the search continues with the largest blob in one of the lists discarded. Then if there is still no match, the largest blob in the other list is discarded, and so on.

After the initial match is found, one proceeds with the matching by taking an *unmatched* blob from the first list as a candidate along with its two closest *matched* neighbors and looking for the corresponding *unmatched* blob in the second list, using the corresponding two *matched* neighbors in the second list for triangulation. If a match is found, the new matched blobs are put in the matched set. If not, the unmatched blob from the first list is discarded.

This process continues until no more blobs remain to be matched in one of the lists.

The matching of distances, angles, and sizes are all measured to within predefined tolerances. The performance of the matching algorithm does not appear to be sensitive to these tolerances, as they were set once when the system developed and were not changed thereafter. This is an important advantage and will be tested as more types of images are matched.

The result of the match is shown in Fig. 1, in which a line has been drawn between the particle center positions in the TEM and STEM image for each particle. The result is clearer when all three figures are superimposed and viewed in color as is the practice in our laboratory.

References

1. R. C. Bolles, "Robust feature matching through maximal cliques," in *Imaging Applications for Automated Industrial Inspection and Assembly*, SPIE 182: 140-149, 1979.
2. Details of the algorithm are to be published soon by the author.

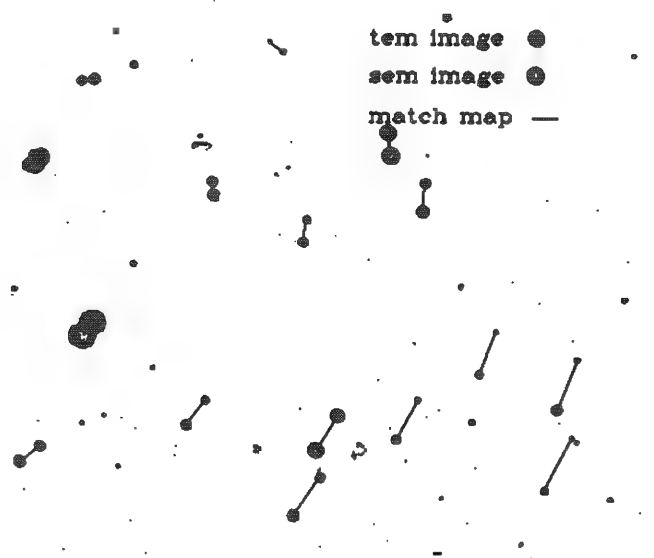


FIG. 1.--SEM and TEM thresholded (binary) images superimposed on match map that connects images of corresponding particles with straight lines. The two images can be distinguished because TEM particles appear solid and SEM images appear as rings. Note that simple rotation about large particles to upper left that are nearly overlapping will not bring SEM and TEM images into registration.

CHOICE OF COLOR SCALES IN ANALYTICAL MAPS

K. F. J. Heinrich and C. E. Fiori

The use of colors to represent information from electron probe area scanning was first advocated by Duncumb¹ and is now widely practiced.² We consider here the special case in which a predefined set of colors is used to represent levels of one parameter such as signal intensity or concentration of one element in a specimen.

Scales of this type are frequently used in a wide variety of maps, from representation of geographic variables (e.g., distribution of precipitation, altitude, or mean temperature over a geographic area) and images of celestial signals--such as x rays--to pictures of human and animal bodies, in function of a signal such as irradiated heat of nuclear magnetic resonance. Many scales follow the sequence of colors in the rainbow; but the sequence of colors often cannot be interpreted intuitively, and the observer must frequently consult the representation of scale affixed to the image. We shall try to establish criteria in the choice of scales in which the color sequence can be intuitively recognized by individuals of normal color perception.

Colors can be distinguished by three properties: hue (e.g., red, orange), saturation (from pure gray tones to saturated "pure" colors), and brightness. The spectrum obtained by decomposition of polychromatic white light (such as sunlight) is a sequence of frequencies, from 400 nm (blue violet) to 800 nm (red). This spectrum is often used as a base of a color scale, since its sequence is universally known. In the usual chromaticity diagram,³ which is a convenient representation of observable colors, the saturated colors are arranged along the curved border of the field; less saturated colors, including white, are inside the field. The figure is completed by the drawing of a straight line between the frequency extremes, from violet to red. On color monitors, the available colors lie within a triangle formed by the "primary colors" red, green, and blue, which are emitted by individual phosphors.

Brightness is not represented in the diagram; for instance, all levels of the gray scale (from white to black) are superposed in the area called "white." The full representation of available colors, including brightness, requires a tridimensional representation.

The rainbow scale is used often in practice; others include:

- (a) a scale based on the passage of "warm" to "cold" colors,
- (b) the gray scale, and
- (c) the altitude scale for geographic maps, which goes from deep blue for deep areas of the ocean to white for high mountains, passing through green, yellow, and brown colors (brown is an orange of low brightness).

This latter scale is quite arbitrary from the point of view of color perception, but known to everybody. It has usually two points of discontinuity: one at sea level, and another at the "snow level." Such discontinuities are useful to designate an important level, such as the zero level of an electrostatic field.

The gray scale has the clearest sequence; even a completely daltonic person can see which of two adjacent gray tones is brighter. Its disadvantage is in the fact that gray levels are only perceived in relation to their surroundings and are difficult to recognize as such. Therefore the observer cannot identify a given level (except black and white) on a complicated map in more than five or six gray levels, without comparing it to the other levels.

The hues of the rainbow scale, on the other hand, are easy to recognize; they have common names and are distinguishable to most observers. Although hue perception is also

Author Heinrich is at the National Bureau of Standards, Washington, DC 20234; author Fiori is at the National Institutes of Health, Bethesda, MD 20205.

enormously influenced by the illumination and the surroundings, the naive observer can compensate for these factors in most circumstances, and recognize hues such as green, orange, or cyan (greenish blue). However, there are the following serious limitations in the recognition of the sequence:

1. We can easily produce and recognize colors intermediate between the extremes of the rainbow (violet and red). In fact, we think of the hues as arranged in a "color circle"; hence it is not clear where a scale based only on hue starts and ends.
2. Differences in brightness levels are always observed, and may interfere even with a carefully designed hue scale. In most practical scales yellow, which is in the middle of the scale, is considered brighter than red or green, on either side of it, and can therefore be taken to be an end point of the scale.
3. In many instrumental set-ups, the three variables defining a color cannot be adjusted individually; for instance, if magenta (purple) is produced by turning on fully both the red and the blue phosphor, it will be brighter to the eye than the primary colors; and the same occurs with yellow and cyan. Perceived fluctuations of brightness are particularly perturbing in the perception of a scale based on hue.
4. Constructors of scales for maps seem often more concerned with contrast and "colorfulness" than with sequence.

It is preferable to erect a scale in which perceivable brightness increases with each step and each level is uniquely tagged by its hue. However, the perceived brightness of colors of differing hue is somewhat subjective. Therefore, the gray scale should be dominant and the hues should not be fully saturated, and should change gradually along the color circle.

It is quite unnecessary to use all available hues. Good maps in only two hues, at various levels of saturation and brightness, can be found in geographic atlases, where they are used to show variables such as population density or precipitation level. Such as considerate use of colors is usually easier to interpret than some of the garish images that adorn the covers of many science magazines.

References

1. P. Duncumb, in V. E. Cosslett, A. Enstrom, and H. H. Pattee, Eds., *X-ray Microscopy and Microradiography*, New York: Academic Press, 1957, 435.
2. K. F. J. Heinrich, *Electron Beam X-ray Microanalysis*, New York: Van Nostrand Reinhold, 1981, 542.

FOURIER ANALYSIS AND PROCESSING OF HIGH-RESOLUTION ELECTRON MICROSCOPE IMAGES

Javier Tejeda and J. M. Dominguez E.

Image processing by computer methods has been a recent subject of development.¹⁻³ The ideal system to perform image analysis consisting of a digitizing unit plus a computer is suitable to work on-line with the microscope. On the other hand, later analysis by computer of recorded images gives a great deal of useful information; this stage is the step previous to the final on-line configuration.

Following the latter method, electron micrographs are digitized by a microdensitometer in a $25 \times 25 \mu\text{m}$ square window for high resolution. The optical density data are stored on magnetic tape and transferred to a VAX 11/750 for analysis.

From the full image a square section of workable size (128×128 or 256×256 pixels) is selected, and the Fourier transform (i.e., optical transform) is obtained. Figure 1 shows a zeolite micrograph and its corresponding Fourier transform. The horizontal and vertical streaks are caused by the fact that one edge does not exactly match the opposite one and periodicity is destroyed. By fading the picture to a constant value on the edges the streaks are eliminated (Fig. 2). This "electronic aperturing"¹ also has the advantage of simulating the cross section of the laser beam used on optical diffraction studies of the same micrograph (Fig. 3).

References

1. W. Krakow, *Proc. 10th Intern. Congr. EM, Hamburg*, 1982.
2. M. Tomita, H. Hashimoto, T. Ikuta, Y. Yakota, and H. Endo *ibid.*, 1: 521, 1982.
3. Y. Yokubo, S. Moriguchi, J. Hosoi, and J. Nash, 1983 *Ann. Meeting MRS*, Boston, Mass. Symp. N, 96.

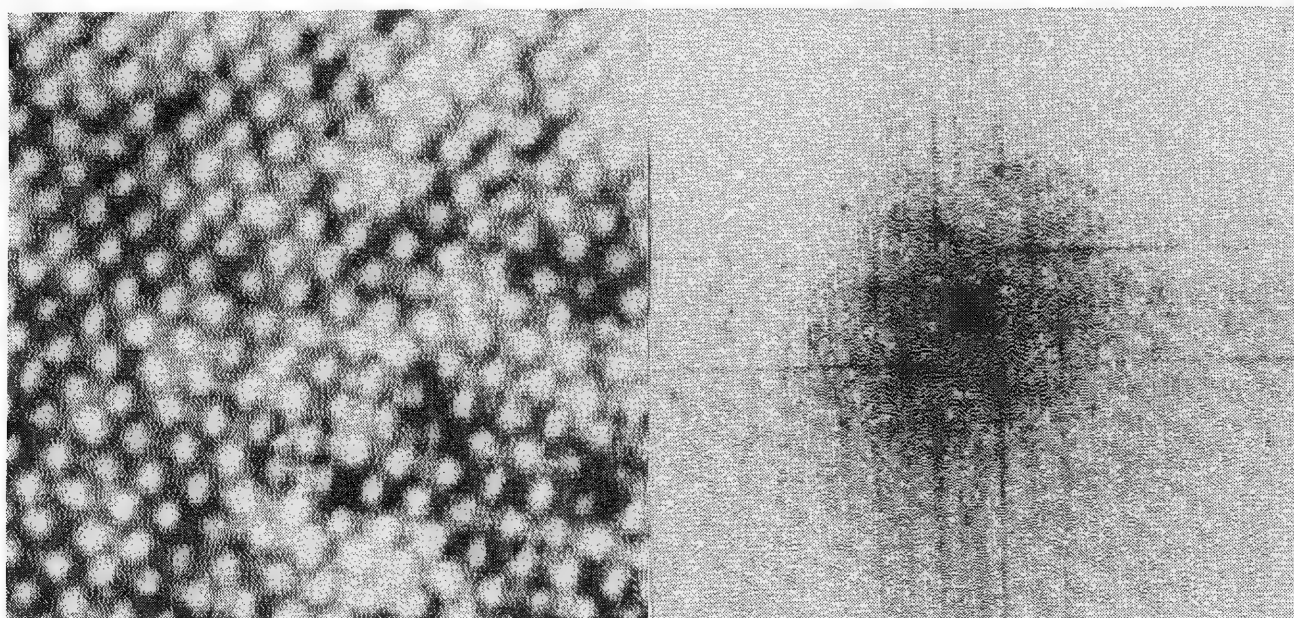


FIG. 1

The authors are at the Instituto Mexicano del Petróleo, Av. Eje Central Lázaro Cárdenas 152, C.P. 07730, México 14, D.F.

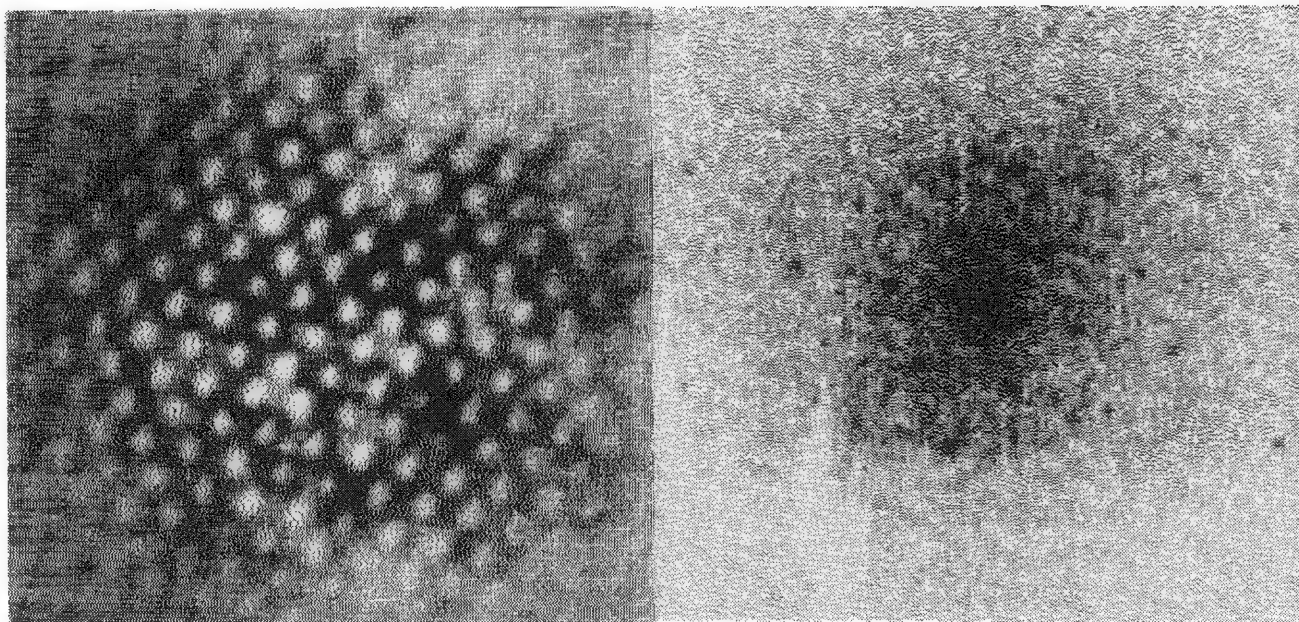


FIG. 2

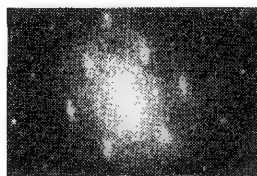


FIG. 3

CONTINUUM CORRECTION OF X-RAY IMAGES IN SCANNING ELECTRON COLUMN INSTRUMENTS

C. E. Fiori, C. R. Swyt, and K. E. Gorlen

An x-ray image in the conventional scanning electron microscope, electron beam x-ray micro-analyzer, or scanning transmission electron microscope is usually formed in a manner analogous to the secondary or backscattered electron or bright-field images. A focused electron beam is scanned over an area of a specimen surface in synchronism with the electron beam of a cathode-ray tube (CRT). The area which is scanned by the CRT beam is fixed (usually 10×10 cm); the area scanned by the beam on the specimen surface is variable and results in useful magnification of typically 10 to 10 000 \times when the specimen is "bulk." In an x-ray map from bulk specimens the magnification is limited primarily by the size of the excitation volume. In the analytical electron microscope the upper magnification limit is determined primarily by statistical considerations and can be greater by a factor of ten or more.

The intensity of the beam in the CRT is modulated by the short rectangular voltage pulse caused by the detection of an x-ray photon. The effect of a pulse is to cause a single "dot" of light to appear on the CRT screen; hence the term "x-ray dot map." When an x-ray image is produced in an energy-dispersive spectrometer (EDS) in an analytical electron-column instrument, a potentially serious artifact occurs due to the poor peak-to-background ratio. The purpose of this communication is to discuss this artifact and describe a procedure to reduce its effect to a negligible level. We also briefly discuss continuum correction when the detector is a wavelength-dispersive spectrometer (WDS).

Statement of the Problem

X rays result from two types of inelastic or energy-loss interactions between fast beam electrons and target atoms. In one case a beam electron interacts strongly with a core electron and imparts sufficient energy to remove it from the atom. A characteristic x ray is occasionally emitted when the ionized atom relaxes to a lower-energy state by the transition of an outer shell electron to the vacancy in the core shell. The x ray is called characteristic because its energy equals the energy difference between the two levels involved in the transition and this difference is characteristic of the element. By counting characteristic x rays we obtain a measure of the number of analyte atoms present.

The second type of inelastic interaction occurs between a fast beam electron and the nucleus of a target atom. A beam electron can decelerate in the Coulomb field of an atom, which consists of the net field due to the nucleus and core electrons. Depending on the deceleration a photon is emitted which can have any energy ranging from near zero up to the energy of the beam electron. X rays that emanate due to this interaction process are commonly referred to as continuum or Bremsstrahlung x rays.

In the usual procedure of forming an x-ray image with the energy-dispersive spectrometer system, two channels of the multichannel analyzer are defined as limits such that the channels between include slightly more than one-half the height of an x-ray peak of the analyte. Whenever an x ray is detected and its resulting voltage pulse falls between the limits specified by these channels, a single pulse is sent to the display CRT to form a single "dot" of light. Any x-ray photon within the energy of interest (whether a characteristic or continuum x ray from the specimen, or continuum from the environment) is processed since there is no way to tell one from the other.

When the height of a characteristic peak in an x-ray spectrum is of the same order as the height of the continuum at the same energy, it should be obvious that the contrast of the resulting x-ray image is as much a function of the physical processes responsible for continuum

The authors are at the National Institutes of Health, Bldg. 13, Rm. 3W13, Bethesda, MD 20205. They wish to thank Dr. D. E. Newbury of the National Bureau of Standards for providing the aluminum wire specimen.

generation as of the desired characteristic generation. Consequently, a serious artifact can result which, in the worst case, manifests itself as a high-contrast x-ray image of an element that is not even present in the specimen. Indeed, any "bulk" specimen with phases that differ in average atomic number by more than several per cent (depending on the number of x-ray counts in the image) can produce lovely images for any element the operator wishes. In the case of "thin" specimens the problem is compounded since the number of generated continuum photons at any given energy is also proportional to the mass-thickness of the specimen.

Discussion

In the x-ray dot map technique we move the electron beam over the face of the recording oscilloscope in synchronism with the beam over the specimen surface. The synchronous beams are displaced by having horizontal and vertical velocity components v_x and v_y imparted to them; v_x is typically between 500-2000 times v_y . The direction in which the velocity component is greater is commonly called the line direction and the other direction is called the frame direction. When the beam reaches the end of a line on the oscilloscope it is inhibited from producing light and moved to the beginning of the next line, and the scan is repeated. When an x-ray photon selected for mapping is detected from a location on the specimen, a bright dot appears at the corresponding location on the CRT. The dots comprising the image can be stored photographically, each dot saturating the film. Since the usual photographic film is capable of approximately 15 shades of gray from black to white, the dot map technique considerably underuses the capability of the film. Variations in the x-ray production and hence the analyte concentration can only be deduced from variation in the spatial distribution of the dots.

A method alternative to continuous beam rastering is discrete rastering, accomplished with what is usually called a "digital scan generator." In this technique the x and y velocity components of the synchronous electron beams are not constant but remain zero for a finite period of time and then the beam is rapidly stepped to the next point. The displacements along the line direction are equal. When the end of the line is reached, the beam is moved back to the beginning of the line and displaced one step along the frame axis with the step size equal to the line step. Each point in the image at which the beam dwells is called a "pixel." For x-ray imaging purposes it is common to use between 128 and 512 points along the "line" and the same number of lines in the "frame."

Discrete rastering is convenient for application with the digital computer. Since the area on the specimen surface is scanned point by point, in computer memory we can define this matrix of points as a two-dimensional array. If the beam remains at any given pixel long enough for a given beam current, beam voltage, and specimen type, it is probable that many pulses will be generated during the dwell time. These pulses can be counted and the value of the count stored along with the pixel coordinates. With appropriate circuitry the counts in this array can be displayed at the appropriate coordinates on the CRT with the brightness at each point proportional to the number of counts. We shall call such a display an *x-ray intensity map* (to distinguish it from the x-ray dot map). An intensity map can fully utilize the gray scale of photographic film. Figure 1 compares the acquisition of an x-ray image using both the "dot" method and the "intensity" method. The number of detected photons is the same in both cases. Note the considerably improved visibility with the "intensity" map. The specimen is an iron and iron-aluminum alloy with intermetallic phases, and the element being imaged as a dot map is scandium (the $K\alpha$ line at 4.088 keV). Since scandium is not present in the specimen we know that the images are pure artifact; the contrast mechanism is average atomic number.

With discrete rastering and the digital computer to store and process the data, it is possible to produce an x-ray intensity map with the average contribution of the background removed at each pixel. The following section describes a procedure to accomplish this goal.

Methods to Separate the Characteristic and Continuum Radiation: EDS

Procedures that accomplish removal of the continuum contribution to x-ray EDS spectra can be classified into one of two categories: modeling or filtering. Background modeling consists of measuring a continuum energy distribution or calculating it from first principles and combining this distribution with a mathematical description of the detector response function. The resulting function is then used to calculate an average background spectrum that can be

subtracted from the observed spectral distribution. Background filtering ignores the physics of x-ray production, emission, and detection; the background is viewed as an undesirable signal to be removed, by modification of the frequency distribution of the spectrum by digital filtering or Fourier transform methods.

Either continuum modeling or filtering will suffice for our purposes. However, a method that does not require an explicit model is more flexible and is clearly advantageous in applications such as imaging of irregular specimens and applications in the analytical electron microscope operating in the energy region above 50 keV. In the latter case one can in principle calculate specimen continuum from a model. However, in practice the calculated continuum rarely accounts for the background since a significant proportion of the background does not originate from the impact point of the primary electron beam but rather from such sources as the specimen support or holder. For our application we have therefore chosen the top-hat digital filter.

The top-hat digital filter was first applied to energy dispersive x-ray spectra by Schamber.¹ The algorithm is both simple and elegant; calculations can be performed very quickly by a computer. The latter point is extremely important since we require the calculations to be made on the fly at every pixel and within the pixel dwell time. Briefly stated, counts in a group of adjacent channels of a spectrum are "averaged" and the "average" assigned to the center channel of the group; the procedure is repeated at each channel as the filter is stepped through that part of the spectrum from which we wish to remove the continuum. One may describe the averaging by the following equation, using the notation of Statham.²

$$y_i' = \frac{1}{2M+1} \sum_{j=i-M}^{i+M} y_j - \frac{1}{2N} \left(\sum_{j=i-M-N}^{i-M-1} y_j + \sum_{j=i+M+1}^{i+M+N} y_j \right) \quad (1)$$

where y_i' is the contents of the i th channel of the filtered spectrum and y_j is the contents of the j th channel of the original spectrum.

The filter is divided into three sections: a positive, central section consisting of $2M+1$ channels centered in turn at each channel in the region of interest; and two side sections each containing N channels. The average of the counts in the side sections is subtracted from the average in the central section.

The effect of this particular averaging procedure is as follows: If the original spectrum is curved concave upward across the width of the filter centered on a particular channel, the average is negative; if the curvature is convex the result is positive. The greater the curvature, the larger the value.

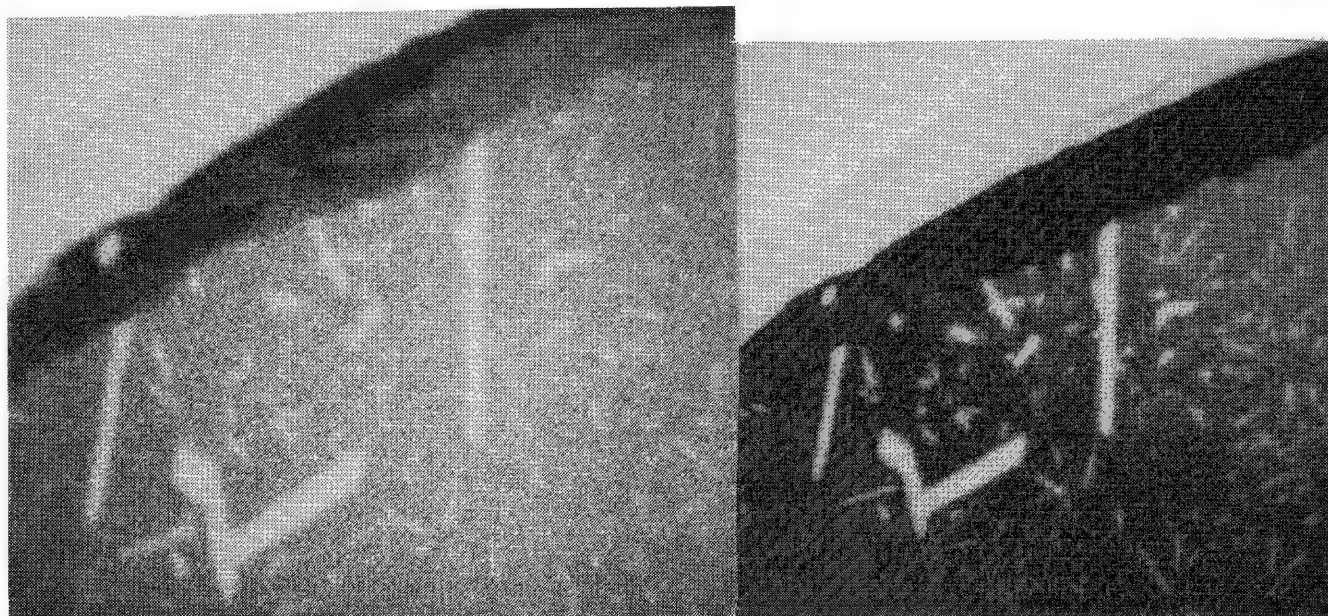


FIG. 1.--Element imaged is scandium (K line at 4.088 keV). Scandium is not present in specimen; image is pure artifact, and contrast mechanism is average atomic number. Dot map (left) and intensity map (right) contain same number of counts; intensity map has considerably greater visibility.

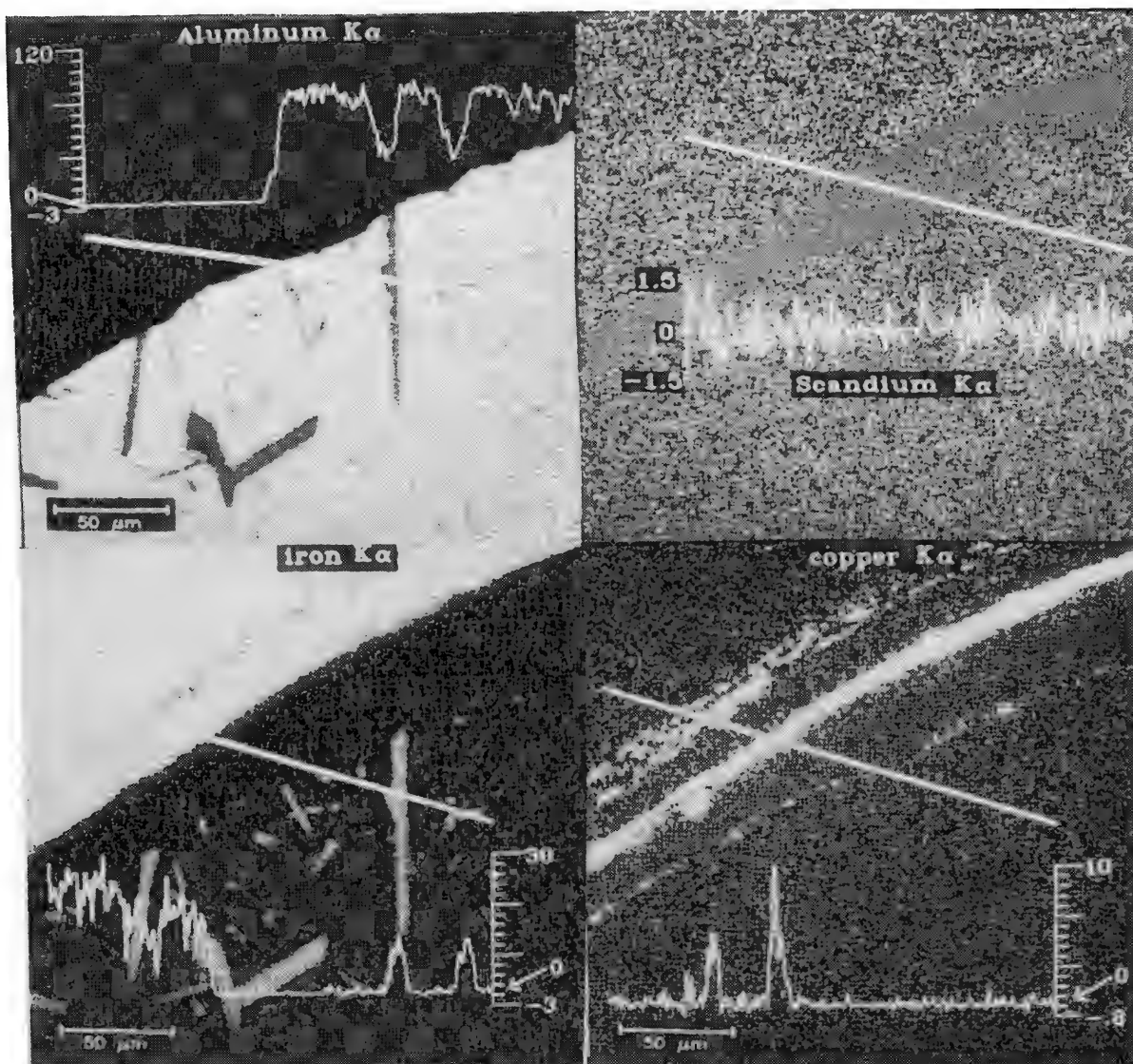


FIG. 2.--Digitally filtered, deadtime corrected Al, Sc, Fe, and Cu (see text for details). Specimen is from failed household electrical junction box. Iron-rich area is part of steel plate that held Al wire; aluminum-rich area is part of wire (note iron-aluminum intermetallic phase); copper region is from plate coating. Linescan through image shows signal variance along line. Numbers on vertical axis are counts per pixel. By nature of digital filter algorithm, numbers are real rather than integer and have much less variance associated with them than their absolute value would suggest. Mean is zero throughout scandium image.

In order for the filter to respond with the greatest measure to the curvature found in spectral peaks, and with the least measure to the curvature found in the spectral background, the width of the filter must be carefully chosen. For a detailed treatment of the subject see Schamber and Statham.^{1,2} In general, the width of the filter for any given spectrometer system is chosen to be twice the full width at half the peak maximum amplitude (FWHM) of the Mn K α peak, with the number of channels in the central section equal to, or slightly more than, the combined number of channels in the side sections.

The final step in the application of the digital filter is to extract a quantity to be assigned to the coordinates of each pixel to represent the characteristic intensity. We choose the sum of the averages of counts in the central section computed at each channel in the filtered region, since this quantity provides the highest peak-to-background ratio.

Regional Variance in Background-corrected Images

Background-corrected images remove a serious artifact but also create another, which is fortunately much less serious. The background-corrected count at each pixel in the image is proportional to the elemental concentration at the corresponding point in the specimen. Since the average effect of the continuum is removed, its only contribution to the image is increased noise. However, if the contribution of the continuum varies greatly from one part of the image to another, one would expect the variance, due to the continuum, in the corrected image to be greatest from regions with the greatest continuum contribution. The effect is shown in Fig. 2, which is a *digitally filtered intensity map* of the same specimen and area as in Fig. 1. Part A of the image is background-corrected aluminum, part B is background-corrected iron, part C is background-corrected scandium, and part D is background-corrected copper. Since scandium is not present in the alloy, there is no "contrast" in the background-corrected image, but there is increased variance correlated with regions of the specimen with higher average atomic number. The increased "noise" in these regions attracts our attention to them but we are not inclined to infer the presence of scandium, as we would in an image not background corrected, such as Fig. 1. This "speckling" of an image is an unavoidable artifact and should not be a cause for concern. Indeed, once one understands the origin of the increased variance, the feature can be used as a tool.

Choice of Scale for Background-corrected Images

When we remove the average effects of the background from a region of an image that does not contain the analyte, the mean count of the region is zero. A mean of zero implies that half the pixels have negative values. We would like to be able to assign the "zero" regions of an image to the darkest gray of the gray scale, i.e., "black." The observer can immediately interpret a region of dominant black as having no analyte. However, by this assignment we essentially "clip" the negative values, since there is no shade of gray to assign to them. The net result of neglecting the negative values is to "bias" the regions that contain no analyte to a mean which has a positive value. The greater the original variance, the greater is this biased mean. An alternative procedure is to set the minimum pixel intensity in the entire image to black. The latter method of setting the brightness scale of background-corrected images requires the author of the micrograph to identify regions that are "zero" with some symbol on the micrograph or comment in the figure caption. The observer must then be able to interpret certain gray levels as representing zero and negative values but numerical information is not compromised.

Dead-time Correction for Digitally Acquired EDS Images

The Si(Li) detector amplifier system produces an output pulse which can be many tens of microseconds long for each processed x-ray photon. Consequently, dead-time losses are high and we can easily attain a condition in which the amplifier cannot process the detected x-ray photons fast enough and the output count rate for the analyte *decreases* for an increase in total input count rate. If we spend the same time at each pixel during the acquisition of an image under high-count-rate conditions, several bizarre artifacts can occur. A particularly insidious one is that regions of a specimen that contain higher concentrations of analyte can appear darker in the image than regions that contain less. This, and other contrast reversal problems, can be avoided by a simple logic gate, so that pixel dwell time is determined not by "real" time but rather by amplifier "live" time.

Methods to Separate the Characteristic and Continuum Radiation: WDS

Since the wavelength-dispersive spectrometer is a single-channel device, it is not possible to obtain a measure of both continuum and characteristic signals simultaneously on the same spectrometer. However, there are several other ways to obtain a measure of the continuum. If time and radiation damage are not considerations it is possible to record sequentially two images under identical conditions from the same spectrometer, one characteristic and one continuum. These images are then subtracted to leave a net characteristic image. Before subtraction it is best to "nearest-neighbor" smooth the continuum image.

Rather than record the two images separately it is possible to interleave the acquisition such that the spectrometer is moved between characteristic and continuum wavelengths at the

end of each "line" of the image, which is then repeated for the other signal. If the electron column has two spectrometers, it is of course possible to obtain a measure of the continuum for one spectrometer from the other. It is a trivial matter to scale the efficiencies of the two before the subtraction. The single spectrometer approach has the significant advantage that the specimen is viewed from a single direction. Specimen self-absorption effects due to different x-ray path lengths are therefore not a problem.

If the second spectrometer is an EDS the differences in dead-time correction must be reconciled. In our laboratory we accomplish this reconciliation by dedicating a separate high-speed amplifier ($< 0.5 \mu s$ shaping time) to the EDS channel. Since high count-rate capability is the only requirement in our application, loss of spectral resolution is not a problem. It is sometimes useful to place a beryllium or carbon absorber between the EDS and specimen to remove superfluous photons lower in energy than the measured continuum band.

Figure 3 is an example of a WDS characteristic image, continuum corrected from a simultaneously acquired EDS image. The specimen is human brain (from the hippocampus) and the element being imaged is aluminum, which is present in the most intense regions at approximately the 200-500ppm level (dry weight, after probe analysis).³ The image was acquired with 512^2 pixels over a 16h period. The current was 2×10^{-7} A and the accelerating potential was 15 kV. The specimen was nominally 20 μm thick mounted on a carbon substrate. In this image it was extremely important to remove the possibility that the contrast was due to average atomic number or mass thickness effects and so a background correction was imperative. This remarkable image could not have been obtained with the "dot" map technique, and indeed exploits both computerized acquisition and the excellent current stability of the present-day electron column. Although 16 h (or more) seems like an inordinate length of time in which to obtain an image, we must remember several things: A microprobe that costs \$0.25-0.5 million and sits all night (and all weekend) doing nothing is sinful; an image requires a large number of collected characteristic photons which can only be obtained by an increase in analysis current, acquisition time, or both; digital images can tell many things about a specimen that line scans and point analyses only hint at--and the only reason we did not use them in the past is simply that we could not get them.

Conclusion

Background correction of digitally acquired x-ray images has been discussed in this paper and several examples were presented. However, background correction must be considered one of the more trivial applications of the new computerized image-acquisition systems that are rapidly becoming available at rapidly decreasing cost. We are about to witness a revolution in our field.

Appendix

The top-hat digital filter described by Eq. (1) can be applied to an x-ray spectrum in a time proportional to the number of channels by calculating the summations in the formula from the difference of two pre-calculated summations; i.e.,

$$\sum_{j=k}^h y_j = \sum_{j=i-M-N}^h y_j - \sum_{j=i-M-N}^{k-1} y_j = S_h - S_{k-1} \quad (A-1)$$

$$\text{where } S_i \text{ is calculated from } S_0 = 0, S_i = y_i + S_{i-1}. \quad (A-2)$$

Rewriting Eq. (A-1) in terms of S gives

$$y_i = \frac{S_{i+M} - S_{i-M-1}}{2M+1} - \frac{S_{i-M-1} - S_{i-M-N-1} + S_{i+M+N} - S_{i+M}}{2N} \quad (A-3)$$

Equations (A-2) and (A-3) form the basis for the following Pascal procedure:

```

PROCEDURE TopHatFilter(
  VAR y:ARRAY[y1..yh:INTEGER] OF REAL; { original spectrum }
  VAR f:ARRAY[f1..fh:INTEGER] OF REAL; { filtered spectrum }
  M:INTEGER; { 2M+1 channels in central section }
  N:INTEGER); { N channels in side sections }

```



```

VAR
  i,p,q,r:INTEGER;
  S:ARRAY[0..MaxSpectrumChannels] OF REAL;

BEGIN
  S[0] := 0;
  FOR i := 1 TO y1-y1+1 DO S[i] := y[y1+1-1] + S[i-1];
  p := N; q := N+M+M+1; r := N+M+M+N+1; { initialize filter section
  indices }

  FOR i := 0 TO y1-y1-(N+M+M+N) DO BEGIN
    f[f1+i] := (S[q]-S[p])/(2*M+1) + (S[p]-S[i]+S[r]-S[q])/(2*N);
    p := p+1; q := q+1; r := r+1; { advance filter }
  END;
END; {TopHatFilter}

```

For general case x-ray spectra, we recommended choosing $M = N$. Thus, there are $4N + 1$ channels in the top-hat filter, N in each of the two side sections and $2N + 1$ in the center section. Since the center section should span an energy range approximately equal to the Full Width at Half Maximum (FWHM) of the x-ray peak, N can be calculated as follows:

$$N = \frac{\text{FWHM}}{2K}$$

where K is the number of electron volts per x-ray spectrum channel. The number of channels filtered equals the number of channels in the center section ($2N + 1$), which requires a total of $6N + 1$ channels centered at the peak energy to be sampled and processed.

References

1. F. H. Schamber, "A modification of the linear least-squares fitting method which provides continuum suppression," in T. G. Dzubay, Ed., *X-ray Fluorescence Analysis of Environmental Samples*, Ann Arbor Science Publishers, 1977, 241.
2. P. J. Statham, "A comparative study of techniques for quantitative analysis of the x-ray spectra obtained with a Si(Li) detector," *X-ray Spect.* 5: 16-28, 1976.
3. R. M. Garruto, R. Fukatsu, R. Yanagihara, D. C. Gajdusek, G. Hook, and C. E. Fiori, "Imaging of calcium and aluminum in neurofibrillary tangle-bearing neurons in Parkinsonism-Dementia of Gaum," *Proc. Natl. Acad. Sci.* 81: 1875-1879, 1984.

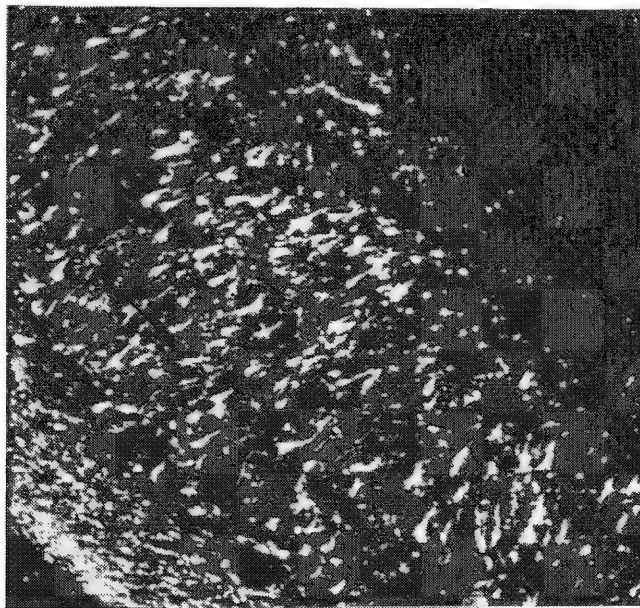


FIG. 3.--Background-corrected WDS Al image (200-500 ppm of Al) from human brain, 1mm full field; see text for other details.

11 Quantitative Electron Probe

SURFACE TILT EFFECTS ON THE EFFECTIVE CURRENT FACTOR

J-F Tian and John C. Russ

The classic ZAF equations used for correction of electron microprobe intensities include, as part of the "Z" term, a correction for the loss of potential ionizations due to the backscattering of electrons with energy above the critical excitation energy of the element being measured. This term is generally called R, the effective current factor. The most common equations^{1,2} used for its calculation are polynomial functions of Z (atomic number) and U (overvoltage = E_0/E_C), which have been fit to measured data and/or Monte-Carlo results; R is a dimensionless parameter with value less than 1.

Strictly speaking, the calculated R values apply only to the case of normal incidence of the electron beam striking the sample surface (the classic microprobe geometry). However, most scanning electron microscopes, whether fitted with energy- or wavelength-dispersive x-ray systems, are used extensively to perform analysis of specimens that do not meet this criterion. This may be due to either attempts to measure locally flat regions on irregular specimens, which are therefore not perpendicular to the beam, or the need to tilt even flat, polished samples to permit the x-ray detector to view the surface. The latter case applies to our SEM, in which the ED detector is at the same height as the sample surface, and tilt angles of 25-45° are common.

When the surface is tilted from the normal, it is expected from a simple understanding of the electron interactions with the sample that the loss of energy due to backscattering will increase (R will decrease). Most programs that ignore this effect make the tacit assumption that the R term, which appears on top and bottom of the ratio of unknown to standard, simply cancels out any effect due to tilt. Of course, if the standard and unknown are at the same tilt, this is a more reasonable assumption than when they are not.

To our knowledge, only two programs have introduced a term in the R equation to adjust for surface tilt. Although R for perpendicular incidence is calculated as a function of Z and U, the multiplicative terms introduced did not include any Z dependence, and one was a function solely of tilt. NBS Frame-B² used a function of tilt angle S and overvoltage U, obtained by empirical fit to Monte-Carlo data:

$$R/R_{\text{norm}} = \exp \{ [\log(0.753/U) + 0.8994] * [\sec(S) - 1 + (S/90)] \}$$

This equation was, however, dropped from subsequent versions of Frame. The second model,³ based on a dramatically oversimplified spherical model for the excited region, with a constant stopping power term, is a function only of S. It showed fair agreement with measured data at 45°.

In order to assess the importance of the tilt effect on R, and obtain measured data that could be used to determine the dependence on Z, U, and S, we measured x-ray intensities on pure specimens of Al (Z = 13), Cu (Z = 29) and Pb (Z = 82). Over the practical working range of accelerating voltage in our SEM (JEOL JSM-2), we were able to work at the following overvoltages:

Aluminum [$E_C(K)$ = 1.56]: U = 4.5, 6.0
Copper [$E_C(K)$ = 8.98]: U = 2, 3, 3.5
Lead [$E_C(M)$ = 2.61]: U = 3, 4.5
[$E_C(L)$ = 13.04]: U = 2, 3

For each material, a polished sample surface cut at 45° to the normal specimen plane

The authors are at North Carolina State University, Raleigh, NC 27695.

(parallel to the stage axes) was oriented by variation of stage tilt and rotation to produce a wide variety of tilt and x-ray takeoff angles. For each tilt angle (from 15 to 80°), several very different takeoff angles were used. All the intensities were determined by recording the x-ray spectrum in a Dapple Microplus+ ED system for 50 or 100 sec, fitting a straight line under the isolated alpha peak, and integrating in a 1.2 FWHM energy window.

For each measurement, the known takeoff angle was used to calculate the absorption from Heinrich's $F(x)$ expression⁴ with Moll's geometric correction.⁵ With the self-absorption of the x rays in the material thus corrected, the other terms in the ZAF equation cancel and the remaining variation in intensity for a given elemental standard, at a given overvoltage, is due to the effect of surface tilt on R .

It was also necessary to correct for beam-current variations, by measuring a reference x-ray intensity at a common surface orientation before and after each measurement. In addition, since we were unable to work at tilt angles down to zero, each curve is plotted to extrapolate to the R value for perpendicular incidence, as in Ref. 2. The agreement between the values obtained using different takeoff angles [$F(x)$ values varying from nearly 1.0 to about 0.6] was quite good. The smallest errors arise at intermediate angles; for large and small tilt angles, the error due to stage precision dominates (for large angles, via the effect on R ; for small angles, via the absorption correction).

For each material, the mean estimated R (relative to the expected R for normal incidence) was measured over the ranges of S and U described. Figure 1 shows the resulting curves. They may be compared to the curves that would be predicted by the existing models, which are shown in Fig. 2. The models do not entirely explain of the observed behavior, in the following respects:

1. The variation of R with tilt is quite small for tilt angles below about 30° and for low- Z materials. Hence, for these circumstances, ignoring the R_{tilt} correction is probably acceptable.

2. Although the relatively flat shelf at low tilt angles is in general agreement with both models, the measured data show that the angle at which the curves depart significantly from the flat behavior and begin to drop more sharply depends on atomic number Z , as summarized in Table 1, based on values obtained from third-order polynomial fits to the data (the curves shown in Fig. 1).

TABLE 1.--Effect of Z on decline of R vs tilt (tilt angle at which R declines by 10 or 20% relative to normal incidence).

Element	Al	Cu	Cu	Cu	Pb	Pb
Overvoltage	4.5	3.5	3.0	2.0	4.5	2.0
Drop in R						
10%	58	53	51	54	37	32
20%	70	64	63	63	50	47

This result is not surprising, as the chief role of atomic number is to change large-angle scattering of electrons, and consequently to alter the shape of the electron-excited region. (Higher Z produces a broader region for a given depth, with the scale controlled by accelerating voltage.) This consideration would predict that for higher- Z materials, where the breadth of the excited volume is greater, a lower tilt angle would show the onset of an increased drop in R (as more backscattered electrons left with energy above E_C). Indeed, at least qualitatively, this is what we observe. Neither model incorporates any Z dependence, and so cannot predict this behavior.

3. The magnitude of the effects is not in quantitative agreement with either model. Certainly, the sphere model is anticipated to be inadequate for large tilt angles. But the shape of the more complex Frame-B model is also noticeably different from the measured data.

4. From the magnitude of the effect, it seems clear that even if standards and unknowns are measured at the same tilt angle, if the angle exceeds about 40° and there are significant differences in average atomic number between standards and unknowns, ignoring the variation in R will cause errors in the results. If the unknowns are tilted and the standards are not, the errors can be substantial. For the case where "standardless" ZAF methods are used, the pure-element intensities are calculated from equations that incorporate an R term. If no tilt adjustment is included and the unknown surface is tilted by about 40° or more, the same

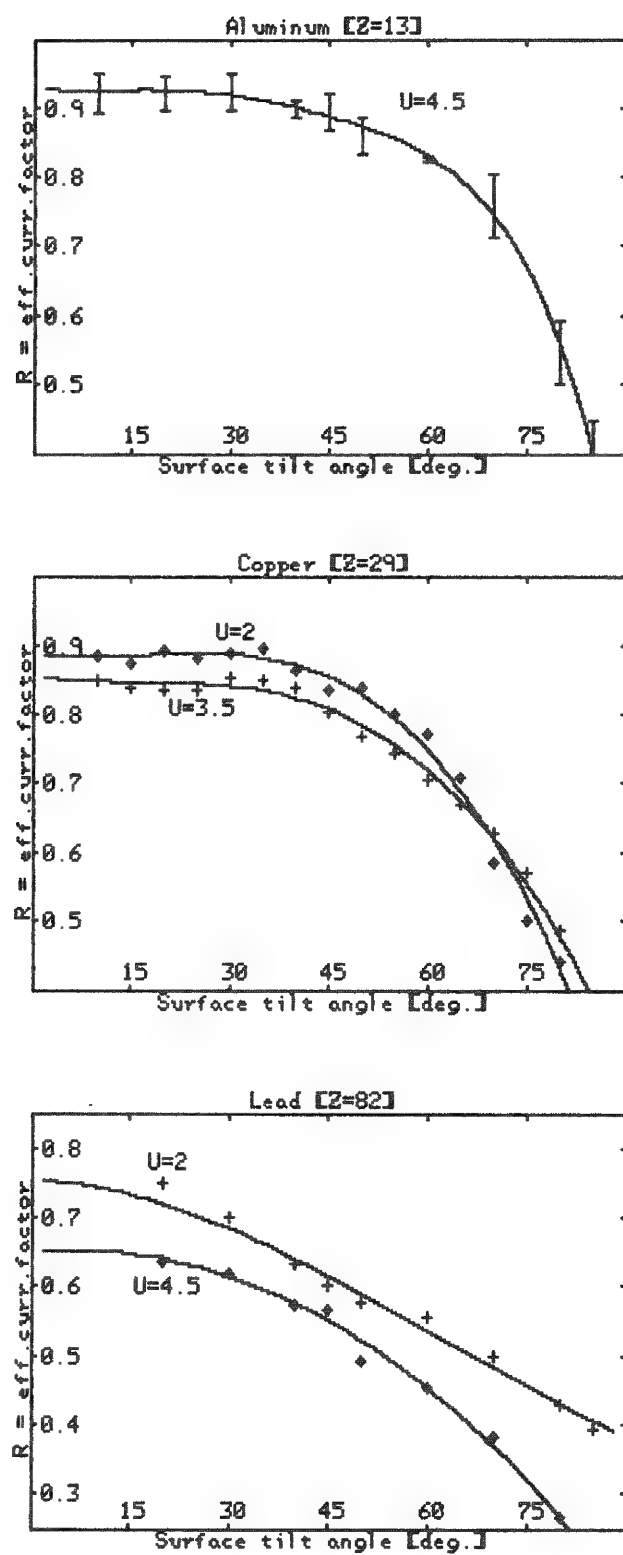


FIG. 1.--Measured variation in R factor with surface tilt angle, for elements Al, Cu, and Pb.

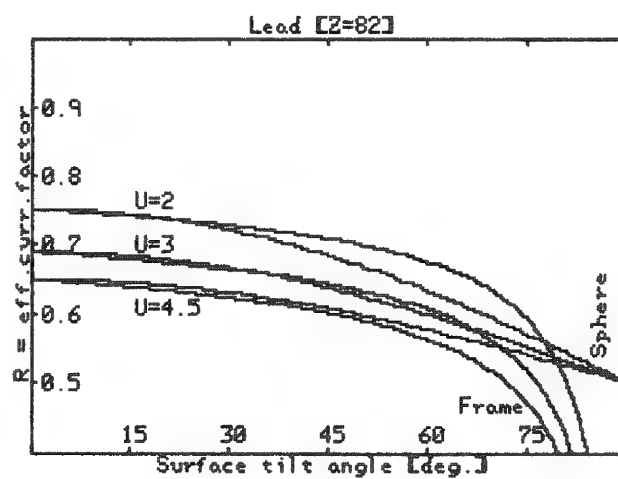
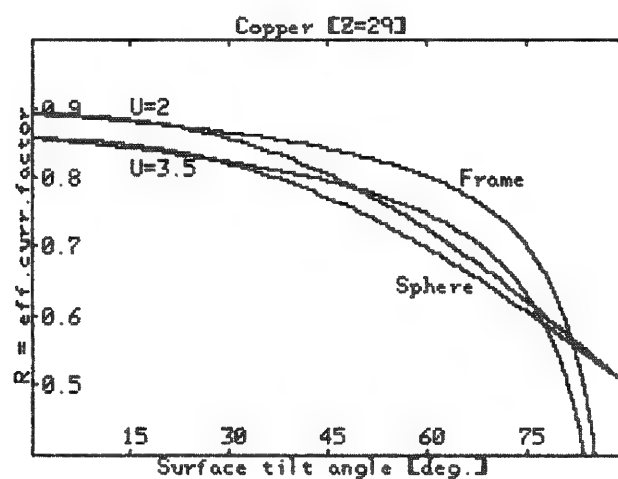
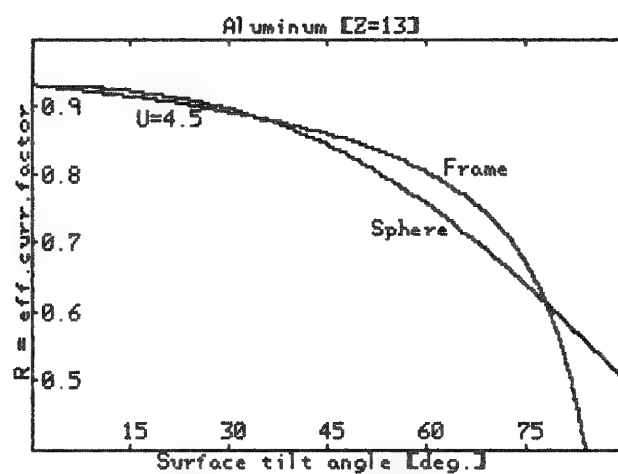


FIG. 2.--Predicted variation of R factor with surface tilt, for elements and overvoltages used for measurements.

errors will appear:

We suggest that more measurements be made, to allow more appropriate universal functions to be devised. These terms should then be applied in all ZAF routines, since the majority of microanalysis instruments in use at present either permit or require the surface angle to be inclined, and indeed often include the tilt angle within the absorption correction.

References

1. H. Yakowitz, R. L. Myklebust, and K. F. J. Heinrich, *FRAME: An On-line Correction Procedure for Quantitative Electron Probe Microanalysis*, NBS Tech. Note 796, October 1973.
2. P. Duncumb and S. J. B. Reed, "The calculation of stopping power and backscatter effects in electron probe microanalysis," in K. F. J. Heinrich, Ed., *Quantitative Electron Probe Microanalysis*, NBS Special Technical Publication 298, 1968, 133-154.
3. J. C. Russ, "Quantitative microanalysis with minimum pure element standards," *Microbeam Analysis--1974*, 22.
4. K. F. J. Heinrich, in T. McKinley, Ed., *The Electron Microprobe*, New York: Wiley, 1966, 296.
5. S. Moll, N. Baumgarten, and W. Donnelly, "Geometrical considerations for ZAF corrections in the SEM," *Microbeam Analysis--1977*, 33.

SOFT X-RAY ANALYSIS WITH THE USE OF A 'WINDOWLESS' ED SYSTEM

Glyn Love, V. D. Scott, and A. O. Sandborg

Energy-dispersive analysis of soft ($< 1\text{keV}$) x rays is becoming increasingly popular as more manufacturers are including provision for 'windowless' operation of the x-ray detector. However, most published work has been concerned with qualitative analysis of elements such as carbon and nitrogen and comparatively little attention has been paid to producing quantitative information. In the present paper a practical procedure is described for carrying out quantitative analysis of ultra-light elements (atomic number less than 11) by means of an EDAX ECON detector with a 711 analyzer system. The effectiveness of the technique is evaluated by a comparison of ED data with those obtained by wavelength-dispersive (WD) spectrometry under similar experimental conditions.

Data Acquisition

The following procedure is recommended for soft x-ray analysis.

1. Rather than use the 'windowless' mode a thin aluminized plastic window should be placed in front of the detector so as to minimize the likelihood of contaminating the silicon detector by hydrocarbons from the vacuum system and to prevent excitation of the detector by light photons (e.g., from cathodoluminescent specimens).
2. A low electron accelerating voltage is preferable, say, less than 15 kV. In this way the efficiency of soft x-ray emission is maximized, the possibility of high-energy electrons entering the detector is eliminated, and the size of the ZAF correction is kept within tolerable limits.
3. Low input count rates (less than 2000 cps) should be employed when recording data, since the pulse pile-up correction becomes ineffective for low-energy x rays because of the inability of the fast discriminator to detect x rays below $\sim 1.5\text{keV}$.
4. The duration of an analysis should be timed manually e.g. by means of a stop watch. This procedure is necessary because the EDAX system's automatic dead time correction becomes unreliable when the spectrum contains a large proportion of low-energy x rays.¹ However, if both the counting period and the number of counts per second stored in the multichannel analyzer are noted, dead-time effects may be accounted for if the spectrum is scaled according to a calibration curve¹ or, more rigorously, by means of an appropriate formula.²

Spectrum Processing

The essential problems, as with the analysis of higher-energy x rays, involve removal of the background and dealing with the large number of x-ray lines that overlap those of the ultra-light elements.

Our method of predicting the x-ray continuum intensity is based on the Kramers expression. However, before the method can be applied, extraneous components of the background, not related to the x-ray continuum, must be removed. One such component is the steeply rising level of the background at low energies (Fig. 1), which is due largely to electronic noise. Unfortunately, the ED system is incapable of distinguishing between noise and genuine signals produced by x-ray photons. However, if the electron beam is switched off, a spectrum consisting solely of noise may be accumulated (the number of noise counts depends only on the counting time) which can then be subtracted from the original spectrum to give

Authors Love and Scott are at School of Materials Science, University of Bath, Bath, England BA2 7AY; author Sandborg is at EDAX International, Prairie View, IL 60069. SERC support for this work is acknowledged.

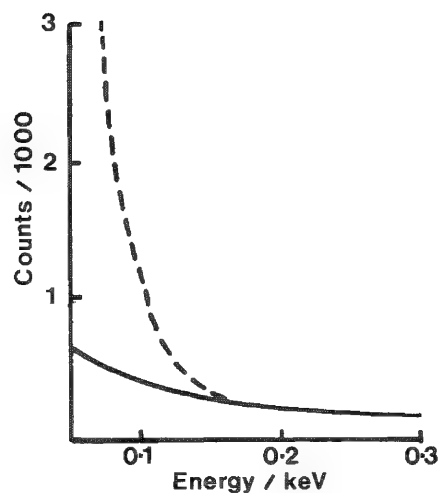


FIG. 1.--Low-energy x-ray spectrum from copper: dashed line, recorded spectrum; solid line, with noise counts subtracted and revealing a "spur."

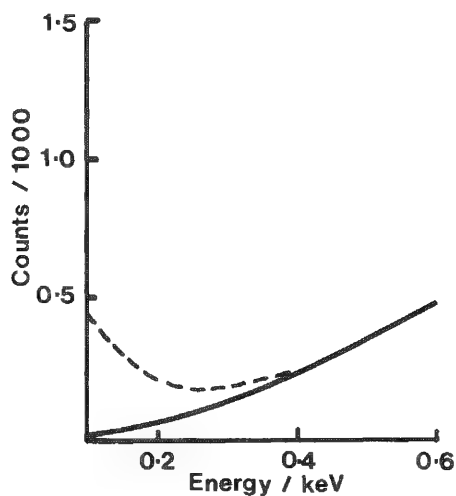


FIG. 2.--Low-energy spectrum from copper: dashed line, with noise counts subtracted; solid line, with both noise and spur subtracted.

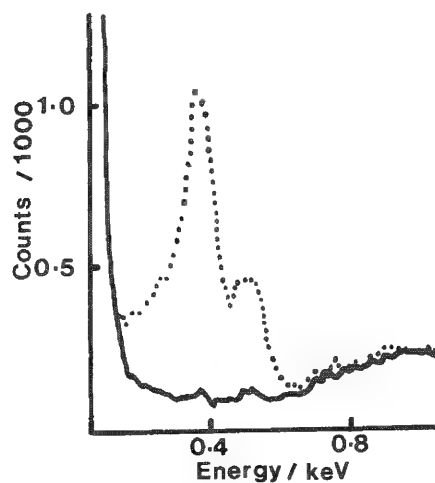


FIG. 3.--Spectrum from silicon nitride: dotted line, recorded spectrum showing nitrogen K peak and small oxygen peak from surface contamination; solid line, calculated background.

a noise-free background (Fig. 1).

Examination of a large number of noise-subtracted spectra reveals that there is yet another artifact present in the background, which we have termed the "spur." The spur is evidenced by a slight rise in the background at low energies (Fig. 1). (If the background consisted solely of continuum the intensity should become negligible as the x-ray energy tends to zero because such weak radiation will be totally absorbed in the specimen and thin plastic windows of the detector.) The spur is not associated with residual noise because its size is related to the total number of counts contained in the spectrum rather than the counting period. A possible cause is incomplete charge collection in the silicon detector, although the exact mechanism has not yet been established. Fortunately, the size and shape of the spur are independent of electron accelerating voltage and atomic number of the specimen so that it may be represented by a simple formula² and then subtracted to leave a background that consists solely of continuum x rays (Fig. 2).

The method adopted for continuum removal is essentially that proposed by Smith et al.,³ in which a continuum spectrum from a reference standard (e.g., silicon) is used to predict the background in the specimen of interest. The continuum from the reference standard is corrected channel by channel for all sample-dependent effects to produce a "normalized" background, representative of a hypothetical sample of atomic number 1 in which no electron backscattering losses or x-ray absorption effects take place. To establish continuum intensity for the specimen of interest, one carries out the procedure in reverse, this time scaling the normalized background using appropriate atomic number and absorption effects for the specimen. (These data will not be known initially so that the procedure must be performed iteratively.) An advantage of the method is that the detector efficiency response need not be explicitly known. Some modifications were required since Smith's approach had never been used to predict the shape of the low-energy continuum. These modifications involved use of a different absorption correction; employment of the original form of Kramers's law; and, in order to eliminate the need to correct for electron stopping power, choice of a reference standard of atomic number similar to that of the specimen. The result of a background fit after contributions from both noise and spur are added is shown for a spectrum of silicon nitride; here the background was calculated by use of a silicon reference standard (Fig. 3).

Deconvolution of overlapped peaks by means of least-squares fitting of spectra from standards was adopted. This approach was preferred to the alternative of using generated Gaussian peaks because of the difficulty in fitting the low-energy tails of the soft x-ray peaks.

A summary of the spectrum processing procedure is given below:

1. Spectra are acquired for a fixed period of time from the specimen, elemental standards, and appropriate continuum reference standard.
2. Spectra are scaled to account for dead-time effects and then noise and spur are removed.
3. The spectrum from the silicon reference standard is corrected for absorption and electron backscattering losses.
4. This normalized continuum is scaled to the atomic number of the specimen being analyzed according to the atomic number dependence given by Kramers. Absorption corrections and electron backscattering effects relevant to the specimen are then imposed. This procedure is carried out iteratively.
5. Noise and spur effects are reincorporated to give the background profile.
6. In the event of overlap, peaks from appropriate standards (with backgrounds removed as indicated above) are used together with the calculated background for the specimen to match the original recorded spectrum by least squares analysis.

Comparison of Data from EDS and WDS

The first set of specimens and standards was selected such that no problems of peak overlap arose. Because of chemical bonding effects in ultra-light element spectra it was necessary to integrate the peak profiles obtained by use of WDS. Measurements were carried out at two electron accelerating voltages and the data are presented in the form of x-ray intensity ratios ($k = I_{\text{specimen}} / I_{\text{std}}$) in Table 1. Included in the table are the corresponding k ratios obtained by ED analysis after the spectra have been processed as described above.

The two sets of k values are close, which indicates that our procedure works well for these systems.

The second set of specimens all suffer more or less from overlapping peaks. However, here again, the ED results differ by only a few per cent from the WD values (Table 2).

Conclusions

A practical method for recording and processing low-energy ED spectra has been described. It is shown that application of the method gives data in good agreement with those provided by wavelength-dispersive analysis. Although the method developed here strictly applies only to an EDAX ECON detector and 711 analyzer, it is anticipated that a similar approach could be applied to equipment produced by other manufacturers.

References

1. D. J. Bloomfield et al., "Evaluation of dead-time corrections in EDS analysis," *X-ray Spectrom.* 12: 2-7, 1983.
2. D. J. Bloomfield et al., "Quantitative light element analysis using an energy dispersive detector: Pt. 1, Dead time and the low energy spectrum," *X-ray Spectrom.*, in press.
3. D. G. W. Smith et al., "The atomic number dependence of the x-ray continuum intensity and the practical calculation of the background in energy dispersive electron microprobe analysis," *X-ray Spectrom.* 4: 149-156, 1975.
4. D. J. Bloomfield and G. Love, "Quantitative light element analysis using an energy dispersive detector: Pt. 2, Continuum removal and peak deconvolution," *X-ray Spectrom.*, in press.

TABLE 1.--Comparison of k ratios obtained by WD and ED: light-element peaks clearly resolved.

X-ray line	Specimen	Standard	k ratios- WD		k ratios-ED	
			7kV	15kV	7kV	15kV
F _K	PbF ₂	MgF ₂	0.196	0.105	0.208	0.110
O _K	NiO	Al ₂ O ₃	0.444	0.458	0.454	0.463
C _K	SiC	Graphite	0.0951	0.0374	0.0933	0.0366
C _K	Fe ₃ C	Graphite	0.0497	0.0191	0.0504	0.0198

TABLE 2.--Comparison of k ratios obtained by WD and ED: light-element peaks overlapped by those from heavier elements.

X-ray line	Specimen	Standard	k ratios - WD		k ratios-ED	
			7kV	15kV	7kV	15kV
F _K	MnF ₂	MgF ₂	0.339	0.144	0.363	0.148
O _K	Fe ₂ TiO ₅	Al ₂ O ₃	0.593	0.472	0.589	0.460
O _K	MgCr ₂ O ₄	Al ₂ O ₃	0.826	1.060	0.837	1.100
N _K	Nitrided Steel	Si ₃ N ₄	0.258	0.451	0.252	0.284

DEVELOPMENT OF A NEW ABSORPTION CORRECTION FOR EPMA

D. A. Sewell, Glyn Love, and V. D. Scott

It has become apparent over recent years that the Philibert absorption correction must be replaced if any progress is to be made in improving quantitative electron-probe microanalysis (EPMA) data. Not only is this correction totally inadequate when absorption effects are large, as in ultra-light (atomic number less than 11) element analysis, but it is often inappropriate when high electron beam energies are employed. Current attempts to develop better absorption corrections fall essentially into two categories.

The first method can be considered as a theoretical approach in which ionizations produced by an electron flux are calculated and the distribution with depth of generated x-rays in a target derived. The x-ray absorption factor may then be readily deduced from these distributions by incorporation of appropriate mass absorption coefficients. In essence, such methods^{1,2} lead to formulas that may be regarded as rather more sophisticated forms of the original Philibert expression; consequently, they suffer many of the limitations of their predecessor.³

The second approach ignores the physics involved in electron-induced x-ray emission and seeks to produce an empirical expression which can describe x-ray distributions [$\phi(\rho z)$ curves] for a range of target materials and electron energies. Provided that appropriate analytical formulas are developed that match $\phi(\rho z)$ curves with sufficient accuracy, the absorption factor may be then derived as above. However, the question is, how accurate does the curve-fitting model have to be in order to perform satisfactorily?

Modeling the x-ray distribution by means of a modified Gaussian profile has been proposed⁴ and should, in principle, provide a very accurate fit; any errors would arise only from the equations used to describe the profile. However, initially the treatment did not appear to give consistently good $f(\chi)$ data but recent improvements⁵ may to some extent overcome the deficiencies in the original equations. As an alternative it has been suggested⁶ that exact curve fitting is not essential for an effective absorption correction and that a simple quadrilateral shape may be adequate. Work on developing this quadrilateral model is described in the present paper.

The Quadrilateral Model

The absorption factor is defined as

$$f(\chi) = \frac{\int_0^\infty \phi(\rho z) \exp(-\chi \rho z) d\rho z}{\int_0^\infty \phi(\rho z) d\rho z} \quad (1)$$

where $\chi = \mu/\rho \csc \theta$, θ is the x-ray take-off angle, and μ/ρ is the mass absorption coefficient. In the quadrilateral model, $\phi(\rho z)$ is replaced by an equation expressed in terms of the coordinates A, B, and C of the profile illustrated in Fig. 1: A with coordinates $0, \phi(0)$; B, the maximum of the $\phi(\rho z)$ curve, by $\rho z_m, \phi(\rho z_m)$; C, with coordinates $\rho z_n, 0$, is close to, but not exactly, the x-ray range in the target. Between A and B, $\phi(\rho z)$ is written as $m_1 \rho z + C_1$; between C and D, as $m_2 \rho z + C_2$, where m_1 , m_2 , C_1 , and C_2 are:

The authors are at the School of Materials Science, University of Bath, Bath, England BA2 7AY. SERC support for this work is acknowledged.

$$m_1 = \frac{\phi(\rho z_m) - \phi(0)}{\rho z_m}, \quad C_1 = \phi(0), \quad m_2 = \frac{\phi(\rho z_m)}{\rho z_m - \rho z_n}, \quad \text{and } C_2 = m_2 \rho z_n$$

The denominator in Eq. (1) is simply the area under the curve and is also written in terms of the above coordinates. Substituting for $\phi(\rho z)$ in Eq. (1) one then obtains,

$$f(\chi) = \frac{2 \int_0^{\rho z_m} (m_1 \rho z + C_1) \exp(-\chi \rho z) d\rho z + 2 \int_0^{\rho z_n} (m_2 \rho z + C_2) \exp(-\chi \rho z) d\rho z}{\phi(\rho z_m) \rho z_n + \phi(0) \rho z_m}$$

Next, expressions are required for the coordinates that describe their variation with atomic number (Z), electron energy (E_0), and overvoltage ratio (U_0). Results based on a limited number of $\phi(\rho z)$ curves have produced the following equations, although they may well be modified as the research proceeds.

- (i) $\phi(0)$ is given in an earlier paper⁷
- (ii) $\phi(\rho z_m) = \phi(0) (1 - 0.58 \exp(-0.4U_0)) [1.9 + (Z/250)]$
- (iii) $\rho z_m = \rho z (0.3 - 0.25 \ln \eta)$, where ρz is the mean depth of x-ray generation and η is the backscatter coefficient
- (iv) ρz_n , as given in an earlier paper⁸

Both ρz_m and ρz_n are expressed in terms of the mean depth of x-ray generation. This is deliberate since advantage is then taken of the scaling properties of $\phi(\rho z)$ curves⁹ and the model is also constrained to work accurately for values of $f(\chi) > 0.5$, where ρz controls the magnitude of the absorption correction factor.

Assessment of Quadrilateral Model

Values of $f(\chi)$ were calculated for a number of systems by use of the quadrilateral model. The data were then compared with corresponding $f(\chi)$ values derived from a Monte Carlo method.⁸ Figure 2 shows results for two typical systems; the curves indicate how closely the two calculations agree. For aluminum at 10 kV, $f(\chi)$ values lie within 5% of the Monte Carlo predictions provided that $f(\chi)$ is greater than 0.1. A similar conclusion may be drawn from carbon data at 10 kV. Clearly, these may be regarded as extreme cases of absorption since EPMA conditions are unlikely to be chosen whereby 90% of x ray absorbed in the target.

The results demonstrate that use of a simple quadrilateral profile to describe the distribution of x rays generated in the target is adequate for formulating an absorption correction. Nevertheless, some refinement of current equations is being undertaken to increase precision and, for this purpose, a more comprehensive series of Monte Carlo calculations is being utilized that cover a larger number of systems and probe conditions. So far the simplified Monte Carlo model⁸ has been employed for this purpose although it may yet prove necessary to adopt a more sophisticated treatment. Consequently, in parallel, the validity of such Monte Carlo calculations is being assessed by comparisons with experimental measurements on a series of tracer-type specimens, with data recorded on samples inclined to the incident electron beam and on ultra-light element specimens, since the objective is to produce a universal procedure for quantitative EPMA.

References

1. J. Ruste and C. Zeller, "Correction d'absorption en micro-analyse," *C. R. Acad. Sci.* 284B: 507-510, 1977.
2. W. Reuter, "The ionisation function and its application to electron probe micro-analysis of thin films," in G. Shinoda, K. Kohra, and T. Ichinokawa, Eds., *X-ray Optics and Microanalysis*, Tokyo: Tokyo University Press, 1972, 121-130.
3. V. D. Scott and G. Love, *Quantitative Electron Probe Microanalysis*, Chichester: Ellis Horwood Ltd., 1983.

4. R. H. Packwood and J. D. Brown, "Quantitative electron probe microanalysis using Gaussian $\phi(\rho z)$ curves," *X-ray Spectrom.* 11: 187-193, 1982.
5. G. F. Bastin et al., "Evaluation of the use of Gaussian $\phi(\rho z)$ curves in quantitative electron probe microanalysis : A new optimisation," *X-ray Spectrom.*, in press.
6. G. Love et al., "An improved absorption correction for quantitative analysis," *Proc. 10th Intern. Congr. X-ray Optics and Microanalysis*, in press.
7. G. Love et al., "The surface ionisation function, $\phi(0)$, derived using a Monte Carlo method," *J. Phys.* D-11: 23-31, 1978.
8. G. Love et al., "A simple Monte Carlo method for simulating electron-solid interactions and its application to electron probe microanalysis," *ibid.*, D-10: 7-23, 1977.
9. H. E. Bishop, "The prospects for an improved absorption correction in electron probe microanalysis," *ibid.*, 7: 2009-2020, 1974.

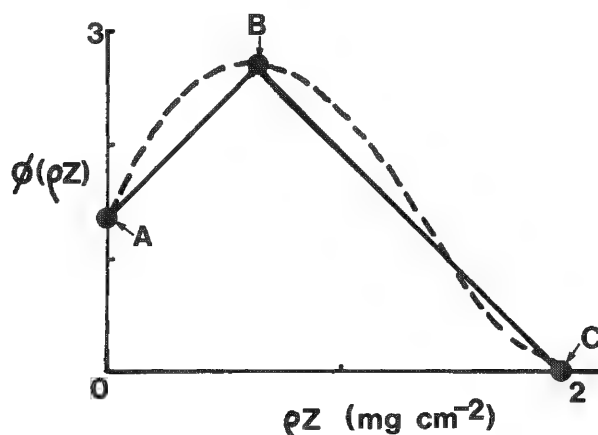


FIG. 1.--Dashed line, Monte Carlo $\phi(\rho z)$ distribution from aluminum at 10 kV; solid line, representation of $\phi(\rho z)$ by quadrilateral profile.

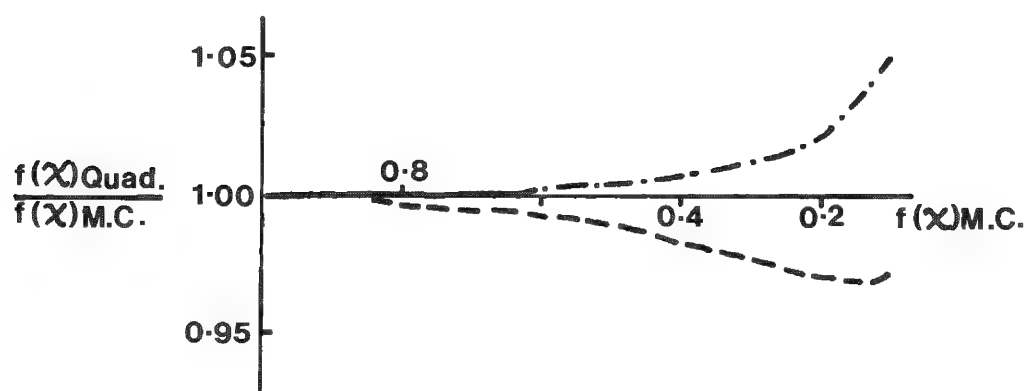


FIG. 2.--Plots of $f(\chi) \text{ quad}/f(\chi) \text{ mc}$ vs $f(\chi) \text{ mc}$: dashed line, aluminum matrix, 10kV electron probe voltage; dash-dot line, carbon matrix, 10kV electron probe voltage.

USE OF A MONTE CARLO ELECTRON TRAJECTORY SIMULATION FOR QUANTITATIVE ANALYSIS OF THICK FILMS IN THE ELECTRON-PROBE MICROANALYZER

D. E. Newbury, R. L. Myklebust, and Eric Steel

Thick films form a class of samples for which neither conventional electron-probe microanalysis (EPMA) with bulk sample matrix correction procedures or high beam energy analytical electron microscopy (AEM) is appropriate. Thick films can be defined as those whose thickness is a substantial fraction (e.g., > 0.25) of the electron range at typical EPMA operating energies, e.g., 15–20 keV. The films may be free standing or they may overlay a bulk substrate. Although free-standing thick films could be analyzed in the AEM, the thickness of such films would require substantial modification of the usual AEM quantitative analysis procedure in order to account for significant scattering, absorption, and fluorescence, which are minor effects in typical AEM analysis situations. Although the EPMA is well suited for obtaining useful x-ray spectra from thick films, the conventional ZAF (atomic number-absorption-fluorescence) matrix correction procedure yields errors which are substantially greater than those found in the analysis of bulk targets of the same composition. In thick films, electron scattering and x-ray absorption and fluorescence differ significantly from the behavior observed in bulk targets, but the calculated ZAF corrections presume bulk behavior. Monte Carlo electron trajectory simulation techniques can provide a unique view of the problems of thick film analysis and form the basis for an advanced correction scheme.

Experimental and Calculational Procedures

The most obvious effect of the thickness on the ZAF-calculated compositional values is a large deviation of the sum of the concentrations from a total of unity. Simple normalization serves to restore the concentrations to values that reflect the actual excited mass of the sample, but substantial analytical errors remain after first-order correction of sample thickness effects by normalization. To examine the behavior of thick films, a wedge-shaped specimen of NBS Standard Reference Material 470 (glass K-411) was prepared by ion milling.¹ Analyses at various thicknesses were performed at a beam energy of 20 keV by energy-dispersive x-ray spectrometry. Quantitative data reduction with pure element standards was carried out by means of the NBS theoretical matrix correction procedure FRAME C, with the oxygen content calculated by stoichiometry.² The normalized concentrations and the non-normalized total, which is an indirect measure of specimen thickness, are listed in Table 1 for several sample thicknesses. Systematic deviations in the concentrations are observed, with the largest deviation for magnesium.

For comparison to the experimentally determined concentrations, "specimenless analysis" was carried out. That is, a Monte Carlo electron trajectory simulation was first used to calculate the emission of x rays from hypothetical thick films and pure element standards and these intensities were then used for input to a ZAF quantitative analysis procedure. (Strictly speaking, since fluorescent radiation is not included in the Monte Carlo calculation, only atomic number and absorption corrections should be carried out.) The details of the Monte Carlo simulation used in this work have been described in the literature.^{3,4} For the present calculations, 20 000 electron trajectories were simulated for each film thickness and bulk standard. From these calculated intensities, a set of intensity ratios,

$$k = i(x, \text{sample})/i(x, \text{standard}) \quad (1)$$

The authors are at the National Bureau of Standards, Washington, DC 20234. (Contribution of the U.S. National Bureau of Standards; not subject to copyright.)

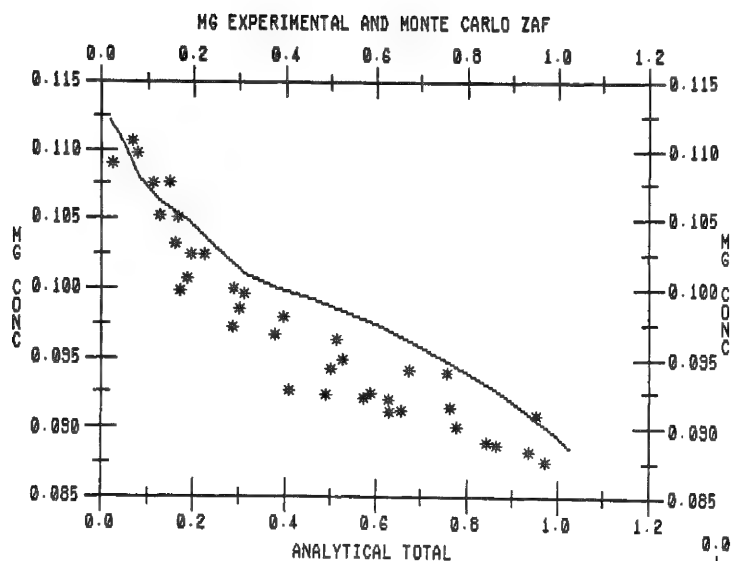


FIG. 1.--Comparison of calculated Monte Carlo/ZAF concentrations (line) and experimentally determined ZAF concentrations (points) for magnesium in K-411 films.

FIG. 2.--Comparison of calculated Monte Carlo/ZAF concentrations (lines) and experimentally determined ZAF concentrations (points) for calcium in K-411 films.

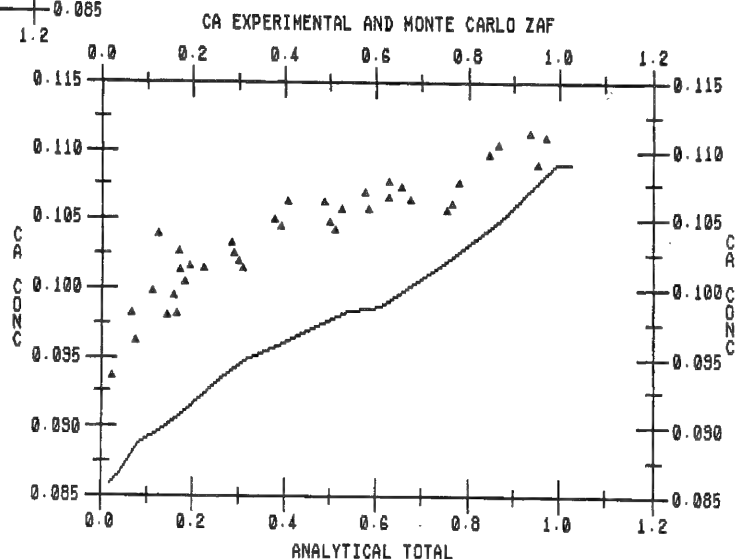


TABLE 1.--Analyses of K-411 films.

Total*	Mg	relative error	Si	relative error	Ca	relative error	Fe	relative error
0.112	0.108	+22%	0.244	-3.9%	0.096	-14%	0.125	+12%
0.224	0.102	+15%	0.249	-2.0%	0.101	-9%	0.121	+8%
0.302	0.0984	+11%	0.250	-1.6%	0.102	-8%	0.124	+11%
0.490	0.0923	+4.3%	0.254	0%	0.106	-4.5%	0.121	+8%
0.780	0.0901	+1.8%	0.260	+2.4%	0.108	-2.7%	0.112	0%

* Total calculated from final ZAF concentrations
(Beam energy 20 keV; pure element bulk standards; NBS FRAME C data reduction)

TABLE 2.--"Specimenless analysis;" Monte Carlo simulation and ZAF correction. (Calculations of emitted x-ray intensities from bulk targets at 20 keV, 40° takeoff angle; intensities in photons/electron; ZAF correction by NBS FRAME procedure; oxygen calculated by stoichiometry.

Target	Mg	Si	Ca	Fe
Mg	1.01E-2			
Si		8.32E-3		
Ca			4.41E-3	
Fe				2.36E-3
K411	4.94E-4	1.56E-3	4.60E-4	2.36E-4
SRM conc.	0.0885	0.254	0.111	0.112
k-value	0.0489	0.188	0.104	0.100
ZAF conc.	0.0915	0.257	0.110	0.112
Relative error	+3.4%	+1.2%	-0.2%	0%

was formed for all elements x . The set of Monte Carlo k -values was then processed through the NBS FRAME ZAF program to yield final concentrations, which could be compared to the original hypothesized composition and final errors determined.⁵ Oxygen was calculated by stoichiometry. Table 2 contains an example of the calculated intensities from a bulk target of K-411 and bulk pure element standards, the resulting k -values, and the ZAF-corrected concentrations. For a bulk target of K-411, the agreement between the composition input to the Monte Carlo calculation and the output from the ZAF corrections is within 3.5% relative for the worst case.

For the thick films, plots of the calculated concentrations for magnesium and calcium as a function of the total of the concentrations are shown in Figs. 1 and 2. In addition experimentally determined concentration values from the wedge specimen are also plotted. The agreement between the Monte Carlo calculations and the experimentally determined ZAF concentrations is within 5% for magnesium but a systematic deviation is observed for calcium throughout the thickness range, with the experimental concentrations above the Monte Carlo/ZAF predicted values. The origin of the deviation for calcium is not yet understood, but it is interesting to note that the shape of the predicted curve follows the experimental data with a nearly constant offset from the absolute values.

Discussion

The magnitude of the relative errors observed in the actual analyses of thick films given in Table 1 indicates that the special nature of thick films cannot be ignored if accurate analysis is to be achieved. Quantitation by a ZAF procedure followed by normalization provides a first level of correction, but relative errors of $\pm 20\%$ can still be expected. To reduce these errors, the Monte Carlo simulation can be incorporated into an analysis procedure for thick films of unknown composition and thickness. The starting point for such a procedure is the normalized concentrations from a ZAF analysis as an initial estimate of the film composition. Monte Carlo calculations are then made for this hypothetical composition and the film thickness, if known, or for a range of film thicknesses if the exact value is unknown. These calculated intensities are used with Monte Carlo calculations of intensities from standards as input to the ZAF calculation. By comparison of the input and output compositions from this Monte Carlo/ZAF procedure as a function of sample thickness, correction factors can be determined that can be applied to the ZAF-calculated composition of the real sample. Because of the repeated use of normalization in this procedure, one must properly account for unmeasured light elements such as oxygen, which can often form 40% or more of the total by weight.

Conclusions

The initial results on K-411 glass suggest that this can be a useful procedure for improving the accuracy of analysis of thick films. Additional calculations and experiments on other film compositions, particularly those containing heavy elements, are needed to understand the origin of systematic errors in order to further improve the procedure and to confirm its applicability to a wide range of sample compositions.

References

1. Standard Reference Material 470, Mineral Glasses for Microanalysis, available from the Office of Standard Reference Materials, National Bureau of Standards, Washington, D.C. 20234.
2. R. L. Myklebust, C. E. Fiori, and K. F. J. Heinrich, *FRAME C: Compact Procedure for Quantitative Energy-dispersive Electron Probe X-ray Analysis*, National Bureau of Standards Technical Note 1106, Washington, 1979.
3. D. E. Newbury and R. L. Myklebust, "Monte Carlo electron trajectory simulation of beam spreading in thin foil targets," *Ultramicroscopy* 3: 391-395, 1979.
4. D. E. Newbury and R. L. Myklebust, "Monte Carlo electron trajectory calculations of electron interactions in samples with special geometries," in *Electron Beam Specimen Interactions for Microscopy, Microanalysis, and Lithography*, Chicago: SEM Inc., 1984, 153-164.
5. H. Yakowitz, R. L. Myklebust, and K. F. J. Heinrich, *FRAME: An On-line Correction Procedure for Quantitative Electron Probe Microanalysis*, National Bureau of Standards Technical Note 796, Washington, 1973.

USE AND ABUSE OF QUANTITATIVE WAVELENGTH-DISPERSIVE X-RAY MICROANALYSIS

R. B. Marinenko

In theory, quantitative electron probe microanalysis (EPMA) appears to be straightforward and is therefore attractive to the novice, particularly today when commercial data reduction procedures are readily available. Comparison of an "unknown" specimen with a standard specimen sounds like an uncomplicated procedure. Yet there are many pitfalls an experimentalist can encounter if proper analysis parameters are not maintained. Errors and their sources are discussed in detail by Heinrich.^{1,2}

The intention here is not to reiterate what is present in the literature but to show that even the experienced microprobe analyst can encounter unanticipated errors. Without close observation and redundant measurements, some of these errors might have gone unnoticed. A few interesting cases from some recent wavelength-dispersive (WDS) analyses will be described.

Charging

In a study of an iron-chromium alloy, two spectrometers with LiF crystals, one vertical and the other horizontal, were positioned on the chromium $K\alpha$ peak, and the third, a vertical spectrometer with a LiF crystal, was positioned on the iron $K\alpha$ peak. The specimen and standard mounts had been freshly polished and they were left uncoated to avoid the possibility of counting errors from an unevenly distributed carbon film. A generous amount of silver paint was therefore used to provide a path for electrons from each specimen to the sample mount. Count rates were below 20 000 counts/s and counting times were chosen so that at least 100 000 counts were accumulated at each point.

In Table 1 are the results of two experiments, in which chromium was analyzed on the C vertical spectrometer in Experiment 1 and on the B vertical spectrometer in Experiment 2. There is considerable disparity in the calculated concentrations for both iron and chromium between the two experiments as well as between the spectrometers. This disparity is further illustrated in the extreme right column of Table 1, where there is no consistency in the ratio of the counts observed by the horizontal spectrometer (A) to either one of the vertical spectrometers (B or C).

Obviously there was a serious error, attributable to either the detector system or the specimen. Charging was not a serious consideration when the problems were first observed because there was no indication of charging on the electrometer used to measure the beam or specimen current. But there was no history of any serious problems like these with the spectrometers or detectors on this instrument. Replicate measurements on a given point and on several points on the standards confirmed that there was reasonable reproducibility.

As a first attempt to try to solve the problem, based on previous similar results observed when charging was undeniably occurring, the standard and sample specimens were carbon coated. The results of the subsequent analysis are tabulated in Table 2, in which there is excellent agreement in the k-values and concentrations for the vertical and horizontal spectrometers as well as with the expected results. The data showed excellent reproducibility within and between points on all specimens.

Since carbon coating alleviated the problem, some kind of charging must have been occurring. Probably a charge was accumulating on the surface of the uncoated plastic (epoxy) mounting material, as a result of re-scattering from the polepiece of the final lens. This charge apparently shifted the beam off the focus of one of the spectrometers and left it in better focus for the other.

The author is at the Center for Analytical Chemistry, National Bureau of Standards, Washington, DC 20234

TABLE 1.--Analysis of an iron-chromium alloy. (Concentrations in wt.%, calculated with FRAME from corrected data; 20 kV; beam current, 4×10^{-8} A.)

<u>Exp.</u>		A(horiz.)	<u>Spectrometer</u> B(vert.)	C(vert.)	<u>Ratio of Counts</u>	
#1	Ele.	Cr	Fe	Cr	A/C	
	Conc.	.1403	.9010	.1176	Cr Std.	.886
					Alloy	1.05
#2	Ele.	Cr	Cr	Fe	A/B	
	Conc. a	.0932	.1537	.8566	Cr. Std.	1.46
	b	.0830	.1575	.8403	Alloy	1.16

TABLE 2.--Analysis of iron-chromium alloy after carbon coating. (Concentrations calculated with FRAME from corrected data; 20 kV; beam current, 4×10^{-8} A.)

	A(horiz.)	<u>Spectrometer</u>	C(vert.)
Element	Cr	B(vert.) Cr	Fe
k-value	.1268	.1254	.8891
Conc.(wt. %)	.1013	.1001	.9037
Expected Conc.	.1010	.1010	.8984

TABLE 3.--Analysis of phosphorus in Al-Mg-P glasses. (Concentrations in wt.%; 10 kV, beam current 5×10^{-8} A, $10 \times 10\mu\text{m}$ scanning raster.)

<u>Glass</u>	WDS 1	<u>EPMA Experiment</u>	WDS 2	<u>Wet Chem.</u>
		EDS		
K-496	20.71	32.71	32.57	32.76
K-497	19.70	31.22	31.06	31.59
K-1013	19.72	31.60	31.21	32.46

TABLE 4.--Analysis of lead-germanium glasses. (Concentrations in wt.%)

<u>Glass</u>	<u>Nominal Values</u>	<u>Wet Chem. Analysis</u>	<u>WDS(FRAME)</u>	<u>EPMA EDS(FRAMEC)</u>	<u>WDS(COR)</u>
K-453					
Ge	28.65	28.60	29.87	29.90	28.35
Pb	54.51	54.16	54.17	53.31	54.38
K-591					
Ge	26.36	26.27	27.47	27.55	26.32
Pb	55.10	54.86	54.48	54.28	54.58
K-968					
Ge	26.27	26.10	27.42	27.32	25.94
Pb	54.91	54.89	54.45	54.32	54.78

Peak Shift

For low-atomic-number elements the x-ray peak location depends on the chemical bonding. Thus, when specimens containing magnesium, aluminum, or silicon are analyzed, a standard close in composition to the unknown is most desirable to avoid peak shifts between the specimen and standard. For example, when glasses containing the oxides of the above elements are analyzed, the oxides are better standards than are the elements. These chemical shifts are discussed by several authors.³⁻⁵ Heinrich,² when discussing chemical peak shifts, mentions that one must be careful in selecting standards for elements up to atomic number 20. But most of the cited literature discusses only elements up through atomic number 14.

Peak shifts due to chemical bonding were therefore not anticipated in the quantitative analysis of phosphorus in three NBS glasses we were studying. The two acceptable standards for phosphorus were gallium phosphide and apatite [$\text{Ca}_5(\text{PO}_4)_3\text{F}$]. Gallium phosphide was the preferred standard because the concentration of phosphorus is close to 30 wt.%, which is approximately the same phosphorus content as in the glasses. Also, the purity and stoichiometry were probably more reliable than for the apatite which is a natural mineral. In Table 3 are the results of the analysis of the phosphorus in these glasses.

In the first analysis (WDS 1), the phosphorus concentration is more than 10 wt.% lower than expected. Yet in the EDS analysis, where the entire integrated peak is used in the data reduction procedure (FRAMEC),⁶ the calculated phosphorus concentration is correct. Several wavelength scans through the phosphorus peak of GaP and the NBS glasses demonstrated that indeed there is a peak shift of about 0.0004 sin units which results in a subsequent loss of peak intensity of about 30% or more. The same shift was not observed for apatite and the glasses.

In subsequent analyses with the GaP standard, the spectrometer position was peaked independently for the standard and glasses. The results are listed in the extreme right column of Table 3, labelled experiment WDS 2. This procedure resulted in a marked improvement in the results.

Data Reduction Procedures

Matrix correction procedures are generally used by the electron-probe analyst with considerable confidence. This attitude is usually justified, but occasionally situations arise in which large errors are observed. We recently encountered some problems because of the unusual nature of the material being analyzed.

Three lead-germanium NBS glasses were being quantitatively analyzed for eventual SRM certification. This particular combination of elements is unusual and had not been previously analyzed in this laboratory. The glasses were repeatedly analyzed by use of different standards and voltages. The data reduction programs used for matrix corrections were FRAME (for WDS) and FRAMEC (for EDS), both of which were developed at NBS.^{6,7} The germanium concentration calculated from these programs was consistently more than 3% (relative) higher than expected. Some of these results are listed in Table 4, where they are compared to the nominal values and to the results from the wet chemistry analyses.

After several experiments confirmed that the error was not in the experimental procedures, we realized that the $L\beta$ fluorescence correction for lead was not included in the FRAME programs. Fluorescence correction calculations are cumbersome and very time consuming. And the fluorescence correction from the $L\beta$ lines is generally very small if not insignificant; therefore, it was not included in the original FRAME programs to reduce the program storage space and to reduce the calculation time. This correction, though, is included in the NBS extended data reduction procedure, COR.⁸ The results obtained from COR are in the extreme right column of Table 4, where a noticeable improvement in the germanium results can be seen.

Conclusion

These are just a few of the problems one could encounter in quantitative EPMA. In these particular cases, we were aware of the errors because we knew what values to expect from our analyses; some errors might have gone undetected had the compositions been totally unknown or had we not been making redundant measurements. For example, in experiment 2 in Table 1, the totals for determinations a and b for iron and chromium on spectrometers B and C are close to 100%. Such results could be deceptive to the unsuspecting analyst.

Also when very accurate results are desired, the microprobe analyst should be prepared. The simpler data-reduction procedures are generally quite good and adequate for most routine quantitative analyses. But in the extreme case, like the lead-germanium analysis above, an alternative, more extensive calculation procedure should be available.

References

1. K. F. J. Heinrich, *Adv. in X-ray Anal.* 11: 40, 1968.
2. K. F. J. Heinrich, *Electron Beam X-ray Microanalysis*, New York: Van Nostrand Reinhold, 1981.
3. T. R. Sweatman and J. V. P. Long, in G. Mollenstedt and K. Gaukler, Eds., *Proc. 5th Int. Conf. X-ray Optics and Microanalysis*, Berlin: Springer, 1969, 432.
4. T. R. Sweatman and J. V. P. Long, *J. Petrol.* 10: 332, 1969.
5. A. Meisel, Ed., *Roentgenspectren und chemische Bindung*, Leipzig: Karl Marx Universität, 1966.
6. R. L. Myklebust, C. E. Fiori, and K. F. J. Heinrich, *FRAME C: A Compact Procedure for Quantitative Energy Dispersive Electron Probe X-ray Analysis*, NBS Tech. Note 1106, 1979.
7. H. Yakowitz, R. L. Myklebust, and K. F. J. Heinrich, *FRAME: An On-line Correction Procedure for Quantitative Electron Probe Microanalysis*, NBS Tech. Note 796, 1973.
8. J. Henoc, K. F. J. Heinrich, and R. L. Myklebust, *A Rigorous Correction Procedure for Quantitative Electron Probe Microanalysis (COR)*, NBS Tech. Note 769, 1973.

A RE-EXAMINATION OF THE CHARACTERISTIC FLUORESCENCE CORRECTION

R. L. Myklebust and R. B. Marinenko

In classical quantitative electron probe microanalysis, the matrix correction factors have been separated into four terms. These terms are normally called the absorption, atomic number, fluorescence, and continuum fluorescence correction. Most computer programs employed in quantitative analysis only use the first three correction factors. This procedure is satisfactory for most specimens since the fluorescence due to the continuum for standards and for specimens is similar.¹ For the following discussion we shall ignore the continuum fluorescence since it makes an insignificant contribution, less than 0.3% relative, for the examples used. Both the absorption and atomic number corrections have an effect on every analysis. Of these effects, probably the most extensively studied factor is the absorption correction.² For most analyses, this is also the largest factor in the quantitative procedure.

For fluorescence to occur, a characteristic x-ray line (element b) in a specimen must be near to and on the high-energy side of the x-ray absorption edge for the measured x-ray line of another element (element a) in the specimen for this correction to be necessary. Fluorescence of element 'a' x rays by element 'b' x rays excite more x rays from element 'a' than would be excited directly by the incident electrons. If this effect is not corrected, the calculated concentration of element 'a' will be greater than its actual concentration in the specimen. Because of the mismatch in the relative energies of the exciting line and the absorption edge, the fluorescence by characteristic x-ray lines is insignificant for many specimens.

The largest effects are due to fluorescences by K x-ray lines. Fluorescences by L x-ray lines produce a much smaller effect, and fluorescences by M x-ray lines are generally ignored since they are considered to be too small to have any effect at all. It must also be remembered that fluorescences may be present even though the exciting x-ray line from element 'b' may not be the measured line for that element. This is the case for K-beta x-ray lines and for the many x-ray lines in the L series that are not measured.

In the following discussion, we examine two of the expressions used to compute the characteristic fluorescence correction as well as some of the parameters used in these expressions. Experimental data exhibiting large corrections for characteristic fluorescence will be used to test the different procedures.

Theory

For the purpose of this study, it was necessary to select materials that exhibit a large characteristic fluorescence correction but have minimal other matrix effects. One binary alloy of iron and chromium and one ternary alloy of iron, nickel, and chromium were selected for these comparisons. These alloys are also interesting since electron microprobe analyses of them usually produce results in which the chromium concentrations are greater than the actual concentrations.

The two expressions for characteristic fluorescence that we shall compare are the full calculation of fluorescence² and a simplified version due to Reed.³ Complete derivations of both expressions have been described by Heinrich.² The expression for the full calculation of characteristic fluorescence is

$$\frac{I_{fa}'}{I_{pa}'} = \frac{C_b}{2} \frac{I_p(b)}{I_p(a)} \frac{\mu(ab)}{\mu(*b)} \frac{r_a - 1}{r_a'} \omega_a P_a \left(\frac{\ln(1 + u)}{u} + \frac{\ln(1 + v)}{v} \right) \quad (1)$$

The authors are at the Center for Analytical Chemistry, National Bureau of Standards, Washington, DC 20234.

I_{fa}'/I_{pa}' is the ratio of the emitted x-ray intensity of element 'a' excited by element 'b' to the emitted primary intensity of element 'a' in the specimen. C_b is the mass fraction of element 'b', $I_p(b)/I_p(a)$ is the ratio of generated primary intensities for each pure element, and $\mu(ab)$ and $\mu(*b)$ are the mass absorption coefficients for the exciting line of 'b' in element 'a' and the specimen, respectively. The term $(r_a - 1)/r_a'$ is the ratio of ionizing absorptions to total absorptions for element 'a', ω_a is the fluorescence yield of element 'a', and P_a is the weight of the analytical line of element 'a'. The value of u is $X(*a)/\mu(*b)$, where $X(*a)$ is the product of the cosecant of the x-ray emergence angle and the absorption coefficient for the analytical line of element 'a' in the specimen $\mu(*a)$, and v is $[450\,000/(E_0^{1.65} - E_v^{1.65})]/\mu(*b)$. This expression as modified by Criss and Birks⁴ was used in the program COR⁵ which was employed to obtain some of our results below.

The second or simplified expression (Reed's) is

$$\frac{I_{fa}'}{I_{pa}'} = \frac{C_b}{2} p_{ij} \frac{A_a}{A_b} \left(\frac{U_b - 1}{U_a - 1} \right)^{1.67} \omega_b \frac{r_a - 1}{r_a} \frac{\mu(ab)}{\mu(*b)} \left(\frac{\ln(1 + u)}{u} + \frac{\ln(1 + v)}{v} \right) \quad (2)$$

where many of the terms are the same as in the previous expression. This is the expression used in the FRAME^{6,7} programs developed at NBS and in many of the other computer programs in use today. A_a and A_b are the atomic weights of the elements, U_a and U_b are the over-voltages for the x-ray lines for elements 'a' and 'b', and ω_b is the fluorescence yield for the x-ray line of element 'b'. The constant in the numerator of v was defined as 333 000 in the FRAME^{6,7} programs. p_{ij} is defined as 1 for K-K or L-L fluorescence, 4.2 for L-K fluorescence, and 0.24 for K-L fluorescence. These values assume for a K-fluorescence that both the K-alpha and K-beta lines of element 'b' will excite the analytical line of element 'a'. It is therefore not necessary to make separate calculations for K-alpha and K-beta lines. The same is assumed for L-lines. This scheme does fail, however, when only the K-beta line fluoresces the analytical line such as Co K-beta exciting the Fe K-lines. Also, the $(r_a - 1)/r_a$ term is defined as 0.88 for K-lines and 0.75 for L-lines. Equation (2) has been used in the programs FRAME⁶ and FRAME C.⁷ The FRAME program was used to obtain the results for comparison with the results below from COR.

In addition to comparing the two fluorescence correction calculations, we also compared results using different values for the fluorescence yields. COR used values for fluorescence yields that were available prior to the publication of the compilation of data by Bambynek et al.⁸ Equation (3) could be selected in COR if values were not available in the table of values stored in COR. For K-shell yields, the equation is

$$\omega_K = Z^4 / (1.06 \times 10^6 + Z^4) \quad (3)$$

Some of the COR data were fitted empirically for use in the FRAME programs. For K-shell yields in FRAME,

$$\omega_K = \exp[2.373 \ln Z - 8.902] \quad (4)$$

The result is that both programs use similar fluorescence yields (at least for the K-shell). For the L-shell, COR uses the individual subshell yield as modified by the Coster-Kronig transition probabilities; and the FRAME programs use the average L-shell fluorescence yield. The results from both original programs were compared below with results from both programs but with the later fluorescence yield values compiled by Bambynek whose fit to the data was used for the K-shell yields in COR and FRAME.

$$\omega_K / (1 - \omega_K) = (0.015 + 0.0372 \cdot Z - 0.64 \times 10^{-6} \cdot Z^3)^4 \quad (5)$$

where ω_K is the K-shell fluorescence yield and Z is the atomic number.

Discussion

An examination of the various fluorescence yields produced the values in Table 1. Experimental data were taken from Bambynek et al.⁸ Clearly, the fluorescence yields from

Bambynek are much higher than all of the previous values used in the FRAME and COR programs and should generate larger fluorescence corrections.

Table 2 contains mass fractions of chromium computed with the COR program for some of the fluorescence yields listed in Table 1. In all cases, the results produced by Eq. (5) are distinctly lower than all the previous concentrations of chromium.

FRAME and COR were compared by use of Eq. (5) for fluorescence yield in both programs. Table 3 contains an analysis of each alloy by each program. We have listed four significant figures in these analyses for comparison purposes only. In actual practice, no more than three significant figures should be used. The value of the constant in v makes only a very small difference in the final result; however, the values for fluorescence yields do make a considerable difference. Reed's expression for the fluorescence correction does still appear to be quite adequate for K-K fluorescence. Further work is required to test this correction and the fluorescence yields for L-fluorescences.

References

1. R. L. Myklebust et al., "Comments on the continuum fluorescence correction," *Proc. 5th Conf. Electron Probe Analysis*, 1970, 11A-11C.
2. K. F. J. Heinrich, *Electron Beam X-ray Microanalysis*, New York: Van Nostrand Reinhold, 1981.
3. S. J. B. Reed and J. V. P. Long, *Proc. 3rd Intern. Conf. on X-Ray Optics and Microanalysis*, New York: Academic Press, 1963, 317.
4. J. Criss and L. S. Birks, in T. D. McKinley, K. F. J. Heinrich, and T. D. Wittry, Eds., *The Electron Microprobe*, New York: Wiley, 1966, 217.
5. J. Henoc et al., *A Rigorous Procedure for Quantitative Electron Probe Microanalysis (COR2)*, NBS Tech. Note 769, 1973.
6. H. Yakowitz et al., *FRAME: An On-Line Procedure for Quantitative Electron Probe Microanalysis*, NBS Tech. Note 796, 1973.
7. R. L. Myklebust et al., *FRAME C: A Compact Procedure for Quantitative Energy-Dispersive Electron Probe X-ray Analysis*, NBS Tech. Note 1106, 1979.
8. W. Bambynek et al., "X-ray fluorescence yields, Auger, and Coster-Kronig transition probabilities," *Rev. Mod. Phys.* 44: 716-813, 1972.

TABLE 1.--Fluorescence yields for chromium, iron, and nickel.

	COR	Eqn 3	Eqn 4	Eqn 5	Exper.
Z	Table	COR	FRAME		Data ^c
24	0.272	0.238	0.257	0.282	0.283
26	.291	.301	.310	.347	.342
28	.320	.367	.370	.414	-

TABLE 2.--Chromium concentrations (mass fractions) in two alloys for different fluorescence yields.

Alloy	k-value	Table	Eqn 3	Eqn 5
FeCr	0.1258	0.1029	0.1042	0.1011
FeNiCr	.2204	.1923	.1942	.1899

TABLE 3.--Concentrations in mass fraction.

Element	k-value	C COR	C FRAME ^a	C FRAME ^b	Wet Chemical
FeCr					
Cr	0.1258	0.1011	0.1008	0.1016	0.1010
Fe	.8799	.8970	.8952	.8952	.8984
Total		.9981	.9960	.9969	.9994
NiFeCr					
Cr	0.2204	0.1899	0.1897	0.1908	0.181
Fe	.6882	.7053	.7027	.7032	(.710)*
Ni	.0948	.1048	.1034	.1034	.109
Total		1.0000	.9958	.9974	1.000

^aConstant in v is 333 000. ^bConstant in v is 450 000. *Iron was determined by difference, which leaves some doubt as to actual composition of this specimen.

QUANTITATIVE ANALYSIS OF SILICATE AND OXIDE MINERALS: A REEVALUATION OF ZAF CORRECTIONS AND PROPOSAL FOR NEW BENCE-ALBEE COEFFICIENTS

J. T. Armstrong

The relative accuracy of a series of ZAF expressions and Bence-Albee factors derived from them are evaluated for analyses of a set of mineral standards. The magnitude of errors encountered in determining mixed oxidation state or hydroxyl substitution using various correction procedures are discussed. A new set of Bence Albee coefficients are proposed which provide a better fit to the analytical data.

With the advent of a new generation of electron-beam instruments with higher-efficiency wavelength and energy dispersive detectors, superior beam stabilization, and more sophisticated computer control, it is possible to perform significantly more precise analyses than previously routinely achievable. In geological applications there is often the desire to determine small deviations from stoichiometry on the basis of the analyses' summation or relative cation proportions in order to evaluate the exact composition of defect or solid solution compounds, the relative amount of elements in mixed oxidation states (e.g., $\text{Fe}^{+3}/\text{Fe}^{+2}$), the amount of substitution of OH^- for O^{2-} , etc. Such determinations require high absolute accuracy, not merely high precision, and depend on the standards analyzed and the correction procedures employed.

In a series of papers recently summarized, Heinrich examined the uncertainties inherent in ZAF correction procedures and warned that care must be taken not to overextrapolate the correction procedures by employing standards of greatly differing ZAF properties from the samples analyzed.¹ Unfortunately this advice is not always remembered. In a growing number of geological studies, analyses are performed with simple oxide standards and attention is not paid to the nature of correction procedures employed, yet accuracy is assumed to be of the same level as the precision. Under such circumstances the data can be seriously over-interpreted and lead to erroneous conclusions. In this paper the variability of results produced by use of the various commonly used correction procedures is evaluated for selected samples of geologic interest and a new set of Bence-Albee coefficients based on up-to-date ZAF correction equations is proposed.

Bence-Albee Corrections

One of the most used correction algorithms for electron microbeam analysis of geological materials is the a-factor approach of Bence and Albee.^{2,3} This is an empirical approach based on two assumptions: (1) that there is a simple hyperbolic relation between relative concentration C and relative intensity K in binary oxide systems, the curvature of which can be expressed by an "a-factor" such that $C/K = a + (1 - a)C$; and (2) that in ternary or more complicated oxide systems, the relation between relative intensity and relative concentration can be determined by a linear combination of a-factors such that $a = \sum(c_i a_i) / \sum c_i$. As Heinrich¹ has noted, these approximations are highly accurate for corrections dominated by absorption, less accurate for corrections dominated by atomic number factors, and relatively inaccurate for cases dominated by characteristic fluorescence.

Bence and Albee² emphasized that one could obtain the best results with their correction method by empirically determining a-factors by analyses of a well-characterized set of silicate and oxide standards. However, most investigators using the Bence-Albee procedures

The author is associated with the Division of Geological and Planetary Science, California Institute of Technology, Pasadena, CA 91125. He thanks H. F. Shaw providing raw analytical data used in the comparison of correction procedures for thick polished specimens, and A. L. Albee and A. A. Chodos for helpful discussion. Support from NASA grant NAG 9-43 is acknowledged; Division Contribution #4075 (477).

employ \bar{a} -factors calculated from an early ZAF correction procedure.³ Shaw and Albee⁴ have demonstrated that use of empirically determined \bar{a} -factors produces significantly better analytical results for a set of silicate and oxide standards than the ZAF-calculated \bar{a} -factors, and their laboratory employs these modified factors. Armstrong⁵ subsequently demonstrated, using the same set of analytical data, that use of new modified ZAF correction procedures based on the methods of Packwood and Brown^{6,7} and Love and Scott⁸ produces analytical results comparable to those obtained by the best-fit \bar{a} -factor corrections. This paper evaluates whether \bar{a} -factors calculated from newer ZAF correction procedures produce results comparable to the best-fit \bar{a} -factors or ZAF expressions themselves.

Matrices of \bar{a} -factors were calculated from the following ZAF correction schemes: (1) the Packwood and Brown $\phi(\rho z)$ model^{6,7} as modified by Armstrong,⁵ (2) the Love Scott model,⁷ and (3) the NBS Frame correction program⁸ with the Heinrich-modified absorption correction.¹ The analytical data of Shaw and Albee,⁴ collected at an accelerating potential of 15 keV and take-off angle of 38.5°, were processed with each of the above ZAF corrections and \bar{a} -factor corrections developed from them. The data were also processed by use of the conventional \bar{a} -factors of Albee and Ray³ and the best-fit \bar{a} -factors of Shaw and Albee.⁴ The results are given in Table 1, which shows that best results (lowest mean relative errors) are produced from using the Shaw and Albee best fit \bar{a} -factors and the modified Packwood/Brown and Love/Scott ZAF corrections. The best ZAF-calculated \bar{a} -factor corrections appear to be those of the modified Packwood/Brown and Love/Scott corrections. The highest systematic errors are produced by use of the conventional \bar{a} -factors of Albee and Ray.

Table 2 lists \bar{a} -factor matrices for selected elements calculated from the Armstrong-modified Packwood/Brown and Love/Scott ZAF corrections and compares them to the conventional \bar{a} -factors calculated by Albee and Ray. The factors are for an accelerating potential of 15 keV and a take-off angle of 40° (the standard analytical conditions for the currently commercially available electron microprobes). Examination of the matrices shows that calculated \bar{a} -factors can vary significantly (by as much as 15-20%) depending upon the algorithm employed. For example, the \bar{a} -factor for Mg by FeO is 1.937 for Albee and Ray, 2.013 for Love and Scott, and 2.101 for Packwood and Brown--a difference of 8%; the \bar{a} -factor for Cr by FeO is 0.880 for Albee and Ray, 0.795 for Love and Scott, and 0.797 for Packwood and Brown--a difference of 10%. The largest deviations between the Albee and Ray matrix from the newer ZAF matrices are in cases where either the absorption or the characteristic fluorescence corrections are particularly large.

Determination of Stoichiometry by Electron Probe Analysis

From the variability in \bar{a} -factors shown in Table 2, it is obvious that the calculated compositions may vary considerably according to the correction procedures employed, particularly when standards and samples are dissimilar in composition. Such uncertainties in the accuracy of data correction can result in serious overinterpretation or misinterpretation of sample stoichiometry, as can be seen in the following example. Ti-rich fassaite pyroxene is a mineral commonly found in refractory inclusions in carbonaceous chondrite meteorites, which are thought to contain some of the most primitive minerals that first solidified from the cooling solar nebula. Some Ti in the fassaite in these inclusions is present as Ti^{3+} instead of the common Ti^{4+} . The amount of Ti^{3+}/Ti is used as an indicator of how highly reducing the formation conditions of the inclusions were. The amount of Ti^{3+} is calculated from stoichiometric constraints in pyroxene of four cations for six oxygen atoms. Table 3 presents the results of stoichiometric calculations for a single fassaite analysis using various of the ZAF and \bar{a} -factor correction procedures previously discussed. Simple oxides and silicates were used as standards. The calculated Ti^{3+}/Ti is seen to vary dramatically, depending on the correction procedure employed, from 13% to 66%. This uncertainty due to the correction procedure employed is much greater than the approximately 10% maximum uncertainty in measurement precision. It is significant that major differences are observed in processing data with a particular ZAF correction as opposed to processing with \bar{a} -factors based on that correction--the calculated Ti^{3+}/Ti is 13% using the Love/Scott ZAF correction and 51% using \bar{a} -factors determined by the Love/Scott ZAF correction. (Analysis of a standard glass of fassaite composition indicates that the Love/Scott or Packwood/Brown ZAF procedures yield the most accurate results in this case.)

Conclusions

Uncertainties in the accuracy of the correction procedures employed can be far greater than uncertainties due to measurement precision in calculating sample stoichiometry, particularly when simple oxide and silicates are used as standards. In order to avoid serious overinterpretation or misinterpretation of data, secondary standards similar in composition to the samples should be analyzed along with the samples. It appears that one can get more accurate Bence-Albee corrections using new a -factors based on more up-to-date ZAF correction procedures. However, both new ZAF correction procedures themselves or Bence-Albee corrections based on best-fit empirical factors appear to produce superior results. With the availability of new commercial high-precision electron microprobes with standard geometry, efforts should once again be focused on making "round-Robin," high-precision measurements of k -factors in well-characterized sets of silicate and oxide standards so that the relative accuracy of the various correction procedures can be determined and the best set of Bence-Albee factors can be calculated.

References

1. K. F. J. Heinrich, *Electron Beam X-ray Microanalysis*, New York: Van Nostrand Reinhold, 1981.
2. A. E. Bence and A. L. Albee, "Empirical correction factors for the electron microanalysis of silicates and oxides," *J. Geol.* 76: 382, 1968.
3. A. L. Albee and L. Ray, "Correction factors for electron probe microanalysis of silicates, oxides, carbonates, phosphates, and sulfates," *Anal. Chem.* 42: 408, 1970.
4. H. F. Shaw and A. L. Albee, "An empirical investigation into possible nonlinearities of the microprobe correction factors in the system $MgO-CaO-Al_2O_3-SiO_2$," *Microbeam Analysis--1979*, 227-230.
5. J. T. Armstrong, "New ZAF and a -factor correction procedures for the quantitative analysis of individual microparticles," *Microbeam Analysis--1982*, 175-180.
6. R. H. Packwood and J. D. Brown, "A Gaussian expression to describe $\phi(\rho z)$ curves for quantitative electron probe microanalysis," *X-ray Spectrometry* 10: 138-146, 1981.
7. J. D. Brown, R. H. Packwood, and K. Milliken, "Quantitative electron probe microanalysis with Gaussian expression for $\phi(\rho z)$ curves," *Microbeam Analysis--1981*, 174.
8. G. Love and V. D. Scott, "Evaluation of a new correction procedure for quantitative electron probe microanalysis," *J. Phys.* D-11: 1369-1376, 1978.

TABLE 1.--Mean percent relative errors for analyses of minerals and glasses when processed by various ZAF and a -factor correction procedures.

Correction Procedure	Mean % relative error $\pm 2\sigma^1$			
	MgO	Al_2O_3	SiO_2	CaO
Shaw/Albee a -factor	-0.3 \pm 2.1	-0.1 \pm 3.5	0.0 \pm 1.0	-0.1 \pm 1.8
Packwood/Brown ZAF	-0.1 \pm 2.2	-0.6 \pm 3.4	0.1 \pm 1.2	0.0 \pm 2.0
Packwood/Brown a -factor	-0.4 \pm 2.3	-0.3 \pm 3.4	0.7 \pm 1.5	0.0 \pm 2.0
Love/Scott ZAF	-0.2 \pm 2.2	-0.4 \pm 3.2	0.4 \pm 1.6	0.6 \pm 2.2
Love/Scott a -factor	-0.6 \pm 2.2	0.0 \pm 3.6	1.2 \pm 1.9	0.7 \pm 2.2
NBS/Frame ZAF	0.4 \pm 2.4	0.4 \pm 3.2	1.1 \pm 1.4	0.3 \pm 2.2
NBS/Frame a -factor	0.2 \pm 2.6	0.8 \pm 3.5	1.6 \pm 1.7	0.3 \pm 2.1
Albee/Ray a -factor	1.1 \pm 2.1	1.9 \pm 4.0	2.5 \pm 2.1	1.1 \pm 2.3

¹Mean and standard deviations of the percent relative errors obtained for the multiple analysis of 23 natural and synthetic minerals and glasses. Raw analytical data taken from the work of Shaw and Albee (1979)⁴.

TABLE 2.--a-factor matrices for $E_0 = 15$ keV and $\psi = 40^\circ$.-- a-FACTOR MATRIX CALCULATED FROM ZAF CORRECTIONS OF PACKWOOD & BROWN --

	Na2O	MgO	Al2O3	SiO2	K2O	CaO	TiO2	V2O3	Cr2O3	MnO	FeO	NiO
Na	1.000	1.126	1.236	1.343	1.599	1.773	2.063	2.306	2.544	2.935	3.265	4.039
Mg	2.076	1.000	1.009	1.084	1.221	1.325	1.466	1.588	1.719	1.919	2.101	2.520
Al	1.612	1.720	1.000	.999	1.087	1.163	1.236	1.300	1.382	1.491	1.602	1.854
Si	1.340	1.413	1.474	1.000	.992	1.053	1.090	1.120	1.174	1.228	1.299	1.452
K	1.078	1.110	1.109	1.135	1.000	.858	.935	.937	.969	.964	.994	1.037
Ca	1.034	1.064	1.059	1.082	1.201	1.000	.863	.872	.909	.907	.938	.979
Ti	1.060	1.088	1.079	1.101	1.135	1.163	1.000	.976	.832	.850	.899	.962
V	1.085	1.113	1.103	1.124	1.132	1.162	1.026	1.000	1.012	.808	.870	.955
Cr	1.072	1.100	1.089	1.109	1.097	1.127	1.094	.988	1.000	.973	.797	.905
Mn	1.105	1.133	1.121	1.141	1.114	1.144	1.108	1.096	1.029	1.000	1.015	.877
Fe	1.092	1.119	1.106	1.126	1.088	1.118	1.080	1.064	1.082	.986	1.000	.797
Ni	1.085	1.112	1.099	1.118	1.063	1.093	1.054	1.032	1.046	1.024	1.042	1.000

---- a-FACTOR MATRIX CALCULATED FROM ZAF CORRECTIONS OF LOVE & SCOTT ----

	Na2O	MgO	Al2O3	SiO2	K2O	CaO	TiO2	V2O3	Cr2O3	MnO	FeO	NiO
Na	1.000	1.130	1.242	1.352	1.564	1.741	2.021	2.232	2.450	2.778	3.066	3.719
Mg	2.134	1.000	1.009	1.086	1.196	1.302	1.440	1.547	1.671	1.846	2.013	2.393
Al	1.645	1.756	1.000	.999	1.072	1.149	1.220	1.276	1.354	1.451	1.556	1.790
Si	1.356	1.431	1.494	1.000	.987	1.048	1.083	1.110	1.162	1.211	1.279	1.425
K	1.088	1.120	1.118	1.144	1.000	.858	.935	.935	.965	.959	.987	1.027
Ca	1.044	1.073	1.068	1.091	1.197	1.000	.863	.870	.906	.902	.932	.971
Ti	1.071	1.099	1.089	1.111	1.132	1.161	1.000	.974	.829	.846	.894	.955
V	1.099	1.127	1.116	1.137	1.131	1.162	1.028	1.000	1.011	.806	.867	.949
Cr	1.089	1.116	1.104	1.124	1.098	1.128	1.095	.989	1.000	.970	.795	.901
Mn	1.125	1.153	1.140	1.161	1.117	1.149	1.113	1.096	1.032	1.000	1.014	.874
Fe	1.114	1.141	1.128	1.148	1.093	1.124	1.087	1.067	1.083	.987	1.000	.796
Ni	1.113	1.139	1.125	1.145	1.072	1.104	1.065	1.038	1.051	1.024	1.040	1.000

----- a-FACTOR MATRIX CALCULATED FROM ZAF CORRECTIONS OF ALBEE & RAY -----

	Na2O	MgO	Al2O3	SiO2	K2O	CaO	TiO2	V2O3	Cr2O3	MnO	FeO	NiO
Na	1.000	1.207	1.297	1.405	1.575	1.767	2.000	2.163	2.383	2.677	2.961	3.640
Mg	2.020	1.000	1.042	1.110	1.191	1.311	1.422	1.496	1.619	1.778	1.937	2.303
Al	1.613	1.739	1.000	1.045	1.089	1.173	1.231	1.275	1.358	1.460	1.566	1.803
Si	1.372	1.465	1.524	1.000	1.008	1.071	1.095	1.115	1.171	1.228	1.299	1.453
K	1.097	1.129	1.122	1.145	1.000	.993	.967	.948	.967	.954	.976	1.007
Ca	1.056	1.085	1.074	1.094	1.254	1.000	.921	.899	.918	.906	.926	.953
Ti	1.090	1.116	1.100	1.118	1.181	1.201	1.000	.960	.900	.893	.915	.945
V	1.116	1.142	1.124	1.140	1.171	1.191	1.026	1.000	.989	.897	.919	.949
Cr	1.105	1.129	1.110	1.126	1.134	1.155	1.109	.991	1.000	.944	.880	.914
Mn	1.139	1.164	1.143	1.159	1.149	1.171	1.121	1.111	1.031	1.000	.978	.902
Fe	1.128	1.152	1.131	1.146	1.124	1.146	1.095	1.080	1.096	.990	1.000	.849
Ni	1.126	1.149	1.127	1.141	1.102	1.124	1.073	1.051	1.064	1.040	1.055	1.000

TABLE 3.--Meteorite fassaite analysis processed with various ZAF and a-factor correction procedures.

----- OXIDE WEIGHT % -----									
	MgO	Al2O3	SiO2	CaO	TiO2	Cr2O3	V2O3	FeO	Total
ZAF cor.									
L/S	10.14	18.19	41.29	25.14	2.02	0.17	2.05	0.67	99.67
a-factor									
L/S	10.10	18.23	41.65	25.00	2.02	0.17	2.05	0.67	99.89
P/B	10.16	18.25	41.53	24.85	2.01	0.17	2.03	0.66	99.66
NBS	10.25	18.46	41.90	24.91	2.02	0.17	2.04	0.66	100.41
A/R	10.24	18.61	42.22	25.12	2.05	0.17	2.07	0.67	101.15

----- ATOMIC PROPORTIONS -----											
	Ca+2	Mg+2	Fe+2	Al+3	Cr+3	V +3	Ti+3	Ti+4	Si+4	O -2	%Ti+3/Ti
ZAF cor.											
L/S	0.992	0.556	0.021	0.789	0.005	0.061	0.007	0.049	1.520	6.000	13.12
a-factor											
L/S	0.984	0.553	0.021	0.790	0.005	0.060	0.028	0.028	1.531	6.000	50.62
P/B	0.980	0.558	0.020	0.792	0.005	0.060	0.027	0.029	1.529	6.000	47.70
NBS	0.975	0.558	0.020	0.795	0.005	0.060	0.033	0.023	1.531	6.000	59.26
A/R	0.977	0.554	0.020	0.796	0.005	0.060	0.037	0.019	1.532	6.000	66.44

Corrections: L/S = Love & Scott, P/B = Packwood & Brown, NBS = NBS/Frame,
A/R = Albee & Ray. Data for E0 = 15 keV, Psi = 40.

A GENERAL CHARACTERISTIC FLUORESCENCE CORRECTION FOR PARTICLES, THIN FILMS, AND THICK SPECIMENS

J. T. Armstrong and P. R. Buseck

A rigorous, general characteristic fluorescence correction for electron microprobe analysis of samples of given geometry has been developed, and specific versions of this equation have been formulated for calculation of the fluorescence produced in thin films and spherical particles. These equations are evaluated for representative matrices having large characteristic fluorescence corrections and the results are compared with existing empirical correction equations.

Armstrong and Buseck¹ have developed a rigorous, general characteristic fluorescence correction expression that enables calculation of the amount of fluorescence in samples of given geometries (thick specimens, thin films, and particles). The general equation is difficult to evaluate; it requires numerical evaluation of a six-fold integral. However, specific simplified expressions can be developed for particular geometries such as a thin film of a spherical particle. Unlike a number of simplified approaches, these equations make no assumptions regarding the distribution of primary x-ray production with depth but evaluate the fluorescence contribution by numerical integration of expressions incorporating $\phi(\rho z)$ equations such as those of Reuter,² Packwood and Brown,³ or Armstrong.⁴

These fluorescence expressions have been evaluated for a series of matrices with large characteristic fluorescence contributions, including (1) Fe K α in FeNi₃, (2) Fe K α in Cu₅FeS₄, (3) Cr K α in FeCr₂O₄, (4) Cl K α in KCl, and (5) P K α in K₃PO₄. For thick polished specimens at $E_0 = 15$ keV and $\psi = 40^\circ$, the amount of emitted x rays due to characteristic fluorescence relative to emitted primary x rays (F_f) for these samples is 0.167, 0.102, 0.036, 0.038, 0.022, respectively. Figures 1 and 2 show typical results for the fraction of characteristic fluorescence vs thin-film thickness calculated from the rigorous correction utilizing the $\phi(\rho z)$ expression of Armstrong⁴ and compare the results with those using the empirical thin-film corrections of Nockolds et al.⁵ and of Twigg and Fraser.⁶ As can be seen in the figures, there is a divergence in the three expressions for thick films, as is expected since the empirical corrections^{5,6} do not incorporate accurate expressions for $\phi(\rho z)$ and are designed only for use with relatively thin films. The expression of Nockolds appears to be closer in agreement with the rigorous, theoretical expression than that of Twigg and Fraser; however, all the expressions give about the same results for films less than approximately 1 μm thick, which indicates that either of the simplified expressions is adequate as long as the film is not too thick.

Results of simulations of the fluorescence correction for spherical particles using the Reuter,² Packwood and Brown,³ or Armstrong⁴ $\phi(\rho z)$ model and either employing or not employing a correction for electron sidescatter⁷ are all essentially identical, particularly for small ($< 20 \mu\text{m}$) particles. Typical results, employing a sidescatter-modified Reuter $\phi(\rho z)$, are presented in Table 1, which lists F_f in the particles relative to F_f in thick polished specimens of identical composition. The results indicate that particles as small as 5 μm in diameter can have significant fluorescence corrections (20 to 40% of that in the thick polished specimens). The spherical-particle fluorescence corrections calculated with the rigorous equations are in good agreement with the values obtained from the empirical simplified expressions previously proposed by Armstrong and Buseck¹ (generally better than 10% relative), which shows that these simplified expressions are adequate, particularly for small particles.

Author Armstrong is associated with the Division of Geological and Planetary Sciences, California Institute of Technology, Pasadena, CA 91125. Author Buseck is associated with the Departments of Chemistry and Geology, Arizona State University, Tempe, AZ 85287. Support from NASA grant NAG 9-43 and grants ATM-8022849 and PFR-7617130 from the Atmospheric Sciences Division of the National Science Foundation are acknowledged. Caltech, Division Contribution 4076(478).

Conclusions

The comparison of data produced by rigorous, theoretical fluorescence correction equations with those produced by empirical correction expressions for particles and thin films indicate that the expressions for particles are generally adequate but that the existing empirical expressions for thin films are accurate only for films less than 1 μm thick. The results of calculations using these rigorous expressions show that a 2000 \AA -thick film or a 1 μm -diameter particle typically has about 10% of the relative contribution from characteristic fluorescence that occurs in an infinitely thick polished specimen (TPS), a 1 μm -thick film has about 30 to 40% of the contribution in a TPS, and a 10 μm -diameter particle has more than 50% of the contribution in a TPS. Thus, in extreme cases, certain elements in a 2000 \AA -thick film or a 1 μm particle can have characteristic fluorescence corrections as high as 5 which points up the need for evaluating such corrections for accurate quantitative analysis.

References

1. J. T. Armstrong and P. R. Buseck, "Development of a characteristic fluorescence correction for thin films and particles," *Proc. VIII Internat. Conf. on X-ray Optics and X-ray Microanal.*, 1977, 42A-F; *X-ray Spectrometry*, in prep.
2. W. Reuter, "The ionization function and its application to the electron probe analysis of thin films," G. Shinoda, K. Kohra, and T. Ichinokawa, Eds., *Proc. VI Internat. Conf. on X-ray Optics and Microanal.*, University of Tokyo Press, 1972, 121-130.
3. R. H. Packwood and J. D. Brown, "A Gaussian expression to describe $\phi(\rho z)$ curves for quantitative electron probe microanalysis," *X-ray Spectrometry* 10: 138-146, 1981.
4. J. T. Armstrong, "New ZAF and a-factor correction procedures for the quantitative analysis of individual microparticles," *Microbeam Analysis--1982*, 175-180.
5. C. Nockolds, G. Cliff, and G. W. Lorimer, "Characteristic x-ray fluorescence correction in thin foil analysis," *Micron* 11: 325-326, 1980.
6. M. E. Twigg and H. L. Fraser, "A comparison of two models for the characteristic x-ray fluorescence correction in thin-foil analysis," *Microbeam Analysis--1982*, 37-42.
7. J. T. Armstrong and P. R. Buseck, "Quantitative chemical analysis of individual microparticles using the electron microprobe: Theoretical," *Anal. Chem.* 47: 2178-2192, 1975.

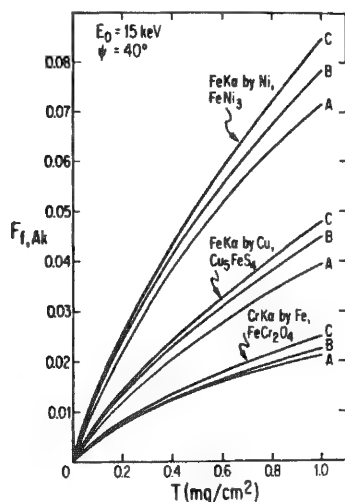


FIG. 1.--Plots of calculated relative characteristic fluorescence F vs thin-film mass thickness T for (1) Fe $K\alpha$ by Ni in FeNi_3 , (2) Fe $K\alpha$ by Cu in Cu_5FeS_4 , and (3) Cr $K\alpha$ by Fe in FeCr_2O_4 . Corrections used in calculations are (A) Armstrong & Buseck, (B) Nockolds et al., (C) Twigg & Fraser. Calculations were made at $E_0 = 15$ keV and $\psi = 40^\circ$. (B) and (C) considerably overestimate amount of fluorescence in thick films and give values greater than for those for infinitely thick, polished specimens.

TABLE 1.--Characteristic fluorescence in spherical particles relative to that in thick polished specimens of same composition.

D (μm)	Fluorescence correction relative to TPS				
	Fe $K\alpha$ in FeNi_3	Fe $K\alpha$ in Cu_5FeS_4	Cr $K\alpha$ in FeCr_2O_4	Cl $K\alpha$ in KCl	P $K\alpha$ in K_3PO_4
100	0.81	0.75	0.89	0.89	0.82
20		0.46	0.67		0.64
10	0.47	0.30	0.50	0.55	0.50
5	0.31	0.19	0.31	0.37	0.32
1	0.09	0.05	0.08	0.08	0.09

Data calculated for $E_0 = 15$ keV and take-off angle = 40° .

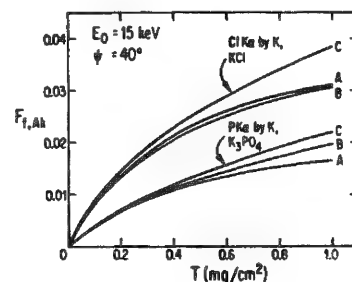


FIG. 2.--Plots of F vs T for (1) Cl $K\alpha$ by K in KCl and (2) P $K\alpha$ by K in K_3PO_4 . Expressions and analytical conditions employed are same as given in Fig. 1.

THE X-RAY CONTINUUM: A BLESSING AND A CURSE

Eric Lifshin

The slowing down of electrons as an electron beam interacts with matter results in the emission of the polychromatic x-ray continuum. It is the principal source of background in the electron-microprobe analysis of bulk specimens. Since determination of the characteristic line intensity after background subtraction is the key to establishing how much of an element is present, and in some cases whether it is there at all, the continuum must be viewed along with the counting time and characteristic line intensity itself as an important factor influencing microanalysis sensitivity. Knowledge of the continuum is particularly important when an energy-dispersive spectrometer (EDS) is used because of its inferior energy resolution relative to a diffraction spectrometer. An EDS smears inherently sharp characteristic lines (a few electron volts) over many tens of electron volts, which leads to low ratios of integrated peak to integrated background and consequently decreased sensitivity. It is therefore not too surprising that when high spatial resolution is not critical, x-ray excitation rather than electron excitation can lead to more than a ten-fold improvement in minimum detectability limits, since it does not excite the specimen continuum.

On the other hand, the x-ray continuum can provide valuable information about a sample. For example, several methods have been developed that relate the continuum intensity to the total mass of a region being analyzed and thus make it possible to use a peak-to-background ratio as a measurement of local mass fraction. In addition, variations in the continuum intensity observed during line scans can be useful in distinguishing changes in surface topography from variations in chemical distribution. However, procedures for measuring the continuum and understanding its role in electron microprobe analysis are not as well established as the more familiar quantitative methods used to convert characteristic line intensity into composition. This paper reviews some of the models that describe the continuum spectral distribution and also examines some of the techniques used to take advantage of the information it conveys.

Historical Background

Much of our present understanding of x rays and how they provide information about the structure and chemistry of matter is based on research performed before 1930. This work was considered so important that principal investigators were the recipients of six Nobel Prizes during that period:¹ W. C. Roentgen (1901), Max von Laue (1914), W. H. and W. L. Bragg (1915), C. G. Barkla (1917), K. M. G. Siegbahn (1924), and A. H. Compton (1927); and had H. G. J. Moseley not been killed at an early age in World War I, he may well have received that honor as well. Individuals involved in both electron microprobe analysis and x-ray fluorescence spectroscopy certainly recognize that Moseley's systematic studies of the unique relationship between atomic number and x-ray wavelength form the basis for qualitative elemental analysis. What is perhaps less well known is that, at about the same time (1913), he recognized that radiation from an x-ray tube consisted "of two kinds, (A) radiation of indefinite wavelength, analogous to white light, (B)...monochromatic radiation, probably characteristic of the platinum"² which was the target he used. He even made some preliminary attempts to characterize the continuum distribution. There was some question at that time whether "general" radiation, which was the name used for the x-ray continuum, might actually be a series of closely spaced lines. W. H. Bragg, himself, raised this point when he wrote:

Possibly this general radiation may eventually be found to consist in part at least of bands of homogeneous rays, but the resolving powers of the spectrometer are hardly sufficient as yet to determine the point.... It is not, however, with this general radiation that I

The author is at General Electric Co. Corporate Research and Development, Box 8, Schenectady, NY 12301.

propose to deal at present.³

Though he was referring specifically to the 1914 paper from which this quote is taken his words were somewhat prophetic, for neither Bragg nor many co-workers in this area of x-ray research spent much time studying the x-ray continuum. Nearly fifteen years later William Duane, whose name we associate with that of Hunt in describing the continuum short-wavelength limit, wrote:

The impact of electrons against atoms produce two different kinds of radiation--the general, or continuous spectrum and the line spectra. By far the greatest amount of energy radiated belongs to the general spectrum and not to the line spectra. In the x-ray region, in particular, the continuous, or general radiation spectrum carries most of the radiant energy. In spite of this, and because the line spectra have an important bearing on atomic structure, the general radiation has received much less attention than the line spectra in the recent development of fundamental ideas in physical science.⁴

Certainly now, almost sixty years after Duane's paper, the situation still has not really changed very much. However, before we discuss events closer to the present, we mention two very important studies: one theoretical, by H. A. Kramers (1923), and the other experimental, by H. Kuhlenskampff (1923).^{5,6} According to Kuhlenskampff (whose measurements were done below 12 kV) the intensity distribution of the continuum is given by

$$I_{\nu} = C[N(\nu_0 - \nu) + N^2b] \quad (1)$$

where ν is the frequency, ν_0 is the limiting frequency, N is the atomic number, and b and C are constants. With a knowledge of these measurements, Kramers set out to show "...how it is possible to account theoretically for the main features of the phenomena of x-ray absorption and continuous x-ray emission...." Viewing the problem as beyond the realm of quantum mechanics at that time, he applied the Bohr correspondence principle in order to calculate

...the radiation which on the classical electron theory which would be emitted by the free electrons in consequence of the change of motion produced by the forces arising from the electric particles in the atom. In view of the approximate character of the result which may be obtained in this way, we are led in the treatment of this problem to introduce simplifications which make the electrodynamical problem much easier.

Then followed over twenty pages of calculations and explanations which, along with the many years that have since past, have led most of us to forget the words "approximate" and "simplification" in the quote contained above. The final result is, in fact, rather simple, namely that

$$I_{\nu} = 4.95s \times 10^{-50} N(\nu_0 - \nu) \quad (2)$$

where s = the number of electrons striking the target per second. It is obviously in good agreement with Eq. (1) from which it differs only in that it does not contain the second term, which is small compared to the first. The second term in Eq. (1) is associated with what is now termed a backscatter correction, which Kramers did not make.

It is interesting, although somewhat difficult, to trace the use and abuse of Kramers's equation since 1923. Revered like Newton's laws and Michelangelo's *David*, it has been used as the cornerstone for a variety of models to facilitate background subtraction as well as thin-film and particle analysis. Sometimes it seems that it would be more appropriate to honor the nameless "adjustable parameters" that have accounted for both the success of Kramers's equation and that of many of our frequently used quantitation schemes.

In addition to looking at some of the initial assumptions, this retrospective also must draw attention to the change in terms and commonly used symbols which further cloud any proper understanding of Kramers's work. Intensity, for example, according to Compton and Allison (1926), refers to

...the average energy emitted between frequencies ν and $\nu + \Delta\nu$, due to a single electron with energy eV traversing a unit area which includes a small number of atomic nuclei of atomic number Z⁷

The definition is similar to that implicitly given by Kramers (who uses the symbol N for atomic number), but is different from the number of photons per second emitted between energies E and $E + \Delta E$, which is what is commonly used today.

We move a few steps backward in the derivation of Eq. (2) to obtain the intensity of continuum x rays emitted from an infinitely thin target:

$$i_v d\sigma dv = \frac{32\pi^2 N^2 e^6}{3\sqrt{3} c^3 m^2 v^2} s A d\sigma dv \quad v < v_0 \quad (3)$$

where m is the mass of an electron, v is the velocity of an electron, c is the speed of light, e is the charge of an electron, $d\sigma$ is the area struck by the electrons, A is the number of atoms per unit area in the bombarded area, and v , N , and s have already been defined. This expression, rewritten by Compton and Allison, is given by

$$i_v dv = \frac{16\pi^2 A Z^2 e^5}{3\sqrt{3} m v c^3} dv \quad v < v_0 \quad (4)$$

To understand why the two expressions are equivalent, the following points should be noted:

1. The square of the electron velocity v is replaced by $2eV/m$ (from $mv^2/2 = eV$, where V is the difference in potential between the anode and cathode of the electron-beam device).
2. The quantity $A d\sigma$ is replaced by the symbol A , since Kramers referred to the number of atoms per unit area (his A) times the area $d\sigma$ actually struck.
3. The term s (number of electron/s) is set equal to 1, so that Eq. (3) is on a per-electron basis.

The thin-film form of the intensity distribution equation (in the form of either Eq. 3 or 4) is as important to present-day work as Eq. (2) because of the interest in thin-film and particle analysis. The bridge between the thin film and bulk equations involves an integration of the intensity function for the thin film from the initial velocity of the electron to a velocity that corresponds to the frequency of interest ($v = mv^2/2h$, where h is Planck's constant).

Renewed Interest in the X-ray Continuum

In the late 1950s renewed interest in the x-ray continuum accompanied the development of the electron microbeam x-ray analyzer. The principal concerns were the practical issues associated with determining sensitivity and background removal in preparation for quantitative analysis. However, we need not always determine the total continuum distribution but rather just a small portion in the vicinity of the characteristic peak of interest. Since crystal diffraction spectrometer resolution was good, peak overlaps were rare and peak-to-background (mainly the continuum) ratios were high for major elements. Therefore, a simple linear interpolation was generally all that was needed to estimate the background under a peak. By the late 1960s and early 1970s the use of EDS on scanning electron microscopes and transmission electron microscopes revived interest in determining the continuum distribution because, in spite of their many advantages, poor energy resolution of EDS relative to crystal-diffraction spectrometers meant that the background had to be more accurately determined over a much broader energy range of the spectrum. It is at this point that Kramers's equation for bulk materials was dusted off and began to reappear in the literature. In 1973 Reed and Ware presented the equation in the following form:

According to Kramers [1923 reference cited] the continuum intensity in photons/s is given by:

$$I(E) = k \frac{E - E_0}{E} dE \quad (5)$$

where E_0 is the incident electron energy, E is the photon energy of the continuum of the point being measured, and k is a constant approximately proportional to atomic number.⁸

Note that intensity is now expressed in photons per second as a result of dividing Kramers's equation by E , the energy per photon, and also that energy rather than frequency finds its way into the equation by redefinition of the constant. At this point Reed and Ware recognized that Kramers's derivation described the continuum as generated within the specimen, and that in order to apply it to spectra observed with energy-dispersive spectrometers it would be necessary to correct for both absorption within the specimen as well as in the

detector itself. They furthermore decided that rather than to calculate the constant k from theory, it would be more effective to back calculate values of k based on actual spectral measurements. Thus the intensity of the observed continuum was given by:

$$I_m(E) = kF(E, \chi, x_i) dE \quad F(E, \chi, x_i) = [(E_0 - E)/E] f(\chi) \exp[-\sum (\mu_i \rho_i x_i)] \quad (6)$$

where $f(\chi)$ is the Philibert absorption correction and the summation includes absorption effects from the beryllium window, gold contact, and dead layer of the detector. The subscript m has been added by the present author to distinguish the measured spectral distribution from that generated in the specimen. [Reed and Ware used $I(E)$ for both.] Furthermore, to achieve a better fit with the data, Eq. (6) was further changed so that "Uncertainties in the theory may be taken into account by means of an additional correction term $F(E)$,"⁸ to give the following:

$$I_m(E) = k[F(E, \chi, x_i) + F(E)] dE \quad (7)$$

Reed and Ware went on to say that: "Since $F(E)$ may be partly dependent on instrumental characteristics, empirical values should be determined for each detector using a number of specimens of known composition." A slightly different approach was taken by Lifshin in 1974.⁹ Spectra from pure elements were measured and the shape of the continuum was back calculated and empirically matched to various functional forms. The result for the intensity distribution generated within the specimen was found to be

$$I(E) = \frac{Z}{E} [a(E_0 - E)^2 + b(E_0 - E) + c] \quad (8)$$

where a , b , and c are constants; thus, if Eq. (8) were written in the older-style intensity units, $I(E)E$, the continuum is described more correctly by a parabolic rather than a linear fit. Fiori (1976) successfully applied this approach to background subtraction as an integral part of quantitative analysis by EDS.¹⁰ Use of this method as well as that of Reed and Ware assumes that absorption corrections for the characteristic and continuum lines are the same. That can only be true if the distribution of excitation is the same and therefore the cross sections for both processes are the same. Although that is not strictly true, the resulting errors do not seem to affect the process of background subtraction seriously. However, they may be more important if exact spectral distribution data are needed for some other purpose.

Use of the Continuum as a Measure of Local Mass

The idea of using the continuum intensity as a measurement of local mass in thin films is contained in a 1975 paper by Marshall and Hall.¹¹ Referring to more laborious methods for determining the total mass thickness of a film, they stated:

A better method is to monitor the mass thickness of the film directly, by use of the continuum of x-rays which specimens emit when bombarded by electrons. This measurement can be taken simultaneously with measurements on characteristic lines, and gives a far quicker method of obtaining the mass concentration of a single element in the film.¹¹

This concept was supported by a theory based on the following equation:

$$W = kEZ \Delta E \quad (9)$$

where W is the energy of the continuous spectrum given off by a thin film, E is the electron energy (easily confounded with the now common notation for the x-ray energy; Compton and Allison refer to eV). Kramers's work was not cited at this point, but rather that of Dyson and also Kirkpatrick and Wiedmann.^{12,13} Dyson experimentally measured continuum distributions from thick targets, and Kirkpatrick and Wiedmann made numerical calculations of the continuum distribution and its production efficiency for both thick and thin films based on Sommerfeld's 1931 relativistic model for the x-ray continuum.¹⁴ Reference to the relativistic cross section disappeared in later papers by Hall (1968, 1971, 1979) and reference was instead made to Kramers's work either directly or through Compton and Allison's description to it. For example, we can find in the 1979 reference the following statement:¹⁵⁻¹⁷

...according to Kramers [1923 reference cited], the detection rate n for continuum radiation generated in the section (detected in some quantum energy band free of characteristic lines and not too close to the energy of the incident electrons) will be proportional to $\sum R Z^2$

where Z is the atomic number of the element r , N the number of atoms of element r per unit area, and the sum is extended over all of the atomic species locally present.¹⁷

Recognizing that Hall's Z is Kramers's N and that Hall's N is Kramers's A , we can see that for a pure element, Hall has taken this key point from Eq. (3). However, Kramers did not discuss the determination of the continuum from a material containing more than one element. In fact, very little work has been done to compare theoretical estimates of the continuum distribution for multielement systems with experimental measurements either for thin-film or for bulk specimens.

Invariance of the Peak-to-background Ratio

According to the Hall method if the characteristic line intensity provides a measurement of the local mass of a particular element and the continuum provides a measurement of the total local mass, then the ratio of the two should be proportional to the local weight fraction. The magnitude of the proportionality constant can then be established from a standard. The result has been a thin-film model which has worked well, particularly for biological systems. An important point is that the standard need not be of the same thickness as the sample as long as they both are relatively thin. Implicit in this discussion is the idea that if two thin samples are of identical composition but differ by, say, a factor of 2 in thickness, the peak-to-background ratio is the same for each. If this is the case, then what (if anything) should limit the independence of the peak-to-background ratio with sample thickness, or geometry for that matter? This area was pursued at about the same time by Statham and Pawley (1978) and also by Small (1978, 1979, 1981). According to Statham and Pawley:

To the extent that characteristic and continuum x-rays are produced in the same region of the sample they are subject to the same absorption and backscatter corrections. This suggests that the ratio of these two quantities should be an indicator of percent concentrations which is fairly independent of particle size or geometry or of the entry point of the electron beam.¹⁸⁻²¹

They then went on to point out that two factors that might cause peak-to-background ratio to vary would be possible fluorescence effects and differences in the cross sections between characteristic and continuum emission. Small's belief in the invariance of the peak-to-background ratio was initially based on experimental data collected on glass fibers and microspheres, where he found that a variation of less than 10% in the peak-to-background ratio was observed for a wide range of particle sizes.

If the peak-to-background ratio does not vary significantly with particle size or geometry, then according to Small equivalent bulk sample intensities could be determined from the following equation:

$$\frac{P}{B}\bigg|_{\text{particle}} + \frac{P}{B}\bigg|_{\text{bulk}} \quad (10)$$

The bulk sample intensity data could then be processed by the conventional ZAF procedure. This method is promising, but even if Eq. (10) applies, there are two potential problem areas when we look at it in the following form:

$$P^*_{\text{particle}} = P_{\text{bulk}} = \frac{B_{\text{bulk}}}{B_{\text{particle}}} \cdot P_{\text{particle}} \quad (11)$$

where P^*_{particle} would be the peak intensity if the particle were effectively a bulk specimen. To use this model, first the background from the bulk sample must be calculated. Although Small reported some progress in this area, we did mention the lack of experimental data and of a good model for the continuum distribution from multielement systems. A second and perhaps more troubling point is the presence of the background intensity from the sample in the denominator of Eq. (11). It is the smallest term of the four and clearly errors due to a lack of adequate counting statistics or the presence of noncontinuum background contributions can lead to serious errors in the bulk composition determination.

Final Comments

This brief review of the studies of the x-ray continuum has been intended to point out

an extremely important factor in electron-beam microanalysis. In spite of this importance, very little experimental or theoretical work has been done relating to it for a very long time. With the much more sophisticated instruments and computers available today, many opportunities exist to measure the spectral distribution, determine cross sections, model multielement systems, and look at the voltage and mass dependence of the continuum from thin films and small particles. There is also a strong need to understand artifacts that can lead to erroneous spectral distribution determinations.

References

1. H. Zuckerman, *Scientific Elite*, New York: Free Press, 1977, 282.
2. H. G. J. Moseley and C. G. Darwin, "The reflexion of the x-rays," *Phil. Mag.* 26: 210-232, 1913.
3. W. H. Bragg, "The influence of the constituents of the crystal on the form of the spectrum in the x-ray spectrometer," *Proc. Royal Soc.* 89: 430-438, 1914.
4. W. Duane, "The character of the general, or continuous spectrum radiation," *Proc. Nat. Acad. Sci.* 13: 662-670, 1927.
5. H. A. Kramers, "On the theory of x-ray absorption and the continuous x-ray spectrum," *Phil. Mag.* 46: 836-871, 1923.
6. H. Kulenkampff, "Continuous Roentgen spectra," *Ann. Phys.* 64: 548-596, 1923.
7. A. H. Compton and S. K. Allison, *X-Ray in Theory and Experiment*, New York: Van Nostrand, 1926, 89-115.
8. S. J. B. Reed and N. G. Ware, "Quantitative electron microprobe analysis using a lithium drifted silicon detector," *X-ray Spectrometry* 2: 69-74, 1973.
9. E. Lifshin et al., "Measurement of characteristic and continuum x-ray production efficiencies," *Proc. 9th MAS Conf.*, 1974, paper 53.
10. C. E. Fiori et al., "Prediction of continuum intensity in energy-dispersive x-ray microanalysis," *Analytical Chem.* 18: 172-176, 1976.
11. D. J. Marshall and T. A. Hall, "A method for the microanalysis of thin films," in *X-ray Optics and Microanalysis*, Paris: Herrman, 1966, 374-381.
12. N. A. Dyson, "The continuous x-ray spectrum from electron-opaque target," *Proc. Phys. Soc.* 73: 924-936, 1959.
13. P. Kirkpatrick and L. Wiedman, "Theoretical continuous x-ray energy and polarization," *Phys. Rev.* 67: 321-339, 1945.
14. A. Sommerfeld, "Ueber die Beugung und Bremsung der Elektronen," *Ann. Physik* 17: 257-330, 1931.
15. T. A. Hall, "Some aspects of the microprobe analysis of biological specimens," in K. F. J. Heinrich, Ed., *Quantitative Electron Microanalysis*, NBS Special Publication 298, 1968, 269-299.
16. T. A. Hall, "The microprobe assay of chemical elements," in G. Oster, Ed., *Physical Techniques in Biological Research*, New York: Academic Press, 1971, 158-275.
17. T. A. Hall, "Problem of the continuum-normalization method for the quantitative analysis of sections of soft tissue," in C. P. Lechene and R. R. Warner, Eds., *Microbeam Analysis in Biology*, New York: Academic Press, 1979, 185-224.
18. P. J. Statham and J. B. Pawley, "A new method for particle microanalysis based on peak to background measurements," *SEM/1978 I*, 469-478.
19. J. A. Small et al., "The production and characterization of glass fibers and spheres for microanalysis," *SEM/1978 I*, 445-454.
20. J. A. Small et al., "Progress in the development of the peak-to-background method for the quantitative analysis of single particles with the electron probe," *SEM/1979 II*, 807-816.
21. J. A. Small, "Quantitative particle analysis in electron beam instruments," *SEM/1981 I*, 447-461.

IMPROVED EDX ANALYSIS BY USE OF X-RAY ABSORPTION FILTERS

J. A. Reffner

Improved EDX analysis of transition metals in low-atomic-number matrices is achieved when an absorption filter is placed between the sample and detector. EDX spectrometers are limited by total x-ray count rate; high count rates increase the system's dead time, their linearity fails, and the detector's energy resolution diminishes. Filters made from low-atomic-number elements selectively reduce the number of x rays from the matrix that reach the EDX detector. Alumina-supported catalysts are used as an example. In a catalyst system such as Co or Ni on alumina, a hydrocarbon or fluorocarbon filter causes a substantial reduction of the aluminum x-ray counts, whereas the higher-energy x rays from Co and Ni are only weakly absorbed. When filters and instrumental parameters are optimized, counting statistics, dot maps, and element distribution line scans improve.

Experimental

Alumina-supported metal catalysts were used to test the use of absorption filters in EDX analyses. Aluminum, carbon, polyethylene (PE), and polytetrafluoroethylene (PTFE) were evaluated as filters. Filters were mounted between the sample and the standard beryllium window of the EDX detector. Each filter was evaluated by recording of the EDX spectrum with and without the filter. All analyses were made with a JEOL JXA-35 SEM and a Tracor/Northern 880 EDX spectrometer system.

Alumina-supported metal catalysts were mounted in an epoxy resin (Buehler EPO-MIX), then ground and polished to give cross sections of the catalyst extrudates. Nickel is commonly found in these catalysts and was used here to monitor the effects of x-ray filters.

The wavelength (or energy) selectivity of filters is shown by the calculated values¹ of the mass absorption coefficient listed in Table 1. The relative transmitted intensity (Table 2) illustrates the expected reduction of the long-wavelength (low-energy) radiation. Experimental x-ray intensity measurements confirm the effectiveness of filters.

Four materials were considered for filters: aluminum, carbon, PE, and PTFE. Although aluminum has a large absorption coefficient for the aluminum x rays, high-energy electrons and x rays cause the filter to produce aluminum x rays. The EDX detector records the aluminum x rays from the sample and the filter, which is totally unacceptable. Graphite rods were cut to produce thin carbon wafers. It was difficult to make these wafers thin enough for reasonable x-ray transmission. PE and PTFE films produced good filters.

Experimental intensity ratios for aluminum and nickel characteristic x rays are presented in Table 3 for various filters. The PE and PTFE are effective in reducing or eliminating the aluminum x-ray counts, but the nickel radiation retains its intensity. Figure 1 compares the filtered and unfiltered spectra from a Ni on Al₂O₃ catalyst. The observation that the x-ray intensity seems higher with filters in the system is unexpected and must relate to dead-time corrections or nonlinearity of the EDX spectrometer at high total count rates.

Conclusions

Selective reduction of x-ray counts from low-atomic-number elements can be achieved by filters. Polyethylene or polytetrafluoroethylene films are effective filters. In real-time experiments the filtering reduces the EDX system dead time. Element distributions by line scans and dot maps are improved.

Detection and quantitation of low levels of a transition metal in a low-atomic-number matrix is also improved when the matrix is filtered out. When the matrix is not contributing to the total count, the beam intensity and/or the detector geometry can increase the emission

The author is Principal Research Microscopist with American Cyanamid Research Laboratories, Stamford, CT 06904.

from the higher atomic number element.

References

1. G. L. Clark, *The Encyclopedia of X-rays and Gamma Rays*, New York: Reinhold, 1963.

TABLE 1.--X-ray mass absorption coefficients for selected elements.

Filter	Mass absorption coefficient for x-ray emission			
	Al (8.32A)	Mo (5.40A)	Co (1.79A)	Ni (1.66A)
Al	5744.9	1690.5	74.3	60.1
C	622.7	183.2	8.05	6.50
F	2008.7	591.1	26.0	21.0

TABLE 2.--Relative x-ray intensity I/I_0 for selected elements after passage through 0.001 density \times thickness filter.

Filter	Relative intensity for x-ray emission			
	Al (8.32A)	Mo (5.40A)	Co (1.79A)	Ni (1.66A)
Al	0.0031	0.185	0.477	0.549
C	0.538	0.835	0.923	0.940
F	0.135	0.554	0.771	0.811

TABLE 3.--Experimental x-ray intensity ratio I/I_0 for x-ray filters.

Filter	Thickness (mm)	Relative x-ray intensity	
		Al (8.32A)	Ni (1.66A)
Al	0.0003	0.725	0.857
Al	0.0012	0.743	0.839
C	1.650	0.000	0.236
PE	0.015	0.405	0.857
PE	0.045	0.090	1.136
PTFE	0.070	0.000	1.124

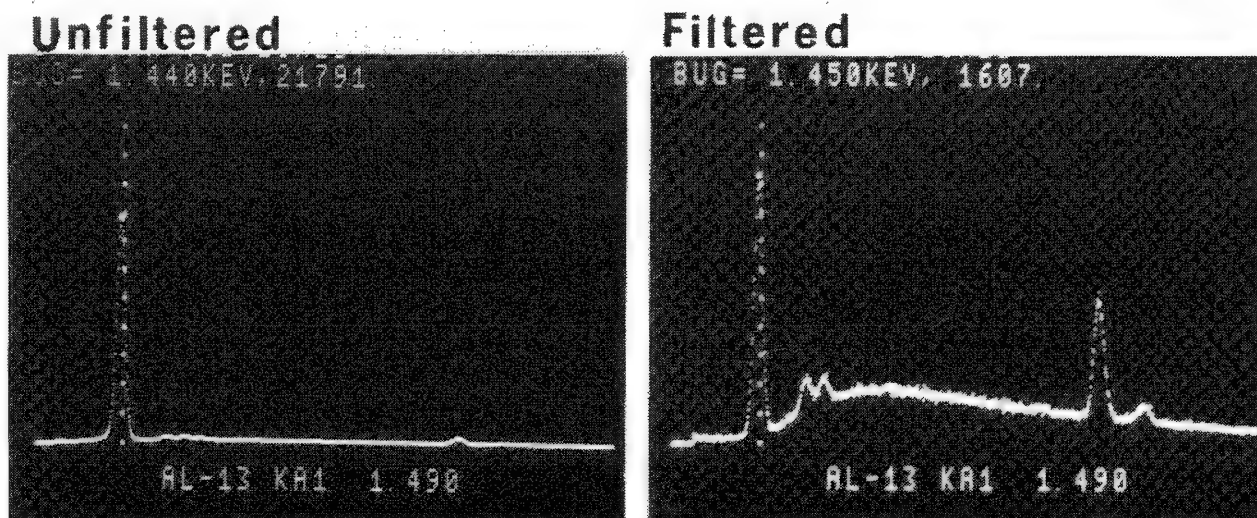


FIG. 1.--Comparison of filtered and unfiltered spectra from Ni on Al_2O_3 catalyst. PE filter 0.045 mm thick.

12 Archaeological Applications

USE-WEAR ANALYSIS OF STONE TOOLS WITH SCANNING ELECTRON MICROSCOPE

Shou Yamada and Muneaki Shimura

In recent years there has been growing interests among prehistorians in use-wear studies of stone tools. The investigation of use-wear on stone-tool edges informs us how ancient stone tools were used and what materials were worked, from direct evidence, not by means of analogy from morphology. Those are important pieces of information for the reconstruction of the life of ancient people. In particular, microwear polish is considered to be the most significant diagnostic trace. There has been only little information about the mechanisms of polish formation, although several polish types that are mainly attributable to worked materials are known. It is clear that this type of information is essential to guarantee a reliability of identification. The present paper describes three different forms of polish experimentally formed on stone surface by friction (use-wear polish, "cotton" pseudo-polish, and "stone" pseudo-polish), with the use of the scanning electron microscope.

Method

Our method is based in Keeley's experimental study of microwear polish.¹ He conducted a large number of experiments of utilization with replicative flint tools, and used the types of microwear polish obtained as a control in the study of microwear polishes found on prehistoric stone tools. Several polish types mainly attributable to worked materials (such as nonwoody plant, wood, bone and antler, dry hide, raw hide, and meat) were distinguished with an optical light microscope (100×). Striations on the polish indicate the direction of movement of the tool edge. These microwear polishes were distinguished from surface alterations that were not the result of use. This result has been confirmed by several authors. The Tohoku University Microwear Research Team has also conducted more than 320 experiments on silicious shale and chert since 1977.^{2,3} The results of this research almost agreed with those of Kelley, though there were certain discrepancies in detail. Almost the same polish types as flint were shown to be produced also on silicious shale and chert.

Only experimental specimens were studied in this study. The topography of microwear polish (use-wear polish), "cotton" pseudo polish, and "stone" pseudo polish were observed. Worked materials include nonwoody plants, wood, soaked antler, boiled bone, and dry hide.

The raw materials used in this study were silicious shale collected from Yamagata Prefecture and chert collected near the Hoshino site in Tochigi Prefecture. Silicious shale was a primary raw material for stone tools in northeast Japan throughout the late paleolithic and neolithic. It is sufficiently silicified and has no lamina, though its components and origin have not been investigated yet. Hoshino chert provides almost all the raw materials for five early paleolithic horizons in the Hoshino site. Chert is a silicious deposit composed of cryptocrystalline silica minerals, such as quartz, opal, or chalcedony. As both of the two raw materials are aggregations of very fine grains, they are isotropic macroscopically and exhibit almost the same morphological features of fracture surface as glass, though secondary cracks were developed in the Hoshino chert.

The specimens experimentally used were cleaned with water and soap, and were sometimes wiped with absorbent cotton immersed in alcohol to remove finger grease. The specimens were first observed with an optical light microscope (100×, 200× and 400×). They were then observed with SEM after vapor deposition of gold.

Author Yamada is at Tohoku University (Department of Archaeology); author Shimura is professor at the Research Institute for Iron, Steel and Other Metals, Tohoku University, Sendai, Japan. Thanks are due to Prof. C. Serizawa and Prof. T. Sudo for directing our attention to use-wear study. J. Fujita helped with the experiments.

Results

The morphological features and the properties of observed polishes are described as follows.

1. *Use-wear Polish*. Use-wear polish is shown in Fig. 1. Developed use-wear polishes commonly had a bright and smooth appearance under the optical light microscope, as if fused. The polish surface was so hard that it was not injured by slight friction. The differences of surface texture corresponding to optical polish types were also observed with the SEM, but they were not very distinctive. Various densities of striations and pits existed on the polish. These observations with the SEM agree with those of Anderson⁴ and Mansur-Franchomme.^{5,6} But whether use-wear polish is additive or abrasive cannot be judged from the appearance. What factors (for example, humidity, texture of worked materials) have been attributable to the variation of surface topography is not clear in the present study.

2. *"Cotton" Pseudo-polish*. Another form of optical polish was formed when stone surface was rubbed with absorbent cotton, paper, cloth, etc. in the dry state. It was named "cotton" pseudo-polish (Fig. 2). This form of polish was also accompanied by striations, and sometimes resembled use-wear polish. Striations on polish were also changed when the direction of rubbing was changed. The polish disappeared when rubbed with absorbent cotton, paper, and cloth containing much water. Use-wear polish was not altered by such treatments. When applied load and duration of work increased, use-wear polish was also formed by dry absorbent cotton. This effect was distinctive on Hoshino chert, and less distinctive on silicious shale.

When observed with the SEM, "cotton" pseudo-polish surface was smooth but it was not fused-like in appearance as use-wear polish. Outlines of crushed grains were seen in the smoothed surface. After being wiped with wet absorbent cotton, the surface exhibited the original granular surface. These effects are explained as transformation and translocation of soft grains caused by slight rubbing.

3. *"Stone" Pseudo-polish*. Keelyey¹ and Mansur-Franchomme⁶ have reported that characteristic optical polish was formed when stone surfaces were rubbed against each other. However, this form of polish was proved to have properties quite different from those of use-wear polish. It was injured by friction with dry absorbent cotton. When rubbed with wet absorbent cotton, the polish did not disappear but was transformed gradually.

When observed with the SEM, this form of polish has different morphological features from the two forms described above. Smoothed surface showed built-up structure, and accompanied many striations and abrasion powder. This texture was well observed with stereomicrophotograph, as shown in Fig. 3.

Discussion

Several explanations of the mechanisms of polish formation have been proposed in the literature. The most recent hypothesis is addressed by Anderson,⁴ which is also supported by Mansur-Franchomme.^{5,6} They believe that microwear polish (use-wear polish) is composed of silica gel. According to their hypothesis, silica minerals of flint are hydriized and silica gel films are formed on the surface. In the case of working plant material, silica accumulated in the plant body was also dissolved and forms an additive silica gel layer. Mansur-Franchomme has determined by x-ray microanalysis that silica is the only component of the microwear polish layer.

We cannot verify this hypothesis from the present study. But it should be noted that at least three possible forms of polish are formed on prehistoric stone-tool surfaces by friction with other materials: use-wear polish, "cotton" pseudo-polish, and "stone" pseudo-polish. The polish phenomenon is not simple. The friction process should be more clearly specified. Careful treatment of specimens is also needed to prevent the formation of "cotton" pseudo-polish. More detailed studies from this perspective should be carried out.

References

1. L. H. Keeley, *Experimental determination of Stone Tool Uses: A Microwear Analysis*, Chicago: University of Chicago Press, 1980.
2. H. Kajiwara and K. Akoshima, "An experimental study of microwear polish on shale artifacts," *Kokogaku Zasshi (Journal of the Archaeological Society of Japan)* 67-71: 1-36,

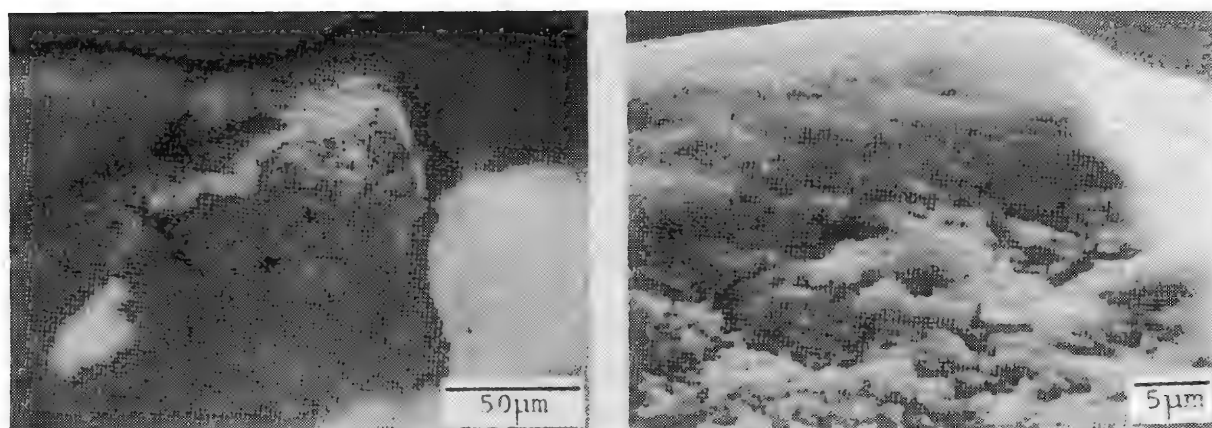


FIG. 1.--Use-wear polish produced by sawing boiled bone (chert): left, optical; right, SEM.

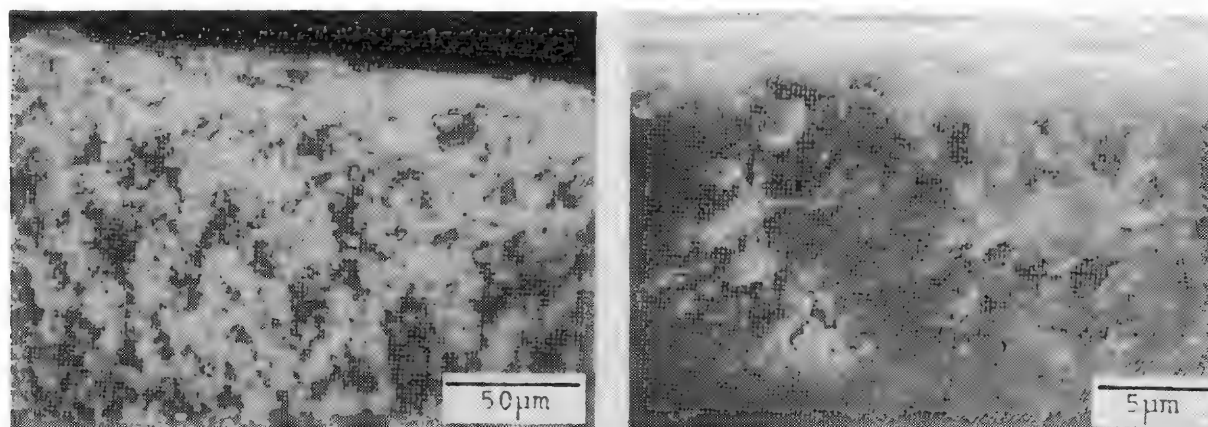


FIG. 2.--"Cotton" pseudo-polish (chert); left, optical; right, SEM.

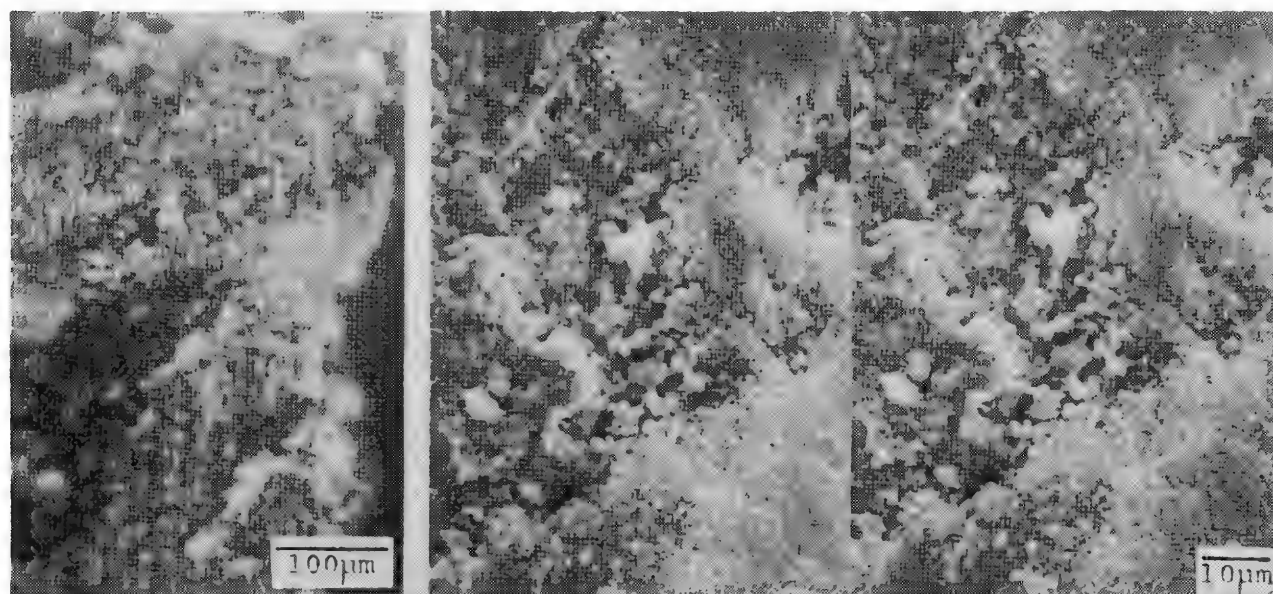


FIG. 3.--"Stone" pseudo-polish (silicious shale): left, optical; right, SEM stereomicro-
photograph.

1981.

3. C. Serizawa et al., "Experimental study of microwear traces and its potentiality," *Archaeology and Natural Science* 14: 67-87, 1981.
4. P. C. Anderson, "A testimony of prehistoric tasks: Diagnostic residues on stone tool working edges," *World Archaeology* 12: 181-194, 1980.
5. M. E. Mansur-Franchomme, "Scanning electron microscopy of dry hide working tools: The role of abrasives and humidity in microwear polish formation," *Journal of Archaeological Science* 10: 223-230, 1983.
6. M. E. Mansur-Franchomme, *Traces d'utilisation et technologie lithique: Exemples de la Patagonie*, Thèse de 3ème Cycle No. 1860, Université de Bordeaux I, 1983.

MICROSTRUCTURAL ANALYSIS OF COPPER ARTIFACTS FROM BATAN GRANDE

S. J. Thorpe and U. M. Franklin

The technology of Central Andean metallurgy has been well documented by excavation, ethno-archaeology, and laboratory simulation of metallurgical activities in various centers whose prime function was metal working, but not metallurgical extraction.¹⁻⁴ Recent excavations by Shimada et al. have revealed mining metallurgical complexes in Cerro Blanco and Cerro de los Cementarios in the La Leche valley on the north coast of Peru.^{5,6} Attempts are now made to understand the prill extraction copper smelting technique. The present study serves to provide microstructure-composition relationships in extracted copper prills and prills retained within the slag phase (in situ) to establish metal-metal and metal-matte equilibria.

Experimental

Samples for analysis were provided in the form of extracted and in situ copper prills and ingots produced by consolidation.⁶ Preliminary bulk compositional analysis of the samples was determined by proton x-ray emission (Pixie) analysis as given in Table 1.⁷ Metallographic sections were prepared for optical, energy-dispersive x-ray, and Auger (SAM) analysis to determine phase analysis and distribution for the impurity/alloying elements Fe, S, As, Pb, and Ca.

Results

The presence of As in the metallic artifacts is important for provenance analysis since the local ore body at Cerro Blanco is a complex of Cu-Pb-Zn oxides and sulfides and is not arsenical in nature. Arsenic does appear in two distinct morphological forms in extracted copper prills:

- (i) in association with Cu and Pb
- (ii) combined in a second phase with Ca

Figure 1 depicts a typical structure of morphology (i) consisting of a central pure Pb region surrounded by an outer ring of Cu-As eutectic embedded in a pure Cu matrix. EDX analysis of the eutectic averages 49 wt% As, very close to the Cu-As eutectic at 50.1 wt% As. Prill BG 80-5 4D was selected for analysis to minimize peak overlap of Mg, which is present in appreciable quantities in all other prills. Elemental distribution is confirmed by x-ray mapping of Cu, As, and Pb in Fig. 2.

The second AS morphology consists of a grain boundary precipitate of a Ca-rich Ca-As phase (Fig. 3) for prill BG 80-5 6F. The Ca:As ratio varies between 3:2 and 4:2, which corresponds closely to Ca_3As_2 in the Ca-As binary, although this analysis requires confirmation by x-ray diffraction. No As was detected in cross sections of remaining extracted copper prills, in situ copper prills, or ingots analyzed.

Analysis of in situ copper prills reveals poor liquid phase separation in the Cu-Fe system (Fig. 4). EDX analysis reveal the phase compositions to be Fe_xCu_y and Fe_yCu_x for $x = 0.89-0.92$ and $y = 0.08-0.11$. In addition, all prills contained a fine particle distribution of $\text{Cu}_x\text{Fe}_y\text{S}_z$ (Fig. 5) consistent with poor phase separation upon solidification. A similar particle distribution was present in both ingot cross sections analyzed.

Discussion

The Cu-As-Pb phase morphology is only prevalent in the outer periphery of prill BG 80-5 5D. Upon solidification, primary Cu precipitates first, followed by an inverse segregation of As to the outer periphery. The Cu-Pb binary exhibits monotectic behavior so a high temperature phase separation is strongly favored. Upon further cooling, the Cu-As eutectic

The authors are with the Department of Metallurgy and Materials Science, University of Toronto, Toronto, Ont., Canada M5S 1A5. They would like to thank Dr. S. Fleming and Mr. S. Epstein for providing the samples and subsequent helpful discussion. One author (S.J.T.) would also like to thank Dr. J. Toguri for his cooperative assistance.



FIG. 1.--Island morphology of Cu-As-Pb located in outer periphery of extracted copper prill G80-5 40.

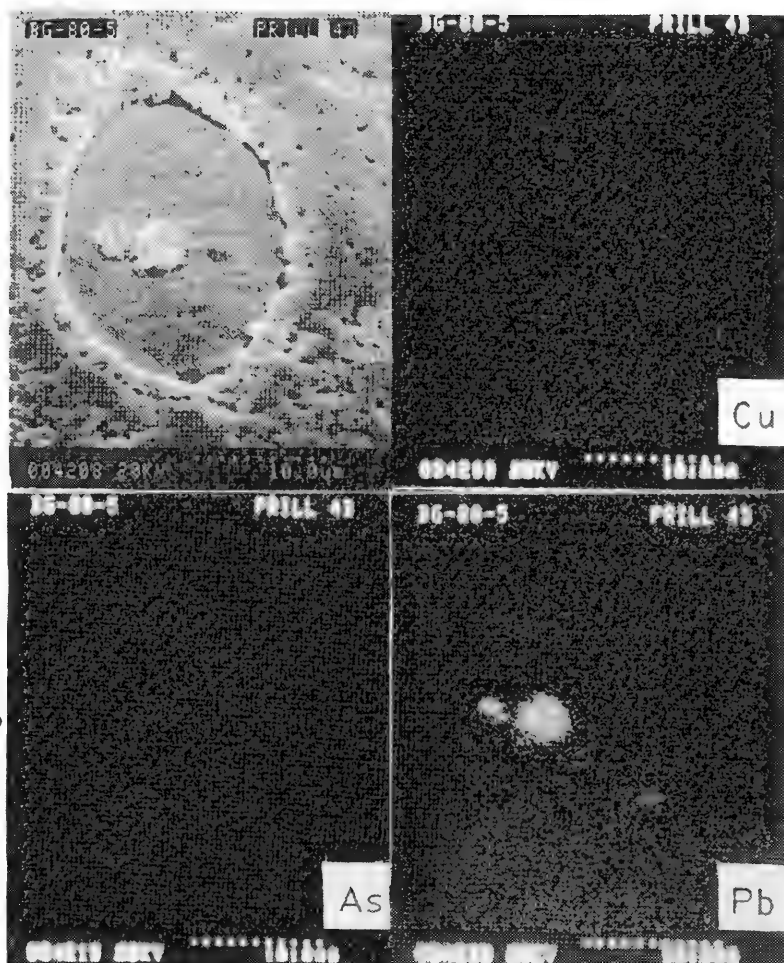


FIG. 2.--Elemental distribution of As, Cu, and Pb by x-ray mapping of island structure of Fig. 1.

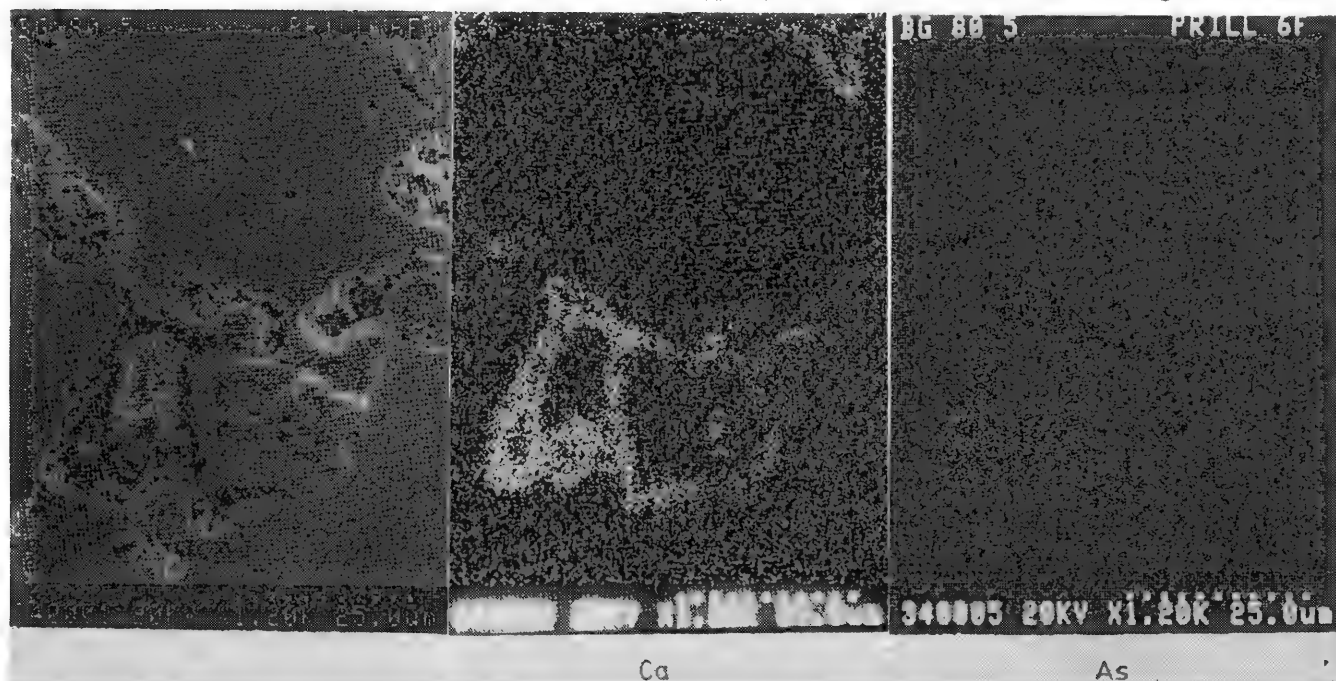


FIG. 3.--Intergranular grain boundary phase of Ca-As in extracted copper prill G80-5 6F.

solidifies, followed by Pb. The solidification path analysis of the Cu-Ca-As intergranular phase is known due to poor definition of the Ca-As binary phase diagram. No As was detected in the ingot analysis or in situ copper prills. The size difference (extracted/in situ copper prills $\sim 10^6:1$ by volume) could strongly affect the thermal history and subsequent As distribution. The difference in As content in the various artifacts by bulk PIXIE analysis (Table 1) and other microanalytical techniques is unresolved. The absence of As in many prills sheds doubt on As addition to Cu as a direct alloying element.

The existence of poor phase separation in the Cu-Fe-S system and miscibility in the Cu-Fe system is indicative of the temperature attainment of 1523 ± 50 K in accordance with equilibria in the Cu-Fe system. Furnace refractory analysis at Batan Grande is consistent with the ability to retain a matte at these temperatures.⁸ The presence of $\text{Fe}_x\text{Cu}_y\text{S}_z$ particulate in both extracted and in situ copper prills and ingots suggest an inclusion carry-over upon remelting. From Fig. 6, the analyzed particulate falls within a miscibility phase field for a temperature of 1423 ± 1473 K. Prills can absorb Fe from the slag, but this process is inhibited by S present in Cu won from sulfide ores.

Conclusions

Microstructure-composition relationships sheds doubt as to the addition of As to Cu as a deliberate alloying element, although a limited database and sampling technique require verification to insure adequate representation. The present phase analysis of copper prills and ingots is consistent with the smelting of sulfide ores.

References

1. E. R. Caley, in W. J. Young, Ed., *Application of Science in Examination of Works of Art*, Boston: Museum of Fine Arts, 1973, 53-61.
2. E. R. Caley and D. T. Easby Jr., *Am. Antiq.* 25: 59, 1959.
3. H. Lechtman, in Young (Ref. 1 above), pp. 38-52.
4. C. C. Patterson, *Am. Antiq.* 36: 286, 1971.
5. I. Shimada et al., "Batan Grande: A prehistoric metallurgical center in Peru," *Science* 216: 952, 1982.
6. S. M. Epstein, "The prehistoric copper smelting industry at Cerro de los Cementerios, Peru: Analysis of the product," *MASCA J.* 2: 58, 1982.
7. F. Folkman, *J. Phys.* 8-E: 429, 1975.
8. O. Reuleaux, *Metall. und Erz* 24: 99-111, 1927.

TABLE 1.--Analysis of the Cerro de los Cementerios metals.

Reference Prills	Elemental Composition (% by weight)										
	Cu	Sn	As	Pb	Fe	Ag	Sb	S	Ni	Mg	Zn
BG 80-5A	94.2	≤ 0.03	1.24	0.71	2.38	0.32	≤ 0.03	0.053	≤ 0.006	0.54	0.61
B	96.0	≤ 0.03	1.04	2.03	0.059	0.44	≤ 0.03	0.093	0.067	0.28	≤ 0.03
C	97.6	≤ 0.03	0.70	0.17	0.96	0.11	≤ 0.03	0.025	0.062	0.32	≤ 0.03
D	99.0	≤ 0.03	0.48	0.057	≤ 0.01	0.20	≤ 0.03	0.013	0.025	≤ 0.05	≤ 0.03
E	92.4	≤ 0.03	0.76	0.23	5.95	0.15	≤ 0.03	0.024	≤ 0.006	0.18	≤ 0.03
F	91.1	≤ 0.03	6.37	0.12	≤ 0.01	0.26	≤ 0.03	0.006	≤ 0.006	1.69	≤ 0.03
Prills(embedded in slag)											
BG 80-7	97.8	≤ 0.03	0.51	0.34	0.34	0.33	≤ 0.03	0.22	0.34	0.35	≤ 0.03
BG 80-8C	96.1	≤ 0.03	0.84	0.33	1.64	0.27	≤ 0.03	0.086	0.029	0.40	≤ 0.03
D	89.1	≤ 0.03	1.03	0.31	8.37	0.26	≤ 0.03	0.065	0.024	0.53	≤ 0.03
Ingots											
BG 80-1	93.7	≤ 0.03	2.76	≤ 0.01	1.45	0.18	≤ 0.03	0.31	0.30	1.30	≤ 0.03
BG 80-2	94.2	≤ 0.03	2.02	≤ 0.01	2.26	0.10	≤ 0.03	0.15	≤ 0.006	1.03	≤ 0.03

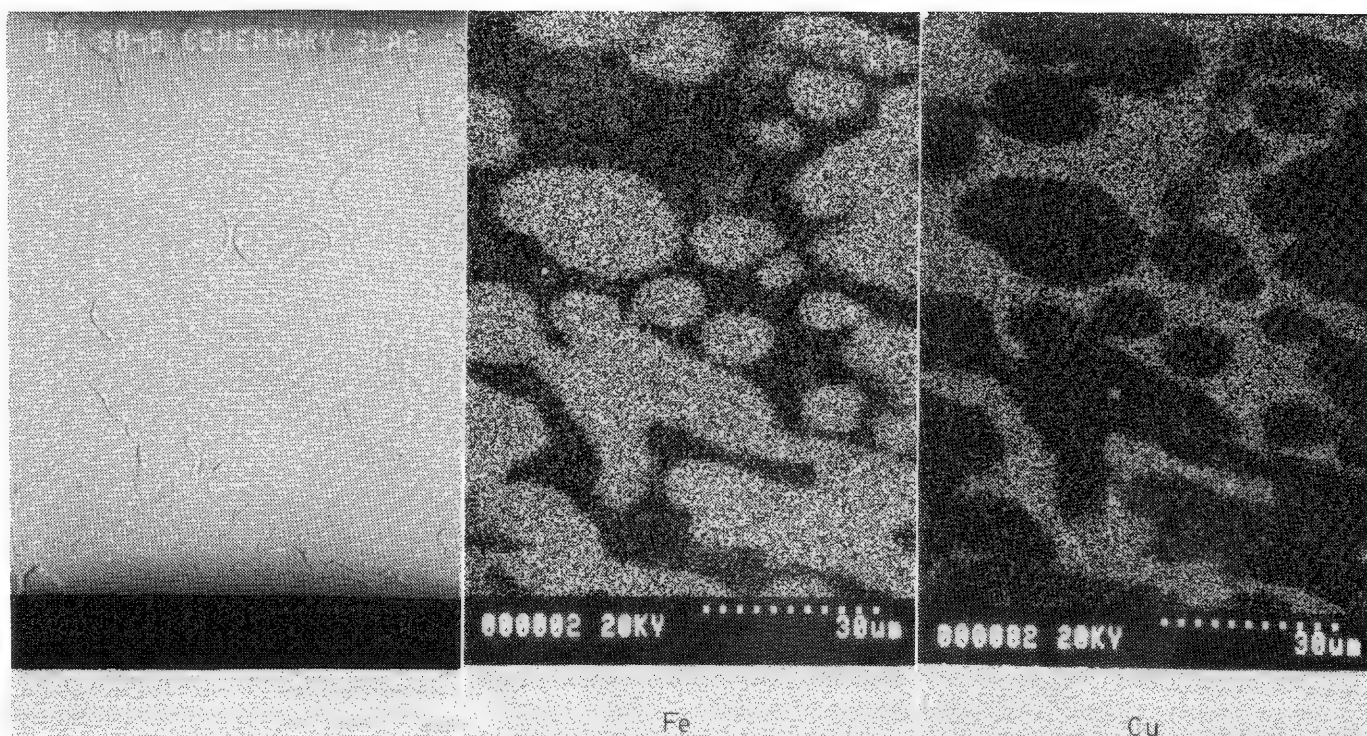


FIG. 4.--Poor phase separation of Fe and Cu in in situ copper prills.

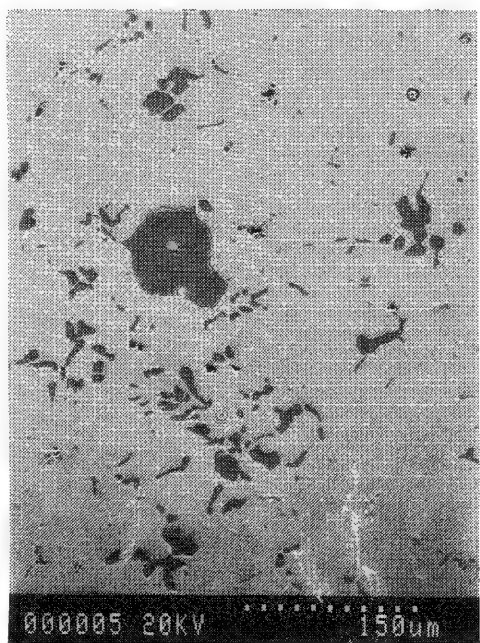


FIG. 5.-- Fe-Cu-S phase distribution found in both in situ and extracted copper prills and ingot samples.

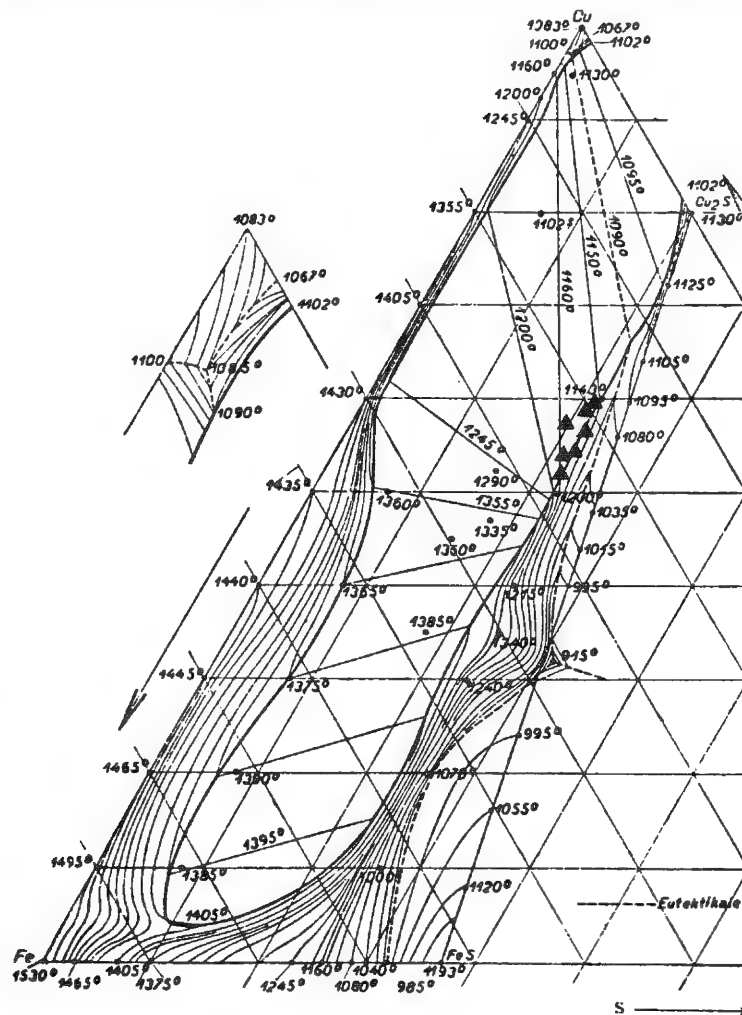


FIG. 6.--Liquidus surface of Fe-Cu-S system indicating analyzed composition of Fe-Cu-S particulate.

THE QUALITY OF WROUGHT IRON EVALUATED BY MICROPROBE ANALYSIS

R. B. Gordon

The utility of bronze tools depends much less on the quality of the metal used to make them than is the case for iron tools. The quality of iron is frequently at issue in archaeological and historical metallurgy and in the economic history of the iron industry. Historical documents are of limited use in the study of metal quality even well into the 19th century because of the absence of quantitative mechanical tests, chemical analyses, and metallography. Evidence from artifacts is therefore most valuable but must usually be obtained from small samples by nondestructive means. I address here the evaluation of the strength properties of wrought iron by metallography and microchemical analysis.

The quality of wrought iron depends on the size and distribution of its slag fibers and its sulfur and phosphorus content. Excessive sulfur makes iron hot short, which is likely to be more of a problem to the ironmaster than the user of a finished product. It has been known since 1784 that phosphorus makes iron cold short¹ and since 1918 that the presence of phosphorus retards cementation in the conversion of iron to blister steel.² The amount of phosphorus in wrought iron depends on the starting materials used and on the chemical composition of the slag in which the solid iron is formed. The composition of the slag also determines its fluidity and hence influences the distribution of slag fibers attained by shingling and rolling. It requires good slag to make good iron. It is most unusual today to find samples of both the slag used and the metal made at an archaeological site, but the fibers in wrought iron are a sample of the slag within which the iron coalesced into a coherent solid. They have been protected from subsequent weathering but may have been modified by reactions with the metal during shingling and cooling. Two studies of slag inclusions in bloomery iron have been published^{3,4} and one on the inclusions in wrought iron made by the conversion of pig.⁵ The mineralogy of bulk samples of bloomery slag was studied by Morton and Wingrove;^{6,7} their work has been critically reviewed and extended by Fells.⁸

Experimental Methods

Results of analysis of the slag inclusions in five samples of wrought iron made between about 1865 and 1870 are reported here. Three are Swedish irons--the best grades of iron available in the U.S. at that time-- and two are from northwestern Connecticut; the latter are samples of the inferior product that had been causing serious problems for American manufacturers of metal products.⁹ Standard metallographic preparation was used and the specimens were examined optically and with the scanning electron microscope. The composition of the slag fibers was determined with a Tracor Northern TN 2000 energy-dispersive x-ray analyzer attached to an Acton Laboratories probe model MS64. The accelerating potential was 15 kV and the sample current 5 μ A. Each run was recalibrated against the Si and Zn K α peaks of willemite. The data were reduced by the method of Bence and Albee.¹⁰

Experimental Results

Wüstite and fayalite crystals in a glassy matrix with fine hercynite and leucite intergrowths are usually found in samples of slag recovered from bloomery sites⁷ but wüstite is often the only crystalline constituent that can be recognized in slag fibers in wrought iron.

The author is at Yale University, New Haven, Conn. He thanks Brendan Caulfield for making the microprobe analyses reported in Table 1 and Dr. Kenneth Barraclough for identifying the three samples of Swedish iron from their makers' marks.

The example in Fig. 1 has primary wüstite (w), a matrix (m) that contains fine crystallites visible with the electron microscope, and a glassy constituent (g). The compositions of these constituents in the samples studied are reported in Table 1. (There is no glassy component in the Swedish irons.) The phosphorus is low in the three irons of superior quality and much higher in the samples of inferior iron.

The analyses show that, of the elements present, only manganese is appreciably soluble in the wüstite. The proportions of SiO_2 , Al_2O_3 , and CaO (which, with the wüstite, should make up the bulk of the slag) are quite different in the different specimen and it would be difficult to estimate the liquidus temperatures of these slags from phase diagrams. The glassy constituent remained liquid after the matrix solidified and was cracked during forging at temperatures below its solidus. The high phosphorus content of the glass is probably responsible for its low melting temperature.

The partition coefficient of phosphorus between slag and metal, $k = \%P(\text{slag})/\%P(\text{metal})$, is large and it is difficult to measure the phosphorus content of the metal accurately with microprobe analysis. Phosphorus concentrations determined by bulk chemical analyses and corresponding slag compositions from which k can be calculated are shown in Table 2. Note that k is much lower for the bloomery than for the finery or puddling process.

In a review of extensive mechanical test data on wrought iron for ships cable, A. L. Holley concluded in 1877 that up to 0.2%P can be tolerated in iron containing 0.03% or less carbon without detriment to the strength properties.¹¹ Recent research on the effect of phosphorus additions to high-purity iron confirms this conclusion but shows that the embrittlement of iron by phosphorus is strongly influenced by the carbon content.¹² If we accept the 0.2%P limit and suppose that a $k \approx 10$, then up to about 4% P_2O_5 in the slag may be tolerated. On this basis, the Salisbury and Collins irons listed in Table 1 would have deficient ductility. Cold shortness in otherwise pure iron is caused by segregation of phosphorus to grain boundaries;¹³ the segregation is confined to a zone only a few lattice spacings wide.¹⁴ In the wrought-iron samples with high phosphorus content the phosphorus is concentrated in the glassy constituent which wets and penetrates the ferrite grain boundaries near the slag inclusions, as shown in Fig. 1. This is expected to be an additional cause of embrittlement in wrought iron containing excess phosphorus. Further studies to test this hypothesis would be useful.

Conclusions

Poor strength properties of wrought iron are most likely to result from excessive or poorly distributed slag particles due to insufficient mechanical working or from phosphorus in excess of 0.2%. The structure of slag inclusions differs from that of bulk slag; only wüstite is ordinarily found as primary crystallites in slag inclusions in wrought iron, and phosphorus, which is strongly concentrated in the slag, forms a glassy constituent of low melting temperature in irons with a high phosphorus content. This glass penetrates ferrite grain boundaries near inclusions. Loss of ductility results from grain boundary segregation of phosphorus within the iron and from the phosphorus-rich glass formed at the slag inclusions. This glass is easily detected with the microscope and its presence is an indication that the iron in an artifact is probably cold short.

References

1. J. Percy, *Iron and Steel*, London: John Murray; 1864, 64.
2. J. E. Stead, "Iron, carbon and phosphorus," *J. Iron and Steel Inst.* 97: 389-412, 1918.
3. R. E. M. Hedges and C. J. Salter, "Source determination of iron currency bars through analysis of slag inclusions," *Archaeometry* 21: 161-175, 1979.
4. J. A. Todd and J. A. Charles, "Ethiopian bloomery iron and the significance of inclusion analysis in iron studies," *J. Hist. Met. Soc.* 12: 63-87, 1978.
5. R. B. Gordon, "English iron for American arms: Laboratory evidence on the iron used at the Springfield Armory in 1860," *ibid.*, 17: 91-98, 1983.
6. G. R. Morton and J. Wingrove, "Constitution of bloomery slags, Part I: Roman," *J. Iron and Steel Inst.* 207: 1556-1564, 1969.
7. G. R. Morton and J. Wingrove, "Constitution of bloomery slags, Part II: Medieval," *ibid.*, 210: 478-488, 1972.

TABLE 1.--Microprobe analyses of slag inclusions in wrought iron.

Iron		FeO	SiO ₂	Al ₂ O ₃	CaO	MgO	MnO	TiO ₂	Na ₂ O	K ₂ O	P ₂ O ₅	SO ₃
JB iron	w	89.1	0.3	0.2	0.0	1.9	7.7	0.0	0.8	0.0	0.0	0.1
	m	25.3	34.1	4.1	18.5	2.7	11.7	0.0	1.5	0.8	0.5	0.8
Munkfors	w	97.4	0.9	0.0	0.0	0.3	0.8	0.0	0.0	0.0	0.3	0.0
	m	72.8	2.0	22.0	0.1	0.0	0.3	0.0	1.2	0.1	0.6	0.0
Little S	w	94.4	0.6	0.2	0.0	0.3	3.2	0.0	0.0	0.0	0.2	0.0
	m	41.1	32.7	3.7	10.0	0.6	7.6	0.0	0.1	0.7	0.9	1.5
Salisbury Refined	w	93.5	1.4	0.2	0.2	0.2	2.2	0.0	1.9	0.0	0.2	0.0
	m	52.7	30.1	2.1	4.5	0.7	5.2	0.1	0.0	1.0	3.2	0.3
	g	54.2	27.2	1.2	5.0	0.7	5.2	0.0	0.0	0.6	5.4	0.0
Collins	w	97.8	0.4	0.0	0.2	0.0	0.7	0.4	0.0	0.0	0.0	0.2
	m	61.7	22.6	1.2	3.4	0.3	1.3	0.1	1.4	0.1	6.7	0.7
	g	62.3	19.0	0.3	2.0	0.4	1.2	0.0	0.8	0.0	8.0	6.2

TABLE 2.--Phosphorus partition coefficient.

Iron	Process*	Ref.	Metal, P	Slag, P ₂ O ₅	k = P(s)/P(m)
J B iron	f	15	0.005%	0.36%	20
Bowling iron	p	16	0.064	3.12	21
U.S.Steel Co.	p	17	0.182	3.82	9
Londonderry N.S.	p	18	0.09	1.66	9
Medieval bloom	b	19	0.8	5.0	2.7
Danebury	b	3	0.58	4.5	3.4
Gretton	b	3	0.46	7.2	6.9

*f = finery, p = puddling, b = bloomery.

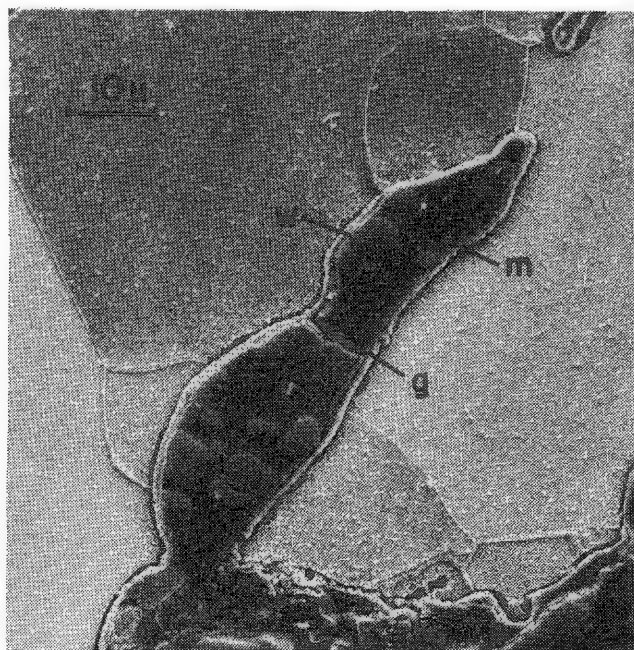


FIG. 1.--Slag inclusion in Salisbury refined iron showing wüstite crystallites (w), crystalline matrix (m), and glass (g).

8. Stephanie Fells, *The Structure and Composition of Archaeological Ferrous Process Slags*, Ph.D. Thesis, University of Aston, 1983.
9. R. B. Gordon, "Materials for manufacturing: The response of the Connecticut iron industry to technological change and limited resources," *Technology and Culture* 24: 602-634, 1983.
10. A. E. Bence and A. L. Albee, "Empirical correction factors for the electron micro-beam analysis of silicates and oxides," *J. Geol.* 76: 382-403, 1968.
11. A. L. Holley, "The strength of wrought iron as affected by its composition and by its reduction in rolling," *Trans. AIME* 6: 101-124, 1877-78.
12. B. E. Hopkins and H. R. Tipler, "The effects of phosphorus on the tensile and notch impact properties of high purity iron and Fe-C alloys," *J. Iron and Steel Inst.* 188: 218-237, 1958.
13. M. C. Inman and H. R. Tipler, "Grain boundary segregation of phosphorus in an iron-phosphorus alloy and the effects upon mechanical properties," *Acta Met.* 6: 73-84, 1958.
14. T. Inoue and Y. Namba, "The influence of the addition of boron on the grain-boundary segregation of phosphorus and fracture behavior of medium-carbon ultra-high strength steel," in R. C. Gifkins, Ed., *Strength of Metals and Alloys*, Oxford: Pergamon, 1983, vol. 2, 787-792.
15. J. Percy, Ref. 1, p. 736.
16. I. L. Bell, *Principles of the Manufacture of Iron and Steel*, London: Geo. Rutledge; 1884, 360.
17. J. M. Camp and C. B. Frances, *The Making, Shaping and Treating of Steel*, Pittsburgh: Carnegie Steel Co., 4th ed., 1919, 224.
18. H. Louis, "On the chemistry of puddling," *J. Iron and Steel Inst.* No. 1: 219-226, 1879.
19. "Iron blooms in the Northwest Passage," *J. Hist. Met. Soc.* 17: 50, 1983.

THE RELATIONSHIP BETWEEN ORE, SLAG, AND METAL COMPOSITIONS IN PRE-INDUSTRIAL IRON

J. A. Todd

The solid-state reduction of iron ore in the pre-industrial bloomery produces a metallic iron sponge intimately mixed with slag products, many of which are incorporated as inclusions in the finally forged products. Compositional analyses of these nonmetallic inclusions by energy-dispersive x-ray analyses can be compared with wet chemical analyses of bulk furnace slags and unreduced ores to yield significant information regarding both the reduction process itself and the level of technology achieved by the smelters. Considerable interest has arisen in fingerprinting the compositional relationships between slag inclusions in excavated iron objects and their parent ores so that archaeologists and historical metallurgists can advance their studies of provenance and trading patterns of iron artifacts. This paper presents analytical data from (1) an Ethiopian bloomery process observed in Dimam in southwest Ethiopia in 1974, (2) Roman ironwork excavated from Longthorpe, and (3) laboratory reductions of archaeological and commercial iron ores in an attempt to clarify these relationships.

Ethiopian Bloomery Iron

In 1974 the Dimi people of southwest Ethiopia were still practicing the traditional bloomery process (in preference to importing and reworking scrap steel) and produced all the iron required for their agricultural tools (digging sticks, hoes, axes, adzes, sickles, etc.), weapons (spears, knives, sacrificing knives), and ornaments (iron bangles and pea bells--to ward off the evil eye--and cowbells) (Fig. 1). They reduced limonite and magnetite ores (Table 1), with charcoal but no added flux, in 1m-high, forced-draft clay furnaces for approximately 4 h to produce sponge iron (Fig. 2), which was later separated from the slag (Fig. 3) and forged to the finished products.¹⁻³ Carbon was lost from the bloom during the forging operation, which resulted in a low-carbon (0.02-0.2%C) product with slag inclusions elongated along the forging direction (Fig. 4). Both single-phase and two-phase inclusions were observed in the Dimi ironwork (Figs. 5 and 6). Many slag inclusions were quantitatively analyzed by a comparison of their energy-dispersive x-ray spectra with those from elemental and mineral standards (Table 2). These analyses were compared with those of the furnace slags (Table 1) and also with laboratory slags produced by reduction of samples of ore in a carbon monoxide atmosphere at 1200 and 1300 C (Table 2).

The limonite and magnetite ores used by the Dimi were associated with aluminosilicate gangue material, much of which was removed by hand sorting. The main compositional variable was MnO (0-3.7% along the mountain range) and in all cases the lime/silica ratio was less than 0.05. This composition was reflected in the laboratory reductions of ores 03 and 06, where the maximum CaO/SiO₂ ratio observed in the slag phase was 0.02 (Table 2). Alkali elements were absorbed as CaO, K₂O from the charcoal (into the slag) during reduction to give a small but significant increase in lime/silica ratio, from 0.04 to 0.2. These oxides concentrated in the iron-aluminosilicate phase rather than the fayalite (2FeO.SiO₂) phase of the two-phase furnace slags. The addition of fluxing agents containing lime (e.g., shells) to the Ethiopian bloomery process would be readily identifiable by comparison of slag and laboratory-reduced ore compositions.

A number of important conclusions could be drawn from the analytical data. (1) The knife and digging stick examined appeared to have been reduced from the low MnO ore, 03, since their slag inclusions contained less than 2.5%MnO, whereas laboratory reductions of

The author is an assistant professor in the Departments of Materials Science and Mechanical Engineering, University of Southern California, Los Angeles, CA 90089-0241.

06 (3.7%MnO) indicate that up to 20%MnO could be found in slags from this ore. (2) The Dimi ores are self fluxing with high iron losses to the slag. (3) Slag and inclusion analyses indicate that temperatures of at least 1300 C and probably 1400 C were reached

TABLE 1.--Chemical analysis of ores and slag.

	03	Ores 04	06	Ethiopian Furnace Slags S1/04	light phase	dark phase
Fe ₂ O ₃	77.37	55.79	53.4	41.37	EDX	EDX
FeO	--	--	--	--	66.0	27.3
SiO ₂	6.7	17.71	12.3	28.73	27.7	41.9
MnO	--	--	3.7	2.01	2.2	1.1
Al ₂ O ₃	1.29	11.18	8.2	21.94	--	15.7
CaO	--	--	0.5	5.73	--	2.7
MgO	--	--	trace	--	1.4	--
%moisture loss	2.52	3.35	--	--	--	--
%combined H ₂ O	11.72	10.77	--	--	--	--
P ₂ O ₅	0.27	0.64	0.97	--	0.8	2.1
S	0.01	0.01	<0.1	0.02	--	--
TiO ₂	--	--	2.5	--	0.3	6.7
K ₂ O	--	--	--	--	--	2.1
TOTAL	<u>99.88</u>	<u>99.45</u>	<u>---</u>	<u>99.80</u>	<u>98.4</u>	<u>99.6</u>
CaO SiO ₂	--		0.04	0.20		0.06

TABLE 2.--Analyses of inclusions and reduced ores.

	Inclusions			Reduced Ores (1300°C)		
	single phase	2-phase light	dark	03	06 light phase	dark phase
FeO	53.4	98.3	55.9	37.7	87.1	46.2
SiO ₂	26.6	0.6	20.9	35.5	1.8	27.0
MnO	1.3	--	0.3	0.8	8.8	16.9
Al ₂ O ₃	8.3	--	6.2	18.3	--	7.5
CaO	4.0	--	2.6	0.5	--	0.3
P ₂ O ₅	4.4	--	10.4	--	--	0.3
TiO ₂	0.6	0.7	--	6.6	--	--
MgO	--	--	1.6	--	--	--
K ₂ O	2.3	--	2.3	0.2	1.8	0.9
CuO	--	--	--	1.1	--	1.9
TOTAL	<u>100.9</u>	<u>99.6</u>	<u>100.2</u>	<u>100.7</u>	<u>99.5</u>	<u>101.0</u>
CaO SiO ₂	0.15		0.12	0.01		0.01

in the furnace. (4) Iron artifacts cannot be readily classified by the phosphorus content of their inclusions since phosphorus partitions into the metal during reduction, but can be subsequently reoxidized from the iron surrounding a slag inclusion during forging. A wide range of inclusion phosphorus contents can be therefore observed.

The study of the Ethiopian bloomery process has shown that it is possible to characterize the ironwork of a specific production center and that for cases where no flux is used, the compositions of slag inclusions in the metal can be related to those of furnace slags and parent ores.

Roman Ironwork

The knowledge gained from the Ethiopian bloomery was applied to the study of nails, roasted ore, and a limited amount of furnace slag excavated from the Roman site at Longthorpe (Table 3). The most interesting aspect of this study was the low phosphorus content of the iron nails (0.06%P max.), slag (1%P), and inclusions (1.7%P) despite the fact that laboratory reduction of the ore produced iron containing 0.8%P. Norwich⁴ has commented on the basic calcareous nature of clay used for furnace construction at the Roman site of Sacrewell and concluded that the clay was deliberately used as a flux for the iron-silicate slags. An alternative explanation suggests the clay was used to minimize the phosphorus content of iron produced in this type of furnace.

Energy dispersive x-ray analyses of the furnace slag distinguished four phases similar to those observed in the inclusions: (i) wüstite, FeO; (ii) a 4:1 mixture of fayalite and calcium silicate, $2\text{CaO} \cdot \text{SiO}_2$; (iii) small angular particles resembling leucite, $\text{Al}_2\text{O}_3 \cdot \text{K}_2\text{O} \cdot 4\text{SiO}_2$; and (iv) a complex phase containing alkali oxides and phosphorus. The lime, MgO, and K₂O contents of the inclusions observed in the nails are higher than would be expected if these elements were absorbed from the charcoal. Assuming that the nails were not imports to the Longthorpe site, there appears to be strong evidence for the use of basic furnace clays in order to control the phosphorus content of the iron and produce a significantly advanced, low-phosphorus (not cold short) product compared to that of the Ethiopian bloomery process.

Laboratory Reduction of Ores

A series of low-grade British ores and high-grade Swedish magnetites were reduced under laboratory conditions at temperatures in the range 1100-1300 C to investigate their suitability for the bloomery process. Detailed analyses are presented in Ref. 1 and summarized briefly in this paper. The British ores were chosen with lime/silica ratios of 0.1, 0.34, and 3 to give individual slag phases containing up to 9%, 47%, and 67% CaO and average slag lime/silica ratios in the range 0-0.2, 0.2-0.4, and 1, respectively. The slag phases produced by the high lime ore and the titanium bearing magnetite were extremely viscous, which would suggest that additions of flux or lower-grade material would be essential for satisfactory reduction in the simple bloomery. The most easily reduced ores were the low-grade self-fluxing ores, similar to the Dimi ores, which produced fluid slags in the temperature range 1100-1300 C by incurring high iron losses to the slag. The high-grade ores used in modern blast furnaces do not appear to be suitable starting materials for the pre-industrial furnace.

The three studies presented above show that meaningful conclusions regarding (a) relationships between ore, slag, and inclusion chemistries, (b) use of fluxes, and (c) the level of technology of the bloomery process can be drawn by comparisons between minor element concentrations in slag phases and parent ores. The combination of metallurgical analyses with archaeological and ethnographic documentation of bloomery processes presents a powerful tool for characterizing the iron work of specific production centers and investigating networks of trade.

References

1. J. A. Todd, *Studies of Primitive Iron Technology*, Ph.D. Thesis, Cambridge University, 1976.
2. J. A. Todd and J. A. Charles, "Ethiopian bloomery iron and the significance of inclusion analysis in iron studies," *J. Historical Metallurgical Society* 12: 68-87, 1978.
3. J. A. Todd, "Studies of the African iron age," *J. Metals* 31: 39-45, 1979.

TABLE 3.--Analyses of Roman ores, slag, and inclusions.

	Ore	Ore	Slag	light phase	medium phase	Inclusions		single phase	single phase
						dark phase			
Fe ₂ O ₃	73.7	63.3							
FeO	--	--	66.39	98.3	35.3	67.3	3.5	20.4	
SiO ₂	8.6	8.6	23.93	2.0	39.9	24.8	54.5	46.3	
Al ₂ O ₃	4.3	2.3	5.38	--	4.4	3.2	11.7	8.9	
TiO ₂	0.3	0.2	--	--	0.5	--	0.6	0.6	
CaO	trace	2.0	2.33	--	5.0	3.9	15.9	9.4	
MgO	trace	trace	--	--	7.9	0.8	3.8	2.8	
MnO	0.08	2.8	--	--	1.3	--	--	0.9	
P ₂ O ₅	1.10	1.85	0.95	--	--	1.8	--	--	
S	0.02	--	--	--	--	--	--	--	
K ₂ O	--	--	--	--	4.2	--	9.9	6.3	
TOTAL	---	---	98.98	100.3	98.5	101.8	99.9	95.6	
CaO SiO ₂		0.23	0.1		0.13	0.16	0.29	0.20	



FIG. 1.--Iron artifacts manufactured in Diman. Left to right, diggin stick, spear, hoe, black iron bangle, sickle, cowbell, sacrificing knife.

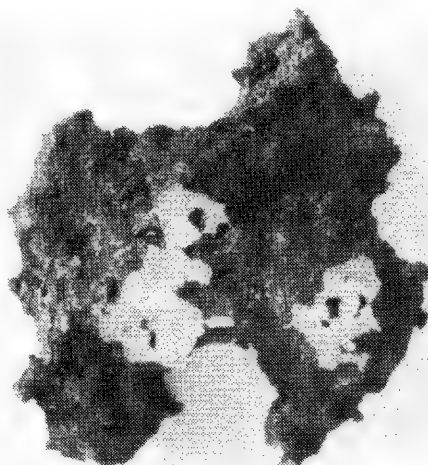


FIG. 2.--Fragment of iron bloom.

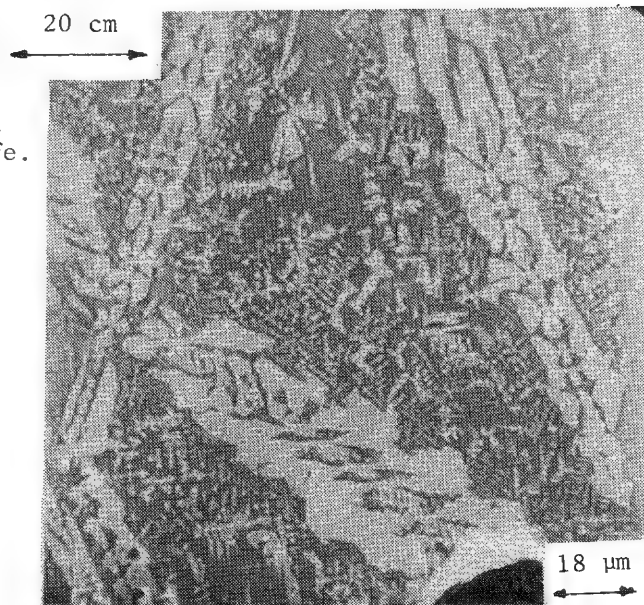


FIG. 3.--Metallographic section of furnace slag containing fayalite in iron-alumino-silicate matrix.

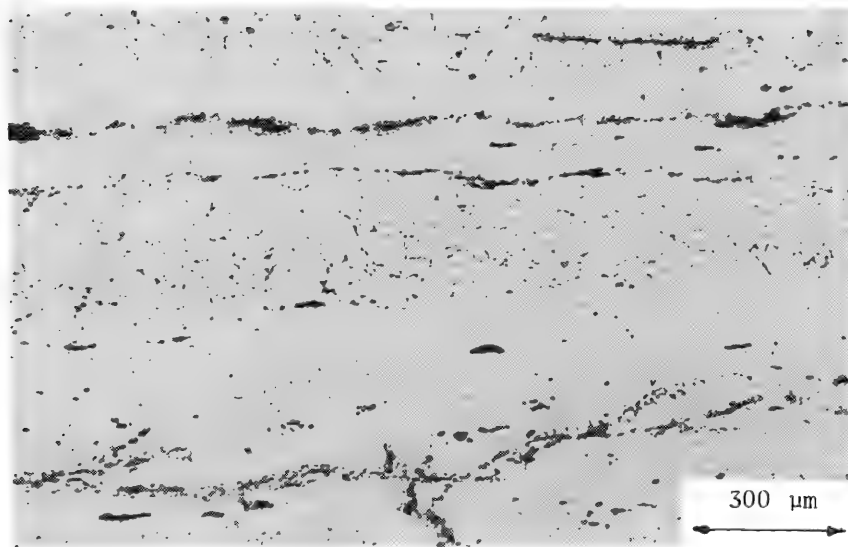


FIG. 4.--Metallographic section of knife showing inclusions elongated along direction of forging.

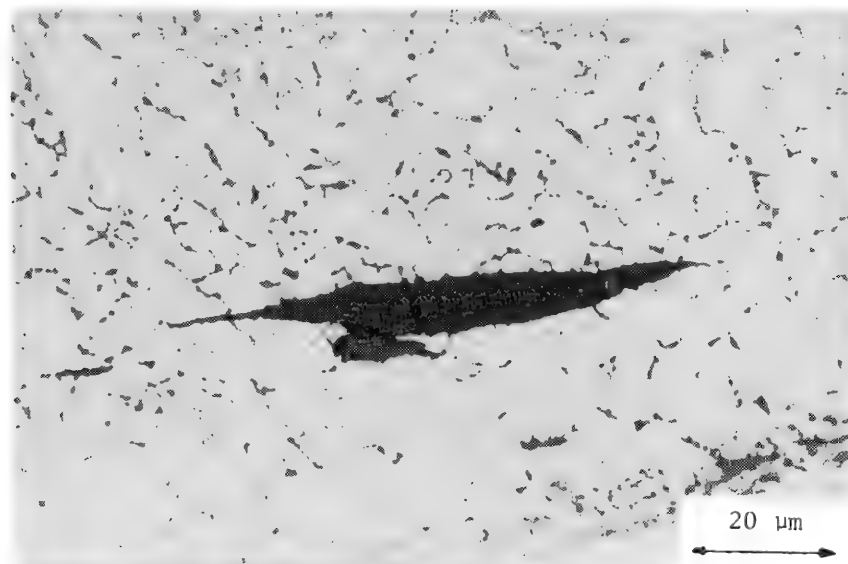


FIG. 5.--Single-phase inclusion in knife section.

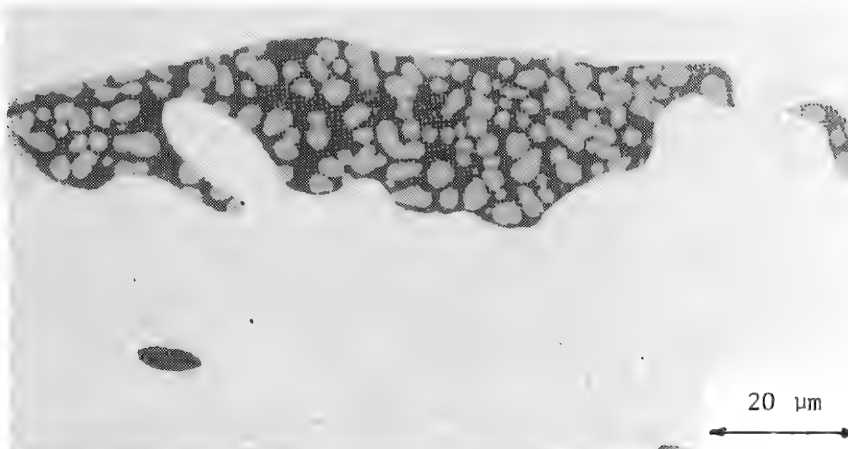


FIG. 6.--Two-phase inclusion containing wüstite and fayalite.

MICROPROBE ANALYSIS OF EARLY COPPER ARTIFACTS FROM THE NORTHERN SINAI AND THE JUDEAN CAVES

M. R. Notis, Heidi Moyer, M. A. Barnisin, and David Clemens

A number of significant archaeological finds have been made in Israel related to the development of early copper metallurgy and smelting practice, and dates as early as the 3rd/4th millennium B.C. Among them are the mining and smelting finds made at Timna;¹ the casting enclave at Abu Matar;² and the large hoard of cast copper objects found at the caves in Nachal Mishmar^{3,4} and smaller finds at Nachal Badir,⁵ both locations in the Judean Desert. Controversy exists as to the cultural origins or possible commonality of these finds.⁶ The use of metallographic and microanalytical techniques to study metal objects found at some of these sites might shed light on this problem.

Previous analyses exist for the ores found at Timna⁷ and Abu Matar.⁸ Timna ores are mainly nodular chalcocite and malachite,⁷ whereas the ore found at Abu Matar is mainly malachite and cuprite with some chalcocite.⁸ In both cases they are free of arsenic, and therefore pose a dilemma with respect to the high bulk arsenic levels reported for maceheads from both Abu Matar and Nachal Mishmar.⁴ The copper metal finds at Timna are consistent with smelting from the in situ ores.⁹ We have therefore obtained a number of metal objects from Abu Matar and the Judean Desert in order to compare the results with each other and against the reported ore analyses.

Copper Piece from Abu Matar

The first sample examined was a small piece of copper from Abu Matar that was found together with pieces of ore and crucibles, and is possibly a splashing from the casting of a large piece. Examination by scanning electron microscopy (Fig. 1) indicated the structure to be typical of cast crude copper and to contain many blowholes due to gas evolution and a large number of second-phase spherical inclusions. EDS analysis of the metal matrix indicated only copper to be present, and the inclusions to be copper sulfide.

Axehead from Safadi (loc. 307) near Abu Matar

This piece has been the focus of previous study by optical metallography.⁸ Initial examination in the SEM reconfirmed the previous findings that the piece has a cast-and-worked structure. Again, EDS analyses of the metal matrix detected only copper. However, three distinct types of inclusions were found. First, there is a copper oxide second phase with morphology typical of the copper-copper oxide eutectic (Fig. 2). There are numerous inclusions that contain mostly nickel, copper, and sulfur; Fig. 3 shows one of these inclusions with the x-ray line scan for Ni superimposed. The inclusion thus appears to be nickel-copper sulfide, and is therefore problematic since nickel has not been reported to be present in any of the ore analyses.¹ The Abu Matar metal analysis given by Dayton⁶ (quoted from Key⁴) and indicating the presence of Ni is erroneous and the object should be properly identified as coming from Nachal Mishmar. Although the presence of Ni in the axehead from Safadi warrants further study, the lack of detectable arsenic in the copper matrix still points to consistency with fabrication from local ore source.

A third type of inclusion (Fig. 4) is found only near the surface of the axehead and is found to contain only silica. It is believed that these are probably quartz grains included in the piece during casting and originating from either the casting crucible or mold material.

The authors are affiliated with the Department of Metallurgy and Materials Engineering, Lehigh University, Bethlehem, PA 18015.

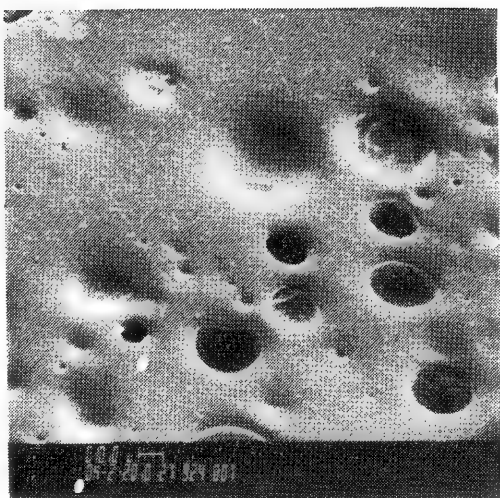


FIG. 1.--Copper object from Abu Matar. Secondary-electron image (SEM) showing blowholes and sulfide inclusions.

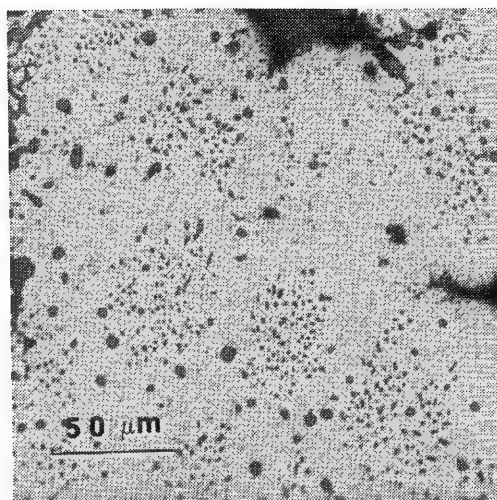


FIG. 2.--Axehead from Safadi-Abu Matar. Optical photomicrograph showing copper-copper oxide eutectic.

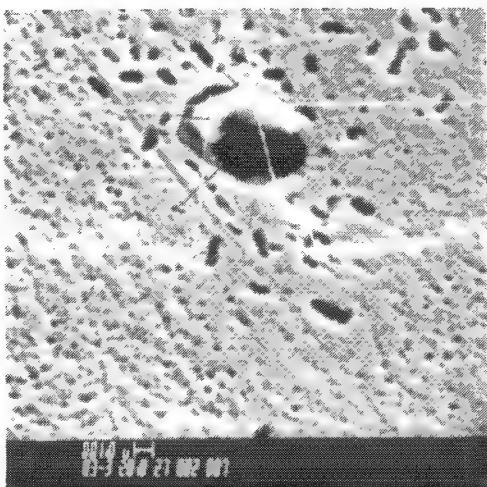


FIG. 3.--Axehead from Safadi-Abu Matar. Secondary-electron image (SEM) of inclusion with Ni K α linescan superimposed.

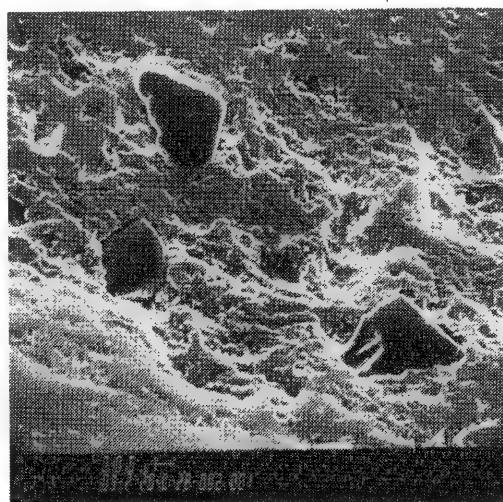


FIG. 4.--Axehead from Safadi-Abu Matar. Secondary-electron image (SEM) of silica inclusions near surface.

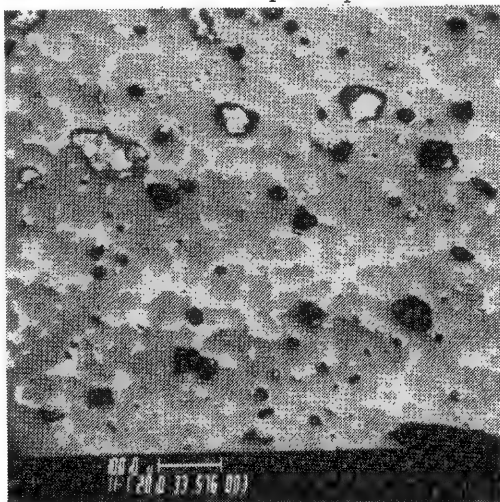


FIG. 5.--Macehead from Judean Desert. Back-scattered electron image (microprobe) indicating two-phase matrix and inclusions.

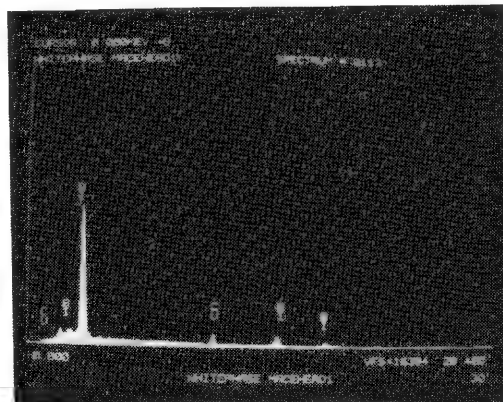


FIG. 6.--Macehead from Judean Desert. EDS x-ray spectra showing high Bi content in inclusions.

Macehead from Judean Desert (Aharoni 52-01-82-F, 46938)

This macehead is of a shape similar in form to those shown on p. 119 of the work by Bar-Adon;³ the inside of the shaft hole still contained the clay center around which the head had been cast. The clay is not completely enclosed in cast metal, as is shown on p. 235 of Bar-Adon.³ Microprobe examination of a polished metallographic section (Fig. 5) indicated the majority of the structure to be a two-phase material. The major phase, occupying about 90% of the cross-sectional area, is a Cu-Sb-As alloy giving the following approximate analysis: 95.3 Cu-2.4 Sb-2.4 As (wt.%). The minor phase appears to be a complex intermetallic sulfide with approximate composition 61.3 Cu-25.3 Sb-7.8 As-bal. S (wt.%). In addition to these phases there are at least two other types of inclusions found in much smaller amounts--copper sulfide with a small amount of Sb and As, and a copper-bismuth phase with small amounts of Sb and S (Fig. 6). The overall alloy composition appears to have a combined Sb + As analysis of $9. \pm 0.6$ (wt.%).

It appears that this macehead has been smelted and cast from a "gray ore" or fahlerz containing tetrahedrite (Cu_3SbS_3) and chalcocite (Cu_2S). These types of ore may have an appreciable portion of the Sb replaced by As, and Bi concentrations typically run quite high. This ore is distinctly different from those found at Timna⁷ and Abu Matar,⁸ but it also appears to be different from the maceheads found at Nachal Mishmar, Nachal Seelim, and Abu Matar, all of which have little Sb content.³ It thus appears that considerably more detailed and updated microanalysis is warranted on these maceheads as a group.

References

1. B. Rothenberg, R. F. Tylecote, and P. J. Boydell, *Chalcolithic Copper Smelting*, Archaeometallurgy Monograph No. 1, 1981.
2. J. Perrot, "The excavation of Tell Abu Matzr, near Beersheva," *Israel Exploration J.* 5: 17-40, 1955.
3. P. Bar-Adon, *The Cave of the Treasure*, Israel Exploration Society, 1980.
4. C. A. Key, "Ancient copper and copper-arsenic alloy artifacts: Composition and metallurgical implications," *Science* 146: 1578-1580, 1964.
5. Y. Aharoni, "Expedition B," *Israel Exploration J.* 11: 11-24, 1961.
6. J. Dayton, *Minerals, Metals, Glazing and Man*, London: Harrap, 1978, 149-150.
7. C. Milton, E. J. Dwornik, R. B. Finkelman, and P. Toulmin, "Slag from an ancient copper smelter at Timna, Israel," *J. Hist. Met. Soc.* 10: 24-33, 1976.
8. R. F. Tylecote, B. Rothenberg, and A. Lupu, "Examination of metallurgical material from Abu Matar, Israel," *ibid.*, 8: 32-34, 1974.
9. J. Roeder, J. Sculac, and M. Notis, "The precipitation of iron in early smelted copper from Timna," *Microbeam Analysis--1984*, 243.

THE PRECIPITATION OF IRON IN EARLY SMELTED COPPER FROM TIMNA

J. F. Roeder, J. F. Sculac, and M. R. Notis

The archaeological site at Timna in the Aravah Region of Southern Israel is one of the most important sites relevant to the beginnings of metallurgical practice. First, it is a site where complete furnaces, tuyeres, slags, ores, and copper ingots have been found in situ¹ and representing different stages in metallurgical development, dating as early as the Chalcolithic Period (4th millenium B.C.). Second, because of the nature of the iron content of the copper ingots² and some of the unique iron artifacts which have been found,³ it may be the strongest evidence that demonstrates that early iron smelting and metallurgy developed directly from copper metallurgy. For this study, a small piece of a copper ingot found at the site identified as Timna Site 2 (sample no. 575) was provided by Beno Rothenberg, the director of the excavations at Timna.

Three morphological forms have been reported in the literature for the iron-rich phases found in high copper-iron alloys: (1) a primary iron phase originating during solidification, and often dendritic in form;^{1,2,4} (2) small spherical coherent solid-state precipitates;⁵⁻¹⁴ and (3) intermediate-size star-shaped or cuboid precipitates.^{4,8,9,14}

Milton et al.² noted that copper from Timna was strongly magnetic and then confirmed the presence of metallic iron by metallographic examination. Later work,¹ with copper samples taken from modern simulation smelting experiments thought to have been performed under similar conditions to those used at Timna, showed the presence of randomly oriented dendritic iron in the copper matrix. This form of iron is due to overdriving caused by a high-volume air blast in the presence of excess charcoal, which reduces the iron oxide present in the smelt. These dendrites result from the limited solubility of iron in copper below the liquidus as shown in the Cu-Fe phase diagram (Fig. 1).

In the present study, electron probe microanalysis was performed on the Timna specimen with a JEOL 733 Superprobe. All measurements were performed at 20 kV and 10 nA by use of Cu and Fe K α radiation. The iron dendrites are easily revealed by imaging of back-scatter electrons (Fig. 2) or Fe K α x-ray emission (Fig. 3). The bulk composition was determined to be 3.66 w/o Fe-95.39 w/o Cu (4.14 a/o Fe) by area scan techniques. Point counting indicated the iron dendrites to have a copper content of 9.6 ± 0.3 w/o Cu (8.5 a/o Cu). Both are consistent with a melt temperature of 1170 ± 30 C. Point counting in the copper matrix away from any visible second phase gave a composition of 1.27 ± 0.08 w/o Fe (1.44 a/o Fe) consistent with the reduced low temperature solubility of Fe in Cu, and the presence of solid-state iron precipitates too small in size to be analyzed by the microprobe.

Studies of precipitation and aging of Cu-Fe alloys have shown that the precipitation of spherical coherent γ -Fe particles⁵ occurs from the supersaturated solid solution at temperatures below the peritectic reaction temperature of ~ 1095 C. This coherency occurs because the lattice parameters of Cu ($a_0 = 0.3615$ nm) and γ -Fe ($a_0 = 0.3590$ nm) are very close in size and both possess the face-centered cubic structure.⁶ The transformation is known to be caused by overaging⁷⁻⁹ and/or plastic deformation¹⁰ but can be suppressed by impurity additions.^{11,12} It has been noted that precipitates smaller than a critical size will not transform⁵ even in the presence of plastic deformation and that for aging temperatures below 800 C, no thermal treatment can transform the paramagnetic γ -precipitate to the α -ferromagnetic form in the absence of plastic deformation, even when greatly overaged.⁸ When the $\gamma \rightarrow \alpha$ transformation occurs, the transformed precipitates consist of $\{112\}_\alpha$ type twins¹³ and have a near Kurdjumov-Sachs orientation relationship with the copper matrix.⁵ It has also been demonstrated that the $\gamma \rightarrow \alpha$ transformation occurs when the elastic constraints of the surrounding matrix are

The authors are affiliated with the Department of Metallurgy and Materials Engineering, Lehigh University, Bethlehem, PA 18015. They thank H. Moyer for performing the microprobe measurements.

removed, as through electrolytic extraction.¹² These observations have led to the suggestion that the $\gamma \rightarrow \alpha$ transformation does not occur when the precipitates do not contain the crystal defects necessary to nucleate or allow the martensitic transformation to proceed.¹⁴

The morphology of the overaged precipitate has been observed in a number of the above studies. Easterling and Miekko-Oja¹⁴ used replication techniques in TEM to show that aged precipitates have a cuboidal shape. Furnace-cooled specimens prepared by Boltax⁹ contain cuboidal and star-shaped precipitates large enough to be resolved by optical microscopy. Cooke and Aschenbrenner⁴ show similar structures for furnace-cooled alloys; however, they indicate that alloys with 2-4% Fe, remelted at 1200 C and quenched in water, are also ferromagnetic, most likely due to transformation of small residual Fe-dendrites formed during cooling, as this result is inconsistent with other studies describing solution treating and quenching experiments from below the peritectic temperature.^{8,9}

The morphology characteristic of the overaged precipitate was observed in the current study during examination of the Timna specimen. Figure 4 is a backscattered electron image, and Fig. 5 is an Fe-K α x-ray image, showing the star-shaped precipitate morphology and indicating the high Fe content. As the resolution of these precipitates was poor, a thin foil was cut and ion-thinned, and the specimen was examined by TEM for better resolution and identification of these precipitates. A bright-field image (Fig. 6) obtained on a Siemens Elmiskop I 100kV electron microscope shows the star-shaped appearance of these precipitates; their common alignment indicates a possible fixed orientation relationship with the matrix. Further investigation was performed on another thin foil on a Philips EM400T operating at 120 kV. As problems were encountered with specimen thinning and as the precipitates are not uniformly distributed within the foil, it was extremely difficult to find areas with both the matrix and precipitates thin enough to produce simultaneous diffraction. One such selected area diffraction pattern is shown in Fig. 7; a dark-field image produced from one of the precipitate spots is shown in Fig. 8 and appears to illuminate only one part of the star-shaped precipitate. Tentative indexing of the pattern indicates a [011] axis for one set of spots and a [112] for the other. Both patterns appear to be FCC and to bear a fixed orientation to each other, but different from that expected from the transformed γ -Fe precipitates. We believe that small particles nucleated during solidification would not be aligned as is observed in Fig. 6 and would not necessarily show a simple orientation relation to the matrix that would have solidified afterwards. Therefore, we believe that the observed star-shaped precipitates were formed in the solid-state during slow cooling in the smelting furnace but maintained their FCC structure, possibly because of impurity stabilization and in the absence of plastic deformation. In any event, further study is warranted to establish the orientation relation between these precipitates and the matrix. A better understanding of the conditions under which they form might yield useful information concerning furnace conditions during smelting.

A further point deserves mention with respect to the possibly misleading statement by Cooke and Aschenbrenner⁴ that a hand-held magnet will conclusively indicate the presence of metallic iron in a copper sample. As discussed previously, when iron precipitates in the solid state, as small coherent particles in copper-rich iron-copper alloys, it has the FCC structure and is paramagnetic. Pure Cu is diamagnetic but the solid solution of FCC ϵ -Cu is also paramagnetic. The paramagnetic γ -Fe precipitates transform to ferromagnetic α -Fe only under the deformation/aging conditions described previously. Third elements also have an effect on the $\gamma \rightarrow \alpha$ transformation; e.g., nickel¹² can completely suppress the transformation when present in amounts greater than ~5%, and similar effects have recently been observed¹¹ for the presence of Sn and Si. More work is needed in the area of other archaeologically important third elements (e.g., As, Bi, Sb) and their effect on the magnetic transformation.

References

1. B. Rothenberg, R. F. Tylocote, and P. J. Boydell, *Chalcolithic Copper Smelting*, Archaeometallurgy Monograph No. 1, 1981.
2. C. Milton, E. J. Dwornik, R. B. Finkelman, and P. Toulmin, "Slag from an ancient copper smelter at Timna, Israel," *J. Hist. Met. Soc.* 10: 24-33, 1976.
3. "New discoveries reveal second period of Egyptian mining," *IAMS Newsletter*, No. 1, 1980.
4. S. R. B. Cooke and S. Aschenbrenner, "The occurrence of metallic iron in ancient copper," *J. Field Archaeology* 2: 253-260, 1975.

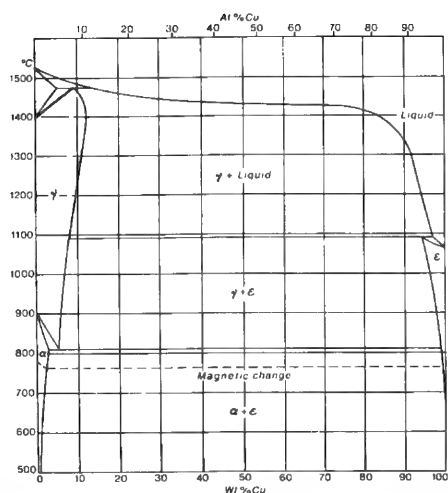


FIG. 1.--Cu-Fe phase diagram.¹⁵

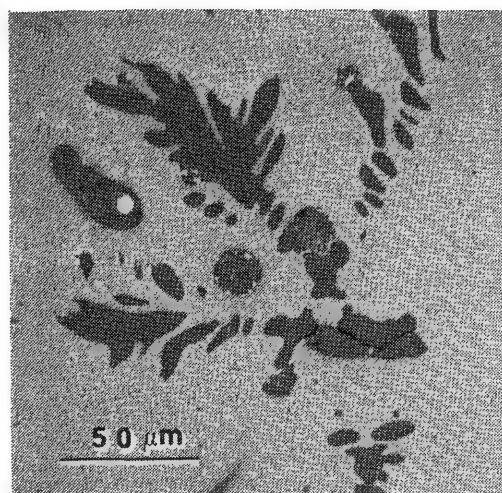


FIG. 2.--Backscatter electron image (microprobe) of iron dendrites in copper matrix.

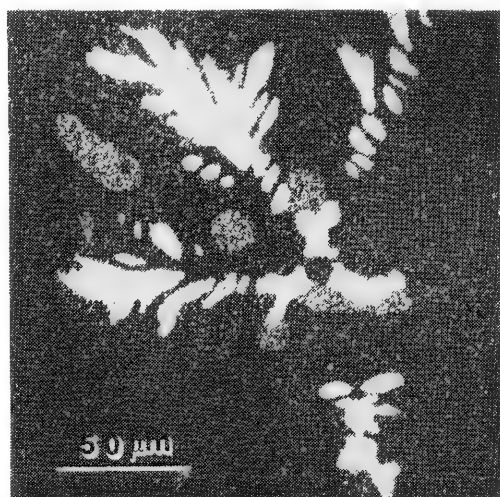


FIG. 3.--Fe K α x-ray image (microprobe) of iron dendrites in copper matrix.

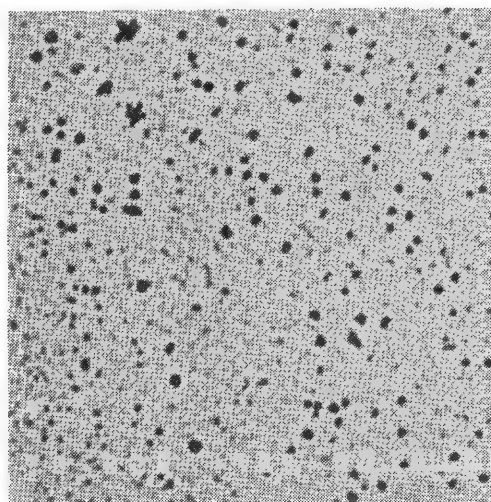


FIG. 4.--Backscatter electron image (microprobe) of iron precipitates in copper matrix.

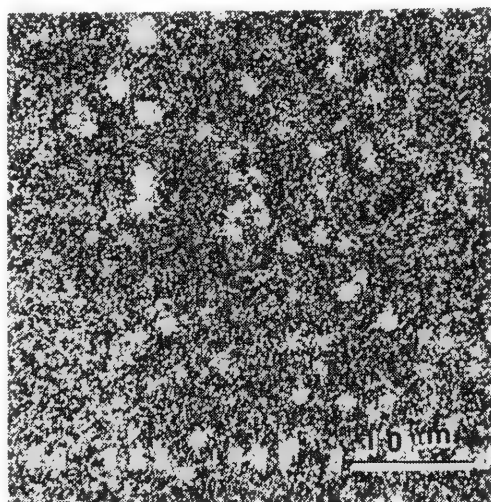


FIG. 5.--Fe K α x-ray image (microprobe) of iron precipitates in copper matrix.

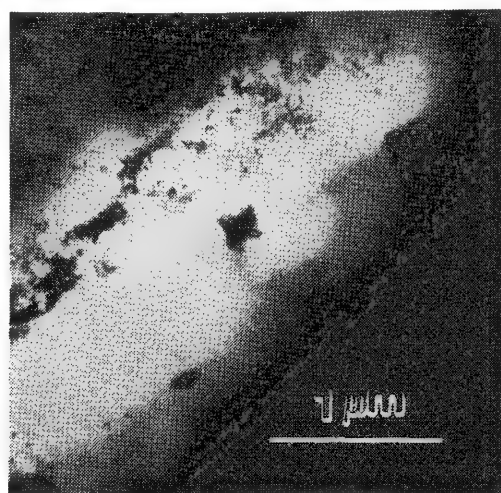


FIG. 6.--Bright-field TEM of star-shaped precipitates.

5. K. E. Easterling and G. C. Weatherly, "On the nucleation of martensite in iron precipitates," *Acta Met.* 17: 845-852, 1969.
6. J. B. Newkirk, "Mechanism of precipitation in a Cu-2.5 pct. Fe alloy," *Trans. AIME* 208: 1214-1220, 1957.
7. P. E. Cech and D. Turnbull, *J. Metals* 6: 45, 1954.
8. J. M. Denney, "Precipitation kinetics and structure in a Cu-2.4% Fe alloy," *Acta Met.* 4: 586-592, 1956.
9. A. Boltax, "Precipitation processes in copper-rich copper-iron alloys," *Trans. AIME* 218: 812-821, 1960.
10. C. S. Smith, "Structures and ferromagnetism of cold-worked copper containing iron," *Phys. Rev.* 57: 337, 1940.
11. D. Stroz, T. Panek, and H. Morawiec, "Influence of the addition of a third element to the precipitation process in Cu-Fe alloys," *Mat. Sci. and Eng.* 58: 43-53, 1983.
12. K. E. Easterling and P. R. Swann, "Nucleation of martensite in small particles," *Acta Met.* 19: 117-121, 1971.
13. R. Monzen, A. Sato, and T. Mori, "Structural changes of iron particles in a deformed and annealed Cu-Fe alloy single crystal," *Trans. Jap. Inst. Metals* 22: 65-73, 1981.
14. K. E. Easterling and H. M. Meikka-Oja, "The martensitic transformation of iron precipitates in a copper matrix," *Acta Met.* 15: 1133-1141, 1967.
15. The Cu-Fe System after *Smithells Metals Reference Book*, London: Butterworth, vol. 7; the $\gamma/(\gamma + L)$ boundary after A. A. Bochvar, A. S. Ekatova, E. V. Panchenko, and Y. F. Sidokhin, *Dokl. Akad. Nauk SSSR* 174: 863-864, 1967.

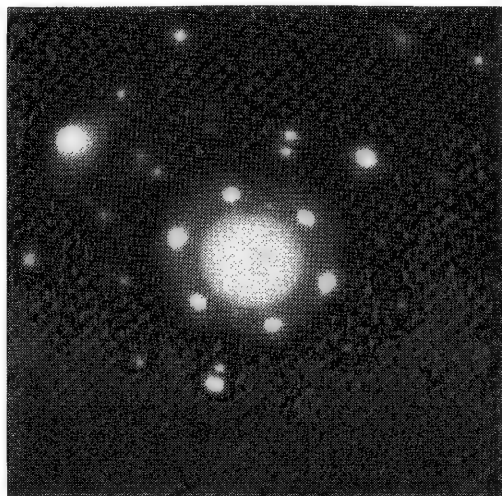


FIG. 7.--Selected-area diffraction pattern with precipitate and matrix spots superimposed.



FIG. 8.--Dark-field image (TEM) of star-shaped precipitates.

AN ANALYTICAL STRUCTURE DETERMINATION OF A SAUGUS PIG

K. S. Vecchio and A. R. Marder

Saugus Iron Works (Hammersmith Works) at Lynn, Massachusetts, was the first successful foundry operation in North America. A metallurgical analysis of an iron pig taken from the Saugus site was undertaken to examine and interpret the structure and composition of the iron. The determination of the structure and composition of the pig will provide an understanding of its processing history.

Chemical analysis of the pig revealed a high phosphorus level (1.92%), high sulfur level (0.11%), and low levels of silicon and manganese (0.04 and 0.02%, respectively). The total carbon content was determined to be 2.59%, the Carbon Equivalent value was 3.24, and the Fluidity Factor was 3.56 as calculated from the chemistry.

Optical metallographic examination revealed the structure to be essentially that of white cast iron. The microstructure consisted of large pearlite colonies, as a result of the proeutectic austenite transformation, in a eutectic matrix of ledeburite. The ledeburite consisted of small pearlite colonies (originally austenite) embedded in cementite (Fe_3C). A microhardness study of the matrix was performed on a Leitz MiniLoad 2 Microhardness Tester at 100 g load to verify the cementite structure.

The microstructural examination was extended to Scanning Electron Microscopy (SEM) performed on a JEOL 733 Microprobe. Backscatter-electron imaging of the microstructure revealed a different structure (due to atomic number contrast) at the pearlite/carbide boundary in a rod-like or lens-like morphology (Fig. 1).

Energy-dispersive x-ray spectroscopy (EDS) and wavelength-dispersive x-ray spectroscopy (WDS) mapping was performed revealing that the pearlite/carbide boundary structure was the iron-phosphide eutectic (Fig. 2). The phosphide eutectic solidifies below 930 C, the temperature at which the other iron constituents solidify, and thus appears at the interface. Quantitative microprobe analysis was performed to determine the phosphide level at the interface region in an attempt to establish the iron/phosphorus content.

An inclusion study was further performed in the microprobe, and two types of inclusions were found. Most of the inclusions located were sulfur based, and WDS analysis revealed that only some inclusions contained manganese. The second type of inclusion found was a titanium-based slag inclusion.

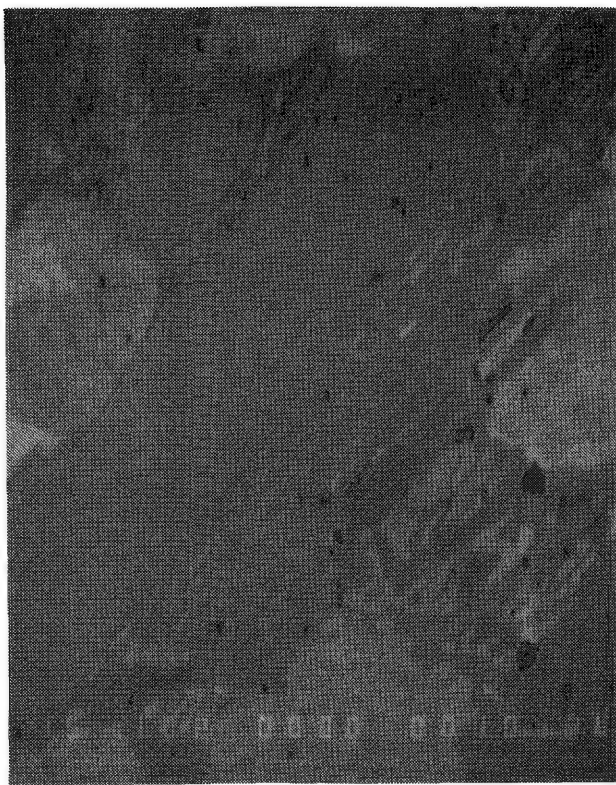


FIG. 1.--Backscatter electron image of pearlite/carbide boundary (1000 \times).

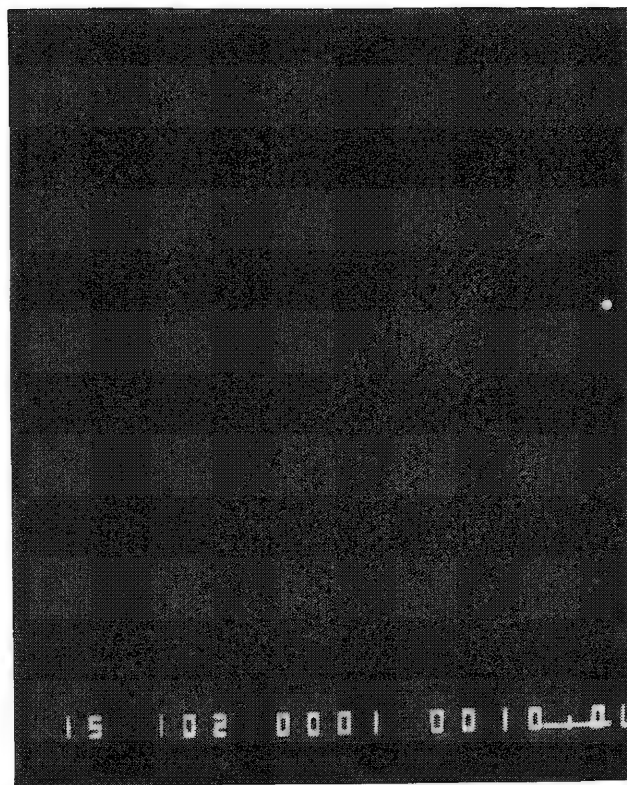


FIG. 2.--WDS x-ray map for phosphorus revealing phosphide structure at pearlite/carbide boundary at same region as Fig. 1 (1000 \times).

MILLI- AND MICROPROBE PIXE FOR THE ANALYSIS OF ANCIENT BRAZING OF GOLD

Guy Demortier

Proton-milliprobe (500 μm in diameter) and microprobe (5 μm in diameter) used to induce characteristic x rays of elements have been proved to be an accurate method for nondestructive elemental analysis of narrow regions of solders on ancient and antique gold artifacts.¹ During the study of more than 2500 narrow regions on more than 200 gold artifacts lent by 6 museums and 8 private collectors, we have observed the presence of cadmium in narrow regions of solders on several among them whose origins are Syria, Iran, or the south of Italy.² Gold brazing alloys containing cadmium have been manufactured in our laboratory by use of only means available in antiquity. Concentrations in such alloys are compared with those of ancient artifacts.

Experimental

Ion-beam techniques in archaeology and the arts have been developed in several laboratories;³ among them prompt methods of detection of characteristic x- and γ -ray signals during the ion-beam bombardment allow topographical investigations (milliprobes and microprobes).

The proton milliprobe system works with the artifact at atmospheric pressure. The incident proton beam (0.5 mm in diameter) crosses a thin (12 μm) foil of Al and reaches the sample situated at a distance of 1 cm in the air. The diameter of the beam is about 0.7 mm at the target position. The x-ray and γ -ray analyses are performed with energy-dispersive solid-state detectors. The thickness of the analyzed surface layer is less than 5 μm . For gold and silver matrices, this thickness is representative of the bulk material, as demonstrated on several items where scratchings have been made and measurement has been repeated, and also by comparison of our results on gold and silver coins with those obtained by 10 MeV proton activation on a thickness of more than 400 μm . Quantitative results are obtained by comparison with known reference materials. True concentrations are extracted from the area of each characteristic peak by use of such known parameters as stopping power of materials, mass attenuation coefficients of x rays, and geometry of the irradiated surface, but also the secondary fluorescence, mainly from absorption of gold L rays in copper.⁴ When such corrections are performed, we obtain the true concentrations of a known alloy containing 25% Au, 31% Cu, 27% Ag, and 17% Cd with an accuracy better than 5% on each element when a sample containing 75% Au, 13% Cu, 6% Ag, and 6% Cd is taken as reference material.⁴

No significant application of PIXE and PIGE to bronzes and brasses can be expected because of the important corrosion of these less noble metals.⁵

The proton microprobe of L.A.R.N. works with a spatial resolution better than 3 μm . The vacuum chamber that holds the sample is large enough to accommodate artifacts up to 30 cm. The scan is done mechanically as well as electrostatically.

Analysis of Solders on Artifacts

The great majority of solders on antique gold jewelry items are obtained by local fusion, without any brazing alloy, or with a Cu-Ag-Au alloy. The soldering of fine granulations (e.g., in Etruscan jewelry) is often achieved by the process of diffusion bonding rediscovered in 1947 by Litteldale.⁶

Cadmium is sometimes present in the regions of solders on gold artifacts from Syria and Iran. When the relative concentrations of Cu-Ag-Cd in the solders on old artifacts worked out in rich gold alloys are plotted in ternary diagrams, one observes that the general trend of the data lies in a region going from the Ag corner to the Cu-Cd axis when absolute

The author is at L.A.R.N., Facultés Universitaires Notre-Dame de la Paix, 22 Rue Muzet, B-5000 Namur, Belgium.

concentration of Cd is observed to increase. The ratio of Cu on Cd concentrations is then nearly constant (Fig. 1). On the other hand, when the same data are collected for modern soldering alloys, the general trend points to the Cd corner, which indicates that the Cu/Ag ratio is now constant (Fig. 2). Other differences between modern and antique soldering alloys are reported elsewhere.²

Microprobe measurements (Fig. 3) have confirmed the general trend of the Cu-Ag-Cd ternary diagram computed from milliprobe data. The use of beams 0.5 mm in diameter is often sufficient to explore the regions of solders without overflowing in the contiguous material.

Information from Old Metallurgical Handbooks

The ancient Greek name of gold solder is chrysocolla, in modern mineralogy an hydrated copper silicate.

It is generally recognized that the term chrysocolla reported in old metallurgical handbooks is malachite, a copper carbonate. We have been highly surprised to read in a copy from the 15th century in the 33rd book of the elder Pliny's *Natural History* (1st century) that the color of natural chrysocolla was yellow and that only "argenteous" gold may be soldered with that chrysocolla, but that gold alloyed with copper is not easily soldered with the same chrysocolla. Surprisingly, no comment on this remark may be found in the literature! Pliny's report would make sense if cadmium sulphide (natural greenockite) was used as chrysocolla.² This point is discussed below.

Experimental Archaeology

We have reproduced, by very rudimentary means, soldering alloys by melting a natural cadmium sulfide (an orange-yellow mineral which appears sometimes on blendes) in gold. A few milligrams of gold are heated at a temperature sufficient to melt the gold and to form a little sphere in the bottom of a carbon crucible. Cadmium sulfide powder is then sprinkled into the melted gold and dissolves at once. The small sphere of the new alloy is then microscopically analyzed. Each alloy sample appears to be quite homogeneous. The centers of the alloy spheres often contain less cadmium than the surface but the difference in these concentrations is always less than 20%. In antiquity bronze and brass were also elaborated by mixing (in an oven) of tin and zinc minerals with copper minerals.⁷

We have established that the solubility of the cadmium sulfide in gold or gold alloys reaches saturation when the cadmium content lies between 1 and 10%. Addition of copper minerals before introduction of the cadmium sulfide enhances the cadmium solubility in gold. No dependence of the silver content has been observed.² Thermal analysis of such mixtures indicates that the melting point of the alloy may be lowered below 750 C even when its degree of fineness is greater than 850/1000. Spark source mass spectrometry used for the analysis of trace elements indicates that at least 95% and sometimes all of the sulfur (introduced with the cadmium sulfide) is eliminated during the alloying procedure. These soldering alloys obtained by dissolution of cadmium sulfide in a gold matrix up to saturation (indicated by the presence of yellow "strings" floating over the melt surface in the crucible when additional cadmium sulfide is poured in the liquid gold) show a bigger endothermic peak than commercial soldering alloys. The compositions of these soldering alloys remain constant during the short time of heating necessary for brazing.

When cadmium sulfide powder is mixed into turnings of gold and then heated to melting, dissolution takes a longer time than when greenockite is sprinkled in liquid gold. Furthermore, the alloy obtained by this procedure is less homogeneous. The sphere of gold-cadmium alloy appears in that case as a gold-rich alloy at the bottom of the crucible with a black deposit appearing at the top. When such a sphere is gently compressed the black coating is easily separated. The measured elemental concentrations also show correlation between copper and cadmium contents. This correlation is observed in both the data on the black deposit, where the gold content is less than 5%, and in the gold-rich alloy obtained simultaneously.² This behavior begs the question of whether cadmium sulfide cannot be used to purify gold! The corresponding ternary diagram of copper cadmium silver (Fig. 4) is very similar to that observed for artifacts. Is the production of this black deposit related to Pliny's remark on the difficulty of brazing copper-gold alloys with chrysocolla?

The temperatures of liquidus and solidus for ternary alloys Au-Cu-Cd obtained by this alloying procedure have been recently studied.⁸

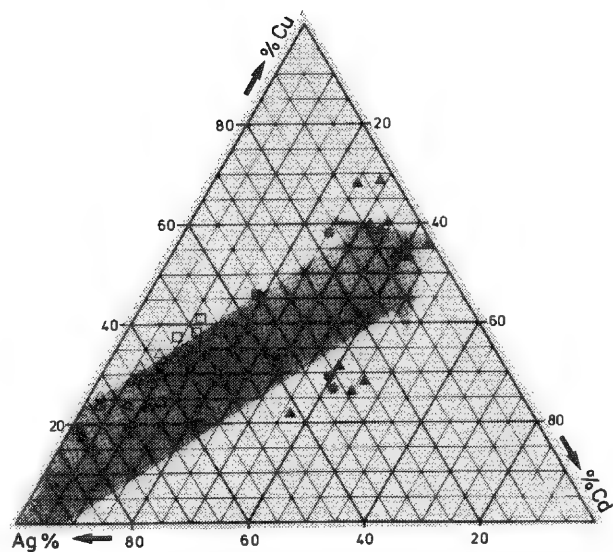


FIG. 1.--Ternary diagram showing relative concentrations of Cu-Ag and Cd in gold alloy of solders on antique gold artifact (Roman necklace, 1st century). Open triangles, open squares, black squares, asterisks, and black triangles indicate increasing Cd content in various regions of solders (milliprobe technique).

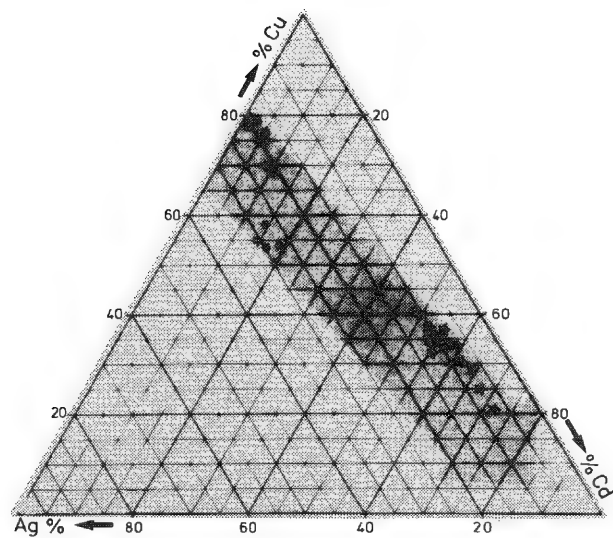


FIG. 2.--Ternary diagram showing relative concentrations of Cu-Ag-Cd of modern gold alloys. Different symbols are used for different soldering alloys used for brazing (milliprobe technique).

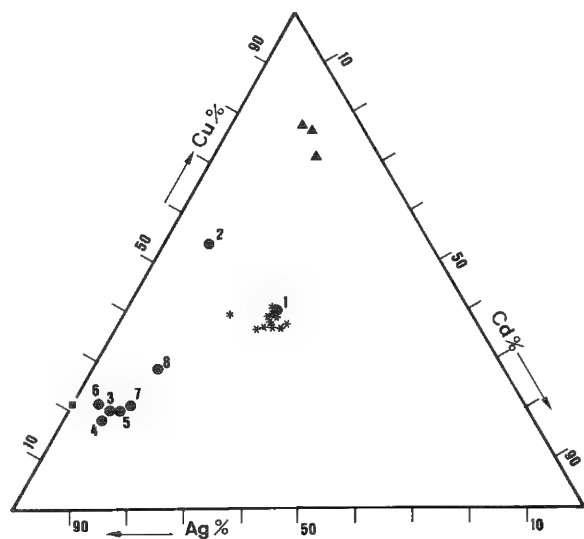


FIG. 3.--Ternary diagram showing relative concentrations of Cu-Ag-Cd in very narrow regions of solders of Roman necklace (microprobe technique).

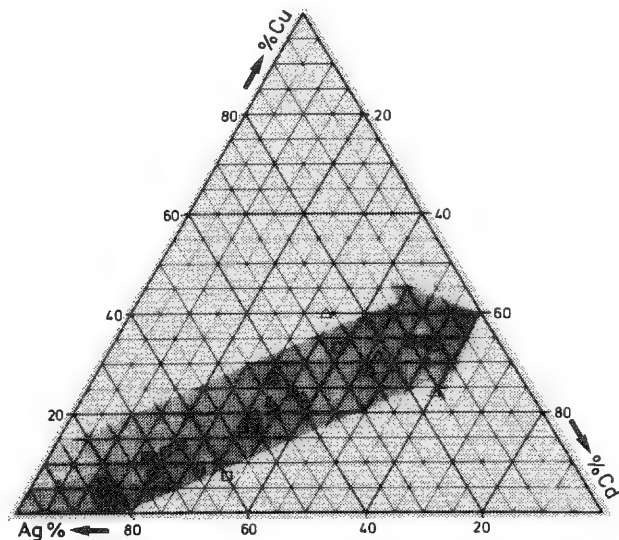


FIG. 4.--Ternary diagram showing relative concentrations of Cu-Ag-Cd in soldering alloys obtained by dissolution of CdS in liquid Au-Cu-Ag alloys. Open squares, black squares, and open triangles are used for increasing copper concentration (1, 4, 12%) in basic gold-copper alloys (milliprobe technique).

Conclusions

Milliprobe PIXE (with the sample under irradiation in the air) has been successfully used for accurate and rapid elemental analysis of narrow regions in solders of ancient gold artifacts. The diameter of the beam (0.7 mm) at the target position is generally small enough to explore the actual solder without irradiation of the neighborhood. Microprobe PIXE (3-5 μm) (with the sample in the vacuum) may also be used to confirm the milliprobe results.

As cadmium has been found in solders of artifacts from the 1st to 9th century A.D. whose origins are Iran and Syria, we have reproduced in laboratory, by rudimentary means (minerals, a carbon crucible, and fire) soldering alloys containing cadmium by dissolution of a yellow mineral (CdS: greenockite) in melted gold and gold copper alloys.

The alloy obtained by this procedure is suitable for gold brazing. Our observations on the properties of these soldering alloys are in fairly good agreement with the version of the 33rd book of Pliny's *Natural History* (1st century A.D.) concerning the soldering of gold artifacts containing copper.

References

1. G. Demortier and T. Hackens, *Nucl. Instr. and Methods* 197: 223-236, 1982.
2. G. Demortier, *Gold Bulletin* 17: 27-38, 1984.
3. J. R. Bird, P. Duerden, and D. J. Wilson, *Nuclear Science Applications* B1: 357-526, 1983.
4. B. Van Oystaeyen and G. Demortier, *Nucl. Instr. and Methods* 215: 299-313, 1983.
5. G. Demortier, T. Hackens, and F. Bodart, *Revue d'Archéométrie*, Supplément III 1981, Actes du 20ème Symposium, Paris, 1980, 63-72.
6. H. A. P. Litteldale, British patent 415 181, 1936.
7. J. R. Marechal, *Revue Archéologique Sites* 19: 20-22, 1984; J. R. Marechal, *La Préhistoire de la métallurgie et ses prolongements*, Sites, Avignon (France), 1983.
8. A. Boullar, Vermeyen-Moor, Z. Gabelica, and G. Demortier, *Proc. Conf. Association Française de Calorimétrie et d'Analyse Thermique*, Brussels, May 1984, in press.

THE USE OF SEM FOR POLLEN MORPHOLOGICAL STUDIES OF CLIMATE-SENSITIVE SPECIES

Rekha Dodia

We have carried out detailed SEM studies of the modern pollen of genera for which species level identification can yield climatic clues. The paper describes the ecological requirements of various species of *Quercus* and *Pinus* and their morphological characteristics relevant to palaeoclimatic studies in Kashmir.

There are five species of genus *Quercus* in the Western Himalayas: *semecarpifolia* Smith, *dilatata* Lindl, *incana* Roxb, *ilex* L., and *glauca* Thunb. In their distribution and ecological requirements, these species are very different from one another. *Quercus glauca* is subtropical; the rest belong to temperate regions. *Quercus ilex* is a typical xerophyte; other species occur in moist situations; but all the species are evergreen. *Q. incana* and *Q. semecarpifolia* may occasionally grow under xerophytic conditions but then the tree is stunted and gnarled under such conditions, which suggests that such an ecology is not normal for these two species. In their requirement for light, *Q. dilatata* is more shade tolerant; *Q. incana*, a moderate light demander; and *Q. semecarpifolia*, shade intolerant. *Q. ilex* grows on dry, stony or rocky grounds and on hot slopes. *Q. incana*, *Q. glauca*, and *Q. dilatata* grow on deep, rich, well-drained soils with a heavy rainfall and ample soil moisture; *Q. semecarpifolia* prefers a region of heavy snowfall and moderate rainfall. Moreover, they also show a distinct altitudinal zonation, as follows:

Species	Altitudinal range in m
<i>Q. glauca</i>	600-1800
<i>Q. incana</i>	600-2400
<i>Q. ilex</i>	600-2700
<i>Q. dilatata</i>	1500-2700
<i>Q. semecarpifolia</i>	2400-3600

As to distribution, *Q. ilex* is distinctly western and extends from the Punjab to the western Mediterranean and even up to the Atlantic; the other species are either eastern or north eastern, distributed from east to west along the Himalayas to China, Burma, Korea, and Japan. *Q. glauca* alone extends to Afghanistan in the west.

Preparation of Pollen Samples for SEM Studies

Pollen grains were acetolyzed by Erdtman's acetolysis method and dehydrated by means of absolute alcohol. After alcohol was decanted the centrifuge tubes, which contain pollen samples, were kept in an inverted position to remove alcohol totally. Dried pollen samples were sprinkled on a double-sided Scotch Tape, which was stuck onto metal stubs. The stubs were cleaned thoroughly with acetone before use. A coating was made with a 400A-thick gold film. Scanning electron micrographs were taken with the help of S. 4-10 Cambridge stereo-scan at various magnifications.

SEM Microphotographs of Quercus Species and Their Morphology

Erdtman has described *Quercus* pollen grain as prolate, tricolporoidate, and granular.² Under the light microscope any *Quercus* species shows the abovementioned characters, so it is very difficult to distinguish one from the other. But the ecology is different for each species as mentioned earlier in the text. And if they could be distinguished from each other then it would be very useful in fossil pollen studies when they are used as climate indicators. In this paper efforts have been made to identify them with the help of SEM

The author is at the Physical Research Laboratory, Ahmedabad 380 009, India.

studies. Two characters, ornamentation and colpi, were used as diagnostic features because these characters can be easily observed under the SEM.

Ornamentation. All five species have granular ornamentation. Some differences were noticed in their granular shape and their placement. The five species were separated into two groups according to the abovementioned characters.

The first group comprises *Quercus semecarpifolia* and *Q. dilatata* (Fig. 1). The ornamentation is characterized by amorphous grains placed together with space in between that simulates a reticulate pattern.

In the second group, comprising *Q. ilex*, *Q. incana*, and *Q. glauca*, the grains are round in shape and placed closely, with very little space in between (Fig. 2).

Vishnu-Mittre (1963) had divided these species into the abovementioned groups on the basis of the distribution curve of the polar axis. In the first group, the polar axis ranges between 25 and 29 μm ; in the second group, between 30 and 34 μm .

Colpi. If we take colpi into consideration, the five species can be separated into the three broad groups.

The first group comprises *Q. ilex* and *Q. incana*. The colpi are very long, running from pole to pole. Possibly the apcolpium is very small. The colpi are narrow, almost slit-like in structure; hence the mesocolpium is very large (ca 5 μm at the equator). The colpi ends are pointed (Fig. 3).

The second group comprises *Q. glauca* and *Q. semecarpifolia* (Figs. 4 and 5). The colpi are wide open, leaving a small mesocolpium (ca 2 μm) at the equatorial region. In *Q. glauca*, the one end of the colpi seems blunt; the other end is not very clear in the photograph. But if both the ends of the colpi are blunt and wide then this feature distinguishes *Q. glauca* from *Q. semecarpifolia*, as in the latter both ends are pointed.

The third group comprises only *Q. dilatata*, in which colpi seem to have an ora in their center, which is why they are called colpoidate. Only in this species could an ora-like structure be seen; the rest seem colpate grains. The colpi are broad in the center with tapering ends (Fig. 6).

To sum, the following diagnostic description of the individual species can be made.

1. *Q. glauca*. Prolate, colpate, granular with round granules placed closely together leaving only a little space. The colpi may be blunt-ended and wide (subtropical species).

2. *Q. ilex* and *Q. incana*. Prolate, colpate, granular. The granules are amorphous, placed jointly, leaving little space in between. The colpi are very narrow and long, running pole to pole. (Both species belong to temperate climate.)

3. *Q. dilatata*. Prolate, colpoidate, granular, granules, amorphous, placed leaving some space in between, which simulates reticulate ornamentation.

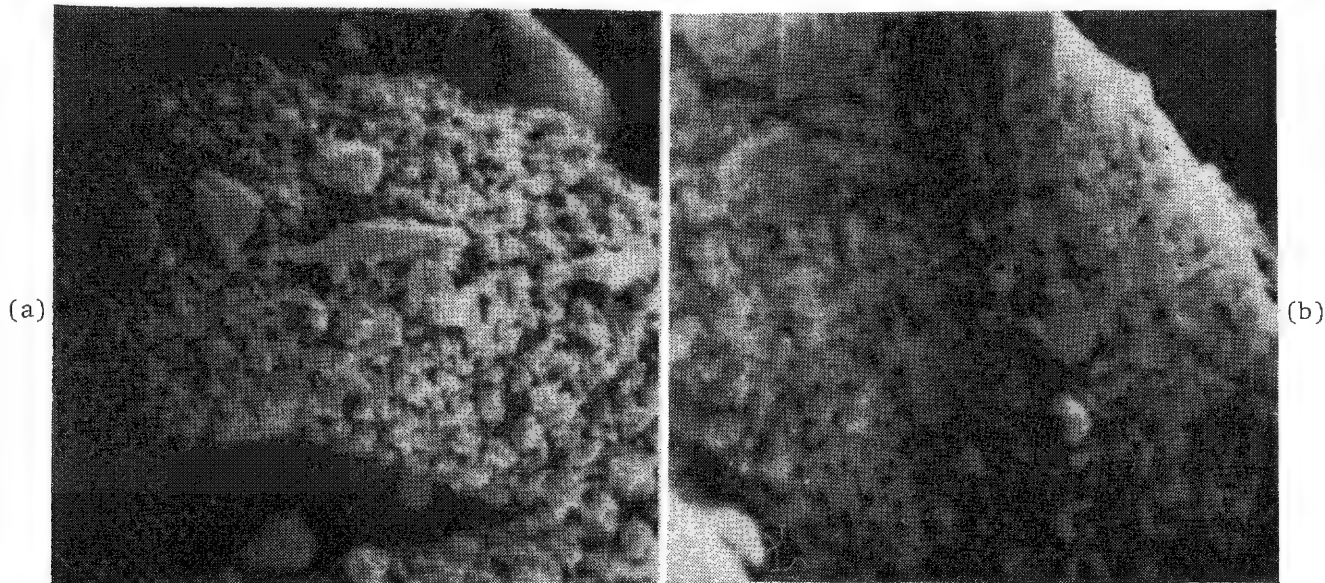


FIG. 1.--(a) *Q. semecarpifolia* and (b) *Q. dilatata* show magnified exine stratification. Granules are amorphous and comparatively thinly populated (10 000 \times).

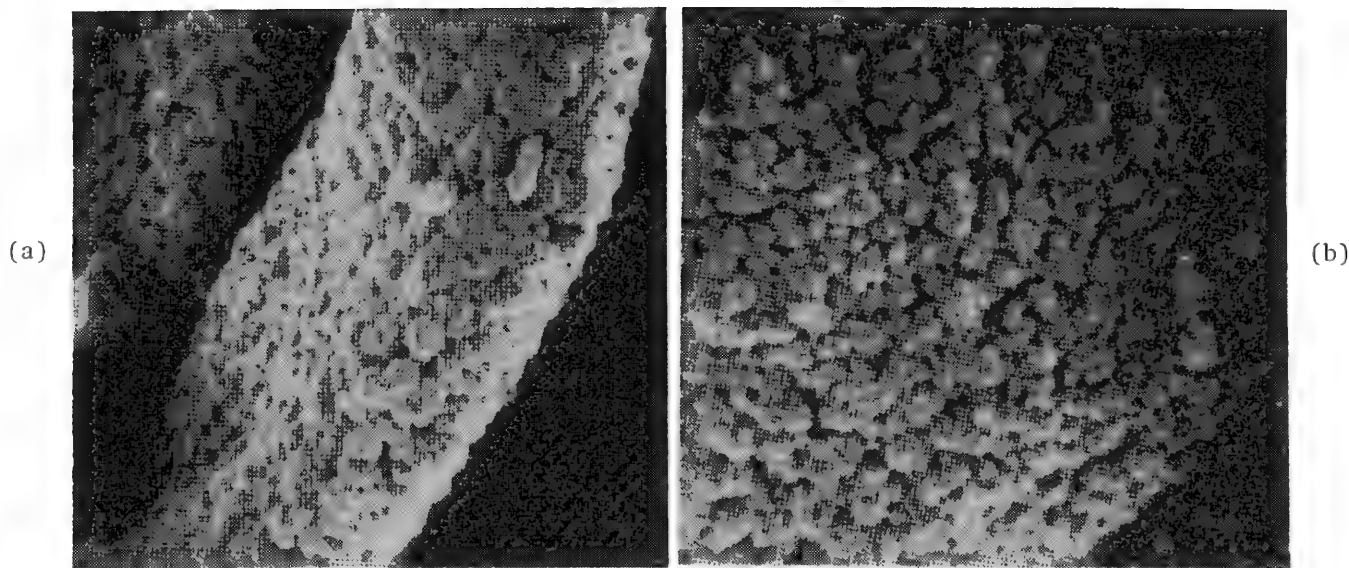


FIG. 2.--(a) *Q. incana* and (b) *Q. glauca* show magnified exine stratification. Granules are round in shape and thickly populated (10 000×).

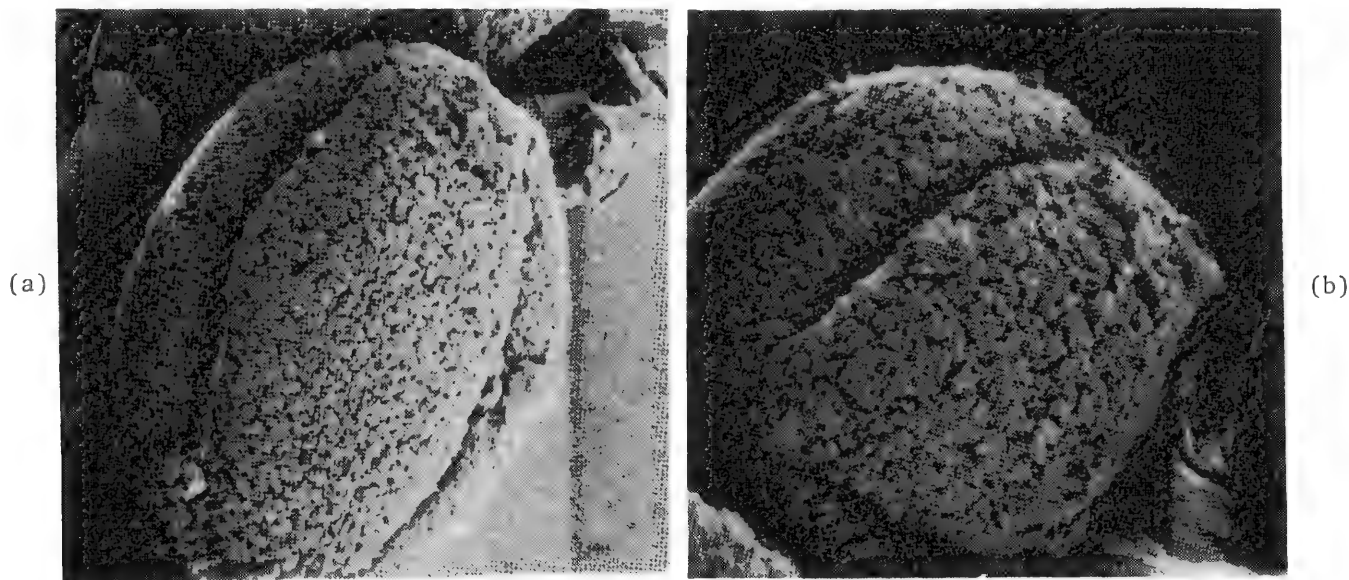


FIG. 3.--(a) *Q. ilex* (4000×) and (b) *Q. incana* (5000×) show colpi and mesocolpium. Colpi are narrow and long, with pointed ends.

4. *Q. semecarpifolia*. Prolate, colpate granular granules, amorphous placed, leaving some space in between, which simulates reticulate ornamentation. Colpi wide open, long with pointed ends.

It is important to identify *Pinus* up to species level, because the two species of *Pinus* are totally different ecologically and hence very good indicators of climate. Efforts were made to distinguish them under the light microscope as well as SEM, but satisfactory results have not been obtained so far. Further studies are going on with the help of SEM, and we hope that in the near future distinguishing features will be determined and reported.

References

1. G. Erdtman, *An Introduction to Pollen Analysis*, Waltham, Mass. 1954.
2. G. Erdtman, 1952. *Pollen Morphology and Plant Taxonomy-1. Angiosperms*, Waltham, Mass., and Stockholm, 1952.
3. V. Mittre and G. Singh, "On the pollen of the Western Himalayan oaks," *J. Indian Bot. Soc.* 42: 130-134, 1963.

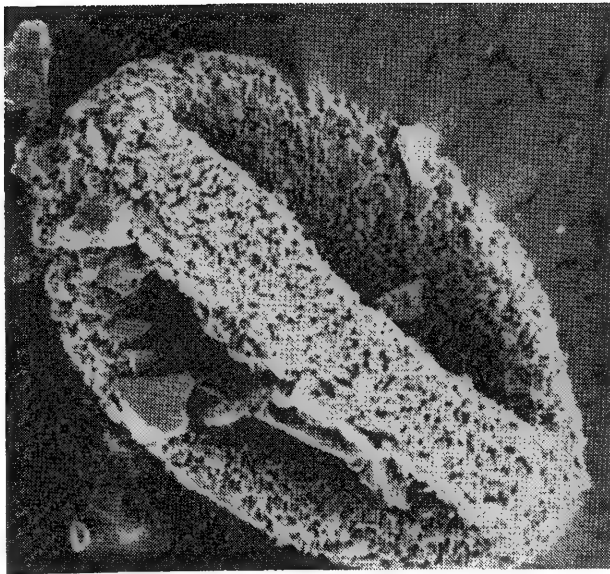


FIG. 4.--*Q. glauca* shows calpus, part of mesocolpium; upper end of calpus is wide and blunt (5000 \times).

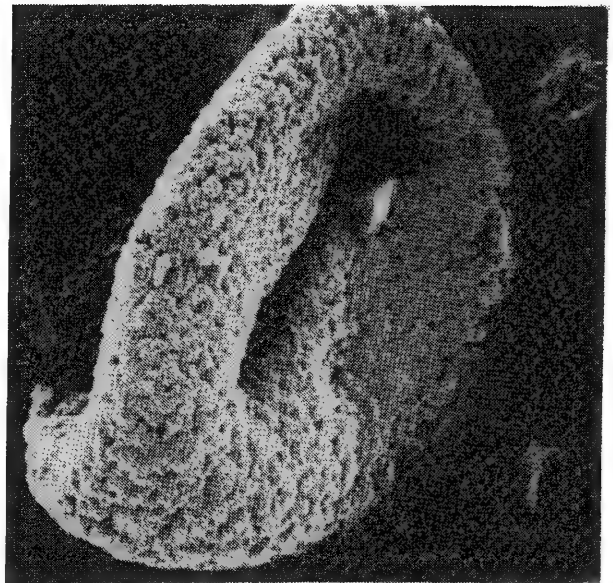


FIG. 5.--*Q. semecarpifolia* shows calpus, part of mesocolpium; calpus is wide open with pointed ends (5000 \times).

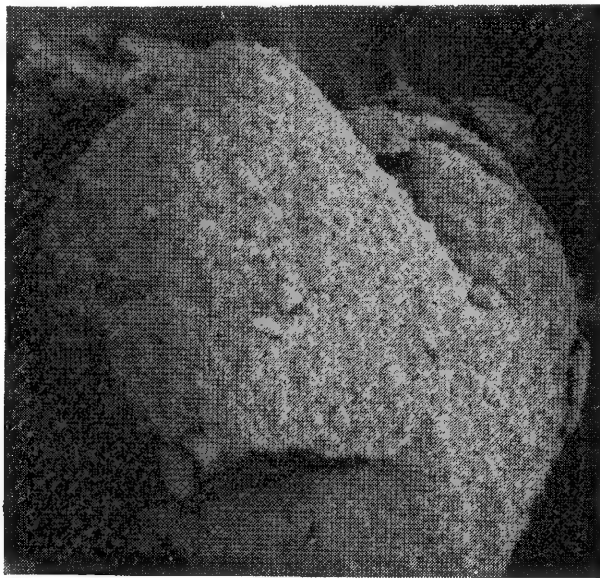


FIG. 6.--*Q. dilatata* shows calpus with ora in center (5000 \times).

RUST ANALYSIS OF THE INARIYAMA SWORD

T. Murata and M. Sasaki

In 1972 a rusted iron sword was found at Inariyama burial mound in the city of Gyoda, Saitama prefecture, 50 miles northeast of Tokyo. Five years later, 115 gold-inlayed Kanji Chinese characters were revealed on both sides of the sword under thick rust layers during corrosion protection treatment for display. This was a sensational find because it is the oldest Japanese written in the vacant period in Japanese history up through the 6th century.

The overall appearance of the front and back surfaces of the sword is shown in Fig. 1. Archaeologists and historians have clarified that the sword was specially prepared in Japan in 471 according to the Western calendar for a person who was buried in the mound during the reign of Emperor Yuryaku. At present the sword is designated as a national treasure and is being displayed at Sakitama Museum in Saitama prefecture.

Experimental and Results

Analysis of the Rust Pieces. Both structural and chemical analyses were made on a small number of compact rust pieces collected from the vicinity of the characters that read TAKAHI (Fig. 2). The largest piece, weighing 0.1 g, was chosen for analysis by CMA (computer-aided microanalyzer) and microfocused x-ray diffraction. Five other pieces were used for chemical analysis; the rest were kept for future investigation.

Composition of the Rust and Cu Condensation. The results obtained through ICP analysis are shown in Table 1, where considerably high concentration of Cu is to be noted, which suggests that the original iron ore is most likely copper-bearing magnetite, Fe_3O_4 . At that historical period, copper-bearing magnetite ores were produced only on the Asian continent, namely China or Korea, which means that the iron or steel used for the sword was possibly manufactured there and brought to Japan afterwards.

The largest rust piece was examined by CMA at its cross section. The backscattered electron image is shown in Fig. 3; a portion is enlarged in Fig. 4 where the light area corresponds to Fe_3O_4 , the dark area to α , γ - Fe_2O_3 and the curved dark line to cracks. The high concentration of Cu is shown on the backscattered electron image by numbered crosshatched areas (Fig. 5). Quantitative analysis for Cu at these areas was made: they range from 2.4 to 90% (assuming Cu to be CuO). The Cu is always concentrated in the Fe_3O_4 zone. The role of Cu in rust formation of iron and steels has not been clarified yet, but Tamura et al.¹ suggest that the Cu ion accelerates the formation of Fe_3O_4 from $\text{Fe}(\text{OH})_2$ as a catalyzer and thus tends to agglomerate to form either CuO or Cu_2O . The average Cu concentration by chemical analysis is about 0.35% and the original Cu content in the steel is estimated at around 0.2-0.3%, if one considers a compact rust layer under a very low corrosion rate: 0.001 mm/yr and a very small ratio of volume of solution to reacting surface. It is a reasonable value for Cu-bearing magnetite ore.

Carbide Remains in the Rust Layers. The close-up view of backscattered electron image of the Fe-enriched zone (Fig. 5) clearly indicates the presence of white networks similar to the pearlite structure of low-carbon steels. This observation was confirmed by micro-focused Laue pattern analysis to be Fe_3C networks. The two-dimensional distribution at grain boundaries suggests that the steel contained approximately 0.2-0.3% carbon and was cooled slowly from above 910 C, so that it was not quenched to martensite structure. The observation of carbides in ancient metallic oxides was first made by Knox² as evidence that the metal oxides were once steel.

Nonmetallic Inclusions. Analysis of nonmetallic inclusions was made with the elongated one shown in Fig. 6. It consists of glassy silicates and can be observed throughout the

The authors are with Nippon Steel Corp.

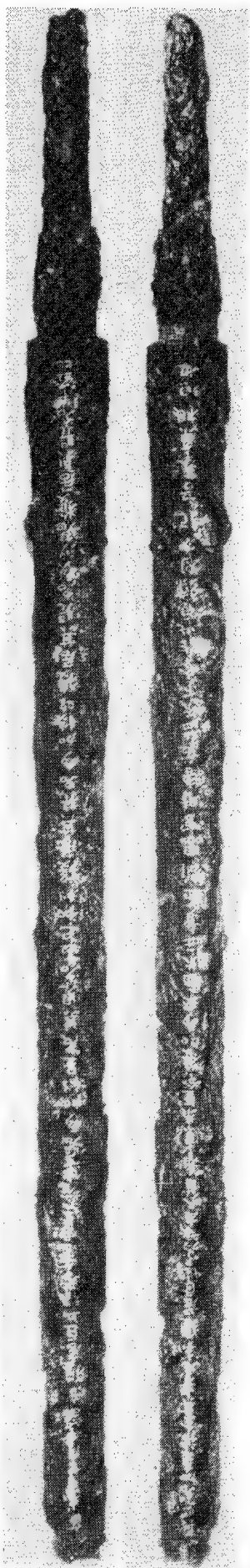


FIG. 1.--Overall appearance of Inariyama sword: back (left) and front (right) surfaces.

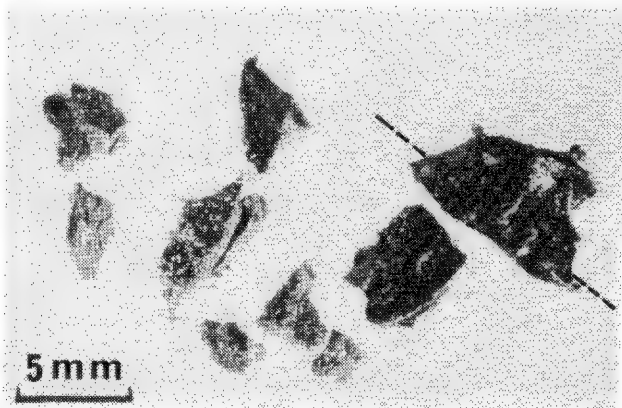


FIG. 2.--Rust pieces examined in this study.

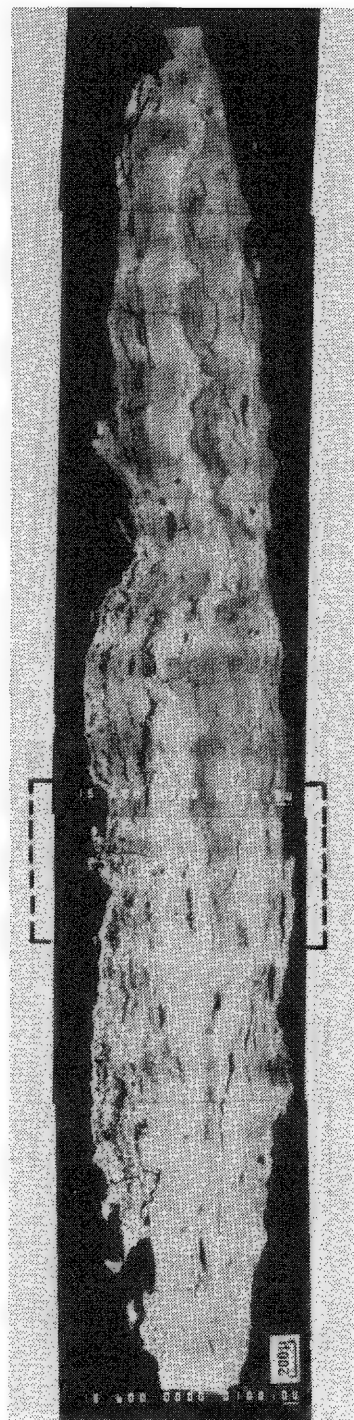


FIG. 3.--Cross-sectional view by backscattered electron image: metal side, right.

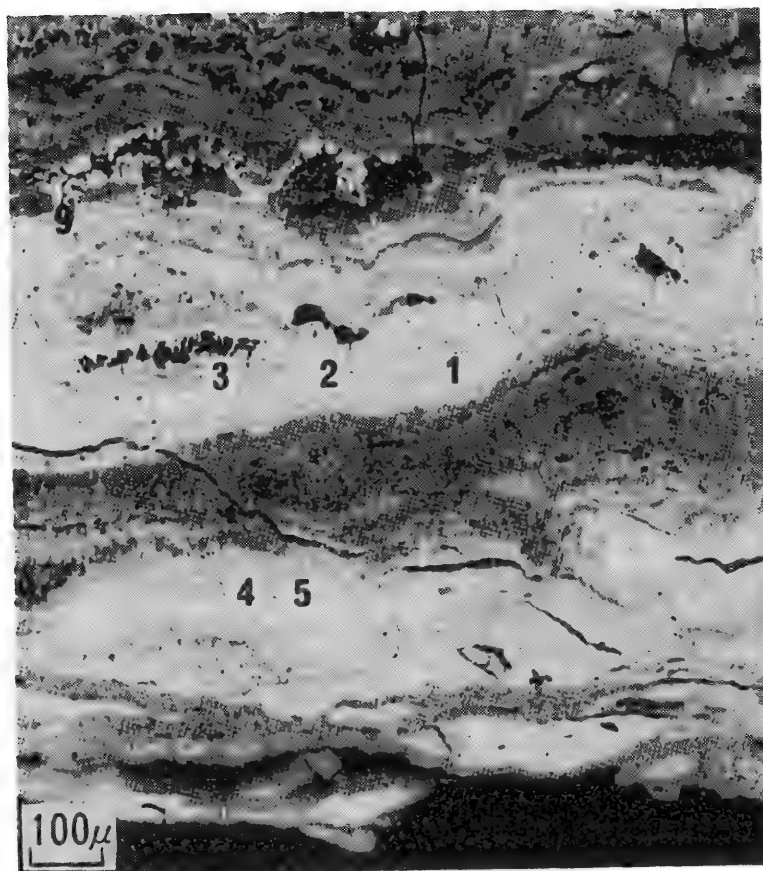


FIG. 4.--Enlarged view of Fig. 3. Numbers correspond to those in Fig. 5.

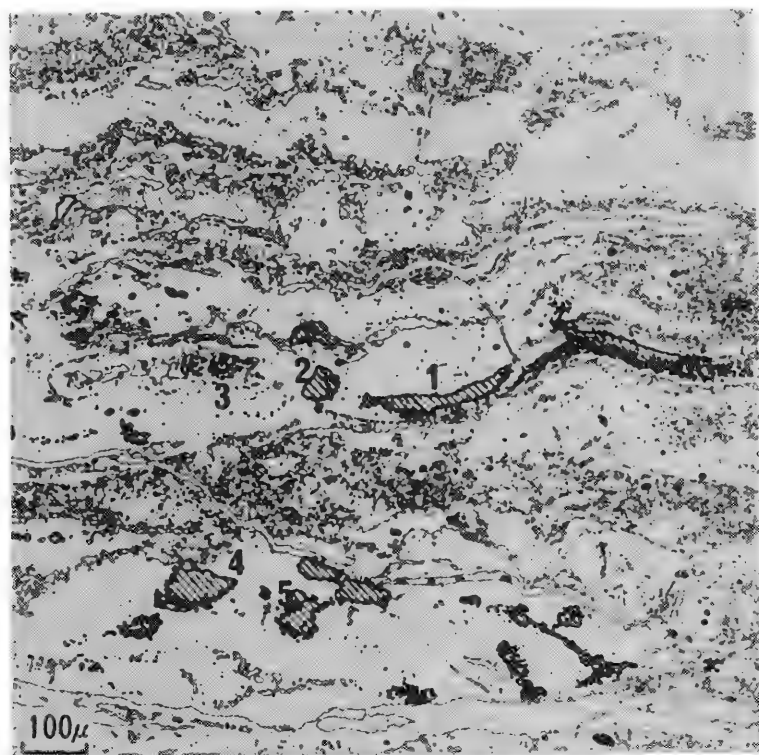


FIG. 5.--Backscattered electron image at rust cross section with superimposition of Cu-enriched zone indicated by crosshatching.

magnetite zones. Their average chemical composition is shown in Table 2.

The main phase is composed of the $\text{CaO-Al}_2\text{O}_3\text{-SiO}_2$ system and contains a lot of alkaline components, which suggests that the inclusions are slag formed during refining. In order to estimate the original flux composition, CaO , MgO , K_2O , Na_2O , Al_2O_3 , and SiO_2 were chosen as the main components; their percentages are illustrated in Table 3. They are likely to be calcinated materials of a mixture of shells, clay, and local sands. Further study is required before clear conclusions can be drawn as to the iron-making process of that period.

Summary

Through the microanalysis of compact rust pieces, the original ore, carbon content, heat treatment, hardness and approximate iron-making process could be assessed.

References

1. H. Tamura et al., *J. Colloidal Interface Sci.* 90: 133, 1980.
2. R. Knox, *Archaeometry* 6:43, 1963.

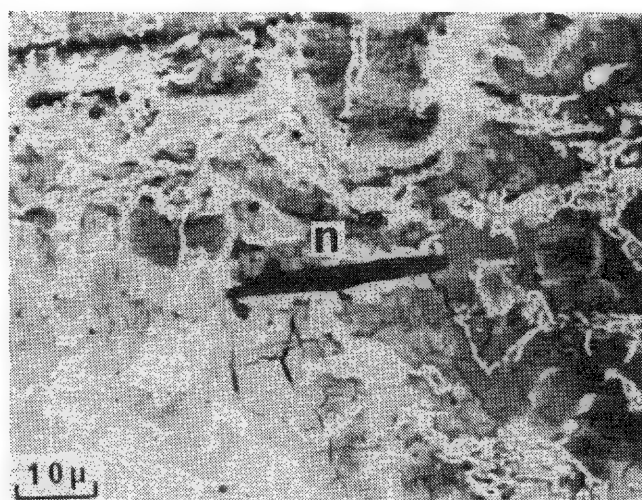


FIG. 6.--Nonmetallic inclusion (n), probably slag.

TABLE 1.--Chemical composition of compact rust pieces by ICP.

Element	Cu	Mn	Ca	Mg	Al	Ti
(%)	0.35	0.18	0.025	0.006	0.018	<0.01

TABLE 2.--Quantitative analysis of nonmetallic inclusions in compact rust layers by CMA.

Sample No.	Chemical Component (%)								
	FeO	MnO	CaO	MgO	K ₂ O	Na ₂ O	Al ₂ O ₃	TiO ₂	SiO ₂
1	19.0	2.0	12.3	2.8	2.4	2.8	7.3	0.6	38.4
2	10.8	0.9	13.8	5.1	3.8	1.7	11.2	0.6	50.4
3	2.8	1.7	20.1	2.9	2.1	1.6	8.3	1.1	58.3
4	8.9	1.3	11.7	3.3	3.0	1.9	11.7	0.7	56.2

TABLE 3.--Percentage of main components found in glassy inclusions.

Sample No.	Chemical Component (%)					
	CaO	MgO	K ₂ O	Na ₂ O	Al ₂ O ₃	SiO ₂
1	18.6	4.5	3.6	4.5	11.1	58.2
2	16.0	5.9	4.4	2.0	13.0	58.5
3	21.5	3.1	2.2	1.7	8.9	62.4
4	13.4	3.8	3.4	2.2	13.4	64.1
Average	17.4	4.3	3.4	2.6	11.6	60.8

ANALYTICAL ELECTRON MICROSCOPY OF EARLY STEEL FROM THE BACQAH VALLEY, JORDAN

K. H. Liu, H. Chan, M. R. Notis, and V. C. Pigott

The presence of a needle-like precipitate within ferrite grains of archaeological iron and steel specimens has been taken as paradigm that these precipitates are nitrides,¹⁻³ and the pickup of nitrogen is then accepted as strong evidence that the object has been heated in contact with an ammonia-bearing fuel such as animal dung. Because the solubility of nitrogen in iron is small (≈ 0.1 wt%), very few of the bulk chemical analyses presented in these studies¹⁻³ demonstrate direct chemical evidence for the presence of nitrogen.

In a recent paper on early iron from Thailand,⁵ the authors identified such needle-like precipitates as iron carbide (or *possibly* nitride) formed during quench-aging. Further investigation in the recent metallurgical literature reveals that this needle-form precipitate is indeed typical of quench-aged carbides; this finding brings into doubt the previous attributions of this precipitate form as nitrides in the archaeological literature. Direct micro-analytical study could be important in determining whether this precipitate form is due to the presence of carbides, or nitrides, as this factor ultimately bears on the interpretation given archaeological artifacts in terms of their fabrication history. We have therefore re-examined an iron object (Sample I55)⁶ from the Bacqah Valley, Jordan, which contains these needle-like precipitates and which we have previously attributed to be nitrides.

The microstructure of Sample I55 corresponds to that of a hypoeutectoid steel and is composed of pearlite, ferrite, and precipitated phase(s) of broadly varying size in the pro-eutectoid ferrite and in the ferritic component region of the pearlite (Fig. 1). The overall morphology is typical of that observed in a cast or seriously overheated condition. Most of the pearlite appears lamellar, but in some regions of the pearlite colonies, the cementite is spheroidized. The ferrite appears with variable morphology: massive ferrite (Fig. 1), network ferrite around prior austenite grain boundaries, and ferritic Widmanstätten plates, which appear to be the predominant form within the structure (Fig. 2). There are also three different categories of precipitated phase: small needles (Fig. 3), larger needles or plates (Fig. 1), and a more massive or blocky form which sometimes appears along prior grain boundaries (Fig. 4). The majority of the present study was concerned with the small needle-type precipitates in the ferrite.

Specimens were ion-thinned or electropolished and were examined in a Philips EM400T electron microscope at 100 kV. Bright-field (Fig. 5) and dark-field images, and selected area diffraction patterns typical of the small precipitates (Fig. 6) in the ferrite matrix were obtained. From the diffraction pattern, the orientation relation between ferrite and precipitate was determined to be

$$(001)_{\alpha} \parallel (125)_p \quad [010]_{\alpha} \parallel [\bar{1}3\bar{1}]_p \quad [\bar{1}00]_{\alpha} \parallel [\bar{3}\bar{1}1]_p$$

This orientation relationship does not match any of the published relationships for nitrides in ferrite, and is also different from the orientation relationship determined by Pitsch and Schrader⁷ for cementite precipitates in ferrite. Nor is the relationship consistent with that given by Pitsch⁸ for cementite and ferrite in pearlite, but it is similar in that the indices given by Pitsch for ferrite are found for the precipitate and vice versa. We are trying to resolve this apparent inconsistency at present.

Electron diffraction patterns were also obtained from the pearlite areas (Fig. 7), and the relation between cementite and ferrite in pearlite was determined as:

$$(100)_c \parallel (011)_{\alpha} \quad [010]_c \parallel [2\bar{1}1]_{\alpha} \quad [00\bar{1}]_c \parallel [11\bar{1}]_{\alpha}$$

Authors Liu, Chan and Notis are associated with the Department of Metallurgy and Materials Engineering, Lehigh University, Bethlehem, PA 18015; author Pigott is associated with MASCA, University of Pennsylvania, Philadelphia, PA 19104. The authors thank D. Calvert, J. Michael, and S. Baumann for their help in specimen preparation and in microscopy.



FIG. 1.--SEM image showing pearlite and proeutectoid ferrite with large and small needle-like precipitates.



FIG. 2.--SEM image showing Widmanstätten ferrite.

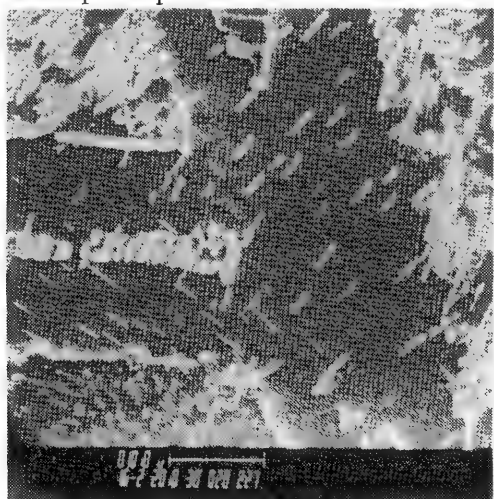


FIG. 3.--SEM image showing small needle-like precipitates in Widmanstätten ferrite and in pearlite regions.

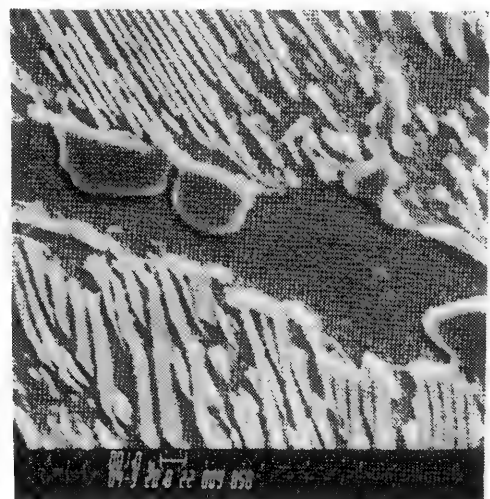


FIG. 4.--SEM image showing blocky or massive carbides.

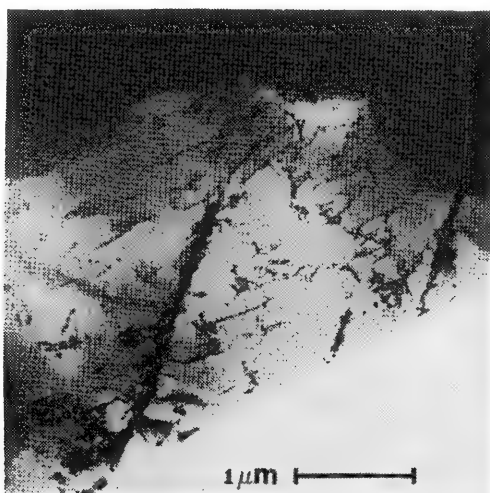


FIG. 5.--Bright-field TEM image of small needle-like precipitates in ferrite matrix.

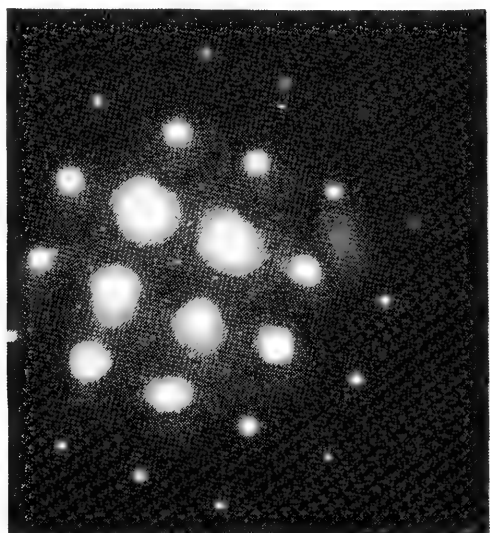


FIG. 6.--Selected area diffraction pattern of region from Fig. 5.

This present result, obtained in a hypoeutectoid steel, coincides with that given by Bagaryatskii⁸ but obtained on a hypereutectoid steel.

Electron energy loss spectra for these precipitates were obtained by means of a GATAN Electron Energy Loss Spectrometer attached to the Philips EM400T. In all, seven or eight spectra were obtained from precipitates of different sizes and shapes. The results were similar and a typical spectrum obtained from one single precipitate is shown in Fig. 8; there is a carbon loss peak in the region of 286 eV, but no evidence for the presence of nitrogen was found.

Last, and in cognizance of its insensitivity to small volume fractions of a second phase below about 1%, x-ray diffraction spectra were obtained on a Philips APD3600; all peaks proved to be from metallic iron and cementite and no evidence for the presence of nitrides was found.

Within the range of our observations--from microstructural studies, from electron diffraction study to determine crystallographic relationships, and from direct microanalytical examination using EELS--all evidence indicates the needle-like precipitates to be carbides. Based on the microstructure of the steel, it appears that during cooling from the austenitic region the specimen underwent a Widmanstätten transformation under relatively large undercooling conditions, i.e., roughly estimated to be an undercooling of about 200 C. The ferrite that formed (both proeutectoid and within the pearlite structure) is therefore supersaturated with respect to carbon. Following the Widmanstätten transformation, the carbide precipitation process intervenes not only in the Widmanstätten ferrite but also in the ferritic portion of the pearlite structure.

It therefore appears that microstructural studies alone are not sufficient to identify the precipitate and that microanalytical techniques open a new scale of examination that can be helpful in the interpretation of the fabrication history of archaeological artifacts.

References

1. J. R. Marachal, "The presence of nitrogen in ancient iron objects," *Mem. Sci. Rev. Met.* 60: 135-142, 1963.
2. H. H. Coghlan, "Etruscan and Spanish swords of iron," *Sibirium* 3: 167-174, 1956-57.
3. J. Piaskowski, "Metallographic study of ancient iron objects found in the Koszalin Region," *Slavia Antiqua* 27: 231-252, 1980.
4. A. S. Keh and W. C. Leslie, *Mat. Sci. Res.* 1: 208, 1963.
5. V. C. Pigott, A. R. Marder, W. A. Schauffler, and J. A. Penny Jr., "Prehistoric iron in Southeast Asia: New evidence from northern Thailand," in *Proc. Symp. Origins of Agriculture, Metallurgy, and the State in Mainland Southeast Asia*, New Zealand, 1983, to be published.
6. V. G. Pigott, P. E. McGovern, and M. R. Notis, "The earliest steel from Transjordan," *MASCA J.* 2[2]: 35-39, 1982.
7. W. Pitsch and A. Schrader, *Arch. für Eisenhütt.* 29: 715, 1958.
8. W. Pitsch, *Acta Met.* 10: 79, 1962.
9. Y. A. Bagaryatskii, *Doklady Akad. Nauk. SSSR* 76: 1161, 1950.

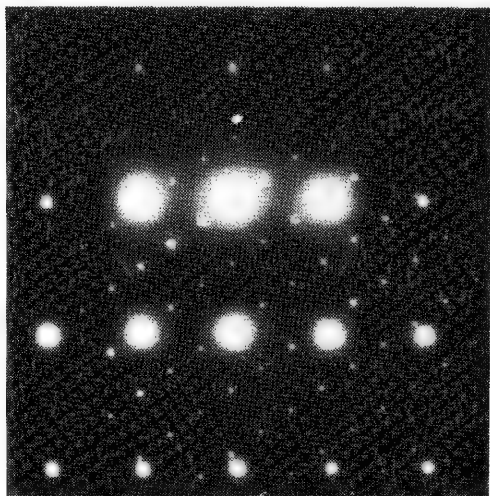


FIG. 7.--Selected area diffraction pattern free from pearlite region.

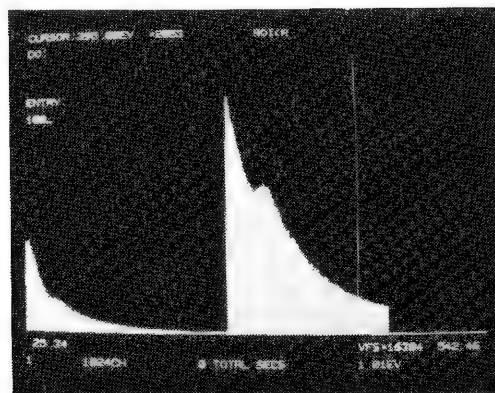


FIG. 8.--EELS spectra obtained from small needle-like precipitates.

13 Biological Applications

SYSTEMATIC RESEARCHES IN VARIOUS FUNGAL TISSUES STUDIED BY LASER MICROSCOPY

Monique Thibaut and Manuel Ansel

The recent and considerable progress in laser microscopy has been an incentive for mycologists to improve their knowledge of the fungal tissues and to perfect their diagnostic techniques in order to make the indications more precise. Recent classification of the fungi according to their morphology and biochemistry has made it possible to redefine some genera by laser microscopy and so to clarify some of the controversies regarding their taxonomy. The primary aims of this investigation, therefore, are to summarize the principles, advantages, and limitations of laser microanalysis and also to provide an understanding of these pathogenic fungi and to reevaluate the current classification.

Experimental

Following a series experiments of a study on fungal tissues, preliminary researches were done of the impact of the laser on fungi. A suitable culture medium (Sabouraud glucose infusion) is inoculated with two species of the genus *Aspergillus*: *A. variegator* Berkeley and Broome, and *A. versicolor* (Vuill.) Tiraboschi. The organisms first grow vegetatively and then fungal tissues are collected, dissected, placed in deionized water, dried, and examined with a laser microscope. This new technique requires care and attention to detail, and has given reproducible results on some 25 samples of each fungus. A microscope combined with a vertically mounted ruby laser was utilized. The laser microbeam is made coincident with the optical path of the microscope. Laser microprobe sampling for emission spectroscopy, employing photographic recording of spectral lines, was applied to elemental analysis of samples. A laser ray beam was then directed onto a definite site of the specimen. The emitted radiation resulting from excitation of atoms of the combusted tissue was analyzed by means of a spectrograph for photographing recording. The spectral composition of the emitted light permits qualitative analysis of the liberated material.

Results

Laser microscopy reveals the presence of calcium, magnesium, phosphorus, copper, boron, and potassium in *Aspergillus variegator*. In *Aspergillus versicolor* this method permits the detection of calcium, magnesium, phosphorus, silicon, iron, copper, sodium, and potassium. No other elements appeared in either species. No attempts were made to obtain quantitative estimates.

Conclusion

Further progress in many areas of mycology can be greatly facilitated by the application of laser microscopy. In our view such an approach is essential in the study of fungal tissues. It allows chemical information to be obtained from the same specimen, permits the detection of 74 elements in the periodic system, and has the advantage of not requiring large masses of tissue. It has opened a new line of research.

Authors Thibaut and Ansel are at Laboratoire de-Parasitologie et Mycologie, 15 rue de l'Ecole de Médecine, F-75270 Paris Cédex 06, France.

LOW-TEMPERATURE ASHING PRECONCENTRATION FOR ELEMENTAL LOCALIZATION IN ION MICROSCOPY

J. T. Brenna and G. H. Morrison

Ion microscopy via secondary ion mass spectrometry (SIMS) is a useful technique for the *in situ* elemental microcharacterization of biological thin sections. Among its advantages as an analytical technique are high sensitivity and the ability to discriminate isotopes of the same element. Though ion microscopy has been successfully used to localize major elemental constituents of thin sections such as Na, K, Ca, Mg, and Cl on the tissue and sub-cellular levels,¹ biologically important trace elements at their ambient levels are of sufficiently low concentration and ionization probability as to preclude imaging from intact resin-embedded thin sections.

Low-temperature oxygen plasma ashing (LTA) is a well-characterized technique used for the preconcentration of inorganic constituents from organic material. In high doses, LTA is known to remove completely organic material (C, H, O, N) while giving quantitative retention for most elements with no detectable contamination.² For resin-embedded biological thin sections mounted on smooth surfaces, LTA treatment produces ash patterns (spodograms) of high morphological integrity.³

The purpose of this study was to characterize the usefulness of LTA pretreatment for the ion microscopic localization of biologically important trace elements at their normal levels in thin tissue sections. Mouse intestine fixed with aqueous reagents served as a model system.

Experimental Procedure

Normal healthy mice were sacrificed via cervical dislocation. Samples of intestine were excised, fixed in 5% glutaraldehyde in phosphate buffer (pH 7.0-7.4) for 1 h, and post-fixed in 1% OsO₄ in buffer solution for 1 h. The specimens were then dehydrated in graded acetone solutions and embedded in Spurr resin. Sections 0.5 μ m thick were cut with glass knives onto deionized distilled water troughs and transferred to 99.999% gold-coated polished silicon wafers. Sections were ashed in a Tracerlab Model LTA-600 Low Temperature Asher at 50 W forward power and 0.2 torr residual O₂ pressure for 4 h to insure complete ashing. The ash residues were analyzed on a CAMECA IMS-3f ion microanalyzer operated with an O₂⁺ primary beam at 5.5 keV energy. Primary ion currents were varied according to the analyte of interest: major elements (e.g., Na) required 5-30 nA, trace elements required 1.0-2.0 μ A for optimal imaging.

Residues were also studied for molecular interferences at nominal masses for trace elements. High mass resolution data were recorded on photographic film and approximately quantified by microdensitometry.

Results and Discussion

Ion micrographs of ⁴⁰Ca (as ⁵⁷CaOH) and ²⁴Mg in ashed intestinal villi are shown in Figs. 1 and 2, respectively. These images of major elements were generated with a primary ion beam current of 30 nA, and illustrate good preservation of elemental morphology after ashing. Intracellular and intranuclear detail are clearly resolved. For Mg, ion micrographs of similar unashed sections require a 2 μ A primary beam to produce images which are generally of inferior quality.

Before attempting to image trace elements, high mass resolution was used to assess the extent of molecular interferences at nominal mass resolution. Our data indicate that

The authors are with the Department of Chemistry, Baker Laboratory, Cornell University, Ithaca, NY 14850. This work was supported by National Institutes of Health and National Science Foundation.

significant interferences occur with most trace elements, with the exceptions of ^{27}Al , ^{63}Cu , and ^{65}Cu . High mass resolution might be used to overcome unwanted peaks; however, the concomitant decrease in intensity for these elements rules out imaging.

Figures 3 and 4 are ion micrographs of ^{27}Al and ^{65}Cu , respectively, in ashed intestine sections. Villi and intestinal glands are clearly discernible. In addition, no emission is observed from the intestinal lumen in Fig. 4, a condition that might exist if the copper was present in the intestine due to contamination during fixation and embedding.

To estimate the elemental intensity enhancement from LTA, pure Spurr resin was doped with calcium and 0.5 μm -thick sections were examined by SIMS before and after ashing. The calcium signal from ashed sections was found to be over 50 times in excess of that obtained from unashed sections under identical analytical conditions. This intensity enhancement for calcium may be expected to be close to the lower limit for intensity enhancement for positive ions, since calcium has a relatively low ionization potential and it is known that oxygen saturation has a more profound effect on relative ion yields for elements of higher ionization potential.⁴

From this information it is clear that application of LTA pretreatment expands the range of ion microscopy for the localization of elements in biological thin sections. This method allows imaging of elemental species that would otherwise be unimagable by SIMS.

References

1. A. R. Spurr, "Applications of SIMS in biology and medicine," *Scanning* 3: 97-109, 1980.
2. G. J. Lutz, J. S. Stemple, and H. L. Rook, "Evaluation by activation analysis of elemental retention in biological samples after low temperature ashing," *J. Radioanal. Chem.* 39: 277-283, 1977.
3. W. Hohman and H. Schraer, "Low temperature ultramicroincineration of thin-sectioned tissue," *J. Cell Biol.* 55: 328-354, 1972.
4. A. A. Galuska and G. H. Morrison, "Oxide bond energies for the calibration of matrix in secondary ion mass spectroscopy," submitted to *Int. J. Mass Spec. Ion Processes*, 1984.

FIG. 1



FIG. 2

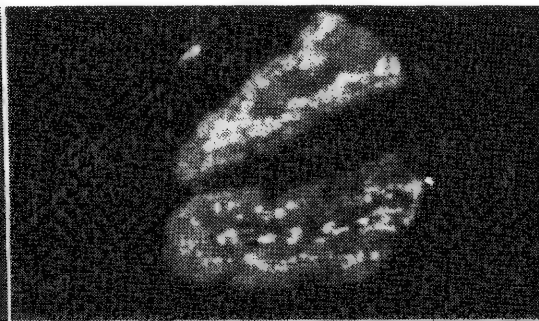


FIG. 3



FIG. 4

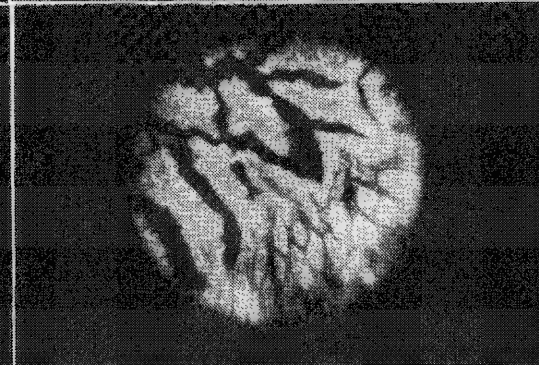


FIG. 1.--Ion micrograph of $^{57}\text{CaOH}$ in ashed mouse intestine, 30nA primary beam current. Villus border, muscle, nuclei, and intranuclear detail clearly discernible, which indicates good preservation of elemental morphology. Field of view, 150 μm . FIG. 2.--Ion micrograph of ^{24}Mg under same conditions. Muscle and nuclei again resolved, but distribution different from that in Fig. 1. FIG. 3.--Ion micrograph of ^{27}Al in mouse intestine, 2 μA primary beam current. Intestinal glands and villi are resolved. Field of view, 400 μm . FIG. 4.--Ion micrograph of ^{65}Cu under same conditions. Intestinal glands, villi, and muscle are resolved.

WATER CONTENT DETERMINED FROM ANALYSIS OF FREEZE-DRIED THIN SECTIONS

R. R. Warner, M. C. Myers, and D. A. Taylor

Water content is an important parameter in many biological analyses. Local water content has often been determined in microprobe studies by the Rick technique applied to freeze-dried thin sections.¹ Two previously unrecognized assumptions of the Rick technique limit its general application for water analysis. An equation has been derived that removes these two restrictions of the Rick technique.

In a microprobe analysis of biological tissue, the determination of local water content is important in two respects. First, the concentration of an element expressed in units per liter of water is directly related to the force governing the element's diffusion, which thus provides information regarding the expected direction of element movement. Second, in some tissues the distribution of water is itself the major focus of investigation. For example, dry chapped skin is thought to result from inadequate water in the upper cellular layers;² consequently, methods for measuring the water content of skin have received increasing attention.³ Of existing methodology, the electron microprobe offers unique opportunities for absolute quantitation of water in any tissue combined with precise analytical spatial resolution.

Two microprobe analytical procedures, those of Hall⁴ and Rick,¹ are available for measuring water in biological thin sections. Both procedures are based on the measurement of mass, which is determined from the continuum intensity.⁵

The Hall technique provides a direct measurement of local water content. Regions of a sample are analyzed first in the frozen-hydrated state and then again after freeze-drying. The difference in mass between these two sample states represents the water content of that region.³ A disadvantage of the Hall technique is the requirement for analysis in the frozen-hydrated state; few laboratories have this technology.

The Rick technique does not require frozen-hydrated tissue analysis; the water content is determined solely from analysis of freeze-dried tissue. With this technique, a standard of known dry mass (known water content) is applied to the tissue prior to freezing. Following cryosectioning, the peripheral standard is presumed to have the same thickness as the sample. After freeze-drying, local differences in mass reflect differences in water content. By reference to the peripheral standard, quantitative differences in dry mass (water content) can be determined. Previously this was done using the equation^{4,6,7}

$$F_d = (C_d/C_d')F_d'$$

where d = dry mass, $'$ = standard, C = continuum intensity, F = dry-mass fraction $M_d/(M_d + M_w)$, M = mass, and w = water.

In addition to the requirement that the specimen and standard are of equal thickness, the Rick technique assumes that specimen and standard undergo equal shrinkage during freeze-drying and equal mass-loss during analysis.¹ These may be reasonable assumptions, but there are two previously unrecognized requirements of the Rick technique that severely limit its application for water (or dry mass) analysis. It can be shown that the Rick technique requires the freeze-dried sample and standard to have the same average composition (average Z^2/A , where Z = atomic number, A = atomic weight). Furthermore, the technique requires the density of the frozen-hydrated standard to be the same as that of the frozen-hydrated sample (Hall, personal communication). This latter assumption will not be true for all samples, and in particular will not be true for the analysis of skin where density variations would be expected within the frozen-hydrated skin sample.

The authors are at Miami Valley Laboratories, Procter and Gamble Co., Cincinnati, OH 45247.

An equation that removes these latter two restrictions of the Rick technique has been derived and is shown below:

$$1/F_d = C_d'G/C_dG'[(1/F_d') - (\rho_d' - \rho_w)/\rho_d'] + (\rho_d - \rho_w)/\rho_d$$

where $G = Z^2/A$ and ρ = density. This equation does require knowledge of the density ρ_d of the freeze-dried organic material of the sample. For some tissues like skin, this parameter is well known,^{8,9,10} and water content can be accurately determined from analysis of freeze-dried tissue.

References

1. R. Rick et al., "Quantitative determinations of cellular electrolyte concentrations in thin freeze-dried cryosections using energy-dispersive x-ray microanalysis," *ibid.*, 517-534.
2. I. H. Blank, "Factors which influence the water content of the stratum corneum," *J. Invest. Dermatol.* 18: 433-440, 1952.
3. A. Triebkorn, M. Gloor, and F. Greiner, "Comparative investigations on the water content of the stratum corneum using different methods of measurement," *Dermatologica* 167: 64-69, 1983.
4. T. A. Hall, "Problems of the continuum-normalization method for the quantitative analysis of sections of soft tissue," in Lechene and Warner, Eds., *Microbeam Analysis in Biology*, New York: Academic Press, 185-208, 1979.
5. T. Hall, "The microprobe assay of chemical elements," in G. Oster, Ed., *Physical Techniques in Biological Research*, New York: Academic Press, 2d ed., vol. 1A, 157-275, 1971.
6. R. Rick et al., "Electron microprobe analysis of the different epithelial cells of toad urinary bladder," *J. Membrane Biol.* 39: 257-271, 1978.
7. J. Mason et al., "Intracellular electrolyte composition following renal ischemia," *Kidney Int.* 20: 61-70, 1981.
8. R. L. Anderson and J. M. Cassidy, "Variations in physical dimensions and chemical composition of human stratum corneum," *J. Invest. Dermatol.* 61: 30-32, 1973.
9. R. J. Scheuplein, *Molecular Structure and Diffusional Processes Across Intact Epidermis*, AD Report 822 655, 1966.
10. C. R. Robbins, *Chemical and Physical Behavior of Human Hair*, New York: Van Nostrand Rheinhold, 1979.

X-RAY MICROANALYSIS IN THE STUDY OF HEAVY-METAL UPTAKE BY FISH CALCIFIED TISSUES

G. R. Sauer and N. Watabe

The scales of teleost fish are dynamic structures whose chemical composition has been shown to reflect that of the aqueous environment.¹⁻³ Previous studies have demonstrated the usefulness of x-ray microanalysis (XMA) in the determination of the chemical composition of fish scales.²⁻⁷ On the surface of the osseous layer of fish scales is a series of concentric ridges called circuli. As a scale grows laterally, the circuli form sequentially such that those circuli located near the scale margin are younger than the circuli located centrally near the scale focus.⁸ Since the relative age of different circuli can be estimated, the use of XMA to determine the elemental composition of each circulus may provide a record of fluctuations in the environmental metal concentrations.

Experimental

Young adult male *Fundulus heteroclitus* were divided into four experimental groups and placed in small plastic aquaria containing artificial seawater. To three of the aquaria, zinc was added in concentrations of 0.1, 1.0, or 10.0 mg/l. The fourth aquarium served as a control. Temperature, salinity, and photoperiod were kept constant and the fish were fed daily.

After 8 weeks under experimental conditions, scales were removed from just above the anterior lateral line with a forceps, rinsed for several minutes in deionized water, freeze-dried embedded in Embed 812 plastic resin, and cut in cross section. The specimen blocks were polished with a diamond bit, mounted on pure carbon stubs, and coated with a thin layer of aluminum in a vacuum evaporator. Details concerning the experimental treatment of fish and specimen preparation have been described previously.²

Specimens were examined with a JEOL JSM-U3 scanning electron microscope (SEM) equipped with an EDAX PV-9100 XMA system. XMA was performed by placing the beam spot at the base of each circulus cross section visible in the scale, which insured that the region analyzed was completely surrounded by calcified tissue. Analytical conditions were: accelerating voltage, 25kV; tilt angle, 0°; take-off angle, 44.8°; magnification, 3000×; spot size, 30 μm; beam current, 1×10^{-11} A; count rate, 600-900; counting time, 300 or 600 L s. These conditions were found to produce very little specimen damage and gave highly repeatable results (coefficient of variation $\leq 2\%$).

Figure 1(a) shows a typical spectrum generated by analysis of a centrally located scale circulus. The major peaks present were calcium and phosphorus due to the hydroxyapatite mineral. Sulfur and potassium were often present in much lower concentrations. In the 1.0 and 10.0 mg/l Zn treatments, Zn peaks were present in the spectra of circuli located near the scale margin (Fig. 1b); Zn peaks could not be distinguished above the background in the control and 0.1 mg/l Zn treatments. The chlorine and aluminum peaks were due entirely to the preparative procedures.

Each spectrum generated was analyzed with an EDAX SW9100 program for background subtraction, peak area integration, and ZAF correction. The weight percentages determined for Zn and Ca were expressed as a Zn/Ca ratio (Fig. 2). A high Zn content of circuli near the scale margin was indicated by a high Zn/Ca ratio. A drop from high to low Zn/Ca ratios occurred over a span of 2-4 circuli. An average of 8 high Zn/Ca circuli preceded the decrease in the Zn/Ca ratio. These observations were consistent in all scales analyzed from the 1.0 and 10.0 mg/l Zn treatments. The difference between the high Zn/Ca and low Zn/Ca regions of the scales was always significant as determined by the Wilcoxon Rank Sum Test ($p < 0.01$).⁹ In the high-Zn/Ca region, the scales from the 10.0 mg/l Zn treatment generally showed higher values than the scales from the 1.0 mg/l treatment, but this difference was not significant ($p > 0.01$).

The authors are at the Marine Science Program, Belle W. Baruch Institute for Marine Biology and Coastal Research, and Electron Microscopy Center, University of South Carolina, Columbia, SC 29208. (Contribution No. 539, Belle W. Baruch Institute for Marine Biology and Coastal Research.)

Discussion

XMA was first applied to the elemental analysis of fish scales by Van Coillie and co-workers.³⁻⁵ These workers observed that the concentration of some elements present in the scales, particularly the heavy metals, was related to environmental concentrations. Atomic absorption spectroscopy (AAS) of fish scales has produced similar results.^{1,2} The advantage of using XMA in this type of study is that the elemental composition of each circulus can be determined separately. Since the chemical composition of each circulus reflects that of the aqueous environment at the time the circulus formed, and the relative age of each circulus can be determined, the scales can serve as a record of temporal fluctuations in environmental metal concentrations. This type of information is not available from AAS, since a relatively large number of whole scales must be ashed before metal determinations can be made.

XMA of scale surfaces has proved to be valuable in the identification of various fish populations.^{6,7} In the present study, we have demonstrated that fluctuations in environmental conditions can be detected by XMA analysis of the elemental composition of individual scale circuli. This technique has a number of potentially very useful applications, such as the detection of changes in pollutant levels, determination of scale growth rates for aging studies, and investigations of migration patterns between different environments. In addition, the technique can be used to study the effects of heavy metals on the basic mechanisms of biomineralization. For example, we have observed that the uptake of Zn by fish scales is accompanied by a decrease in the Ca/P molar ratio.²

The principal problems in XMA of bulk biological material are that the majority of the x rays generated by the electron beam arise from below the specimen surface and that the excitation electrons are dispersed laterally in the sample. These specimen-beam interactions have two major consequences: (1) structures visible at the surface are not necessarily those that are analyzed and (2) the spatial resolution is not adequate for many biological problems.¹⁰ On the other hand, bulk specimens are advantageous because elements present in very low concentrations are easier to detect, background radiation is reduced, and the readily available ZAF correction programs can be utilized. Although it has been suggested that ZAF procedures not be used for many biological materials, they are applicable to mineralized hard tissues.¹¹

We have determined using standard formulas^{10,11} that the maximum excitation volume in our samples can be described by a cylinder with diameter 45 μm and depth 15 μm . This diameter is well within the dimensions of a scale circulus cross section and the orientation of the specimen with respect to the electron beam insures that all x rays generated below the surface arise from calcified tissue. The use of polished scale cross sections eliminates the errors produced by irregular surface topography¹² that have affected other XMA studies of fish scales.³⁻⁷ Expressing the data as elemental ratios rather than absolute concentrations eliminates the need for standards (frequently troublesome in biological XMA¹¹) and reduces much of the variability inherent in biological systems.¹³

For the reasons listed above, we feel that the method outlined here is appropriate for studies involving the elemental composition of fish scales. Although we have been concerned primarily with fish scales in our laboratory, the techniques presented here could be easily applied to the study of other calcified tissues such as bone or otoliths.

References

1. M. I. Abdullah et al., "Environmental dependence of manganese and zinc in the scales of Atlantic salmon, *Salmo salar* (L.) and brown trout, *Salmo trutta* (L.)," *Freshwater Biol.* 6: 161-166, 1976.
2. G. R. Sauer and N. Watabe, "Zinc uptake and its effect on calcification in the scales of the mummichog, *Fundulus heteroclitus*," *Aquatic Toxicol.* 4, 1984 (in press).
3. R. Van Coillie et al., "Use of scanning x-ray microanalysis in the study of environmental problems in fishes," *SEM/1976 VIII*, 597-603.
4. R. Van Coillie et al., "Microanalyse de l'incorporation d'un metal lourd dans les écailles d'un poisson," in *International Conference on Transport of Persistent Chemicals in Aquatic Environments*, Ottawa: National Research Council of Canada, Pt. 2, 41-45, 1974.
5. R. Van Coillie and A. Rousseau, "Composition minérale des écailles du *Catostomus commersoni* issu de deux milieux différents: Etude par microscopie électronique analytique," *J. Fish. Res. Board Can.* 31: 63-66, 19.
6. L. A. Lapi and T. J. Mulligan, "Salmon population identification using energy dispersive x-ray microanalysis," *SEM/1976 VIII*, 591-596.

7. L. A. Lapi and T. J. Mulligan, "Salmon stock identification using a microanalytic technique to measure elements present in the freshwater growth region of scales," *Can. J. Fish. Aquat. Sci.* 38: 744-751, 1981.
8. J. Yamada and N. Watabe, "Studies on fish scale formation and resorption: I. Fine structure and calcification of the scales of *Fundulus heteroclitus* (Atheriniformes: Cyprinodontidae)," *J. Morphol.* 159: 49-66, 1979.
9. M. Hollander and D. A. Wolfe, *Nonparametric Statistical Methods*, New York: Wiley, 1973.
10. J. A. Chandler, "Principles of x-ray microanalysis in biology," *SEM/1979 II*, 595-606.
11. N. C. Barbi, "Quantitative methods in biological x-ray microanalysis," *SEM/1979 II*, 659-672.
12. J. I. Goldstein et al., *Scanning Electron Microscopy and X-ray Microanalysis: A Text for Biologists, Materials Scientists, and Geologists*, New York: Plenum Press, 1981.
13. K. Simkiss and M. Taylor, "Cellular mechanisms of metal ion detoxification and some new indices of pollution," *Aquatic Toxicol.* 1: 279-290, 1981.

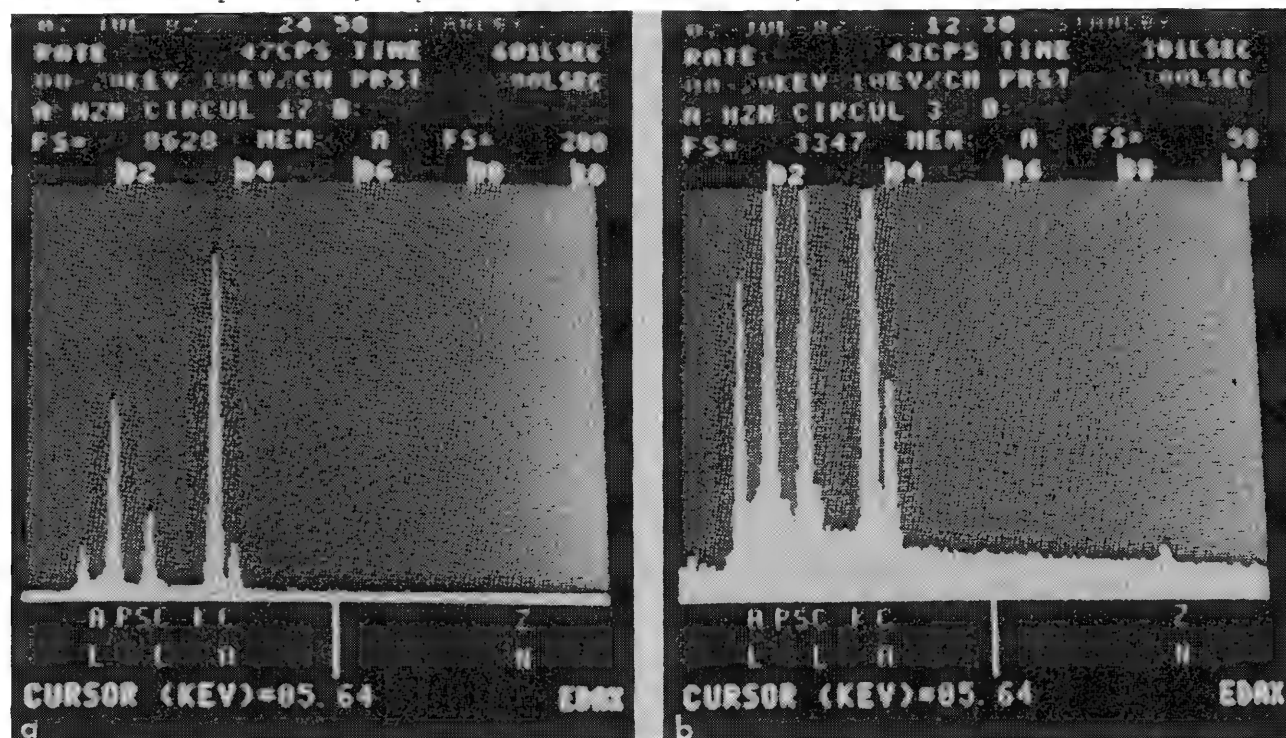


FIG. 1.--Representative x-ray spectra generated by circuli from different regions of one scale: (a) near scale focus, (b) near scale margin (vertical axis expanded); 10.0mg/1 Zn treatment.

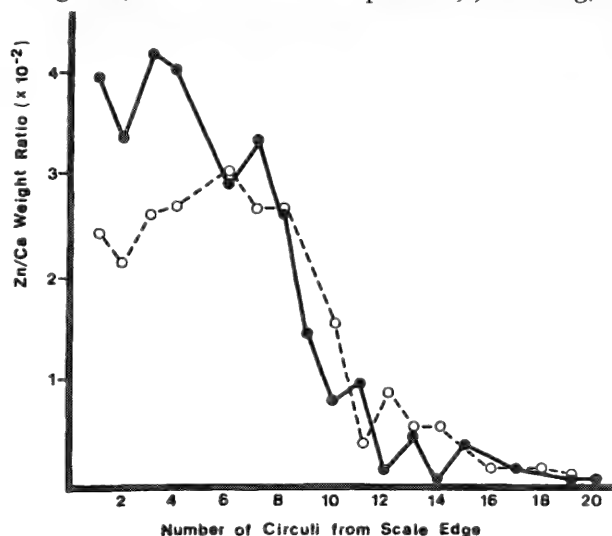


FIG. 2.--Relationship between Zn/Ca weight ratio and circulus position in scale from 10 mg/1 Zn treatment (closed circles) and 1 mg/1 Zn treatment (open circles) after 8 weeks. Each point represents mean of two determinations.

ACCURACY AND PRECISION OF BIOLOGICAL X-RAY MICROANALYSIS: CARDIAC MUSCLE

J. McD. Tormey

Despite continuing advances, uncertainty remains regarding the accuracy and precision of electron-probe microanalysis as applied to diffusible elements in biological samples. This paper presents recent experience with cardiac muscle, and demonstrates that this technique is capable of routinely producing data that are highly reliable.

The samples used in this study were 150 nm thick, freeze-dried, frozen sections. They were probed at ambient temperatures with 100kV electrons, and were analyzed by energy-dispersive x-ray spectroscopy (EDS). The basic analytical approaches were similar to those described by Hall,¹ Schamber,² and Shuman and Somlyo.³ We employed refinements in preparative technique, and an approach to minimizing the errors in Ca measurement that result from the overlap between K and Ca peaks in EDS spectra. We described these technical improvements last year.⁴

Our data show: (1) The analysis of Ca in the 1 mmole/kg dry wt range is both accurate and insensitive to orders of magnitude higher K concentrations. (2) The analyses of all elements, with the possible exception of S, are statistically tight and fall within the range of values expected from the results of other methods. (3) Analysis of variance demonstrates that most of the observed variances can be explained by either counting statistics or biological variation.

Results

Figure 1 illustrates a series of measurements made on freeze-dried frozen section standards that contained low Ca concentrations along with K concentrations ranging from 0 to 1800 mmole/kg dry wt. The K,Ca EDS overlap was deconvoluted as described previously.⁴ The regression line fit to the mean values obtained by microprobe analysis not only is very close to expected but has a correlation coefficient of 0.9997. However, the more impressive aspect of these data is their precision. The statistical precision predicted for each point by least-squares fitting statistics² ranged from ± 1.2 to 1.6 mmole/kg dry wt, and the observed standard deviations (indicated by the error bars) ranged from ± 1.6 to 2.2. We conclude that the presence of overlapping K peaks need cause no significant deterioration of the analytical precision of Ca measurements.

The remainder of the data was obtained from freeze-dried frozen sections of papillary muscles from rabbit hearts.

The data in Table 1 are typical of the microbeam analyses we obtain from such tissue samples. The results are given both in their original units (mmole/kg dry wt) and in recalculated units (mmole/liter H₂O); the latter units are useful because they are the ones most commonly used in the relevant biological literature. The statistical variations are relatively small. Aside from that, the most important aspect of these data is how closely they agree with measurements of the same parameters obtained by use of alternative analytical techniques.

Further evidence of the reliability of our data is provided by Fig. 2, which shows the effect of adding the glycoside ouabain to cardiac muscle. Each of the ouabain-treated muscles was frozen within 2 min of developing total ouabain contracture. The measurements are all from cytosol, which is defined here as any rectangular area of cytoplasm larger

The author is at the Department of Physiology, Center for Health Sciences, UCLA, Los Angeles, CA 90024. The collaboration of JoAnn Hill and Lyle G. Walsh is gratefully acknowledged. This work has been supported in part by Grant R01 HL 31249 from the National Heart, Lung, and Blood Institute and by grants from the American Heart Association Greater Los Angeles Affiliate and the Muscular Dystrophy Association.

TABLE 1.--Intracellular concentration measured in 6l cells from six control cardiac muscle preparations. (Deviations are standard errors of means; aqueous concentrations are calculated on basis of intracellular water content of 77% of wet weight.)

Units	Na	Mg	P	S	Cl	K	Ca
mmoles/kg dry wt	59.6 ±2.9	50.9 ±1.1	475.4 ±4.9	158.4 ±5.5	102.4 ±3.7	496.5 ±8.0	1.1 ±0.3
mmoles/liter H ₂ O	17.8 ±0.9	15.2 ±0.3	142.0 ±1.5	47.3 ±1.6	30.6 ±1.1	148.3 ±2.4	0.3 ±0.04

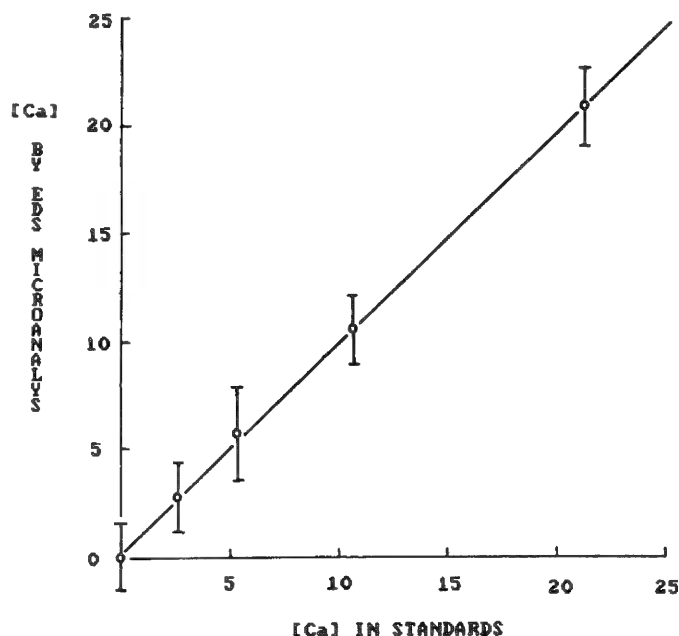


FIG. 1.--Ca measured by electron-probe analysis of thin section standards plotted against known composition. Standards also included K at concentrations up to 1800 mmole/kg dry weight. Despite massive overlapping from K x rays in energy-dispersive spectra, observed variances are not significantly greater than those predicted by fitting or counting statistics. Regression line is $Y = 0.975X + 0.202$. Error bars indicate standard deviations of individual measurements. Number of measurements at each point, 30-42; each point represents at least 6 samples measured on at least 6 different occasions.

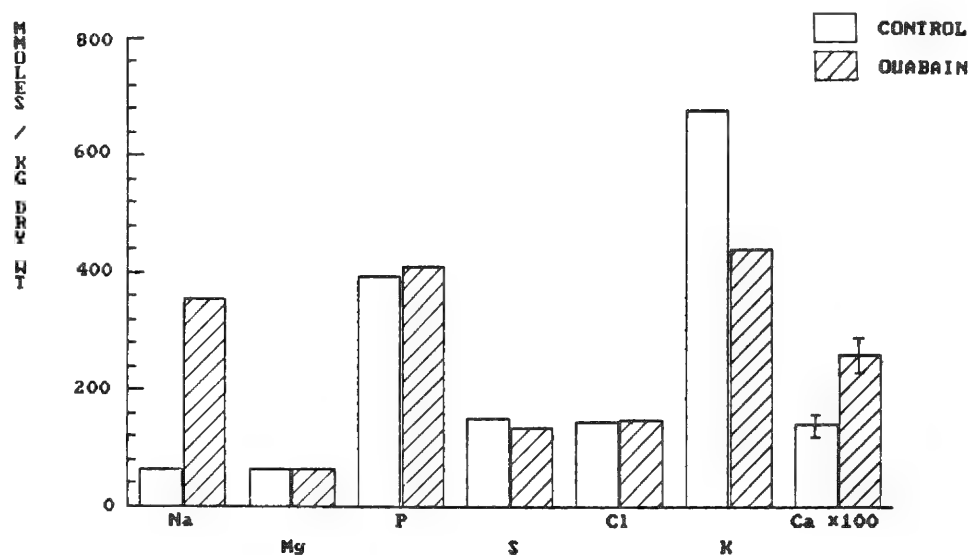


FIG. 2.--Effect of ouabain-induced contracture on elemental composition of cardiac cytosol as measured by electron-probe microanalysis of ultrathin freeze-dried frozen sections; 250 measurements were evenly divided between 6 control and 6 ouabain-treated muscles. Standard errors ranged from 0.2 to 10.9 mmoles/kg dry weight. Scale does not permit depiction of such small errors, except for Ca, which has been scaled up by two orders of magnitude; t tests confirm that only Na, K, and Ca change significantly as result of treatment.

than $10 \mu\text{m}^2$ that lies within a single cell and contains no mitochondria. The statistical scatter of the data is once again quite small. The only significant changes in concentration are those of Na, K, and Ca, and these results agree quantitatively with the results of other methods. Especially noteworthy is the ability to obtain measure a statistically significant change in [Ca] that is only 1 mmole/kg dry wt; the ability to do this by EDS in a biological sample would have seemed unlikely before now.

Multilevel analyses of variance were carried out, and Fig. 3 illustrates the results with the control cytosol data from Fig. 2. The statistical techniques employed are classic,^{5,6} though somewhat arcane. Their rationale and significance in terms of this investigation are elaborated in the next section.

Discussion

Widespread acceptance of microbeam analysis as a tool for biological research requires convincing demonstration that the technique is quantitatively reliable. The first step is a demonstration of accuracy. The exact intracellular composition of tissues such as cardiac muscle is not well known, so that there can be no absolute criteria of accuracy. All that can be done is to show that the results of microanalysis are in reasonable agreement with the range of available data generated by other techniques. Even though these other techniques may be inherently less reliable, they carry the unrefutable advantage of having been accepted before the advent of quantitative biological microbeam analysis.

The analysis of Na is a case in point. The x-ray microanalytical value of 17.8 mM (mmoles/liter H_2O) is lower (both as an absolute concentration and in relation to K concentration) than usually reported for wet chemical analyses of cardiac muscle, e.g., Lee and Fozzard's intracellular [Na] of 33 mM.⁷ Such discrepancies are not surprising, because most of the Na in biological tissues is extracellular, so that wet chemical analysis requires a very accurate estimate of the relative volume of extracellular space. The needed accuracy is hard to achieve given the vagaries of the extracellular tracers available to biologists. Our figure, when multiplied by the accepted value of the cytoplasmic activity coefficient for Na (0.3), is in even better agreement with intracellular ion selective microelectrode measurements. Also, the increase in cytosolic and whole cell [Na] that we measure after development of full ouabain contracture is extremely close to reports in the literature involving both ion selective electrodes and chemical measurements.^{8,9} We conclude that our microprobe measurements of intracellular Na are at least as accurate as those obtainable by other, more widely accepted methods.

The analysis of Ca provides another example. Although total Ca content can be measured by wet chemical methods, Ca is known to be highly compartmentalized. So-called compartmental analysis can be used to apportion Ca analytically among kinetically distinguishable pools, but the anatomical locations and volumes of these pools remain conjectural. In view of this level of uncertainty, our measurements of Ca surely surpass the accuracy of results that involve wet chemistry and compartmental analysis. (We are of course measuring Ca concentration, which parallels Ca activity but exceeds it by orders of magnitude.) The increase of cytosolic [Ca] that accompanies ouabain contracture is especially intriguing. Not only is the rise statistically significant, but its value (1.2 mmole/kg dry wt) correlates closely with the amount of Ca that is required fully to activate cardiac myofibrils.¹⁰

Confidence in the reliability of a method requires much more than a demonstration that it yields measurements which agree *on the average* with the results of other, often inherently inaccurate techniques. For instance, until 18 months ago we found the microanalysis of cytosolic levels of Ca in the presence of K to be highly unreliable. From one day to the next we measured fluctuating levels of Ca whose differences were statistically significant even though the measurements were made on the same sample each day. Fluctuations of this size must arise from major, uncontrolled systematic errors, and they can give rise to spurious results and make meaningful experimentation a practical impossibility. We subsequently found these fluctuations arose from inaccurate spectral deconvolution. The results shown in Fig. 1 are therefore very important, since they show that systematic errors arising from the deconvolution can be virtually eliminated.

Trust in the method may be further enhanced by closer examination of the total variance for each element and by analysis of its components. Confidence is increased by the absence of unacceptably large variance components for which there is no satisfactory explanation.

Analysis of variance is also useful for quantitating biological variation and for optimizing sampling strategy.

The total variance of the measurements for a given element is simply the square of the standard deviation. If an appropriate sampling strategy is used, a straightforward analysis of variance can be used to "deconvolute" the overall variance into its components. The total can thus be understood as the linear sum of all its parts, each of which can accordingly be expressed as fraction of the whole (as in Fig. 3).

We have fractionated the cytosolic variances into five components, each of which adds to the components below it. Starting at the lowest level, they are:

1. *X-ray counting statistics*, estimated in this instance from linear least-squares fitting statistics. Given the statistical nature of x-ray spectroscopy, this component is always present even in the total absence of systematic errors or biological variation.

2. *Within cells*, which is the additional component observed when different but similar regions of the same cell are analyzed. This component is due to biological variation between regions within the cells and to analytical imprecision due to causes other than counting statistics.

3. *Among cells*. This component is attributable to biological variation among cells which lie near one another within a particular section.

4. *Among samples*. This component quantitates any variance among samples from a given heart muscle that is greater than the variance predicted by the foregoing three components. In our experiments, each sample is a section on a different support grid, and each is the product of either a different length of time in storage or of a different cryomicrotomy session and freeze-drying run. Although the magnitude of this component could be attributed to biological variation between anatomical regions, we believe it is due primarily to uncontrolled systematic error.

5. *Among muscles*. Any variance not accounted for by the foregoing components can be attributed to real biological variability from one heart muscle to the next.

Figure 3 shows how markedly the relative contribution made by each variance component differs from one element to the next. In the case of sulfur, for instance, the variance component that originates among samples is highly significant statistically and accounts for 47% of the total variance. Furthermore, this unexpectedly high variance component is observed very consistently both in other anatomical regions of control cells and in ouabain-treated as well as control preparations. We conclude that the microprobe analysis of sulfur is unreliable under our analytical conditions. This conclusion agrees with reports that selective loss of the S results from radiation damage to biological samples undergoing microanalysis at ambient temperatures.^{3,11}

With phosphorus the situation is totally different. Almost all the variance arises within and among cells. There is no significant additional variance that arises among samples or among muscles. The large components at the subcellular and cellular levels are attributable to biological variation. The absence of an among-samples component implies satisfactory precision from one sample to the next and thus appears to rule out systematic errors involving this element.

Calcium demonstrates yet another pattern, in which 69% of the total variance is due to counting statistics. Furthermore, none of the other components is statistically significant. This result shows that biological variation of Ca within control cytosol of these cardiac muscles is relatively small. There is no evidence of systematic errors, and the only limitations on the analyses are those imposed by probe intensity and analysis time.

In the cases of the other elements there are large components of variance that can be attributed to biological variation, e.g., among-cells variance in the cases of Mg and Cl. In the case of Na there is a relatively small, but significant variance component among samples, which suggests the possibility of systematic error.

In conclusion, we have demonstrated that electron-probe microanalysis of cardiac muscle can be carried out with a very high degree of precision and accuracy. The results that can be achieved at the cellular level by microanalysis appear in general to be more reliable than those which can be achieved by any other method.

References

1. T. A. Hall, "The microprobe assay of chemical elements," in G. Oster, Ed., *Physical Techniques in Biological Research*, New York: Academic Press, 2d ed., 1971, vol. 1A, 157.
2. F. H. Schamber, "A modification of the linear least-squares fitting method which provides continuum suppression," in T. G. Dzubay, Ed., *X-ray Fluorescence Analysis of Environmental Samples*, Ann Arbor: Ann Arbor Science, 1977, 241.
3. H. Shuman et al., "Quantitative electron probe microanalysis of biological thin sections: Methods and validity," *Ultramicroscopy* 1: 317, 1976.
4. J. McD. Tormey, "Improved methods for x-ray microanalysis of cardiac muscle," *Microbeam Analysis--1983*, 221.
5. R. R. Sokal and F. J. Rohlf, *Biometry: The Principles and Practice of Statistics in Biological Research*, San Francisco: W. H. Freeman, 1981, 2d ed.
6. P. R. Bevington, *Data Reduction and Error Analysis for the Physical Sciences*, New York: McGraw-Hill, 1969.
7. C. O. Lee and H. A. Fozzard, "Activities of potassium and sodium ions in rabbit heart muscle," *J. Gen. Physiol.* 65: 695, 1975.
8. C. O. Lee et al., "Relation between intracellular Na ion activity and tension of sheep cardiac Purkinje fibers exposed to dihydro-ouabain," *Biophys. J.* 29: 315, 1980.
9. J. H. B. Bridge et al., "Sodium efflux in rabbit myocardium: Relationship to sodium-calcium exchange," *J. Physiol.* 316: 555, 1981.
10. R. J. Solaro et al., "Calcium requirements for cardiac myofibrillar activation," *Circ. Res.* 34: 525, 1974.
11. A. Dorge et al., "Preparation of freeze-dried cryosections for quantitative x-ray microanalysis of electrolytes in biological soft tissues," *Pflügers Arch.* 373: 85, 1978.

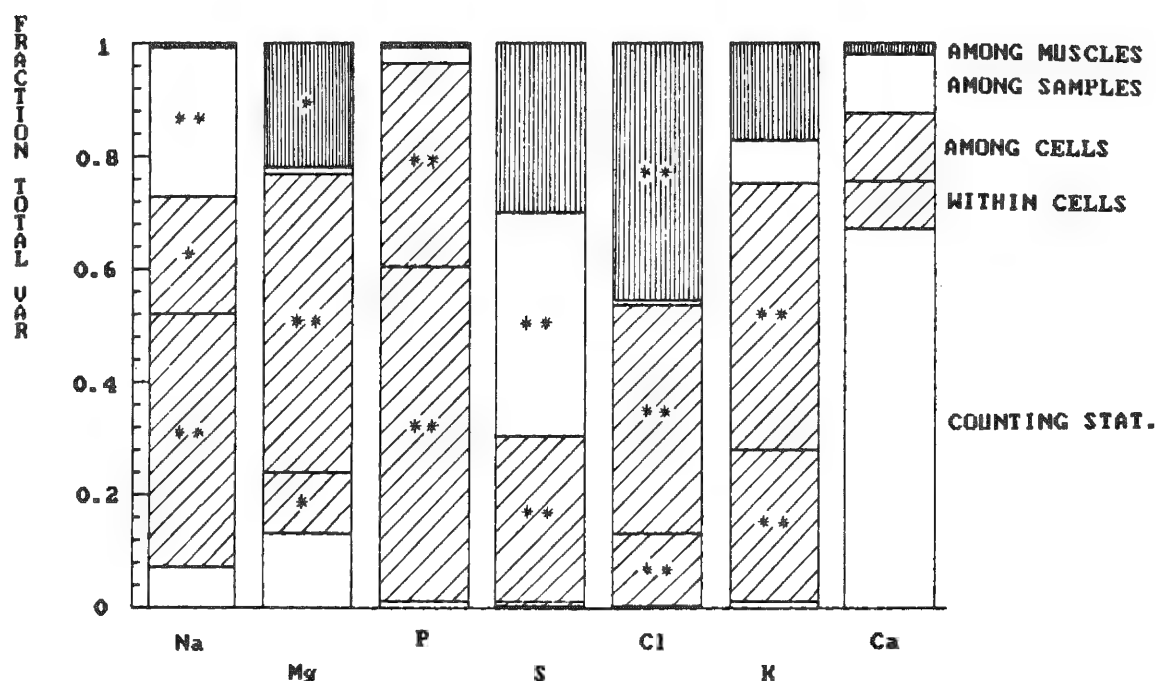


FIG. 3.--Results of multilevel analysis of variance in electron-probe analysis of cytosol compartment of control cardiac muscles. Components of variance originating at each level were estimated. Relative contribution each level makes to overall variance is indicated as fraction of total variance of each element. Presence of * or ** within component indicates that that component is statistically significant at better than the 95% or 99% probability levels, respectively. For further details, see text.

ELEMENTAL ANALYSIS OF LABIAL GLANDS IN CYSTIC FIBROSIS

K. T. Izutsu, D. E. Johnson, and E. Wang

In the past an understanding of the glandular dysfunctions associated with cystic fibrosis (CF) has been hampered by the lack of an appropriate experimental model. Thus, considerable effort has been expended in the study of animal models of uncertain applicability (e.g., reserpinized rats and mice), or conveniently available human tissues that may not be relevant to studies of exocrine gland abnormalities (e.g., erythrocytes and cultured fibroblasts).

Experimental advances in human salivary and mucous gland studies have thus far lagged behind those in the above tissues. However, Mangos has studied metabolic processes, elemental distributions and secretion regulating factors in human parotid glands obtained from CF patients after death.¹ Still, this experimental approach results in several difficulties including the fact that significant changes in intracellular elemental concentrations occur after death, and such changes could obscure any CF-related changes.

We have developed a salivary gland experimental preparation that overcomes objections concerning species and tissue relevance. This preparation is the human labial salivary gland studied after biopsy from control and CF patients. Since there is considerable evidence to suggest that intracellular ion concentrations are abnormal in salivary glands of patients with CF, we are using this new preparation and energy-dispersive x-ray microanalysis in a study to measure directly subcellular elemental distributions in these tissues.

Experimental

Labial salivary gland fragments are obtained from one half of the lower inner lip about 10 mm beneath the vermilion border. Three salivary gland fragments between 1 and 2 mm in their longest dimension are excised and either placed in formalin for light microscopy or positioned on stainless-steel chucks such that they rest on their dissected end. This configuration decreases the likelihood of sampling injured cells. The sample is frozen by quick immersion in rapidly stirred Freon 22 (-156 C) and cooled with liquid nitrogen, and the frozen lobules are stored in liquid nitrogen until sectioned.

A Sorvall MT2-B cryoultramicrotome and glass knife are used to prepare thin sections. The cold bowl temperature is maintained at -100 C. A knife clearance angle of 7° and the lowest cutting speed is used. Dry cut sections are transferred to copper double grids precoated with formvar and carbon. Grids are folded, stamped with a copper rod, placed in a heavy brass container at liquid nitrogen temperature, and transferred to an Edwards high-vacuum evaporator. Sections are dried overnight at 10⁻⁵ to 10⁻⁶ Torr. When the samples reach approximately 10 C, they are warmed under vacuum to a few degrees above room temperature to prevent rehydration, and brought to room pressure with dry nitrogen gas. Grids are stored under vacuum in a dessicator until analyzed.

Elemental Analysis

Freeze-dried sections are examined in a JEOL-100C electron microscope in both conventional and scanning modes. All x-ray spectra are collected in the STEM mode by use of a KEVEX 7000 spectrometer with a 30mm² detector. The spectra are analyzed by use of a digital-filter, least-squares fitting routine developed by Shuman et al.² Binary salt

Author Izutsu is with the Departments of Oral Biology and Oral Medicine; authors Johnson and Wang are with the Center for Bioengineering, University of Washington, Seattle WA 98195. Supported by NIH Grant R03 DE 06487.

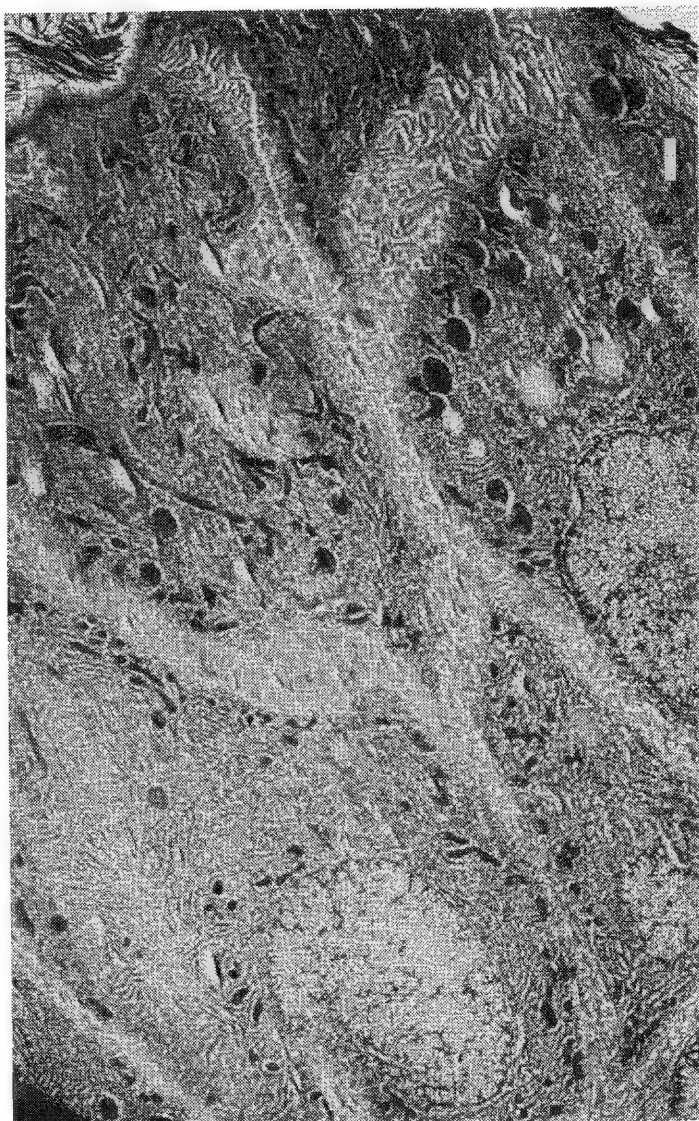
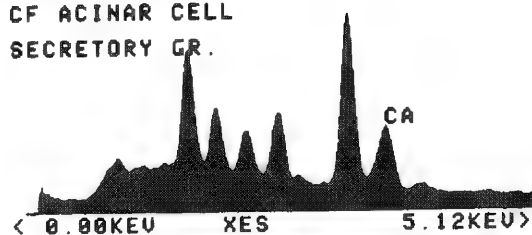


FIG. 1.--Conventional transmission micrograph of unstained, freeze-dried cryosection of human minor gland. (Bar = 1 μ m).

HUMAN MINOR GLAND
CF ACINAR CELL
SECRETORY GR.



HUMAN MINOR GLAND
CONTROL ACINAR CELL
SECRETORY GRANULE

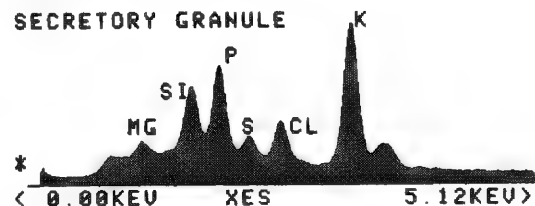


FIG. 2.--X-ray spectra from secretory granules of control and CF patients.

TABLE 1.--Comparison of secretory granule concentrations in labial salivary gland from control subjects and patients with cystic fibrosis (uncorrected for mass loss).

Secretory Granules	Na	Mg	P	S	Cl	K	Ca
Controls (n=38)	67 ± 5	61 ± 9	208 ± 20	104 ± 9	149 ± 13	466 ± 32	143 ± 11
Cystic Fibrosis patients (n=60)	136 ± 16	66 ± 8	215 ± 14	143 ± 7	220 ± 15	617 ± 29	138 ± 8
P(t)	.001	NS	NS	.001	.001	.001	NS

P(t) = significance level for unpaired t-test between groups.

standards are used to establish relative counting efficiencies, and an albumin specimen is used to establish an absolute standard for S. The resulting concentrations are stored on a CDC Cyber 170-750 computer.

Elemental concentrations in different cellular compartments and between groups are compared by a t-test and by nested, one-way analysis of variance (ANOVA).

Results

This study compared findings in 6 patients with CF (5 males and 1 female between 18 and 30 yr) and 6 controls (3 males and 3 females between 21 and 30 yr).

Acinar cells were commonly observed in freeze-dried cryosections, but duct cells were not (Fig. 1). Intracellular and extracellular spaces were clearly discernible. Nuclear and cytoplasmic regions were discernible, as were secretory granules. Mitochondria were most easily identified in cell sections containing few secretory granules. At least a few secretory granules were observed in nearly all cells, but cells similar in appearance to serous cells of the rat parotid gland were relatively infrequently observed. However, such cells with large numbers of secretory granules yielded cytoplasmic x-ray spectra that were similar to those obtained from acinar cells with few secretory granules.

CFs vs Controls

Comparison of elemental concentrations in intracellular acinar spaces of patients with CF and controls yielded several significant differences. Cytoplasmic concentrations of P, S, and K were elevated in patients with CF. These same concentrations plus Ca were significantly elevated in nuclei from patients with CF. Secretory granules in patients with CF had elevated levels of Na, S, Cl, K (Table 1 and Fig. 2). The above t-test results are not yet confirmed by ANOVA.

Testing for Systematic Measurement Differences Between Groups

An analysis of covariance was performed by comparison of regression relationships between each of the elemental concentrations in each of the intracellular spaces and system parameters (such as size of area analyzed, beam current, x-ray continuum counts obtained from the film and from the section, the χ^2 evaluation of the fit between the observed spectrum and the calibration standard peaks, and the Ca and Si concentrations) for controls and patients with CF. It was concluded that differences in these parameters could not account for the observed differences in intracellular elemental concentrations between controls and patients with CF. In addition, there were no strong correlations between elemental concentrations in the various acinar intracellular spaces and disease severity.

Differences in Osmolarity

Table 2 shows the estimated differences in osmolarity between glands from controls and from patients with CF. Differences in osmolarity were estimated from the sum osmolarity $NA + K + Cl$. Statistically significant differences were found in secretory granules, cytoplasm, and nuclei; values from CF glands exceeded control values. However, only the osmotic difference for secretory granules appeared to be an appreciable one (a 42% increase vs 11% increases for cytoplasm and nuclei). This finding may be relevant to the pathophysiology of mucous glands in CF. This possibility is independent of the ionic state of the additional elements in the CF granules because if they are bound, that suggests the secretory product is different; and if they are ionized, that would result in a greater number of osmotically active particles. Introduction of the secretory granule contents into the lumina would result in different osmotic and ionic milieus for the mucus from controls and patients with CF. Hence, even if the primary structure of mucus is unaltered in CF, ionic-strength considerations would predict that mucus secreted in conjunction with the contents of the present CF secretory granules would be denser and more tenacious than that from the present control granules.³

Comparison with Previous Results

The present quantitative results are in at least qualitative agreement with several earlier salivary gland studies although none was performed with human labial glands. The

results of Schneyer & Schneyer,⁴ based on flame photometry data, can be used to calculate a cellular K concentration in the rat submandibular gland of approximately 627 mM/kg dry mass when the conversion factor for converting from mM/kg wet weight to mM/kg dry mass obtained by Sasaki et al.⁵ is used. Since cellular space consists primarily of cytoplasmic, nuclear, and secretory granule spaces, and since the K content of secretory granules is appreciably less than that in the other two spaces, it appears that the Schneyers' results are in good agreement with our result.

The microprobe results of Sasaki et al.⁵ in mucous cells of the dog submandibular gland and of Roomans et al.⁶ in mucous cells of rat submandibular glands are also qualitatively similar to the present results.

Summary of Findings

These results indicate that resting labial glands in patients with CF have altered intracellular elemental concentrations, and that these changes are not strongly affected by disease severity. The CF related differences were not accounted for by systematic differences in specimen preparation or analytical procedures. The observed increase in P and S concentrations are consistent with the previously reported increase in rates of synthesis and secretion of secretory products in tracheal bronchial mucous glands,⁷ because such increased rates could require increased levels of RNA (accounting for the increased P) and of substrates for mucus synthesis (accounting for the increased S). The explanation for the elevated K concentration is still unknown, although it is conceivable that a cellular metabolism may be coupled to the transmembrane potential or vice versa.

References

1. J. A. Mangos, "Isolated parotid acinar cells from patients with cystic fibrosis: Functional characterization," *J. Dent. Res.* 60: 797-804, 1981.
2. H. Shuman, A. V. Somlyo, and A. P. Somlyo, "Quantitative electron probe microanalysis of biological thin sections: Methods and validity," *Ultramicroscopy* 1: 317-339, 1976.
3. P. Y. Tam and P. Verguo, "Control of mucus hydration as a Donnan equilibrium process," *Nature* 292: 340-342, 1981.
4. L. H. Schneyer and C. A. Schneyer, "Electrolyte and inulin spaces of rat salivary glands and pancreas," *Am. J. Physiol.* 199: 649-652, 1960.
5. S. Sasaki, I. Nakagaki, H. Mori, and Y. Imai, "Intracellular calcium store and transport of elements in acinar cells of the salivary gland determined by electron probe x-ray microanalysis," *Japan. J. Physiol.* 33: 69-83, 1983.
6. G. M. Roomans, X. Wei, O. Ceder, and H. Kollberg, "The reserpinized rat in the study of cystic fibrosis: X-ray microanalysis of submandibular gland and pancreas," *Ultrastruct. Pathol.* 3: 285-293, 1982.
7. R. C. Frates Jr., T. T. Kaizu, and J. A. Last, "Mucus glycoproteins secreted by respiratory epithelia from cystic fibrosis patients," *Pediatr. Res.* 17: 30-34, 1983.

TABLE 2.--Estimated differences in osmolarity* between intracellular spaces of glands from controls and from CF patients (uncorrected for mass loss).

Intracellular space	Control	Patients with cystic fibrosis	P(t)**
Secretory granules	683±42 (n=38)	973±41 (n=60)	.001
Cytoplasm	1136±37 (n=45)	1258±29 (n=54)	.01
Nucleus	1386±30 (n=41)	1547±38 (n=43)	.001

*Differences in osmolarity were estimated from Na + K + Cl for each case in each group.

**P(t) = significance level of unpaired t-test.

A GENERALIZED APPROACH FOR THE ANALYSIS OF ISOLATED CELLS BY ELECTRON-PROBE MICROANALYSIS

D. E. Lange, C. B. Donovan, and E. H. Abraham

Over the past several years techniques have been developed for analyzing by electron-probe microanalysis (EPMA) individual cells grown in tissue culture. These techniques have been applied to the study of the kinetics of cellular ion transport arising from modulations of the cell and membrane-bound transport proteins. These modulations can be the result of exposure of the cells to drugs, hormones, or alterations in the ionic composition of the bathing medium. The approach can also be used to detect functional consequences of genetic variation in the molecular structure of the transport proteins. To facilitate these studies, software has been developed for use with a Tracor Northern automated (TN-2000/1310) Cameca MBX or JEOL 733. The locations on the cells to be analyzed were selected by the investigator and saved, and automated data collection was then begun for the elements of interest. Locations on the substrate of cell free surfaces were selected to assess x-ray background counts. Data reduction was performed with a separate Flextran program, which allows regression analysis and elimination of outlier data points. Population data were compared by Student's t-test or analysis of variance (ANOVA). The reduced data were stored on computer floppy disk, and because the analysis was nondestructive, the segments containing cells were also saved. To date we have reanalyzed samples two years after the initial electron-probe evaluation with no significant difference in data generated.

The analysis of individual cells by means of EPMA poses potential problems since the x-ray generation volume extends into the substrate even at low kilovoltages. Moreover, the situation is further complicated by the fact that the cell thickness and hence the cell mass analyzed varies with position in a single cell, from cell to cell, and from population to population. One approach to these problems was to choose a beam diameter small enough to be confined to one cellular compartment (e.g., the cytoplasm) and yet large enough to average over any subcellular organelles contained within the compartment of interest. A beam spot diameter of 10-15 μm has satisfied these requirements for many cell types. It was also necessary to have some measure of the local cell dry mass. Macromeasurements frequently rely on measurements of protein content to normalize measurements of other cellular constituents. For flux studies it was desirable to have a marker that was maintained constant during a cell history that results in perturbations of other cellular species. We have found that the elements carbon and phosphorus fulfill these requirements in a variety of conditions. The carbon signal was useful when the cells were grown on a noncarbon substrate (e.g., silicon). Our approach has been to analyze a relatively large subset of our sample populations and to compare linear regression slopes obtained from x-ray intensity data for an element of interest to that of carbon or phosphorus. Initial testing of this approach has been carried out by use of populations of fibroblasts grown on pyrolytic graphite segments.^{1,2} Figure 1 shows an SEM image of two adjacent fibroblast populations.

Two schedules were developed for use with a modified version of Sandia TASK to set up and

Author Lange is at the Department of Geological Sciences, Harvard University, Cambridge, MA 02138. Authors Donovan and Abraham are at the Metabolism Division of Children's Hospital Medical Center, Boston, MA 02115; Dr. Abraham is at present in the laboratory of Professor Guido Guidotti at the Department of Biochemistry and Molecular Biology, Harvard University, Cambridge, MA 02138. The work was supported in part by NIH (AM0 6485) and NSF grants. The authors are indebted to Prof. Robert Dymek and the Department of Geological Sciences, Harvard University, for instrument time for development of these programs. We thank Prof. J. L. Breslow for guidance and generosity in this project; Dr. M. Canessa and Ms. A. Spalvino for the atomic absorption measurements; and Charles Nielsen, JEOL-USA, for assistance in adapting the data-collection programs for use on a JEOL-733.

TABLE 1.--Atomic absorption measurements of intracellular ion concentrations. (Double-label-corrected values using ^{14}C urea and ^3H sucrose.) Values expressed as means \pm S.E.

	Wash medium	
	Iso-osmolar sucrose	Water (distilled deionized)
Wash time (s)	12.0	12.0
Cell volume (pL)	2.75 \pm 0.34	2.72 \pm 0.66
K (mM/L)	175.6 \pm 23.8	170.5 \pm 6.3
Na (mM/L)	32.1 \pm 4.9	41.0 \pm 3.4
Number of samples	5	6

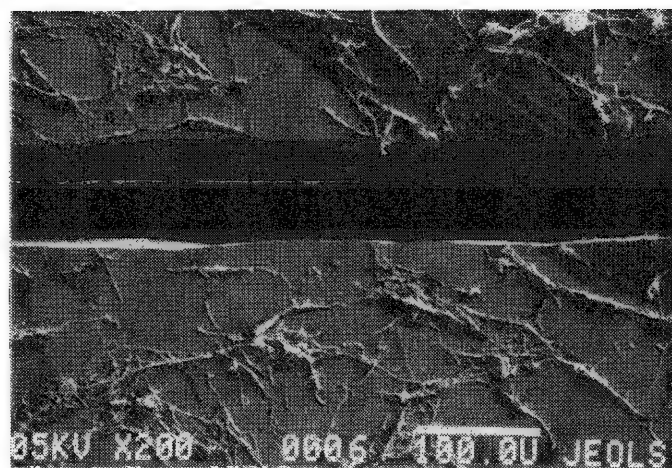


FIG. 1.--SEM photograph showing two adjacent populations of human fibroblasts grown on polished pyrolytic graphite segments.

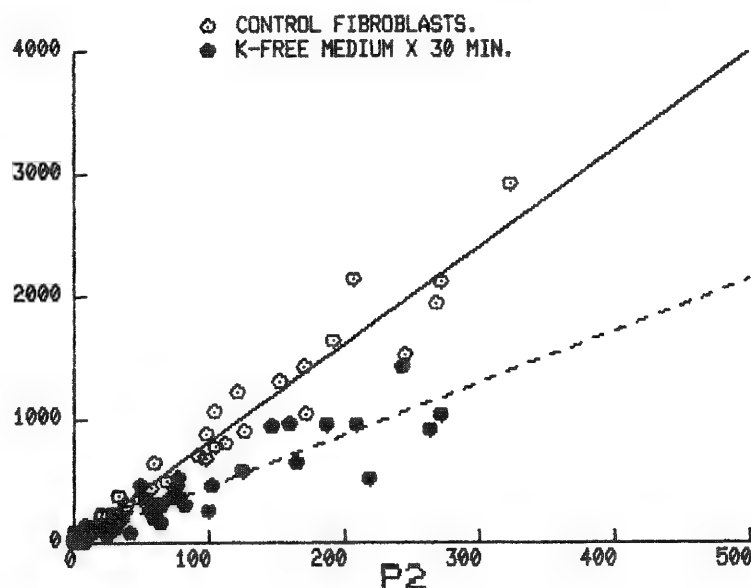
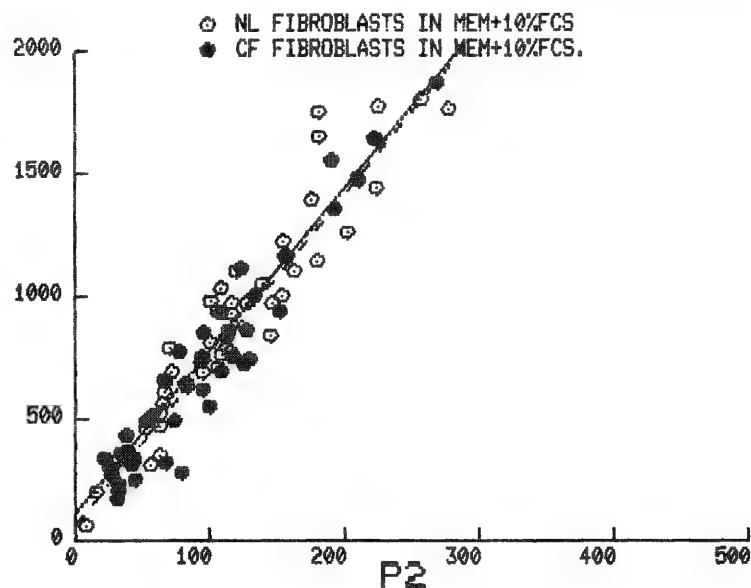
FIG. 2.--Visual comparison of regression related information about two populations of fibroblasts (produced by CELL analysis package). (a) K (x-ray) vs P (x-ray) counts of two populations that show no significant difference; open circles (solid line) are data from normal population, filled circles (dashed line) from diseased state (cystic fibrosis). (b) case for which single population of cells has been switched from normal medium (control) to potassium-free medium: difference in potassium content is highly significant, as shown by comparison of regression curves of the two populations ($P < 0.001$).

	○	●	
M	6.60	6.71	2000
B	106.4	56.3	
R2	0.892	0.915	
M0	7.30	7.14	1500
R20	0.977	0.976	
N	46	43	

K3

	○	●	
M	7.90	4.21	4000
B	19.0	20.4	
R2	0.953	0.850	
M0	8.01	4.35	3000
R20	0.975	0.922	
N	41	45	

K3



analyze the freeze-dried cells.³ The first schedule sets up an individual point table for each sample with entry via a joystick switch after positioning the stage to the desired location to be analyzed. The x, y, and z coordinates of up to 50 points may be entered in each point table. Any or all of the positions may be checked with the FOCUS command. A second schedule performs the actual analysis and storage of data. To minimize beam damage to the cells and analytical time, the spectrometers were each set to an element of interest and the stage was then sequentially positioned to each location in a previously defined point table. This approach was more efficient, since the stage was moved considerably fewer steps between locations than a spectrometer between elements. On completion of a point table, the data were saved and a new point table was commenced. Typical analyses include seven elements (sodium, potassium, chlorine, phosphorus, calcium, magnesium, and sulfur) with the more potentially volatile elements chlorine and sulfur analyzed first. One spectrometer was continuously tuned for either phosphorus or carbon with each cycle of analysis. On completion of a cycle, the next set of elements were automatically set up and each point table was again called up and processed. With excellent instrument stability, the only limitations to a probe run was the storage capacity of the computer system. Our runs require 2-3 h of operator setup time followed by up to 20 h in the automated analysis mode with up to 40 sample populations analyzed and approximately 2000 individual cells studied.

The data reduction program was designed for use with a VT125 as a graphics terminal. Once the data were collected, the data reduction program, CELL, was called up and processing began. Data from each cycle were assembled so that each sample population could be treated separately. The population averages, standard deviations, and linear regressions of up to 14 pairs of elements were obtained. Outliers were determined graphically from inspection of the regression plot of relevant binary combinations of elements; e.g., element vs phosphorus. Points more than two standard deviations from the rest of the points were excluded from further analysis. With outliers removed, statistical tests comparing two (Student's t-test) or more (ANOVA) sample populations were performed by comparisons of the slopes obtained by linear regression.⁴ To minimize the effect of analyses which were only slightly above the background, analyses that had net counts of less than three times the square root of the background were excluded from statistical tests. In the comparison of slopes, a test was also made to check whether a slope was statistically equal to 0, and if so a warning message was printed. The methods used could not statistically distinguish between two or more slopes if any were statistically equivalent to 0. Figures 2(a) and 2(b) present typical regression comparisons.

We have been using macromasurements to reduce the data further to more physiologic units. The concentrations of ions per liter of cell water were measured as follows. Cells were grown to confluence on the probe substrate. After washing, the substrates were immediately quenched in liquid nitrogen and freeze-dried. Multiple disks with freeze dried cells were then dissolved in 0.1% Acatonox (Scientific Products, McGraw Park, Ill.) for at least 4 h at room temperature and then vortexed vigorously. Other replicates were saved as standards for the electron probe. Aliquots of the cellular suspension were analyzed for K⁺ in a Perkin-Elmer model 5000 atomic-absorption spectrophotometer. Cell numbers were determined by a Coulter counter. Intracellular and intercellular trapped volumes were determined by a double-label technique described by Vasquez et al. using ¹⁴C urea and ³H sucrose as the total and extracellular volume markers, respectively.⁵ These data allowed determination of intracellular potassium concentration in variously loaded populations of cells after correction for trapped extracellular media. Table 1 presents representative values for fibroblasts in control medium with either an isoosmolar wash or a distilled-water wash showing the good correlation by either approach. The values of potassium determined by macromasurement can be equated to the slope of the K (counts) versus P (counts) regression determined by the electron probe. We refer to this latter slope as K/P. Figure 3 was a calibration curve for probe K/P values and the corresponding atomic absorption measurements for intracellular potassium. One can extend these values to all other elements analyzed by including segments of the probe support coated with pure salt solution. For example, a segment with KCl microcrystals allows determination of K and Cl relative x-ray counting efficiencies and hence conversion of the slope of the Cl (counts) versus P (counts) into Cl intracellular concentration.

Figures 4(a, b) show the results of combining the ANOVA and the cell standards to investigating fluxes. The bar graphs show the effect on intracellular ion contents of exposing fibroblasts to potassium-free medium for up to 3 h. Each bar was the average of 6 replicate determinations, approximately 300 cells probed (50 cells on each segment), for the same

strain of fibroblasts (S-411). The error bars show the standard deviation in intracellular K, Na, and Cl within the groups of segments harvested at the three time points. The ANOVA program applied to the populations shows that variation within groups was not significant but variation among groups after K-free treatment for 30 min or 3 h is highly significant ($p < 0.001$). Figure 4(b) shows the results of ANOVA applied to the Ca, Mg, or S vs P regression slopes. The Mg or S vs P regression slope among-group variation was not significant. Intracellular contents is stable for these elements during exposure of cells to K-free medium. The Ca vs P regression slopes showed significant decrease upon exposure to K-free medium: the Ca content was reduced to about half within 30 min and remained constant at that level at 3 h (intermediate points not shown). These studies show that $T_{1/2} < 5$ min for Ca efflux, and ~ 20 min for K efflux.

References

1. E. H. Abraham, J. L. Breslow, J. Epstein, P. Chang-Sing, and C. Lechene, "Preparation of individual human fibroblasts and study of ion transport," submitted to *Am. J. Physiol.*
2. E. H. Abraham, C. B. Donovan, and D. E. Lange, "Application of electron probe microanalysis to tissue culture studies of normal cellular physiology and genetic disease," *Microbeam Analysis--1984*, 285.
3. W. F. Chambers, *SANDIA-TASK '78: An Electron Microprobe Automation Program*, Albuquerque, N.M.: Sandia National Laboratories Report SAND78-1149, 1978.
4. J. H. Zar, *Biostatistical Analysis*, Englewood Cliffs, N.J.: Prentice-Hall, 1974.
5. B. Vasquez, F. Ishbashi, and B. Howard, "Measurement of intracellular volume in monolayers of cultured cells," *In Vitro* 18: 643-649, 1982.

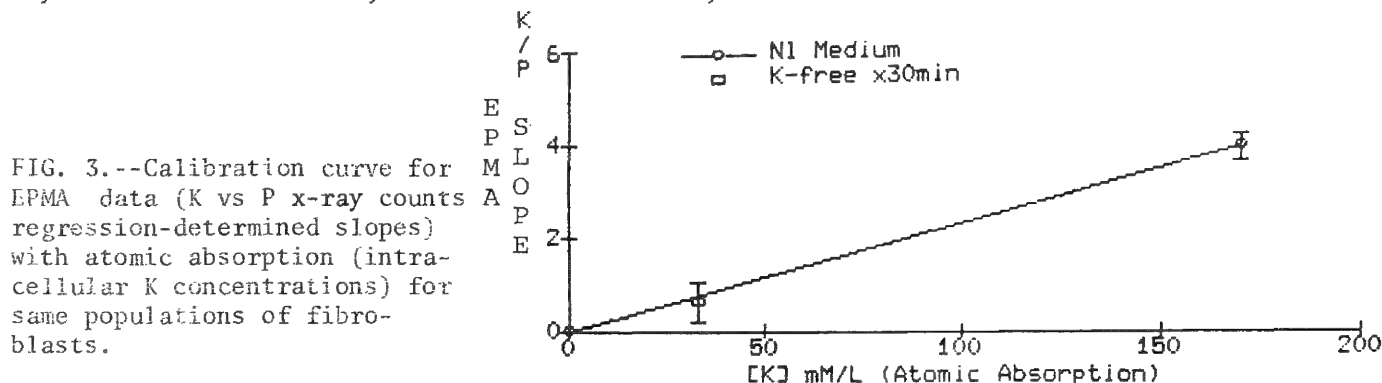


FIG. 3.--Calibration curve for EPMA data (K vs P x-ray counts A regression-determined slopes) with atomic absorption (intracellular K concentrations) for same populations of fibroblasts.

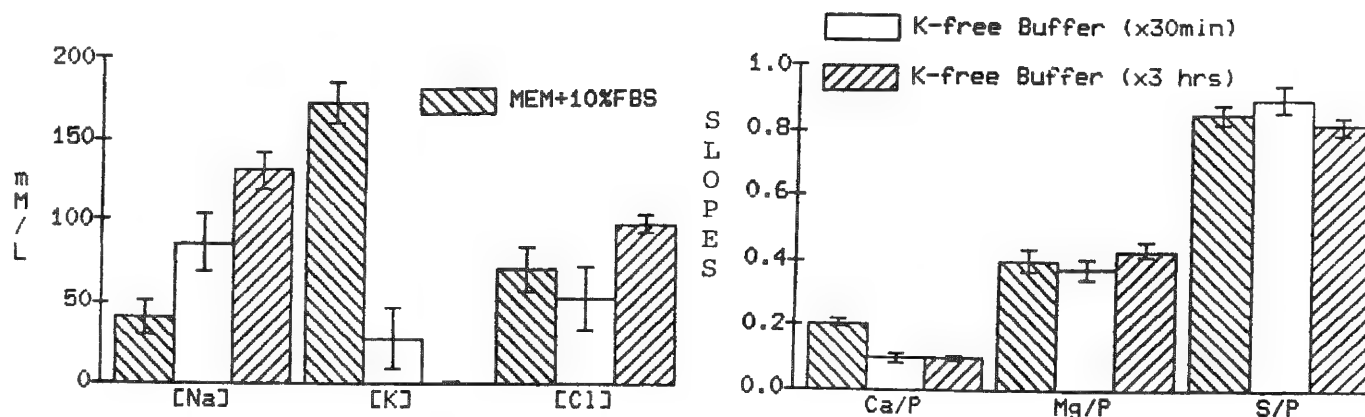


FIG. 4.--(a) Time course for exposure of normal fibroblasts to K-free medium for 3 h. Values of intracellular concentrations for K, Na, and Cl in control cells are compared to time points at 30 min and 3 h after exposure to K-free medium. Changes in contents reflect cellular K efflux and Na influx in normal human fibroblasts. Error bars show SD about mean for concentration values of 6 replicate populations of fibroblasts for each condition. Differences among treatments were highly significant ($p < 0.001$) as determined by ANOVA comparison of slopes (Na, K, or Cl x-ray counts vs P x-ray counts). X-ray counts for Na, K, Cl, and P were measured simultaneously, then converted to concentrations (mM/L) by use of standards cell calibration curves (Fig. 3) and standard salt regressions (not shown). (b) Analysis for Ca, Mg and S in same fibroblasts as in (a); results shown in form of slopes for x-ray counts vs P.

APPLICATION OF ELECTRON-PROBE MICROANALYSIS TO TISSUE CULTURE STUDIES OF NORMAL CELLULAR PHYSIOLOGY AND GENETIC DISEASE

E. H. Abraham, C. B. Donovan, and D. E. Lange

Electron-probe microanalysis (EPMA) can be used to identify and quantify small amounts of many biologically important elements. This technique has been applied to biological systems where elemental analysis has been performed on single cells or even subcellular organelles. These studies have generally been performed with cells or tissues removed directly from the living organism. In such experiments, it is often difficult to study specific effects on ionic composition of the cells or tissue. To assess the influence of genetic and environmental factors in this regard more accurately, we have developed a technique that allows us to study the ionic composition of cells grown in tissue culture by electron-probe microanalysis. A special feature of this technique is that many different populations of cells can be examined under identical analytical conditions. Although it is possible to make macrom measurements on cell culture cells, electron-probe techniques are particularly useful where the cells can be generated only in limited quantities, or where there are heterogeneities within the population of cells such as a mixed population of cells. In addition to examining normal transport physiology and transport phenomena associated with cellular differentiation, we have found the approach ideally suited to determining effects of cellular exposure to drugs and/or hormones, and to comparison of genetic disease derived cells with normal controls. This approach has important implications for prenatal diagnosis and heterozygote screening for genetic diseases such as cystic fibrosis.

Materials and Methods

Preparation of the Cell Supports. Polished pyrolytic graphite disks (E. Fullam, Schenectady, N.Y.) or p-doped (boron) silicon wafers (Monsanto Chemical Co.) were used as supports for electron-probe analysis. Each type of support was subdivided prior to cell plating. In the case of the graphite disks cleavage resulted from an initial point fracture in the center of the disk, which divided it in half along the anisotropic axis of the graphite. We performed subsequent cuts parallel to this axis by lightly percussing the disk with a single-edge razor blade, allowing it to be divided into as many as 40 individual segments (Fig. 1). In the case of the silicon ships the subdivision was produced either by a dicing machine or a diamond-tipped glass cutter.

Cells and Media. Initial development was carried out on human fibroblasts.¹ Human cells were derived from several sources. Monocytes were obtained from peripheral venous blood samples.² Fibroblasts and epithelial cells were derived from percutaneous biopsy samples and amniotic fluid samples. Epithelial cultures can be studied in the short term by use of the initial outgrowth of skin biopsy tissue, or in the long term by use of irradiated 3T3 cell feeder layers.³ Figure 2 shows representative cell types for EPMA.

Recently, we have been developing a routine method for preparing cultures of urinary epithelial cells of human origin in culture. This method was based on work described by Felix

Authors Abraham and Donovan are at the Metabolism Division of Children's Hospital Medical Center, Boston, MA 02115; Dr. Abraham is at present in the laboratory of Professor Guido Guidotti at the Department of Biochemistry and Molecular Biology, Harvard University, Cambridge, MA 02138. Author Lange is at the Department of Geological Sciences, Harvard University, MA 02138. The work was supported in part by NIH (AM0 6485) and NSF grants. We thank Dr. J. L. Breslow for guidance and generosity in this project; Charles Nielsen, JEOL-USA, for assistance in development of the 733 automation for these analyses; Anthony Laudate and Linda Lopez, JEOL-USA, for assistance with the SEM's; and Dr. S. Cole for preparation of the monocyte cultures.

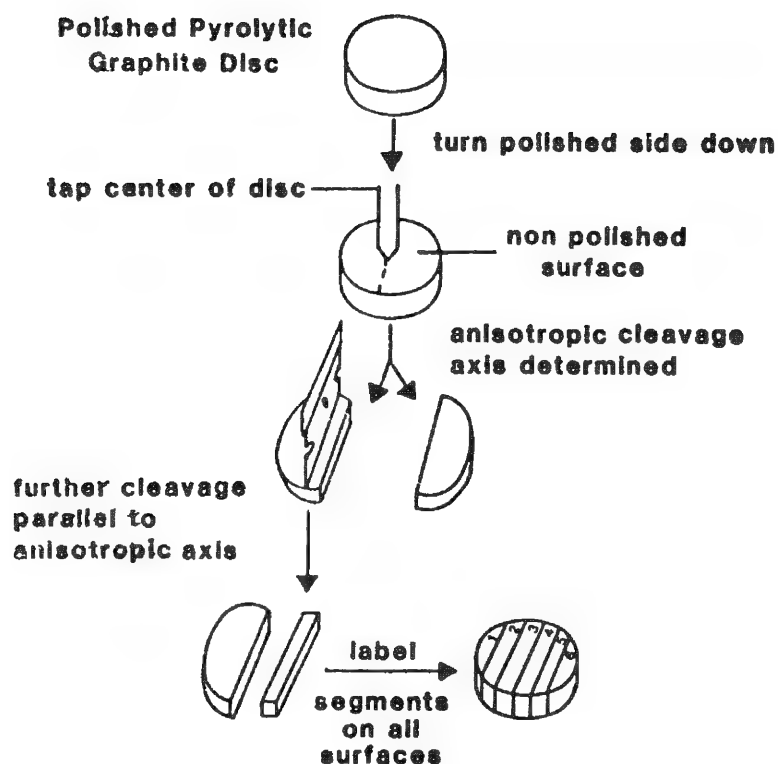


FIG. 1.--Disk-cleavage process for preparation of segments from polished pyrolytic graphite disks.

et al.,⁴ but we have made the following observation: whereas, in general, urinary epithelial cells are rarely obtained from urine specimens after the neonatal period, we have succeeded when patients were administered intravenous aminoglycoside therapy. With patients receiving either Gentamicin or Tobramycin, it has been possible to obtain fairly numerous epithelial colonies even from adults, up to 20 to 30 colonies per 100 ml of urine. The processing includes spinning the urine at 800×G for 10 min and resuspending the pellet in MEM plus 10% Fetal Calf Serum (FCS) with added penicillin and streptomycin. Initial epithelial colonies were noted at 1-2 weeks of plating.

Cell stocks of dividing cells (fibroblasts, epithelial, myocytes) were maintained on plastic petri dishes maintained at 36.5 C in a 5% CO₂/95% air, humidified incubator in Eagle's minimal essential medium containing 10% fetal calf serum and supplemented with 900 mg/l glucose and 6.6 mg/l sodium pyruvate. Prior to each experiment, cells were washed with Earle's balanced salt solution, detached from the petri dish with trypsin (0.05% trypsin, 0.05 mM Na₂ EDTA), suspended in MEM, centrifuged for 2 min, resuspended in fresh MEM, and plated onto the probe supports (either pyrolytic carbon or silicon wafer segments). The plating inocula generally contained between 10 000 and 100 000 cells/ml, or between 200 and 1000 cells per segment at 48 h after plating on the probe support. Plated cells were generally incubated for 24 to 72 h to allow for cell attachment and division.

Experimental Protocol. In various experiments the cells on the disk segments were placed in test media at 36.5 C in either regular MEM or potassium-free medium. The cells were treated with a variety of factors that affect ion transport present or absent (serum, ouabain, amiloride). At the end of experimental treatments the cells were washed and rapidly frozen and then freeze-dried. From comparison of a variety of wash solutions, we have found that distilled deionized water at pH = 7.0 and 3 C was optimal for many probe studies. Figure 3 presents a schematic representation of the cellular processing.

Electron Probe Microanalysis. The freeze-dried segments were assembled in a stainless-steel holder in the case of the graphite segments, and were attached with silver paint in the case of silicon segments. The segments were then inserted into the stage of a JEOL 733 SuperProbe. With the JEOL plural stage up to 160 segments can be inserted simultaneously in-

to the column. At present for a typical probe run we enter the coordinates of 2000-3000 cells on 40-50 segments. The accelerating voltage was 11 kV, the beam current 200 nA, the beam diameter either 10 or 15 μm . The characteristic $K\alpha$ x-ray lines were analyzed for potassium, chlorine, phosphorus, calcium, sulfur, sodium, and magnesium. With silicon segments, carbon $K\alpha$ x-ray lines were also analyzed. Four elements were analyzed simultaneously in individual cells for 10 s. Off sample backgrounds were measured for 60 s at locations distant from the cells on each segment. Details of automation and data reduction are discussed in an accompanying paper.⁵

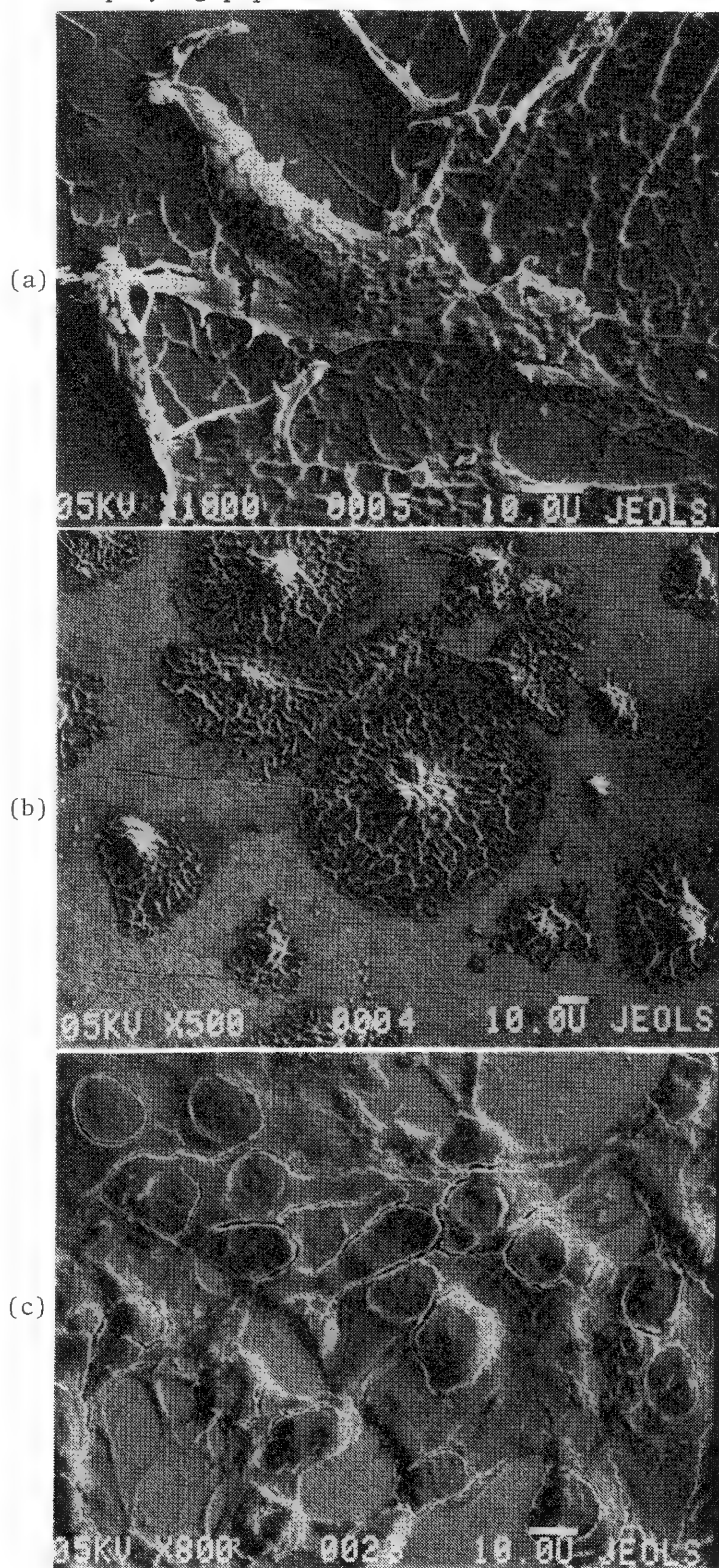


FIG. 2.--Representation and SEM micrographs of several cell types routinely analyzed by EPMA: (a) fibroblasts and (b) monocytes on pyrolytic graphite segments; (c) epithelial cells on silicon substrates.

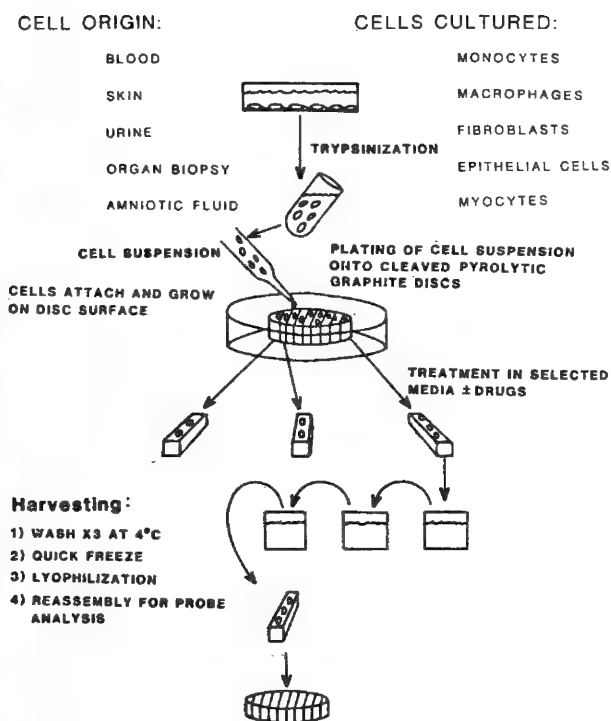
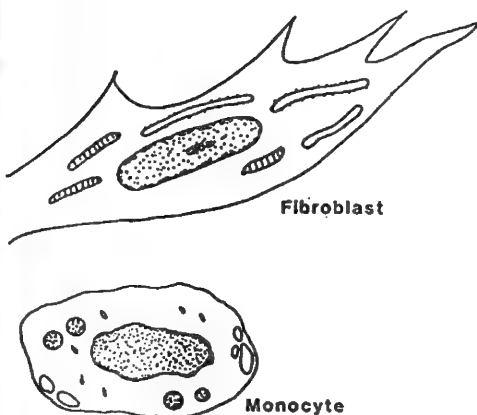


FIG. 3.--Schematic depiction of preparation of cultured cells for EPMA.

Results and Discussion

With these electron-probe methods we have been investigating ion transport in a variety of cell types from normal individuals and from cystic fibrosis (CF) patients. We have been able to demonstrate differences between CF and normal ion permeabilities most consistently in epithelial cells. This result was not surprising since the disease is known primarily by its epithelial-cell manifestations, of which the most extensively studied are the increased sodium and chloride concentrations in the sweat (a product of epithelial structures, the sweat ducts). This phenomenon has served as the basis of the only reliable diagnostic test of the disease, the so-called sweat test.⁶

Our electron-probe methods permit investigation of the alterations of epithelial cell permeabilities that may be related to the observed sweat abnormalities in CF. Normal and CF fibroblasts, and monocytes and epithelial cells in normal medium (control) generally show minimal differences in the intracellular contents of the various ionic species analyzed by EPMA. Differences in content have been demonstrable after the cells undergo perturbations. One series of our experiments tests the effect of inhibiting active transport of the (Na-K)ATPase by the incubation of the cell in potassium-free medium (in the presence or absence of ouabain). These conditions inhibit most active transport and result in maximal influx of Na into the cells. CF epithelial cells show a more rapid increase in intracellular Na content and decrease in the intracellular K content than controls. For a further comparison of the rates of accumulation of cellular Na after exposure to potassium-free medium, we exposed the cells to serum and/or amiloride (Fig. 4). The same techniques are being applied to epithelial cells derived from amniotic fluid, and may make prenatal diagnosis of CF by EPMA feasible. Figure 5 shows a configuration of the probe segments that could extend the present studies to diagnostic purposes in CF. A similar configuration could be used in other diseases such as hypertension or diabetes, which have observed cellular ion transport defects.

References

1. E. H. Abraham, J. L. Breslow, J. Epstein, P. Chang-Sing, and C. Lechene, "Preparation of individual human fibroblasts and study of ion transport," submitted to *Am. J. Physiology*.
2. P. L. Einstein and H. R. Colten, "Synthesis of the second component of complement by

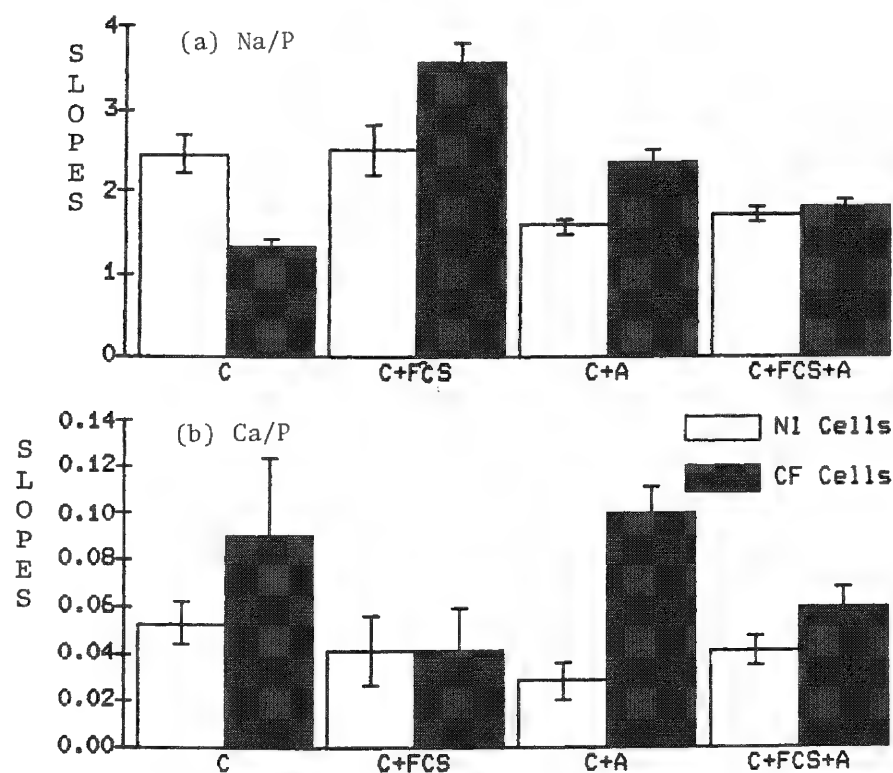


FIG. 4.--EPMA approach to comparison CF and normal cultured urinary epithelial cells: (a) cellular sodium and (b) cellular calcium in normal (NI) and CF cells 30 min after transfer from normal medium with serum to potassium-free medium (C) in presence or absence of 0.1 mM amiloride (A) and/or 10% fetal calf serum (FCS). About 30 normal and 30 CF cells analyzed in each condition. Populations transferred to C-medium show significantly increased uptake of sodium in normal cells over CF cells; Ca content in CF cells is elevated over normals in C medium in presence or absence of amiloride. Effects are significant at 0.001 level. In presence

of FCS and amiloride, normal and CF cells are not significantly different in terms of either sodium or calcium content.

long-term primary cultures of monocytes," *J. Exp. Medicine* 143: 114-135, 1976.

3. J. G. Rheinwald and H. Green, "Serial cultivation of strains of human epidermal keratinocytes: The formation of keratinizing colonies from single cells," *Cell* 6: 331-343, 1975.

4. J. S. Felix, T. Sun, and J. W. Littlefield, "Human epithelial cells cultured from urine: Growth properties and keratin staining," *In Vitro* 16: 866-874, 1980.

5. D. E. Lange, C. B. Donovan, and E. H. Abraham, "A generalized approach for the analysis of isolated cells using electron-probe microanalysis," *Microbeam Analysis--1984*, 281.

6. H. Shwachman, A. Mahmoodian, and R. K. Neff, "The sweat test: Sodium and chloride values," *J. Pediatrics* 98: 576-578, 1981.

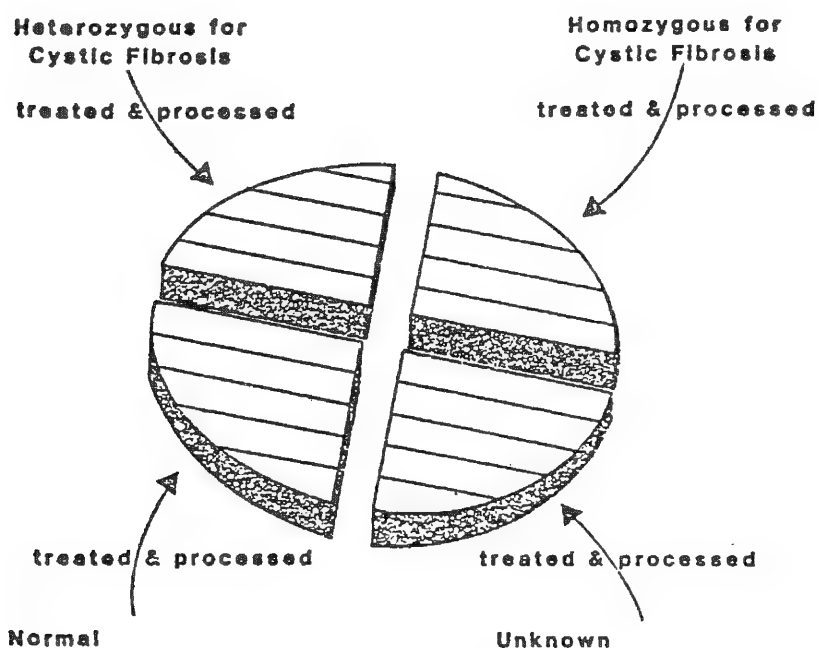


FIG. 5.--Prototype for electron-probe microanalysis for CF diagnosis: configuration of graphite chips that could be used for testing of multiple populations.

CRYOTRANSFER OF ULTRATHIN CRYOSECTIONS FOR X-RAY MICROANALYSIS

H. K. Hagler

An often asked question is whether a cryotransfer cold stage is necessary for x-ray microanalysis of ultrathin cryosections of fresh frozen tissues. If the removal of water were the only concern, the answer would be no, provided care was exercised to prevent the rehydration of the dry cryosections when they were handled. Generally, tissue sections that are less than 1 μm in thickness are dry within 5 min at -90°C in a good cryotrapped high-vacuum system.¹ When an external freeze drier is used, once the tissue sections are dry, they are warmed to room temperature, carbon coated, and transferred either to a dessicator or the electron microscope. The handling and transfer of sections must be carefully conducted in a dry-box system to prevent rehydration of the sections.² With regard to avoiding rehydration of the tissue, the cryotransfer cold stage and external freeze driers are theoretically equivalent, but in practice the cryotransfer stage is much easier to use.

Routine fixation, dehydration, and embedding techniques are designed to stabilize proteins and lipids while removing water and unstabilized lipid before plastic embedding. Freeze drying of fresh tissue sections is quite adequate for removal of water but does nothing to remove or stabilize lipid unless a low-temperature osmium vapor fixation step is used before the temperature of the sections reaches the melting point of the lipids.³

One of the consequences of cell injury is lipid deposition within the cell;^{4,5} the amount of deposition depends on the severity of injury. There are also some tissues (e.g., adipose tissue) that are composed almost entirely of lipid. In an effort to determine the consequences of the lipid content, rat adipose tissue was frozen with a pair of copper-jawed pliers cooled with liquid nitrogen. The tissue was mounted and sectioned in a Dupont Sorvall FS-1000 cryosystem interfaced with a MT-5000 ultramicrotome. The 100-120nm thin sections were collected dry using a bamboo splinter, placed on a formvar-coated 50-mesh copper grid, sandwiched with a top formvar film, and placed in a Gatan model 626 cryotransfer cold stage. The sections were cut and transferred to the electron microscope at -120°C . The cold stage was warmed to -90°C for freeze drying in the electron microscope column. The ultrastructural preservation of the cell proteins, lipids, and diffusible elements were quite good. The stage was then warmed to $+25^\circ\text{C}$ in the electron microscope. At about $+10^\circ\text{C}$ the lipid drops were observed to melt, and the surface tension of the liquid lipid destroyed all cell structure that had been previously visible. From this simple experiment it is concluded that for cells with a high lipid content, a cryotransfer cold stage is necessary if one wishes to avoid the addition of osmium to the tissue and to study the elemental content by x-ray microanalysis. Thus for studies of cell injury and cells with a high lipid content, the use of a cryotransfer stage is a requirement in order to avoid loss of structure and possible redistribution of diffusible elements due to the presence of lipid.

References

1. T. A. Hall and B. J. Gupta, "The localization and assay of chemical elements by microprobe methods," *Quarterly Rev. Biophysics* 16: 279-339, 1983.
2. J. McD. Tormey, "Improved methods for x-ray microanalysis of cardiac muscle," *Microbeam Analysis--1983*, 221-228.
3. F. D. Ingram and M. J. Ingram, personal communication.
4. L. M. Buja et al., "Sites and mechanisms of localization of technetium-99m phosphorous radiopharmaceuticals in acute myocardial infarcts and other tissues," *J. Clin. Invest.*
5. D. W. Bilheimer et al., "Fatty acid accumulation and abnormal lipid deposition in peripheral and border zones of experimental myocardial infarcts," *J. Nucl. Med.* 19: 276-283, 1978.

The author is at the Department of Pathology, University of Texas Health Science Center at Dallas, 5323 Harry Hines, Dallas, TX 75235. The collaboration of Dennis Bellotto and typing of D. Granville are gratefully acknowledged. Supported in part by the National Institutes of Health Ischemic Heart Disease Specialized Center of Research grant HL17669.

14 Computer-assisted Analysis

QUANTITATIVE ELECTRON-PROBE MICROANALYSIS OF CARBON IN BINARY CARBIDES

G. F. Bastin and H. J. M. Heijligers

Among the many problems connected with quantitative electron probe microanalysis of light elements ($Z < 10$),¹ there is one problem that, although recognized as early as 1975,² has been grossly neglected since then and that is the fact that intensity measurements for these elements can no longer be performed at the maximum of the emission peak. Instead, intensities have to be measured in an integral fashion--a direct consequence of the fact that in the K-ionization process of (for example) carbon the bonding electrons are involved, which leads, apart from shifts in the peak position that can be easily accounted for, to serious alterations in the shape of the C-K α peak, leading in turn to an absolute necessity for integral measurements. If this factor is neglected errors of 30-50% are made, depending on the type of carbon standard. In the present case of binary carbides the problem can be overcome by the introduction of so-called Area/Peak (A/P) factors for each carbide, which represent the ratio between the (true) Area k-ratio and the Peak k-ratio. Once these have been established, future measurements can simply be carried out on the peak and multiplication by the appropriate A/P factor yields the correct k-ratio.

The next major problem is the choice of a correction procedure for matrix effects, of which absorption no doubt represents the major part. Unfortunately any correction procedure has to face the fact that the mass absorption coefficients for carbon are only known with little accuracy. An effort has therefore been made to produce a new set of consistent coefficients using the "thin-film" approximation of Duncumb and Melford.³ Our own correction program,⁴ based on the use of modified Gaussian $\phi(\rho z)$ curves, was finally used to convert the measured k-ratios into concentrations, with excellent results: A relative root-mean-square value (calculated/true composition) of 3.7% over 117 k-ratios measured between 4 and 30 keV.

Experimental

For the measurements 14 binary carbides have been used (mostly of the groups IVA-VIA metals), the majority of which were prepared by arc-melting techniques in our own laboratory. With a few exceptions (line-compounds) the carbon content was determined independently by conventional combustion techniques.

Accurate Area/Peak factors with respect to Fe₃C as a carbon standard were measured by stepping the spectrometer (JEOL 733 microprobe, take-off angle 40°) in small increments over the appropriate spectral range of the C-K α peak and accumulating a large number of counts after each step. These counts were stored in the channels of a multichannel analyzer and displayed on the screen of a CRT. Finally the net (background subtracted) areas under the peak for both the unknown carbide and Fe₃C were used to calculate the Area k-ratio. From the same spectra the Peak k-ratio was established. In this way a total of about 600 spectra were recorded, for some carbides over the full kV range; for others, mainly between 4 and 12 kV. All spectra were stored on floppy disk. As these measurements required long dwell-times (up to 3 h) on the same spot it was found imperative to use some kind of anticontamination device; an air jet turned out to be the only efficient option in the long run. Finally, for improved statistics and to overcome the problem of slight inhomogeneities inevitably present in some carbides, a large number of peak k-ratio measurements were performed on 13 carbides at 9 different voltages between 4 and 30 kV. At each kV 50 measurements were carried out automatically on preselected areas of the specimen. This latter set

The authors are at the Laboratory for Physical Chemistry, University of Technology, P. O. Box 513, NL-5600 MB Eindhoven, The Netherlands.

of data, after multiplication by the appropriate A/P factors to yield the Area k-ratios, served as the database to which our correction program (BAS) was finally applied.

Results and Discussion

First it was established that the A/P factors for carbon were independent of voltage, contrary to earlier expectations,² and that those for the metals were equal to 1. Figure 1 represents the results of the A/P measurements for carbon. The conspicuous sawtooth-like appearance, which is completely synchronous with the beginning and ending of a new period in the periodic system, is caused by the fact that carbides of notoriously strong carbide-forming metals like Ti, V, Zr, and Nb tend to yield relatively narrow and unambiguous emission peaks, whereas carbides of elements like Si, Fe, Mo, and W tend to develop shoulders in their profiles. As a consequence profiles of the former group have most of their intensity concentrated in a small region centered around the position of the maximum, with the result that peak intensity measurements would lead to a pronounced overestimation. The reverse applies to the latter group. It is quite obvious that errors of up to 30% are possible if only peak measurements were carried out in the present case with Fe₃C as a carbon standard. This error range would even deteriorate to 50% if glassy carbon with its broader peak had been used as a standard.

Figure 2 shows the results of the peak k-ratio measurements relative to Fe₃C for TiC and ZrC which must be considered as two typical examples in the sense that in all carbides in which the absorption for C-K α radiation is lower than in the Fe₃C standard, the k-ratio vs kV-curve exhibits a kind of saturation after an initial rise, followed by a downward bend (see upper curve in Fig. 2). The opposite is always found in systems with stronger absorption (lower curve). As mentioned, we have tried to use the "thin film" model,³ to test the existing sets of mass absorption coefficients on their internal consistency. If ever the conditions for this model to apply were satisfied, it would surely be in the present case for C-K α radiation beyond 30 keV.

According to Duncumb and Melford,³ the limiting k-ratio can be written as:

$$k = \frac{\phi(0)_{\text{MeC}}^{\text{C}} \cdot (\mu/\rho)_{\text{Fe}_3\text{C}}^{\text{C}} \cdot \chi_{\text{MeC}}^{\text{C}}}{\phi(0)_{\text{Fe}_3\text{C}}^{\text{C}} \cdot (\mu/\rho)_{\text{MeC}}^{\text{C}} \cdot \chi_{\text{Fe}_3\text{C}}^{\text{C}}}$$

where $\phi(0)$ is the surface ionization (calculated according to Ref. 5), μ/ρ is the mass absorption coefficient, and χ is the weight fraction of carbon. The superscript refers to the type of radiation (C-K α) and the subscript to the type of carbide. Two of the most recent sets of mass absorption coefficients for the examples in Fig. 2 are given in Table 1, together with our own final values. The limiting peak k-ratios predicted by the thin film model using these various sets are indicated in Fig. 2 by dashed lines. It is evident that our set provides a better agreement between the predicted limiting k-ratio and the one extrapolated from the measurements up to 35-40 keV, than either of the other sets; and this conclusion is valid for all other carbides too.

Further support for the choice of the present mass absorption coefficients can be found in the results of the calculations of our correction program (BAS) in Fig. 3.

The fact that the calculated compositions are almost independent of voltage and the level merely shifts in a vertical direction according to the choice of absorption coefficients could be taken as an indication that the $\phi(\rho z)$ curves predicted by our model are at least fairly realistic. Anyhow, with the new set of coefficients a relative root-mean-square value (calculated/true composition) of 3.7% is obtained over 117 measurements, which shows that with proper care and procedures an accuracy can be obtained which is comparable to that of heavier elements. More details of this work will be supplied in separate publications.

FIG. 1.--Variation of area/peak factors for C K α radiation for various carbides relative to Fe₃C with atomic number of metal.

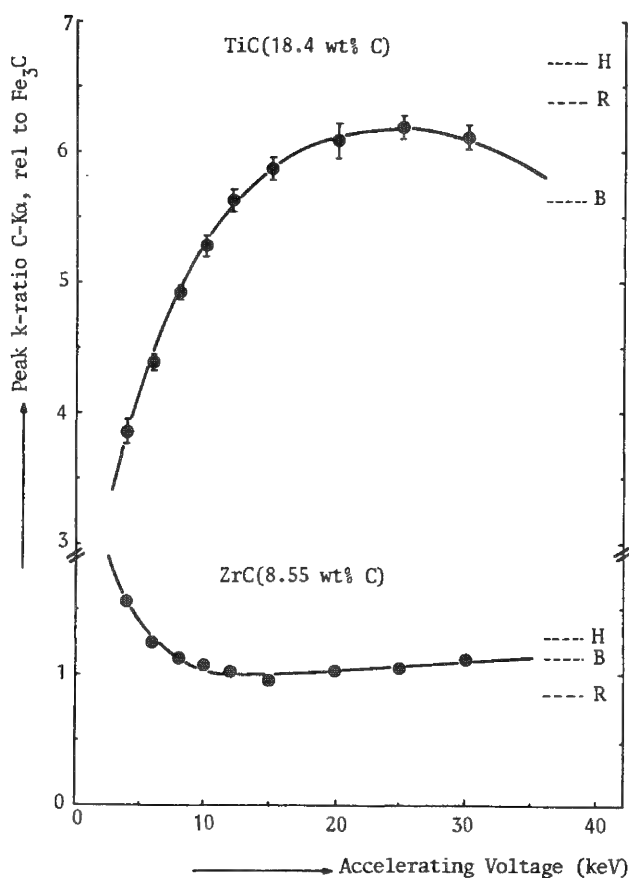
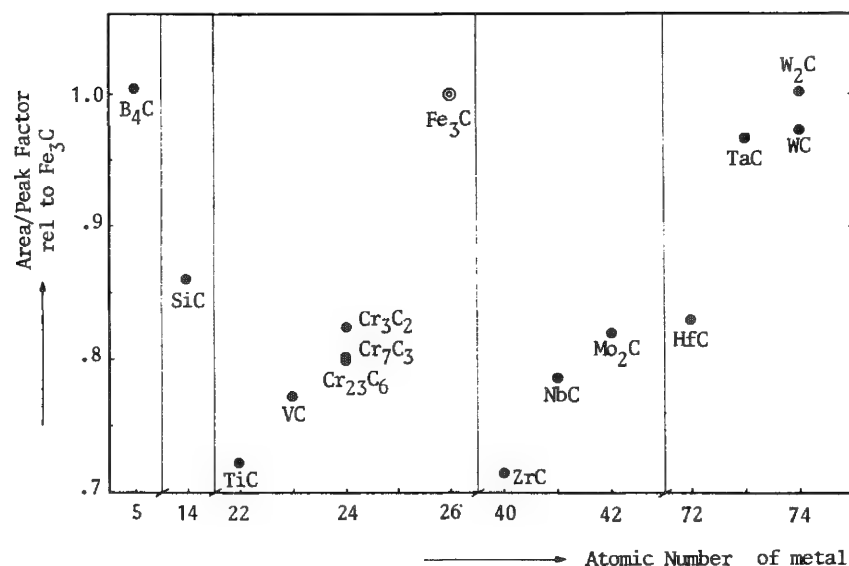


FIG. 2.--Peak k-ratios for C K α radiation relative to Fe₃C for TiC and ZrC versus probe voltage. Dashed lines indicate limiting k-ratio according to mass absorption coefficients of Henke (H),⁶ Ruste (R),¹ or present work (B). Bars indicate standard deviation. For ZrC measurements standard deviation smaller than dot size. Take-off angle 40°.

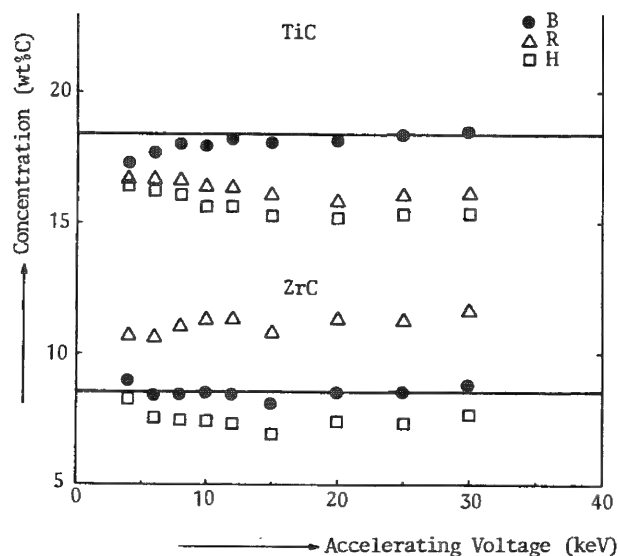


FIG. 3.--Compositions calculated according to BAS program. Results for different sets of mass absorption coefficients indicated (see also Fig. 2).

References

1. J. Ruste, "Principes généraux de la microanalyse quantitative appliquées aux éléments très légers," *J. Microsc. Electron.* 4: 123-136, 1979.
2. W. Weisweiler, "Elektronenstrahl-Mikroanalyse von Kohlenstoff: V," *Microchim. Acta* 1975(II): 179-194, 1975.
3. P. Duncumb and D. A. Melford, "Quantitative applications of ultrasoft x-ray microanalysis in metallurgical problems," in R. Castaing et al., Eds., *X-ray Optics and Microanalysis*, Paris: Hermann, 1966, 240-253.
4. G. F. Bastin, F. J. J. van Loo, and H. J. M. Heijligers, "Evaluation of the use of Gaussian $\phi(\rho z)$ curves in quantitative electron probe microanalysis: A new optimization," *X-ray Spec.*, 1984, in press.
5. G. Love, M. G. Cox, and V. D. Scott, "The surface ionisation function $\phi(0)$ derived using a Monte-Carlo method," *J. Phys. D-11*: 23-31, 1978.
6. B. L. Henke et al., "Low energy x-ray interaction coefficients: Photoabsorption, scattering, and reflection," *Atomic Data and Nuclear Data Tables* 27: 1-144, 1982.

TABLE 1.--Most recent sets of mass absorption coefficients for carbon K α radiation for the examples in Fig. 2.

Absorber	Mass absorption Coefficient according to		
	Ruste ¹	Henke ⁶	Present Work
C	2373	2350	2373
Ti	8094	8090	9400
Fe	13300	13900	13500
Zr	31130	21600	24000

DESIGN AT THE SOFTWARE-OPERATOR INTERFACE: CONSIDERATIONS ON PROGRAMMING FOR EFFICIENT USE OF MODERN INSTRUMENTATION

Thad Mauney and Pierre Van Espen

The time has arrived when essentially every major analytical instrument constructed has as an option, if not as a standard feature, an attached computer for control of the device and processing of measurements. New developments in instrumentation in the research laboratory commonly incorporate a computer as a peripheral if not a central part of the design. The scientist and scientific programmer must control a new breed of servants: how do we program these things so that using them is easier than doing without them? In this paper we consider some aspects of this problem, and propose strategies to avoid encumbrance with awkward or inappropriate software. We emphasize the problems involved with programming of dedicated real-time minicomputers interfaced to "major instruments" such as mass spectrometers, but many of the remarks apply equally to scientific computation in general.

Criteria

We contend that consistent criteria for evaluating program quality are identifiable, and that these criteria relate directly to the scientific utility of a program and its potential commercial value. The value of a scientific instrument control program depends on its ability to meet several simultaneous needs of the user.

1. The program must perform the computations necessary for the solution of a particular scientific problem with adequate accuracy, precision, and speed for the users' instrumental, scientific, and schedule requirements.
2. It must be user controllable by inputs that are easily read, understood, used, and remembered; this quality has come to be called "user friendliness."
3. The computations must be performed reliably, so that operator input errors or unanticipated instrumental output does not result in loss or corruption of data, in incorrect instrument operation, or in program crash; and that corrupt or unreliable data are neither generated nor accepted.
4. The program and its data should be shareable; the users often need to transfer data between programs, between computer systems, and between institutions, and the programs need to be exchanged between machines or between institutions. The structure of the program must facilitate these transfers.

In this paper we explore the second criterion, concerning the structure of communication between the program and its user, as a problem of scientific importance. Careful design of that communication in its linguistic structure, vocabulary, and display format is intrinsic to the production of programs that adequately solve scientific problems.¹

Operator I/O (Input/Output) as a Language

The procedure of interactive computation can be regarded as a man-machine conversation conducted in a special language. The structure of that language strongly influences the type, speed, quality, and content of the conversation, and thereby the value of the program; careful attention to the design of this language for efficiency of communication is intrinsic

The authors are at the Department of Chemistry, University of Antwerp (UIA), Universiteitsplein 1, B-2610 Wilrijk, Belgium. This work was supported by the Inter-ministerial Commission on Science Policy of Belgium through grant 80-85/10, and by the National Science Foundation of Belgium (NFWO).

to the development of high-quality programs. The program-user exchange of information is a language in the sense that it consists of a finite set of elements (numbers, words, mnemonics, special keystrokes, or other signs) governed by a set of grammar rules laid down explicitly or implicitly in the program.² The grammar of user input may permit only a predefined sequence of entries, or may allow a wide variety of complex strings to be entered. Program output is also a language, though quite restricted, consisting of symbols, numbers, and words that indicate the state of the program or the content of memory locations. One can examine the structures of these languages, list the valid elements, and specify the grammar, and thereby locate inconsistencies that complicate both program structure and user training. As a framework for comparison we classify user input languages into five levels of structure and list some properties of each.

1. *Modified batch mode.* The user must input a sequence of elements in a predefined order, with or without program prompts, and each program or program section executes as a single process. Although the program runs concurrently with the user input, that can hardly be called interactive computing.

2. *Sequential conversation structure.* The user may select branches at predefined program steps that tailor the executed process to the current task, e.g., PLOT/NO PLOT, LOG/LINEAR, or pause till ready. We term this a sequential input language because the order of allowed inputs is fixed within the program. The grammar consists of lists of allowed entry elements for each program step, and the allowed vocabulary can differ from step to step. Such structures can be represented by tree-type branching diagrams.

3. *Command interpretation.* In this structure the element entered by the user initiates a process within the program, and, after executing a process, the program returns to a state awaiting further input. These "verb" inputs may be used in any order desired provided that it is consistent with the logical necessities of the system, for example to load data before plotting a spectrum. These structures can be represented by diagrams of the program states, indicating all of the processes and allowed transitions.¹

4. *Extended command interpretation.* Additional data can be entered along with the command verbs if the grammar includes with the table of verbs, tables of data specifiers, data formats, and rules for ordering and separation in an input sentence. One highly efficient and widely used type of grammar is the leading verb command language, which places data with specifiers, as needed, after the verb and before carriage return.

5. More complex structures may allow redefinition of language elements, definition of "macro-instructions," or even the use of an interpreted programming language on line for instrument control. These structures are appropriate in some cases, but involve complexities outside the scope of this paper.

Examples

Some distinct levels of sophistication in program control and I/O implementation can be compared in three programs for instrument automation developed over the last few years in our laboratory. Two programs, LAM³ and OLDLAM,⁴ acquire and process spectral data from a laser microprobe mass spectrometer (Leybold-Heraeus LAMMA 500), and SIDAP⁵ (Sims Data Acquisition Program) controls a secondary ion mass spectrometer (Cameca IMS-300). All run under RT-11 on DEC LSI-11 processors. Differences between the programs reflect differences in needs at time of development and differences in the tasks appropriate to the instruments.

The initially developed package for LAMMA control, called here OLDLAM, is a collection of semi-independent programs related through their common data set. Within each program, for example the spectrum acquisition program, user input is prompted and must be entered in fixed sequence. When a different function, say displaying a spectrum, is required then a separate program is run, in which user input is again fixed in sequence with prompts from the program. This structure addressed the need of the laboratory for rapid implementation of a usable basic system, but has several drawbacks:

- Transfer of data between modules is cumbersome
- Modules include large sections of redundant code
- Operator time is wasted on disk access in loading programs for each function
- Installation of new functions involves still more redundant code

To streamline data processing, the recent program LAM combined all the instrument-control and data-manipulation functions into one program (overlaid) which accepts command words and initiates appropriate processes. This scheme greatly speeds the response and minimizes the number of user entries required at each step since all of the current status information is available to all modules through common storage blocks. In addition, the implementation of a command interpreter allowed the use of verbs from natural language as commands to simplify training of operators. In this program three distinct grammars are operational at separate program levels: the command level consists of a grammar of verbs only, shortening of which to the minimum unambiguous form is allowed; within each process data entry is sequential, with program prompts, and where a default is appropriate a carriage return alone selects the default; an exception is the spectrum display process, within which special function keys are enabled and subprocesses are initiated by the implicit verbs of the special keystrokes.

The structure of SIDAP is similar to that of LAM in that all processes are contained within one program and a command interpreter initiates user-selected processes; a more complex grammar permits data to be included in the command line after the verb of the form

VERB[/Data_specifier[=Data]][/Data_specifier[=Data]][/...]

where the square brackets [] denote optional elements. This procedure enables the parameters of the process to be input when a change is needed, but otherwise the previous or default values are used. The language elements are thus the verb, specifying the process to be executed; the data descriptor, marked by a leading slash /, specifying which parameter is to be changed; and the datum, marked by a leading equivalence sign =, specifying the new value by a numeric or alphanumeric string.

The data descriptor(s) and datum(a) are parsed from the command line as the verb is interpreted, so that these elements are optional and position independent. Interpretation of the data descriptor and datum is made within the process activated by the verb, so the command interpreter need not include highly function-specific code. This construction reduces user input because redundant parameter information need not be given, for example in repeating a depth-profile analysis. Compactness of the input is increased by permitting abbreviation of the verbs and data descriptors to the minimum unambiguous form. Complex tasks can be controlled through the many data descriptors; though only a few are used in ordinary work, all possible instrument controls are accessible through the command lines.

In these examples various syntaxes have been used for particular scientific needs. Where the number of optional parameter entries is large, as in the SIMS case, a leading-verb syntax makes things easier. When few instrumental parameters are computer controlled, as in the LAMMA case, the language was simplified by omitting the possibility for trailing data. Where a process requires user input for completion or where certain inputs should be enforced (e.g., logging the LAMMA laser intensity), prompted sequential syntax is used.

When several syntaxes are employed within a program it is easy to become careless in programming and write routines *ad hoc*, forgetting considerations of consistency. Experience has convinced us that for simplicity in program structure, program maintainance, and user training, when several syntaxes are used in a program these syntaxes should carefully be kept consistent among the various processes.

Selection of Vocabulary

Great value must be placed on wise selection of vocabulary of both the input and output languages. The vocabulary determines the number of keystrokes required for each entry, and the ease of learning and remembering the language. There is currently a trend toward so-called "natural language entry," but it is important to distinguish between the use of elements with appropriate cognate words in natural language and the application of natural-language grammar. For keyboard entry genuine natural language is too cumbersome. Natural language is verbose; it must be so in order to accommodate the complexity of concepts humans wish to convey, and it must include redundancy to minimize miscommunication. We contend that I/O languages, in order to be efficiently used, must consist of sequences of elements which are clearly and correctly meaningful in the natural language of the user, but which are grammatically simplified from the natural language to be compatible with the I/O hardware employed.

Program I/O creates conventions in nomenclature used in the laboratory by the workers, so that it is significant to examine whether that nomenclature is well planned and scien-

tifically appropriate. To avoid degradation of human communication, the computer-operator language should be designed so that every language element is used in a way which is logically consistent with its cognate in the human scientific language. We can see no excuse that would justify implanting a new name in the language of the laboratory where a simple, logical, and widely understandable word from natural language would suffice, yet commercial and university programmers are alike guilty of inventing cute names, confusing nouns and verbs, and using hashed variable names in output.

Conclusions

Communication between humans and computer programs is conducted in an artificial language, the quality of which influences the quality of scientific work done with that program. As a step in program design, this language can be subjected to syntactic analysis like any other language. The potential benefits of this analysis include improvements in

- teaching the language to users
- use of the syntax checking in input error detection
- avoidance of awkward program structures
- efficiency of program construction
- minimization of I/O dedicated code

For instrumentation programs we favor a command interpreter structure, where the commands have direct cognates in natural language. We feel that the leading-verb command syntax is useful for most automated instruments found in the laboratory at present. The I/O language is an intrinsic part of programs, often occupying over half their length. Implementation of a command interpretation package that could be applied to new instrumentation problems by changing only vocabulary tables and process subroutines would be a valuable contribution to the community; it would increase programming efficiency, operator efficiency, and transportability of programs. Finally, we point out that because the quality of communication between user and program so strongly influences its utility, the commitment of time and effort to careful design of this communication (which in our experience can easily exceed half the programming effort) is well rewarded and should be accepted by both the programmer and the laboratory supervisor.

References

1. W. M. Newman and R. F. Sproull, *Principles of Interactive Computer Graphics*, New York: McGraw-Hill, 1973.
2. D. Gries, *Compiler Construction for Digital Computers*, New York: Wiley, 1971.
3. H. Nullens, University of Antwerp, unpublished 1981.
4. T. Mauney, University of Antwerp, unpublished, available from the author, 1983.
5. M. Van Craen, P. Van Espen, and F. Adams, "A versatile and user-friendly computer system for the CAMECA IMS-300 secondary ion mass spectrometer," *Rev. Sci. Instrum.* 53: 1007-1011, 1982.

THE APPLICATION OF AN AUTOMATED MICROPROBE PROCEDURE FOR THE EVALUATION OF ELEMENTAL SEGREGATION IN ALLOYS

R. V. Heyman

High-temperature, high-strength superalloys are generally processed through an intricate melting, remelting, and forging process into wrought product forms. These products are typically used as blade support rotating disks for land-based and aircraft turbines. Such applications call for stringent quality standards. One of the factors that affects the mechanical properties of these alloys is the extent of elemental segregation, as they tend to exhibit heavy elemental segregation. Since it is not practical to eliminate all the segregation, a rapid, reliable, and reproducible method for measuring its extent is required. The Electron Microprobe has proved to be a very useful tool in measuring segregation.

At the 1983 meeting the many changes in the ARL software that this rapid measurement required was outlined. In review, a central rectangular region of a standard metallographic sample $7500 \times 7000 \mu\text{m}$ is analyzed. If the alloy has not been analyzed previously, a complete Bence-Albee or Magic ZAF quantitative analysis for all 200 randomly selected points within this region is performed, to yield a reference for later rapid analyses. A rapid procedure is necessary because a normal 7 to 8 element analysis of 200 points takes 12-18 h, and a rapid analysis of up to 4 elements at 100 different points takes 3-6 h. The rapid procedure is performed in the following manner. A complete ZAF analysis at a randomly selected location for all the relevant elements in the alloy is followed by peak-only measurements at various randomly selected locations for a specified number of "key" elements (no more than the number of spectrometers) for an operator-specified number of analyses. A complete ZAF analysis is then performed at another randomly selected location. The cycle is then repeated until all but one of the required analyses are done. The last analysis is always another complete ZAF analysis. In this manner, a data file is obtained containing approximately 100-200 analyses from 100-200 different locations. All the data are stored on a flexible disk for later use.

Additional software is required to make comparisons among various alloy production parameters practical. An editing routine removes spurious results caused by analyses of included carbides or nitrides. The data for each element are then plotted on a cumulative probability plot. Under ideal conditions, and given a sufficiently large statistical population, the plot is a straight ascending line whose slope is a measure of the segregation. A typical plot is shown in Fig. 1. However, a normal histogram plot is sometimes also necessary so that the presence of possible bimodal phase formation can be checked graphically (Fig. 2). If the same y axis "windows" are used for the plots of two different analyses of samples formed under two different melting procedures, a qualitative comparison is very simple. These plotting routines have been written in ARL basic and transmit HPGL instructions through a DL-11 board with an RS.232 interface to a Hewlett-Packard 7470A plotter.

In the following example, the Electron Microprobe was run at 25 kV. A $10\mu\text{m}$ -diameter beam was used for P917 and a $20\mu\text{m}$ -diameter beam was used for P931. Previous examination of this alloy showed that this change in beam size has a negligible effect on the results. Work with various alloys has shown that any beam size focused to $75 \mu\text{m}$ or less is usable, but that depends somewhat on the alloy being analyzed.

Figures 3 and 4 are plots of the alloy 718 after treatment at two different homogenization cycles. The sample represented in Fig. 4 was treated at a higher temperature and for a longer time than that in Fig. 3. (This is the type of data we wanted to obtain, as it allows us to select the optimum time and temperature parameters that produce the most homogeneous alloy possible and to evaluate the effect of changing these parameters.)

The author is at Cameron Iron Works, Box 1212, Houston, TX 77251.

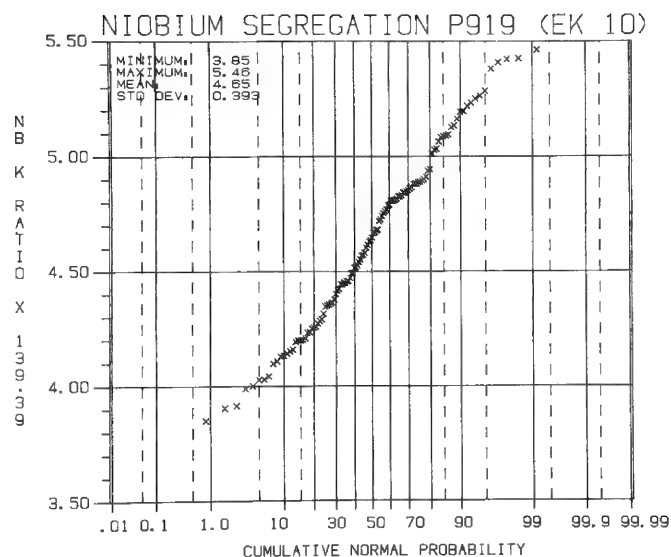


FIG. 1.--Typical segregation probability plot (718 alloy).

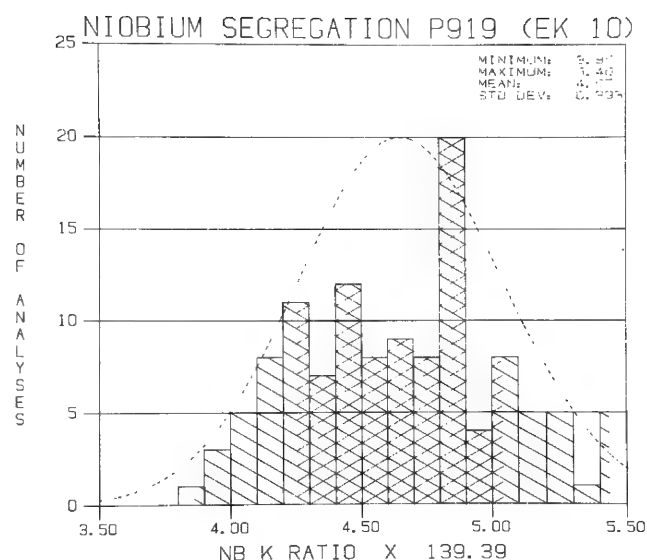


FIG. 2.--Typical segregation histogram plot (718 alloy).

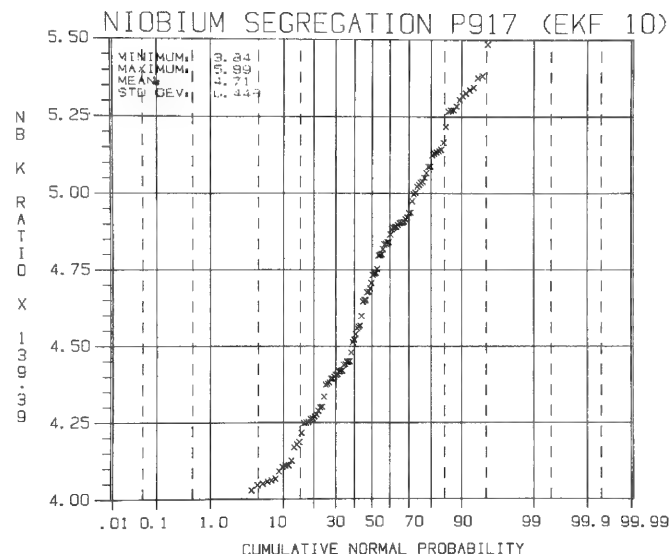


FIG. 3.--718 alloy segregation after homogenization cycle.

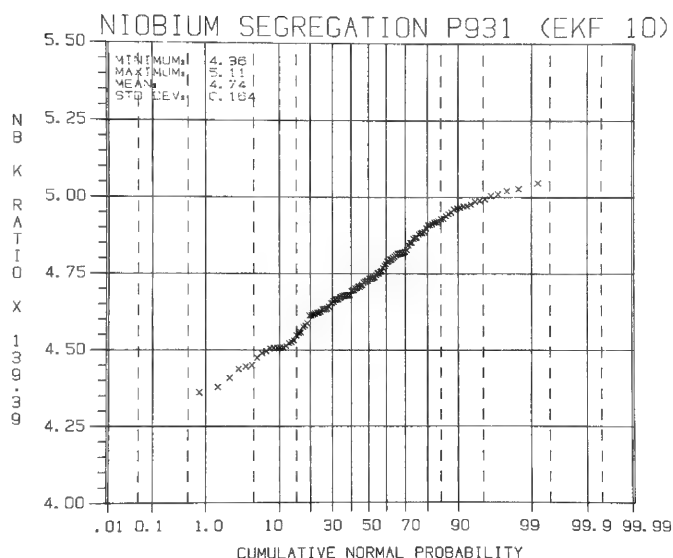


FIG. 4.--718 alloy segregation after longer homogenization cycle at higher temperature.

However, the rapid-analysis technique must be applied carefully to avoid a dangerous pitfall. Since the rapid-analysis runs generate only k ratios, an average of the corrections generated by the complete analyses made in a rapid run is calculated. This average is then used to correct all the rapid-analysis values prior to plotting. Usually this procedure works very nicely and gives results comparable to that of a complete analysis run (Figs. 5 and 6). However, for some elements in some alloy systems, the procedure breaks down (Figs. 7 and 8). The exact reason for the breakdown is not known at present; perhaps the correction factor is changing too rapidly with concentration for an average correction factor to be usable in this concentration range. Therefore, the rapid system must be qualified by a comparison of the results obtained by it with the results obtained by the slower full-analysis system for each element of each alloy that is to be analyzed with the rapid system.

These segregation analysis procedures (both rapid and all-element) have proved themselves to be reliable qualitative procedures for determining the degree of elemental segregation (nonhomogeneity) present in the alloys that we produce, which has resulted in a refinement of our melting procedures and helps us to produce a higher-quality alloy at a lower cost than was previously obtainable.

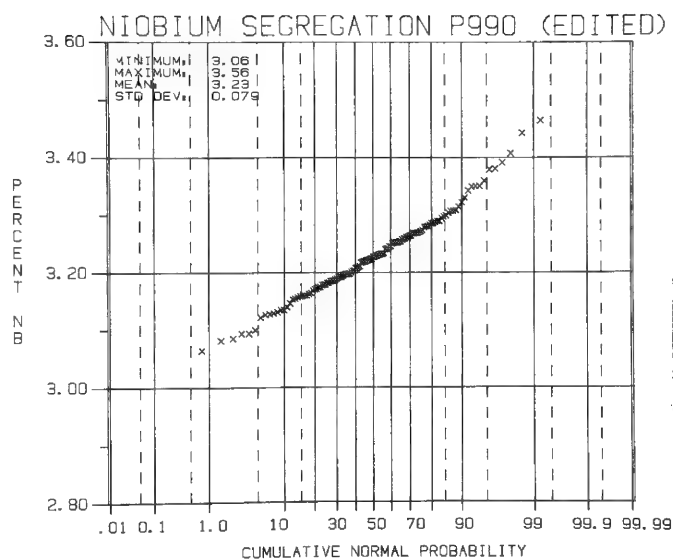


FIG. 5.--Nb segregation in René 95 from all-element analysis.

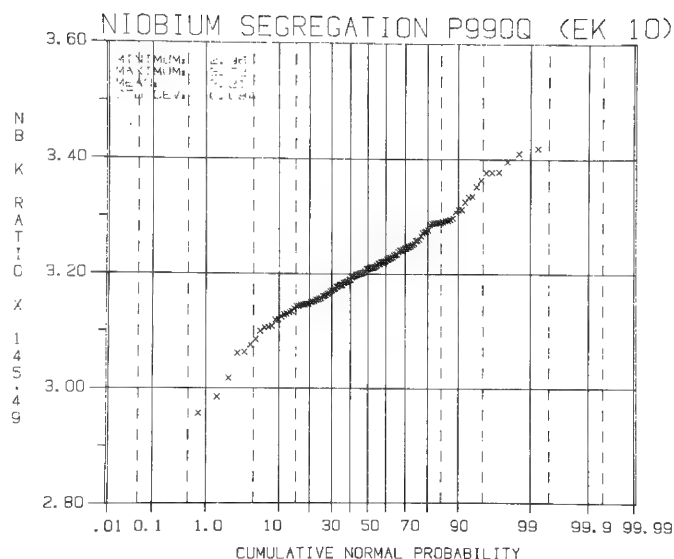


FIG. 6.--Nb segregation in René 95 from rapid analysis.

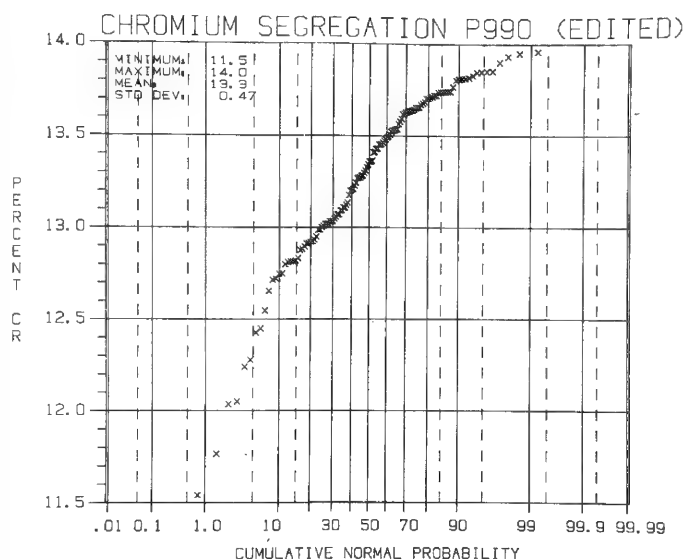


FIG. 7.--Cr segregation in René 95 from all-element analysis.

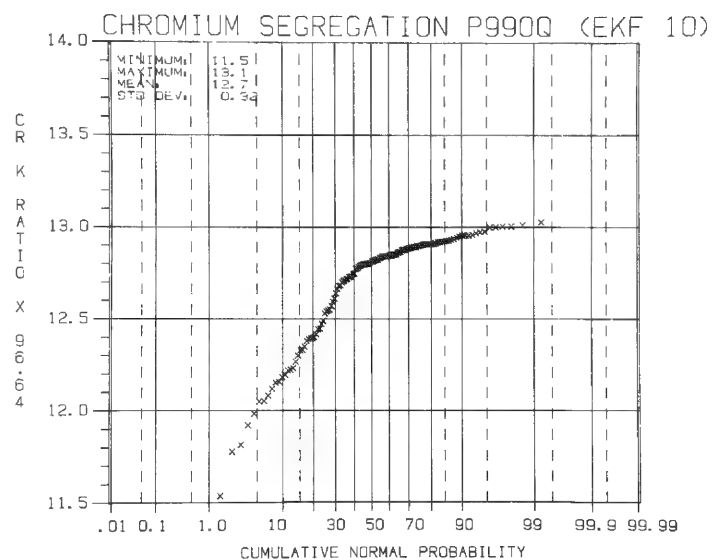


FIG. 8.--Cr segregation in René 95 from rapid analysis.

15 Materials Applications

SEGREGATION ANALYSIS OF MELT-GROWN CRYSTALS OF Fe-Ni ALLOYS WITH THE USE OF ELECTRON MICROPROBE

Ram Sellamuthu and J. I. Goldstein

The segregation behavior of solute elements is of importance in the preparation of materials by zone refining and the Czochralski process. We have carried out the present study to understand the segregation behavior of S, P, Ge, Ir, and C in melt-grown crystals of Fe-Ni alloys.

Experimental

Alloy crystals were grown from the melt by the Bridgman technique in which the liquid alloy, contained within an alumina crucible, was withdrawn from a gradient heating furnace at a slow rate. This procedure promotes the growth of solid crystals with a planar solid-liquid interface. The details of this procedure and the master alloy preparation methods have been given previously.^{1,2} The compositions of the alloys used in this study are listed in Table 1. Figure 1 illustrates the general microstructural features of alloy 1, melt-grown with a planar interface. The microstructure consists of a proeutectic phase, γ (f.c.c.), and two eutectics. Small amounts of sulfide inclusions form within the proeutectic phase. The phosphide eutectic consists of γ , $(\text{FeNi})_3\text{P}$, and FeS. The sulfide eutectic consists of γ and FeS.

A JEOL 733 microprobe with an automated stage was used. X-ray intensities were measured by wavelength-dispersive spectrometers (WDS). An accelerating voltage of 15 kV was used to obtain optimum peak-to-background (P/B) intensities for elements with high (Fe and Ni) and low (P and S) characteristic x-ray energies. For Ge and Ir, 30 kV was used to obtain a high P/B ratio. To obtain a large number of x-ray counts, a high beam current (100–200 nA) was used. The x-ray counting times used for P, Ge, and Ir were between 60 and 200 s. Pure elements were used as standards for Fe, Ni, Ge, and Ir; FeS and $(\text{FeNi})_3\text{P}$ were used as standards for S and P, respectively. By linear interpolation, the value of the background intensity at the peak position was determined from the values of x-ray intensities measured at slightly above and below the characteristic wavelength.

X-ray intensities for Fe, Ni, S, and P were measured with an operating voltage of 15 kV and a $50 \times 50 \mu\text{m}$ raster scan at intervals of about 1 mm along the crystal. Smaller intervals were used near the end of the proeutectic region. Since the sample is about 15 mm long (Fig. 1), it was possible to use broad-beam analysis without sacrificing spatial resolution. The x-ray data were converted to compositions by a ZAF matrix correction program. If the alloy contained either Ir or Ge, the data were retaken at 30 kV. The computer-controlled specimen stage in the microprobe was used for relocating the sample during the second run. In the eutectic region, 20 to 40 measurements were made to obtain an average composition of the eutectic.

Meteoritic cohenite $(\text{FeNi})_3\text{C}$, which contains 6.67% C, was used for the C standard. The background intensity was measured on a C-free Fe-Ni ferrite sample. A liquid-nitrogen cold finger was used to minimize C contamination of the sample. X-ray data were obtained for 60 s with a defocused beam of $20 \mu\text{m}$ in diameter, a beam current of 100 nA, and an operating voltage of 5 kV. The use of a low voltage reduced the x-ray absorption effect for C. Two methods for data reduction were employed. In the first method, the x-ray data were converted to composition by a ZAF calculation. In the second method, a calibration curve of x-ray intensity for C, less its background, measured in Fe-Ni-C alloys of known compositions vs wt% C was constructed. The background-corrected x-ray data for C obtained from the melt-grown alloys were converted by interpolation to composition with the use of the calibration curve.

The authors are at Lehigh University, Bethlehem, PA 18015. NASA support under grant NAG 9-45 is acknowledged.

EFFECT OF SCALE ON INTENSITIES FROM HETEROGENEOUS ALUMINUM BRONZES

Inge Simonsen, T. M. Hare, and J. C. Russ

It is well known that the classic quantitative correction routines assume that the specimen being analyzed is a homogeneous mixture of the elements present. If each element were present simply as a solid, pure block of material, adjacent to other pure islands of the other elements present, there would be no interelement effects, and the measured K-ratios would simply be the area fractions of each element. In other words, the Z, A, and F factors would all be unity. Many real samples have a structure which is heterogeneous, and applying ZAF corrections to the measured intensities may be inappropriate. The degree or size scale of the heterogeneity that will affect the results depends on the specific elements present and the conditions used for analysis.

To illustrate this problem, we prepared a specimen of aluminum bronze (11.8% Al, 88.2% Cu). This produces a fine martensitic structure when quenched, but can be heat treated by holding at temperatures just below the eutectoid transformation temperature (565 C) to produce pearlitic (lamellar) structures with varying interplanar spacings. The two phases that are present contain 9.4% Al and 15.6% Al, respectively. Figure 1 shows a representative microstructure.

Regions about 40 μm in diameter were analyzed in these samples, by spreading of the electron beam. The accelerating voltage used was 20 kV, and the takeoff angle in our microprobe (AMR-1) is 15° . Pure aluminum was measured before and after each series of 5 analyses, and values were interpolated to obtain K-ratios for each measurement. After measurement, the mean free spacing was determined from photomicrographs, with the contamination marks on the specimen surface used as guides.

The data show that the aluminum intensity (K-ratio) for very fine lamellar samples (down to the 0.5 μm limit of our measurement technique) were substantially lower than the intensities from coarser structures. Figure 2 shows a plot of the results. The trend toward higher intensities at larger mean free spacings is quite clear.

An additional experiment was performed on two locations which contained visually uniform lamellae, one with a rather fine spacing and the other somewhat coarser. These regions were measured twice, once with the lamellae aligned perpendicular to the x-ray takeoff direction, and again aligned parallel to the direction. The latter condition produced higher measured Al intensities. The two vertical bars in Fig. 1 show the intensity values from these measurements. Of course, we do not know whether the lamellae chosen were actually perpendicular to the surface or not.

On a qualitative basis, it is clear that these data illustrate the effect of different absorption of the aluminum x rays in passing through the different phases, which have quite different mass absorption coefficients for the relatively low-energy Al $K\alpha$ x rays. The increased intensity from the high-aluminum phase, when the absorption is reduced because of the lower copper content, is significant. The magnitude of the effect would be much smaller for a higher energy line, or with a higher takeoff angle. For the case of the rotation experiments, there may also be some effect of surface relief due to the etch applied to the material to reveal the structure, but the data seem in general consistent with the balance of the measurements.

The mean depth of excitation of Al $K\alpha$ x rays in this material is about 0.3 μm , and with a 15° takeoff angle, this means that the emitted x rays pass through a lateral distance of well over 1 μm . If the x rays encounter predominantly one of the two phases present, the emitted intensity will depend on the individual phase mass absorption coefficients, rather than that of the average composition of the matrix. Since absorption is an exponential

The authors are at North Carolina State University, Raleigh, NC 27695.

function, the intensities from each phase do not add to give the same result as would be obtained from the homogeneous material with the same mean composition.

Computing the effect of microstructural scale requires some assumptions about the geometry of the phases involved. The eutectoid structure typical of aluminum bronze (and common steel) may be approximated by parallel plates of the two end member phases, since the spacing is quite uniform over the distances relevant to analysis. Of course, there is a variation in the observed spacing of the lamellae due to the orientation of the plates with respect to the polished surface. The expected relative intensity from a randomly oriented microstructure is obtained by numerical integration over all possible angles of plate orientation (inclination angles) and surface orientation (angle between lamellae and spectrometer).

The integration considers the phase where the x rays originate, the path length, and the relative proportion of each of the absorbing phases along the x-ray path. The relative densities (7.68 and 6.93 g/cc) and weight fractions of each eutectoid phase are used to determine the absorption coefficients. The point of origin (generation) is varied in both the z direction, according to Brown's $\phi(\rho z)$ function,¹ and from all lateral positions from the middle of one lamella through one repeat cycle. Two histograms are obtained for the probability that an x ray generated from each of the two phases (for all depths of excitation) encounters a given composition.

The shape of the generation curves are similar in both phases, and so the total generated aluminum K α intensity was taken as proportional to the weight fraction of Al present in each phase. By weighting with the geometric probability functions, one can compute the expected relative intensity measured for each surface orientation. When these intensities are summed over all angles, the curve in Fig. 3 is obtained. On the arbitrary intensity scale used, 1 corresponds to the case where all x rays generated in each phase are absorbed only in that phase, and zero corresponds to complete homogeneity. The shape agrees qualitatively with the observed data, and shows the effect of lamellar spacing on measured intensities. Note that even for quite coarse spacings, the curves approach 1 very slowly.

This procedure is much more direct and rapid than Monte Carlo calculations for the same range of possible microstructures and orientations. Any other structure, including one with preferred orientations, that can be described analytically, so that the integration over all orientations can be performed (for instance, spheroidized precipitates), should be susceptible to the same procedure.

References

1. J. D. Brown and W. H. Robinson, *Microbeam Analysis*--1979, 238.

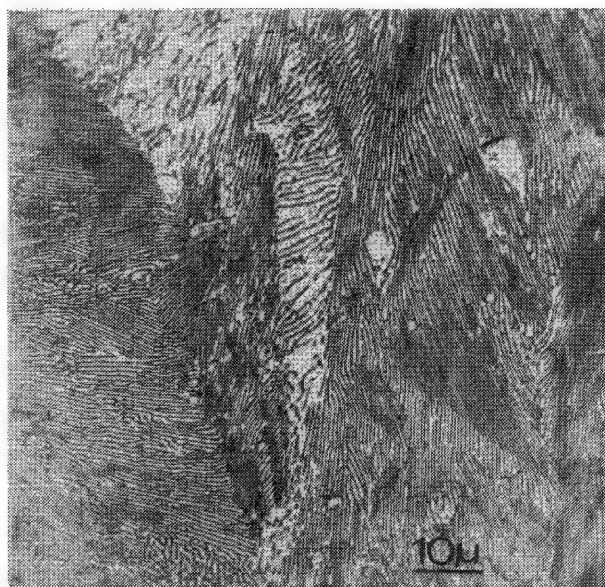


FIG. 1.--Representative eutectoid microstructure of aluminum bronze.

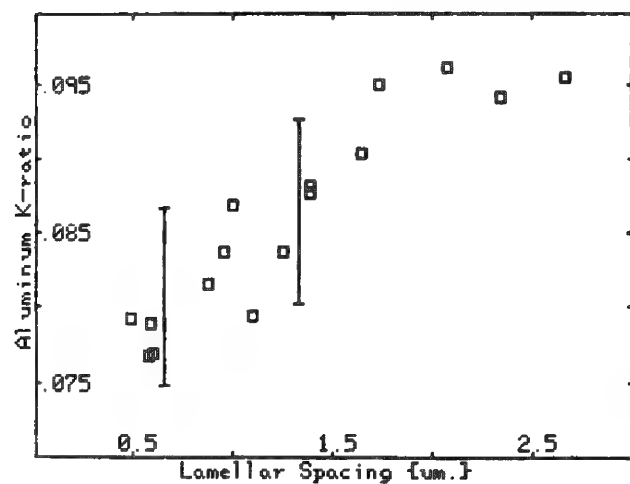


FIG. 2.--Measured aluminum K-ratios (points) on eutectoid structures with varying lamellar spacings. Vertical bars show measurements on two individual regions, with orientation parallel or perpendicular to x-ray takeoff direction.

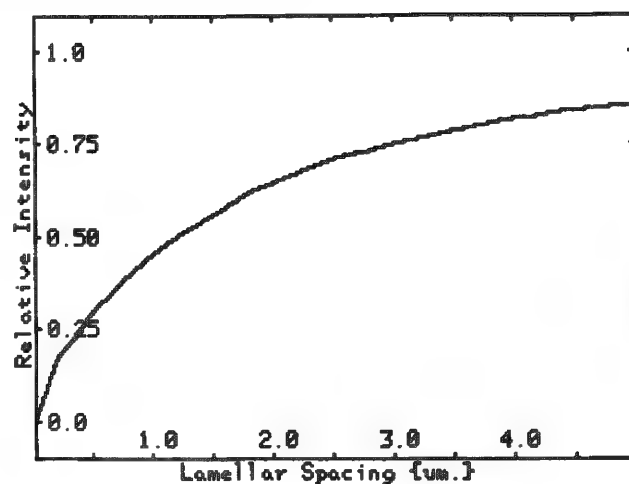


FIG. 3.--Calculated variation in intensity as function of lamellar spacing, by use of numerical integration with depth and analytical integration over all possible orientations of lamellae.

WIDE-ANGLE ECP OF INSONATED ALUMINUM

K. R. Breen, P. J. Moran, and A. M. Leimkuhler

Wide-area Electron Channeling Patterns (ECP) and SEM photomicrographs were taken of an aluminum rod, predominantly single crystal, before and after insonation at 20.5 kHz. The approximately one-half wavelength (resonant length) rod showed a localized region of deformation about 10 mm wide with prominent slip lines. The ECP exhibited change only in the deformation region. In this region there was a narrowing of the 200 and 311 channeling bands followed by a shift in the channeling pattern. Changes in the pattern's orientation combined with SEM micrographs of the specimen surface will be further studied in an attempt better to understand ultrasonically produced deformation.

The study of the effects of ultrasound on metals is of interest to material scientists and microscopists alike. It has been studied by those interested in metal fatigue and failure analysis¹ and by those interested in material processing. Ultrasound superimposed on static stress has been found greatly to reduce the amount of static stress required for plastic deformation, and thus aid material processing.²

Microscopists in particular have shown interest in this topic. Langenecker³ in 1966 applied 20kHz ultrasound to a thin section of aluminum for in situ observation in a transmission electron microscope and found an increase in dislocation density. Kromp et al.⁴ have looked at surface fatigue damage due to insonation at 20 kHz of polycrystalline copper specimens of resonant length in the SEM. Stickler et al.⁵ used selected area electron channeling patterns (SA ECP) to examine ultrasonically induced fatigue failure in a 316 stainless steel tube.

A comprehensive review of ECP theory, practice, and applications has been presented by Joy et al.⁶ ECP result from signal variations that occur as the angle between the incident beam and the crystal lattice of the specimen is varied. ECP degrade with crystal deformation; thus, by calibration with samples of known deformation, elastic⁷ and plastic⁸ deformation may be measured. Wide-area ECP are obtained when an SEM is operated at low magnification (approximately 20 \times) on a large single crystal. At this magnification the angle variation is the scan angle itself.

Experimental

A specimen was fashioned from an aluminum rod 10 mm in diameter by machining of screw threads on one end to allow attachment to an ultrasonic horn. The rod was single crystal except for a small, secondary crystal at the other end, approximately 0.5 cm³ in volume. A flat 8 mm wide and 102 mm long (80% of resonant length) was mechanically polished parallel to the specimen axis. To remove the surface damage from grinding, the sample was rotated in a chemical polishing solution of 75% orthophosphoric acid, 12% glacial acetic acid, 3% nitric acid, and 10% water at 95-100 C.⁹

Wide-area ECP were taken in an ISI 60A SEM equipped with a Robinson backscattered detector. The operating voltage was 30 KeV, the emission current 10⁻⁴ A, and the incident current (measured in a Faraday cup) was of the order of 10⁻⁷ A. In order to decrease the divergence angle as recommended by Joy,⁶ the final lens was on, but at only a low percentage of the voltage needed for focusing on the aluminum surface to occur. The sample was positioned at a working distance (W.D.) of 10 mm but the final lens was set for a W.D. of 45 mm, which amounted to reducing the current to the final lens to 10 to 20% of its normal value.

Author Breen is a graduate student and author Moran is an assistant professor at Johns Hopkins University (Department of Material Science and Engineering), Baltimore, Md.; author Leimkuhler is at David Taylor Naval Ship Research and Development Center, Bethesda, Md.

A sample holder (Fig. 1) was made for the aluminum rod with opposing screws along its length to hold the sample in position and to act as markers. A piece of silicon single crystal of (112) orientation was affixed to the holder for reference to act as a channeling standard. For each ECP the specimen current was set on the silicon crystal to approximately 115×10^{-9} A, which resulted in a specimen current of 120×10^{-9} A on the aluminum crystal. Photomicrographs of aluminum were taken at two angles to allow two channeling bands 200 and $31\bar{1}$ to be examined.

The sample was insonated with a Branson Tapped Catenoidal horn at 20.5 kHz. The power was supplied with an ENI model EGR-1600 power generator matched with an ENI model EVB-1 piezoelectric transducer matchbox. The technique for measuring displacement amplitude positions along the specimen's length was taken from Sirian et al.¹⁰ A point-contact piezoelectric detector acted as an amplitude detector. Relative amplitude vs position measurements were taken on a sample insonated at a low power level. Actual displacement measurements at the experimental power level were made by direct observation in an optical microscope and used to scale the relative measurements. Several low-power insonation runs were made on the sample to ascertain displacement amplitude curves prior to the high-power run that caused deformation. The high-power insonation at 20.5 kHz lasted approximately 1 min (1.2×10^6 cycles) and resulted in the appearance of slip lines near the middle of the specimen and sample heating.

Results

The appearance of slip lines delineated a localized region of deformation near the center of the aluminum specimen where maximum strain of a resonant length crystal would be predicted. The maximum strain on the specimen, E_{\max} , was calculated from the relation $E_{\max} = kE_0$, where the wave number $k = 2\pi/\lambda$ and E_0 is the maximum displacement amplitude.¹⁰ The maximum strain was found to be approximately 4×10^{-4} .

The bright area near the center of the aluminum rod shown in Fig. 1 is the deformation region. This region may be broken down into two zones. Photomicrographs of the first zone show a braided appearance crossed by slip lines (Fig. 2). In the second zone, slip lines are still present but the deformation braids are more tightly spaced. The ECP of the first zone show a marked reduction in the width of the 200 and the $31\bar{1}$ bands (approximately 30%). In the second zone both these bands are shifted, perhaps due to rotation within the crystal. No obvious linewidth or image contrast degradation was apparent in these two zones, although more quantitative analysis is in progress. These results and those of further tests will be used to help understand ultrasonic deformation mechanisms.

References

1. W. A. Wood and D. E. MacDonald, "Metal fatigue at ultrasonic frequency," *Proc. 1st Int. Symp. High Power Ultrasonics*, 1970, 50-52.
2. B. Langenecker, "Ultrasonic treatment of specimens in the electron microscope," *Rev. Sci. Instr.* 37: 103-106, 1966.
3. *Ibid.*, p. 103.
4. W. Kromp et al., "Direct observation of surface fatigue damage in the SEM," *Metallurgical Trans.* 4 (April): 1167-1169, 1973.
5. R. Stickler et al., "Application of the SA-ECP method to deformation studies," *SEM/1971 I*, 473-480.
6. D. C. Joy et al., "Electron channeling patterns in the scanning electron microscope," *J. Appl. Phys.* R81-122, 1982.
7. G. E. Davis and M. E. Taylor, "A new method for the investigation of stress in MIS devices using SEM electron channeling patterns," *J. Vac. Sci. Technol.* 19: 1024-1029, 1981.
8. A. W. Ruff, "Deformation studies at sliding wear tracks in iron," *Wear* 40: 59-74, 1976.
9. W. J. Tegart, *The Electrolytic and Chemical Polishing of Metals in Research and Industry*, London: Pergamon Press, 1959.
10. C. R. Sirian et al., "Method of measuring elastic strain distribution in specimens used for high frequency fatigue testing," *Proc. Intern. Conf. Fatigue and Corrosion Fatigue up to Ultrasonic Frequencies*, Engineering Foundation, Champion, Pa., USA, 25-30 October 1981, 1-16.

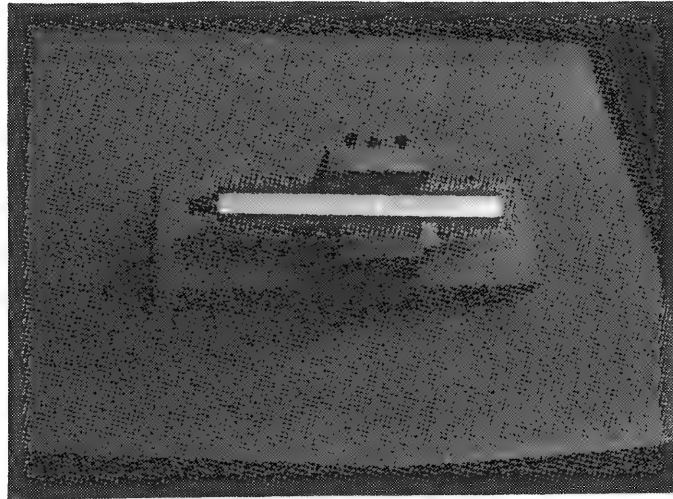
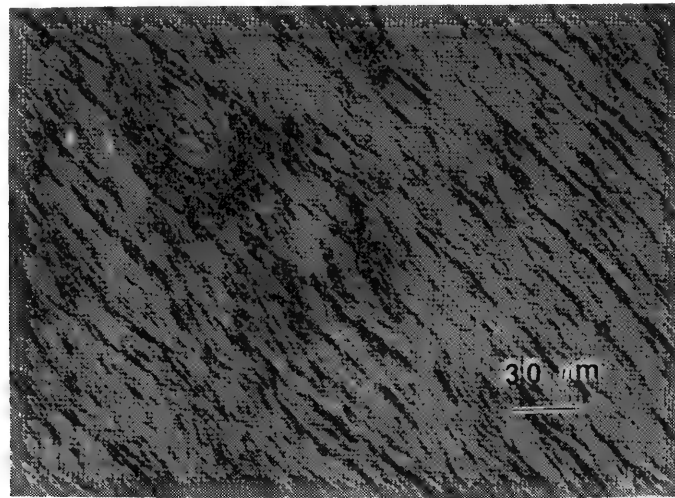
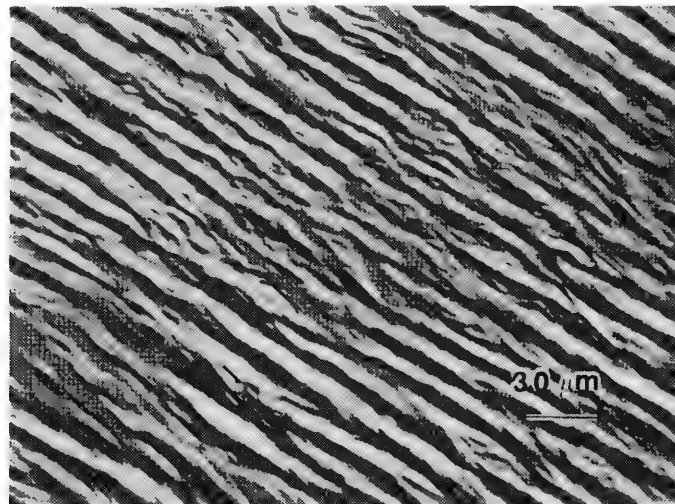


FIG. 1.--Long, bright rod is aluminum test piece and shows localized deformation near center; rectangular block below rod is silicon reference on sample holder.



(a)



(b)

FIG. 2.--Slip lines shown in deformed region, with (a) optical micrograph and (b) SEM micrograph.

CHARACTERIZATION OF THE SUSPENDED SOLIDS IN A STEEL PLANT EFFLUENT WITH THE USE OF ELECTRON-OPTICAL AND X-RAY DIFFRACTION TECHNIQUES

J. V. Twork and Sudhir Mehta

Millions of gallons of water are used every day in steel plants for both process and cooling-water requirements. After use in the mills, the water is treated to remove the majority of the contaminants and then discharged into the local water system or recycled to the plant for further use. The primary freshwater source for a plant is usually the local river or lake water, which also contains a certain amount of suspended solids. These suspended contaminants can have an impact on the water quality of the steel plant wastewater discharge and on the efficiency of the plant's water treatment facilities. In order to quantify the impact, the suspended solids in both intake and discharge water must be fully characterized. Scanning Electron Microscope (SEM)-based automated image and x-ray analysis,^{1,2} together with x-ray diffraction studies, can provide total characterization of the inorganic suspended solids in these waters. The purpose of this study was to use these techniques to analyze suspended solids on a particle-by-particle basis in the intake and the discharge waters and use this information to quantify the amount of river water solids that are carried over through the plant's water system.

Experiment

The SEM-based automated particle analysis was performed on an Amray 1600 (Turbo) SEM fitted with TN-2000 Multichannel Analyzer (MCA) Energy Dispersive X-ray Spectroscopy (EDS) system. Software packages developed by Fritz et al.³ were used for simultaneous determinations of size, shape, and chemical types of the particles. Particulate samples suitable for the analysis were prepared by filtering 30 ml of water through 0.1 μ m Nuclepore filters. Prior to filtration water samples were mixed with nonionic dispersant and agitated in an ultrasonic bath to break up any particle aggregates. The filtered particles supported on the Nuclepore filter were coated with carbon and examined in the SEM in the backscatter electron imaging mode. The analysis was carried out at 1000 \times magnification, and a database consisting of size, shape, characteristic x-ray intensity, and chemical types for every particle was created.

The chemical typing of particles was done on the basis of x-ray diffraction and EDS analysis. Preliminary x-ray diffraction studies showed that quartz, calcite, and iron oxides, as well as mica and clay minerals, were the major mineral phases; EDS analysis indicated that Al, Si, K, Fe, Mn, and Ca were the prominent elements present in these particles. Based on this information and on an estimate of the ranges of concentrations of elements in the most likely mineral phases, several chemical types for these solids were created. Table 1 lists various categories of chemical types that were used for automated typing of the particles in this study.

Results and Discussion

Particle Chemistry and Size. The results of the automated analysis for the solids in the intake and the discharge wastewater are shown in Tables 2 and 3. The data in Table 3 show that about 10% of the number of particles in the treated discharge water are iron-rich. The remaining 90% of the particles have chemistries similar to that of the particles from the intake river water (Table 2). The presence of iron-rich particles in the discharge water is attributed to mill scale, which is predominantly FeO (90%) generated in the

The authors are at Homer Research Laboratories, Bethlehem Steel Corp., Bethlehem, PA 18016.

TABLE 1.--Classification scheme for characterization of inorganic filtered solids; values shown are minimum characteristic x-ray peak intensities.

Particle Type	Relative Peak Intensity					
	Al	Si	K	Fe	Mn	Ca
Al-rich	85	0	0	0	0	0
Si-rich	0	82	0	0	0	0
Fe-rich	0	0	0	50	0	0
Ca-rich	0	0	0	0	0	40
Al-Si-K	30	60	5	0	0	0
Si-Ca-Al	11	65	0	0	0	21
Si-Fe-K	0	50	8	40	0	0
Al-Si-Fe	21	36	2	23	10	2
Mn-Si-Al	8	12	0	5	70	0

NOTE: "Composite" classification is given to particle which does not fit into any of the above categories.

TABLE 2.--SEM-based automated analysis: results for suspended particulates in intake river water.

Type	No. of Particles	%	Relative Peak Intensity of Elements						Average Particle Diameter (microns)
			Al	Si	K	Fe	Mn	Ca	
Si-rich	40	24.24	3	90	1	2	0	1	2.7
Ca-rich	1	0.61	4	5	5	6	0	79	0.7
Fe-rich	1	0.61	0	22	3	66	3	3	0.7
Al-Si-K	5	3.03	27	56	13	3	0	0	4.2
Si-Fe-K	1	0.61	27	56	13	3	0	0	4.2
Al-Si-Fe	3	1.81	16	42	7	18	9	4	2.3
Composite	114	69.09	16	56	7	10	5	3	2.4
	165	100.00							

TABLE 3.--Sem-based automated analysis: results for suspended particulates in plant discharge water.

Type	No. of Particles	%	Relative Peak Intensity of Elements						Average Particle Diameter (microns)
			Al	Si	K	Fe	Mn	Ca	
Si-Rich	129	53.97	2	90	1	2	1	1	1.6
Fe-rich	23	9.62	3	7	1	79	2	4	1.4
Al-Si-K	7	2.93	26	59	11	1	0	0	1.6
Si-Fe-K	2	0.83	9	49	11	26	2	0	1.4
Al-Si-Fe	1	0.42	21	48	6	15	3	3	1.7
Composite	77	32.22	10	64	4	8	5	5	1.7
	239	100.00							

hot-forming of steel. The data also indicate that the average particle size of suspended solids in the discharge water is smaller than that of solids in the intake water (1.7 vs 4.2 μ m). This result can be explained by the settling of the larger particles in the plant's supply basin and settling lagoons.

Weight Fraction. The weight fractions of each of the particle categories in the sample were also calculated from the density of the most likely mineral phase of the particles, average volume of the particle (determined from the average particle diameter), and the fraction of the total number for each particle phase. The results of these calculations for the two water samples are shown in Tables 4 and 5. The data show that the river water solids comprise 88.4% of the total inorganic solids in the discharge water. The remaining solids are iron-rich particles that were not removed by treatment in the settling lagoon.

Impact of Organic Solids. In addition to suspended inorganic solids, the waters also carry a certain amount of insoluble organic solids, the concentrations of which were determined separately. To determine the absolute contribution of inorganic solids, the SEM data

were corrected to reflect the organic component of the total suspended solids. This correction was made by use of the annual average total suspended solids at the two locations and recalculation of the weight fraction attributed to the river water solids as determined by the SEM analysis. With this approach it was determined that 77% of the total suspended solids in the discharge water were river water solids that had been carried through the plant's water system prior to treatment.

Conclusion

This study clearly shows that the SEM-based automated particle analysis together with x-ray diffraction studies can be effectively used for rapid and accurate determination of the contribution of the river water solids to the plant's wastewater discharge as well as in measuring the removal efficiencies of various constituents by the plant's wastewater treatment facilities.

References

1. R. J. Lee and J. F. Kelly, "Overview of SEM-based automatic image analysis," *SEM/1980 I*, 303-310.
2. J. F. Kelly, R. J. Lee, and S. Lentz, "Automated characterization of fine particles," *SEM/1980 I*, 311-322.
3. G. S. Fritz, J. J. McCarthy, and R. J. Lee, "Interactive software for automated particle analysis," *Microbeam Analysis--1981*, 57-60.

TABLE 4.--Mineral phase and weight fraction for each particle category in river water solids.

Type	Mineral Phase	Density (gm/cm ³)	Particle Volume (1x10 ⁻¹² cm ³)	Fraction	Weight (1x10 ⁻¹² g)
Si-rich	Quartz	2.65	10.3	.2424	66.2
Ca-rich	Calcite	3.3	0.2	.0061	0
Fe-rich	Scale	5.6	0.2	.0061	0.1
Al-Si-K	Illite	2.75	38.9	.0303	32.4
Si-Fe-K	Biotite	3.0	0.4	.0061	0.1
Al-Si-Fe	Biotite	3.0	6.4	.0181	3.5
Composite	Mica	2.8	7.3	.6909	141.2
					243.5

$$\text{Fe-rich (plant solids)} = \frac{0.1}{243.5} \times 100 = .04\% = \text{negligible}$$

$$\text{River solids} = 100\%$$

TABLE 5.--Mineral phase and weight fraction for each particle category in discharge water solids.

Type	Mineral Phase	Density (gm/cm ³)	Particle Volume (1x10 ⁻¹² cm ³)	Fraction	Weight (1x10 ⁻¹² g)
Si-rich	Quartz	2.65	2.2	.5397	31.4
Fe-rich	Scale	5.6	1.4	.0962	7.5
Al-Si-K	Illite	2.75	2.2	.0293	1.8
Si-Fe-K	Biotite	3.0	1.4	.0083	0.3
Al-Si-Fe	Biotite	3.0	2.6	.0042	0.3
Composite	Mica	2.8	2.6	.3222	23.5
					64.8

$$\text{Fe-rich (plant solids)} = \frac{7.5}{64.8} \times 100 = 11.6\%$$

$$\text{River solids} = \frac{64.8-7.5}{64.8} \times 100 = 88.4\%$$

MORPHOLOGICAL STABILITY OF β - γ PHASE INTERFACES IN Ni-Cr-Al ALLOYS

S. M. Merchant, M. R. Notis, and J. I. Goldstein

An understanding of interfacial stability in diffusion-bonded structures is necessary to explain the origin of multiphase products, e.g., as in the formation of β -NiAl and γ' -Ni₃Al intermediate phases during pack aluminization of Ni-based (γ -solid solution) superalloys. In the present study, the electron microprobe analyzer was used to examine the morphological stability of β - γ phase interfaces in Ni-Cr-Al alloys at 1150 C.

Experimental

Solid-solid diffusion couples consisting of a common terminal β -NiAl (Ni-50 at/o Al) end member and a series of γ -alloys nominally containing Ni-10,20,30,40 at/o Cr and pure Ni were fabricated. The Ni-50 Al alloy was directionally solidified and γ -alloys were cast in Cu-molds, and subsequently homogenized at 1000-1200 C for more than 5 days. Disks were sectioned out of the rods and polished down to 0.25 or 1 μ m diamond polish. The disks were held together in a stainless-steel clamp and the assembly was encapsulated in fused silica capsules backfilled with argon. All diffusion couples were isothermally heat treated at 1150 C for 49 h. In order to retain the high temperature structures the annealed capsules were quenched into water and immediately broken. The couples were sectioned parallel to the direction of diffusion by a slow-speed diamond saw, polished, and examined metallographically.

Quantitative wavelength-dispersive x-ray microanalyses were performed with a JEOL 733 Superprobe operating at an accelerating voltage of 15 kV and 10 nA beam current. Spectral intensities were reduced to quantitative compositional values using the Tracor Northern ZAF matrix correction procedure which utilizes the Magic IV program developed by Colby.¹ Pure-element standards were employed during the analyses. The beam voltage of 15 kV gives a satisfactory overvoltage for Ni; however, it is quite high for Al. The resultant strong absorption for Al K α in Ni is significant. A compromise was therefore made in choosing the given operating conditions without the loss of spatial resolution attendant on higher beam currents. An absorption correction² of 80-120% was necessary for the conversion of Al intensities with use of the ZAF program. Counting times of 20-60 s were employed. The precision specimen stage of the microprobe was used for locating the sample under a stationary beam. In the vicinity of interfaces and within intermediate phases, step sizes of 1 μ m were used; they were increased to 5 or 20 μ m away from these regions of the diffusion couples.

Results and Discussion

Microstructures typical of the reaction diffusion zone produced in β - γ diffusion couples with various end-member compositions are shown in Fig. 1. The β vs pure Ni (not shown) and β -Ni10Cr (Fig. 1a) couples showed an intermediate γ' -layer. The γ' -phase exhibits planar interfaces with both β and γ regions, except in the vicinity of Kirkendall pores and grain boundaries. The β -Ni20Cr (Fig. 1b) and β -Ni30Cr (not shown) couples did not contain any intermediate phases and these bonded producing a planar β - γ interface. The β -Ni40Cr couple (Fig. 1c) showed an intermediate α -layer with an irregular α - γ interface. The α -phase tended to be laterally associated with regions of β , so that alternate layers of α + β were found touching the γ region; some regions were found where the α -phase appeared to be in continuous contact with the γ -phase.

Microprobe scans across regions such as shown in Fig. 1(a) indicated two discontinuities in composition at β - γ' and γ' - γ interfaces; a single discontinuity was observed when traversing across a planar β - γ interface in the diffusion couple shown in Fig. 1(b). Microprobe

The authors are at Lehigh University, Bethlehem, PA 18015. NSF support under Grant DMR-8023955 is acknowledged.

data taken across a planar β - α - γ region in the reaction diffusion zone of the β -Ni40Cr couple (Fig. 1c) are shown in Figs. 2(a) and (b). Typical errors associated with microanalysis are shown in Fig. 2(b), which illustrates the concentration variations across the α -layer. These errors were calculated using the 3σ criterion discussed by Goldstein et al.²

The microprobe data have also been plotted on the 1150 C isothermal section of the Ni-Cr-Al system (Fig. 3),³ to designate the reaction diffusion paths of β - γ couples investigated. Such paths do not convey any spatial or kinetic information. However, the composition paths do represent an equilibrium configuration. If multiphase regions are present, composition paths that cross these regions of the phase diagram exhibit equilibrium compositions of co-existing phases. These plots therefore serve to check the quality of microprobe data obtained from discontinuities in compositions of interphase interfaces when compared with a previously known and accurately determined phase diagram. The uncertainties in phase boundaries³ shown on the 1150 C isothermal section (Fig. 3) are clearly reflected in the β -Ni30Cr and β -Ni40Cr diffusion couples. Extrapolation of concentration gradients to interfaces and errors associated with these boundaries cannot be discussed at present, as accurate phase boundary compositions are required. Work is being carried out to determine the extent of the $\alpha + \beta$, $\alpha + \gamma$, and $\beta + \gamma$ regions at 1150 C.³

The transition from a stable or planar to an unstable or nonplanar interface with the systematic variation in Cr content of one of the end-members of the diffusion couple can be indexed by means of the diffusion paths and phase-equilibrium relationships. The formation of γ' in the β -pure Ni diffusion couple can easily be explained in terms of diffusion flux balances at the interfaces.⁴ As γ' can take up to 8 a/o Cr in solid solution at 1150 C, its appearance in the β -Ni10Cr couple is accountable by a simple extension of the binary analog. Diffusion couples containing Ni20Cr and Ni30Cr exhibit interfacial compositions that nearly coincide with the β and γ phase boundaries, which indicates that the reaction path follows a tie-line within the $\beta + \gamma$ region. Consequently, these couples form a planar interface.⁵

Electron microprobe data across the interdiffusion region of the β -Ni40Cr couple indicates that the reaction path varies smoothly within the β -phase field, enters the α -region, and leaves it to vary again within the γ -phase field. Unlike in the two preceding cases this couple is unable to attain direct β - γ equilibrium and the system takes the easiest path available to approach equilibrium, namely through the α -phase. A phenomenological description to explain this interfacial breakdown is being examined⁶ and results will be published elsewhere.

It is interesting to compare results of this study with a similar investigation⁷ on pack aluminized Ni-20, 35, and 50 Cr alloys. In that work, samples were annealed at 1160 C for 3 h. An agglomerated layer of α of nearly constant composition (~ 91 to 93 Cr, < 1 Al) was observed in addition to an $\alpha + \beta$ layer, where the β -region contained about 40Al-6Cr, balance Ni. The Ni-20Cr and Ni-35Cr alloys showed interfacial compositions of 11Al-24Cr and 10Al-30Cr, balance Ni, respectively. Although experimental conditions in the present study and the previously reported work⁷ are slightly different, the microprobe data show good agreement. Interfacial concentrations from both studies however, do not agree with phase boundary compositions and hence the isothermal section warrants further investigation.

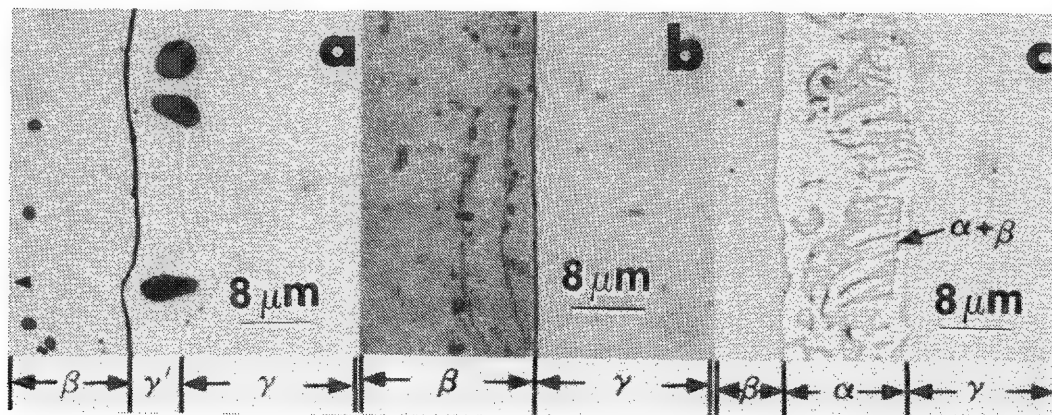
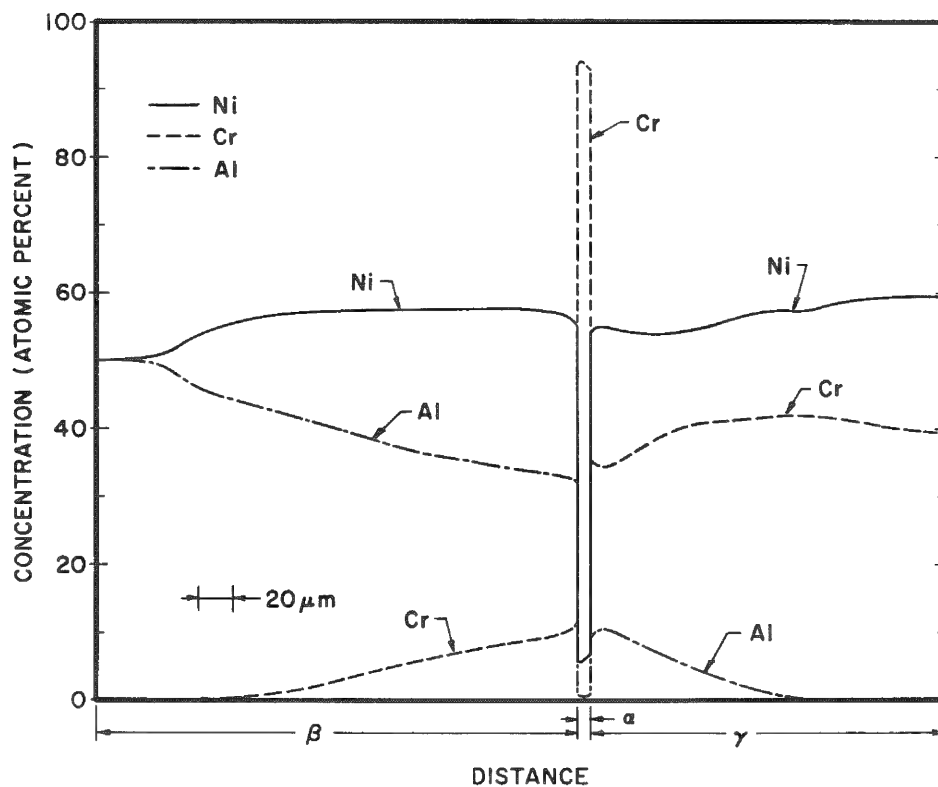


FIG. 1.--Typical microstructures of reaction diffusion zone in β - γ couples: (a) β -NiAl vs Ni-10 Cr, intermediate γ' layer; (b) β -NiAl vs Ni-20 Cr, planar β - γ interface; (c) β -NiAl vs Ni-40 Cr, intermediate layers of α and $\alpha + \beta$.

(a)



(b)

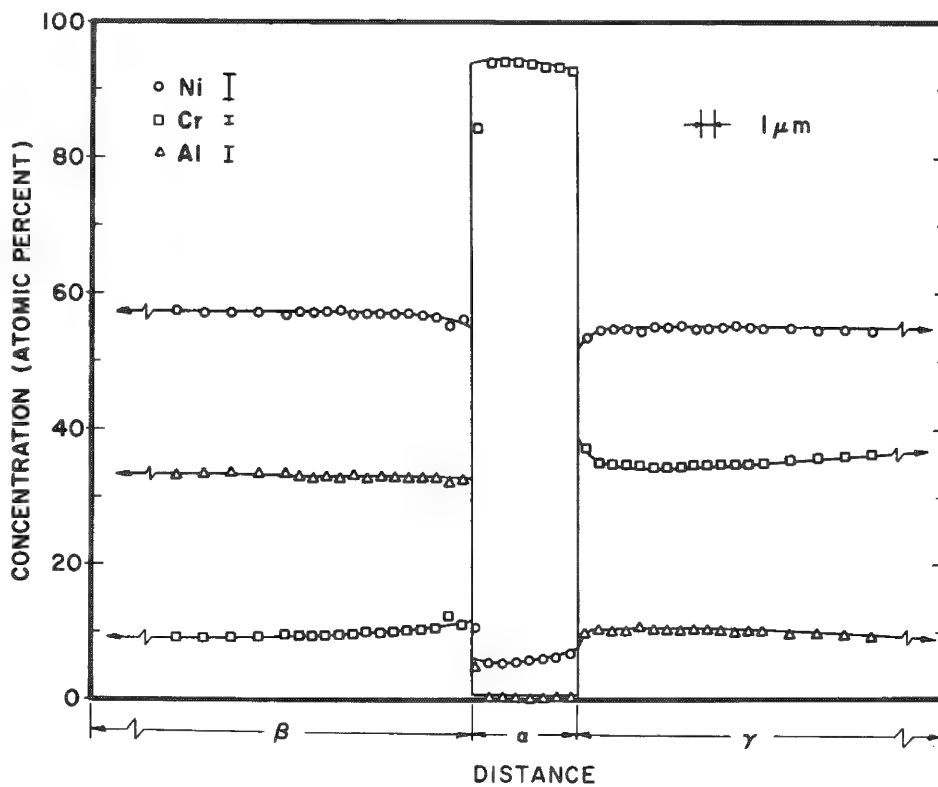


FIG. 2.--Microprobe data taken across β vs Ni-40 Cr diffusion couple annealed at 1150 C for 49 h: (a) trace across entire region; (b) region near β - α - γ interface.

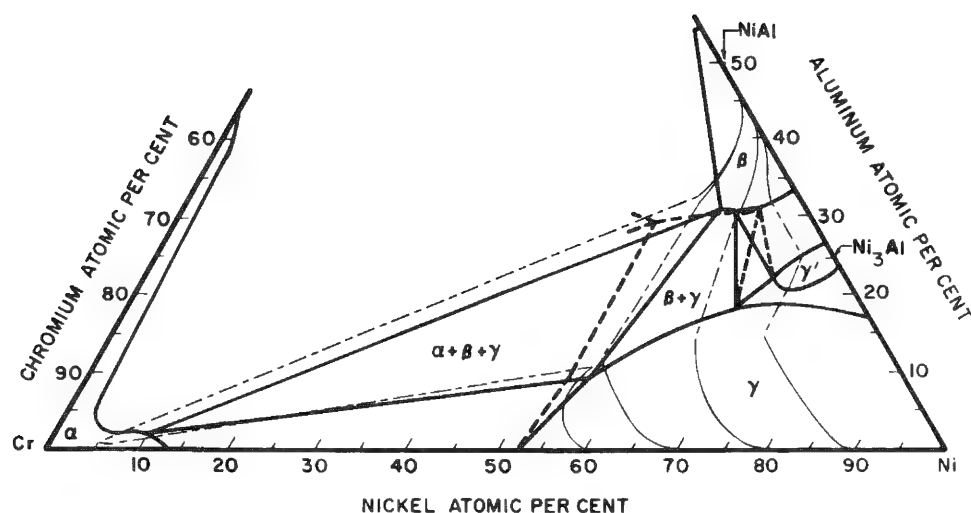


FIG. 3.--Reaction diffusion paths plotted on 1150 C isothermal section of Ni-Cr-Al system. Compositional variations shown by thin solid lines in single-phase and phantom lines in two-phase regions, respectively. Phase boundaries shown in thick dashed and solid lines.

References

1. ZAF Matrix Correction Procedure for Bulk Samples, TN-2120, Tracor Northern, Inc., Middleton, Wis., 1981.
2. J. I. Goldstein et al., *Scanning Electron Microscopy and X-ray Microanalysis*, New York: Plenum Press, 1981.
3. S. M. Merchant and M. R. Notis, *Mat. Sci. Engr.*, to be published.
4. R. Glitz et al., *Metall. Trans.* 13A: 1921, 1982.
5. J. S. Kirkaldy and L. C. Brown, *Can. Met. Quart.* 2: 89, 1963.
6. S. M. Merchant, Ph.D. work, Lehigh University, 1984.
7. M. R. Jackson and J. Rairden, *J. Vac. Sci. Tech.* 17: 81, 1980.

ENHANCEMENT OF CATHODOLUMINESCENCE IN ZnSe COOLED TO LIQUID-NITROGEN TEMPERATURES WITH THE USE OF AN SEM

A. Sicignano, S. Colak, C. J. Werkhoven, and W. F. van der Weg

A conventional SEM was adapted for cathodoluminescence (CL) characterization of materials by the addition of optical ports, photomultiplier (PM) detectors, and a 0.25m grating spectrometer. In addition, the temperature of the sample can be controlled between near-liquid-nitrogen (90 K) and room temperature. This system is used to classify the CL of a variety of luminescence materials: ZnSe, CdS, GaAs, and rare-earth phosphors.

The CL is collected through two separate paths: (1) directly onto a PM (total CL), or (2) with the use of an optical spectrometer. The CL signal from either path can be used to view the sample in the e^- -beam raster mode. In addition, wavelength spectral scans (400 to 900 nm) can be plotted from specific sample areas.

We have observed enhancement of CL intensity in ZnSe, following electron-beam irradiation at near-liquid-nitrogen temperatures. These irradiation experiments were done in an SEM on a large number of different bulk and epitaxially prepared samples at an electron beam energy of 27 keV and current densities in the range of 0.1 to 0.001 A/cm². The observed changes in CL depended on irradiation energy and exposure time. These changes in CL were measured at different e^- -beam densities. The degree to which different samples were affected varied greatly, and distinct CL enhancement was not observed in all samples.

The intensity of the band-edge emission (free and bound exciton recombination around 452 nm, 2.75 eV) and the deep level emission bands generally increased in the irradiated area at 100 K (Fig. 1). In most cases these changes were accompanied by a decrease in the luminescence bands due to free-to-bound transitions (470 nm, 2.60 eV). At room temperature, some samples showed a large enough enhancement in the overall CL emission to allow the identification or reading of patterns which were previously written at 100 K.

At very low e^- -beam excitation currents (<0.01 A/cm²), the previously irradiated areas gave less overall CL intensity as compared to unirradiated areas. However, as the beam current was increased to 1 A/cm², the irradiated areas showed a higher superlinearity in their light emission and the overall integrated intensities were higher.

These types of annealing effects could only be achieved when the sample was close to 100 K. The e^- -beam power densities used for these experiments were one to two orders lower than the levels required to melt the ZnSe materials.¹

Since this is not a melt recrystallization process, and depends on the specific sample and its temperature, another explanation was sought. The effects of the irradiation can be explained by the mechanisms for the recombination enhanced diffusion of defects and/or impurities in the host lattice.^{2,3} In the case presented here a selective gettering of defects and impurities toward higher defect concentration areas or toward the e^- -beam excitation boundaries occurs. This gettering creates regions of better quality ZnSe with less nonradiative recombination.

At low-current-density excitation, the newly created electron-hole pairs, or excitons, can diffuse over larger distances in previously annealed regions toward the (previously created) higher defect areas and recombine nonradiatively. This effect is shown in Fig. 2(c).

When the current density excitation is increased, carrier-carrier scattering⁴ in the excited region decreases the diffusion length, and the effect of higher radiative recombination in the better (previously annealed) areas is observed as increased CL intensity (Fig. 2a).

Authors Sicignano and Colak are with Philips Laboratories, Briarcliff Manor, NY 10510; author Werkhoven is at Philips Research Laboratories, Signetics, Sunnyvale, Calif.; and author Van der Weg is at Philips Research, Netherlands.

Conclusion

Permanent localized changes in the luminescence properties of some ZnSe materials have occurred when they were irradiated with an e^- -beam at 100 K.

References

1. K. N. Ratnakumar, R. F. Pease, D. J. Bartelink, and N. M. Johnson, *J. Vac. Sci. Technol.* 16(6), 1979.
2. L. C. Kimerling, *Solid State Electronics* 22: 1391, 1978.
3. W. T. Stacy and B. J. Fitzpatrick, *J. Appl. Phys.* 49(9), 1978.
4. F. J. Blatt, *Physics of Electronic Conduction in Solids*, 1968, 269.

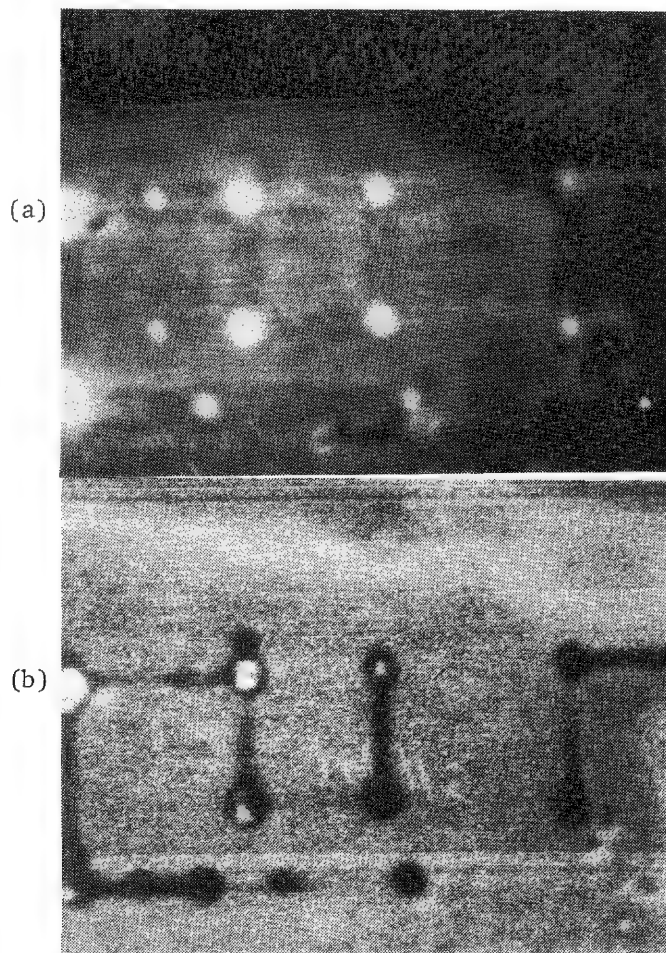


FIG. 2.--CL imaging of selectively annealed ZnSe under varying e^- -beam current densities: (a) 4 A/cm², (b) 0.125 A/cm², (c) 0.0125 A/cm².

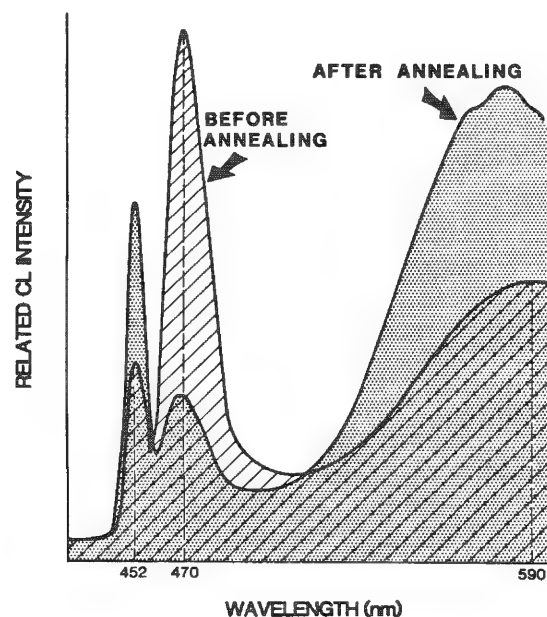
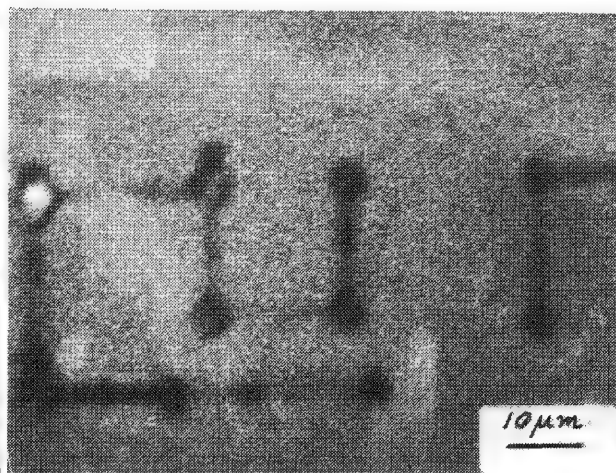


FIG. 1.--Comparison of CL spectral response from ZnSe sample 16092 before and after low-temperature e^- -beam annealing.



INFLUENCE OF PROBE SETTING IN SIMS QUANTITATIVE ANALYSIS

J. M. Lang and F. Degrevé

Secondary Ion Mass Spectrometry (SIMS) is a well-established quantitative analysis method. Its greatest advantages are its very large dynamic range and its low detection limit for most elements.¹ It is well known that the presence of an oxidizing gas phase around the sample greatly enhances the positive secondary-ion yield. This phenomenon has been extensively studied previously, and it was shown that the important factor is the fractional oxygen coverage of the surface θ . Precise quantitative analysis requires a maximum coverage for maximum ion yield. These results were obtained on machines with a static low-current-density primary beam (defocused beam), where this condition is easily satisfied, and were transposed on machines with a high-current-density probe rastered on the analyzed surface. The purpose of this paper is to examine the validity of this hypothesis. The experiments were carried out on a Cameca IMS-3F SIMS ion microscope. The sample was an homogeneous Al-4% Cu alloy. Primary ions were Ar^+ ions accelerated at 8 keV.

A Theoretical Model for the Evolution of θ under a Rastered Ion Probe

When a surface is rastered by an ion probe in an oxygen atmosphere ($\sim 10^{-4}$ torr), the oxygen surface coverage is governed by two antagonist phenomena: oxygen is brought to the surface by the surrounding gas phase and oxygen is sputtered away by the ion probe.

This situation is schematized as suggested by Blaise² for one spot on the surface in Fig. 1. During the irradiation (time $\tau \approx 10^{-5}$ s) θ decreases according to a law $\theta_{1,i}(t)$, where i is the cycle number. When the probe moves away, the spot "recovers" during T ($\approx 10^{-1}$ s) and θ increases according to a law $\theta_{2,i}(t)$. $\theta_{1,i}(t)$ is an important quantity since it governs the actual ion emission; it can be calculated as a function of oxygen pressure, primary beam current density, τ , and T . Figure 2 presents the variation of θ with time t as predicted by the above model for four different primary-beam-current densities. It shows that transients are observed and that the lower the current density, the longer the transient. Surprisingly it shows that the higher the current density, the lower the steady-state coverage.

Experimental Verification

The oxygen coverage θ cannot be easily measured, but as the secondary ion current $I_{\text{Al}}^+ \propto \beta(\theta)S(\theta)I_p$ [where $\beta(\theta)$ is the ionization coefficient, $S(\theta)$ is the sputtering yield, and I_p is the primary intensity], the evolution of I_{Al}^+ can be interpreted qualitatively in terms of θ . Figure 3 represents the variation of $I_{\text{Al}}^+(\theta)$ as a function of time and should be compared with Fig. 2. The validity of the model is demonstrated: as the primary beam current increases, the transients are shorter and the steady-state secondary currents decrease.

This last paradoxical result shows that the increase of I_p is counterbalanced by the decrease of $\beta(\theta)S(\theta)$ as the steady-state θ_{st} decreases. When $\theta=0$, I_{Al}^+ again increases with I_p .

Practical Consequences

When analyzing quantitatively a sample with a rastered probe one must verify that the surface is saturated with oxygen by adjusting the experimental parameters which influence θ (oxygen pressure, T , τ , I_p); otherwise errors of as much as a factor of 5 can be made in extreme cases.

The authors are with Cegedur Pechiney, Centre de Recherche, B. P. 27, F-38340 Voreppe, France.

References

1. F. Degrève, *J. Microsc. Spectro. Electron.* 6, 1981.
2. G. Blaise, private communication.

FIG. 1.--Evolution of oxygen coverage θ under a rastered probe (schematic).

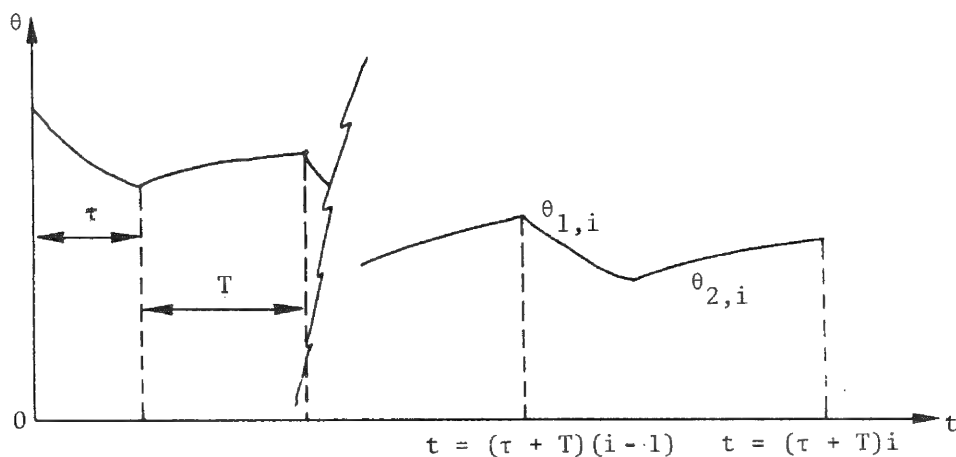


FIG. 2.--Variation of θ as predicted by model [$\tau = 10^{-1}$ s, $p(O_2) = 5 \times 10^{-5}$ Torr] Ni ($\times 10^{21}$ ions/cm²): 1:1, 2:10, 3:100, 4:1000.

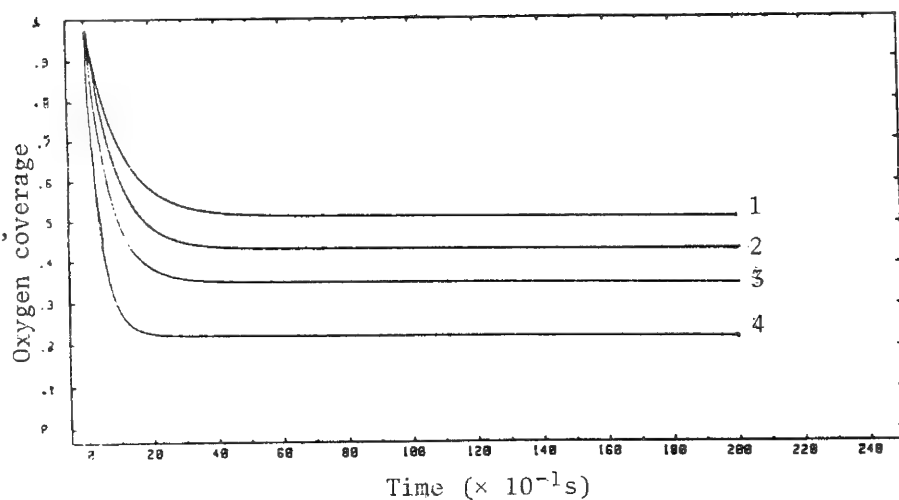
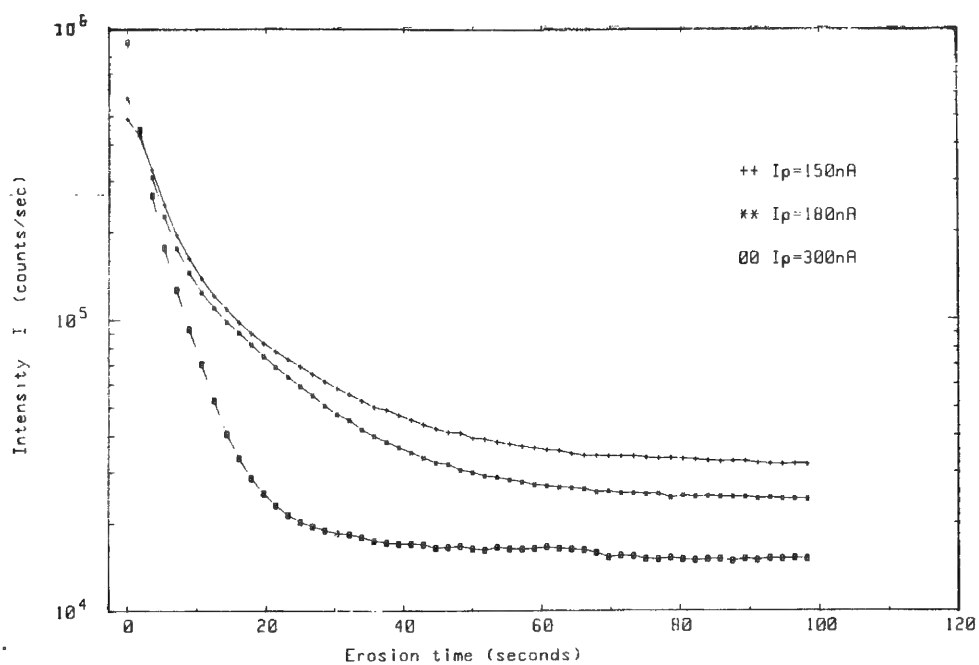


FIG. 3.--Effect of Ar⁺ primary intensity on Al⁺ signal [$p(O_2) = 10^{-6}$].



AUGER SPECTROSCOPY OF CERAMIC GRAIN BOUNDARIES

Robert Sherman

Auger spectroscopy of insulators is complicated by electron beam damage and by surface charging. The grain boundary chemistry of three ceramics, one partially stabilized zirconia and two silicon carbides (hot pressed and sintered), was analyzed by Auger spectroscopy. An important part of the investigation was the identification of electron beam damage and the subsequent interpretation of that data. This paper discusses the nature of the damage and how spectra were acquired to minimize the influences of electron beam effects.

Auger electron spectroscopy (AES) has been used extensively over the past several years to study boundary chemistry of ceramics. In these studies, segregants or second phase components have been identified in alumina,¹ silicon nitride,² silicon carbide,^{3,4} and other systems. As is well known, Auger spectroscopy of insulators often involves overcoming the surface charging problem that is due to the secondary yield being different from the incident beam current. Marcus et al.⁵ discuss the surface charging problem and its relationship to the chosen incident beam voltage. Generally, shifts of several eV in peak position are experienced due to surface charging effects.

A second and more difficult problem associated with Auger spectroscopy of insulators involves electron beam damage of the materials being analyzed. Generally, this form of damage can include electron simulated desorption or adsorption, compound dissociation, surface enhanced diffusion, surface heating, volatilization, etc. Articles by Carriere and Lang,⁶ and by Pontano and Madey,⁷ discuss the problems of electron beam damage and surface charging, and they suggest wisely that "AES of materials with potential susceptibility to beam damage be executed and interpreted with caution."⁶

Experience has indicated that the above problems can be alleviated by use of low incident beam voltage or low current densities (defocused beam, TV raster, or low beam current) when an auxillary electron gun is not available. By following the above advice, or the advice in the Physical Electronics manual,⁸ one negates several capabilities of the Auger microprobe and the Auger technique. Low voltages and low current densities reduce the signal-to-noise ratio, sensitivity to weak peaks, and spatial resolution.

In this paper, Auger analysis of three ceramics, a calcium partially stabilized zirconia and SiC (hot pressed and sintered), is discussed. These ceramics displayed the results of electron beam damage and surface charging effects. These effects were identified before the resultant Auger spectra of IG and TG species in both ceramics were interpreted. An Auger Microprobe, Model 595, from Physical Electronics was used in the above studies.

Partially Stabilized Zirconia

Partially stabilized zirconia (PSZ) offers unique properties compared to other strong ceramics, especially in terms of fracture toughness. This increased toughness is due to a stress-assisted martensitic transformation of tetragonal phase precipitates to the monoclinic phase at the crack tip. The large volume expansion and resulting compressive stresses are believed to retard growing cracks in PSZ. Previous researchers^{9,10} have observed intergranular facets to be sites of fracture initiation and intergranular crack growth in water vapor. Both researchers suggested that grain boundary chemistry may be responsible for the intergranular nature of fracture and for environmentally assisted subcritical crack growth.

The investigated material was a 3.7 wt% calcium PSZ prepared by Dr. M. V. Swain

The author is at Southwest Research Institute, San Antonio, TX 78284. Part of this research was supported by the Internal Research Program at Southwest Research Institute.

(CSIRO, Australia). The Auger Microprobe was operated at an initial accelerating voltage of 3 keV. Initial beam currents ranged from 200 to 10 nA. The effects of electron beam damage were observed at all beam currents, but were most severe at higher currents.

Auger spectra (Fig. 1) indicated the presence of oxygen, calcium, zirconium, and silicon on the intergranular fracture surface; the transgranular fracture surface exhibited evidence of only oxygen, calcium, and zirconium. An enhancement of the calcium concentration by a factor of about four was observed on all intergranular facets, independent of the amount of porosity.

The spectra for both silicon and zirconium indicated that they were in an oxide chemical state, not an elemental state. (No chemical state information can be deduced from the calcium peak shape.) This conclusion was based upon comparison of our spectra with other published spectra. The identification of silicon as an oxide¹¹ was based upon the peaks at 79 and 65 eV, and a weak peak at 1612 eV (not shown).

The identification of the zirconium peaks as zirconium oxide was based upon comparison of the spectra in Fig. 1 with published spectra of elemental and oxidized zirconium.¹¹⁻¹³ A peak at 147 eV dominates the Auger spectrum of elemental zirconium, and side peaks occur at 174, 128, 120, and 90 eV. Upon oxidation, Auger peaks involving valence electrons (127, 147, and 174 eV) of elemental zirconium were strongly attenuated, but Auger peaks involving core electrons (90 and 120 eV) were not attenuated. Also, peak shifts of several electron volts to lower energies were observed.¹³ A portion of the peak at 149.5 eV was believed to be due to electron beam damage. By observation of the secondary-electron counts in real time, it was possible to monitor growth in the 149.5 eV peak at the expense of the 142 eV peak. With this small change in the 149.5 eV peak, changes due to excessive electron beam currents in the other zirconium peaks were not expected.

A high-energy peak for zirconium is known to exist at 1845 eV.¹¹ Spectra from transgranular regions indicated that a peak shift to approximately 1835 eV occurred. The shift in energy of the high-energy zirconium peak is similar to peak shifts observed in other metal oxides.¹¹ Peak shape changes are not discussed due to the weakness of this high-energy peak and the resulting low signal-to-noise characteristics of the spectra at high energies.

The above observations at low incident beam currents are believed to be indicative of the true grain boundary chemistry. Spectra acquired at higher electron beam currents displayed the effects of electron beam damage. With these spectra, incorrect chemical state information dominated the spectra. The silicon peak was typical of elemental silicon and had a peak-to-peak height (PPH) similar to the oxygen PPH. The calcium peak displayed no shifts, but its PPH was also similar to that of oxygen. The Zr 149.5 eV peak widened and covered the Zr 142 eV and was of similar PPH as the Zr 120 and 90 eV Auger peaks.

SiC

Two silicon carbides, one hot pressed with alumina additives (NC 203, Norton Co.) and the other sintered (SiC, Carborundum Co.) with boron and carbon additives, were analyzed by Auger spectroscopy to relate the intergranular chemistry to processing methods and failure modes.⁴ This investigation used accelerating voltages and incident beam currents ranging from 10 to 2 keV and 300 to 10 nA, respectively.

For the hot pressed material, Auger spectra from IG and TG regions are shown in Fig. 2. Upon comparison, the grain facets indicate the additional presence of aluminum (oxidized), calcium, and nitrogen, and a weak zirconium peak. The Si peak shapes (both high- and low-energy peaks) from both IG and TG regions are similar to each other and similar to previous work on SiC.³ The high-energy aluminum peak is typical of alumina, but the low-energy aluminum peak was shifted to a higher energy. None of the other elements displayed any peak shifts, and the source of the aluminum peak shift is not understood, though electron beam damage may have been responsible.

Past work on hot pressed silicon carbide suggested that the grain boundary phase is an aluminum silicate with possible calcia impurities.¹⁴⁻¹⁶ In this work, the Si (oxide) peak would be observed between the alumina and silicon 92 eV peak, yet no obvious peak was detected. Though the spectrum in Fig. 2(a) was obtained at an accelerating voltage of 10 kV, no evidence of silicon oxide was observed at a lower accelerating voltage and current (3 eV, 10 nA, and 0.25 eV/step). Silica and silicate materials are susceptible to electron beam

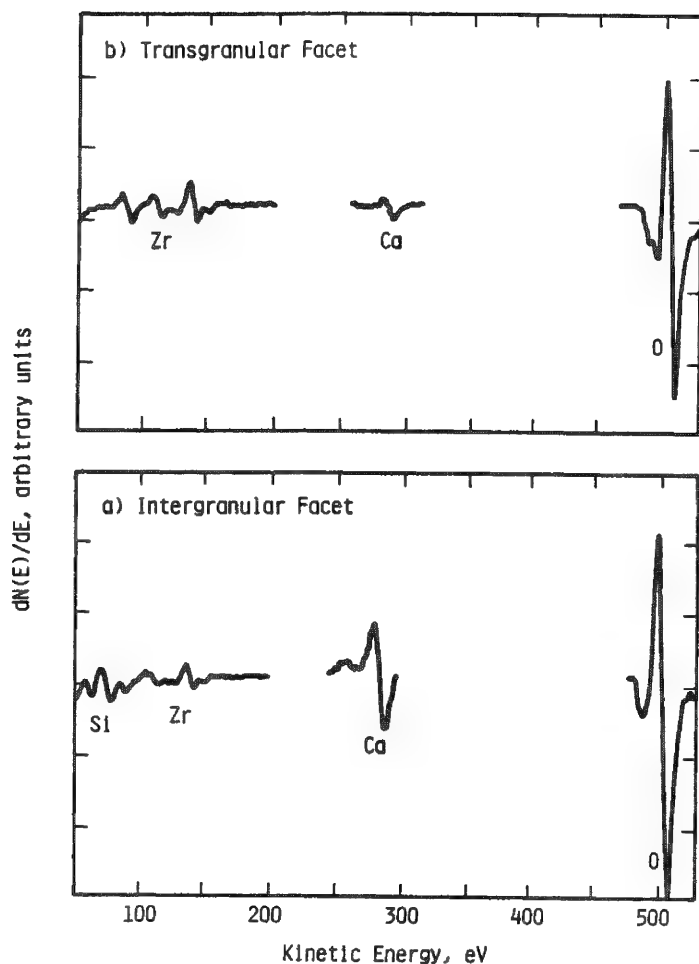


FIG. 1.--Auger spectra from (a) intergranular and (b) transgranular regions of Ca-PSZ. Spectra acquired at 3 keV and 10 nA.

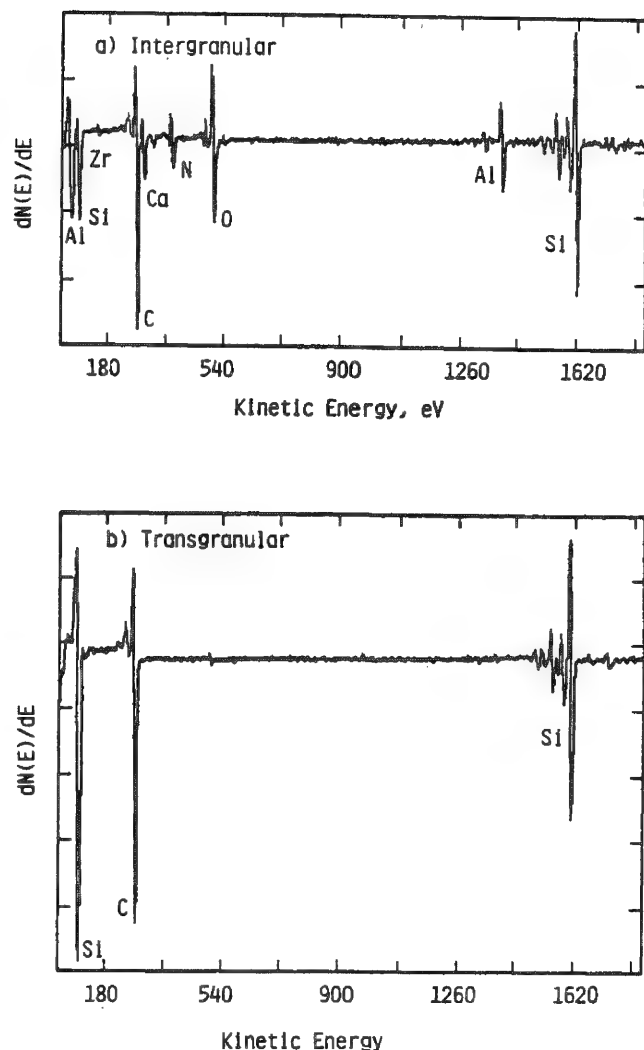


FIG. 2.--Auger spectra from (a) intergranular and (b) transgranular regions of hot pressed SiC. Spectra acquired at 10 keV and 100 nA.

damage, but it is believed that no electron beam damage occurred in this study. This was supported by spectra from a SiO_2 on Si thin film acquired under similar conditions (10 and 3 keV); the spectra displayed no evidence of electron beam damage. Therefore, silicate or silica species may not be components of the grain boundary phase.

Sintered silicon carbide displayed predominately transgranular fracture with many faceted voids. Auger multiplex spectra from IG and TG regions are shown in Fig. 3(a) and (b), respectively. The spectra from both regions were very similar, which shows that the sintering aid, boron, may have dissolved into the bulk SiC grains. No detectable electron beam damage occurred for the sintered SiC, but peak shifts of several eV were observed (and were corrected).

Conclusions

The above Auger analyses indicate that spectroscopy of ceramic grain boundaries can be performed and interpreted if possible electron beam damage effects are taken into account. Acquired Auger spectra from PSZ and SiC did display the effects of surface charging and electron beam damage. Efforts to minimize the above effects by low beam currents succeeded and the resultant Auger spectra yielded information on the differences between intergranular and transgranular chemistry of these ceramics.

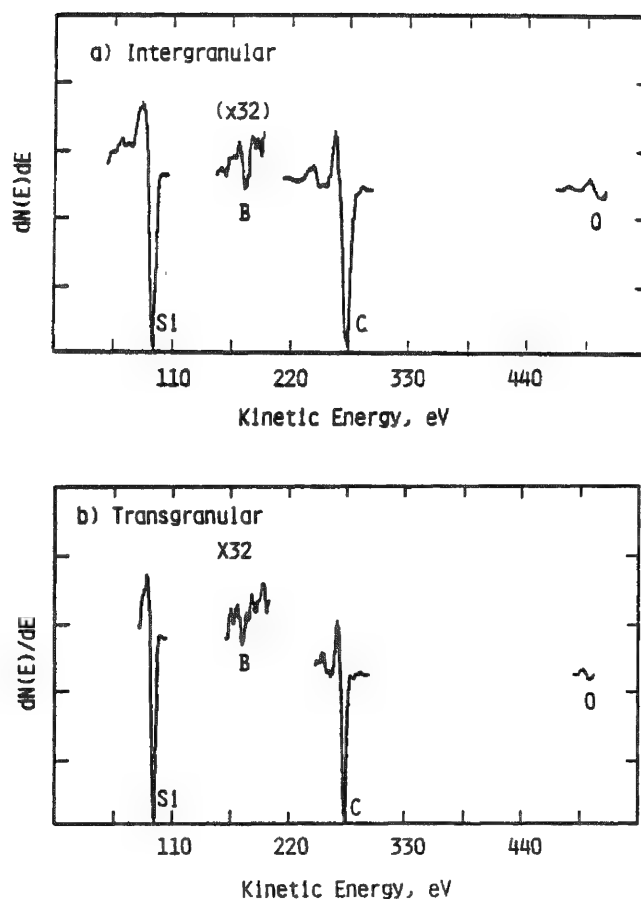


FIG. 3.--Auger spectra from (a) intergranular and (b) transgranular regions of sintered SiC. Spectra acquired at 10 keV and 50 nA.

References

1. W. C. Johnson, *Met. Trans.* 8(A): 1413, 1977.
2. R. Kossowsky, *J. Matr. Sci.* 8: 1603, 1973.
3. R. Hamming, G. Grathwohl, and F. Thummler, *J. Matr. Sci.* 18: 3154, 1983.
4. R. Sherman, *J. Am. Cer. Soc.*, submitted 1984.
5. H. L. Marcus, J. M. Harris, and F. J. Szalkowski, in R. C. Brandt, D. P. H. Hasselman, and F. F. Lange, Eds., *Fracture Mechanics of Ceramic*, New York: Plenum Press, 1974, 387.
6. B. Carriere and B. Lang, *Surf. Sci.* 64: 209, 1977.
7. C. G. Pantano and T. E. Madey, *Appl. of Surf. Sci.* 7: 115, 1981.
8. *SAM 595 Users Guide*, Physical Electronics, 1983.
9. R. W. Rice, K. R. McKinney, and R. P. Ingel, *J. Am. Cer. Soc.* 64: C-175, 1981.
10. L. K. Lenz and A. H. Heuer, *ibid.*, 65: C-192, 1982.
11. L. E. Davis, N. C. MacDonald, P. W. Palmberg, G. E. Riach, and R. E. Weber, *Handbook of Auger Electron Spectroscopy*, Eden Prairie, Minn.: Perkin Elmer, 1978.
12. J. Danielson, *J. Vac. Sci. Tech.* 20: 86, 1982.
13. G. N. Krishan, B. J. Wood, and D. Cubicott, *J. Electrochem. Soc.* 128: 191, 1981.
14. F. F. Lange, *J. Matr. Sci.* 10: 314, 1975.
15. A. G. Evans and F. F. Lange, *J. Matr. Sci.* 10: 1659, 1975.
16. F. F. Lange and J. L. Iskoe, in J. J. Burke, A. E. Gorum, and R. N. Kotz, Eds., *Ceramics for High Temperature Applications*, Brookhill Publishing, 1974, 223-238.

A SCANNING NUCLEAR MICROSCOPE

W. G. Morris, H. Bakhru, and A. W. Haberl

Chemical and microstructural analysis based on the use of high-energy particles is now quite common. The use of accelerators to generate beams of He ions from 1 to 4 MeV, and the analytical techniques of Rutherford backscattering spectrometry (RBS) and particle-induced x-ray emission (PIXE) have been described in many articles during the past 10 years.¹⁻⁵ The reviews by Cookson are particularly noteworthy.^{6,7} The 1980 Conference on applications of Accelerators in Research and Industry had a session devoted to Trace Analysis with Ion Beam and Microprobes.⁸ Some early instruments obtained beams of micron dimensions through collimation,¹ and recently the addition of a probe-forming lens has been used to gain both working distance and beam current intensity. Cylindrically symmetrical (solenoid) lenses⁹ and quadrupole multiplets have been developed for this purpose,¹⁰⁻¹⁶ with a greater use of the latter.

The success of a relatively simple quadrupole doublet lens at Sandia by Doyle et al.¹² encouraged us to try to adapt a similar system to the 4 MeV Dynamitron accelerator in the Physics Department of the State University of New York at Albany. This particular accelerator has considerably more beam current available than the Van de Graaff type of machines, which opens up the possibility of (a) obtaining a higher current in the typical 5-10 μm beam size of other nuclear microprobes, (b) reducing the beam size to 1-2 μm while still maintaining a usable beam current, and (c) having sufficient beam current available to generate a secondary-electron signal that could be used for forming a scanned image of the surface.¹⁴ It is very important to be able to view the surface of the sample to locate the particular features to be analyzed. The present smallest practical beam size obtainable for high-energy ion beams appears to be about 1 μm .¹³ Other applications of microbeam techniques include ion channeling to obtain localized crystal orientation and perfection information.^{17,18}

Design Considerations

The critical optical components of the present configuration of the instrument (Fig. 1) are the adjustable 4-way micron slits and the quadrupole doublet lens, both similar to those used by Doyle¹² and manufactured by Kovar Engineering, Waltham, Mass. The polepieces of the lens are electrically isolated from the rest of the system and can be used for electrostatic deflection of the beam. The line and frame deflection waveforms are mixed to adjust aspect ratio and image rotation. Deflection voltages of ± 150 V deflect the beam approximately ± 50 μm if only the exit polepieces are used. Greater deflection, and greater distortion, are realized if both sets of polepieces are connected in parallel. The controls for the lens current supplies were connected such that focus and astigmatism could be independently controlled.

The signals we wish to detect are secondary electrons (for imaging), backscattered He ions (RBS), and emitted x rays (PIXE). The secondary-electron detector is a conventional plastic scintillator on a light pipe leading to a photomultiplier tube. The scintillator is aluminized and biased at +10 kV.¹⁴ The RBS detector is located at a backscatter angle of 160° . A Si(Li) energy-dispersive x-ray detector is at present being fitted to the chamber. Data from the NS-625 multichannel analyzer are fed to an Apple II computer for display and analysis.

The Syntek SYM-1 microcomputer board was programmed to generate the line and frame

Authors Bakhru and Haberl are at The State University of New York at Albany, NY 12222; Morris is at General Electric, Corporate Research and Development, Box 8, Schenectady, NY 12301.

SCANNING NUCLEAR MICROSCOPE
GENERAL ELECTRIC AND STATE UNIVERSITY OF NEW YORK

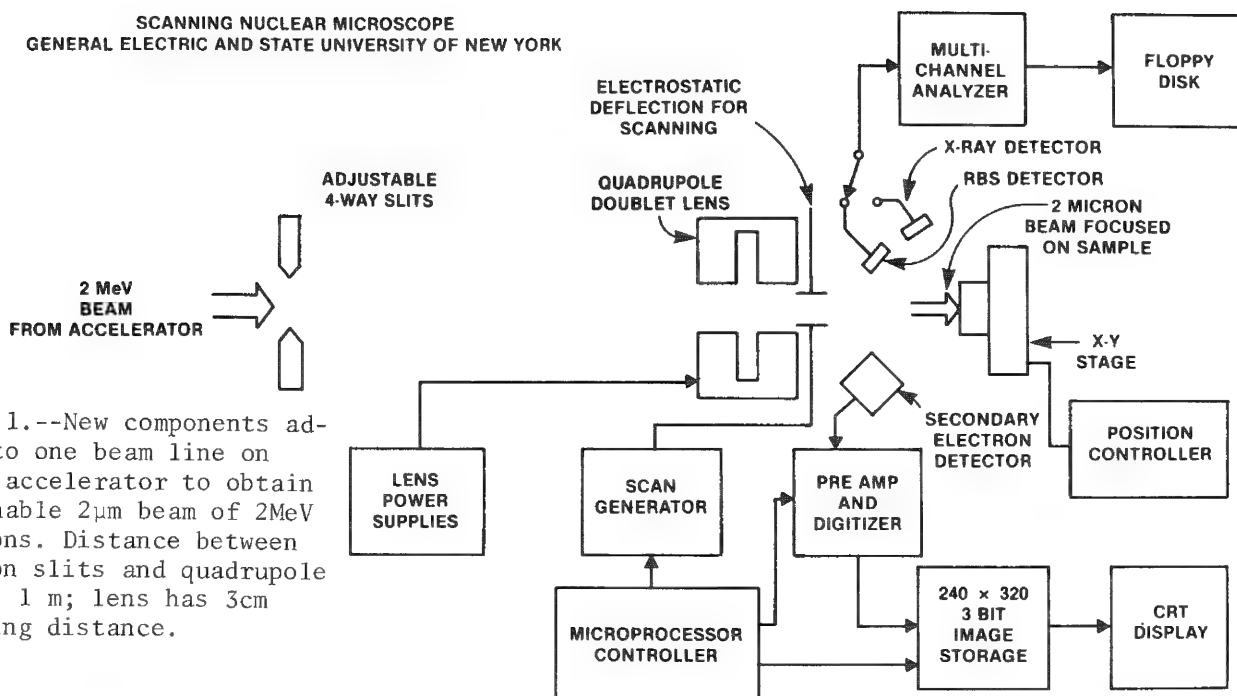


FIG. 1.--New components added to one beam line on SUNY accelerator to obtain scannable $2\mu\text{m}$ beam of 2MeV He ions. Distance between micron slits and quadrupole lens, 1 m; lens has 3cm working distance.

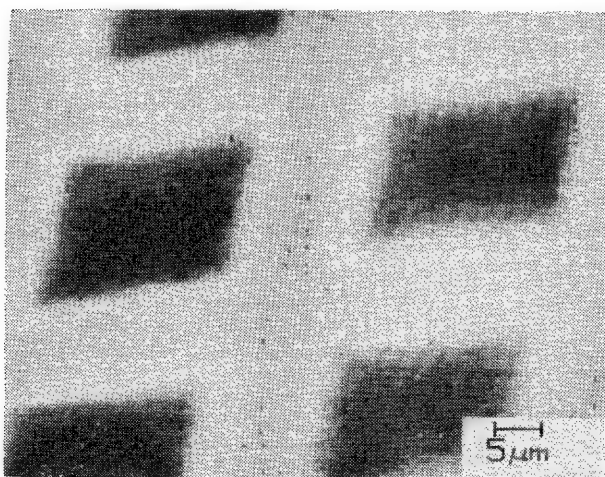


FIG. 2.--Image of 1000-mesh Cu grid formed by collection of secondary electrons emitted as $2\mu\text{m}$ beam of 2MeV He ions is scanned across sample. Frame time, 5 s; beam current, 1 nA.

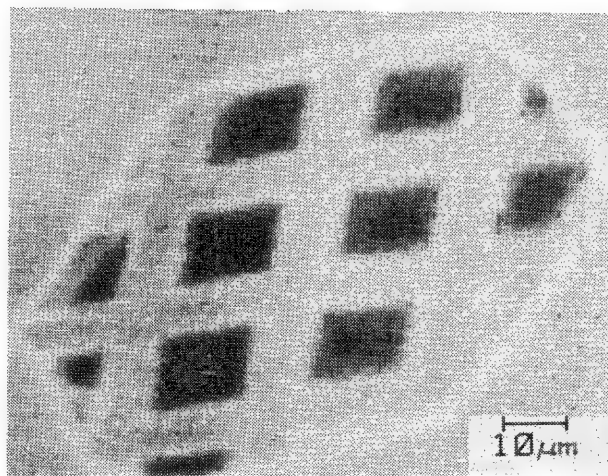


FIG. 3.--Lower magnification of 1000-mesh Cu grid sandwiched between 200-mesh grids. (Image distortion originates within scanning system.)

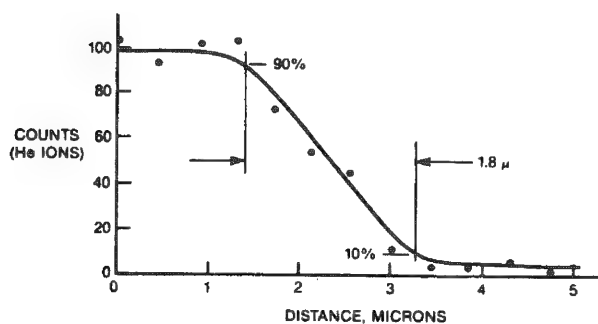


FIG. 4.--Number of backscattered particles from Cu grid of Fig. 2 as beam is scanned across edge of one grid bar; 80% of beam intensity is within $1.8\mu\text{m}$ beam diameter.

deflection voltages via digital-to-analog converters. The same microcomputer was used to digitize the video signal from the secondary-electron detector via a voltage-to-frequency converter. The image is stored $320H \times 200V$ pixels, with 3 bits (8 gray levels) per pixel. The digitizing time is approximately 80 μ s per pixel, which gives a frame time of about 5 s. The image is continuously read from memory and displayed at TV rate on a conventional monitor. This approach provides flexibility for individual addressing of lines for stationary line scans, and points for spot mode. There is memory space for expanding the image to 16 gray levels in the future.

Since the electrostatic deflection gives a field of view of only about $100 \times 100 \mu$ m, a sample stage driven by stepping motors was included to give a total accessible area of 2×2 cm, also controlled by the Apple microcomputer. A connection between the SYM-1 and Apple allows the digitized image to be stored on the Apple floppy disk.

Results

Figure 2 shows a 1000-mesh electroformed copper grid, with some tilt and aspect ratio distortion apparent. Figure 3 shows a lower magnification with the 1000-mesh grid sandwiched between 200-mesh grids with hexagonal openings. If the beam is stepped across the edge of one of the grid wires seen in Fig. 2, and the Cu RBS signal plotted as a function of distance, it is seen that 80% of the beam is contained within a diameter of 1.8μ m (Fig. 4). A portion of a microelectronic circuit is shown in Fig. 5. The contrast is low, and vertical bars due to 60Hz fluctuations in the beam current can be seen. The line scan was synchronized to the 60Hz power-line frequency. The Rutherford backscatter spectrum from point A in Fig. 5 is illustrated in Fig. 6. This spectrum was taken with a 2μ m beam, a current of 1 nA as measured in a Faraday cup, and a collection time of 60 s. The spectrum agrees reasonably well with the presumed layered structure on the silicon wafer. Figure 7 shows a bright region on the surface of a microelectronic circuit. RBS analysis with the beam positioned on this area shows that the particle possibly contains carbon and rests on top of the metallization layer. The peaks from Mo and W probably come from the tails of the beam which extend beyond the edge of the particle.

Future Work

The major accomplishment at present is achieving a 2μ m beam with a beam current of 1.5 nA. However, reduction of beam current fluctuations is necessary for secondary-electron images of better quality. Since we elected to rely on the scanning imaging system to locate features to be analyzed, it must be of adequate quality easily to relocate areas previously seen in light-optical or SEM images. An auto steering feedback system is used to keep the 2MeV ion beam properly aligned on the slits, and on occasion this control loop has become unstable, causing either beam current fluctuations at the sample or beam deflection. An additional memory plane may be added to the image storage system to give a 4-bit (16 gray levels) digitized image. If the beam current fluctuations can be reduced, the black level might be suppressed for effectively greater contrast. It may be possible to obtain a reduction of beam size to about 1μ m by incorporation of rotation correction as mentioned by Martin.¹⁵ A solid-state energy-dispersive x-ray detector is on order at present and will be attached to the system for PIXE.

References

1. R. Nobiling, Y. Civelekoglu, B. Povil, D. Schwalm, and K. Traxel, "Collimation of ion beams to micrometer dimensions," *Nucl. Inst. and Meth.* 130: 325-334, 1975.
2. F. W. Martin, "Advantages of heavy ions for high resolution microscopy," *ibid.*, 149: 475-481, 1978.
3. G. J. F. Legge, C. D. McKenzie, and A. P. Mazzolini, "The Melbourne Proton Microprobe," *J. Microsc.* 117(Pt. 2): 185-200, 1979.
4. G. J. F. Legge and I. Hammond, "Total quantitative recording of elemental maps and spectra with a scanning microprobe," *J. Microsc.* 117(Pt. 2): 201-210, 1979.
5. P. A. Cahill, "Proton microprobes and PIXE systems," *Ann. Rev. Nucl. Part. Sci.* 30: 211-252, 1980.
6. J. A. Cookson, "The production and use of a nuclear microprobe of ions at MeV energies," *Nucl. Inst. and Meth.* 165: 477-508, 1979.

7. J. A. Cookson, "The use of the PIXE technique with nuclear microprobes," *ibid.*, 181: 115-124, 1981.
8. In *Proc. Conf. Application of Accelerators in Research and Industry*, published in *IEEE Trans.* NS-28, 1981; the session on Trace Analysis with Ion Beam and Microprobes is on pp.1369-1428.
9. C. J. Maggiore, "Materials analysis with a nuclear microprobe," *SEM/1980 I*.
10. M. Prins and L. J. B. Hoffman, "The Eindhoven Proton Microbeam," *Nucl. Inst. and Meth.* 181: 125-129, 1981.
11. J. C. den Ouden, A. J. J. Bos, R. D. Vis, and H. Verheul, "A proton microbeam under construction," *ibid.*, 181: 131-133, 1981.
12. B. L. Doyle, N. D. Wing, and P. S. Peercy, "Nuclear microprobe analysis," *Micro-beam Analysis--1981*, 79-86.
13. F. Watt, G. W. Grime, G. D. Blower, and J. Takacs, "A coupled triplet configuration of the Oxford microprobe," *IEEE Trans.* NS-28: 1413-1416, 1981.
14. P. A. Younger and J. A. Cookson, "A secondary electron imaging system for a nuclear microprobe," *Nucl. Inst. and Meth.* 158: 193-198, 1979.
15. F. W. Martin, "Electrical rotation of quadrupole lenses," *ibid.*, 189: 93-96, 1981.
16. F. W. Martin and R. Goloskie, "An achromatic quadrupole lens doublet for positive ions," *Appl. Phys. Lett.* 40: 191-193, 1982.
17. S. A. Ingarfield, C. D. McKenzie, K. T. Short, and J. S. Williams, "Semiconductor analysis with a channeled helium microbeam," *Nucl. Inst. and Meth.* 191: 521-526, 1981.
18. J. C. McCallum, C. D. McKenzie, M. A. Lucas, K. G. Rossiter, K. T. Short, and J. S. Williams, "Channeling contrast microscopy: Application to semiconductor structures," *Appl. Phys. Lett.* 42: 827-829, 1983.

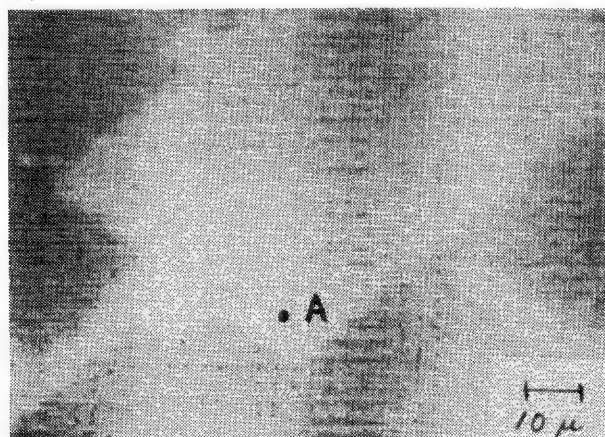


FIG. 5.--Secondary-electron image of metalization pattern on microelectronic circuit. Beam was positioned at A to obtain Rutherford backscattering spectrum

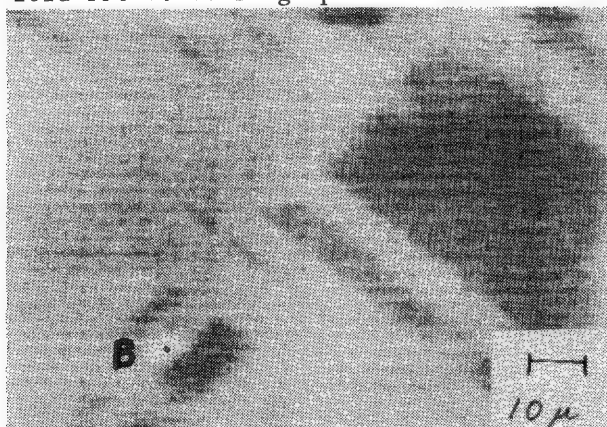


FIG. 7.--Bright region was seen at B on microelectronic circuit, possibly surface particle or defect.

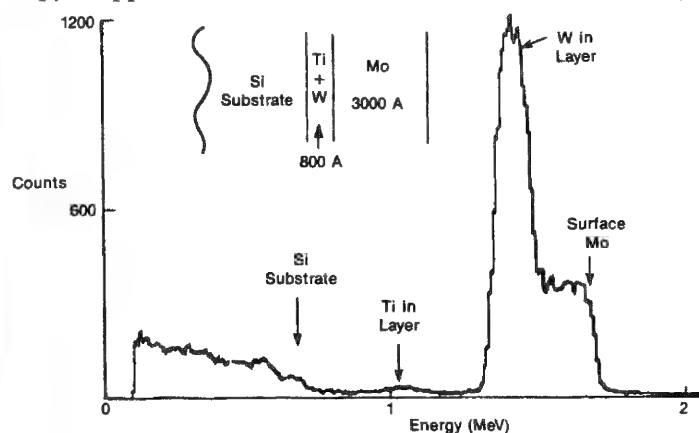


FIG. 6.--Rutherford backscattering spectrum from A in Fig. 5. Features corresponding to metallization layer are labeled. Beam current, 1 nA; spectrum collected for 60 s.

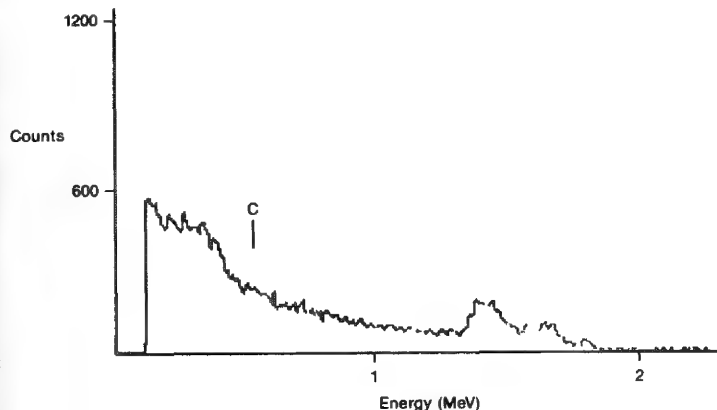


FIG. 8.--Analysis at B of Fig. 7 shows particle possibly contains carbon and presumably rests on top of metallization. Beam current, 1 nA; spectrum collected for 60 s.

INCREASED REPRODUCIBILITY OF HIGH MASS RESOLUTION SIMS

W. H. Robinson, J. D. Brown, D. D. Johnston, and W. M. Lau

The results obtained from high mass resolution secondary ion mass spectrometry (SIMS) analysis of implanted species in semiconductor materials should be highly reproducible. Several factors (vacuum conditions, charging, crater-wall effect) influence the observed secondary ion intensities. In addition, there may be limitations in the design and construction of the SIMS instrument. High-precision isotope measurements have been described¹ that used a Cameca IMS-3f SIMS instrument modified by the addition of high-stability power supplies and new software to compensate for field instabilities, drift, and hysteresis. Others have stressed the importance of the digital-to-analog converter (DAC) in positioning the magnet to the correct mass for reproducible high mass resolution analysis.²

In order to evaluate these effects and to increase the speed and flexibility of SIMS analysis, a major revision of the Cameca software was undertaken. The instrument was originally controlled by twelve independent software programs residing on magnetic tape, of which only one program at a time may be loaded into the memory of the computer. By eliminating redundant sections of code and revising the program structure, the software was compressed into one program in which several enhancements were included. One improvement was in locating the mass of interest under high mass resolution conditions. The original software allowed two options, manual adjustment of the magnetic field or a centroid calculation. There are difficulties with both methods: manual adjustment depends on the skill of the operator to adjust a potentiometer while viewing an LED display of signal intensity and either method may be complicated by the presence of local peaks as in Fig. 1. A scan through this mass range of Fig. 1 would place the centroid between the first and second peaks.

The new software displays the mass spectra on the computer's graphics device and offers the user a cursor that may be positioned at the peak of interest to determine the DAC value. The DAC is set to a precision of 19 bits and is composed of two numbers, the first in the range $\pm 2^{15}$, the second between 0 and 7. These DAC values may then be entered during the calibration stage of a depth profile, isotope, or step scan analysis. The DAC values are determined only after hysteresis effects have been taken into account.

These software revisions have enabled the user to evaluate resolution conditions quickly and to obtain high mass resolution depth profiles showing enhanced reproducibility.

References

1. J. T. Armstrong, J. C. Huneke and G. J. Wasserburg, "Precision and accuracy of high resolution isotopic measurements with the ion microprobe and systematics of ion formation," *Microbeam Analysis—1982*, 202-204.
2. W. C. Harris, doctoral thesis, Cornell University, 1983.

Authors Robinson and Brown are at the Faculty of Engineering Science and the Centre for Interdisciplinary Studies in Chemical Physics, The University of Western Ontario, London, Canada N6A 5B9; authors Johnston and Lau are at Surface Science Western, The University of Western Ontario, London, Canada N6A 3K7.

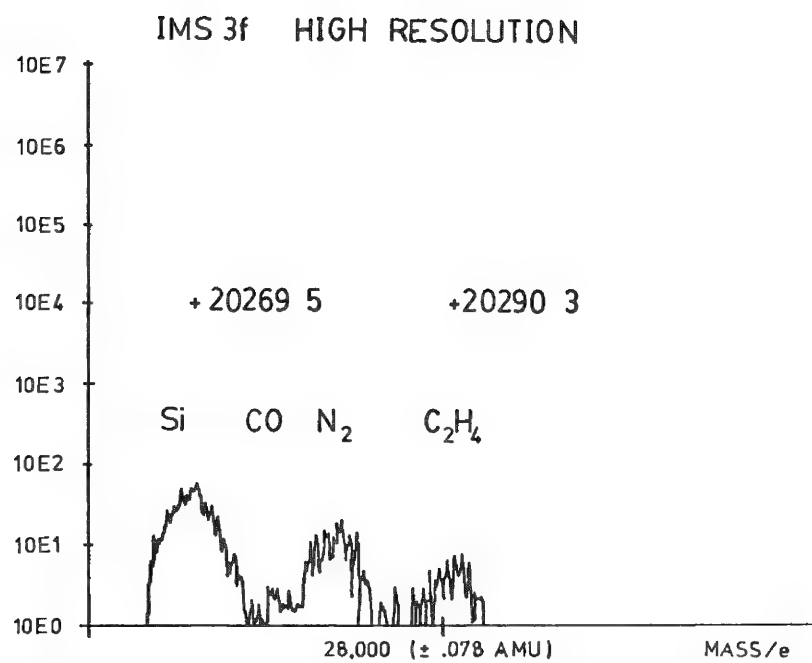


FIG. 1.--High mass resolution spectrum of silicon in gallium arsenide.

THE MATRIX EFFECT IN DEPTH PROFILING OF IMPLANTS IN $\text{Al}_x\text{Ga}_{1-x}\text{As}$ BY SECONDARY ION MASS SPECTROMETRY

W. H. Robinson and J. D. Brown

Secondary ion mass spectrometry (SIMS) is a highly sensitive technique for determining the depth distribution of dopant species in semiconductor materials. The observed secondary ion yields are influenced by experimental conditions and by the SIMS matrix effect. The semiconductor materials GaAs and $\text{Al}_x\text{Ga}_{1-x}\text{As}$ are used in the fabrication of a number of electrical and optoelectrical devices. The characterization of dopant distribution in such materials is the undertaking of this study.

The secondary ion yield, which is the number of detected secondary ions of a given species per sputtered atom of the same species, is very sensitive to chemical changes in the sputtered surface. It has been reported that the ionization probability is related to the degree of oxidation of the surface.¹ Oxidation is in turn controlled by the availability of oxygen and metal-oxygen bond strengths. When the ionization probability was normalized to that of GaAs it was found that the ionization probability of various ions was related to Al content in a linear manner.¹ In a similar fashion, another study² has shown that the secondary ion yields and sputtering yields are linearly related to the matrix concentration. These studies both utilized O_2^+ primary ion species.

On the other hand, studies by Pivin et al.³ have indicated that secondary ion intensities are related to the atomic concentrations in a more complex manner, analogous to the influence coefficient equations used in x-ray spectrometry and other analysis techniques.

Analysis of implants of silicon and chromium in matrices of $\text{Al}_x\text{Ga}_{1-x}\text{As}$, with x being 0, 0.05, 0.2, and 0.4 has been carried out. The analysis was performed on a Cameca IMS-3f with a primary beam mass filter, with oxygen and cesium used as primary ion species. In addition to a quantitative analysis of the SIMS matrix effect, the dopant distributions can be characterized at a number of primary ion beam energies to illustrate artifacts of ion beam knockon and mixing.

References

1. C. Meyer, M. Maier, and D. Bimberg, "Matrix effect and surface oxidation in depth profiling of $\text{Al}_x\text{Ga}_{1-x}\text{As}$ by secondary ion mass spectrometry using O_2^+ primary ions," *J. Appl. Phys.* 54: 2672-2676, 1983.
2. A. A. Galuska and G. M. Morrison, "Matrix calibration for the quantitative analysis of layered semiconductors by secondary ion mass spectrometry," *Anal. Chem.* 55: 2051-2055, 1983.
1. C. Meyer, M. Maier, and D. Bimberg, "Matrix effect and surface oxidation in depth profiling of $\text{Al}_x\text{Ga}_{1-x}\text{As}$ by secondary ion mass spectrometry using O_2^+ primary ions," *J. Appl. Phys.* 54: 2672-2676, 1983.
2. A. A. Galuska and G. M. Morrison, "Matrix calibration for the quantitative analysis of layered semiconductors by secondary ion mass spectrometry," *Anal. Chem.* 55: 2051-2055, 1983.
3. J. C. Pivin, C. Rocques-Carmes, and G. Slodzian, *Intern. J. Mass Spectrom. Ion Phys.* 26: 219, 1978.

The authors are at the Faculty of Engineering Science and the Centre for Interdisciplinary Studies in Chemical Physics, The University of Western Ontario, London, Canada N6A 5B9.

Author Index

- Abraham, E. H., 281, 285
 Adams, F., 19
 Adar, F., 121
 Adesida, I., 68, 70
 Agarwal, U. P., 125
 Al-Saleh, K., 65
 Alvarez, J. L., 103
 Andersen, M. E., 115
 Ansel, M., 264
 Armstrong, J. T., 208, 213
 Atalla, R. H., 125
 Bakhru, H., 327
 Barnisin, M. A., 240
 Bastin, G. F., 291
 Benoit, D., 169
 Blanc, M., 169
 Boyer, H., 107
 Breen, K. R., 309
 Brenna, J. T., 265
 Bright, D. S., 173
 Brown, J. D., 331, 333
 Brown, Z. A., 145
 Buseck, P. R., 213
 Calvo, F. A., 157
 Chan, H., 261
 Clarke, N. S., 31, 40
 Clemens, D., 240
 Colak, S., 319
 Craighead, H. G., 73
 Crisp, J. A., 143
 Davey, A. R., 31, 40
 Degreve, F., 321
 Demortier, G., 249
 Dilks, A., 139, 149
 Dingle, T., 23
 Dodia, R., 253
 Dominguez E., J. M., 177
 Donovan, C. B., 281, 285
 Doyle, T. E., 103
 Fatiadi, A. J., 14
 Fiori, C. E., 175, 179
 Fletcher, R. A., 14
 Fox, P., 49
 Franklin, U. M., 227
 Friel, J. J., 55
 Goldstein, J. I., 303, 315
 Gordon, R. B., 231
 Gorlen, K. D., 179
 Graham, S. C., 139, 149
 Griffiths, B. W., 23
 Guerra, V., 59
 Guilemany, J. M., 157
 Haberi, A. W., 327
 Hagler, H. K., 290
 Hare, T. M., 306
 Hearn, P. P., 145
 Heidersbach, R., 61
 Heijligers, H. J. M., 291
 Heinrich, K. F. J., 175
 Hercules, D. M., 15
 Hertzberg, R. W., 131
 Hess, D. R., 65
 Heyman, R. V., 299
 Hlava, P. F., 87
 Hollister, L. S., 143
 Isaacson, M., 68, 70
 Izutsu, K. T., 277
 Johnson, D. E., 277
 Johnston, D. D., 331
 Joy, D. C., 81
 Kirkendall, T. D., 165
 Kirkland, E., 68
 Kulick, C. G., 143
 Lang, J. M., 321
 Lange, D. E., 281, 285
 Leapman, R. D., 45
 Leidheiser, H., Jr., 111
 Leimkuhler, A. M., 309
 Lifshin, E., 215
 Lin, P. S. D., 99
 Liu, K. H., 261
 Love, G., 191, 195
 Lugand, L., 169
 McCarthy, J. J., 1
 Manson, J. A., 131
 Marder, A. R., 247
 Marinenko, R. B., 201, 205
 Matson, R. J., 93
 Mauney, T., 19, 295
 Maze, W., 143
 Mehta, S., 55, 312
 Merchant, S. M., 315
 Moran, P. J., 309
 Morelli, J. J., 15
 Morris, W. G., 327
 Morrison, G. H., 265
 Moyer, H., 240
 Murakami, K., 65
 Murata, T., 257
 Muray, A., 68, 70
 Myers, M. C., 267
 Myklebust, R. L., 198, 205
 Newbury, D. E., 27, 198
 Notis, M. R., 240, 243, 261, 315
 Park, D., 139
 Peters, K.-R., 77
 Pickering, H. W., 65
 Pigott, V. C., 261
 Porter, J. R., 135
 Purcell, F., 61
 Reffner, J. A., 221
 Remmel, T. P., 165
 Rimnac, C. M., 131
 Robinson, W. H., 331, 333
 Roeder, J. F., 243
 Romig, A. D., Jr., 7, 87
 Ruckman, J. C., 31, 40
 Russ, J. C., 161, 186, 306
 Russ, J. Ch., 161
 Sakarcian, M., 135
 Sakurai, T., 65
 Salazar, J. M., 157
 Sarkar, D., 135
 Sasaki, M., 257
 Sauer, G. R., 269
 Schroder, W. H., 30
 Scott, V. D., 191, 195
 Sculac, J. F., 243
 Sellamuthu, R., 303
 Sewell, D. A., 195
 Sheng, T. T., 97
 Sherman, R., 323
 Shimura, M., 223
 Saignano, A., 319
 Simons, D. S., 27
 Simonsen, I., 306
 Sisson, V. B., 143
 Small, J. A., 27
 Smith, D. C., 107
 Sommer, A. J., 111
 Soto, L., 121
 Steel, E. B., 27, 198
 Steinkampf, W. C., 145
 Strobe, 154
 Swyt, C. R., 45, 179
 Tatlock, G. J., 49
 Taylor, D. A., 267
 Tejeda, J., 177
 Thibaut, M., 264
 Thorpe, S. J., 227
 Tian, J.-F., 186
 Tighe, N. J., 127
 Todd, J. A., 235
 Tormey, J. McD., 272
 Tsuo, Y. S., 93
 Tworck, J. V., 312
 van der Weg, W. G., 319
 Van Espen, P., 295
 Vecchio, K. S., 247
 Wang, E., 277
 Warner, R. R., 267
 Watabe, N., 269
 Werkhoven, C. J., 319
 Worrel, W. L., 59
 Yamada, S., 223
 Yost, F. G., 87

Notes